UNIVERSITAT POLITÈCNICA DE CATALUNYA
BARCELONATECH
Department of Civil and Environmental Engineering
Division of Geotechnical Engineering and Geosciences

Tesi per compendi de publicacions – Thesis by publications

ROCKFALL ANALYSIS:

Failure, fragmentation and propagation characterization

A FRACTAL FRAGMENTATION OF ROCKFALLS

PhD Thesis

Roger Ruiz-Carulla

Supervisor: Jordi Corominas

Barcelona, 2018

UNIVERSITAT POLITÈCNICA DE CATALUNYA

School of Civil Engineering of Barcelona
UPC BARCELONATECH

Abstract:

The present thesis aims at the analysis of the fragmentation of rockfalls. The fragmentation is a complex phenomenon poorly understood with a lack of tools to reproduce it on rockfall simulators. The effect of fragmentation on the hazard assessment and mapping is significant and it may substantially modify the risk scenario. The analysis of the empirical data acquired in a series of inventoried natural rockfalls and real-scale drop tests, clearly suggests that fragmentation displays a fractal behavior. Based on these observations, a fractal fragmentation model is proposed heare, adapting the basics of Perfect (1997) to the specific case of rockfalls. An important development of the thesis presented is the procedure to characterize the rockfall mass before and after the fragmentation, which include the methodology to measure the block size distributions of the deposit, the use of Unmaned Aerial Vehicles (UAV) equipped with digital camera digital, and the photogrammetric analysis to reconstruct the detached block volumes based on 3D models and discrete joint characterization. The block size distributions before and after the fragmentation are related with the proposed model, using the real data to calibrate the model parameters by back analysis. The methodologies and the model proposed contribute to the understanding of the fragmentation phenomenon and have the capability to reproduce the entire block size distribution and the calculation of the number and volume of the fragments. They also allow the quantification of the areas of the fresh faces created due to breakage, which may be related to the required fragmentation energy. The final goal of the ongoing research is the implementation of fragmentation behavior on a rockfall simulator which is currently under developed within the Rockmodels project (https://rockmodels.upc.edu/es), and modify the criteria to calculate the probability of impact used in hazard mapping and in quantitative risk assessment studies. The results of the fragmentation model may also contribute to the analysis of the efficiency and to the design of the rockfall protection systems.

Resum:

La present tesis es centra en el fenomen de la fragmentació en despreniments rocosos. La fragmentació és un fenomen complex de difícil caracterització i de la que ens manquen eines per a la seva modelació en programes de simulació de caiguda de blocs. Tanmateix, els efectes de la fragmentació sobre les prediccions i els conseqüents mapes de perill poden comportar modificacions en l'escenari de risc. A partir d'un conjunt de dades empíriques obtingudes mitjançant l'inventari de despreniments naturals, s'ha observat un clar comportament fractal. A partir d'aquestes observacions, s'ha proposat un model de fragmentació fractal adaptant la descripció de Perfect (1997) al cas específic del despreniment rocós. Una part important del desenvolupament de la tesi són les metodologies utilitzades per a la caracterització de la massa rocosa abans i després de la fragmentació, des de metodologia per mesurar distribucions de volums de blocs al dipòsit, fins a la utilització de drons i fotogrametria digital per reconstruir el volums dels blocs abans de caure a partir de models 3D i de la caracterització discreta de les discontinuïtats del massís. Les distribucions de volums de blocs abans i després de la fragmentació és relaciones mitjançant el model de fragmentació proposat, utilitzant les dades reals per calibrar els paràmetres del model per retro anàlisis. La utilització de les metodologies proposades i del model de fragmentació ajuden a la comprensió del fenomen, permeten la reproducció de la distribució de blocs sencera amb una estimació del nombre de blocs i el seus volums. També permet una quantificació de la superfície nova creada en cares fresques degut a la ruptura, que es vincula amb l'energia dedicada a la fragmentació. L'objectiu final d'aquesta recerca és la implementació de la fragmentació en un simulador de caiguda de blocs que es troba en desenvolupament en el marc del projecte Rockmodels (https://rockmodels.upc.edu), així com modificar els criteris de càlcul de probabilitat d'arribada que s'utilitzen per elaborar els mapes de perill i els estudis quantitatius del risc. Les conclusions poden canviar la manera com es dissenyen els sistemes de protecció contra despreniments.

Resumen

La presente tesis se centra en el fenómeno de la fragmentación en desprendimientos rocosos. La fragmentación es un fenómeno complejo de difícil caracterización y de la que nos faltan herramientas para su modelación en programas de simulación de caída de bloques. Sin embargo, los efectos de la fragmentación sobre las predicciones y los consecuentes mapas de peligro pueden conllevar modificaciones en el escenario de riesgo. A partir de un conjunto de datos empíricos obtenidos mediante el inventario de desprendimientos naturales, se ha observado un claro comportamiento fractal. A partir de estas observaciones, se ha propuesto un modelo de fragmentación fractal adaptando la descripción de Perfect (1997) en el caso específico del desprendimiento rocoso. Una parte importante del desarrollo de la tesis son las metodologías utilizadas para la caracterización de la masa rocosa antes y después de la fragmentación, desde metodología para medir distribuciones de volúmenes de bloques en el depósito, hasta la utilización de drones y fotogrametría digital para reconstruir el volúmenes de los bloques antes de caer a partir de modelos 3D y de la caracterización discreta de las discontinuidades del macizo. Las distribuciones de volúmenes de bloques antes y después de la fragmentación se relacionan mediante el modelo de fragmentación propuesto, utilizando los datos reales para calibrar los parámetros del modelo mediante retro análisis. La utilización de las metodologías propuestas y del modelo de fragmentación ayudan a la comprensión del fenómeno, permiten la reproducción de la distribución de bloques entera con una estimación del número de bloques y sus volúmenes. También permite una cuantificación de la superficie nueva creada en caras frescas debido a la ruptura, que se vincula con la energía dedicada a la fragmentación. El objetivo final de esta investigación es la implementación de la fragmentación en un simulador de caída de bloques que se encuentra en desarrollo en el marco del proyecto Rockmodels (https://rockmodels.upc.edu), así como modificar los criterios de cálculo de probabilidad de alcance que se utilizan para elaborar los mapas de peligro y los estudios cuantitativos del riesgo. Las conclusiones pueden cambiar la forma en que se diseñan los sistemas de protección contra desprendimientos.

ACKNOWLEDGMENT:

N'he fet 30. 30 anys anant a l'escola. Els útlims 10 a l'escola de camins. Segurament passa a totes les etapes de la vida, però els últims anys han sigut els més interessants. La tesina final de carrera era sobre gestió de bases de dades espacials amb eines GIS, aprofitant les practiques que feia a GISA amb la MªPau i dirigida per en Jordi i la Nieves. Els tres heu sigut referents importants per a mi. De la mà d'en Jordi vaig entrar a la recerca durant el master. Moltes gràcies Jordi, sempre t'ho he dit, em vas salvar fent-me entrar en un món que crec que és el meu. No sé mai com agraïr-te la paciència que tens amb mi i tot el que he aprés de tu encara que sovint no ho sembli. De veritat, moltes gràcies per tot Jordi. Gràcies Nieves per ajudar-me sempre amb tot, amb un somriure i resolent cada obstacle eficientment que en venen d'altres. Gràcies Pau, per ensenyar-me tantes coses, per les converses de la vida i per ajudar-me a madurar. Encara em queda.

La tesina de master i aquesta tesi no haurien sigut posibles sense l'Olga. Moltes gràcies Olga per portar-me a tot arreu amb el Nissan, per les converses sobre aquest món i per advertir-me i guiar-me. Mai oblidarem el despreniment al Cadí que gairebé acaba amb aquesta història. Sempre recordarem aquell sopar celebrant que erem vius, i com aquella experiència ens va fer apropar-nos l'un a l'altre, i sobretot a la fotogrametría i finalment als drons. Moltes gràcies per tot Olga, per la paciencia i per les correccions.

Durant la última etapa ha arribat un nou company. Hábil, escalador i treballador. Gerard, moltes gràcies per l'esforç i les ganes que poses en tot el que fem, i per viure segons les teves conviccions. Ets un exemple. Espero que seguim endavant i que poguem seguir compartint moltes coses.

Vaig arribar al seu despatx d'urgència quan Yesa era una gran emergencia. José, muchas muchas gracias por todo. Els pitis a la porta, les conyes que ens portem i tot plegat fan que el dia a dia amb tu al despatx em senti còmode i acollit. Sempre explico que tinc molta sort de que em toques estar en aquesta taula on sóc ara mateix davant teu. Moltes gràcies per tot.

Marcel, ets l'únic que no t'he tingut com a profe, però sempre hem tingut una molt bona relació sense saber molt bé d'on sortia. Complicitat natural. Tu, el José, la Nieves i el grupet m'heu ajudat moltissim a sentí-me un més entre vosaltres. Moltes gràcies. De veritat. Estic segur que molts doctorands no se senten tant a gust com jo em sento entre vosaltres, com en una familia.

A tot l'equip, Josep, Albert, Carol, Felipe, Amparo, Joan, moltes gràcies per tot el suport durant aquest projecte i el que ens queda.

No és habitual fer agrïments extensos i detallats, però no penso escriure una altra tesi. A la tercera va la vençúda diuen.

Són 10 anys a l'escola i molts profes que ens han ensenyat a pensar, a ordenar i entendre el món. Moltes gràcies a tots. Marcote, Dani, Martí, Susana, Camino, Estela, Imma, Bordonau, Joa, Calvet, Nue, Marta, Lloret i Suriol (combo), padres geotécnicos Alonso, Núria, Gens, Ledesma, Sebas, Jean i segur que m'en deixo. A tots, moltes gràcies per ajudar-me a crèixer

L'escola és un col·lectiu, i tots hi sumem. Al bar, Jordi, Toni, Manoli, Vicente i Vanesa, moltes gràcies. Hi ha gent amb qui conectes i de la que t'alegres quan estiguin bé i et preocupes quan els fan patir. Moltes gràcies Eva i Oscar (un altre combo) per tot el suport durant aquests anys. Moltissimes gràcies per fer entre tots un entorn i un grup de gent tant agradable.

Tots els companys de tesi i d'hores d'estudi i de "patí": moltes gràcies pels dinars, els debats politics, els moments d'alegria i d'angoixa compartits a la plaça. Sobretot gràcies Laura, per escoltar-me cada matí, pels pitis amb passeig de tardes i per les converses de la vida. Moltes gràcies a tots: Nuria, Angels, Rotman, Paula, Nuria, Albert, Albert Carles, Miki, Laura, Nabil, Quim, Oriol, Guillem, Mireia, Carme, i els sobrevinguts temporals, Marvin i sobretot Robi. Motles gràcies pels debats i pels àpats que compartim.

Joan, Ivan Pau i Sjædric: sou l'equip. Moltes gràcies per les patidakes d'escacs, els debats politics i les sortides de camp. Moltes gràcies Sjædric per tot, sense tu no hauria fet tot el que he fet. Gràcies per ajudar-me sempre, amb l'impressora 3D, amb els drons, amb el matlab o amb el que faci falta. No cal que t'ho digui. Gràcies. Solà, gràcies per ajudar-me sempre a fer tot alló que ens proposem, per posar-hi ganes i entussiasme enlloc de barrers i problemes. Gràcies. Nandu, Roger, Rubèn, Edu, Aryu, Gerard, sé que no us dedico prou temps i us vull agraïr la vostra comprensió i amistat incondicional. Moltes gràcies.

I a la meva familia, moltes gràcies per saber entedrem. Montserrat, Robert, Martí i Roseta, gràcies per fer-me sempre costat i ajudar-me a crèixer com a persona. Sense vosaltres no seria qui sóc i no podria haver fet res del que he fet. Pel genotip i pel fenotip. Mil gràcies.

Aina, no tinc paraules per agraïr-te tot el que fas per mi. Sóc conscient que no sóc fácil. Moltissimes gràcies. Per fer-me sortir de la bombolla, portar-me coses del món a casa i portar-me a mi pel món. Amb tot l'amor del món, moltes gràcies. Ara, iniciem nous projectes que ens faran crèixer i madurar junts. Amb una banyera i dos xiclets construirem un coet, perquè ens porti lluny d'on som, per tenir clar d'on venim, per tenir clar el que tenim.

INDEX

1. Introduction

Evans and Hungr (1993) and Hungr et al. (2014) reserved the term fragmental rockfall for the events in which, the individual fragments move as independent rigid bodies interacting with the ground surface by means of episodic impacts. They distinguished it from the term rock avalanche in which masses of fragments move as a granular flow. In fragmental rockfalls, the detached rock mass, which often includes discontinuities, disaggregates breaks or both, after the first impacts on the ground. The resultant fragments propagate independently downhill (Figure 1). The deposit of a fragmental rockfall is a set of rock blocks of different sizes scattered on the ground surface. In the case of mid to large-size fragmental rockfalls (over several hundred of cubic meters), a more or less continuous Young Debris Cover (YDC) can be formed as well. Understanding the fragmentation process is fundamental for the analysis of the rockfall hazard, since it is a critical input datum for calculating the trajectories and the run-out of the rock fragments, the encounter probability with the elements at risk and the expected impact energies.

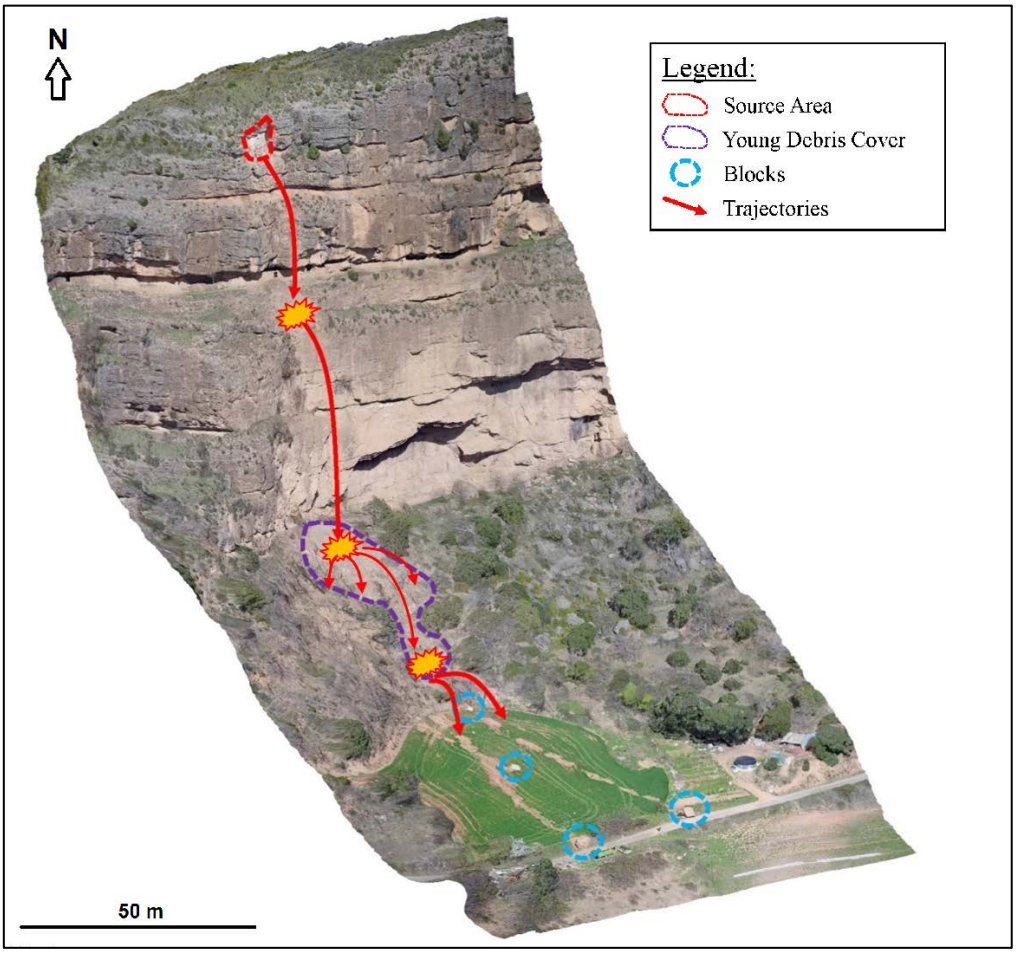

Figure 1. Fragmental rockfall at Gurp, Central Pyrenees, Spain. A Young Debris Cover (YDC) is formed just below the rockfall source (purple polygon). Four large individual blocks (blue circles) followed both independent and divergent trajectories after the impact on the ground.

The block size distribution of the blocks deposited in a rockfall event, or Rockfall Block Size Distribution (RBSD) is product of the fragmentation phenomenon.

The detached mass from the cliff can be a single block or a rock mass with joints, defining an initial distribution of block volumes known as the In situ Block Size Distribution (IBSD) (Lu and Latham, 1999). Our studies focus on the fragmentation phenomenon based on the changes of the block size distribution from the initial state (IBSD), to the final deposit (RBSD) (Figure 2). We also propose a fragmentation model that uses the IBSD as input, and using 2 or 3 control parameters, is able to reproduce the natural observed RBSD.

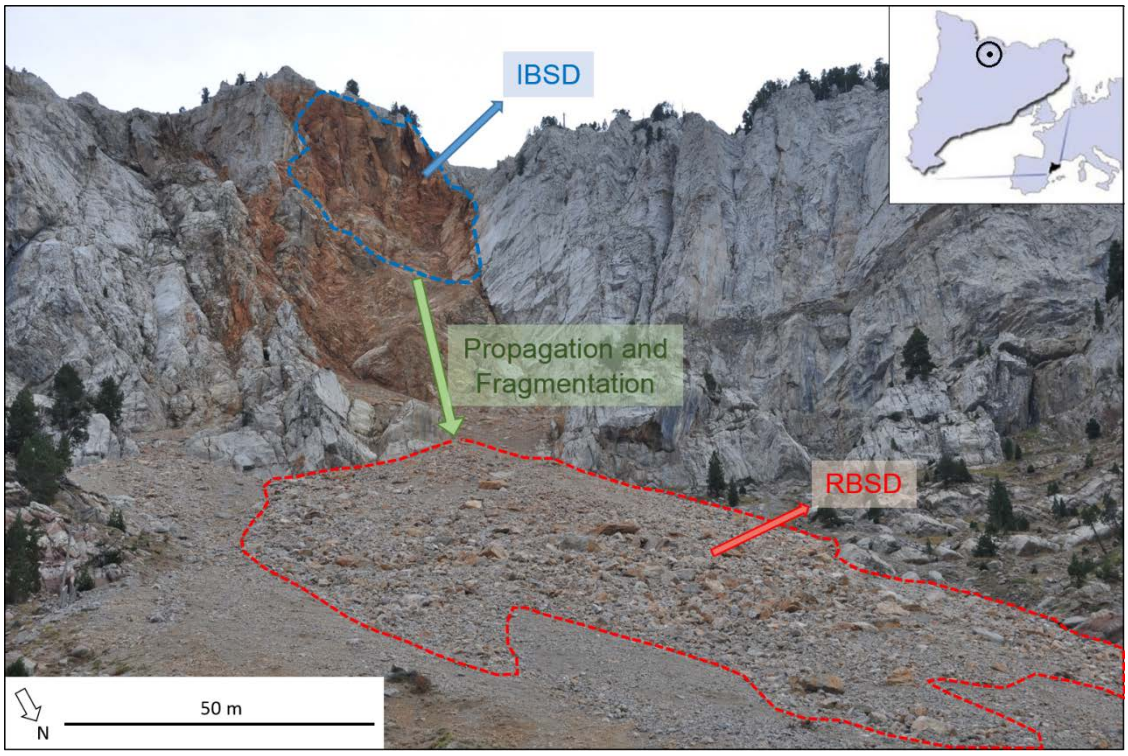

Figure 2. Fragmental rockfall of Cadí, near the village of Vilanova de Banat, Catalan Pyrenees. The detached rock mass may be formed by a group of block precutted by the joint pattern on the massif.

Our research is based on empirical observations and measurements, collecting data from real fragmental rockfalls and from real-scale tests in a quarry. For this reason, PART I of the thesis is focused on "Rockfall characterization and measurements" and PART II is focused on "Real-scale fragmentation tests". The data obtained show a fractal pattern of the fragments block size distributions. Based on these observations, a fractal fragmentation model is proposed and calibrated, which is presented in PART III: "Rockfall Fractal Fragmentation Model". The methodologies developed for the characterization of rockfalls and the unstable rock masses as well as the lessons learned on the fragmentation process can be easily implemented. This is shown in PART IV: "Applications", where they have been applied to the indentification of the maximum credible failure in the steep slopes of Andorra and in the Quantitative Risk Assessment analysis

considering fragmentation in a natural resort in which visitors are exposed. The thesis is composed of a set of publications and original chapters as follows:

The thesis is composed of 11 documents organized in 4 parts:

2 articles already published as a first author in journals included in the JCR
1 article already published as a co-author in journals included in the JCR
1 article submitted (under review): as a co-author in journals included in the JCR
3 articles published as a first author in peer-reviewed conferences and symposia
2 manuscripts to be submitted to journals
2 original chapters

PART I: Rockfall characterization and measurements

Chapter 2: Publication in Landslides (2015): Ruiz-Carulla R, Corominas J & Mavrouli O. (2015). **A Methodology to Obtain the Block Size Distribution of Fragmental Rockfall Deposits.** Landslides, Volume 12, Issue 4: 815–25. doi:10.1007/s10346-015-0600-7.

Chapter 3: Congress publication (2016): Ruiz-Carulla R., Corominas J & Mavrouli O. (2016) **Comparison of block size distribution in rockfalls.** 12th International Symposium on Landslides (ISL 2016) Landslides and Engineered Slopes. Experience, Theory and Practice – Aversa et al. (Eds) © 2016 Associazione Geotecnica Italiana, Rome, Italy, ISBN 978-1-138-02988-0.

Chapter 4: Congress publication (2017): Ruiz-Carulla R, Corominas J & Hürlimann M (2017). **Experiences with UAV for the stady of slope mass movements.** IX Simposio Nacional de Taludes y Laderas Inestables, Santander. Publicado por: CIMNE, Barcelona, España (2017) ISBN: 978-84-946909-5-2. **Communication awarded** by the Scientific Committee of the IX Simposio Nacional de Taludes y Laderas Inestables (Santander, 2017) as the "*Best communication"* in "*Site investigation, characterization, and mapping*" category.

Chapter 5: Original unpublished chapter: **Unstable rock mass characterization with UAV.**

Chapter 6: Original unpublished chapter: **Fragmental rockfall inventory.**

PART II: Real-scale fragmentation test

Chapter 7: Congress publication (2016): R. Ruiz-Carulla, G. Matas, A. Prades, J.A. Gili, J. Corominas, N. Lantada, F. Buill, O. Mavrouli, M.A. Núñez-Andrés, J. Moya (2016). **Analysis of rock block fragmentation by means of real-scale test.** International Symposium Rock Slope Stability 2016, Lyon, France, Proceedings

Chapter 8: Publication in preparation: **Comparative analysis of 4 real-scale fragmentation tests.**

PART III: Rockfall Fractal Fragmentation Model

Chapter 9: Publication in Landslides (2017): Ruiz-Carulla R, Corominas J & Mavrouli O (2017). **A fractal fragmentation model for rockfalls**. Landslides, Volume 14, Issue 3: 875-879. doi.org/10.1007/s10346-016-0773-8

Chapter 10: Publication to be submitted: Ruiz-Carulla R & Corominas J. **A performance of a rockfall fractal fragmentation model**.

PART IV: Applications

Chapter 11: Publication in Landslides (2018): Corominas J, Mavrouli O & Ruiz-Carulla R, (2018) Magnitude and Frequency relations: are there geological constraints to the rockfall size? Landslides Landslides, Volume 15 Issue 5, pages: 829-845. doi.org/10.1007/s10346-017-0910-z

Chapter 12: Publication submitted (under review): Corominas J, Matas G & Ruiz-Carulla R, (2018) **Quantitative Analysis of Risk due to Fragmental Rockfalls** (paper submitted)

1.1 Thesis objectives

The thesis is focused on two main objectives:

1. Unstable rock mass identification and failure characterization based on 3D models obtained by Lidar or digital photogrammetric technics with UAV pictures.

2. Fragmentation on rockfalls: block size distributions characterization from the initial state of the rock mass in the cliff to the final deposit of rockfall fragments. To propose a fragmentation model able to simulate the fragmental behavior, based on real observations.

In order to improve the understanding of the fragmentation phenomenon in rockfalls, the present thesis focusses on: 1. Characterization of unstable rock masses on a cliff. In particular, their initial state defined by the total volume and the joint pattern defined by the In situ Block Size Distribution (IBSD). 2. Characterization of the fragmental rockfalls through the Rockfall Block Size Distribution (RBSD) of the deposited blocks. 3. Proposition of a model which input is either a single block or an initial IBSD, allowing the simulation of the observed RBSD data using a set of parameters. Figure 3 is a sketch showing the fragmental rockfall and the block size distributions in terms of relative frequency.

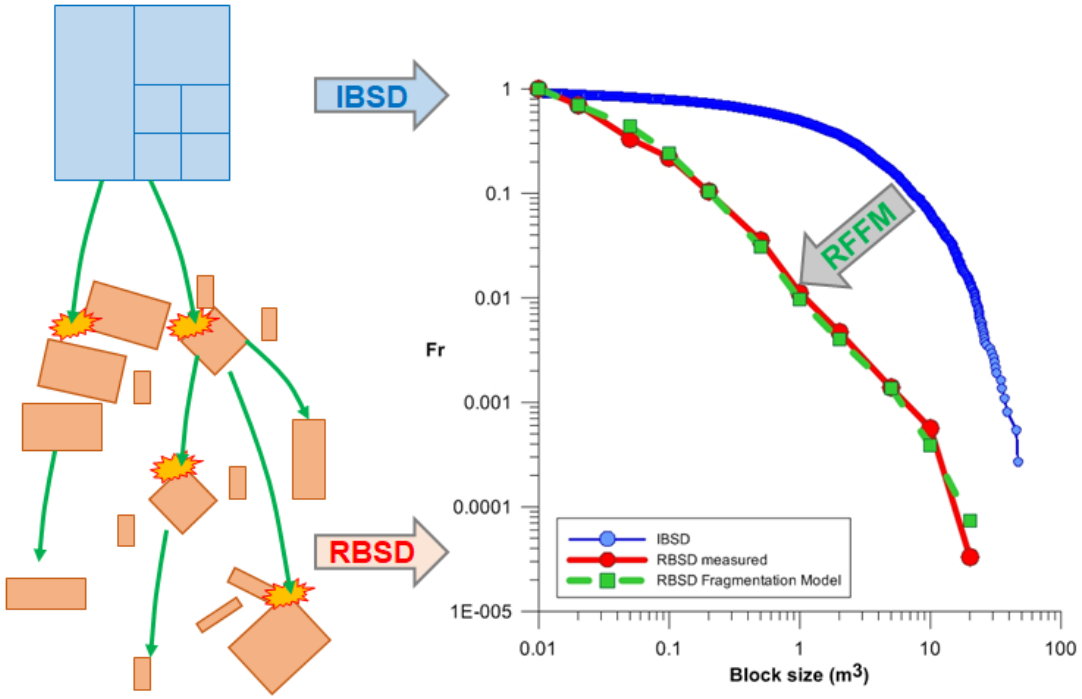

Figure 3. Fragmental rockfall conceptual scheme and block size distributions in terms of relative frequency: IBSD as intial state, RBSD obtained from field measurements and RFFM as results of the proposed fractal model.

1.2 Fragmentation of rockfalls

Fragmentation of brittle materials is a stochastic phenomenon, adding uncertainty to the modelling efforts of calculating risk associated to rockfall events. The last decades, the research has been focused on blocks shape characterization, the description of the terrain, the roughness, the restitution parameters and so on. It is fundamental to address the knowledge of fragmentation and the characterization of the whole fragment size distribution for its implication in the analysis of hazard.

As an example of a fragmental rockfall, the scheme of Figure 4 shows the case of Gurp rockfall (See Chapter 6). The rockfall event involves 100 m^3 of rock mass, falling from about 100 meters height. At the base of the cliff, a high energy impact creates an explosive fragmentation with a wave of dust covering the vegetation and flying debris causing impacts up to a height of 5 meters. As a result of the impact, it is formed a Young Debris Cover (YDC) with a gradational range of block sizes (Ruiz-Carulla et al, 2015, Hantz et al, 2014). Part of the blocks remain in-place deposited and the rest are ejected downslope. Some of them will break in subsequent impacts between the two reference sections named Trail 1 and Trail 2 (Figure 4). Large blocks may cover large runout distances. In the Gurp rockfall, 3 large blocks crossed the Trail 2 and continues rolling and bouncing over the field, two of them reaching the road.

The probability of impact over the Trail 1 section (crossing the YDC zone) should take into account the number of fragments and their velocities and heights (Figure 5). Trail 2 and Road sections have lower density of blocks, less block per square meter of the affected section. However, the bigger blocks reach the road.

In fragmental rockfall scenarios, the probability of impact is not the percentage of blocks of a certain volume that reach or cross a defined section (like Trail 1), simulated individually. Notice that a single block may generate a distribution of fragments in terms of volumes and in terms of spatial distribution that increases the probability of impact. For this reason, we focus our efforts in to measure, describe and reproduce block size distribution generated in fragmentation process.

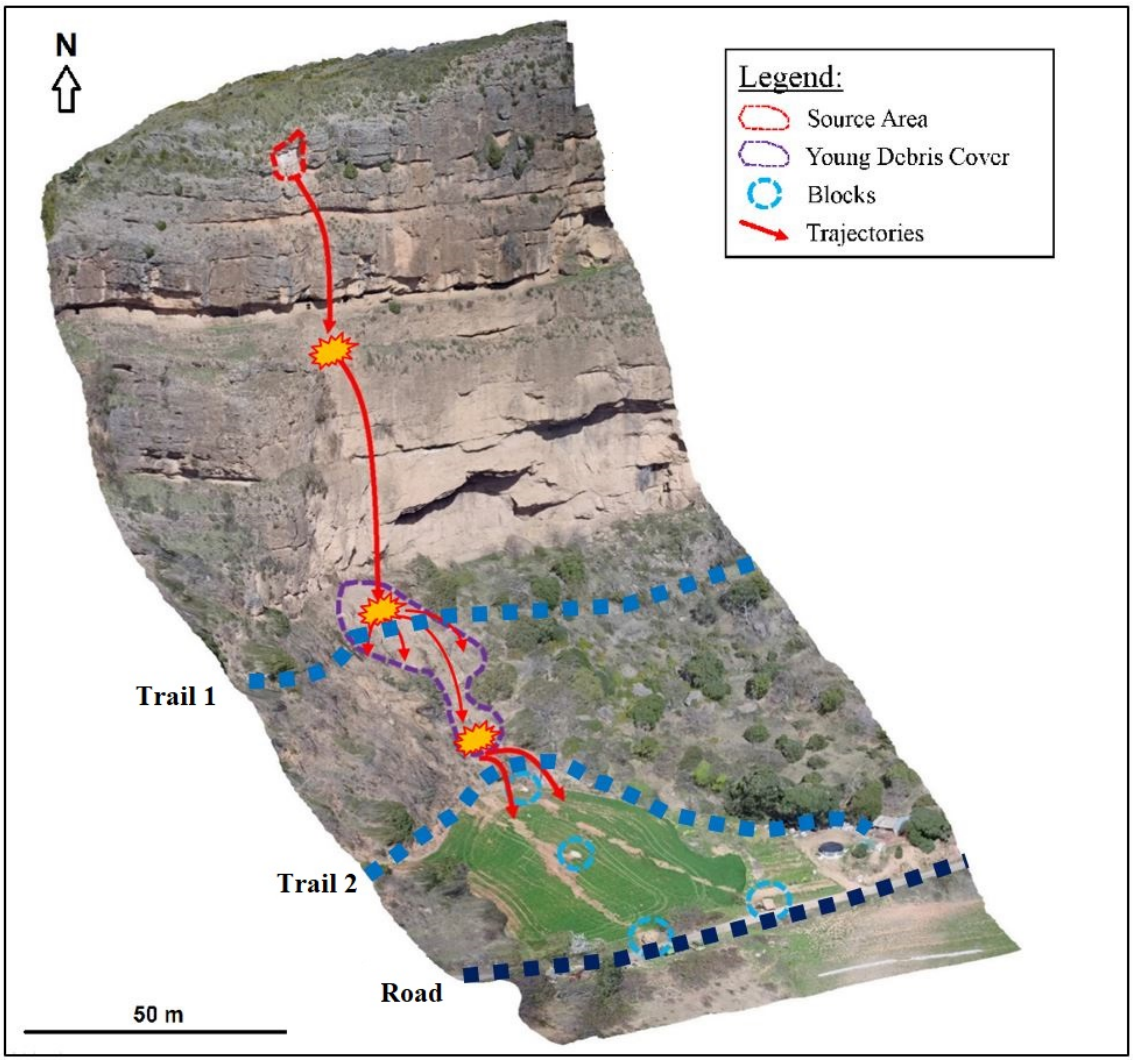

Figure 4: Fragmental rockfall scheme based on the 3D model obtained in the inventoried rockfall on Gurp.

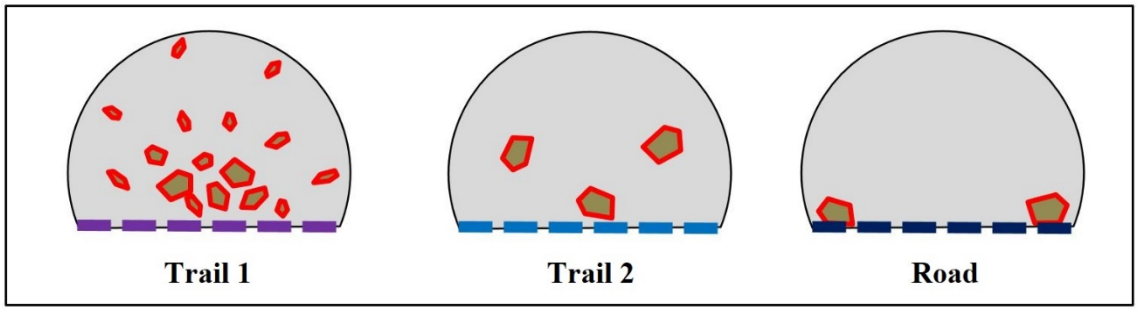

Figure 5: Schematic reference sections of Trail 1, 2 and Road with the fragments crossing the section. Notice how the fragmentation of the rock mass, generating hundreds of fragments, may increase the probability of impact against somebody walking along the Trail 1, Trail 2 or a vehicle travelling along the road. However, the blocks mass reduction implies a decrease of the runouts and a reduction of the impact energy of each block.

The description above, consider the whole rock mass detached as a massive single block of 100 m^3. This assumption may overestimate the impact energy on the bottom of the cliff. Another possibility is that the rock mass breaks in its first impact against the cliff at the mid height (Figure 4) and then the remaining energy and trajectories of each block has to be estimated individually from this point. Moreover, the total rock mass detached may be a single massive rock mass or a group of blocks already separated by joints. The list of block volumes from the cliff is defined as In Situ Block Size Distributions. In this case, the rock mass released may disaggregate when tilting after its detachment (Figure 6). An accurate study of the potential unstable rockfall mass on the cliff, and the characterization of the joint sets that define the IBSD, are necessary. The former is input parameter in a fragmentation characterization study or for modelling purposes.

Figure 3 shows an example of disaggregation of the mass from the source when the rock mass tilt as consequence of the detachment. In the example obtained from a recording of cleaning tasks, an operator pushes the rock mass tilting it, producing the toppling of the whole unstable mass. When the tilt angle reaches the 60 degrees, the mass disaggregates completely following the joint set as there is not enough cohesion in the joints to hold the blocks together. Then the question is, should the impact energy be calculated for each individual block or for the total detached mass? On the other hand, fragmentation will reduce the volume of the biggest blocks: Therefore, in trajectory analyses they cannot be used to calibrate directly the restitution parameters of the ground. Furthermore, the blocks forming the IBSD will probably interact and collide each against the other. The knowledge total volume detached is required and is a good descriptor of the total energy involved in the phenomenon. However, the whole IBSD is necessary to describe the initial state of the rock mass, for the fragmentation analysis comparing it with the deposited fragments distribution.

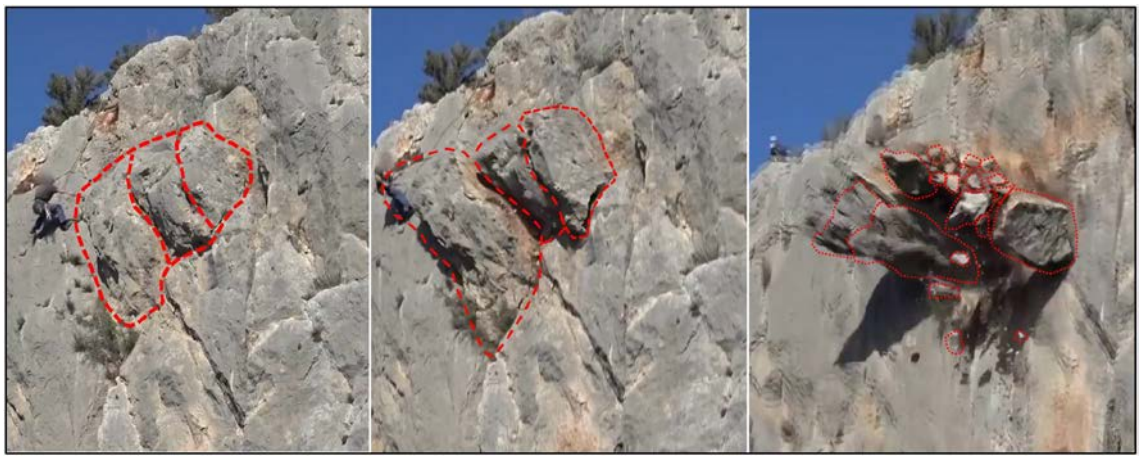

Figure 6: Sequence extracted from the video “Major Rock Fall Occurs Next to a Climber in Chulilla, Spain” on Youtube, showing the disaggregation of a rock mass in a toppling failure mechanism describing an IBSD.

The hazard analysis of rockfall is focused on trajectory simulators. A huge effort was made by many authors in developing trajectory simulators and methodologies to characterize the rockfall hazard: using high resolution 3D numerical models (Agliardi et al 2003); trajectory simulator with an stochastic impact model (Bourrier et al, 2009); evaluating the parameters that control de propagation simulation (Crosta et al, 2004); reviewing the rockfall mechanics (Dorren 2003) and characterizing the hazard zones based on the kinetic energy (Jaboyedoff et al 2005). Recent studies evaluate the effect of different resolutions of the Digital Elevation Model used in raster format and the advantatges of the use of Point Clouds to describe the terrain and the overhangs (Noël, et al 2017a). Restitution parameters and the terrain roughness influence on the energy consumption in order to predict the runout of the blocks (Agliardi et al. 2009; Crosta et al. 2015; Gischig et al. 2015; Matas et al, 2016; Nöel et al, 2017b,). Hazard characterization of a rockfall scenario is based on trajectory simulations, where a significant part of the tasks is the calibration of the restitution parameters (Kim et al. 2015). In places with previous rockfall events, it is common to use the volume and location of some big blocks in order to calibrate the restitution parameters, considering the blocks unbreakable during the propagation (Chau et al. 2002; Gischig et al. 2015; Asteriou et al. 2012, Li and Lan, 2015). The main hypothesis is that there is no fragmentation. However, fragmentation often occurs during the propagation, and the blocks observed on the deposit are fragments from bigger blocks that breaks due to impacts. Then, the use of the location and volume of these fragments to calibrate the restitution coeficients may involve errors in terms of energies absorbed by the terrain. The restitution parameters may become artificial parameters to control the energy balance and stop the blocks close to the observations.

The probability of impact of rockfalls is often defined as the percentage of blocks of a certain volume that reach a certain point from a high number of simulations (Guzzetti et al., 2002; Jaboyedoff et al 2005). In reality, a single block can produce hundreds of fragments after its breakage as we observe in real-scale tests (Gili et al. 2016; Ruiz-Carulla et al. 2016). Then, the probability of impact after fragmentation depends on the whole fragment size distribution, the total number of fragments generated and the velocity and trajectory of each one defining the impact energy. Focusing on structures and protection systems, the multi-impact effect due to fragmentation is obviated in the design processes. Multiple fragments increase the probability of impact against an important part of structures, as piles in protective fences or in house structures. The fragility curves of the exposed elements should consider it.

Another interesting effect of fragmentation are “flight bullets”. These smaller fragments, generated in fragmentation explosive stage, can be ejected at high velocities and create new parabolic trajectories with high heights, trespassing fences and reaching longer runout distances. An efficient fragmentation may produce a “rain” of fragments over a road, and may be more

hazardous than the same total volume concentrated in a single block in terms of affected area and probability of impact, also impacting to multiple objects or vehicles. Restitution parameters obtained based on the location of these small fragments considering the rockfall source area will yield unreliable results.

The fragmentation of a rock block is a very complex phenomenon due to the high degree of anisotropies and weakness structures in contrast of the main industrial man created materials. Rock fragmentation, has been considered in a wide range of fields of study related with tunneling or blasting, often related with mining proposes (Aler et al. 1996; Bakar et al. 2014; Chakraborty et al. 2004; Cunningham 1983 and 1987; Faramarzi et al. 2013; Gheibie et al. 2009; Hudaverdi et al. 2010; Peng et al 2009; Saavedra et al. 2006). However, for rockfall trajectory analyses purposes it is usually obviated.

T he type of a single impact can be exemplified hitting a rock block with a geological hammer. A single impact can be applied on a corner, an edge or a face of the block (Figure 4). On a real rockfall, multiple impacts can be produced at the same time over an edge or a face of the block. The impact direction relative to a joint set or weakness plane of anisotropy produce different results. Tavallali (2010) analyzed the effect of the layer orientation on Brazilian tests, observing larger relative fracture length and smaller energies required with the alignment of the applied forces and the bedding planes of the tested sandstones. We can imagine it hitting a sedimentary block with a hammer parallel or not to the predominant planes of weakness (Figure 4). Real rock masses may have multiple planes of weaknesses, related to the genesis of the material and to the stress history. Then, the probability to get a more or less efficient impact direction is related to the number of anisotropies and the shape of the block. As we can observe this behavior on real-scale test (Giacomini et al. 2009 ; Gili et al 2016; Ruiz-Carulla et al. 2016) it is a stochastic process difficult to be modelled, but may be managed using stochastic or a controlled variation of some parameters, for example, over a survival rate of each block.

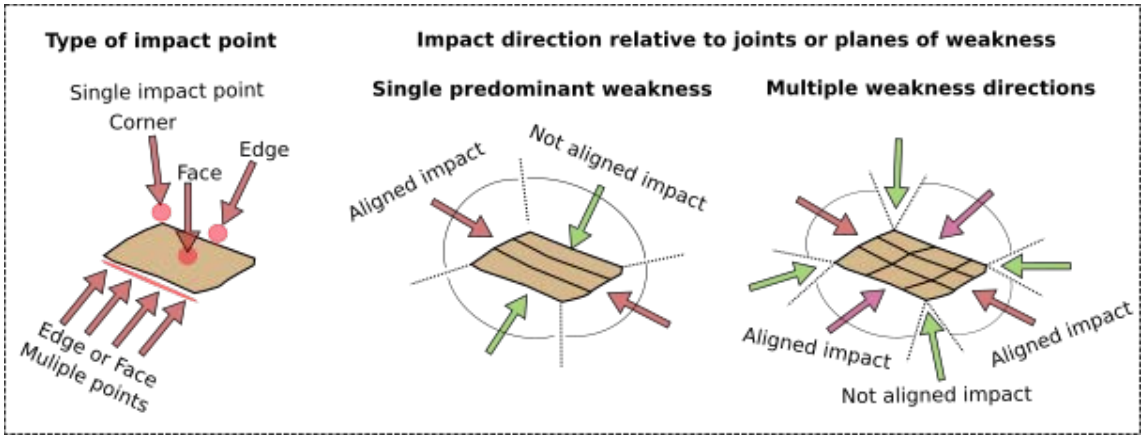

Figure 7: Types of single or multiple impacts on a rock block and examples of impact direction relative to planes of weakness.

Discrete elements methods can work considering the anisotropy, the joint sets and the shape of the blocks (Wang & Tonon 2010; Shen et al. 2017; Zhao et al. 2017). However, it is not a deterministic problem in terms of capability to describe with high degree of certainty what will happen due to the high number of factors dealing with fragmentation phenomenon. For these reasons, the impact type and relative direction are not been taken into account in this approach. However, for a real judgment expertise criterion, the shape of the blocks and the number of different imperfections systems has to be considered. Studies from energetic estimation on fragmentation (Hou et al 2017) and supported by real scale tests (Giacomini et al. 2009 ; Gili et al. 2016) reach this conclusion.

Due to difficulties to study the impact forces directions and the wave of stress propagated inside the block, the energetic analysis is widely applied (Hou et al, 2017). The basis of many fragmentation theories uses the crushing work ratio that denotes the work used to break a volume of rock. This ratio is used to relate the energy and the size reduction commonly described as a diameter before breakage (D) and after breakage (d) (Rittinger 1867; Kick 1885 and Bond 1952, 1961; Cunnungham, 1987; Grady DE. 1985; Hardin 1985). This description means that the rock mass redistribution after fragmentation is described using an average size. Alternatively, they are measured by sieving characterized by a diameter or areas in image analysis. The more relevant theories from Rittinger (1867), Kick (1885) and Bond (1952, 1960) uses this descriptor, and also all the theories based on these. The mentioned theories consider different aspects on fragmentation energy consumption and how to estimate the crushing ratio. However, they use a single diameter as average size to describe the final fragments distribution and sometimes a shape coefficient for the whole distribution (Hou et al. 2017).

The main dominant idea is that the energy consumption on fragmentation should be proportional to the area of the new fractures generated or propagated if they already exist (Blasio & Crosta 2016). Part of the energy is transferred to the fragments generated which propagate with a certain velocity after the impact. Both, the energy transferred and the kinematics of the fragments after the breakage upon the impact may be determined using Discrete Elements Methods analysis (Zhao et al. 2017).

Part of the energy is absorbed by the ground and the elastic parameters both the falling rock mass and the terrain are considered in the elastic impact theory (Hou et al, 2017). The breakage criterion based on the energy or the velocity (Hou et al, 2017) can help in the comprehension of the phenomenon. However, from our point of view, a single average size of the falling mass is not enough, and the whole fragment size distribution is necessary to characterize the rockfall hazard and improve the quantitative risk evaluation.

Haug (2016) analysed the energy budget of fragmentation in rockfalls and rockslides using experiments. In a way similar than Bowman (2012), different angles of the inclined plane were tested and a block sliding until its impact against the bottom base. The geometrical descriptors that defined the scenario were the relative fall height of the center of mass, the aspect ratio of the mass, and the travel distance. Another parameter used in this study was the potential energy relative to the cohesion, used as a descriptors of the energy available and the resistance to breakage, respectively. The parameter describing the fragmentation is the "degree of fragmentation", which is defined as the proportion between the largest fragment volume and the initial volume. This definition of the degree of fragmentation assumes that the size of largest fragments describe the entire fragment size distribution.

The fragments of the forefront of the block may be ejected at high velocities during the impact (Haug et al, 2017; Zhao et al, 2017). At the same time, other fragments from the bottom and rear part of the block may move at lower velocities. Haug (2017) observed a power law relationship between the degree of fragmentation and the ratio between the specific potential energy and the cohesion, and that the aspect ratio depends linearly with the degree of fragmentation. The increase of the degree of fragmentation reduces the run out distance of the center of mass of the deposit (Haug 2017, Bowman et al, 2014, Matas et al, 2017). He concluded that the front of the deposit travel farther away with increased degree of fragmentation. We argue this reasoning, because the increase of the fragmentation degree (or other descriptor) should diminish the energy of each fragment, and then, the reduction of the run out distance in a natural fragmental rockfall scenario. However, in a single impact, fragmentation may generate small and medium fragments from the frontal part of the block that can describe new parabolic trajectories with longer runout distance. As mentioned in the introduction, the "flight bullets" fit to this behavior. Another specific case is when the shape of block may control the stoppage of the block, and if the block breaks, a new mobility possibility appears, which increasing the run out distance of the new fragments. These are the cases of the studies of Haug (2017) and Zhao (2017). We have observed this behavior in real-scale fragmentation test in quarry (Gili et al 2016).

The energy scenario is also an important point in the fragmentation analysis. Considering the energy consumption proportional to the new area created, the bigger a block, the greater is the energy required to break it. An increase of the number of fragments implies an increase of new areas created, and then, more energy is spent in breakage. At the same time, the type of impact contact (face, edge or a vertex of the block) and the relative orientation between the maximum impact force direction and the main weakness anisotropy may control de fragmentation pattern. For all these reasons, fragmentation process is a very stochastic process and difficult to describe and understand. Experimental studies (Giacomini et al 2009); Gili et al, 2016) were not able to

find an energy threshold in real scale fragmentation tests. It is necessary to notice that all the tests were carried out within the same order of magnitude of energy.

Haug et al 2016 studied the energy budgets of the fragmentation in rockfalls and rockslides. The focused on the displacement of the center of mass and the energy budget of 109 experimental rockslides using a rock analogue material. They defined a characteristic fragment size and the largest fragment. The fragmentation degree is found to depend linearly on the aspect ratio of the experimental sample and on its cohesion (as power law). In these rockslides experimetns, the travel distance of the front of the deposit increases with the degree of fragmentation. In contrast, the center of mass reduces the mobility with the degree of fragmentation, suggesting an increased energy consumption. The characteristic fragment size that describes the degree of fragmentation is taken as the largest fragment due to the difficult in sieving the deposited material and obtain the whole size distribution. Therefore, the degree of fragmentation (defined as m_c) is the relation between the initial mass and the largest fragment mass after the experiment. It has also been used by Nocilla et al, 2009 to characterize the degree of fragmentation of rockfalls. In the present thesis, the whole size distribution of the deposits (Rockfall Block Size Distribution) is considered. The degree of fragmentation in terms of m_c may describe well the single block cases. However, in the cases where the detached mass is a set of blocks (IBSD), is not possible to link the largest fragment with a single initial block. In the model (RFFM) proposed in this thesis, survival rate parameter is defined which is the analogue to the degree of fragmentation in terms of m_c, and a set of parameters is used to generate the rest of the fragment size distribution. In rock avalanches, Charriere et al, (2015) follow a similar criterion and compare the initial and the deposited block size distribution. In rock avalanches, more energetic than rockfalls, part of the rock mass may produce clouds of dust (Crosta et al, 2007) completely disintegrating the rock mass, and exerting some control on the run out distances (Davies et al 1999, Locat et al 2006).

The fragmentation is a natural phenomenon that may be characterized by means of fractals (Perfect 1997). In order to study it, the author highlights the requirement of well detailed descriptions of the rigid bodies before and after the fragmentation phenomenon. The present research is focused on the observation and description of the main geometric descriptors and the block size distribution characterization on real fragmental rockfall based on a fractal fragmentation concept. In order to characterize the intial state of the rock mass, we have to reconstruct the detached rock mass and the IBSD based on the joint pattern present on the cliff. In order to achieve it, the use of UAV and digital photogrammetrics techniques should be considered. 3D models of the scar, in point cloud format are useful in order to quantify the joint pattern on the cliff (Gates et al, 2012; Gigli & Casagli 2011; Haneberg et al, 2006; Buyer, et al 2017). Also in order to define geometries for dicrete elements methods (Firpo, et al 2011).

1.2 Summary

PART I: Rockfall measurements and characterization

The PART I of the present thesis, describes the methodologies and techniques used and developed in order to collect the relevant parameters of the rock mass and for the characterization of the fragmental rockfalls. **Chapter 2, "A methodology to obtain the block size distribution of fragmental rockfall"** describes how to obtain the RBSD of a rockfall debris by means of sampling plots. The results show a clear fractal behavior on the block size distribution that can be fitted to a power law. The analysis of the RBSD of several rockfall events is included in **Chapter 3, "Comparison of block size distributions in rockfalls"**. It presents the different RBSD obtained in rockfalls with a wide range of conditions in terms of total volume, geometrical conditions of the slope, lithology and terrain properties. The paper ends with the correlation between the free fall height and the exponent (or slope) of the power laws that can be fitted to each RBSD, which relates the amount of energy to the slope of the fitted power law. The main conclusion is that the fragmentation process cannot be characterized only by the final product of the process, which is the RBSD. The analysis and characterization of the fragmentation have to consider the initial state of the rock mass and the comparison between the IBSD and the RBSD. This reason motivated the study of the unstable rock masses, the reconstruction of the detached volume and the joint pattern characterization in order to obtain the IBSD to be compared against the RBSD on each rockfall inventoried. To this end, we first ensembled our own UAV (Unmanned Aerial Vehicles or drones) to take pictures and prepare high-resolution 3D models using digital photogrammetric techniques such as the structure from motion algorithms. **Chapter 4, "Experiences with UAV on mass movements characterization"** is a short publication reviewing how these new technologies allow the obtention of a high amount of information that can be used to deal with: real terrain profiles (with overhangs), joint pattern characterization, unstable rock mass identification, 4D measurements for erosion-deposition studies or landslide deformation. The main advantage in using these techniques is the increase of the measurement capabilities and, at the same time, the reduction of risk during the field works by avoiding the exposure to the hazardous locations. **Chapter 5: "Unstable rock mass characterization with UAV"**, presents more in detail the procedure we developed (including applications for rockfalls inventories), the acquisition systems tested, the data formats and how to manage the 3D information in order characterize the joint pattern and identify unstable rock masses. Finally, with all this new knowledge in data acquisition, we revisit the inventoried rockfalls as well as new ones, collecting the data that is presented in **Chapter 5: "Fragmental rockfall inventory"**. These data are then used to calibrate the proposed fragmentation model, as well as to support other

research lines like trajectographic simulators or RBSD measurements based on raster or 3D point cloud analyses. Figures 8 to 10 are examples of tools, products and results of the field work carried out to characterize the fragmental rockfalls. Figure 8 shows the RBSD obtained and pictures of the rockfall inventoried. The inventory contains data of a wide range of rockfalls volumes, from 2,6 m^3 to 10,000 m^3, and different lithologies (limestone, schist, sandstone and conglomerate).

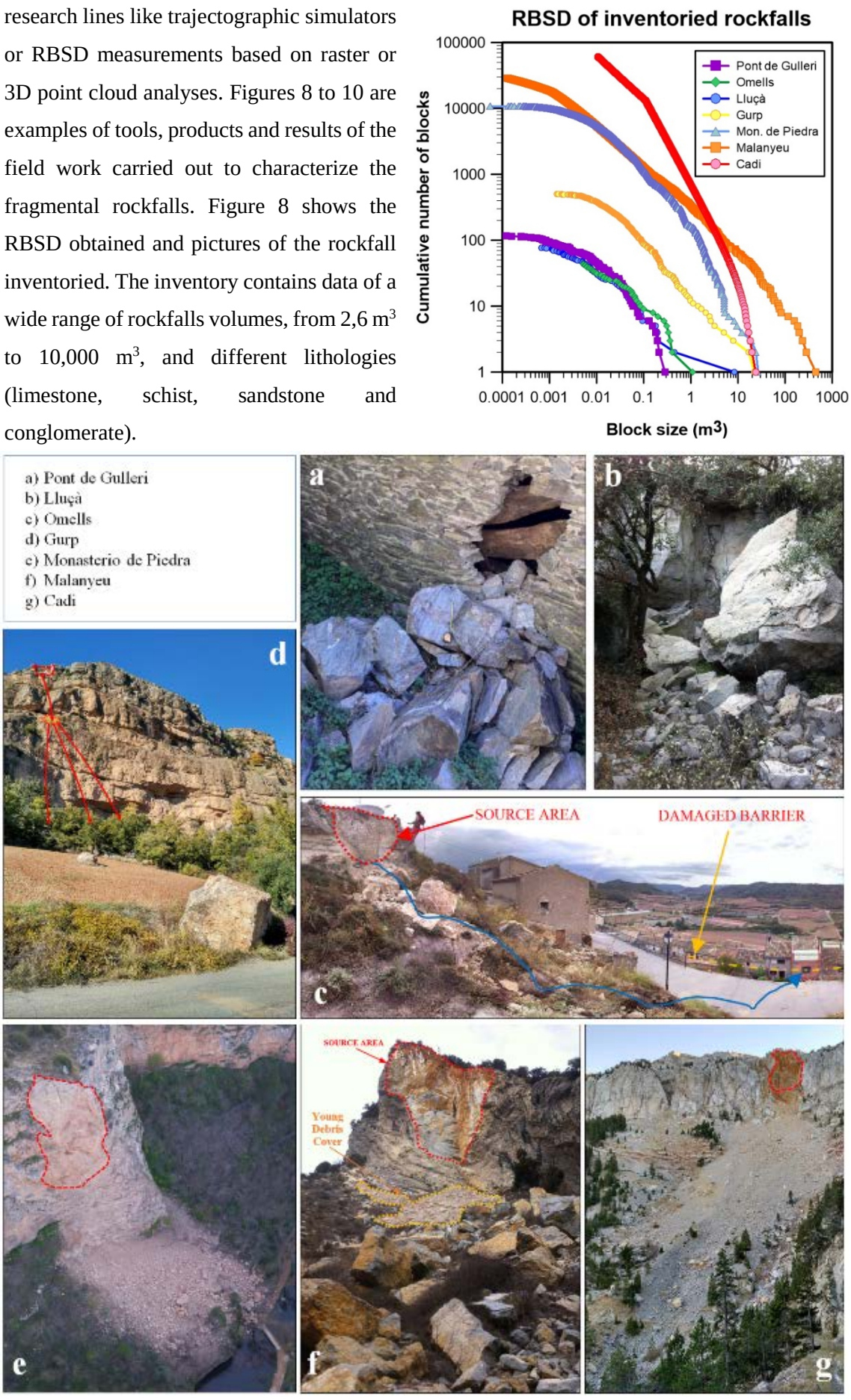

Figure 8: RBSD obtained (up right) and photos of the seven inventoried fragmental rockfall events.

Figure 9 shows a 3D model of a fragmental rockfall inventoried (Monasterio de Piedra) and the drone used (DJI-Inspire 2). After the rockfall event, an important unstable rock mass was characterized for further risk studies. Figure 10 shows the visual joint identification over a texturized 3D model and the outcrop modeling of the joints that define the unstable volume using a 3D point cloud.

Figure 9: Texturized 3D model of a fragmental rockfall inventoried (Monasterio de Piedra), whereafter the rockfall event, an important unstable rock mass (orange volume) was characterized for further risk studies.

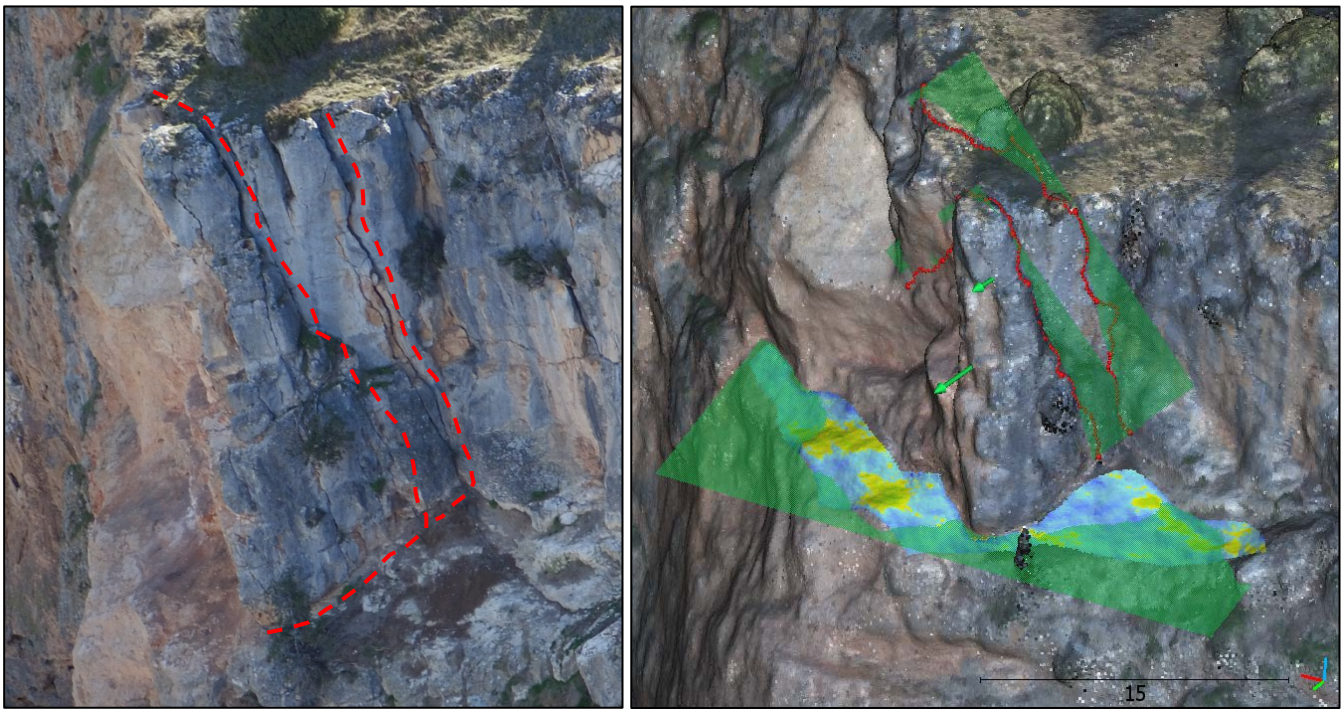

Figure 10: Visual identification of joints on a texturized 3D model (left) and joints outcrop modeling (right).

PART 2: Real-scale fragmentation test

The study of fragmentation phenomenon in natural rockfalls involves important uncertainties particularly on the size and characteristics of the initially detached rock mass and on the deposit of fragments. The real-scale fragmentation tests carried out in quarries (Figure 11) have provided high-quality data in a very controlled scenario with the possibility to repeat the test several times.

Figure 11: Picture of real-scale fragmentation test (test nº 4) performed in a limestone quarry.

We performed 4 real-scale fragmentation tests (Figure 12) dropping rock blocks with volumes ranging between 0.17 m^3 and 5 m^3. The main features recorded during the tests are: initial volume using a tape and a 3D photogrammetric reconstruction, fragments' volumes, 3 high-speed cameras for trajectories reconstruction by videommetry, seismic recording, targets located on the scenario coordinates and UAV flights for 3D scenario reconstruction and measurements improvements.

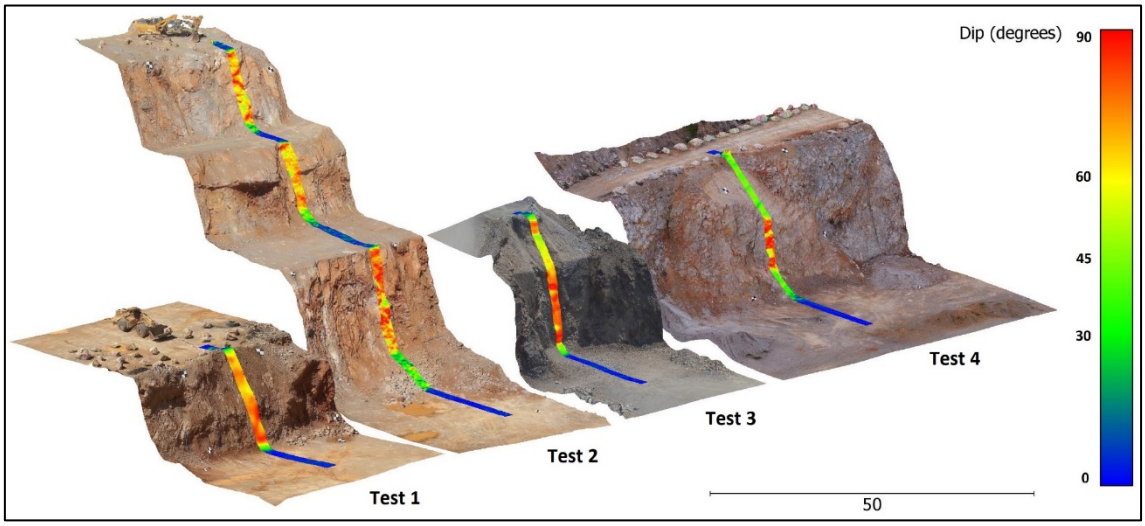

Figure 12: 3D models of the test sites with a profile coloured by the slope angle.

The **Chapter 7: "Analysis of rock block fragmentation by means of real-scale test"** is a short communication presenting the preliminary results of the test nº 1 and 2. The communication contains the correlation between the exponent of the fitted power laws of the block size distributions (BSD) of the fragments, and the number of fragments measured. No correlation is found between the number of fragments and the kinetic energy nor with the Schmidt hammer measurements. However, it must be taken into account that the range of kinetic energies generated in the quarry tests is much less than the range observed in nature (natural rockfalls). The **Chapter 8: "Comparative analysis from 4 real-scale test"** discusses more in-depth the data obtained from the four tests realized. The first part of the chapter is focused on the techniques and methodologies used to capture as much information as possible on each test, with special attention on the measure of volumes. For the purpose of this thesis, the most relevant information collected is the BSD of the fragments for each block tested (Figure 13). A total of 124 blocks were tested and 2907 fragments were measured with a tape. The BSD obtained are colorized by low (purple), medium (orange) or high (green) exponent of the fitted power law.

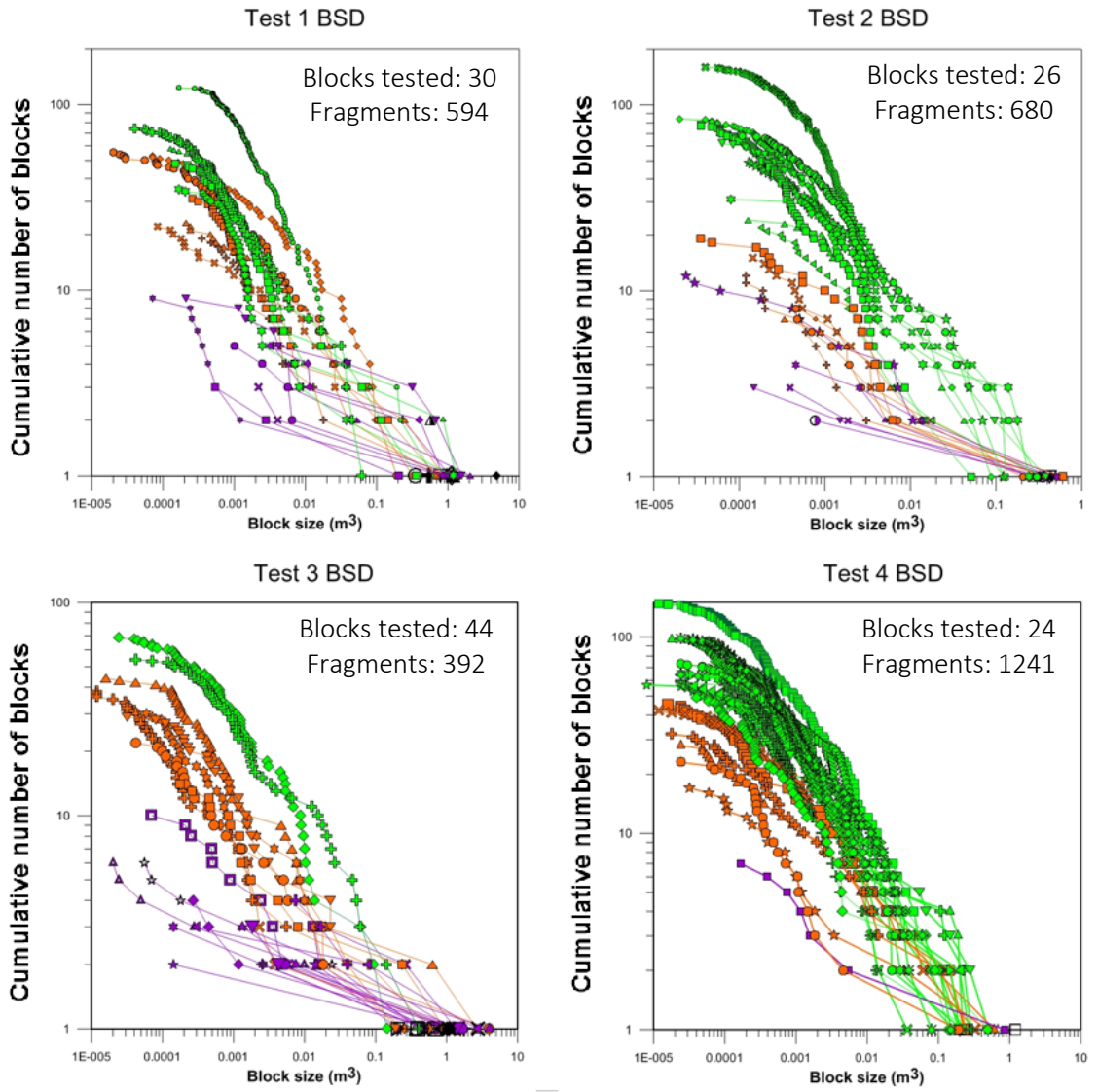

Figure 13: BSD of fragments measured for each block tested, from test 1 to 4, colored by low, medium or high exponent of the fitted power law on each distribution.

The Survival rate (*Sr*) is defined here as the largest fragment volume measured over the initial volume. Then, a *Sr=1* means that the block remains intact. Two blocks with the same *Sr* may produce a different number of blocks. Then, the *Sr* and the number of fragments are both necessary to characterize fragmentation. Figure 14 (left) shows the Survival rate and the number of fragments produced in each block tested. The smaller the *Sr* value, the larger the number of fragments produced. However, it is not a direct relation, and the same number of fragments may be generated with a wide range of Sr and vice-versa. Furthermore, *Sr* is not directly related to the potential energy as shown in Figure 14 (right) exemplifying that is not possible establish a fixed energetic threshold. All the blocks from the same test site were dropped from the same height, however, the potential energy varies because a range of block volumes was used in the test.

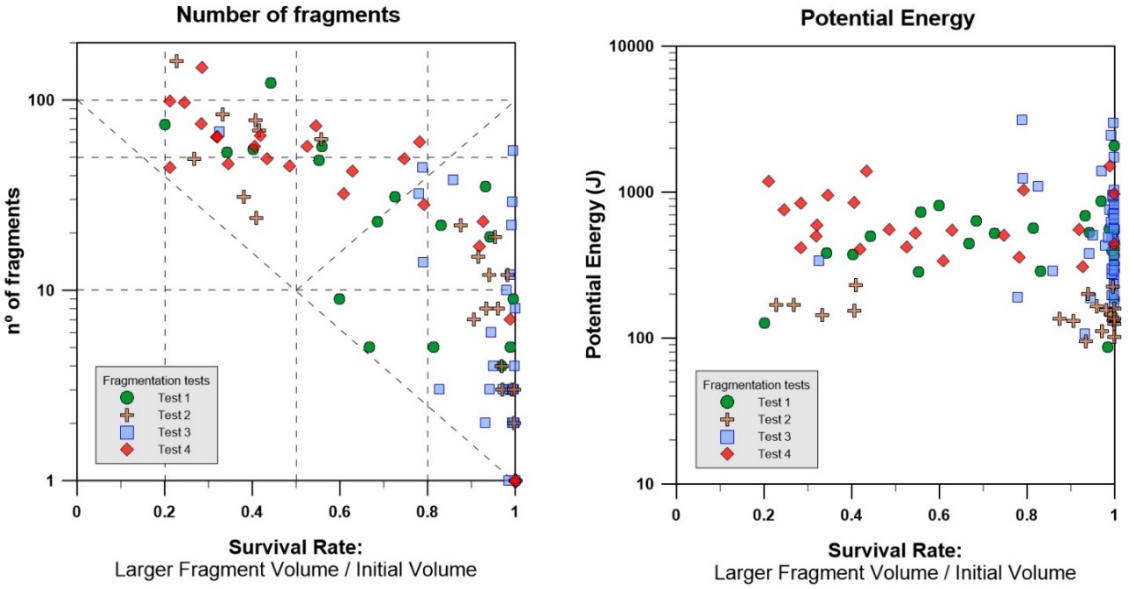

Figure 14: Survival rate versus number of fragments produced on each block tested (left) and versus the potential energy of each block (right).

Plotting the number of fragments versus the *Sr* by test sites (Figure 15) distinct patterns are observed. Blocks of Test 1 show a wide range of behaviors. Some blocks remain intact while others break completely, with *Sr* ranging from 1 to 0.2 and progressively increasing the number of fragments. The impact angle, whether the impact takes place on a vertex, edge or face of the block, the relative orientation between the anisotropies of the rock block and the impact surface, and the rigidity of the ground, are controlling factors of the fragmentation process. Blocks from test 2 show a contrasting behavior represented by two differentaited groups of *Sr>0.85* and *Sr<0.55*, generating less or more than 20 fragments, respectively. In this test, blocks impacting against a more rigid substrate, doing a sharp impact sound (high frequency), generate more fragments and lower values of *Sr*.

Test 3 is a steep slope with soft materials at the flat platform below. The blocks released impact tangentially over the slope and remain intact until their contact with the flat platform below. As the latter is composed of fine soft material, most of the blocks of Test 3 remain virtually unbroken, with *Sr* > 0.8-0.9. Despite the high *Sr* values, the number of blocks generated ranges from 1 (no breakage) to 50. Only one of the blocks broke because it impacted upon a deposited block, (similar rigidity). The breakage yielded *Sr* close to 0.3 and more than 50 fragments. Finally, Test 4 the blocks were dropped from a height of 8.5 meters above a stiff fault plane surface inclined 42º. The total height of the fall is 23.6 m. As the fault plane (see Figure 11) has high rigidity and the slope geometry allows a more normal component of the impact force than the other tests, the blocks break in an explosive way, most of them producing more than 40 fragments and even more than 100. However, the *Sr* ranges from 1 (or 0.8) to 0.2. Test 3 and 4 show opposite behavior, highlighting the importance of terrain rigidity and impact angle.

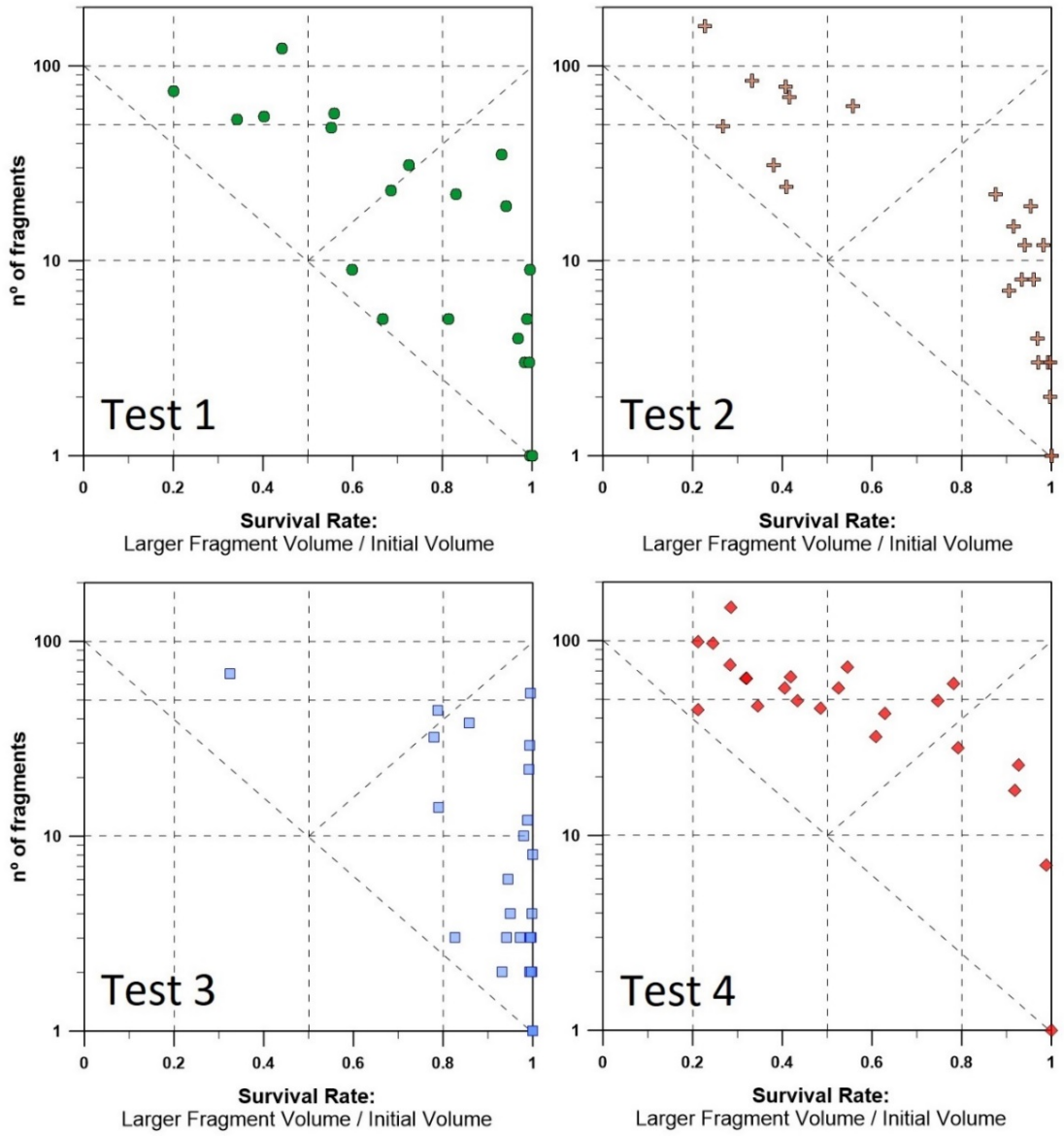

Figure 15: Survival rate versus number of fragments produced on each block tested separtly by test sites.

PART 3: Rockfall Fractal Fragmentation Model

The block size distributions collected in our fragmental rockfall inventory, and also from real-scale fragmentation tests, show a fractal pattern. Based on this, a fractal fragmentation model is proposed in **Chapter 9: "A fractal fragmentation model for rockfalls**". The initially detached rock mass consists of either an individual block or a jointed rock mass. In the latter, the intersection of the joints individualizes rock blocks whose volumetric distribution is the In-situ Block Size Distribution (IBSD), that will be the input of the model. The methodology to obtain the estimation of the IBSD is also explained in this chapter. The size distribution of the fragments generated as a result of the impact and breakage of the initial blocks is the Rockfall Block Size Distribution (RBSD), used in order to calibrate the model. The fragmentation of a rock mass can be quantified by comparing the block size distributions before and after the impact. Figure 16 is a sketch showing the fragmental rockfall and the block size distributions in terms of relative frequency.

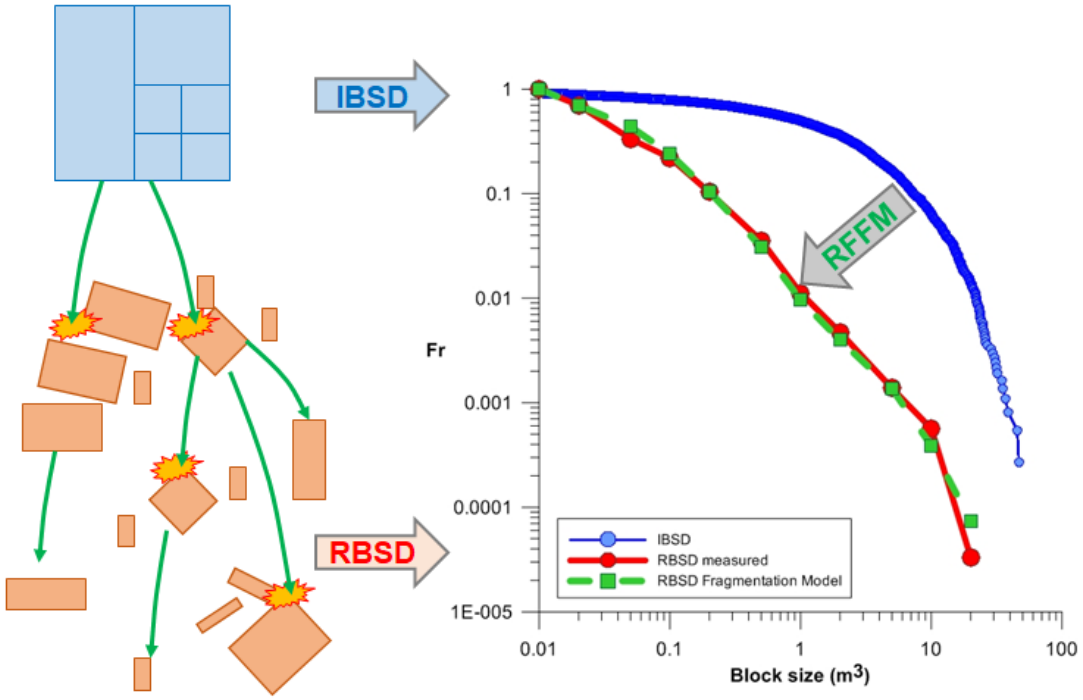

Figure 16: conceptual scheme (left) of the block size distributions from the initial state (IBSD) to the final deposit (RBSD), and the adjusting of the proposed Rockfall Fractal Fragmentation Model (RFFM) to the measured RBSD from the IBSD as input (right).

The main idea of fractal behavior is the reproduction of the same behavior in several orders of magnitude, in this case, creating fragments from an initial volume. Figure 17 shows a conceptual scheme of the RFFM proposed, where: 1) the geometric factor "*b*" controls the proportions between the initial volume and the fragments generates; 2) the Probability of failure "$P(1/b^i)$"

defines the proportions of the block that break producing fragments. The model proposed in chapter 9 works with iterations, applying the same construction rules in each iteration ("*i*" on Figure 17) using the before generated fragments as new initial blocks.

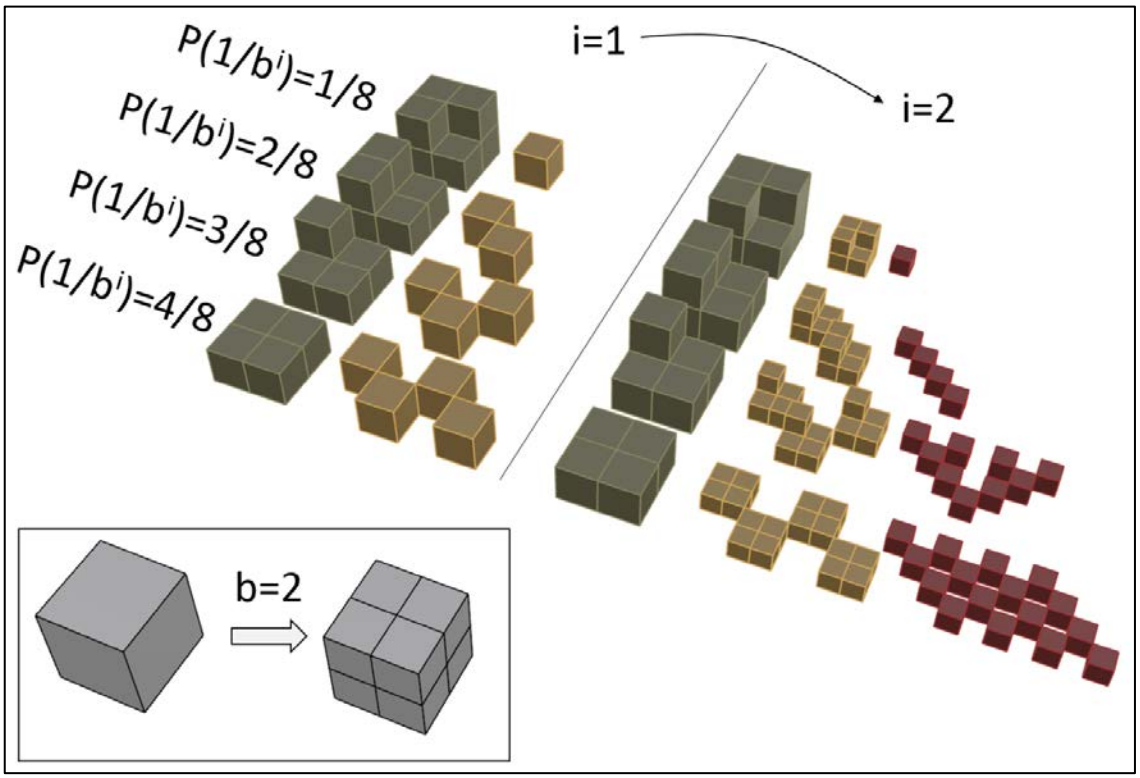

Figure 17: Scheme of the fractal fragmentation model (scale-invariant) using b=2 and examples of smaller block generation for $P(1/b^i)$=1/8, 2/8, 3/8 and 4/8=0.5, considering 1 or 2 iterations.

The model input is the IBSD as a list of volumes. In order to estimate the IBSD, a 3D model of the scar is obtained by means of digital photogrammetry techniques. The latter is used to reconstruct the detached volume and to indentify the joint sets. Finally, we cut the reconstructed volume with the modeled joints assuming infinite persistence. Figure 18 shows two possible volume reconstruction (A and B) and the IBSD obtained using 4 or 5 sets of joints to cut it.

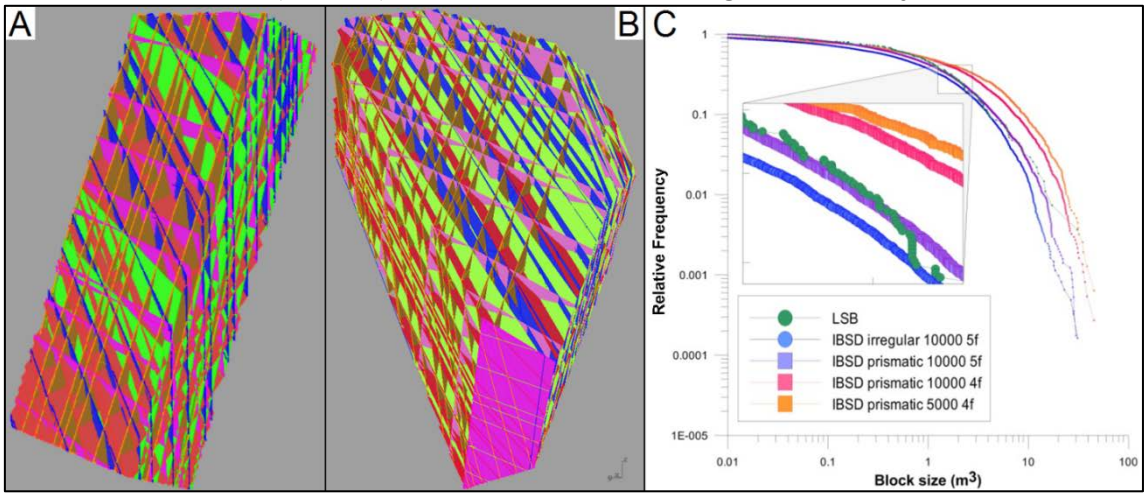

Figure 18: IBSD generated taking a prismatic volume (A) or a reconstructed irregular volume of the detached rock mass (B), and the corresponding IBSD (C) considering 4 or 5 fully persistent joint sets.

The model is calibrated using the inventoried Cadi rockfall event. Figure 19 shows the results in terms of relative frequency (A) and in terms of the cumulative number of blocs (B). The IBSD is the input distribution (blue), the RBSD is the distribution of blocks obtained from field measurements (red), and the block size distribution resultant of the model (green) is named RBSD_RFFM. The proposed model in Chapter 9 works using bins, classifying the blocks in size classes. Then, each block is defined by an average size of the bin. Due to this, the mass balance cannot be accomplished. A survival rate is defined in order to quantify the proportion of blocks of each bin size that breaks, allowing a percentage of blocks remaining unbroken.

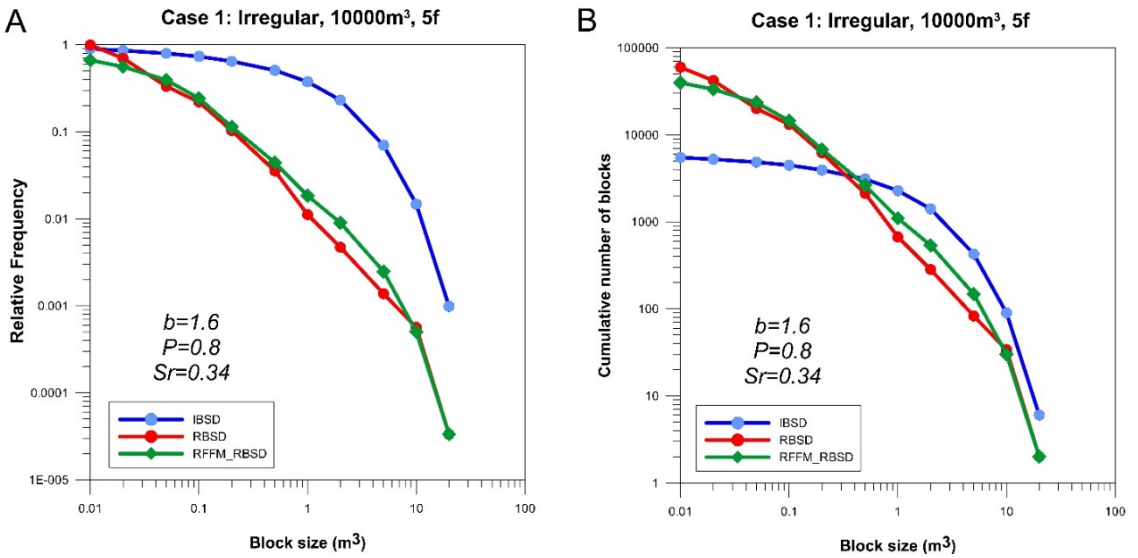

Figure 19: IBSD (irregular shape, 5 joint sets), RBSD from the measurements in the field and RFFM_RBSD generated using the Rockfall Fractal Fragmentation Model; in terms of relative frequency (A) and the cumulative number of blocks (B) versus block size.

We identify the main limitations of the proposed mode: 1) cannot accomplish the mass balance due to the use of bins: 2) the shape of the block size distributions produced depends on the number of iterations; 3) the methodology follows implies the generation of fragments of equal sized in each iteration. The latter is arguable when the initiator is a single block like the used in the real-scale fragmentation tests or in small rockfalls. In order to overcome these limitations, we propose some model upgrades in **Chapter 10: Performance of a rockfall fractal fragmentation model".** The most important upgrade of the model is the use of the formulation in terms of the cumulative number of blocks, avoiding the classification in bins and applying the model on each initiator block. With this upgrade: 1) the iteration process is not requiered, and then, the parameters of the model no longer depend on the number of iterations; 2) the model satisfies the mass balance and 3) the model produces a distribution of fragments in a cumulative way, with fragments continuously decreasing in size as it is observed in reality. Another upgrade of the model is the use of scale-variant behavior with the formulation proposed also by Perfect (1997), allowing the reproduction of block size distributions with an irregular shape. Notice that the

Survival rate (*Sr*) defined in Chapter 9 as the proportion of blocks of each bin that remain unbroken have no sense in the upgraded model without bins, because all the input blocks are initiators that may break or not. At the same time, the use of scale-variant formulation introduces a parameter defined by Perfect (1997) as a *probability of survival*, that defines the largest fragment produced by an initiator. Here, the *probability of survival* has been renamed as Survival rate to define the largest fragment over the initial block volume. We calibrate the upgraded model using the data collected from 7 inventoried rockfalls. We use the same set of parameters for all the blocks of each rockfall event, being a set of average parameters of the fragmentation model, despite the fact that the set of parameters may be specific of each block, depending on the impact conditions. Figure 20 shows the results of the model calibration with the rockfall events of Gurp, Monasterio de Piedra, Malanyeu, and Cadi.

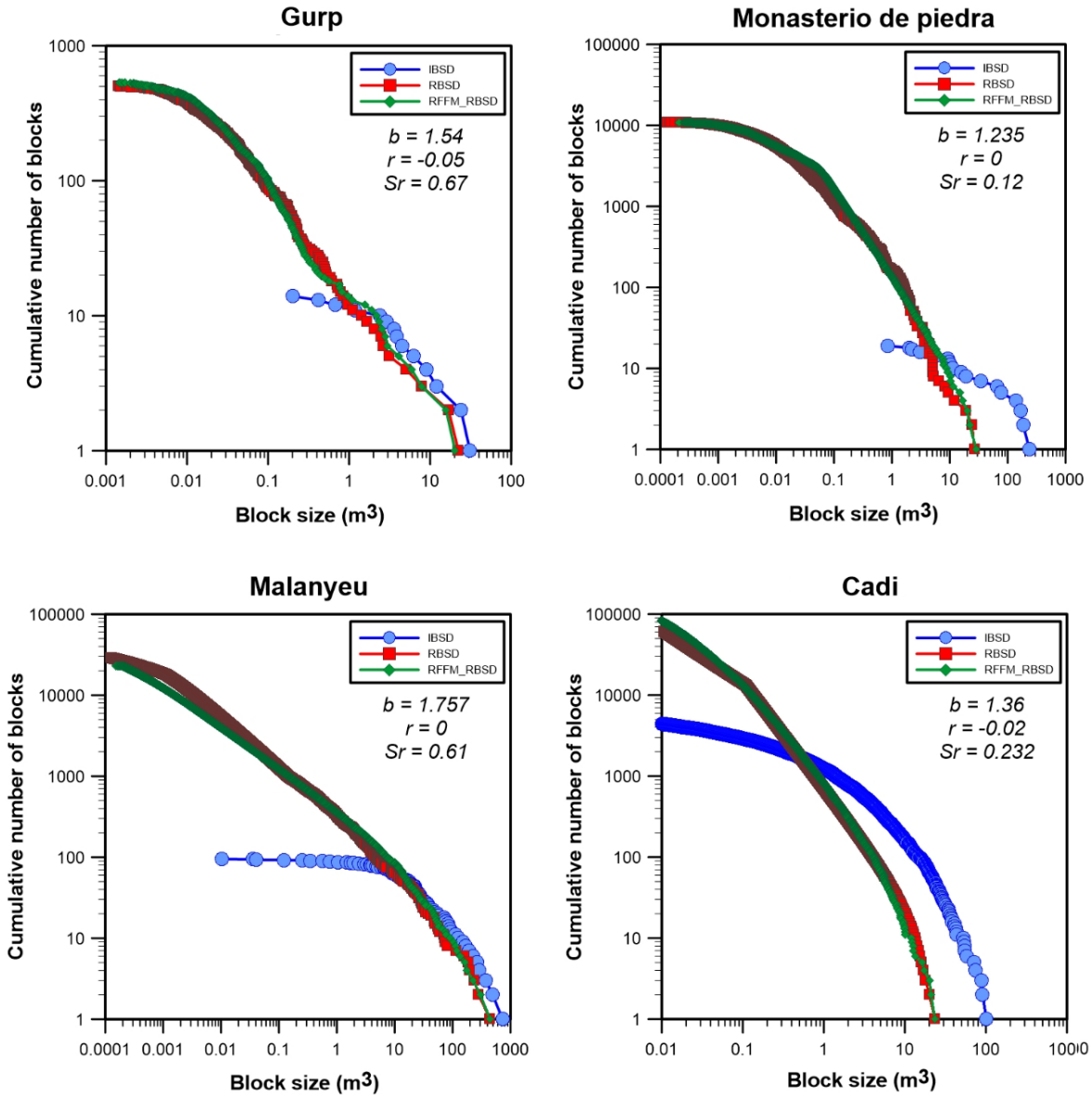

Figure 20: RFFM calibrated using the RBSD and the IBSD of the Gurp, Monasterio de Piedra, Malanyeu and Cadi rockfall events.

The model is able to reproduce correctly the number of blocks as well as the entire block size distribution. The number of fragments increases with the total rockfall volume as may be expected (Figure 21, left). Pont de Gulleri rockfall (PdG in Figure 21) shows a higher number of blocks than the other cases, also normalizing the number of blocks by the total rockfall volume (Figure 21, right). The higher or lower value of the initial number of blocks is related to the degree of fracturation of the rock mass, as well as to the uncertainties in the IBSD estimation procedure.

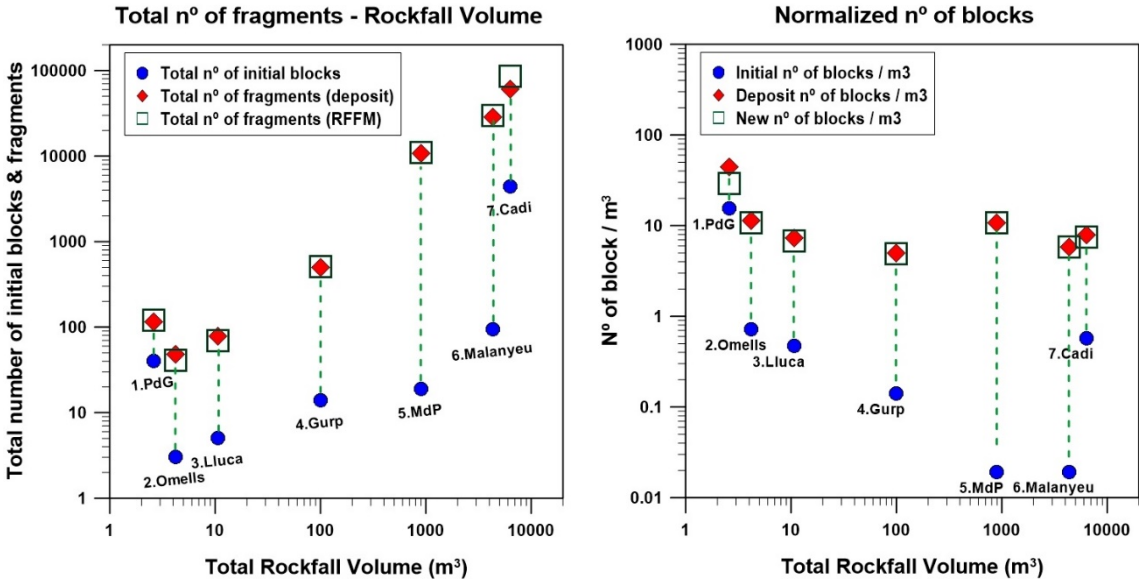

Figure 21: Left: Total number of initial blocks (from the IBSD estimation, blue dots), fragments measured on the deposit (red dots) and fragments resultant from the model calibration (green squares); Right: number of blocks normalized by the total rockfall volume.

We calculate the new surface area created by comparing the total fragment surface area and the initial surface area of the IBSD. The new area created, which may be related to the fragmentation energy, shows good correlations with the total rockfall volume and with the total potential energy (Figure 22).

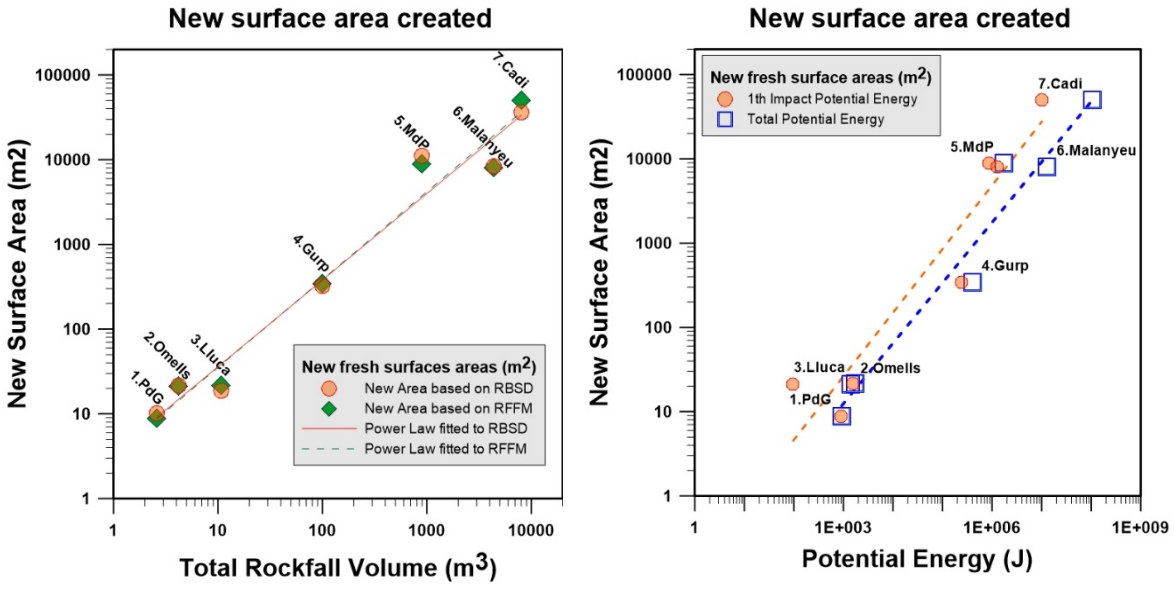

Figure 22: New surface area versus Total rockfall volume (left) and versus Total Potential Energy and 1st Impact Potential Energy (right).

The Specific Surface Area (SSA) is calculated normalizing the surfaces areas by the total rockfall volume, obtaining the Initial, the New and the Total Specific Surface Area (ISSA, NSSA, and TSSA respectively) plotted in Figure 23 (left). Also, the proportion of NA/TA (equal to NSSA/TSSA) is plotted as a percentage. The ISSA column represents the initial surfaces area per volume unit of the IBSD, defining the initial degree of fracturation of the rock mass. The NSSA quantify the new area created by breakage. Then, from our point of view of fragmentation, the bars represent the proportion between disaggregation (surfaces already existing in the IBSD) and breakage (new surfaces). Pont de Gulleri rockfall (PdG) shows the higher values of TSSA, but only the 21% is related with the new area, being the disaggregation the predominant mechanism in this case. Monasterio de Piedra (MdP), Cadi and Omells events, show TSSA values close to 10 m^2/m^3 with different proportion of new surfaces: 87%, 65%, and 49% respectively, being the Monasterio de Piedra the event with greater breakage, followed by the Cadi event. In comparison, Lluçà, Gurp and Malanyeu cases show smaller values of TSSA, and may be interpreted as events with less breakage. In the latter events, a few blocks remain unbroken or less affected: Lluçà with a block of 8,5 m^3 over the 10,7 m^3 of total detached mass; Gurp with two blocks of more than 20 m^3 over the total 100 m^3 of rockfall; and Malanyeu, where the deposit includes 7 blocks greater than 100 m^3, and more than 60 blocks greater than 10m^3, with a maximum boulder of 445 m^3.

The model parameters (*b* and *Sr*) show a good correlation with the proportion of new area over the total area (NA/TA) (Figure 23, right). By decreasing the model parameters, the proportion of breakage over disaggregation increases.

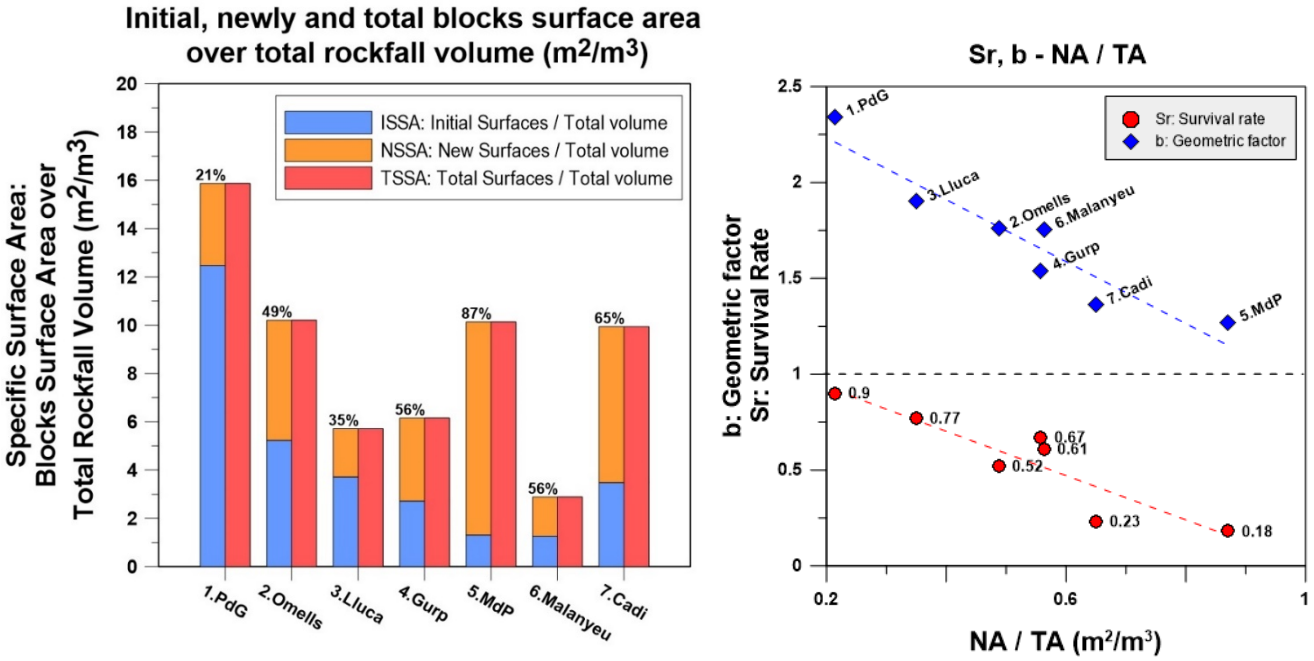

Figure 23: Left: Initial (blue), new (orange) and total (red) specific surface areas of each rockfall inventoried. Right: Model parameters versus Nea Area over Total Area (NA/TA).

PART 4: Applications

The improvements in data acquisition systems by means of UAV surveys and digital photogrammetric techniques, as well as the joint pattern characterization and identification unstable volumes identification, are useful in other research lines. The **Chapter 11: "Magnitude and Frequency relations: are there geological constraints to the rockfall size?"** presents an application of these methodologies in identifying the maximum credible volume at a particular cliff in Andorra. The analysis of the geological structure of the rock mass at the Solà d'Andorra allows us conclude that the size of the failures is controlled by the fracture pattern and that the maximum size of the failure is constrained. by the existence of faults in the rock mass. Finally, fragmentation strongly affects the results of the quantitative risk analysis (QRA). **Chapter 12: "Quantitative Analysis of Risk due to Fragmental Rockfalls"** presents an example of a QRA of fragmental rockfalls. The fragmentation of the falling rock mass is integrated in a rockfall trajectory simulator to quantify runout, impact energy, and the probability of impact. The identification of unstable volumes is also an important part of the risk analysis. Figure 24 shows a group of unstable rock volumes identified and colored by failure susceptibility based on expert judgment and some indicators as previous failures, aperture of fissures, and persistence.

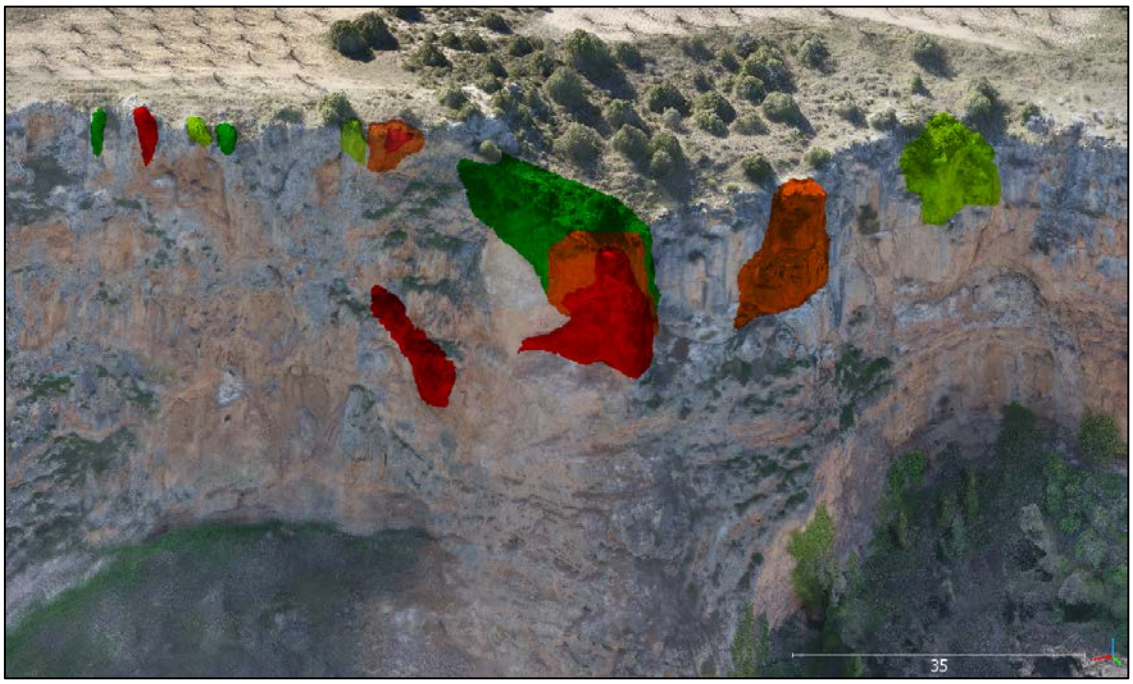

Figure 24: 3D models of the unstable rock volumes identified in Monasterio de Piedra, colored by failure susceptibility from low (green) to medium (orange) and high (red).

The results of the QRA analysis show that fragmentation has a significant but contrasting effect on the calculation of risk. The overall risk may be reduced if the slope where blocks propagate is both long and gentle enough before reaching the analyzed section. The reason is that, compared

to the unfragmented rock masses, the new fragments generate short travel distances with lesser kinetic energy. This effect vanishes in case of large rockfalls. Conversely, the risk increases if rock blocks propagate over steep slopes and the distance to the analyzed section is short. The reason is that the exposure increments due to the generation of a cone of fragments. Our simulations also have shown that the segregation of the visitors' flow has only a minor influence on the results of the risk analysis. Finally, the consideration of fragmentation provides additional criteria for the assessing the efficiency of the rockfall protective measures. Figure 25 shows the results of a rockfall simulation with fragmentation in a case where fragmentation may be favorable in terms of reducing the fragments runout. Figure 26 shows two simulations in a steeper slope (with a single block or an IBSD as the initiator, left and right respectively) where fragmentation plays an unfavorable effect increasing the number of fragments that reach the trail below, increasing the probability of impact and modifying the hazard map characterization.

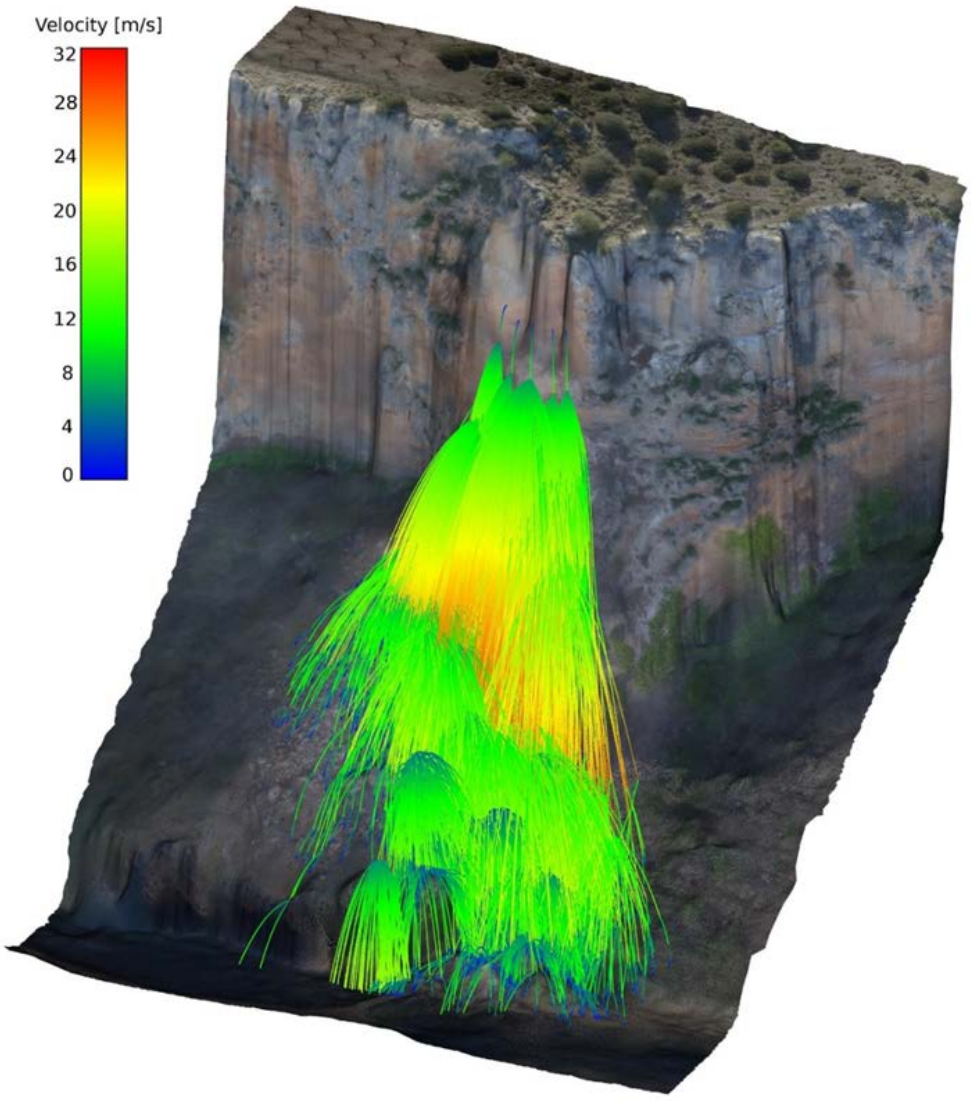

Figure 25: Rockfall simulation considering fragmentation in a case where fragmentation may play a favorable role due to the decrease the runout and the impact energy of each block (from Gerard Matas).

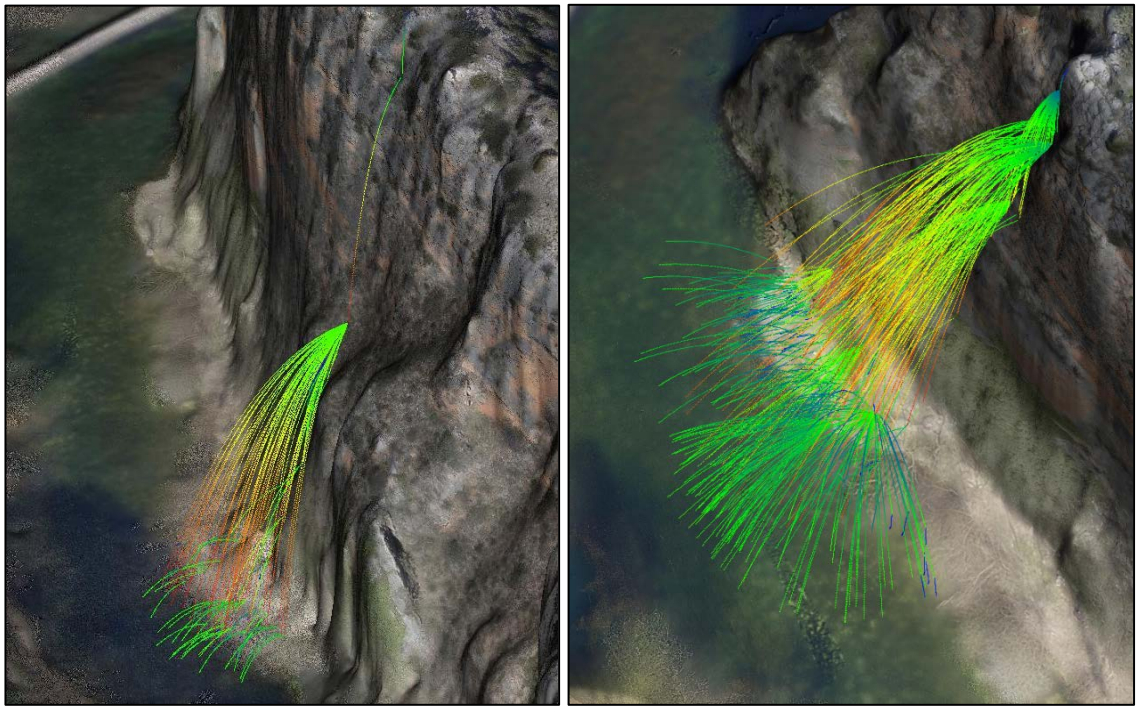

Figure 26: Rockfall simulation considering fragmentation in a case where fragmentation may play an unfavorable role due to the increase of fragments and then, the increase of the probability of impact. Left: with a single block as the initiator. Right: with an IBSD as initiator (from Gerard Matas).

Now, every time that we have to deal with rockfalls and perform risk analysis, hazard maps or trajectory simulations, we have to start asking whether the hypothesis of “no fragmentation” is on the ssafe side. It will depend on each scenario geometry. Figure 27 summarises some of the questions that must be asked in front of a fragmental rockfall analysis. For example, a steeped (a) or a long and gentle slope (b).

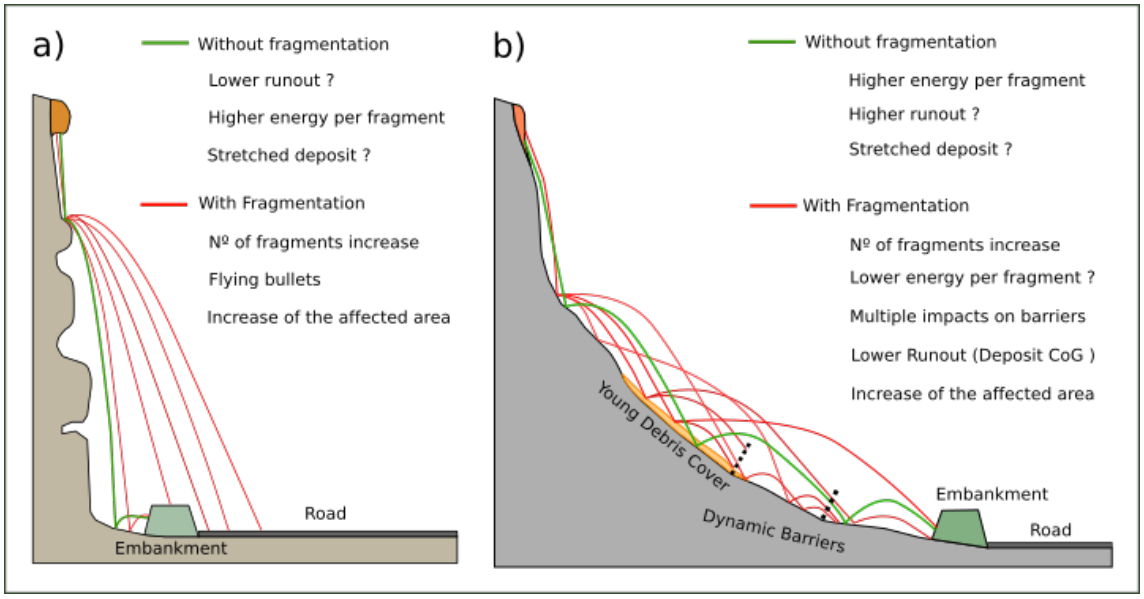

Figure 27: Schema of fragmental rockfall scenarios and possible fragmentation scenarios.

1.3 Tools developed

In order to achieve the main objectives of the present thesis, some tools have been developed. An important time-consuming task has been devoted to the construction of our own drones at the beginning of this technology for civil purposes (2013-2015). In the inventoried rockfalls, the UAV surveys and the digital photogrammetry has played an important role. The huge amount of information and high resolution allows a full recording of the event and the storage of a big amount of data that will be used in future research. To this end, the author of this thesis obtained the drone pilot license necessary to operate under the Spanish regulations. Futhermore, he constructed, in collaboration with Sjædric Moreno, 3 drones: a DJI F-450 quadcopter (Figure 28); an original design of a fiber hexacopter (Figure 29) and a DJI S900 (Figure 30). We also use other drones like DJI Inspire 1 Pro (Figure 30 on the right) and DJI Inspire 2 (Figure 9).

Figure 28: DJI F450 quadcopter mounted and used at the beginning of our research.

Figure 29: Self-constructed and based on our own design of a hexacopter (HexaCarbonFrame), in collaboration with Sjædric Moreno Coscoll as designer, constructor and drone pilot.

Figure 30: DJI-S900 sefl-mounted with a Sony NEX5 camera (left) and DJI-Inspire 1Pro with the camera X5 (right).

From another point of view, some tools have been developed in order to implement the fragmentation models proposed. The fragmentation model proposed in Chapter 9 has been implemented in an Excel worksheet in order to calibrate the model and learn how it works (Figure 31).

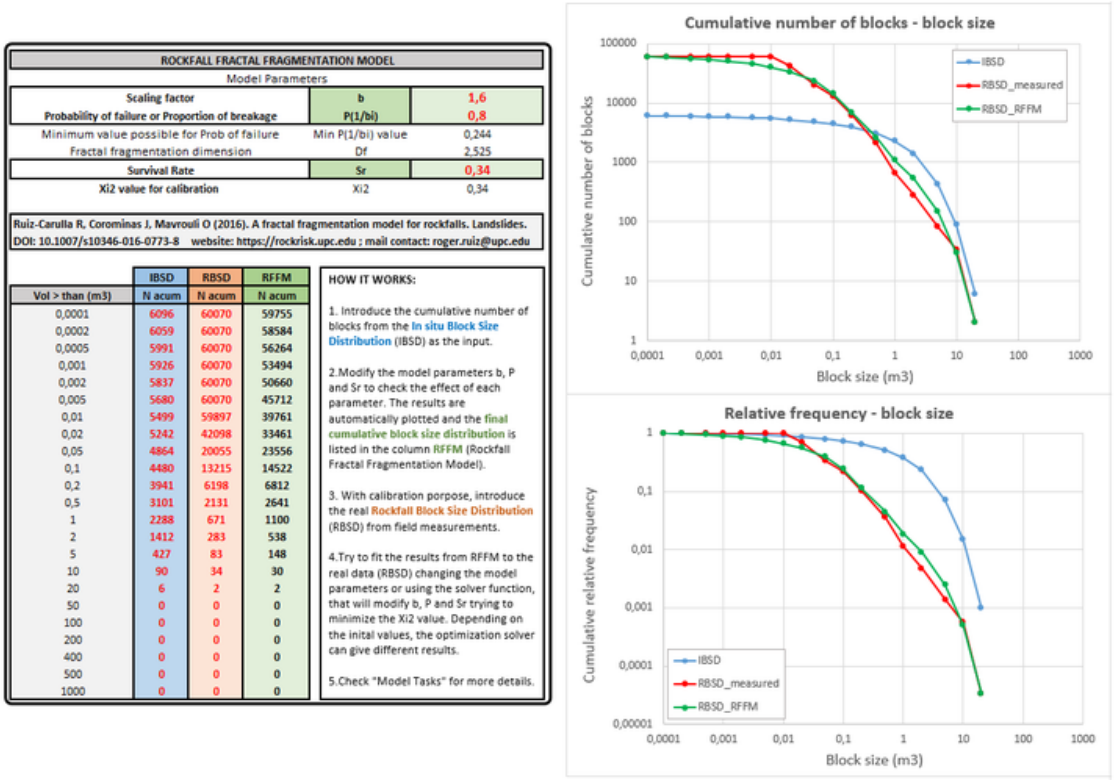

ROCKFALL FRACTAL FRAGMENTATION MODEL

Model Parameters

Scaling factor	b	1,6
Probability of failure or Proportion of breakage	P(1/bi)	0,8
Minimum value possible for Prob of failure	Min P(1/bi) value	0,244
Fractal fragmentation dimension	Df	2,525
Survival Rate	Sr	0,34
Xi2 value for calibration	Xi2	0,34

Ruiz-Carulla R, Corominas J, Mavrouli O (2016). A fractal fragmentation model for rockfalls. Landslides. DOI: 10.1007/s10346-016-0773-8 website: https://rockrisk.upc.edu ; mail contact: roger.ruiz@upc.edu

	IBSD	RBSD	RFFM
Vol > than (m3)	N acum	N acum	N acum
0,0001	6096	60070	59755
0,0002	6059	60070	58584
0,0005	5991	60070	56264
0,001	5926	60070	53494
0,002	5837	60070	50660
0,005	5680	60070	45712
0,01	5499	59897	39761
0,02	5242	42098	33461
0,05	4864	20055	23556
0,1	4480	13215	14522
0,2	3941	6198	6812
0,5	3101	2131	2641
1	2288	671	1100
2	1412	283	538
5	427	83	148
10	90	34	30
20	6	2	2
50	0	0	0
100	0	0	0
200	0	0	0
400	0	0	0
500	0	0	0
1000	0	0	0

HOW IT WORKS:

1. Introduce the cumulative number of blocks from the In situ Block Size Distribution (IBSD) as the input.

2.Modify the model parameters b, P and Sr to check the effect of each parameter. The results are automatically plotted and the final cumulative block size distribution is listed in the column RFFM (Rockfall Fractal Fragmentation Model).

3. With calibration porpose, introduce the real Rockfall Block Size Distribution (RBSD) from field measurements.

4.Try to fit the results from RFFM to the real data (RBSD) changing the model parameters or using the solver function, that will modify b, P and Sr trying to minimize the Xi2 value. Depending on the inital values, the optimization solver can give different results.

5.Check "Model Tasks" for more details.

Figure 31: Excel sheet programmed with the Rockfall Fractal Fragmentation Model proposed.

Chapter 10 presents the upgrades of the model, with a completely new code and new features. The model allows the generation of large and continuously decreasing fragment size distribution from a single block or an IBSD as input. Scale-invariant and scale variant behavior has been implemented with automatic input parameters modifications. The new code has been implemented in Matlab. A graphic interface (Figure 32) is developed to load easily the IBSD and the RBSD from excel files using a button, as well as the exportation of the RFFM results in .txt or excel format. An optimization method has been implemented, minimizing the error (described by the reduced Xi^2) using the RBSD as truth and obtaining the best fitting model parameters on a predefined range of values and precision.

The graphics interface shows the results in terms of the cumulative number of blocks, relative frequency, the percentage of blocks passing, the percentage of volume passing and cumulative volume, all of them versus block size in log-log plots. The program also shows the Xi^2 fragment per fragment and the variation of the probability of failure and the fractal fragmentation dimension in the case of scale variant behavior.

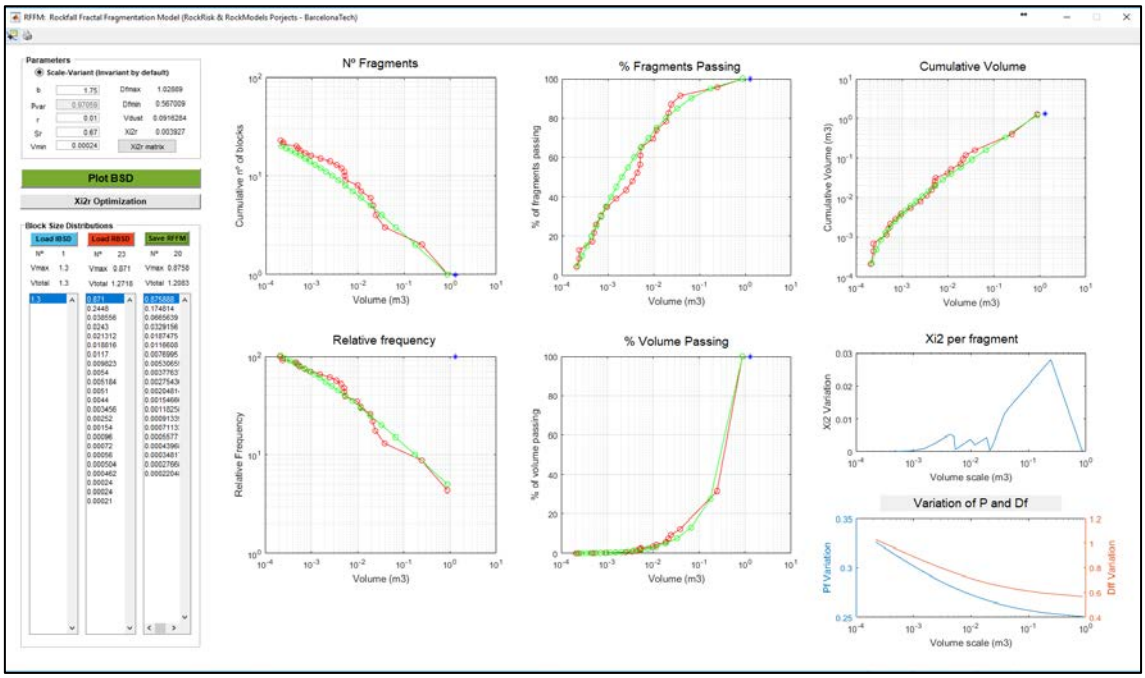

Figure 32: Graphics interface of the Matlab code developed with the upgraded Rockfall Fractal Fragmentation Model presented in Chapter 10.

1.4 Conclusions and future work

The main conclusion of this thesis is that fragmentation of rockfalls cannot be neglected due to its effects on the rockfall risk quantification. The assumption of "no fragmentation" is not always at the safe side.

Fragmentation on rockfalls is a natural process in earth surface dynamics. By measuring fragments from natural rockfalls and listing their volumes, a clear power law is observed (straight line on log-log plot). It indicates the same behavior in several orders of magnitude, becoming a fractal behavior. In order to characterize and reproduce the phenomenon, a fractal fragmentation model for rockfalls is proposed. The model has the capability to reproduce the observed block size distribution by defining the volume and number of fragments. The calibration of the model is carried out using the data from an exhaustive rockfall inventory of 7 fragmental rockfall events. The UAV systems combined with digital photogrammetry are very efficient and useful in order to characterize the scenario generating high-resolution 3D models. To calibrate the results, we measured 7200 fragments in the field with a tape to estimate their volumes.

Breakage of a rock block implies the creation of a new surface area which is related to the energy spent on it. The new surface area created in the fragments of inventoried rockfalls is calculated and shows a satisfactory correlation with the total rockfall volume and with the potential energy of each event. However, real-scale fragmentation tests in a very controlled scenario, show a wide range of results, without correlation with the potential or kinetic energy. This means that there is not possible to define an energetic threshold for each individual block. However, as we introduce more energy in the system, a higher number of fragments and new surfaces are produced.

The real-scale fragmentation tests allow the identification of the factors controlling fragmentation, such as the terrain rigidity or the impact angle. The type of impact (vertex, edge or face) and the anisotropies and planes of weakness inside the rock are difficult to evaluate beforehand and often impossible to predict. Due to this, the phenomenon has a stochastic behavior that should be considered in the analyses.

From the point of view of the risk, fragmentation has contrasting effects: on one hand, the breakage of the falling rock mass increases the number of fragments, and then, and increases the probability of impact. Sometimes, multimpact may be more dangerous than a single impact, depending on the elements exposed and their vulnerability. On the other hand, the breakage implies the reduction in volume, which reduces both the impact energy and the runout distance.

Thus, depending on the geometry of each scenario, as well as the vulnerability of the exposed elements, fragmentation may increase or reduce the rockfall hazard.

In order to identify the control factors, in the future we will enlarge the inventories and carry out more real-scale tests. All the data collected may be used in a Rock Engineering System to weight each controlling factor. Another research line is the simulations with discrete elements methods to build a meta-model to be integrated on a trajectory simulator. It is currenly possible to carry out simulations from "no fragmentation increasing block breakage progressively in order to identify the worst case of each specific scenario.

For these reasons, the main conclusion is the following: Is the assumption of no fragmentation at the safe side of security when performing rockfall simulations? It depends. The disaggregation of the rock mass due to the preexisting block volumes is unavoidable. The breakage behavior may be different at each event, even the rockfall occurs in the same cliff as we observe on specific site inventories in Andorra or in the real-scale fragmentation tests.

Detailed conclusions and future works by parts:

PART I: Rockfall measurements and characterization

About methodologies and techniques to characterize rockfall events

-A sampling-procedure is proposed in Chapter 2 for the construction of the block size distribution of a fragmental rockfall deposit (Rockfall Block Size Distribution, RBSD). The fragments follow power law distributions. The exponent of the fitted power law is related with the fractal dimension and could be used as a descriptor of the fragmentation process. The RBSD from different inventoried rockfalls (Chapter 3) suggests that these exponents could be related to the height of fall and to the proportion of new surfaces generated by breakage, among other factors.

-The RBSD is not enough to study the fragmentation phenomenon, and it should be compared with the initial state of the detached rock mass, defined by the In situ Block Size Distribution (IBSD).

-The estimation of an IBSD depends on the volume detached (shape and location), the joint sets present in the cliff that predefine the number of blocks, and their relative position. For these reasons, a detailed 3D model of the source area is required to estimate the IBSD. The procedure is done by means of 3D point cloud analysis and 3D texturized mesh as best formats to deal with this kind of procedures.

- UAV combined with photogrammetry techniques can provide a large amount of information of high quality. Their use in the description of slope instabilities, characterization of discontinuities, delimitation of unstable volumes, as well as monitoring tasks, will be essential in order to improve the performance, safety and efficiency of the field work (Chapter 4).

-The 3D models allow the generation of high-resolution maps (topography, orthophotos, DEM, etc) as well as the obtention of real terrain profiles from point clouds, particularly the overhangs. The high-resolution orthophotos (0.7 cm/px to 3 cm/px) enable the elaboration of very detailed cartographies and the identification of missing elements in field work.

- The collected data in the fragmental rockfall inventory (Chapter 6) will be used in future developments of rockfall propagation models and to calibrate procedures for automatic volume identification and calculation of fragments using image and 3D analyses.

-The safety during the inventory tasks is importantly enhanced using the UAV, substantially reducing the exposure in the hazardous zones and, at the same time, obtaining a huge amount of high-quality information.

About joint pattern characterization:

-The parameters used in order to fit facets on a point cloud (joint face identification with the plugin *Facet Matching* or other tools) should be tested at every site, due to the variation of the point cloud density, the degree of roughness, the waviness; and the scale relation between the interesting joints and the scenario studied. All of them controls the resultant facets or joints identified.

-The *Compass* tool from CloudCompare (Thiele, et al 2017) is very useful in order to characterize in a fast way the more evident joint faces. Also, the capability to characterize traces improves the characterization of the joint pattern. It may be exported to create volume reconstructions or an IBSD with software like Rhinoceros, Polyworks, or directly to be used in discrete elements methods codes.

-The estimation of the IBSD of each case is based on observed joint faces or traces that are extended with the assumption of infinite persistence. Neither joint spacing measurements nor statistical reconstructions are used. The influence of the IBSD is very important on a rockfall event, defining the initial block volumes that may create different trajectories and breakage processes depending on the propagation scenario. For this reason, the unstable volume identification and the joint pattern characterization is a fundamental tasks in rockfall prevention and analysis studies.

PART 2: Real-scale fragmentation tests

- Real-scale fragmentation tests allow the measurement and observation of the rock fragmentation phenomenon in a very controlled scenario and with the capability of to repeat the experiment. The results show large variations of the breakage behavior for the same conditions within each test.

-The results indicate that the size distribution of rockfall fragments can be expressed by power laws, which exponents are indicators of the degree of fragmentation. Although an energy threshold could be expected for the breakage of the blocks, the kinetic energies measured, the potential energy and the Schmidt hammer values show poor correlations with the number of fragments generated.

- We propose the combination of the Survival rate and the number of fragments as descriptor of the fragmentation. Different behaviors were observed at the testing sites.

-Comparing the data obtained from 4 real-scale fragmentation test, some insights of controlling factors may be derived. The difference between the Test 3 and the Test 4, ranging from Sr and number of fragments defines the possibles ranges that may be used in stochastic simulations.

-All range of fragmentation features are observed in test site 1. A contrasting behaviors is observed in test site 2, the rock blocks that break and the ones that not too much. test site 3, involved very soft terrain of the ground surface. Most of the blocks remain unbroken, with Sr > 0.85, but producing fragments between 2 to 100 fragments. At the other end, testing site # 4, Sr ranges from 0.2 to 0.8. Most of the blocks generate more than 40 fragments. Based on these observations, we conclude that, despite some trends are identified, the fragmentation cannot be modelled in a deterministic way.

-The rigidity or capacity to absorb energy of the terrain is found a main controlling factor of fragmentation in the drop tests. Similarly occurs with the impact angle. Other parameters such as the relative impact direction of the main rock block anisotropies (fissures or planes of weakness of the block) as well of the type of impact (vertex, edge or face) are features that can be hardly taken into account in the simulations. Only discrete elements methods can deal with these features and the deterministic modelling of real events is still a challenge.

-The real-scale fragmentation tests therefore provide a large amount of high-quality data that we will be precoessed in the future: energies, impact angles, initial block fractures studies, as well as all the information needed in order to calibrate fragmentation models, propagation models and discrete elements methods.

PART 3. Rockfall Fractal Fragmentation Model

- Based on the empiricial observations presented in PART I and PART II, we proposed a Rockfall Fractal Fragmentation Model (RFFM). It is model that simulates the passage from from the In Situ Block Distribution (IBSD), to the Rockfall Block Size Distribution, RBSD. The models is based on fractal laws and works using three-parameter. The results of the model may vary depending on the assumptions made for the joint pattern in the procedure to estimate the IBSD.
-The RFFM proposed in Chapter 9 uses bins to classify the IBSD and the RBSD, as well as the results. Because of this, the condition of mass balance is not fulfilled. To overcome this problem, we present in chapter 10 the upgraded model that works with all the blocks from the IBSD, applying the model on each block, avoiding the use of bins and accomplishing the mass balance.

-The upgraded model is able to reproduce the block size distributions observed in both natural fragmental rockfall events and real scale tests. The input of the model may be either a single block or the IBSD. An interesting upgrade of the model is the use of scale-variant formulation, that is able to generate block size distributions with irregular shapes.

- The model parameters are calibrated using the same set of parameters *b, r,* and *Sr* for all the blocks of each rockfall event. The calibrated values of the geometric factor "*b"* range between 1.235 and 2.34, and the Survival rate from 0.18 to 0.9. In all the cases, the Xi_r^2 used to calibrate the model ranges between 0.0004 and 0.018.

-Future trajectory simulators considering fragmentation will be able to apply a different set of parameters for each block at each impact. The controlling factors are the focus of our future

research. Currently, the capacity to absorb the energy of the terrain, despite its relevance is difficult to quantify, as well as the total potential energy, the impact conditions (impact angle) and the shape of the blocks.

-The rock mass properties such as the RMR show a positive correlation with the survival rate, however, the correlation with the geometric factor *b* is weak. Similarly occurs with the correlation with the Uniaxial Compressive Strength and the Tensile Strength without direct correlations. It may be noticed a relation between the 3d surface area of the scar and the total rockfall volume, as well as the number of fragments and new area created in a wide range of orders of magnitude. The new area created is related with the fragmentation energy and seems to be directly correlated with the total rockfall volume as well as total potential energy.

-The specific surface area of the initial blocks (ISSA) and of the resultant fragments (TSSA) are used as fragmentation indicators. The proportions of Initial, New and Total Specific Surface Area of the blocks characterize the fragmentation event. The ISSA (Initial Specific Surface Area) is the one defined by the preexisting discontinuities, and is determined by the IBSD. There exists a direct relationship between the NSSA (New Specific Surface Area) and the breakage of the rock creating new surfaces. Based on this, we interpret the more or less predominant fragmentation behavior based on the proportion of New Surface Area over Total Surface Area (NA/TA = NSSA/TSSA). The model parameters show a clear correlation with the proportion of NA/TA.

-Unfortunately, the number of inventoried cases is too small to generalize these findings. The fragmentation process is a very complex phenomenon where small details that may affect the final results. From real-scale fragmentation test, we observed how 30 similar blocks dropped from the same height on the same place yields Sr ranging between 0.2 and 1 (unbroken) depending on the local impact conditions and the block shape. For these reasons, a probabilistic approach of the fragmentation should still be used.

-The final purpose of this ongoing research is to highlight the influence of the fragmentation on rockfall propagation and provide tools to consider it on a trajectory rockfall simulator. Quantitative risk assessment studies should also consider the implications of fragmentation that can modify the hazard by the number of fragments, the runout, the mass distribution, and then, the impact energies and probabilities of impact.

PART 4. Aplications

-All the knowledge about fragmentation and the tools and data acquisition systems developed and improved during the research for this thesis, can be applied other research domains and to real rockfall assessment cases.

-The magnitude frequency relations are used in a wide range of natural phenomena. Also, for the period of return of a rockfall (or mass movements) of a certain size or magnitude. This relation is also characterized by a power law, and then, can be interpreted as a fractal or with fractal behavior.

-As we observe from the real-scale fragmentation test and from the rockfalls inventories, the fractals laws are not completely scale-invariant, and often the trend on a singular order of magnitude, varies for some reason. The change of behavior can be controlled by the scale of the rock mass with joints, the spacing of the joints, and below the minimum spacing, the rock matrix might affect the slope of the power law.

-The results from the QRA analysis show that fragmentation has a significant but contrasting effect on the calculation of risk. The overall risk may be reduced if the slope where blocks propagate is both long and gentle enough before reaching the analyzed section. The reason is that, compared to the unfragmented rock masses, the new fragments generate short travel distances with lesser kinetic energy. This effect vanishes in case of large rockfalls. Conversely, the risk increases if rock blocks propagate over steep slopes and the distance to the analyzed section is short. The reason is that the exposure increments due to the generation of a cone of fragments. Our simulations also have shown that the segregation of the visitors' flow has only a minor influence on the results of the risk analysis. Finally, the consideration of fragmentation provides additional criteria for the assessing the efficiency of the rockfall protective measures

References

Agliardi F, Crosta G (2003) High resolution three-dimensional numerical modelling of rockfalls. International Journal of Rock Mechanics and Mining Sciences vol. 40, 4, pp. 455-471

Agliardi F, Crosta G, Frattini P (2009) Integrating rockfall risk assessment and countermeasure design by 3D modelling techniques Nat. Hazards Earth Syst. Sci., 9 , pp. 1059–1073 http://dx.doi.org/10.5194/nhess-9-1059-2009

Aler J, Du Mouza J, Arnould M (1996) Measurement of the Fragmentation Efficiency of Rock Mass Blasting and its Mining Applications. Int. J. Rock Mech. Min. Sci. & Geomech. Abstr., 33: 125-139

Asteriou P, Saroglou H, Tsiambaos G. 2012. Geotechnical and kinematic parameters affecting the coefficients of restitution for rock fall analysis. International Journal of Rock Mechanics & Mining Sciences 54: 103–113

Bakar MZ, Gertsch LS, Rostami J (2014) Evaluation of Fragments from Disc Cutting of Dry and Saturated Sandstone. Rock Mech Rock Eng, 47:1891–1903

Blasio F. V., Corsta G. B. (2016) Extermly Energetic Rockfall: Some Preliminar estimates. 12th International Symposium on Landslides (ISL 2016) Landslides and Engineered Slopes. Experience, Theory and Practice – Aversa et al. (Eds) © 2016 Associazione Geotecnica Italiana, Rome, Italy, ISBN 978-1-138-02988-0.

Bourrier F, Dorren L, Nicot F, Berger F, and Darve F. 2009. Toward objective rockfall trajectory simulation using a stochastic impact model. Geomorphology, 110: 68-79

Bowman ET, Andrew Take W (2014) The Runout of Chalk Cliff Collapses in England and France — Case Studies and Physical Model Experiments." Landslides, Volume 12 (2), pp: 225-239. doi: 10.1007/s10346-014-0472-2

Bond F C (1952) The third theory of comminution, Transactions of the American Institue of Mining and Metallurgical Engineers, 193. 494-495

Brideau M, Sturzenegger M, Stead D, Jaboyedoff M, Lawrence M, Roberts N, Ward B, Millard T, Clague J (2012) “Stability Analysis of the 2007 Chehalis Lake Landslide Based on Long-Range Terrestrial Photogrammetry and Airborne LiDAR Data.” Landslides 9: 75–91. doi:10.1007/s10346-011-0286-4.

Buyer A and Schubert W (2017) Calculation the Spacing of Discontinuities from 3D Point Clouds. Symposium of the International Society for Rock Mechanics. Procedia Engineering 191: 270 – 278. https://doi.org/10.1016/j.proeng.2017.05.181

Chakraborty AK, Raina AK, Ramulu M, Choudhury PB, Haldar A, Sahu P (2004) Parametric study to develop guidelines for blast fragmentation improvement in jointed and massive formations. Eng Geol, 73: 105–16.

Charrière M, Humair F, Froese C, Jaboyedoff M, Pedrazzini A, Longchamp C (2015) From the source area to the deposit: Collapse, fragmentation, and propagation of the Frank Slide. Geological Society of America Bulletin. doi: 10.1130/B31243.1

Chau KT, Wong RHC, Wu JJ (2002) Coefficient of restitution and rotational motions of rockfall impacts. Int J Rock Mech Min Sci. 2002;39(1):69–77.

Crosta GB, Agliardi F (2004) Parametric evaluation of 3D dispersion of rockfall trajectories. Nat Hazards Earth Syst Sci 4:583–598

Crosta GB, Frattini P, Fusi F (2007) Fragmentation in the Val Pola rock avalanche, Italian Alps. Journal of Geophysical Research, 112: p. F01006

Crosta GB, Agliardi F, Frattini P, Lari S, Lollino G (2015) Key Issues in Rock Fall Modeling, Hazard and Risk Assessment for Rockfall Protection. Engineering Geology for Society and Territory, Volume 2, pp: 43-58. doi: 10.1007/978-3-319-09057-3_4

Cunningham CVB, (1983) The Kuz-Ram model for prediction of fragmentation from blasting. In: Proceedings of the First International Symposium on Rock Fragmentation by Blasting, 22–26 August , Lulea, Sweden, pp. 439–454

Cunningham CVB (1987) Fragmentation estimations and Kuz-Ram model – four years on. Proceedings of second International Symposium on rock fragmentation by blasting, Keystone, Colorado, p.475–87

Davies TR, McSaveney MJ, Hodgson KA (1999) A fragmentation-spreading model for long-runout rock avalanches. Canadian Geotechnical Journal, 36: 1096-1110

Dorren LKA (2003) A review of rockfall mechanics and modeling approaches. Progress in Physical Geography 27 (1): 69– 87

Evans S, Hungr O (1993) The assessment of rockfall hazard at the base of talus slopes. Canadian Geotechnical Journal 30 :620-636

Faramarzi F, Mansouri H, Ebrahimi Farsangi MA (2013) A Rock Engineering Systems Based Model to Predict Rock Fragmentation by Blasting. International Journal of Rock Mechanics and Mining Sciences 60: 82–94. doi:10.1016/j.ijrmms.2012.12.045.

Firpo G, Salvini R, Francioni M, Ranjith P (2011) Use of Digital Terrestrial Photogrammetry in rocky slope stability analysis by Distinct Elements Numerical Methods. International Journal of rock Mechanics and Mining Sciences 48:1045-1054

Gates WCB, Haneberg WC (2012) Comparison of Standard Structural Mapping Results to 3-D Photogrammetric Model Results : Boundary Transformer Banks Rockfall. American Rock Mechanics Association 12: 368.

Gheibie S, Aghababaei H, Hoseinie S H, Pourrahimian Y (2009) Modified Kuz – Ram fragmentation model and its use at the Sungun Copper Mine. International Journal od Rock Mechanics & Mining Sciences 46: 967-973. doi:10.1016/j.ijrmms.2009.05.003

Giacomini A, Buzzi O, Renard B & Giani, G P (2009) Experimental studies on fragmentation of rock falls on impact with rock surfaces. Int J Rock Mech Min Sci 46:708–715

Gili JA, Ruiz-Carulla R, Matas G, Corominas J, Lantada N, Núñez MA, Mavrouli O, Buill F, Moya J, Prades A, Moreno S (2016) Experimental study on rockfall fragmentation: in situ test design and firsts results. In: Aversa S, Cascini L, Picarelli L, Scavia C (eds) Landslides and engineered slopes, 2: 983-990.

Gischig V, Hungr O, Mitchell A, Bourrier F. 2015. Pierre3D - a 3D stochastic rock fall simulator based on random ground roughness and hyperbolic restitution factors. Canadian Geotechnical Journal 52(9). DOI10.1139/cgj-2014-0312

Grady DE, Kipp ME (1985) Mechanisms of dynamic fragmentation: factors governing fragment size. Mech Mater 4: 311–320

Guzzetti, F., Crosta, G., Detti, R., & Agliardi, F. (2002). STONE: A computer program for the three-dimensional simulation of rock-falls. Computers & Geosciences, 28(9), 1079–1093.

Haneberg WC, Norrish NI, Findley DP (2006) Digital Outcrop Characterization for 3-D Structural Mapping and Rock Slope Design along Interstate 90 near Snoqualmie Pass, Washington." Proceedings 57th Annual Highway Geology Symposium, 1–14.

Hantz D, Rossetti J P, Servant F, D'Amato J (2014) Etude de la distribution des blocs dans un éboulement pour l'évaluation de l'aléa. Proceedings of Rock Slope Stability 2014, Marrakesh, Morocco

Hardin BO (1985) Crushing of soil particles. J Geotech Eng 111(10):1177–1191

Haug ØT, Rosenau M, Leever K, Oncken O (2016) On the energy budgets of fragmenting rockfalls and rockslides: Insights from experiments, J. Geophys. Res. Earth Surface, 121, 1310–1327, doi:10.1002/2014JF003406.

Hou, T., Xu, Q., Xie, H. Xu N, Zhou (2017) An estimation model for the fragmentation properties of brittle rock block due to the impacts against an obstruction. Journal of Mountain Science, Vol 14 (6), pages: 1161-1173. https://doi.org/10.1007/s11629-017-4398-8

Hudaverdi T, Kuzu C, Fisne A (2010) Investigation of the blast fragmentation using the mean fragment size and fragmentation index. International Journal Rock Mechanics & Minning Science, Volume 56, pp: 136-145. http://dx.doi.org/10.1016/j.ijrmms.2012.07.028.

Hungr O, Evans S G, Hazzard J (1999) Magnitude and frequency of rock falls and rock slides along the main transportation corridors of southwestern British Columbia. Canadian Geotechnical Journal, 1999, 36(2): 224-238, 10.1139/t98-106

Hungr O, Leroueil S, Picarelli L (2014) The Varnes classification of landslides types, an update. Landslides 11:167-194

Jaboyedoff M, Dudt JP, Labiouse V (2005) An attempt to refine rockfall hazard zoning based on the kinetic energy, frequency and fragmentation degree. Natural Hazards and Earth System Sciences 5: 621–632

Kim DH, Gratchev I, Berends J, Balasubramaniam A (2015) Calibration of restitution coefficients using rockfall simulations based on 3D photogrammetry model: a case study. Natural Hazrads 78: 1931-1946 DOI 10.1007/s11069-015-1811-x
System Sciences 5: 621–632.

Latham. J. P. Lu. P. 1999. Development of an assessment system for the blastability of rock masses. International Journal of Rock Mechanics & Mining Sciences 36, 41-55. PII: S01 4 8- 90 6 2(98)0 0 17 5 -2.

Li L, Lan H (2015) Probabilistic modeling of rockfall trajectories: a review. Bulletin of Engineering Geology and the Environment 1: 1-14.

Locat P, Couture R, Leroueil S, Locat S (2006) Fragmentation Energy in Rock Avalanches. Canadian Geotechnical Journal 851 (20060135): 830–51. doi:10.1139/T06-045
Lu P, Latham JP (1999) Developments in the assessment of in-situ block size distributions in rock masses. Rock Mechanics and Rock Engineering, 32: 29-49

Matas, G., Lantada, N., Corominas, J., Gili, J.A., Ruiz-Carulla, R., Prades, A. 2017. RockGIS: a GIS-based model for the analysis of fragmentation in rockfalls. Landslides, 14: 1565–1578

F Noël, E Wyser, M Jaboyedoff, C Cloutier, J Locat (2017a) Development of a 3D rockfall simulation model for point cloud topography. EGU General Assembly Conference Abstracts 19, 16699

Noël F, Jaboyedoff M, Cloutier C, Mayers M, Locat J (2017b) The effect of slope roughness on 3D rockfall simulation results. 6th Interdisciplinary Workshop on Rockfall Protection RocExs 2017, p.31-34

Peng S, Zhi-wei X, Hou-quan Z, Yong-nian He (2009) Evolution of Blast Induced Rock Damage and Fragmentation Prediction. In The 6th International Conference on Mining Science & Technology, 585–91

Perfect E (1997) Fractal models for the fragmentation of rocks and soils: a review. Engineering Geology 48:185-198

Rittinger, P. R. "Lehrbuch der Aufbereitungskunde," Berlin, 1867.

Ruiz-Carulla R, Corominas J & Mavrouli O (2015). A Methodology to Obtain the Block Size Distribution of Fragmental Rockfall Deposits. Landslides, Volume 12, Issue 4: 815–25. doi:10.1007/s10346-015-0600-7.

Ruiz-Carulla, R., Matas, G., Prades, A., Gili, J., Corominas, J., Lantada, N., Buill, F., Mavrouli, O., Núñez-Andrés, M.A., Moya, J (2016). Analysis of rock block fragmentation by means of real-scale tests. In: International Symposium Rock Slope Stability. "International Symposium Rock Slope Stability 2016: proceedings". Lyon: Sage, 2016, p. 107-108.

Saavedra JC, Katsabanis PD, Pelley CW, Kelebek S (2006) A neural network model for fragmentation by blasting. In: Proceedings of the 8th international symposium on rock fragmentation by blasting. Santiago, Chile; p. 200–6

Shen WG, Zhao T, Crotsa GB, Dai F (2017) Analysis of impact-induced rock fragmentation using a discrete element approach. International Journal of Rock Mechanics & Mining Sciences, 98: 33–38. http://dx.doi.org/10.1016/j.ijrmms.2017.07.014

Spreafico MC, Franci F, Bitelli G, Borgatti L, Ghirotti M (2017). Intact rock bridge breakage and rock mass fragmentation upon failure: quantification using remote sensing techniques. The Photogrammetric Record Vol 32, Issue 160: Pages 513-536 https://doi.org/10.1111/phor.12225

Tavallali A, Vervoort A (2010) Effect of layer orientation on the failure of layered sanstones under Brazilian test conditions. International Journal of Rock Mechanics & Mining Sciecnes 47: 313-322. Doi: 10.1016/j.ijrmms.2010.01.001

Wang, Y, Tonon, F (2010) Discrete Element Modelling of Rock Fragmentation upon Impact in Rock Fall Analysis. Rock Mech Rock Eng 44: 23–35

Zhao T, Crosta GB, Utili S, Blasio FV (2017) Investigation of rock fragmentation during rockfalls and rock avalanches via 3-D discrete element analyses. Journal of Geophysical Research: Earth Surface, 122 doi:10.1002/2016JF004060

PART I

Rockfall measurements and characterization

2- A methodology to obtain the block size distribution of fragmental rockfall

3- Comparison of block size distribution of rockfalls

4- UAV experiences in mass movements

5- Unstable rock masses characterization using UAV

6- Fragmental rockfalls inventory

2. A methodology to obtain the block size distribution of fragmental rockfall deposits

This chapter reproduces the article published in the Landslides journal, on the procedure to determine the distribution of rock blocks volumes of a fragmental rockfall.

Publication reference:

Ruiz-Carulla R, Corominas J & Mavrouli O (2015). A Methodology to Obtain the Block Size Distribution of Fragmental Rockfall Deposits. Landslides, Volume 12, Issue 4: 815–25. doi:10.1007/s10346-015-0600-7.

Abstract:

Rock masses detached as rockfalls usually disintegrate upon impact on the ground surface. The knowledge of the Rockfall Block Size Distribution (RBSD) generated in the rockfall deposit is useful for the analysis of the trajectories of the rock blocks, run-out distances, impact energies and for the quantitative assessment of the rockfall hazard. Obtaining the RBSD of a large rockfall deposit may become a challenge due to the high number of blocks to be measured. In this paper, we present a methodology developed for mid-size fragmental rockfalls (10^3 up to $10^5 m^3$) and its application to the Cadí massif, Eastern Pyrenees. The methodology consists of counting and measuring block fragments in selected sampling plots within homogeneous zones in the young debris cover generated by the rockfall along with all the large scattered rock blocks. The size distribution of blocks obtained in the sampling plots is extrapolated to the whole young debris cover and summed to the inventoried large scattered blocks to derive the RBSD of the whole rockfall event. The obtained distributions from the fragments can be well fitted by a power law distribution, indicating the scale invariant character of the fragmentation process (Hartmann 1969 ; Turcotte, 1986). The total volume of the rockfall fragments has been checked against the volume at the rockfall source. The latter has been calculated comparing 3D digital surface models before and after the rockfall event.

Keywords: rockfall, fragmental rockfall, block size distribution, volume estimation

1. Introduction

Evans and Hungr (1993) and Hungr et al. (2014) reserved the term fragmental rockfall, for the events in which the individual fragments move as independent rigid bodies interacting with the ground surface by means of episodic impacts. They distinguished it from the term rock avalanche in which masses of fragments move in a flow-like way. In fragmental rockfalls, the detached rock mass, which often includes discontinuities, disaggregates, breaks or both, after the first impacts on the ground. The resultant fragments propagate independently downhill. The deposit of a fragmental rockfall is a set of rock blocks of different sizes scattered on the ground surface. In the case of mid to large-size fragmental rockfalls (more than thousands of cubic meters) a more or less continuous Young Debris Cover (YDC) can be formed as well (Fig. 1). Understanding the fragmentation process is fundamental for the analysis of the rockfall hazard, since it is a critical input datum for calculating the trajectories and the run-out of the rock fragments, the encounter probability with the elements at risk and the expected impact energies.

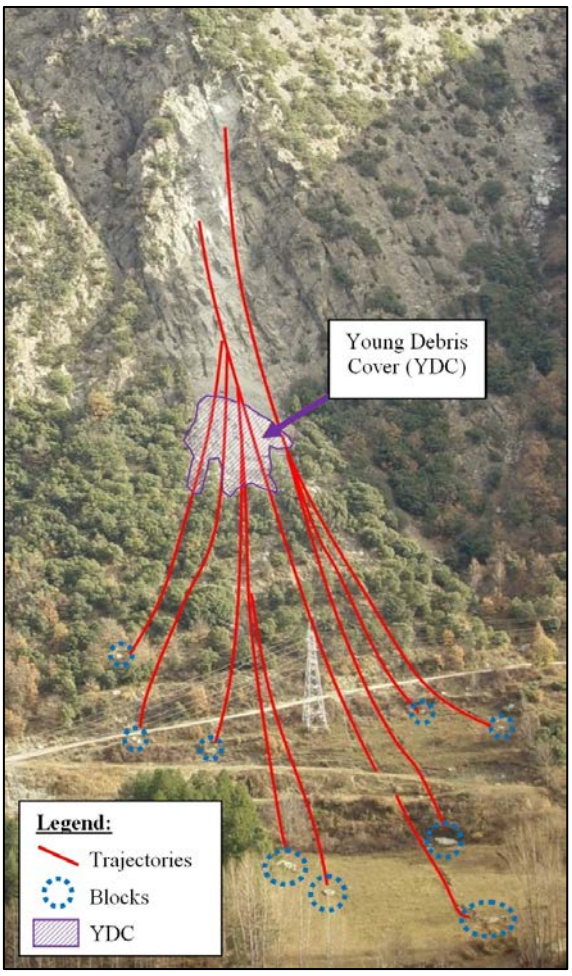

Fig. 1. Fragmental rockfall at La Guingueta, Central Pyrenees, Spain. The trajectories of the large scattered blocks diverge after the impact of the rock mass upon the ground surface. A young debris cover, composed of small-size blocks, has been deposited close to the rockfall source.

The importance of the rockfall fragmentation in the analysis of the rockfall hazard has been discussed by Jaboyedoff et al. (2005) and Corominas et al. (2012). The definition of the initial rockfall volume is crucial when performing the trajectographic analysis. Run-out analyses performed with the originally detached rock mass volume produce results, which are significantly different from those using individual rock blocks (Okura et al., 2000 ; Dorren 2003). Considering the initial rock mass leads to the overestimation of the rockfall kinetic energy and run-out. If the modal or the maximum block fragment size is used instead, the travel distances and the energies obtained are more realistic. However, the frequency and the impact probability are largely underestimated as in reality, the original rock mass splits into a large number of rock fragments, leading to the multiplication of the impact probability by a factor "n" equal to the number of new blocks generated. Taking this into consideration, the assessment of the size and number of blocks produced from an original rock mass is of primary importance for the rockfall risk analysis (Hungr et al. 1999). An indicator of the rockfall fragmentation is given by the Rockfall Block Size Distribution (RBSD).

Several parameters influence the fragmentation process and the RBSD (Dussauge et al. 2003; Wang & Tonon 2010; Hantz et al 2014): the presence of discontinuities in the detached rock mass as well as their persistence, aperture and orientation at the moment of the impact, the impact energy, the rigidity of the ground and the impact angle. However, rockfall fragmentation is a complex physical mechanism that it is still poorly understood and difficult to simulate (Chau 2002; Zhang et al. 2000). A few codes incorporate a fragmentation module for propagation analysis such as HY-STONE (Agliardi & Crosta 2003). It includes a trained neural network (Hecht-Nielsen 1987; Schalkoff 1997) which determines the mass and velocities of the fragments right after the impact. The model is efficient in predicting whether a rock block is broken or not on given impact conditions. It can also approximate well the energy loss due to the failure process and the energy transformation upon impact. However, it has some difficulties in reproducing the fragment size distribution as observed in reality. Salciarini et al. (2009) used a Discrete Elements Model approach to model the fragmentation effects using the software UDEC, and the results of the simulations indicated that the position and the extent of the accumulation zone is strongly affected by rock mass fragmentation. Tests performed in quarries provided some insight into the phenomenon but were not able to indicate impact energy thresholds that produce breakage of the blocks (Giacomini et al. 2009). The observations of Dussauge et al. (2003) suggest that the rockfall fragment sizes are associated with the fracture pattern of the detached rock mass volume at the source. Hantz et al. (2014) found that the deposited rockfall blocks follow a power law.

The investigation of the rockfall phenomenon for the development of predictive models requires the existence of rockfall inventories. Commonly, the rockfall inventories record the total volume

of the detached mass (Dussauge et al. 2002, 2003) or the largest blocks with the longest run out. Complete inventories including deposited blocks of all sizes are difficult to obtain. Several researchers mainly working on rock blasts, have used photoanalytical techniques to obtain the fragment size distribution (Crosta et al. 2007). However these provide results only for the block area and not for the volume. In large rockfall deposits, the large amount of blocks and the extent of the deposits make difficult obtaining the RBSD. To this end, field work should be systematic and well-organized. In this paper we present a methodology to obtain the RBSD based on field measurements.

2. Methodology

Mid-size fragmental rockfalls often generate a more or less continuous young cover of small debris and larger scattered blocks (Fig. 2). Some debris covers have a large extent and display a progressive downhill increase of the average block size. Because of this, obtaining the RBSD may become a challenging task.

Two complementary activities may be performed for measuring the rock blocks and obtaining the RBSD: a) the selective sampling of the young debris cover (YDC); and b) the systematic measurement of the large scattered blocks. The methodology is summarized in Fig. 2.

First, the YDC is divided into homogeneous zones of similar average block size based on visual field observation and orthophoto interpretation (in this case, A1 to A3). At each zone, several sampling plots are defined in which all the blocks larger than a minimum size are measured to obtain the respective block size distribution of the plot. The large scattered blocks are georeferenced using a GPS GARMIN Montana 650 and measured one by one. A few small blocks outside the YDC were also measured and included in this group. Three lengths more or less orthogonal to each other are measured at each block to estimate the volume, assuming that the shape of the blocks is prismatic.

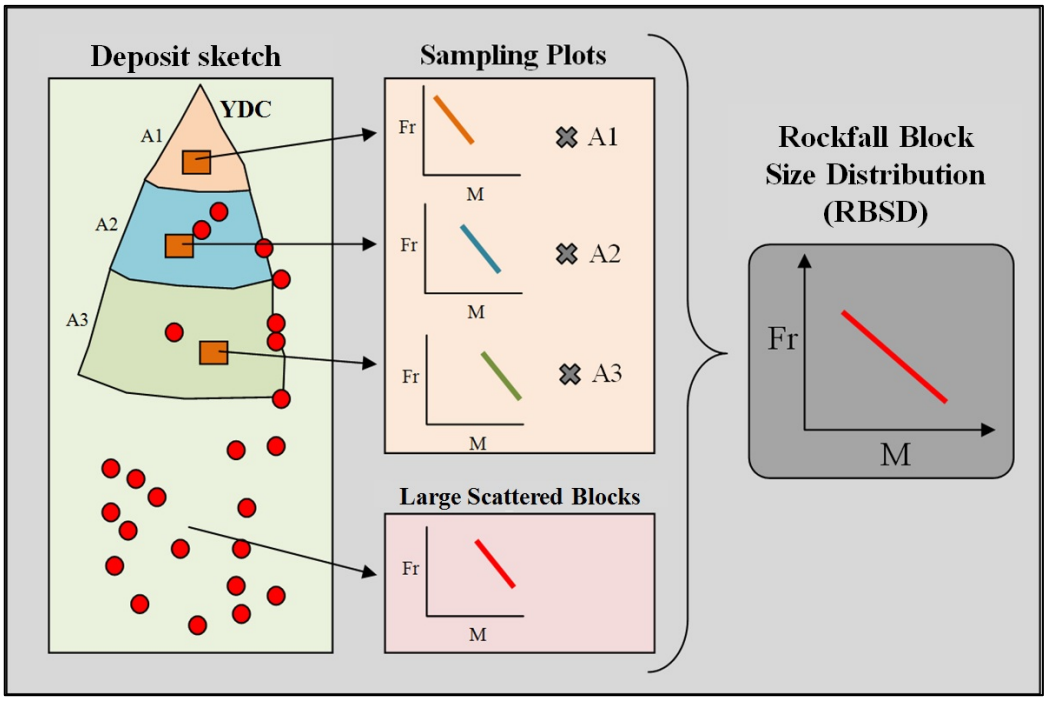

Fig. 2: Methodology followed to prepare the RBSD. The scheme shows the Young Debris Cover (YDC), the sampling plots (orange squares) for each homogeneous zone A1 to A3 (the symbol X stands for weighted multiplication, see step 2 in the text below), and the large scattered blocks. The plots display the block size distribution where "Fr" is the cumulative relative frequency for each block size bin "M".

The RBSD is obtained as follows (Fig. 2):

(1) The measured blocks of each sampling plot (orange squares) are classified in bins (*j*) of different block size ranges. It is convenient to test several bin ranges before choosing one of them (see Clauset 2007), in order to define correctly the shape of the distribution (specially the tail).

(2) Then, the block size distribution for each sampling plot is extrapolated to the whole homogeneous zone. The extrapolation is done for each defined zone (*i*) (for example, in the methodology scheme of the Fig.2 *i*=3), multiplying the number of measured blocks of each block size bin ($n(V_j)_i^{measured}$) with a scaling factor R_i (Eq. 1):

$$n(V_j)_i^{RBSD} = n(V_j)_i^{measured} \cdot R_i \qquad \text{(Eq.1)}$$

Where:; $n(V_j)_i^{RBSD}$: is the number of blocks in the block volume bin (*j*) representing the zone *(i)* in the RBSD; $n(V_j)_i^{measured}$: is the number of measured blocks in the block volume bin (*j)* in the zone (*i)* ; The scaling factor R_i is defined as:

$$R_i = \frac{A_i}{A^{sp}_i} \qquad \text{(Eq. 2)}$$

R_i : is the scaling factor ; A_i : is the area of the homogeneous zone (*i)*; $A^{sp}{}_i$: is the area of the sampling plot selected in the zone (*i)*.

The block size distribution of the Large Scattered Blocks (LSB) is prepared independently. The LSB includes only individual blocks, and does not represent a continuous surface covered by blocks. Hence the LSB distribution is not extrapolated.

Finally, the RBSD is obtained by adding all the afore-mentioned distributions.

$$RBSD: n(V_j)^{RBSD} = \sum_{i=1}^{r} n(V_j)_i^{RBSD} + n_{LSB}(V_j) \qquad \text{(Eq. 3)}$$

Where $n(V_j)^{RBSD}$: is the estimated number of blocks in the block volume bin *(j)* in the RBSD representative of the whole deposit; $n(V_j)_i^{RBSD}$: is the estimated number of blocks in the block volume bin *(j*) in each defined zone *i* ; $n_{LSB}(V_j)$: is the number of Large Scattered Blocks in the block volume bin *(j)*. Finally, the obtained RBSD can be represented either in terms of cumulative number of blocks or as relative frequency.

Several constraints must be overcome. In case that rockfall fragments stop over a previously existing talus slope, only the new deposited blocks associated to the recent event are measured. A key issue is thus differentiating young from old rock fragments. When the reconnaissance is made shortly after the occurrence of the event, this should not be a difficulty. New blocks show distinct fresh broken surfaces, including faces with stained coatings and clay fills, and bright colours (Fig. 3 and 4). If the YDC is formed by a thick continuous deposit in which a percentage of blocks are buried and cannot be measured, then the counting becomes uncertain and this becomes a restriction of the proposed approach.

The definition of the homogeneous zones is based on visual field observation and orthophoto interpretation. It is recommended to select more than one sampling plots at each homogeneous zone in order to double check the distribution obtained. The influence of the number of homogenous zones and the selection of the sampling plots is discussed at section 4(d). The length of the sampling plots must be at least one order of magnitude greater than the length of the measured blocks. Consequently, the area of the sampling plots increases with the size of the blocks. Big boulders found in the YDC are considered large scattered blocks when they are more than one order of magnitude bigger than the rest of the blocks.

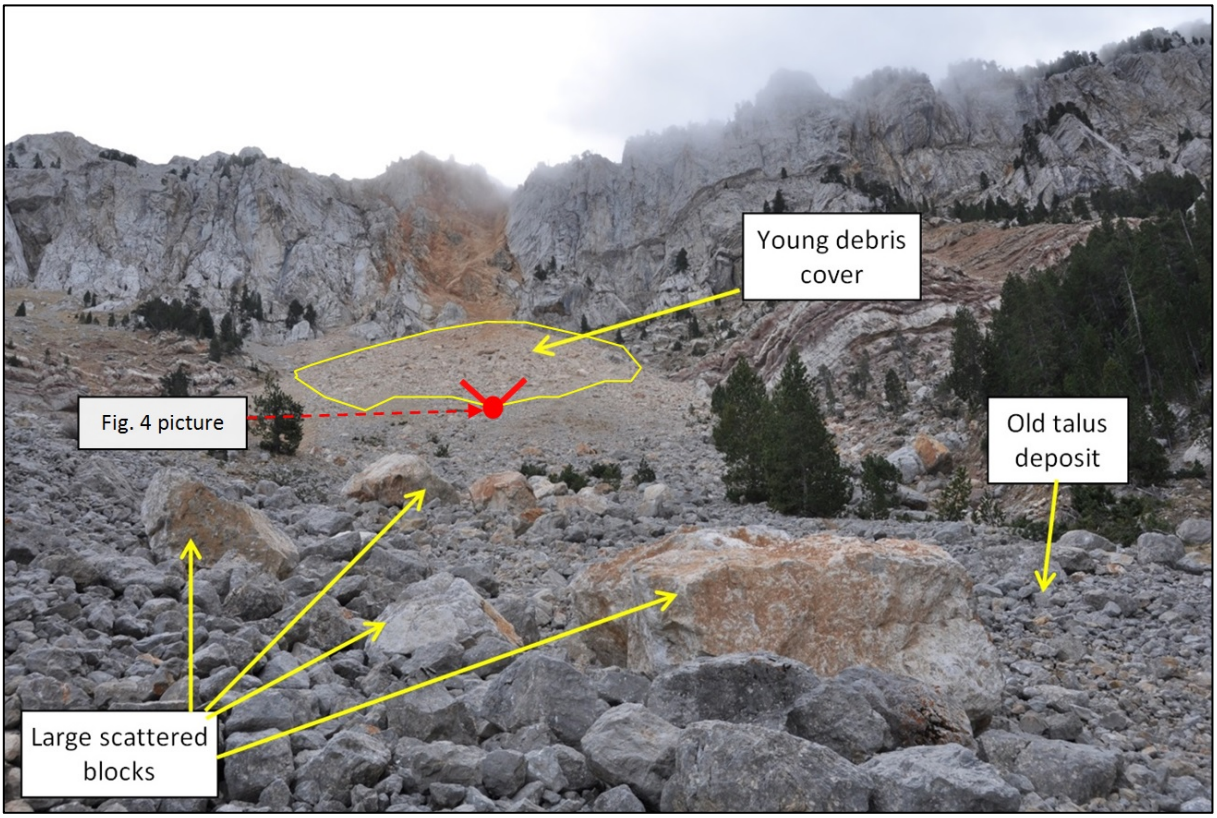

Fig. 3: Large scattered blocks laying on a previously existing talus deposit. New blocks stand out from the old ones by their most vivid (reddish, yellowish) colours. An almost continuous young debris cover is noticeable at the background. The red dot is the location of the picture in Figure 4. Vilanova de Banat rockfall at the Cadí massif, Eastern Pyrenees.

Fig. 4: View of the lower zone of the YDC. Almost continuous debris cover generated by the Vilanova de Banat rockfall, lying on a previously existing talus deposit. New blocks stand out from the old ones by their most vivid colours (reddish, yellowish). Distinct fresh fractures and spalling as a consequence of the impacts are also observed.

3. Application to a case-study

The proposed methodology has been applied to obtain the RBSD of a mid-size fragmental rockfall event occurred near the village Vilanova de Banat in November 2011, on a limestone cliff in the Cadí Sierra, Eastern Pyrenees (Fig. 3 and Fig 4). The rockfall has an initially estimated detached mass of about 10000 m^3 (Fig. 5a, red line). The source area measures 40 meters in width, 40 meters in height (from 2270 m to 2310 m of altitude) and 14 meters in thickness approximately, and it has a wedge shape. A 3D model of the source area and the potentially detachable mass is presented in section 5.

The YDC covers an area of approximately 30000 m^2 extended between the altitudes of 1950 m and 2138 m, with a maximum length of 260 meters and a maximum width of 115 meters (yellow line in Fig. 5b). The YDC is an almost continuous layer of boulders of variable size, between few decimeters in the upper zone of the talus up to one meter in the lowest zone.

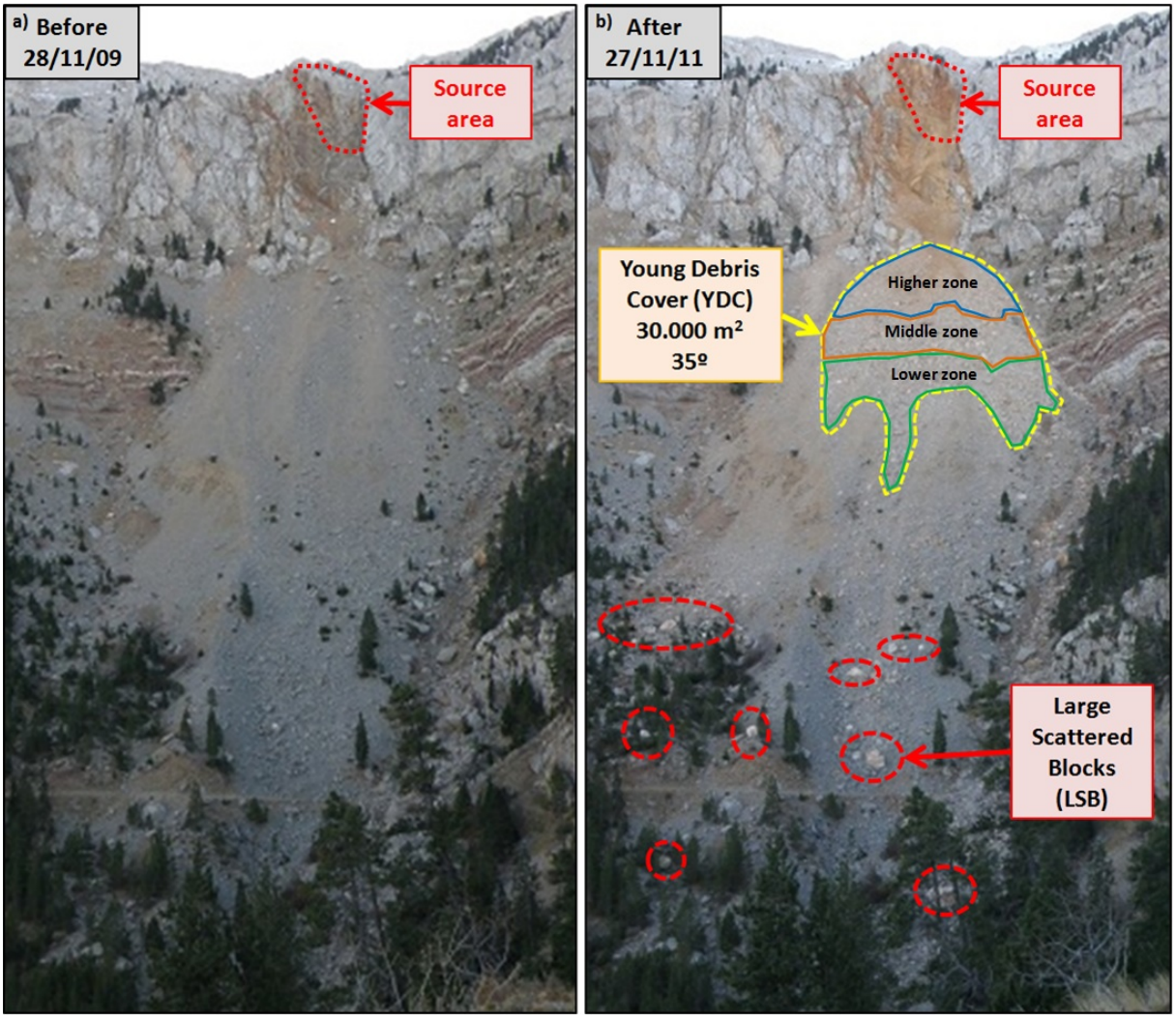

Fig. 5: Rockfall event occurred in November 2011 in Cadí massif, Eastern Pyrenees. 5a shows the rockfall source area before the occurrence of the rockfall event. 5b shows the same area after the rockfall event, including the source area (dashed red line), the young debris cover (dashed yellow line) formed in the upper zone of the talus and the large scattered blocks (dashed red ellipses) deposited in the lower zone of the talus.

Three roughly homogeneous block size zones have been visually identified: the higher, middle and lower zone of the YDC. We further divided the zones in sectors in order to check their size-homogeneity and select sampling plots (SP1 to SP6 in Fig. 6). Table 1 shows the area of the sampling plots (that varies between 25 m^2 and 400 m^2) and the number of blocks measured in each SP. A total of 1500 blocks larger than 0.015 m^3 were measured, which includes both the large scattered blocks (272), and the blocks inside the sampling plots (1252). Block sizes under 0.015 m^3 were not measured due to their large number and because many of them were lost in voids existing among large older blocks. The locations of each large block, and of the corners of the sampling plots, were georeferenced with a GPS.

4. Results

The deposit of the November 2011 rockfall event was mapped including the location of all the measured large scattered blocks, the sampling plots, the delimitation of the defined sectors and the source area (Fig. 6).

(a) Large Scattered Blocks

The large scattered blocks (LSB: green dots in Fig. 6) were mainly found in the western part of the deposit (inside a predominant trajectory path), and also in the lower zone of the deposit, with larger run out than the YDC. Some very big blocks found in the YDC were also considered LSB when they are at least one order of magnitude larger than the rest of the blocks in the sampling plot. The volume of the biggest measured boulder is 30.8 m^3, and the measured maximum runout distance from the source area is 683 meters.

(b) Sampling Plots

The sampling plots 1, 2, 3 and 4 are located in the higher and middle zones in the young debris cover. The sampling plots 1 and 2 have an area of 100 m^2, while the sampling plots 3 and 4 of 25 m^2. The sampling plots 3 and 4 were selected to double check the mesurements of the highest zone where sampling plot 2 is found. The sampling plots 5 and 6, which are located at the lowest part of the YDC, have a predominance of big blocks, and their areas are larger, 400 m^2 and 225 m^2 respectively. We used two sampling plots in the lower zone to double check the block size distribution of the YDC.

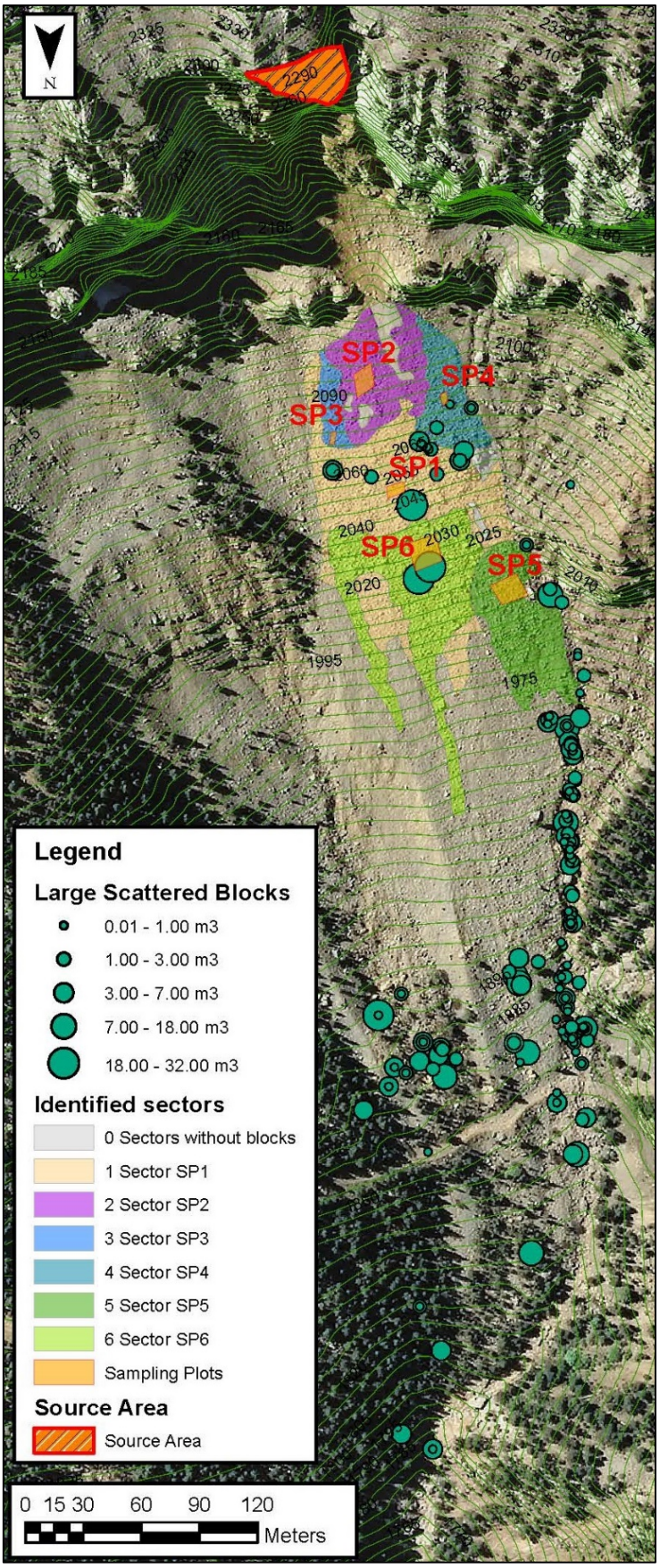

Fig. 6: Orthophoto map showing the location of the six homogeneous sectors of the YDC, sampling plots, the large scattered blocks, and the source area.

(c) Block size distributions

The blocks measured in each sampling plot, as well as the blocks measured as large scattered blocks, were plotted in the Fig. 7, in terms of cumulative number of blocks versus block volume. We tested different bin ranges. The shape distributions obtained using 5, 12 and 19 bins were compared to the original distribution. Our results show low precision shape of distribution using 5 bins, whereas using 12 or 19 the shape is well defined. Based on these results we finally classify the blocks in bins as 0.01-0.02 ; 0.02-0.05 ; 0.05-0.1 ; 0.1-0.2 ; 0.2-0.5 ; 0.5-1 ; 1-2 ; 2-5 ; 5-10 ; 10-20 and 20-50, all of them in cubic meters, covering 4 orders of magnitude.

These block size distributions obtained directly from the measurements in the sampling plots have a very similar slope in a log-log plot, and can be well fitted by power laws. In section 4(d) we have performed a sensitivity analysis of the final RBSD with respect to the SP used (using 6, 4 or 3 SP).

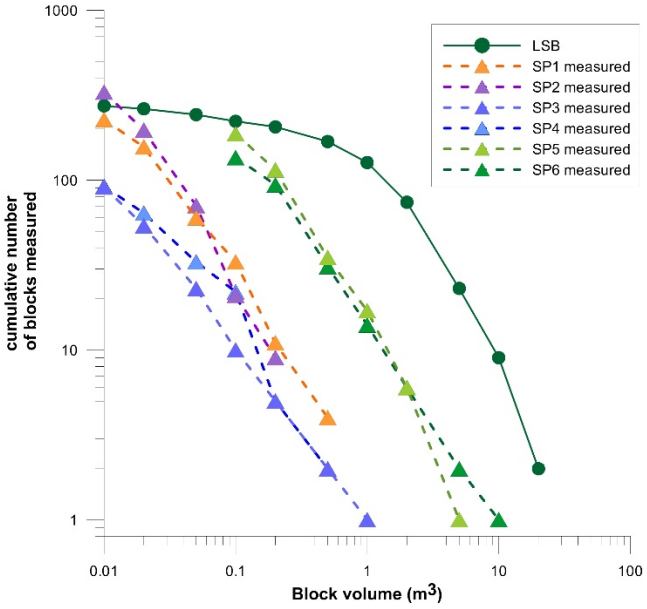

Fig. 7. Cumulative number of blocks measured versus block volume obtained directly from the measurements in the sampling plots (SP) and from the large scattered blocks (LSB)

Figure 7 shows that the block size distributions from the highest zone of the YDC (SP2, SP3 and SP4) are very similar to each other and also to SP1 (middle zone). Furthermore, SP5 and SP6 show a substantial overlap confirming the size homogeneity of the lowest unit of the YDC. It is noticeable that the slope of the obtained distributions is similar for all of them. The measured volumes cover a range of 4 orders of magnitude without gaps.

We classified the data in bins to extrapolate the block size distributions from the sampling plots to the corresponding homogeneous sectors, using the scaling factor for each defined sector (Fig.

8). Adding all of them and the large scattered blocks distribution we obtain the final RBSD representative of the whole deposit, allowing the estimation of the total volume of the rock mass detached. Table 1 shows the scaling factors used to extrapolate the data from the sampling plots to the homogeneous sectors. The extrapolated data, the fitted power laws by linear regression, and the resultant RBSD obtained, are shown in the Fig. 8.

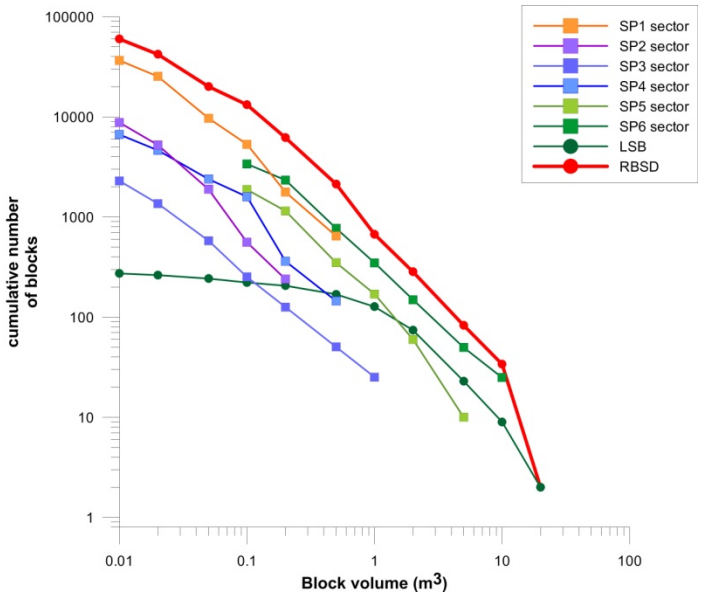

Fig. 8: Block size distributions obtained from the extrapolation of the measurements using the areas ratios, in terms of cumulative number of blocks versus block volume. The obtained RBSD is representative of the whole deposit. The power laws fitted to these distributions are also represented.

The minimum total volume of the rockfall deposit calculated with this procedure is approximately 8000 m^3, involving more than 60000 blocks over 0.015 m^3, based on the data plotted in the Fig. 8.

As a final step, the same block size distributions shown in the Fig. 8 were expressed in terms of cumulative relative frequency. The frequency (F_r or P) block size (V_o) distributions (Fig. 9) of the sampling plots and the large scattered blocks can be also fitted by power laws (Dussauge et al. 2002 ; Crosta 2007) characterized by: a) a constant *C* associated with the minimum significant block size (V_{min}), and b) an exponent *b* which is the slope of the distribution in a log-log representation (Eq. 4).

$$P(V_{\min} \leq V_o) = C \cdot V_o^{-b} \qquad \text{Eq. 4}$$

To estimate the exponent, *b* value, we used the linear regression method and the maximum likelihood estimator because they are the two methods classically suggested in the literature (Dussauge 2003 ; Pickering et al, 1995 ; Clauset et al, 2009). A minimum block size is used to fit the power law to each distribution. Table 2 shows the obtained *C* and *b* values and the minimum

volume used for each frequency - block size distribution plotted in the Fig. 9. The exponent *b* of the fitted power laws ranges between 0.8 and 1.3 obtained using the linear regression method, and between 0.8 and 1.2 obtained using the maximum likelihood estimator method. The fitted power laws using the linear regression show a very good fitting with R^2 ranging between 0.94 and 0.98. The values of the reduced χ_r^2 test for the fitted power laws (using both methods) range between 0.010 and 0.014 (Table 2), significantly lower than 1.

Therefore the proposed power laws describing the global RBSD can be well accepted given the reduced χ_r^2 values of 0.222 and 0.082 for the linear regression and the maximum likelihood methods respectively. The final RBSD obtained was fitted by a power law with C=0.01 and *b*=1.26 using the linear regression method, and a C=0.01 and *b*=1.16 using the maximum likelihood method.

The SP and LSB data represented in the Fig. 9 are plotted block by block in cumulative frequency terms. To obtain the RBSD a previous classification of the data in bins was made to extrapolate the data and to sum it up. This figure, and the same block density of the sectors of each defined zone (Table 1), confirms that the visual selection of the homogeneous zones was appropriate. The block size distributions of SP5 and SP6 show a perfect overlap. For SP2, SP3 and SP4 collected in the highest zone only the SP4 shows a slight shift. In any case, the difference in frequency is less than one order of magnitude for most of the sizes.

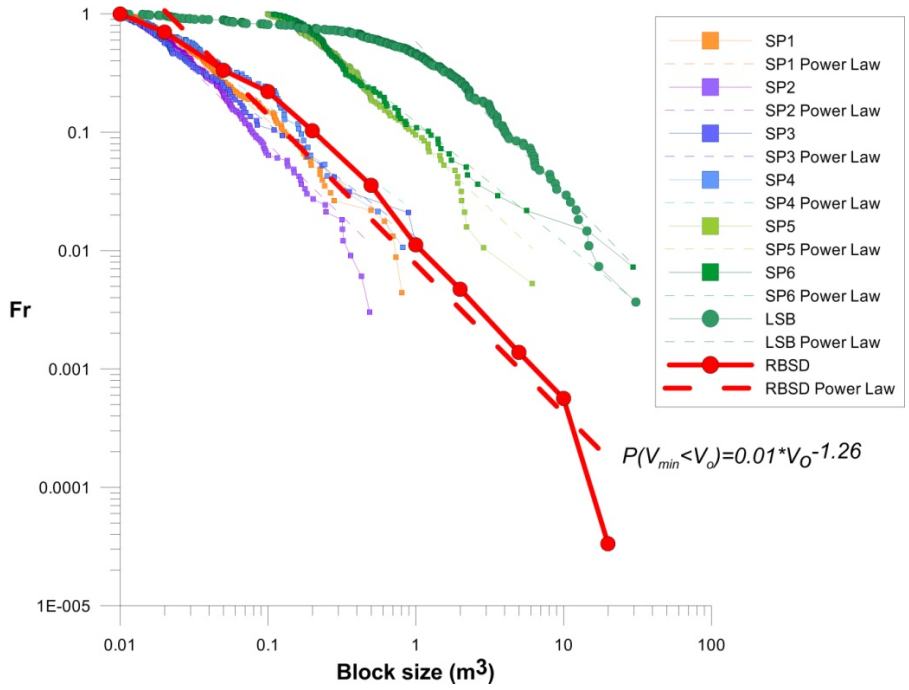

Fig.9: Block size distribution obtained from the 6 sample plots: SP1-6; from the large scattered blocks: LSB; the obtained Rockfall Block Size Distribution: RBSD, and the fitted power law by linear regression method.

The frequency - block size distributions in the Cadí case (Fig. 9) cannot be extrapolated for volumes bigger than the biggest blocks found. Therefore the right end of the total RBSD is determined by the maximum block volume measured, while the extrapolation to the left end is restricted by the total volume of the rock mass detached. For rockfall events bigger than the November 2011 event, the frequency - block size distribution can be used to calculate the probability of having blocks bigger than a given volume. Fig. 10 shows the frequency - block size distribution and the fitted power laws by the linear regression and the maximum likelihood method. It may be observed that the linear regressions yield relative frequencies greater than 1 for block sizes close to the minimum volume used (SP1, SP4, SP5 or RBSD), which does not make sense. This occurs because the method is not able to impose the condition $Fr=1$ when $Vol=V_{min}$. This drawback does not appear when using the maximum likelihood method. In the RBSD case, if the X_r^2 test is used to minimize the error of the fitting, this condition is not fulfilled, maybe due to a rollover effect in blocks size under 0.1 m^3.

Table 1: Summary of blocks measured, area of the sampling plots, area of the homogeneous sectors and scaling factors.

	Nº of blocks measured	**SP area (m^2)**	**Area of the homogeneous sector (m^2)**	**Block Density (nºblocks/m^2)**	**Scaling factor R**
SP1	284	100	16125	2.84	161.3
SP2	400	100	2659	4.00	26.6
SP3	113	25	629	4.52	25.2
SP4	103	25	1810	4.12	72.4
SP5	209	400	3994	0.52	10
SP6	143	225	5610	0.64	24.9
LSB	272	-	-	-	-
TOTAL	1524	875 m^2	30830 m^2		
RBSD	60231 (number of blocks calculated by the extrapolation)				

Table 2: Obtained values of the fitted power laws using Linear Regression and Maximum Likelihood methods.

		Power Law fitted by Linear Regression				**Power Law fitted by Maximum Likelihood**			
	Min. Volume (m^3)	**C**	**b**	**Standard Deviation for b (σ)**	**Test X_r^2**	**C**	**b**	**Standard Deviation for b (σ)**	**Test X_r^2**
SP1	0.01	0.011	1.04	0.07	0.009	0.025	0.79	0.05	0.010
SP2	0.01	0.004	1.22	0.07	0.020	0.012	0.96	0.05	0.011
SP3	0.01	0.013	0.96	0.10	0.002	0.014	0.91	0.09	0.010
SP4	0.01	0.021	0.89	0.09	0.014	0.036	0.72	0.07	0.012
SP5	0.1	0.088	1.18	0.09	0.006	0.117	0.93	0.07	0.010
SP6	0.1	0.121	1.02	0.09	0.004	0.157	0.83	0.07	0.010
LSB	1	1	1.28	0.11	0.029	1	1.06	0.09	0.007
RBSD		**0.01**	**1.26**	**0.38**	**0.222**	**0.01**	**1.16**	**0.35**	**0.082**

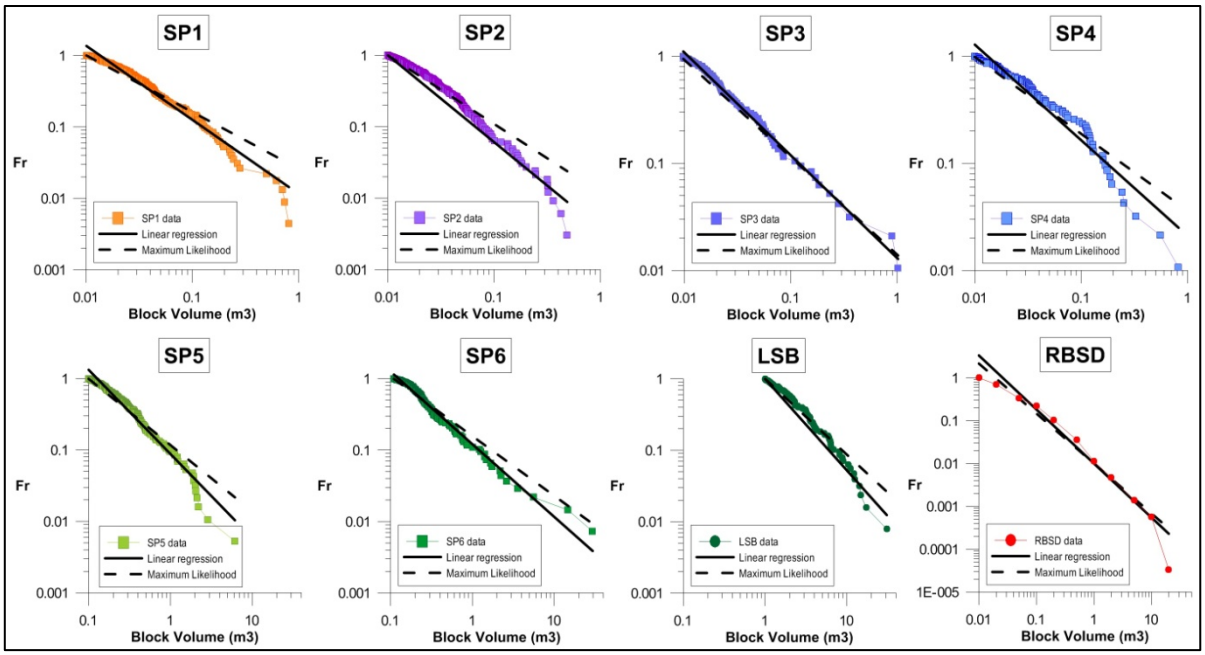

Fig.10: Comparison of the fitted power laws using linear regression or maximum likelihood methods for the frequency - block size distribution for each sampling plot data, the large scattered blocks and the final RBDS.

(d) Repeatability of the block size distributions obtained in the sampling plots

The selected sampling plots in the YDC were: SP2, SP3 and SP4 (higher zone); SP1 (middle zone); and SP 5 and SP6 (lower zone). To verify the degree of representativeness and repeatability of the selected sampling plots we have generated several RBSD using alternatively the data of 3, 4 or 6 sampling plots, with the following combinations: SP1, SP2, and SP6; SP1, SP2, SP5 and SP6; and all of them. In all these cases, the LSB distribution is also used. The merged zones have the same block density (Table 1).

The generated RBSDs have similar shapes and are fitted well by power laws (Fig. 11). The obtained exponents range between 1.26 (six sampling plots), 1.25 (four sampling plots) and 1.22 (three sampling plots). The results show that the visual selection of the block-size homogeneous zones and the sampling plots does not produce significant differences in the obtained RBSD.

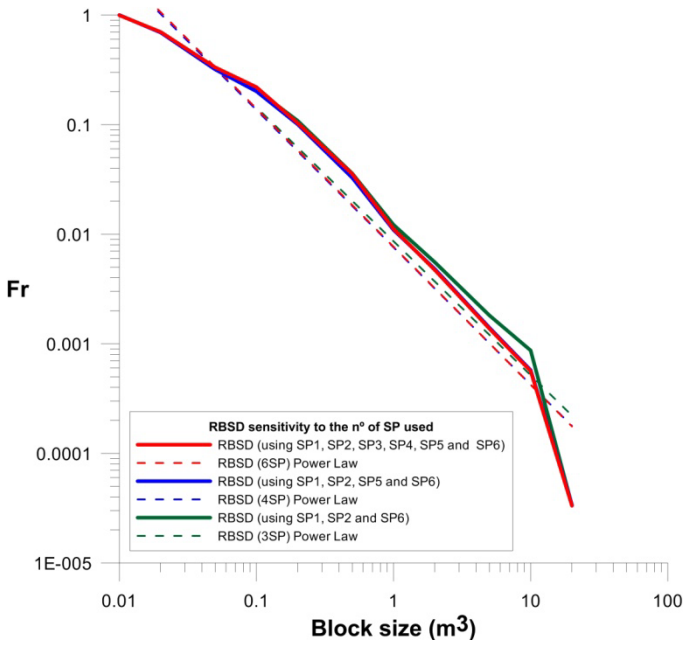

Fig.11: RBSD obtained using six, four or three sampling plots.

5. Checking the obtained rockfall volume.

To validate the proposed procedure, we used an alternative method to calculate the total detached volume from the cliff for the Cadí rockfall event. The total detached volume obtained with the RBSD was approximately 8000 m^3. This corresponds to the minimum volume because blocks smaller than 0.015 m^3 were not measured. This value has been checked against the volume obtained subtracting two Digital Surface Models (DSM). We used the topographic model at 1:5000 scale, of the Cartographic Institute of Catalonia, generated by aerial photogrammetry before the rockfall occurrence. To obtain a DSM of the rockfall scar after the rockfall, we used a digital photogrammetry software with pictures taken from the ground.

The use of two consecutive 3D models to estimate a volume detached from a cliff has been discussed before (Sturzenegger et al., 2009; Firpo et al., 2011 ; Viero 2012). The main limitation of this case is that the topographic model is obtained with aerial photogrammetry (with an accuracy of about 1 metre in X and Y coordinates, and 1.5 m in Z for the 90% of the defined points). Meanwhile, the photogrammetric model of the scar is realised using terrestrial pictures, taken from a direction which is almost perpendicular to the aerial orthophoto. Consequently, the errors of these models are maximum in different directions. To estimate the detached volume, we proceed with the following steps:

a) We used 17 pictures taken by a camera Nikon D90 with a focal length of 60 mm and a resolution of 4288x2848px (12Mp).

b) We tested all the pictures using the software Agisoft PhotoScan and VisualSFM. It uses the Structure from Motion algorithms to identify the matching pixels between pictures, thus allowing working with more than two pictures. It also reconstructs the position where the pictures were taken, readjusts the distortion parameters of the lens, and generates a 3D point cloud (Wu 2011). The final scar DSM used is a mesh based on the 3D point cloud generated.

c) The DSM of the rockfall scar was scaled and georeferenced using seven Ground Control Points (GCP) (Fig.12). The coordinates of these seven GCP were obtained from the orthophoto and from the topographic maps.

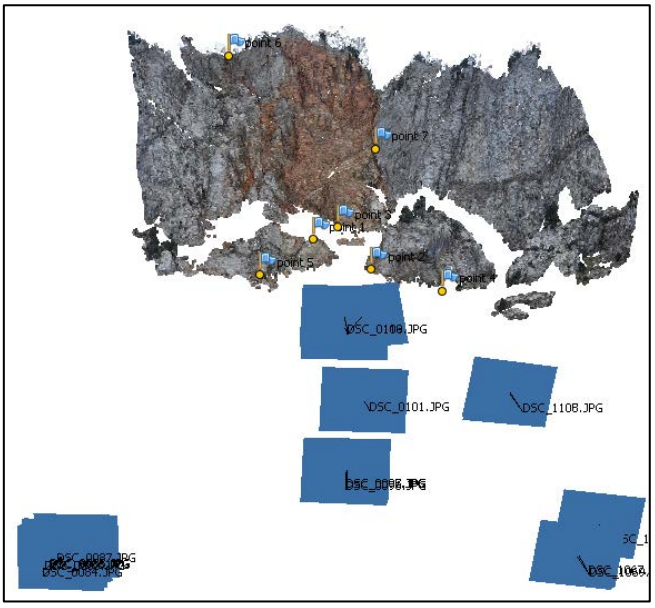

Fig.12: 3D visualisation with the location of the used pictures (blue rectangles) and the Ground Control Points (yellow points)

d) We generated a DSM based on the topographic map at 1:5000 scale prior to the event.

e) Both DSMs have been aligned with the software CloudCompare. To this end, we have first excluded the rockfall detached zone. In this alignment the difference analysis show a distance ranging from 0 to 9.2 m, with a standard deviation of 3.7 m. and a mean distance of 1.1m. The difference here is attributed to the different precision between the topographic DSM, which includes topographic data smoothing where abrupt rock corners are present, and the scar DSM.

f) Then, a new difference analysis between the scar DSM (including the detached zone) and the topographic DSM show differences ranging between 0 and 18.4m (due to inclusion of the

detached volume), a standard deviation of 3.2 m and mean distance of 2.1 m. This difference map (Fig.13b) was used to delineate the detached zone in the cliff (Fig.13a) and to estimate the detached volume.

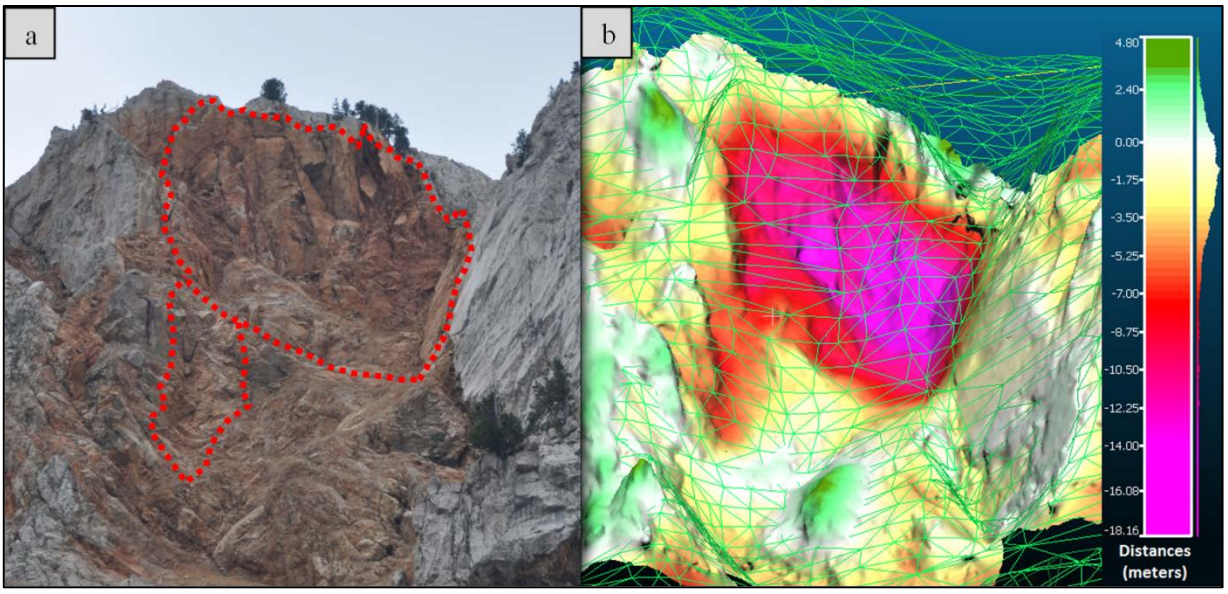

Fig.13: a) Picture of the scar (the rockfall detachment zone is outlined in red). b) Topographic DSM (green mesh), scar DSM coloured by the distances to the topographic DSM.

g) Finally, we used the software Rhinoceros to define a volume using the topographic DSM, the scar DSM, and two main joints identified in the cliff (Fig. 14). The joints are identified in the pictures and over the scar DSM. Their use allows to define the volume according with the field observations where the recent scar is distinguished by its red colour and fresh faces (Fig.13a).

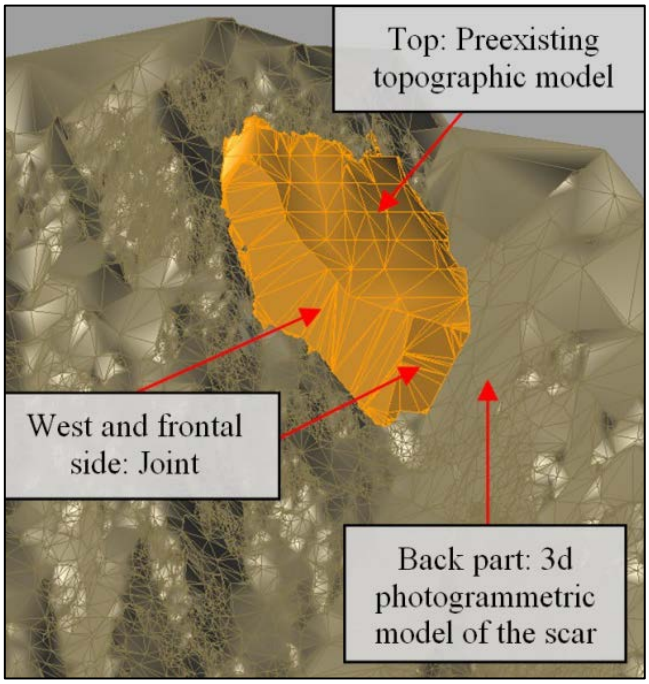

Fig. 14. Detached volume reconstruction (orange volume) based on the topographic DSM (top), the scar DSM coloured in brown (back, laterals and bottom parts) and two main joints (frontal face).

The estimated volume is approximately 10000 m^3, which is bigger than the volume based on measured rock fall blocks (8000 m^3). The 2000 m^3 of difference between both volumes is possibly ought to the fact that approximately the 20% of the rock mass can result in dust and blocks smaller than 0.015 m^3 that were not measured in the field. In fact, by extrapolating the RBSD to a block size of 0.005 m^3, a volume of 10000 m^3 is obtained. Another possible reason for this difference is the uncertainties and the errors associated to the topographic DSM and the scar DSM.

6. Conclusions

The presented sampling–procedure allows the construction of the block size distribution of a fragmental rockfall deposit in a consistent and reliable way. Double checking of the sampling plots has shown that the visual selection of the block-size homogeneous zones was appropriate, obtaining the same block density in the sectors inside each defined zone. The fitted power laws of the RBSD generated using 6, 4, and 3 SP, yielded the following exponents:1.26, 1.25 and 1.22, respectively.

The application to a case study, a mid-size fragmental rockfall deposit in the Eastern Pyrenees, has yielded a RBSD which is well fitted by a power law. In the case of the large scattered blocks, a rollover effect appears related to the voluntary censoring of blocks smaller than 1 m^3 at our measurements. The rest of the obtained block size distributions show a sight rollover effect and can be very well fitted directly with power laws. The RBSD for this particular case shows a rollover effect, suggesting that there is bias due to undersampling of the blocks under 0.1 m^3, as it occurred in SP5 and SP6.

The obtained power law distributions are consistent with the observations of Hartmann (1969), Perfect (1997) and Turcotte (1986) about fragmentation in rocks, where the number of fragments versus size generated by the fragmentation process follow a power law. The exponent of the fitted power law, is related with the fractal dimension, and could be used as a descriptor of the fragmentation process.

The measured volumes cover a range of 4 orders of magnitude. It is also noticeable that the similar slope of these distributions indicates the homogeneity or the scale invariant behaviour of the samples. The power law related with the block size distribution generated at a fragmental rockfall is truncated on the right branch by the maximum volume block detached and on the left branch, by the minimum sampled volume.

The maximum likelihood method used to fit the RBSD with a power law represent better the whole data than the fit using the linear regression method. However the biggest blocks are better fitted by the linear regression method. The power law describing the RBSD can be alternatively calculated excluding bigger volumes as outliers

The total detached volume was estimated 8000 m^3 based on the field measurements. This volume was checked against the volume of the rockfall scar. The latter was obtained by subtracting the scar DSM based on terrestrial digital photogrammetry and the DSM derived from the topographic map prior to the event giving a total of 10000 m^3. The difference in the two volumes can be attributed to the precision errors of the DSMs. Nevertheless, the extrapolation of the RBSD to block volumes up to 0.005 m^3 which were not sampled, can as well compensate for the missing volume.

Acknowledgements

The authors acknowledge the support of the Spanish Economy and Competitiveness Ministry to the Rockrisk research project (BIA2013-42582-P) and the support of the Ministry of Education to the first author (grant code FPU13/04252)

References

Agliardi F, Crosta GB (2003) High resolution three-dimensional numerical modelling of rockfalls. Int. Journal of Rock Mechanics & Mining Sciences 40: 455-471

Chau K T, Wong R H C, Wub, J J (2002) Coefficient of restitution and rotational motions of rockfall impacts. Int. Journal of Rock Mechanics & Mining Sciences 39: 69-77

Clauset A, Shalizi C R, Newman M E J (2009) Power-Law distributions in empirical data. Society for Industrial and Applied Mathematics (SIAM) review. 51(4):664-703

Corominas J, Mavrouli O, Santana D, Moya J (2012) Simplified approach for obtaining the block volume distribution of fragmental rockfalls. E Eberhardt, C Froese, A K Turner & S Leroueil (editors). Landslides and engineered slopes. Taylor and Francis. Vol 2: 1159-1164

Crosta G, Frattini P, Fusi F (2007) Fragmentation in the Val Pola rock avalanche, Italian Alps. Journal of Geophysical Research, 112: p. F01006

Dussauge C, Grasso J, Helmstetter A (2003) Statistical Analysis of Rock Fall Volume Distributions: Implications for Rock fall Dynamics. Journal of Geophysical Research B 108 (B6) (2003) 2286, DOI: 10.1029/2001JB000650

Dussauge C, Helmstetter A, Grasso J, Hantz S, Desvarreux P, Jeannin M, Giraud A (2002) Probabilistic approach to rockfall hazard assessment: potential of historical data analysis. Natural Hazards and Earth Systems Science 2:15-26

Dorren, L K A (2003) A review of rockfall mechanics and modeling approaches. Progress in Physical Geography 27 (1):69– 87

Evans S, Hungr O (1993) The assessment of rockfall hazard at the base of talus slopes. Canadian Geotechnical Journal 30:620-636

Firpo G, Salvini R, Francioni M, Ranjith P (2011) Use of Digital Terrestrial Photogrammetry in rocky slope stability analysis by Distinct Elements Numerical Methods. International Journal of rock Mechanics and Mining Sciences 48:1045-1054

Giacomini A, Buzzi O, Renard B & Giani, G P (2009) Experimental studies on fragmentation of rock falls on impact with rock surfaces. Int J Rock Mech Min Sci 46:708–715

Hantz D, Rossetti J P, Servant F, D'Amato J (2014) Etude de la distribution des blocs dans un éboulement pour l'évaluation de l'aléa. Proceedings of Rock Slope Stability 2014, Marrakesh, Morocco

Hartmann W K (1969) Terrestrial, lunar and interplanetary rock fragmentation. Icarus 2(2):201-213

Hecht-Nielsen, R (1987) Kolmogorov's mapping neural net-work existence theorem. Proceedings of the first IEEE international conference on neural networks. San Diego CA, USA, 11–14

Hungr O, Leroueil S, Picarelli L (2014) The Varnes classification of landslides types, an update. Landslides 11:167-194

Hungr O, Evans S G, Hazzard J (1999) Magnitude and frequency of rock falls and rock slides along the main transportation corridors of southwestern British Columbia. Canadian Geotechnical Journal, 1999, 36(2): 224-238, 10.1139/t98-106

Jaboyedoff, M, Dudt, J P, Labiouse, V (2005) An attempt to refine rockfall hazard zoning based on the kinetic energy, frequency and fragmentation degree. Natural Hazards and Earth System Sciences 5: 621–632

Okura, Y, Kitahara, H, Sammori, T, Kawanami, A (2000) The effects of rockfall volume on runout distance. Engineering Geology 58(2):109–124

Perfect, E (1997) Fractal models for the fragmentation of rocks and soils: a review. Engineering Geology 48:185-198

Pickering, G, Bull, J M, Sanderson, D J (1995). Sampling power-law distributions. Tectonophysics 248:1-20

Salciarini, D, Tamagnini, C, Conversini, P (2009) Numerical approaches for rockfall analysis: a comparison, Proceedings of the 18th World IMACS / MODSIM Congress, Cairns, Australia

Schalkoff, R (1997) Artificial neural network, New York: McGraw-Hill

Sturzenegger M, Stead D (2009) Close-range terrestrial digital photogrammetry and terrestrial scanning for discontinuity characterization on rock cuts. Engineering Geology 106:163-182

Turcotte, D (1986) Fractals and Fragmentation. Journal of Geophysical Research 91. NO B2: Pages 1921-1926

Viero, A, Furlanis, S, Squarzoni, C, Teza, G, Galgaro, A, Gianola, P (2012) Dynamics and mass balance of the Cima Una rockfall (Eastern Alps, Italy). Landslides 10:393-408

Wang, Y, Tonon, F (2010) Discrete Element Modelling of Rock Fragmentation upon Impact in Rock Fall Analysis. Rock Mech Rock Eng 44: 23–35

Wu, C (2011) VisualSFM: A visual structure from motion system. *URL: http://homes. cs. washington. edu/~ ccwu/vsfm*, *9*

Zhang Z X, Kou S Q, Jiang L G Lindqvist P A (2000) Effects of loading rate on rock fracture: fracture characteristics and energy partitioning. Int J Rock Mech Min Sci 37:745–762

3. Comparison of block size distributions in rockfalls

This chapter reproduces an article presented in the 12th International Symposium on Landslides (ISL 2016) and published in the book *Landslides and Engineered Slopes. Experience, Theory and Practice – Aversa et al. (Eds) © 2016.* The chapter is focused on the comparison of blocks size distributionsa from different inventoried rockfalls.

Publication reference:

Ruiz-Carulla, R., Corominas, J. and Mavrouli, O. (2016) Comparison of block size distribution in rockfalls. 12th International Symposium on Landslides (ISL 2016) Landslides and Engineered Slopes. Experience, Theory and Practice – Aversa et al. (Eds) © 2016 Associazione Geotecnica Italiana, Rome, Italy, ISBN 978-1-138-02988-0.

Abstract: Rock masses detached as rockfalls usually disintegrate upon impact on the ground surface. The Rockfall Block Size Distribution (RBSD) generated by the propagation of the rockfall mass is required for the analysis of the trajectories of the blocks, the run-out distances, the impact energies, the quantitative assessment of the rockfall hazard and for the understanding of the fragmentation process. We have measured the volume of the blocks detached in 5 rockfall cases, obtaining the corresponding RBSD. The total volume involved in these rockfall events ranges from 2.6 m3 to 10000 m3. The obtained RBSD can be well fitted by power laws with exponents ranging from 0.51 to 1.27. The results suggest that these exponents may be related to the height of fall (potential energy) and to the proportion of new fractures generated in the rock mass, among other factors.

Keywords: rockfall, fragmental rockfall, block size distribution comparison

1. Introduction

Evans and Hungr (1993) and Hungr et al. (2014) re-served the term fragmental rockfall, for the events in which the rock fragments move as independent rigid bodies interacting with the ground surface through scattered impacts. They distinguished it from the term rock avalanches in which masses of fragments move in a flow-like way. In fragmental rockfalls, the detached rock mass, which often includes discontinuities, it disaggregates, breaks or both after the first impacts on the ground. The resultant fragments propagate independently downhill. The deposit of a fragmental rockfall includes blocks of different sizes scattered on the ground surface. In the case of large fragmental rockfalls (thousands or tens of thousands of cubic meters) a more or less continuous Young Debris Cover (YDC) can be formed.

Understanding the fragmentation process is fundamental for the analysis of the rockfall hazard (Jaboyedoff et al. 2005; Corominas et al. 2012), since it is a critical input datum for calculating the trajectories and the run-out of the rock fragments, the encounter probability with the elements at risk and the expected impact energies. Run-out analyses per-formed with the originally detached rock mass volume produce results, which are significantly different from those using individual rock blocks (Okura et al. 2000; Dorren 2003). The initial rock mass may lead to the overestimation of the rockfall kinetic energy and run-out. If the modal or the maximum block fragment size is used instead, the travel distances and the energies obtained are more realistic. However, the frequency and the impact probability are largely underestimated as in reality, the original rock mass splits into a large number of rock fragments, leading to the multiplication of the impact probability by a factor “n” equal to the number of new blocks generated.

An indicator of the fragmentation degree is given by the Rockfall Block Size Distribution (RBSD) (Giacomini et al. 2009; Hantz et al. 2014; Hartmann 1969). Several parameters influence the fragmentation process and the RBSD (Dussauge et al. 2003; Wang & Tonon 2010) namely: the presence of dis-continuities in the detached rock mass as well as their persistence, aperture and orientation at the moment of the impact, the impact energy, the rigidity of the ground, the impact angle and the velocity.

We have defined different scenarios for the fragmentation of the rockfalls (Figure 1). First, the detached rock mass consist of a single block. The block can either remain intact or break when hitting the ground if there is enough impact energy. Alternatively, the detached rock mass may include joint sets. Within the rock mass, individual blocks of different sizes and shapes may result from the mutual intersection of the joint sets.

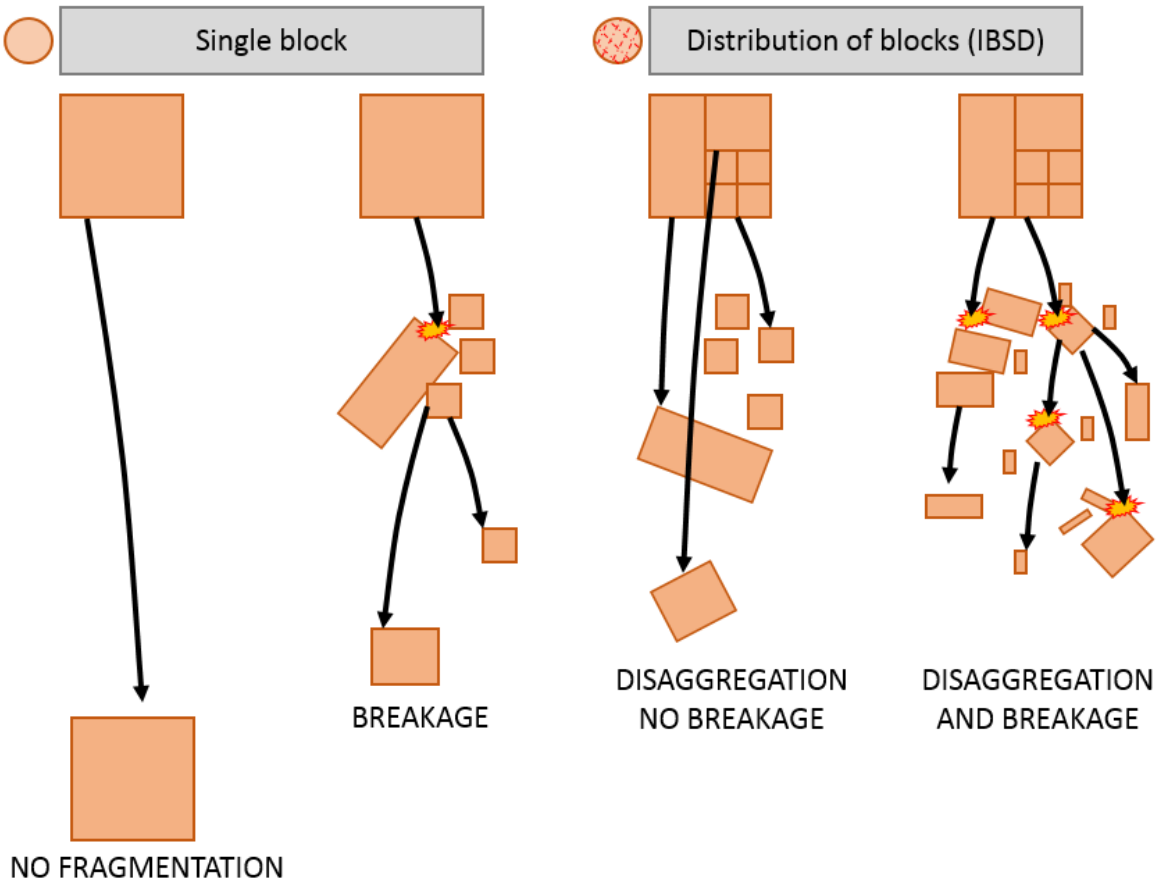

Figure 1. Scheme showing the scenarios of rockfall fragmentation considered. Left: the detached rock mass consist of a single block; Right: the detached rock mass is characterized by an IBSD.

The range of volumes of these blocks can be characterized by the In Situ Block Size Distribution (IBSD). With low impact energy levels, the rock mass will be simply disaggregated and blocks will be bounded mostly by the preexisting joints, generating a RBSD similar to the original IBSD. If the impact energy is enough to break blocks, the generated RBSD must differ from the original IBSD. These differences can be used to characterize the fragmentation phenomenon and to identify the predominant mechanism as disaggregation, pure breakage or a combination of both. The comparison between the IBSD and the RBSD is used to characterize the fragmentation phenomenon in other cases like rock avalanches (Bowman et al. 2014; Locat et al. 2006) or in blastability (Faramarzi et al.2013, Hudaverdi et al. 2012; Latham et al. 1999).

2. Study cases

We have measured the volume of the blocks deposited in 5 rockfall cases located in Catalonia, Spain, obtaining the corresponding RBSD. The rockfall volume involved in these events ranges

from 2.6 m3 to 10000 m^3. The rockfall cases represent 5 different scenarios of volume, lithology, height of fall and surface morphology.

To obtain the RBSD, we measured the blocks using a tape, assuming either a rectangular or triangular prismatic shape of the blocks and measuring 3 dimensions of each one. In the case of large fragmental rockfalls, the size distribution in the Young Debris Cover (YDC), is obtained by measuring all the blocks over a certain volume inside sampling plots, and then extrapolating the distribution over the homogenous zone represented by the sampling plot. The definition of the homogeneous zones, the selection of the sampling locations and the extrapolation procedure is described in detail in Ruiz et al. 2015. The obtained RBSD can be well fitted by power laws with exponents ranging from 0.51 to 1.27.

2.1 Pont de Gullerí rockfall

Pont de Gullerí rockfall took place near Sant Romà de Tavèrnoles village. The measurement of the accumulated blocks gave a detached rock mass volume of 2.6 m^3, and a height of fall of 12 meters (Figure 2 left). The cliff is composed of Cambro-Ordivician schists with a high persistence joint pattern. The fallen blocks are bounded by preexisting joints (Figure 2 right). This allows us to assume that the detached rock mass was disaggregated following the joint pattern. Only one block shows fresh breaks. The block size distribution (RBSD) was obtained by measuring 116 blocks in the deposit, and the curved shape could be related with the In Situ Block Size Distribution (IBSD) (Elmouttie & Poropat 2011) in the cliff. The minimum block volume measured is 1.2*10-4 m^3, and the maximum is 0.28 m^3.

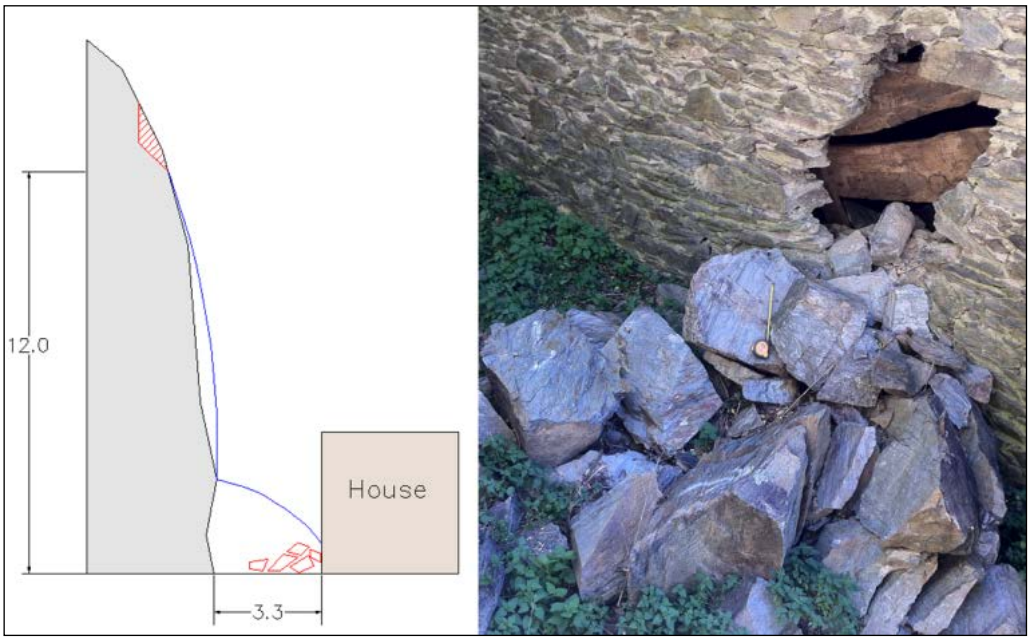

Figure 2. Left: Scheme of the Pont de Gulleri rockfall (distanc-es in meters). Right: Deposited blocks.

2.2 Lluçà rockfall

In the Lluçà rockfall the detached volume is 10.7 m3. The rupture mechanism is predominantly top-pling caused by differential erosion of the underly-ing weak rocks (Figure 3). The rock is grey sand-stone of Upper Eocene age. The detached mass was a single block bounded by two joints filled with roots. The latter might have facilitated their devel-opment. The fallen blocks show fresh faces generat-ed by the impact and abundant fine material gener-ated by the breakage. We measured 77 blocks, with a minimum volume of 6.7*10-4 m3 and a maximum volume of 8.47 m3. The RBSD obtained can be very well fitted by a power law with an exponent of 0.51.

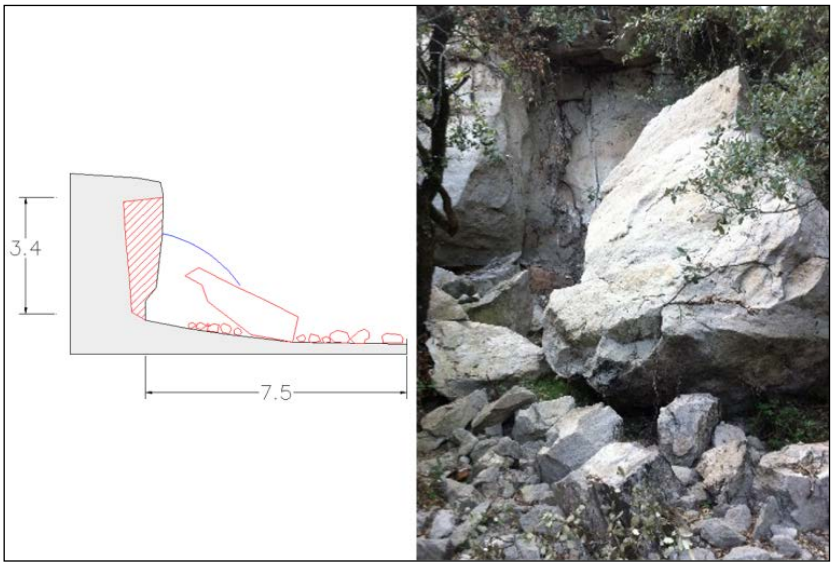

Figure 3. Scheme of the Lluçà rockfall (distances in meters). The high number of small blocks results from the fragmenta-tion of a initial one.

2.3 Omells de na Gaia rockfall

The Omells de na Gaia rockfall is a small-size rock-fall that propagated on a stepped soft ground. It ini-tiated with a free fall of 0.8 m, and the farthest block stopped by impacting on a wall at 22 meters from the source (Figure 4). In the lowest part, the blocks trajectories crossed a paved road and dam-aged a barrier (Figure 5 and Figure 6). The detached rock mass is sandstone of Oligocene age with a vol-ume of 4.2 m3. We measured 48 blocks, with a min-imum and maximum volume of 7*10-4 and 1.1 m3, respectively. The blocks generated by fragmentation show fresh faces formed by the breakage as well as preexisting dis-continuities, mostly sedimentary planes.

The fragmentation of the rock mass during the propagation of the rockfall changed the trajectories of the blocks, modifying the impact energies (Figure 6). The RBSD obtained is well fitted by a power law with an exponent of 0.53.

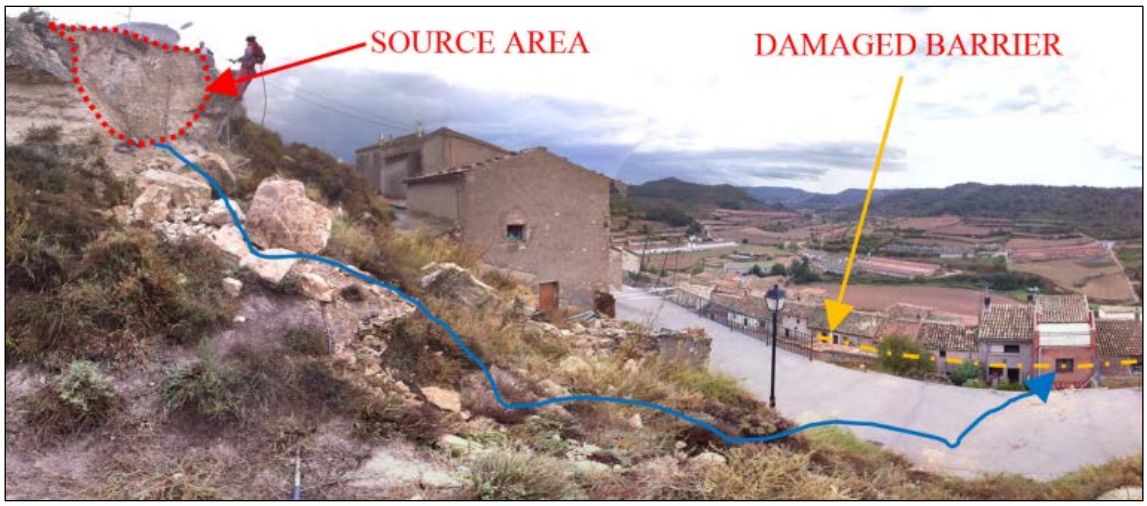

Figure 4. Omells de na Gaia rockfall.

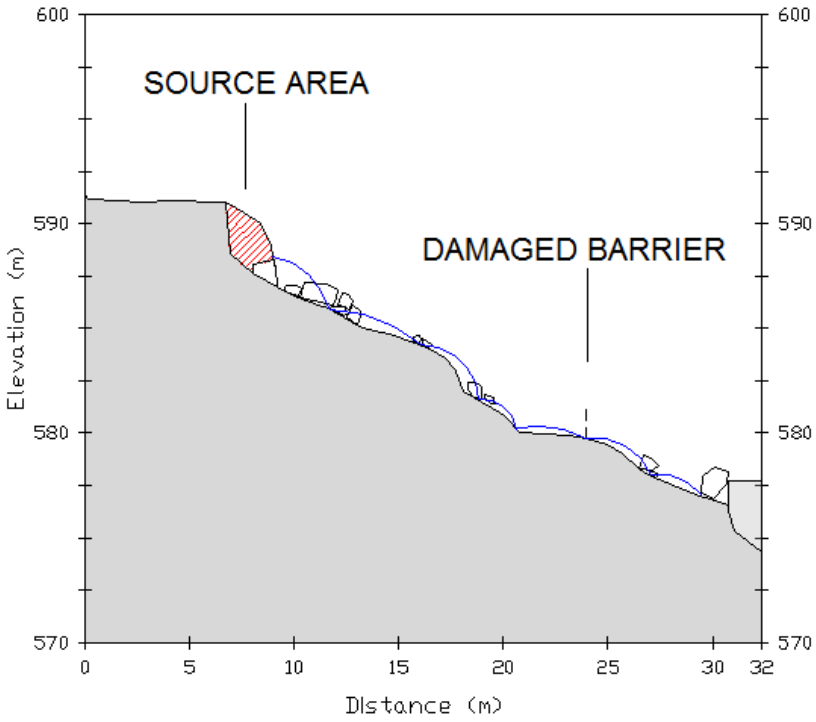

Figure 5. Omells rockfall scheme, with the source area, the tra-jectories and some of the deposited blocks.

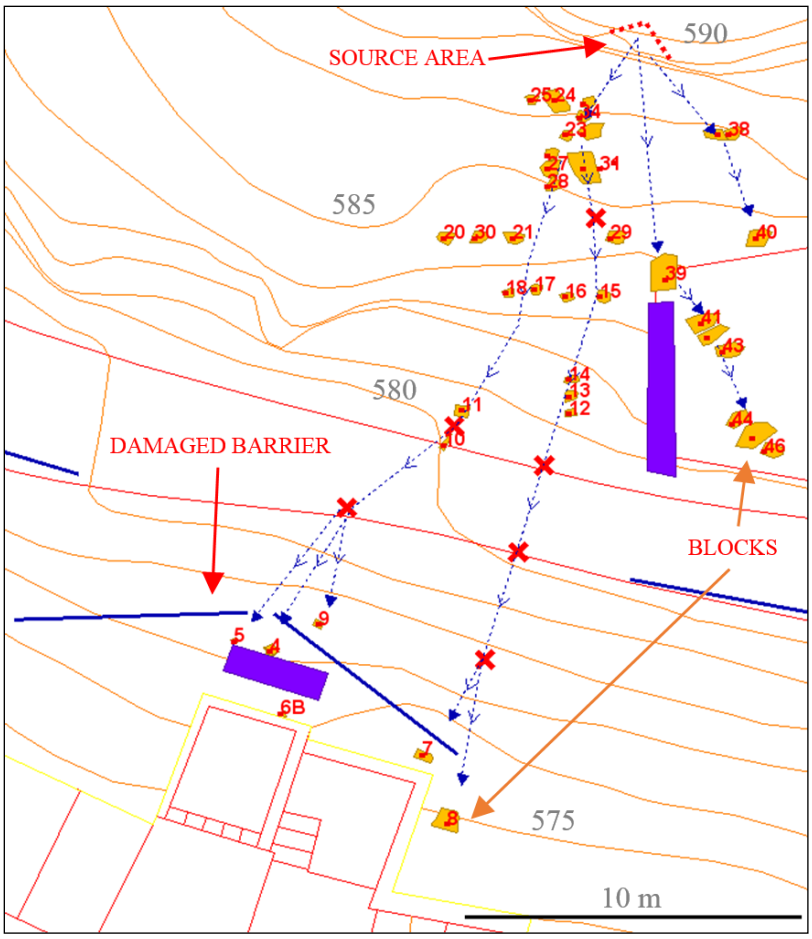

Figure 6. Map of the Omells rockfall, with the source area, the trajectories, the impacts, the deposited blocks and the dam-aged barriers.

2.4 Malanyeu rockfall

The Malanyeu rockfall is a large rockfall, with a total volume detached close to 5000 m^3. The rock is Maastrichtian limestone. The free fall height is less than 10 meters, and the maximum run-out distance is 100 meters, reaching the valley bottom (Figure 7). We measured 2721 blocks, with a minimum vol-ume of 4.2*10-5 m^3 and a maximum volume of 445 m^3. The deposit includes 7 blocks greater than 100 m^3, and more than 60 blocks greater than 10m^3.

In this case, the fragmental rockfall generated a more or less continuous Young Debris Cover (YDC) in the upper part of the deposit with a high concentration of small-size blocks (Figure 8). To obtain the block size distribution from the YDC, we defined 3 homogenous zones, where block sizes are relatively similar. In each zone, we selected a sampling plot. We measured all the blocks over a certain volume inside it (zone 1: 4.2*10-5 m^3, zone 2: 1.4*10-4 m^3 and zone 3: 1.6*10-4 m^3).

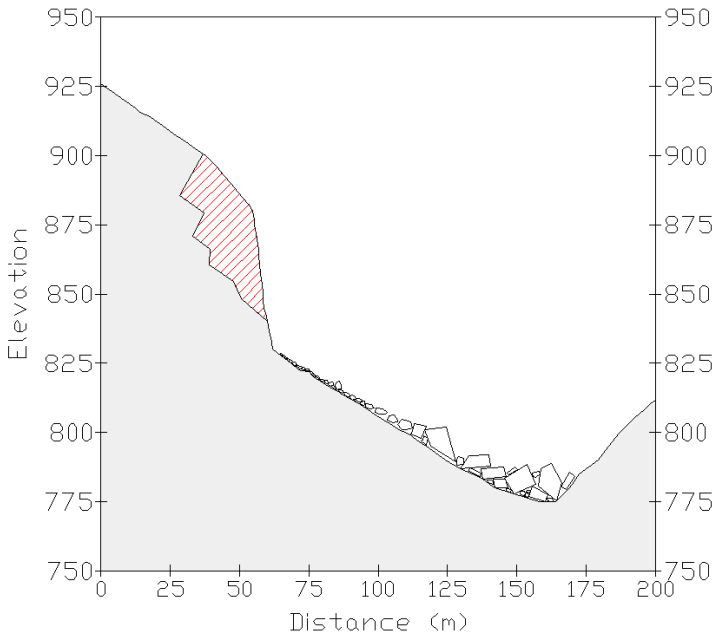

Figure 7. Scheme of the Malanyeu rockfall.

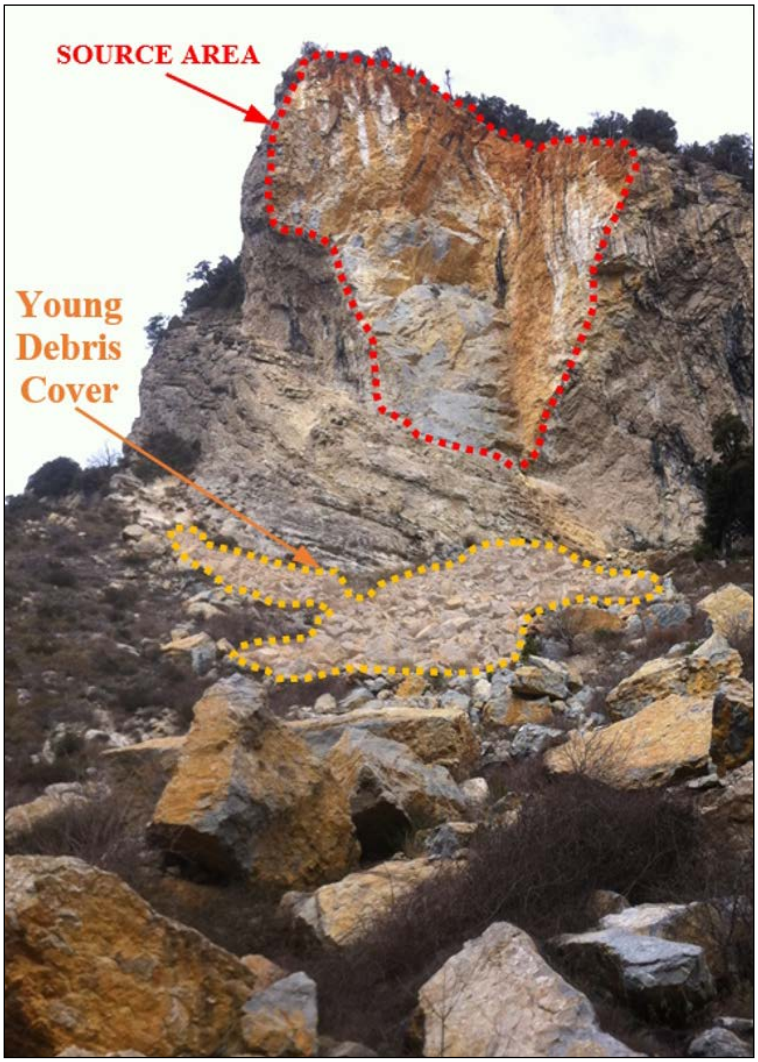

Figure 8. View of the Malanyeu rockfall.

The sampling plots have a square shape, and the area is proportional to the size of the blocks inside (sampling plot in zone 1: 4 m2, zone 2: 16 m2 and zone 3: 6.25 m2). Finally, we extrapolated the block size distribution obtained at the sampling plots to each homogeneous zone. To this end, we used the ratio between the area of the homogenous zone and the area of the sampling plot representative of the zone. See Ruiz et al. (2015), for further details.

The faces of the accumulated blocks are mostly preexisting discontinuities in the rock mass (joints and bedding surfaces). Figure 9 depicts the source area, the boundaries of the homogeneous zones used and the biggest blocks deposited at the lower part of the deposit.

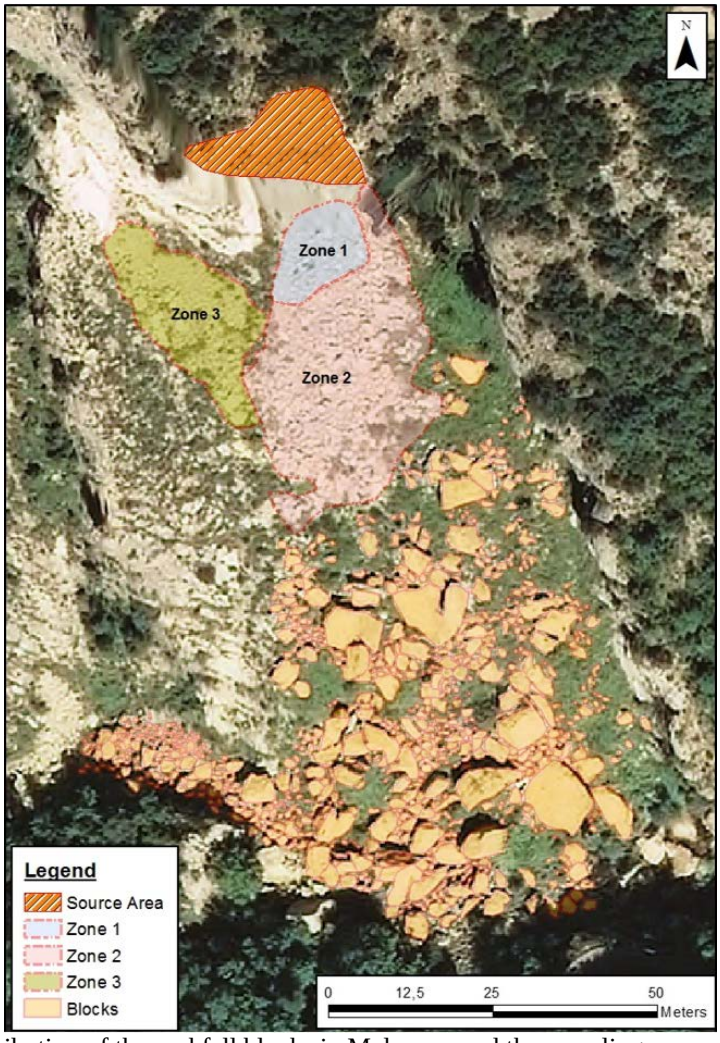

Figure 9. Spatial distribution of the rockfall blocks in Malanyeu and the sampling zones selected.

This case corresponds to a large fragmental rock-fall where the fragmentation is related to both the disaggregation of the rock mass along preexisting discontinuities (joints and bedding planes), and pure breakage. A proof of this is the presence of huge blocks, bounded by preexisting discontinuities in the lower part of the deposit and, on the other side, the blocks of the YDC, showing multiple new faces. The obtained RBSD is well fitted with a power law with an exponent of 0.72.

2.5 Vilanova de Banat rockfall

Vilanova de Banat rockfall is located in Cadi Sierra, in the Eastern Pyrenees. The cliff is made of limestone of Paleocene age. The volume detached is close to 10.000 m^3, based on field measurements and on the reconstruction of the detached mass from a 3D model of the scar generated by photogrammetric techniques (Ruiz et al., 2015). The free fall height is 40 m, and the maximum run-out distance is 740 m (Figure 10).

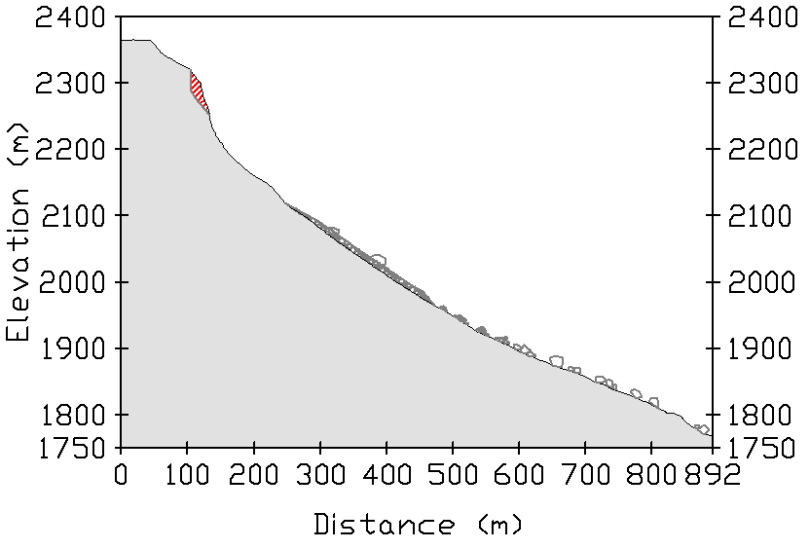

Figure 10. Scheme of the Vilanova de B. rockfall.

The first impacts generated a YDC of 30.000 m^2 (Figure 11). Three roughly homogenous block sizes zones have been identified: the highest, middle and lowest parts of the YDC. We further divided the highest part in 3 zones, and the lowest part in 2 zones (Figure 12). We measured 1252 blocks in 6 sampling plots (one per each defined zone) and 272 as Large Scattered Blocks (LSB). The corners of the sampling plots and each LSB measured were georeferenced with a GPS (Figure 12).

The extrapolation of the block size obtained from the sampling plots to the homogenous zones is explained in detail in Ruiz et al. (2015). The minimum and maximum block volume measured is 1.53*10-3 and 30.8 m^3, respectively. We measured 1524 blocks, in the sampling plots which resulted in 60.000 blocks in the deposit after their extrapolation to the whole YDC.

The blocks deposited have an irregular shape, showing fresh faces related to the breakage and some faces defined by the preexisting joints. Field observations suggest that the deposit was mainly originated by breakage. This is confirmed by the large number of small and medium blocks and the predominance of fresh faces in the blocks. The obtained RBSD can be very well fitted with a power law with an exponent of 1.27.

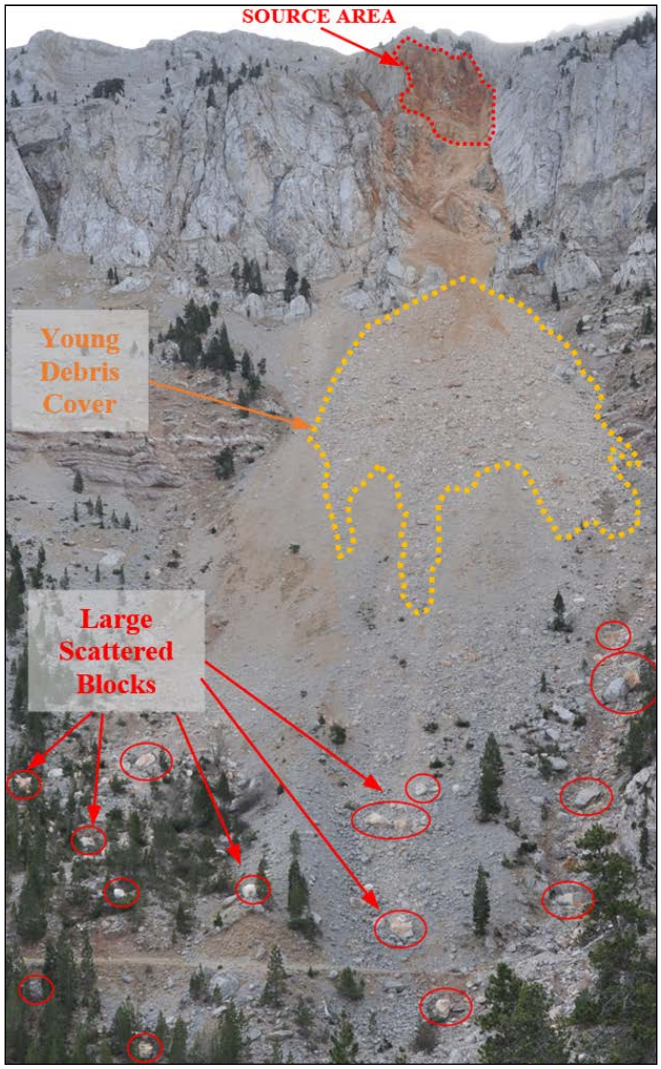

Figure 11. Picture of the Vilanova de Banat rockfall.

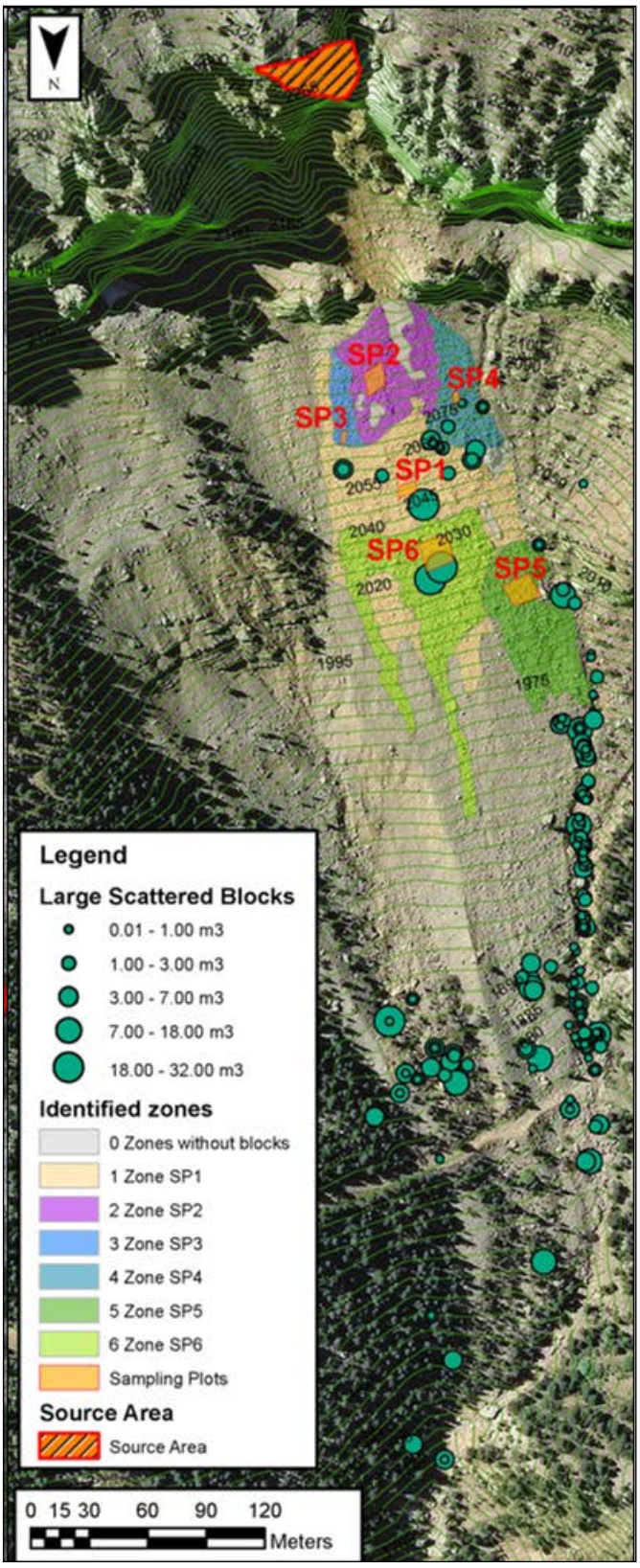

Figure 12. Orthophoto map showing the location of the six homogeneous zones of the YDC, samplings plots, the large scattered blocks and the source area in the Vilanova de Banat rockfall case (Ruiz et al. 2015).

3. RBSD comparison

The obtained RBSD is expected to be related to the predominant fragmentation mechanism of the rock mass during the propagation. The final RBSD de-pends on the IBSD, the geomechanical characteristics of the rock, the impacts energies, the total volume detached and the morphology and rigidity of the ground. The obtained RBSD based on field measurements are plotted in relative frequency terms (Figure 13), while the main attributes are summarized in Table 1.

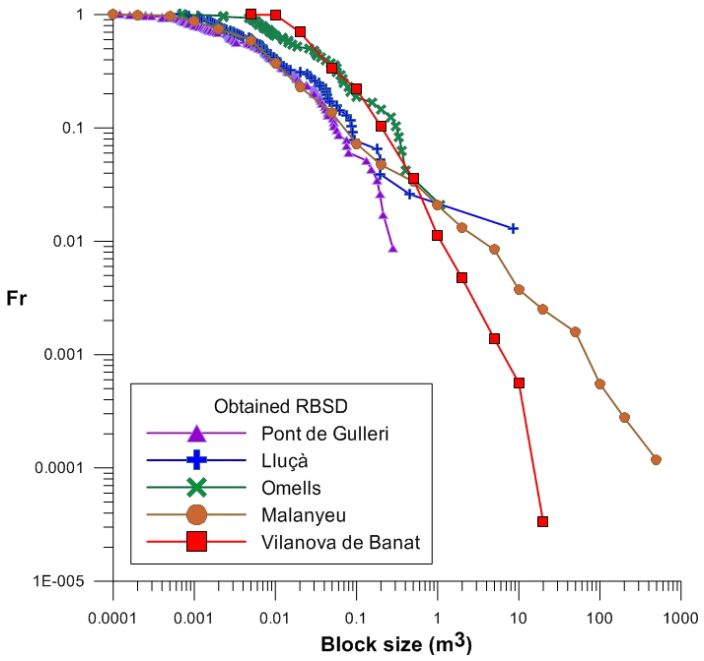

Figure 13. RBSD obtained in relative frequency versus block size.

Table 1. Attributes of the studied rockfalls and their RBSD.

Rockfall case	Exponent of the fitted power law (b)	R^2	Total Volume (m^3)	Free fall height (m)	Lithology
Pont de G	0.92	0.94	2.6	12	Schist
Lluçà	0.51	0.95	10.7	0.6	Sandstone
Omells	0.53	0.89	4.2	0.8	Sandstone
Malanyeu	0.72	0.98	5000	10	Limestone
Vilanova	1.27	0.95	10000	40	Limestone

The description of the RBSD in relation to the observed field features follows:

-Pont de Gullerí case is a disaggregation case, with the blocks clearly delimited by preexisting joints.

-Lluçà rockfall is a case with pure breakage. The total volume detached is 10.7 m3, and the biggest block measures 8.47 m3. The 20% of the original mass was broken from the detached block, generating a distribution of blocks that clearly follows a power law.

-Omells rockfall involves a low fall which progresses on a soft and stepped ground, and the rock is very weak. The fragmentation occurs by breakage of the blocks but is strongly controlled by the anisotropy of the rock produced by the bedding planes. This case is very similar to the Lluçà case.

-The deposit in Malanyeu rockfall shows the influence from the IBSD in the cliff, related with the shape and the volume of the blocks. The fragmentation by breakage is observable mainly in the YDC. The preexisting discontinuities are prevalent features in the faces of the bigger blocks. The low energy (limited fall height) of the rockfall could account for the large number of big unbroken blocks.

-The deposit in Vilanova de Banat rockfall shows more fragmentation by breakage, less big blocks and a high exponent of the fitted power law. Probably, this high degree of fragmentation by breakage is related to the free fall height and to the volume detached, which generate high impact energies at the beginning of the propagation. Furthermore, the IBSD could have an important influence as well.

4. Conclusions

We conclude that the exponent of the fitted power laws to the RBSD can be used to characterize the block size distribution generated in a fragmental rockfall, and it may also provide information on the fragmentation phenomenon. The results suggest that these exponents could be related to the height of fall (Figure 14) and to the proportion of new fractures generated in the rock mass, among other factors. However, to characterize the fragmentation more information is needed on the IBSD, the total volume detached, the impact energies and the morphology and the rigidity of the ground. The disaggregation of the blocks in the case of Pont de Gullerí rockfall suggests that the RBSD is controlled by the preexisting joints in the detached rock mass. The cases of Lluçà and Omells show a very similar behavior, with the difference that in the Omells case, the stepped ground allows more impacts. The Lluçà rockfall has only one impact, allowing the survival of a large block in a low energy scenario. This is confirmed in the latter case by the accumulation of several very large blocks and by the higher presence of preexisting discontinuities in the faces of deposited blocks.

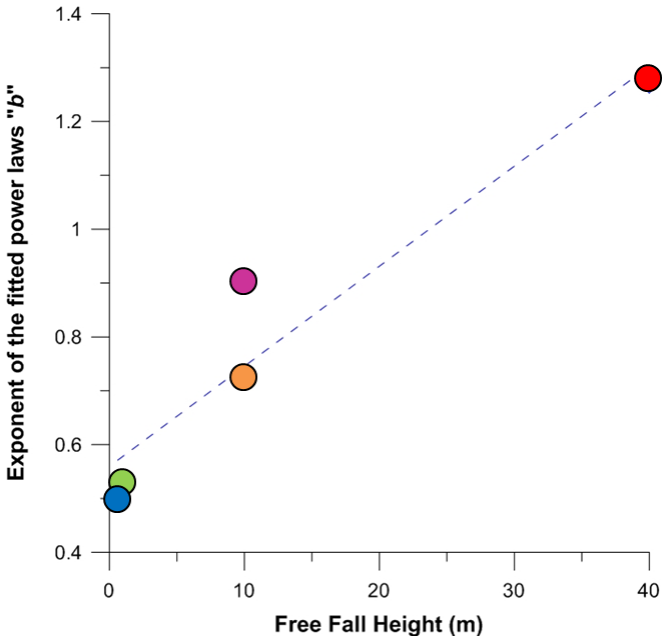

Figure 14. Exponent of the fitted power laws versus free fall height.

ACKNOWLEDGEMENT

The authors acknowledge the support of the Spanish Economy and Competitiveness Ministry to the Rockrisk research project (BIA2013-42582-P) and the support of the Ministry of Education to the first author (grant code FPU13/04252) and the sup-port of the Foundation BBVA (Ayudas Fundación BBVA a Investigadores, Innovadores y Creadores Culturales) to the third author.

References

Bowmann. E.T. Take. W.A. Rait. K.L. Hann. C. 2012. Physical models of rock avalanche spreading behavior with dynamic fragmentation. NRC Research Press. Can. Geotech. J. 49: 460–476 (2012) doi: 10.1139/T2012-007.

Corominas. J. Mavrouli. O. Santana. D. Moya. J. 2012. Simplified approach for obtaining the block volume distribution of fragmental rockfalls. E. Eberhardt, C. Froese, A.K. Turner & S. Leroueil (editors). Landslides and engineered slopes. Taylor and Francis. Vol 2: 1159-1164.

Dussauge. C. Grasso. J. Helmstetter. A. 2003. Statistical Analysis of Rock Fall Volume Distributions: Implications for Rock fall Dynamics. Journal of Geophysical Research B 108 (B6) (2003) 2286, DOI: 10.1029/2001JB000650.

Dorren. L.K.A. 2003. A review of rockfall mechanics and modeling approaches. Progress in Physical Geography 27 (1):69– 87.

Elmouttie. M. K. & Poropat. G. V. (2011). A Method to Estimate In Situ Block Size Distribution. Rock Mechanics and Rock Engineering, 45(3), 401–407. doi: 10.1007/s00603-011-0175-0.

Faramarzi. F. Mansouri. H. Ebrahimi Farsangi M.A. 2013. A rock engineering systems based model to predict rock fragmentation by blasting. International Journal of Rock Mechanics & Mining Sciences, 60, 82-94. http://dx.doi.org/10.1016/j.ijrmms.2012.12.045.

Giacomini. A. Buzzi. O. Renard. B. & Giani. G. P. (2009). Experimental studies on fragmentation of rock falls on impact with rock surfaces. International Journal of Rock Mechanics and Mining Sciences, 46(4), 708–715. doi:10.1016/j.ijrmms.2008.09.007.

Hantz. D. Rossetti. J. P. Servant. F. D'Amato. J. (2014) Etude de la distribution des blocs dans un éboulement pour l'évaluation de l'aléa. Proceedings of Rock Slope Stability 2014, Marrakesh.

Hartmann. W.K. (1969) Terrestrial, lunar and interplanetary rock fragmentation. Icarus 2(2):201–213.

Hudaverdi. T. Kuzu. C. Fisne. A. 2012. Investigation of the blast fragmentation using the mean fragment size and fragmentation index. International Journal of Rock Mechanics & Mining Sciences, 56, 136-145. http://dx.doi.org/10.1016/j.ijrmms.2012.07.028.

Evans. S. Hungr. O. 1993. The assessment of rockfall hazard at the base of talus slopes. Canadian Geotechnical Journal 30:620-636.

Hungr. O. Leroueil. S. Picarelli. L. 2014. The Varnes classification of landslides types, an update. Landslides 11:167-194.

Jaboyedoff. M. Dudt. J.P. Labiouse. V. 2005. An attempt to refine rockfall hazard zoning based on the kinetic energy, frequency and fragmentation degree. Natural Hazards and Earth System Sciences 5: 621–632.

Latham. J. P. Lu. P. 1999. Development of an assessment system for the blastability of rock masses. International Journal of Rock Mechanics & Mining Sciences 36, 41-55. PII: S01 4 8- 90 6 2(98)0 0 17 5 -2.

Locat. P. Couture. R. Leroueil. S. Locat. J. Jaboyedoff. M. 2006. Fragmentation energy in rock avalanches. NRC Research Press. Can. Geotech. Can. Geotech. J. 43: 830–851. doi: 10.1139/T06-045.

Okura. Y. Kitahara. H. Sammori. T. Kawanami. A. 2000. The effects of rockfall volume on runout distance. Engineering Geology 58(2):109–124.

Ruiz. R. Corominas. J. Mavrouli. O. 2015. A methodology to obtain the block size distribution of fragmental rockfall deposits. Landslides. doi 10.1007/s10346-015-0600-7.

Wang. Y. Tonon. F. 2010. Discrete Element Modelling of Rock Fragmentation upon Impact in Rock Fall Analysis. Rock Mech Rock Eng 44: 23–35.

4. Experiences with UAV on mass movements characterization

Conference Publication reference:
Ruiz-Carulla R, Corominas J & Hürlimann M (2017). Experiencias con drones para el estudio de movimientos de ladera. IX Simposio Nacional de Taludes y Laderas Inestables, Santander.

Translated from Spanish to the English language
Ruiz-Carulla R, Corominas J & Hürlimann M (2017). ***Experiences with UAV for the stady of slope mass movements.*** IX Simposio Nacional de Taludes y Laderas Inestables, Santander.

Communication awarded by the Scientific Committee of the IX Simposio Nacional de Taludes y Laderas Inestables (Santander, 2017) as the "*Best communication*" in "*Site investigation, characterization, and mapping*" category.

Abstract:
The UAV (Unmanned Aerial Vehicle or drone) technology has been exponentially developed on the last years. High resolution 3d models from the terrain can be generated by using digital photogrammetry techniques from a collection of pictures obtained with an UAV. These new technologies allow the geometrical characterization in a more efficient way, more secure and with a high resolution. The present communication shows some practical experiences in the measurement of erosion and the associated morphological changes, in rockfall characterization and inventorying, and in the characterization of the joint pattern, necessary for the stability analysis and unstable rock mass identification.

Keywords: UAV, drone, digital photogrammetry, terrain profile, 3d models, point cloud, mass movements, change detection.

1. Introduction

The use of UAV in order to take pictures, combined with the last digital photogrammetric techniques, allow to obtain a wide range of different mapping, geometric and graphic products that can be applied to studies in studies on the field of earth science and engineering. The low height of flight allows collecting high-resolution images and the generation of high quality orthophotos with the desired periodicity. Furthermore, a 3D point cloud reconstruction may be obtained, as well as a 3D texturized mesh and a Digital Elevation Model (DEM) on raster format. From the last, other products are generated like the contour lines, terrain profiles, slope and orientation maps, etc. Also from the point cloud may generate other products like the point cloud by dip or dipdirection, geometrical measurements like Euclidian distance, or separately by X, Y, Z, as well as areas, volumes or terrain profiles. This communication shows the differences between generate a terrain profile from DEM or from point cloud. Without get into the post-processing steps and details, the communication aims to show some possibilities on the use of UAV with digital photogrammetry on mass movements studies.

2. UAV and digital photogrammetry

The popular known as drones should be more technically defines as UAV (Unmanned Aerial Vehicles) or RPAS (Remotely Pilot Aircraft Systems). A wide range of dimensions and types of UAV exist, while the common aircrafts used on science and engineering are drones of less than 25 kg of weight, with 1 meters or less of diameter and typically with a photographic camera as data acquisition tool. These kind of vehicles are controlled by the 18/2014 law in Spain, where the requests to their use are defined, as a specific pilot license, civil responsibility insurance and an entity as flight operator to manage the legal requests.

The UAV are able to flight autonomously thanks to the satellite positioning system and the inertial main unit (GPS and IMU). Drone types can be divided into multirotors and fixed wings devices. Multirotors (Figure 1) have less time of flight per battery than a fixed wings, but multirotors can stay immobile on the air and move it side by side. These lateral displacements, combined with the camera stabilization (or Gimbal), allow to take pictures on frontal and oblique perspectives in front of a cliff, furthermore than the classic zenithal pictures.

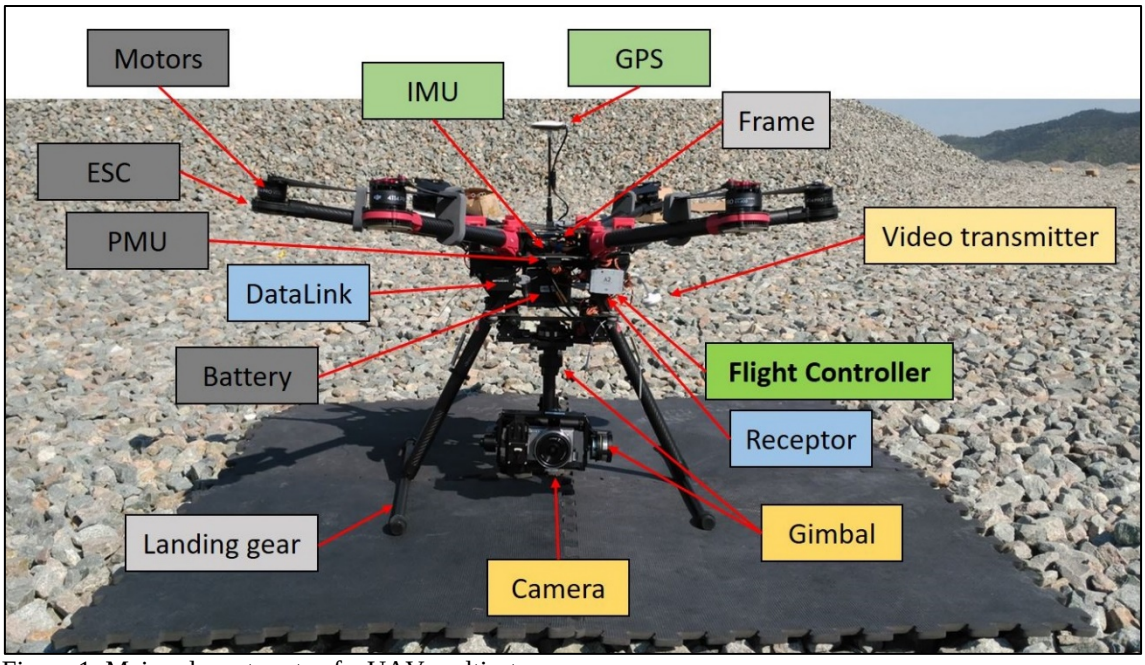

Figure 1: Main relevant parts of a UAV multirotor:

Other important elements on a multirotor UAV are the battery, the Power Main Unit (PMU), the Electronic Speed Controls (ESC) and the motors. A 2.4GHz receptor allows that the drone pilot manage the vehicle with a digital programmable radio, and a secondary communication system (DataLink) allows the control of the drone using a tablet or computer in order to execute autonomous programmed flights. Finally, the camera or the sensor mounted will be the most important part of the drone in terms of data acquisition system. For this reason, the 3 axes stabilization system (or Gimbal) is very important in order to obtain high quality pictures.

Digital photogrammetric software like VisualSFM, Agisoft Photoscan, PIX4D, Accute 3D or others, allows the generation of a wide range of cartographic products and 3D reconstructions. All of them depends on the quality of the images, the focus, the lightening, and the final resolution depends on the distance between the camera and the terrain, the focal length and the sensor size (Thoeni et al, 2014). The low height of flight, below the 120 meters over the ground, allows high resolutions with common values of 3 cm/px (considering a 18mm width sensor with 4608 pixels and a focal length of 15 mm). Reducing the distance between the camera and the terrain the resolution increase, with 1 cm/px at 40 meters of height (p.e.). The velocity of the drone on the air should be properly combined with the pictures frequency in order to arrange a correct overlapping on consecutives pictures to allow a correct photogrammetric reconstruction.

Model georeferentiation may depend on the GPS metadata of the pictures. However, using this data, the obtained models can be erroneously moved between 1 and 10 meters on real referencing. In function of the requirements of each study, may be opportune reduce the position errors to 1 –

5 cm. To this end, it is common the use of a set of targets that can be well identified on the pictures (circles of 30 cm of diameter) and their coordinates measurements with a GPS-RTK to fix the model on more precise coordinates.

For all of these, it is necessary to have some background on topography and photogrammetry knowledge in order to design a flight plan in order to obtain homogeneous results. On the same way, we consider important the drone systems and piloting background, especially on high mountain flights.

3. Application on rockfalls inventories

On landslides characterization, detailed 3D models reconstruction as soon as possible may be very useful in order to characterize the event and register it with other products like orthophotos, digital elevation models and topographic representation, that can helps on cartography, characterization and interpretation tasks.

A rockfall of 100 m^3 occurred in April of 2016, on the village of Gurp, on Tremp basin, in Catalonia. This rockfall event was inventoried in the framework of a research project focused on fragmentation of rockfall. 500 blocks were measured on the deposit by tape attending to measure all the blocks generated by fragmentation. Furthermore, a UAV flight allows the generation of a 3D model of the whole cliff and the deposit zone (Figure 2). The georeferenced model allows the estimation of the detached rock mass based on a detailed 3D model of the scar and an interpretation of the fresh faces and the joint pattern that delimited the detached mass.

These type of 3D models, with the orthophoto and the digital elevation models, allow the measurements of distances, areas, volumes, runouts, and so on, on an easy way, with high precision and in a very secure mode. ·D models make easier the Euclidian distance measurement between two points, as the decomposition in X, Y and Z components or in the opportune system. Angle measurements on 3D models are easier than the required conversions related to the angle measurements on planimetric representation on GIS or CAD.

Is important to notice that the zenithal projection of the study environment that is used on GIS and CAD tools, difficult to deal with cliff and very vertical scenarios, due to a huge amount of information from the cliff surface is comprised on few pixels on zenithal representations. 3D models allow a better representation of these scenarios, as well as obtain frontal or oblique orthophotos in order to work on 2D on high resolution if is required.

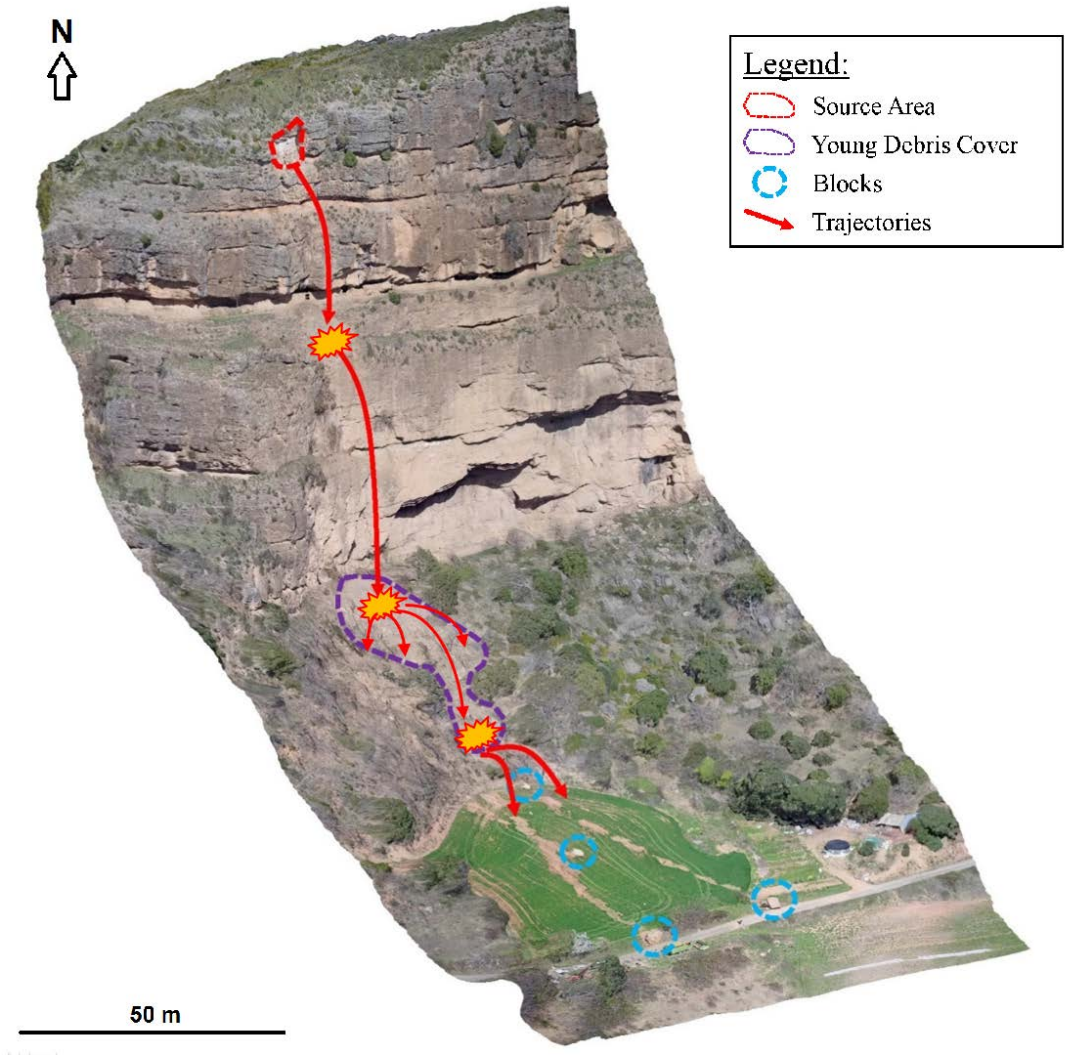

Fig. 2: 3D model of the inventoried Gurp rockfall, in Conca de Tremp, Catalonia.

One of the main benefits on the use of the 3D point cloud instead of Digital Elevation Models (DEM), is in order to obtain terrain profiles. Terrain profiles are the classic and necessary representation on stability and geomorphological studies as well as for evolution interpretation and monitoring. Figure 3 shows the terrain profile from the Gurp rockfall 3D point cloud, and the profiles obtained with digital elevation model, generated with the same point cloud, using 10cm/px (blue) and 2 m/px (red), As DEM are 2D representation, is not able to define two heights on the same XY point, missing the information from overhangs and erosioned zones. The geomorphological, mechanical and evolutive interpretation of this cliff cloud be completely different on these 3 different profiles generated.

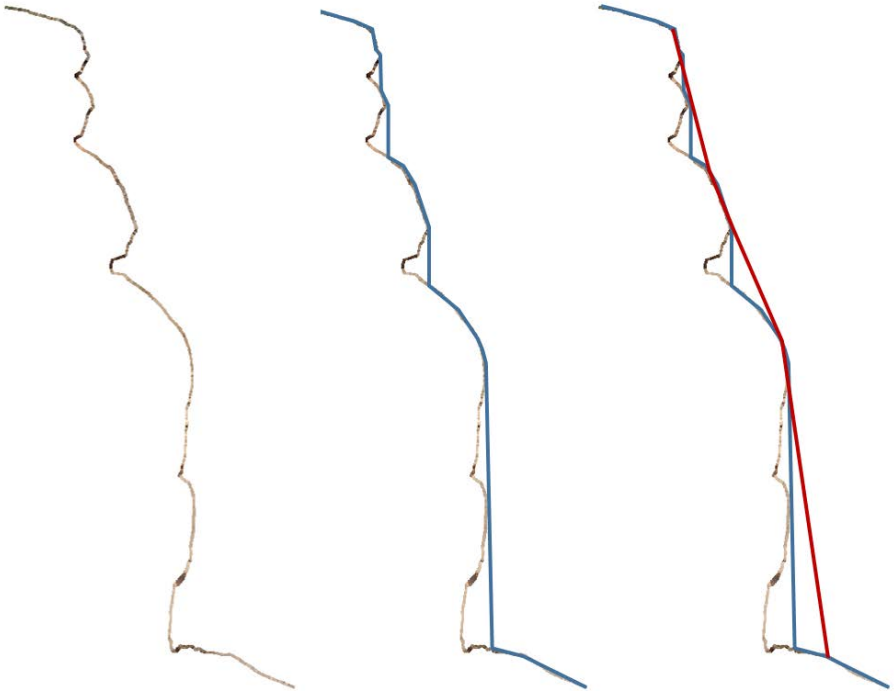

Fig. 3: Terrain profiles from: 3D point cloud (brown); a DEM of 10 cm/px (blue) and a DEM of 2 m/px (red), showing the information missed on overhangs and changing the stability and geomorphology interpretations.

4. Joint pattern characterization

Joint pattern characterization is an important task on rock slope stability analysis. Outcrop modelling and 3D point cloud analysis can be used to characterize joint patterns from 3D point clouds. The normal vector of each point can be calculated considering a buffer zone per each point, and then, the point cloud can be colored by dip or dip direction. Some codes exist in order to identify the joint sets from point cloud like COLTOP3D (Jaboyedoff et al. 2007), DiscontinuitySelfExtractor (Riquelme et al. 2014), CloudCompare (Girardeau-Montaut 2006) o GaiaGeoRoc (Assali 2014). Figure 4 shows a point cloud from Pala Morrano zone on the Natural Park of Aigüestortes (Catalonia), by real color (up) and colored by dip direction (down).

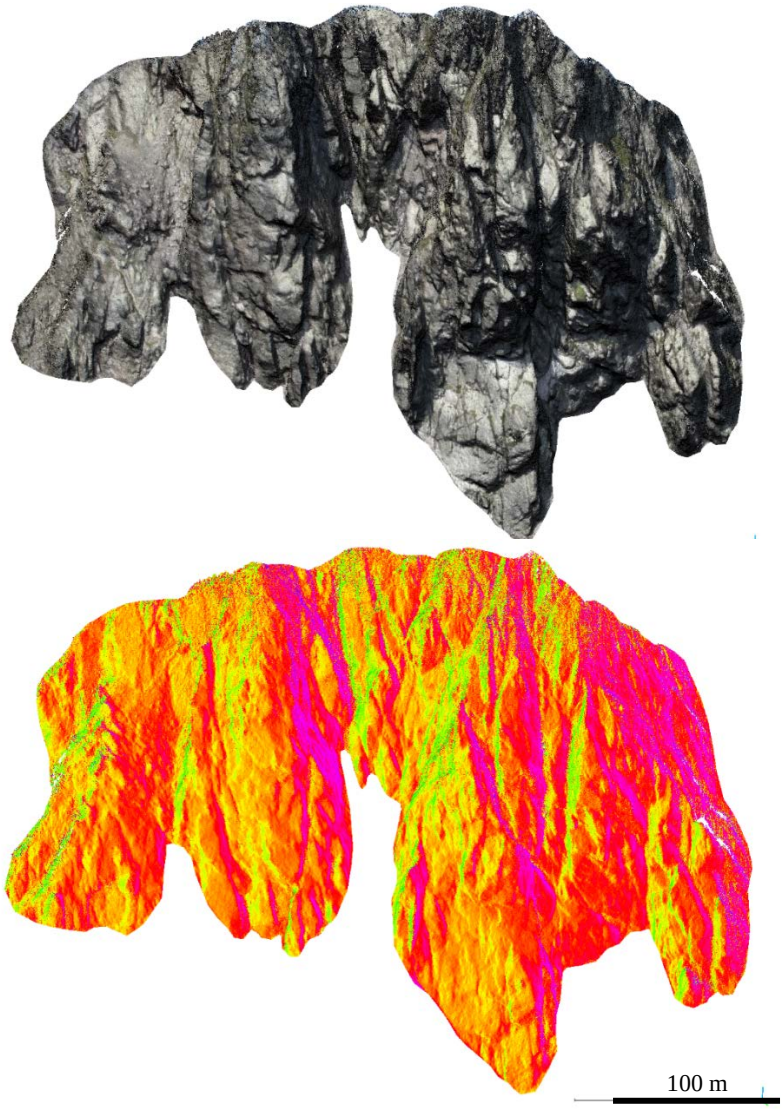

Figure 4 Point cloud from Pala Morrano on real color (up) and colored by dip direction (down).

From 3D point cloud, different procedures may be applied in order to fit and characterize the joint set that creates relief. Figure 5 show a set of joints characterized by planes with a maximum distance of 1 meter against the point cloud, from which a set of families may be identified and plot on a stereographic representation.

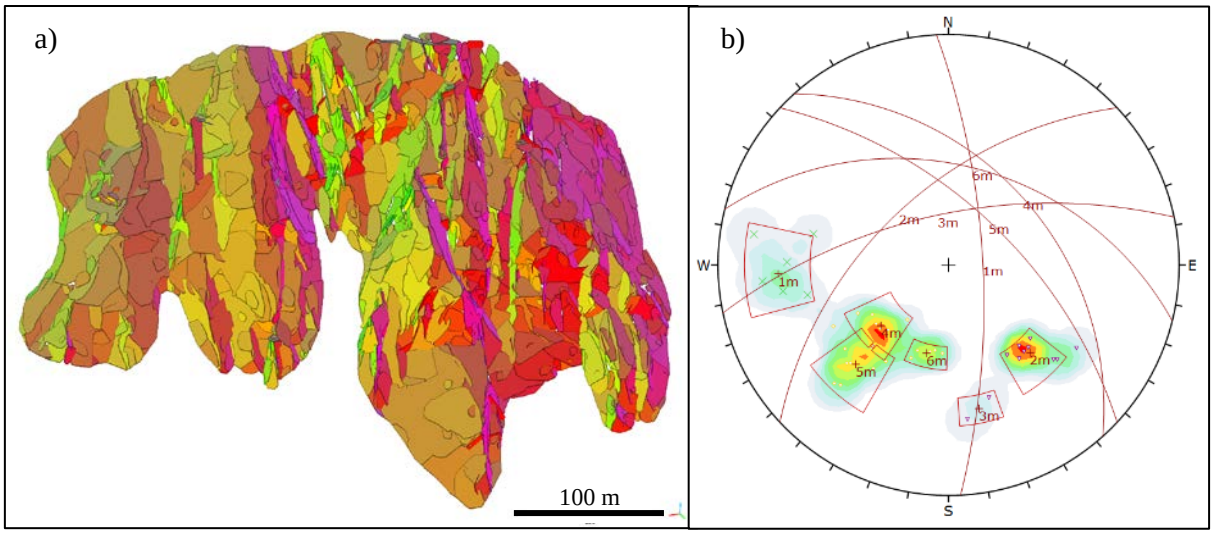

Fig. 5: Planes fitted on the point cloud (a) and the stereographic projection of the joint sets identified (b).

For trace elements, may be useful the use of 3D modeling programs, such as the Rhinoceros, the Polygon or the 3DMAX, for the characterization and the model of the joints, in this case on 3D textured meshes to facilitate their identification. These programs allow to cut the meshes with the modeled joints and with other planes imported from other procedures, facilitating the delimitation of kinematically unstable volumes.

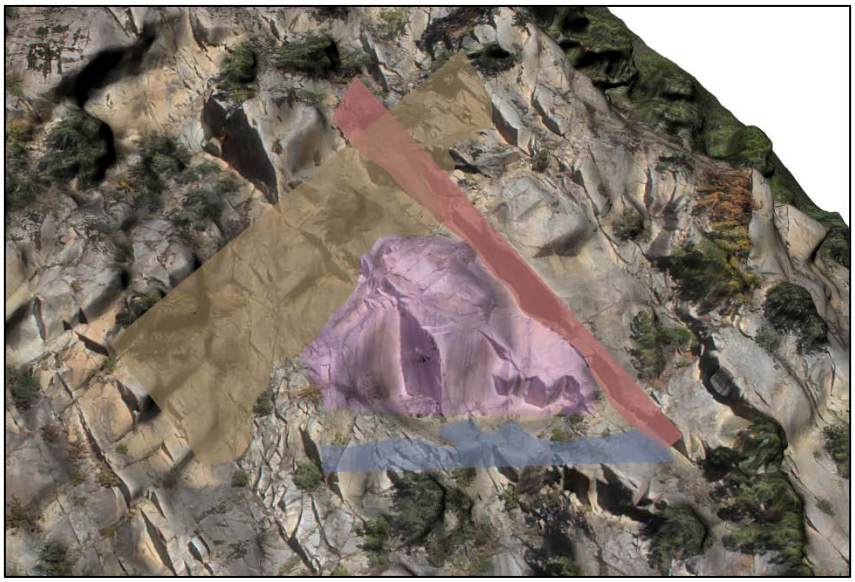
Fig. 6. Unstable rock mass delimitation based on 3D joints modeling.

5. Morphological temporal changes evaluation

The total control in the periodicity of the flights allows the monitoring of zones with the desired frequencies. It is true that weather conditions can be an important inconvenience, but in general, "ad hoc" flights can be made to the measures considered appropriate. For example,

it may be of interest to monitor an area before and after major rain events or volcanic eruptions (Baldi et al 2005).

In Fig. 7 a) there is a general view of the El Rebaixader basin, in front of the town of Senet in the Catalan Pyrenees. It is an active basin with a large area of erosion in the head that contributes sediments of till to generate rockfalls, rocky avalanches or torrential flows depending on the rainfall regimes and the available and accumulated material. It is an inventoried study area with exhaustive control of its activity (Hürlimann et al 2014). In 2016, a series of UAV flights was carried out, which allowed obtaining a digital model of very good quality elevations. The data were contrasted with the last model of elevations that was available obtained by LIDAR airborne techniques in light aircraft (ALS). Fig. 7 b) shows the erosion mapping (in red scale) based on the comparison of the two DEMs at a resolution of 2 meters / pixel conditioned by the resolution of the ALS

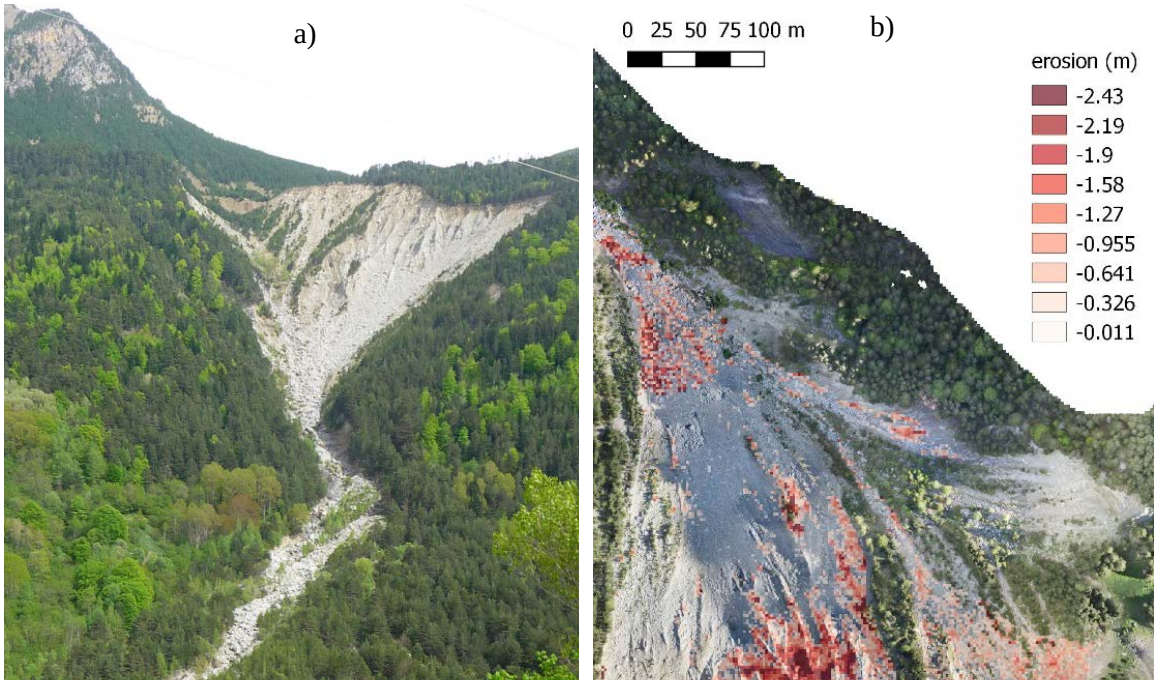

Fig.7 a) General view of the El Rebaixader basin, and b) calculated erosion in the scarp area comparing the DEMs obtained by drone and ALS. The cell size is 2m.

The second case of monitoring is a small landslide in a quarry slope. The following Fig. 8 shows the orthophoto obtained in 2016 (a) and that of 2017 (b). In them, with resolutions of 3 cm, may be perfectly observe the cracks that have ended up generating escarpments, as well as the advance of the lobes of the slide in the west direction. The treatment of these orthophotos with GIS tools allows the cartography of the slide in great detail.

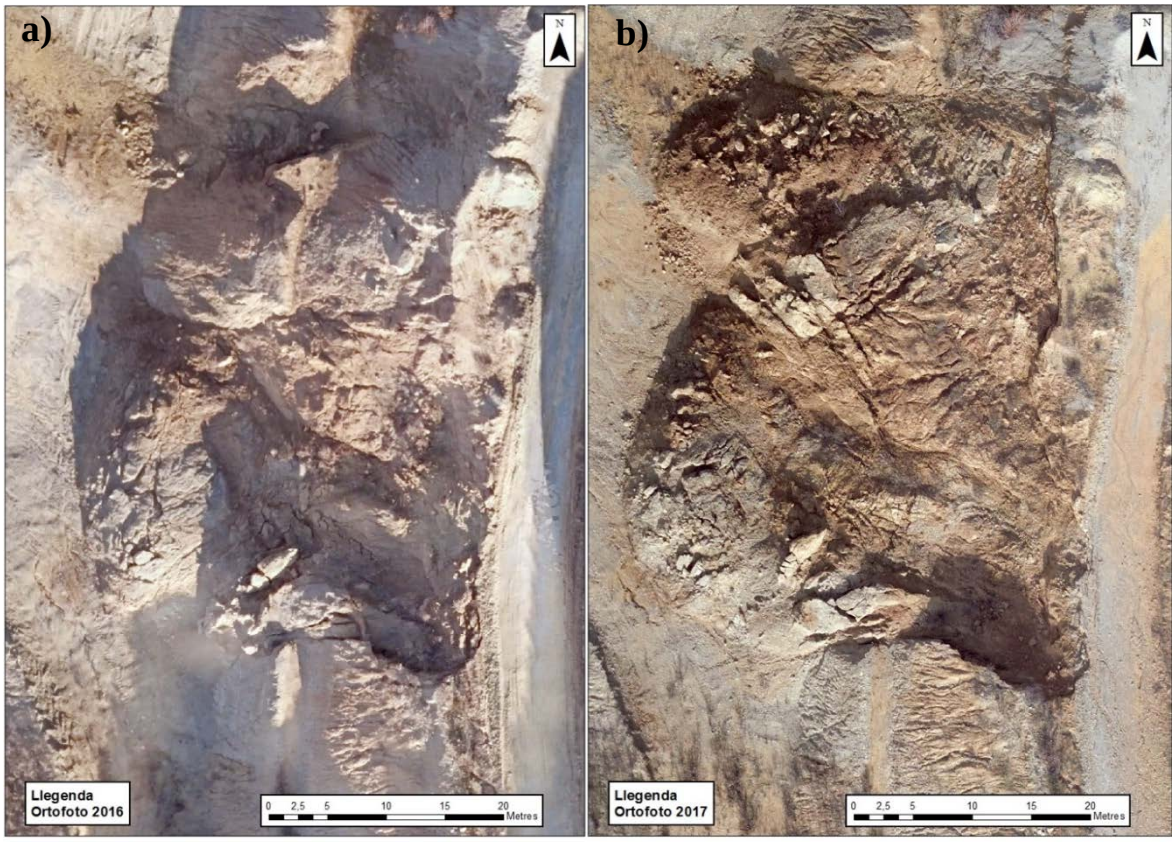

Fig. 8: Orthophoto of 2016 (a) and of 2017 (b) of a rupture of slope of quarry with resolution of 3cm / px.

At the same time, digital terrain models were obtained with which a direct comparison analysis can be carried out in the Z direction. From this, a new map of elevations with the values of increase or decrease of elevation of the points of the terrain is obtained. Fig. 9 shows the comparison of DEMs from 2016 to 2017, perfectly delimiting the area that has fallen losing height (in reds) and the zone that has gained altitude or on which the landslide has been deposited (in blues). The red zones define the escarpments in great detail, while the blue areas define the lobes of the landslide.

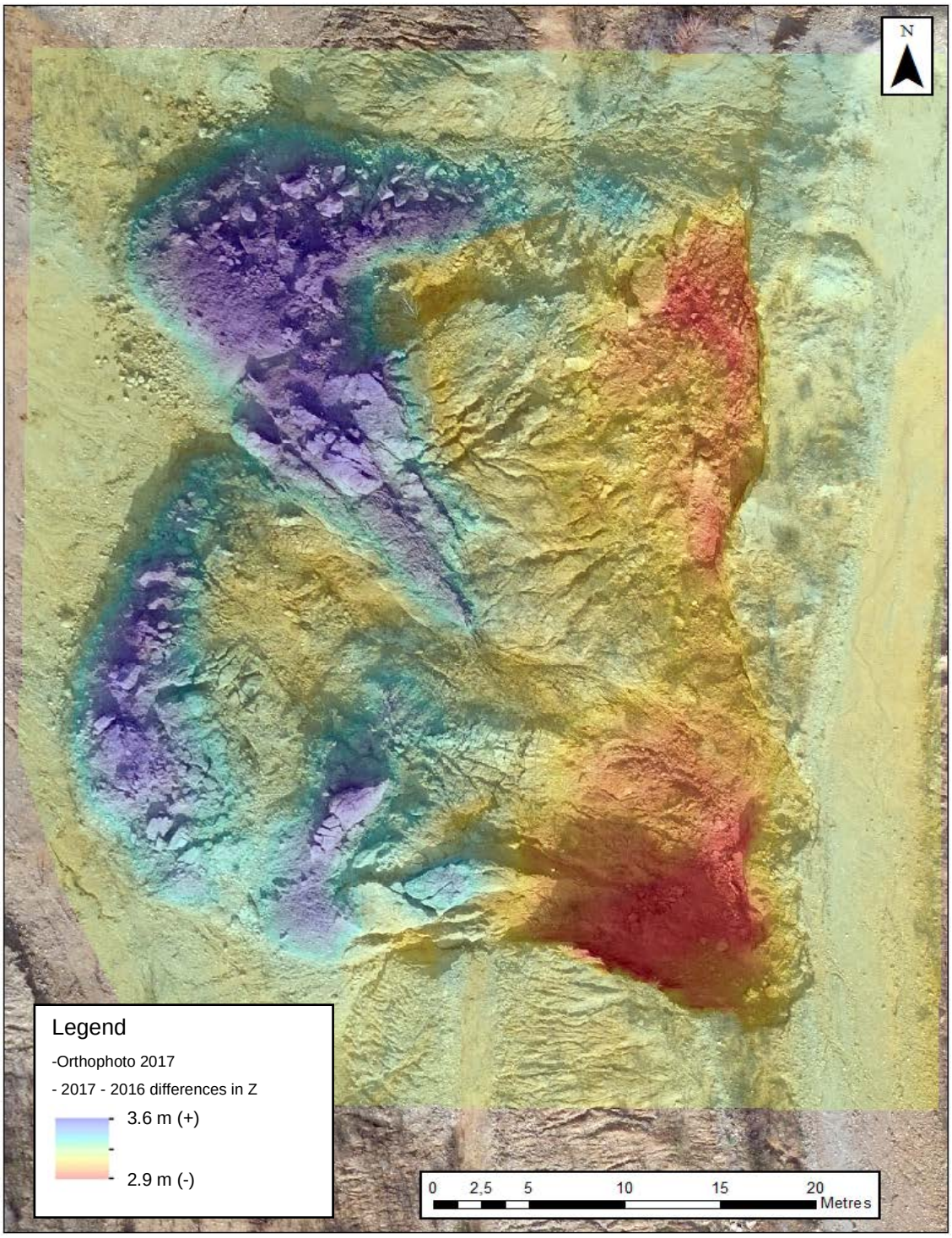

Fig. 9: Map of differences between the two digital models of elevations of 2016 and 2017. In red areas where the level has been reduced (escarpments, high zone of the landslide) and in blue areas that have gained elevation due to the deposit of the lobes of the landslide.

It may make sense to perform the analysis of differences between 2016 and 2017 models in a point cloud format, obtaining the minimum distances between the two models, or the decomposition in X, Y and Z or in the system considered appropriate. Fig. 10 a) shows the point cloud of the 2017 model colored according to the distance to the 2016 model, with the

escarpments in red and the lobes of the slip in blue. The results are slightly different, and according to the sliding morphology it can be important to measure the Euclidean distances in 3D, as well as the internal rotations in the slip body. The escarpments are better identified on the cloud of points represented by slope (Fig. 10b).

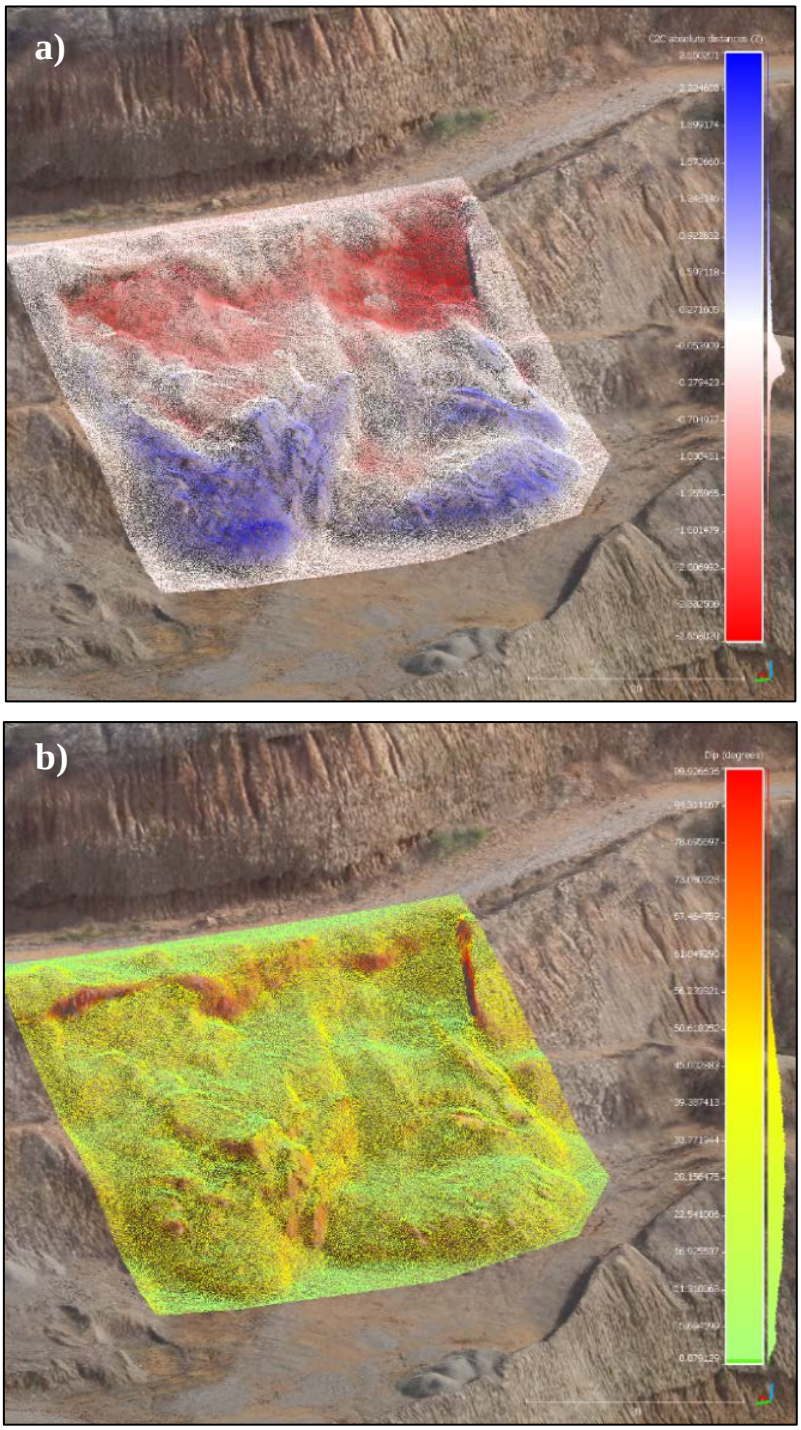

Fig. 10: a) 2017 points cloud colored based on the minimum distance to the 2016 point cloud; and b) Point cloud of 2017 colored according to the slope (red 90º, green 0º).

Finally, it seems interesting the extraction of profiles on the point clouds that allow us to compare the evolution of the profile and colored ground by minimum distance between the two models, where the rotation and the displacement of mass are clearly observed (Fig. 11

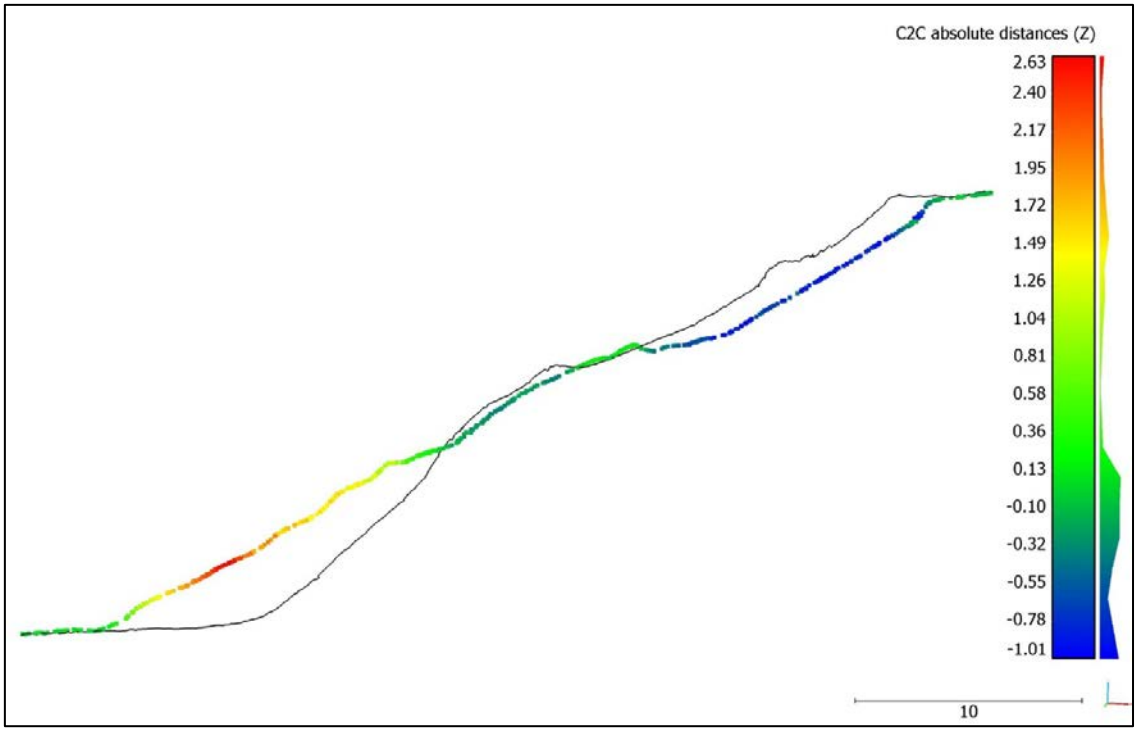

Fig. 11: Profiles on point clouds: 2016 in black and 2017 colored by minimum distance between models.

6. CONCLUSIONS

The uses of drones combined with photogrammetry techniques can provide a large amount of information of high quality. Its application in the description of slope instabilities, characterization of discontinuities, delimitation of unstable volumes, as well as monitoring tasks, will make it an essential tool to improve performance, access to more and better information and improve safety and efficiency in the field works.

7. ACKNOWLEDGMENT

The authors would like to thank the Ministry of Economy and Competitiveness for the financial support of the RockRisk research project (BIA2013-42582-P), the FPU scholarship of the first author (FPU13 / 04252), as well as the grant "Ayudas Fundación BBVA a Innovative Investigators and Cultural Creators "to the third author.

REFERENCES

Assali P (2014) Modélisation géostructurale 3D de parois rocheuses en milieu ferroviaire. Thèse de Docteur de l'Université de Strasbourg. École Doctorale Mathématiques, Sciences de l'Information et de l'Ingénieur.

Baldi P, Fabris M, Marsella M, Monticelli R (2005). Monitoring the morphological evolution of the Sciara del Fuoco during the 2002–2003 Stromboli eruption using multi-temporal photogrammetry. ISPRS Journal of Photogrammetry & Remote Sensingm Volume 59, pp 199-211

Girardeau-Montaut (2006) Detection de Changement sur des Données Géométriques 3D", D. PhD manuscript (french), Signal & Images Processing, Telecom Paris

Hürlimann, M., Abancó, C., Moya, J., & Vilajosana, I. (2014). Results and experiences gathered at the Rebaixader debris-flow monitoring site, Central Pyrenees, Spain. Landslides, 11, 939–953

Jaboyedoff M, Metzger R, Oppikofer T, Couture R, Derron MH, Locat J, Turmel D (2007) New insight techniques to analyze rock-slope relief using DEM and 3D-imaging cloud points: COLTOP-3D software, in: Rock mechanics: Meeting Society's challenges and demands, Proceedings of the 1st Canada – U.S. Rock Mechanics Symposium, edited by: Eberhardt, E., Stead, D., and Morrison, T., Vancouver, Canada, 27–31 May, Taylor & Francis, London, UK, 1, 61–68

Riquelme A, Abellán A, Tomás R, Jaboyedoff M (2014) A New Approach for Semi-Automatic Rock Mass Joints Recognition from 3D Point Clouds. Computers & Geosciences 68. Elsevier: 38–52. doi:10.1016/j.cageo.2014.03.014.

Thoeni K, Giacomini A, Murtagh R, Kniest E (2014) A comparison of multi-view 3D reconstruction of a rock wall using several cameras and a laser scaner. The International Archieves of the Photogrammetry, Remote Sensing and Spatial Information Science, Volume XL-5, ISPRS Technical Commission V Symposium, 23 - 25 June 2014, Riva del Garda, Italy. doi:10.5194/isprsarchives-XL-5-573-2014.

5. Unstable rock mass characterization with UAV

This chapter is focused on the methodologies followed in order to identify and characterize unstable rock volumes based on 3D models obtained with UAV and digital photogrammetric techinques. The methodology is used also for the rockfall inventory (Chapter 6), as well as for the applications presented on Chapters 11 and 12.

Original unpublished chapter

Abstract:

The identification of unstable rock mass is always an important part of the hazard assessment. Nowadays, the use of both UAV and digital photogrammetry allows an easy and safe methodology to characterize a rock cliff. This chapter describes the methodology used to identify and characterize unstable volumes based on 3D point clouds, joint pattern characterization with semi-automatic and manual tools, volume delimitation and kinematic analysis.

Keywords: Unstable rock mass, joint set, UAV, drone, digital photogrammetry, point cloud

1. Introduction

In rockfall hazard or risk assessment studies, the identification and quantification of the potential unstable rock volumes is an important part of the hazard characterization. This chapter presents the methodology used on this thesis in order to identify and quantify potential unstable rock volumes. The methodology is also used to characterize the inventoried rockfalls and other mass movements.

Vertical cliff or steeped terrain are sources of rockfalls. When overhangs are present in the slopes, they often erroneously displayed in 2D representations like topographic maps, digital elevation models and orthophotos. To improve the representation and the information quality, the 3D models should be used. The methodology presented here (flowchart of Figure 1) may be divided in 4 steps: 1. Data acquisition (properly planning and executing an UAV flight); 2. Products generation (by digital photogrammetry techniques); 3. Joint sets identification (using semi-automatic and manual tools); and 4. Potential Volume delimitation (3D mesh cutting). The products generated can be used for slope stability analysis such as the limit equilibrium methods, or, using the accurate 3D models, for define the geometries in discrete element methods.

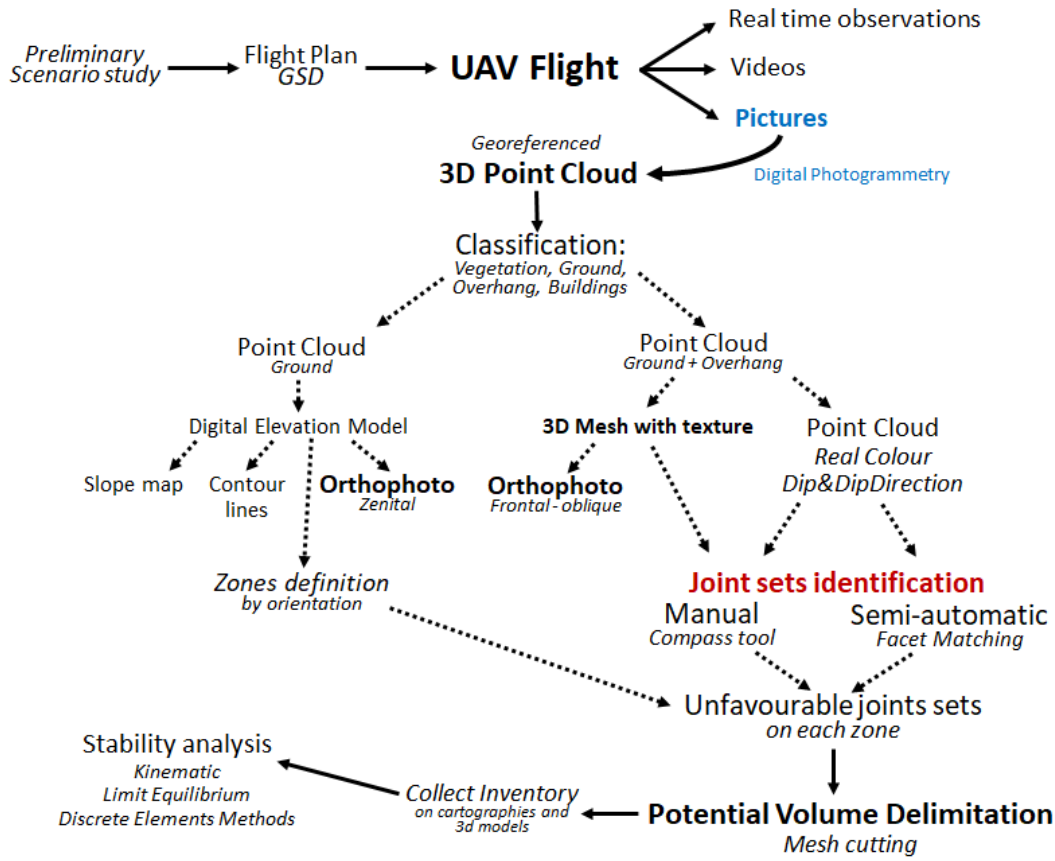

Figure 1: Flowchart of the main steps from UAV flight to the potential volume identification and calculation.

2. Data acquisition

The first step, and one of the most important part on acquisition works, is the selection of the sensor used. In the case of UAV and digital photogrammetry, the camera and the drone will define the quality of the original data obtained. We tested different drones in several landslides scenarios: a little Hubsan H107C (toy) with a camera of 1.3Mp; a self-constructed DJI-F450 with a GoPro Hero 4; a self-constructed HexaCarbonFrame; the DJI-Inspire 1 Pro; the DJI-Inspire 2 and a self-constructed hexacopter DJI-S900 (Figure 2). We used a SONY-NEX5 (14Mp, APS-C sensor) on the hexacopters (HexaCarbonFrame and DJI-S900) and the cameras X5 (16Mp, micro 4/3 sensor) and X5S (20.8, Mp micro 4/3 sensor) with the Inspires 1 Pro and Inspire 2 respectively.

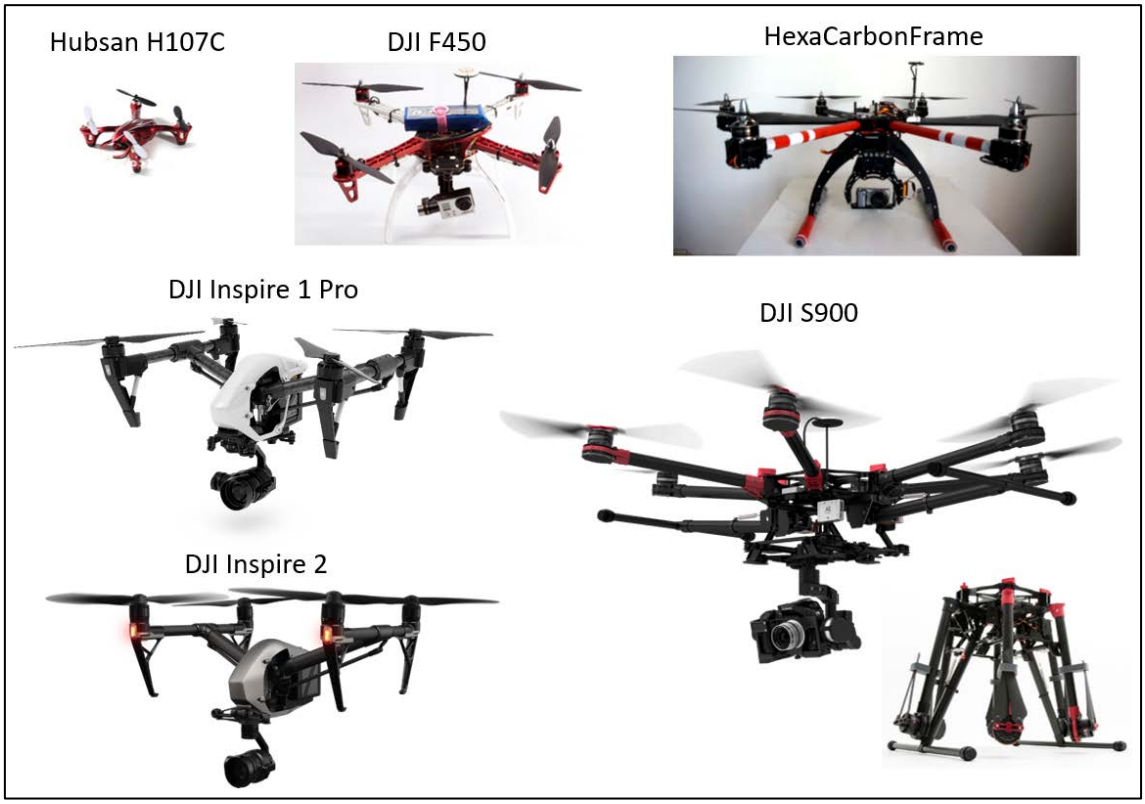

Figure 2: UAV devices tested on landslides site investigation.

The Hubsan H107C, is mounted with a camera of 1.3 Mp. However, it has no GPS neither camera stabilization device (or Gimbal). It was our first experience in 2013. It allowed the generation of a 3D model of a steep rock wall with satisfactory results. DJI-F450 and our own HexaCarbonFrame are drones with a GPS incorporated. It has the capability to program the flight to perform autonomous paths. The gimbal, in these devices, allows the stabilization of the camera obtaining well aligned and clear pictures. The flight time, or battery life, is an important issue in order to plan the acquisition works. Flight duration is usually short, like 10 minutes per battery on DJI-F450 and HexaCarbonFrame. The DJI-Inspire series are "*ready to flight*" drones, with very good performance in terms of camera and gimbal quality, as well as the communication

systems. On the other hand, the Inspire series is restricted to the cameras that can mount due to the specific camera/gimbal port. In this way, the DJI-S900 allow the mount of different typology of acquisition systems, like multispectral cameras or a Lidar. As a powerful hexacopter, the S900 is a good option to flight in high mountain environments with possible strong wind hits. However, as a personal election, the DJI-Inspire 2 has a very good quality image (with the X5S camera), that is the origin of our data, as well as good systems to avoid and detect obstacles, strong wind resistance. It is easy to pilot, and brings more than 20 minutes of flight per battery, being our favorite drone today.

The flight plan has to take into account the Ground Sample Distance (GSD), the real dimension of a pixel projected on the terrain. The GSD depends on the focal length, the sensor dimensions and the distance between the camera and the object or terrain. Typical values of GSD are 3 cm/px from 120 meters of height, the maximum height altitude by law in Spain. Flying close to the terrain or with bigger sensors, the GSD obtained are typically 1.5 – 2 cm/px, creating high resolution 3D models and orthophotos that allows a very detailed maps and a new era of data acquisition in the field.

In order to maintain the same GSD for all the products generated, the distance between the drone (camera) and the terrain should be more or less the same. We prepare always two flight plans: the first, with the camera taking pictures with a Zenital perspective in order to cover the whole study area; and a second flight with frontal and oblique point of view of the cliff and vertical zones to obtain all the information of the rock wall face (Figure 3). To maintain the GSD, the flight plan should maintain the height from the terrain in vertical, and similar distance in frontal and oblique point of views. This can be achieve using preexisting topographic maps and adapting the height of the flight lines, typically flying parallel to the contour lines. Some flight plans can be designed with a secondary path of flight, perpendicular to the first one, in order to obtain more points of view to avoid shadow zones in very irregular terrains like blocky deposits on rock avalanches or fragmental rockfalls (Figure 4).

Programming the frontal and oblique points of view flights and the estimation of the picture size above the ground may be difficult due to the tilted camera position. Often, the oblique pictures are obtained by manual piloted flight, where the main goal is to optimize the picture information on rock face avoiding the sky or the cliff toe. Often is normal to pay more attention to the unstable zones that can be observed on real time during the flight, focusing the pictures on specific parts of the cliff to obtain the best information possible from different point of view, typically to observe the aperture of fractures (Figure 5).

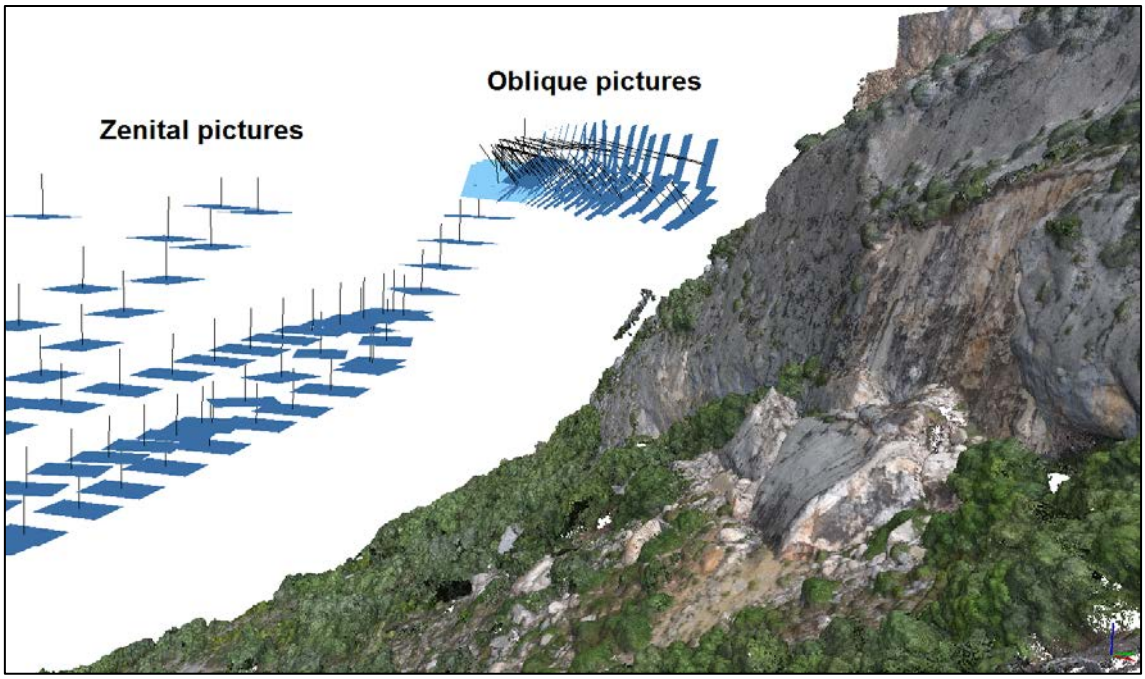

Figure 3: Zenital and Oblique pictures (blue rectangle) on Isona rockfall case study on Catalonia.

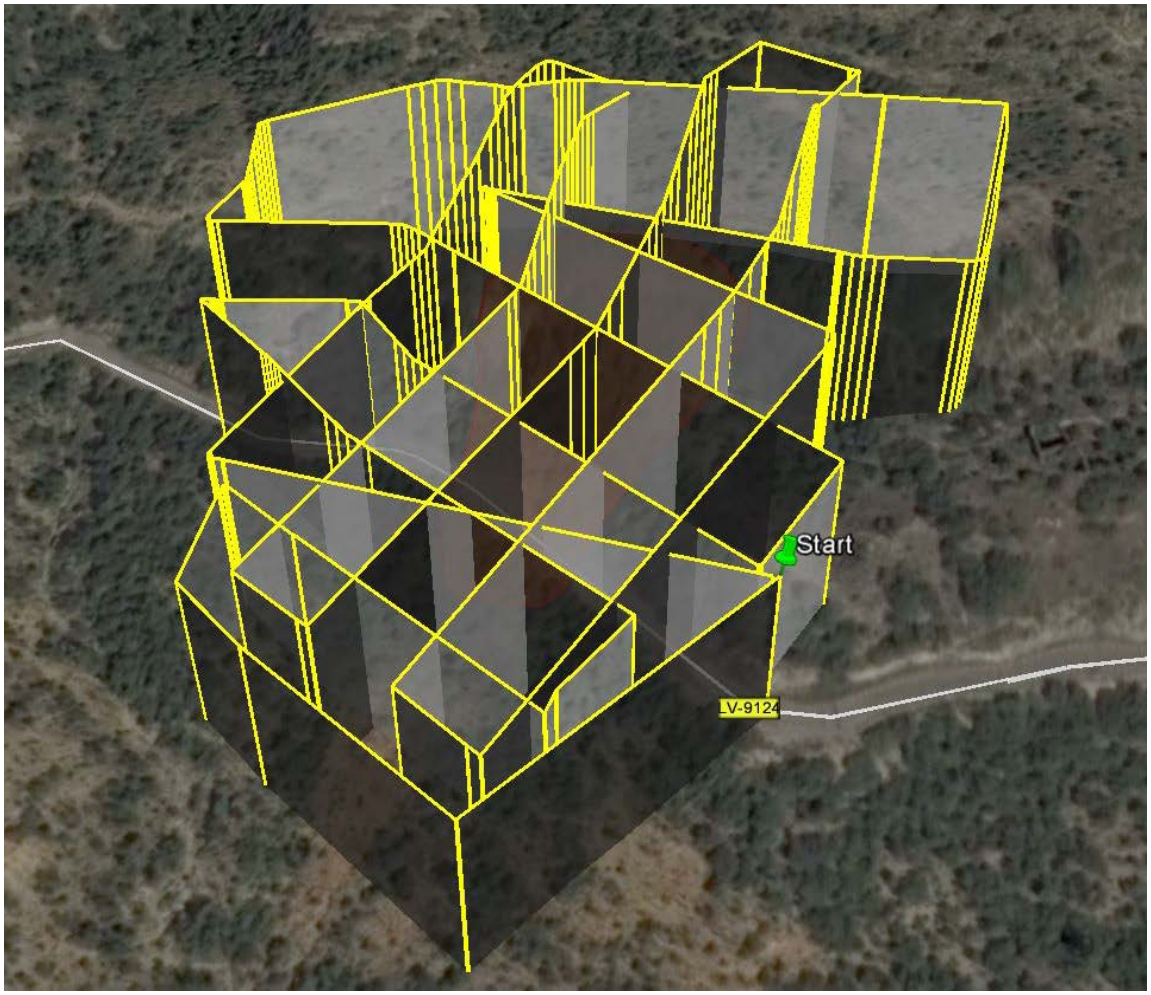

Figure 4: Flight plan on GoogleEarth: two perpendiculars schemes are used in order to cover the whole area from different points of view

Figure 5: Drone pictures from different points of view to observe joint aperture on unstable rock mass identification. The rotation against the unstable volume allows a good view to identify it.

When using frontal and oblique perspectives, it is important to take into account the change of the direction in the sequence of pictures that will be captured. The camera sensor has a rectangular shape. Normally, in a zenital point of view, picture over picture are taken moving the camera to the longer direction of the sensor, going to the upper part of the caption. On the other hand, in frontal and oblique captions, the natural drone movement is a lateral displacement, when picture a picture, the direction is to the right or to the left (Figure 6), against the shorter side of the camera sensor. Then, the overlap calculation is based on the time interval between pictures and the drone velocity, calculating the percentage of area overlapped between two consecutive pictures against the shorter side (or longer side in zenital perspective) of the sensor.

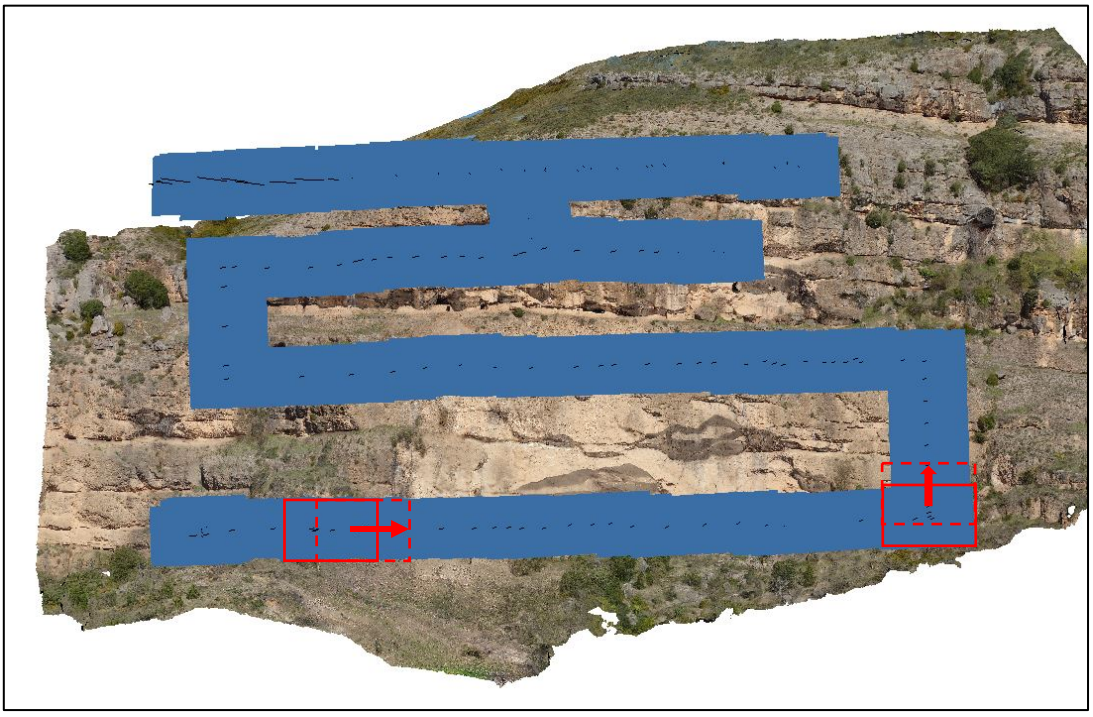

Figure 6: Exemple of frontal pictures, with a lateral displacement of the drone.

In order to design and execute the flight plan, we use the app “Litchi” that allow the creation of the flight path on the website (or in a GIS and import it then in .csv format to Litchi server) and execute it using an Ipad. We also use the “Ground Station” apps originals from DJI to manage, design and execute the flight plans on the HexaCarbonFrame, the DJI S900 and the Inspire drones.

Piloting a drone may be dangerous, and the law at each country must be respected. The Spanish law requires: a pilot license (it requires overcoming both theoretical and practical exams), an insurance and an operational entity as a responsible of the pilots, the drones and the insurances. Security should be always the most important issue in a drone flight, and accidents are common in the drone world.

3. Products generations

The first step is checking the images’ quality and rejecting the low quality pictures if any (pictures with sky, wrong focused or lightened). We use Agisoft Photoscan Professional in order to realize the photogrammetric tasks and the products generation. The software offers a picture quality index in order to identify with a quantitative value from 0 to 1 the unacceptable pictures.

The pictures obtained have an EXIF information on the metadata with the latitude, longitude and altitude, typically in WGS84 reference system. Depending on the final goal, the georeferencing of the final products may be achieved only with the pictures metadata. However, the GPS precisions may leave the final product between 2 and 10 meters moved. In order to fix and improve the quality of the products generated, a set of targets is used, measuring the coordinates with a GPS-RTK. The localization of the center of the target, manually, on the first pictures, is already the first post-processing step.

After locating the targets in the pictures and the alignment of the camera, the dense point cloud can be generated. In order to create different products (2D or 3D) with different information, the point cloud is classified. Classify ground points tool allow the definition of ground points following the next criteria: starts with a grid of cell size length defined, where the lowest point will be defined as “ground”; the besides points will be classified as ground if: the angle between the new point analyzed and the horizon is lower than a defined angle, and if the maximum vertical distance is also lower than a defined distance. Notice how the points that have another point above, on the same planimetric (XY) position but with another altitude, typically ground under vegetation, are already the overhangs on cliff zones. After some iterations on the values to classify automatically the ground points, manual classification is required in order to define the vegetation on a supervised manner. We classify the points in ground, vegetation, overhang (taking the

already classified points as low points) and also buildings. Figure 7 and 8 shows an example of the point cloud (in natural colors and classified respectively) obtained from the Castell de Mur rockfall that occurred in April of 2018 in the Eastern Pyrenees. The ground classification tool allow a good classification of the ground points (brown in Figure 7). Then, the non-classified points are defined as vegetation (green). However, the ground classification tool can be used also to identify the more relevant fragments on a rockfall deposit (red on Figure 7). The classified points as "low points" are identified as overhangs on the cliff zone (purple) and the ground points that have lower points can be defined also as prominent parts of the cliff (blue on Figure 7).

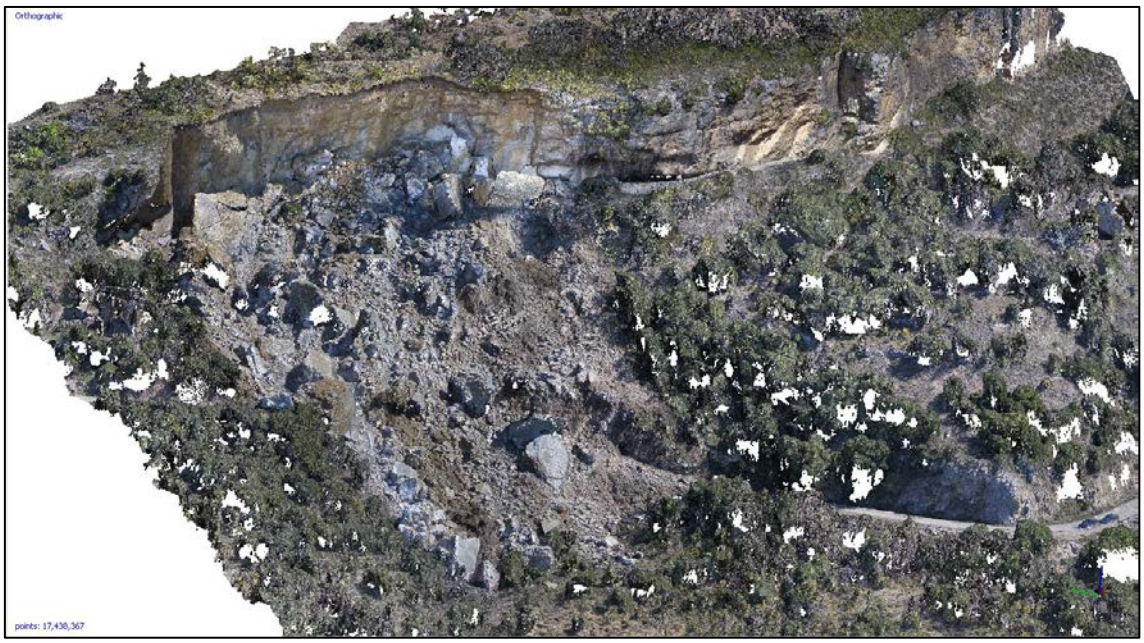

Figure 7: Point cloud by original color from Castell de Mur rockfall.

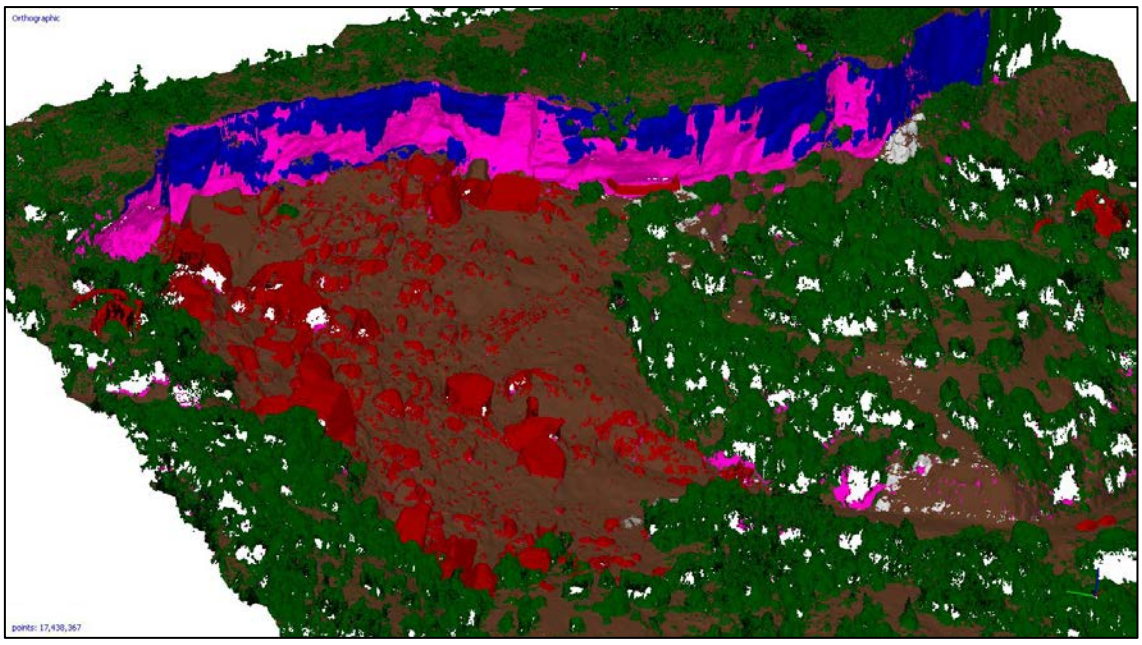

Figure 8: Classified point cloud by: Ground (brown), vegetation (green), main fragments on the deposit (red), overhangs on the cliff (purple) and points above overhangs (blue).

The generation of different products is divided in two ways: for cartographic or 2D representation, and for 3D products.

The points classified as ground are used to create the digital elevation model, avoiding the distortion that vegetation may introduce. Based on this digital elevation model, others products are generated, like the orthophoto, the slope map and the contour lines map (Figure 9). In a study in which unstable rock masses are identified, it may be useful divide the whole study area in zones with the same orientation. For each the cliff face orientation, the unfavourable joint sets on each zone may be defined. Figure 9 shows the maps generated at the site of Monasterio de Piedra. The unstable rock mass identification tasks, as well as the maps and the obtained 3d models, are used in a quantitative risk assessment study (Corominas et al, 2018 submitted) also presented in the chapter 12 of this thesis. The products at high resolution are very useful for rockfall inventorying tasks (chapter 6) and also to locate the final unstable rock mass identified.

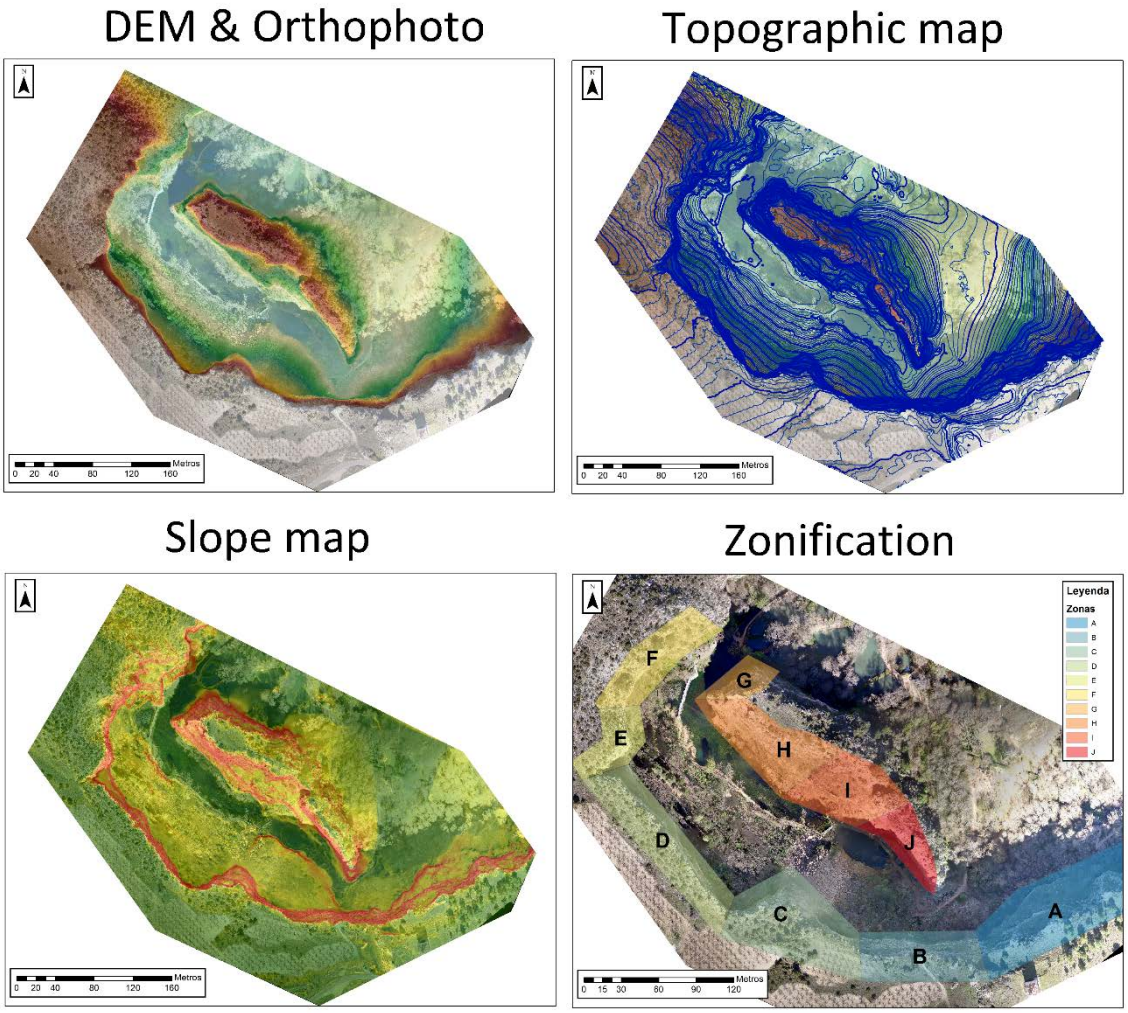

Figure 9: Cartographic product generated for the case of Monasterio de Piedra study (see Chapter 12). Orthophoto and Digital Elevation Model (upper left), Topographic map (upper right), Slope map (lower left) and the Zonation map of each cliff to be analyzed one by one.

The second way to produce models uses the points classified as ground and overhangs, that should be the best option to deal with the cliff information and characterize the joint pattern and identify the unstable volumes. To this end, the ground and overhangs points are exported as point cloud to be analyzed on specific point cloud analysis software like CloudCompare (Figure 10). A simple colorization of the point cloud by dip (slope) may allow the identification of the main patterns and morphology of a rock face. These points are used to create a 3D mesh texturized with the purpose to identify the joint traces.

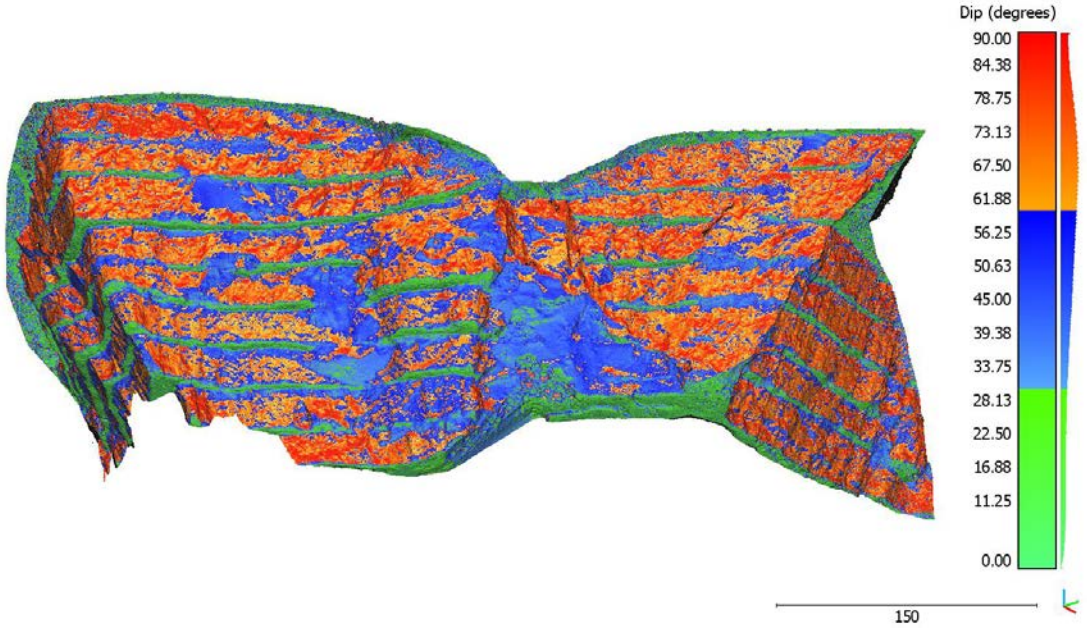

Figure 10: Example of a point cloud of a quarry considering ground and overhangs, colored by dips in order to analyze the joints pattern and the potential unstable volumes.

Another interesting product that can be generated, is the frontal or oblique orthophotos. The frontal orthophotos enable mapping of the joint sets and rock bridges characterization based on high resolution frontal images (Figure 11 up). The original pictures, also in real time during the inspection flight, allow the visual identification of unstable rock mass (Figure 11 down).

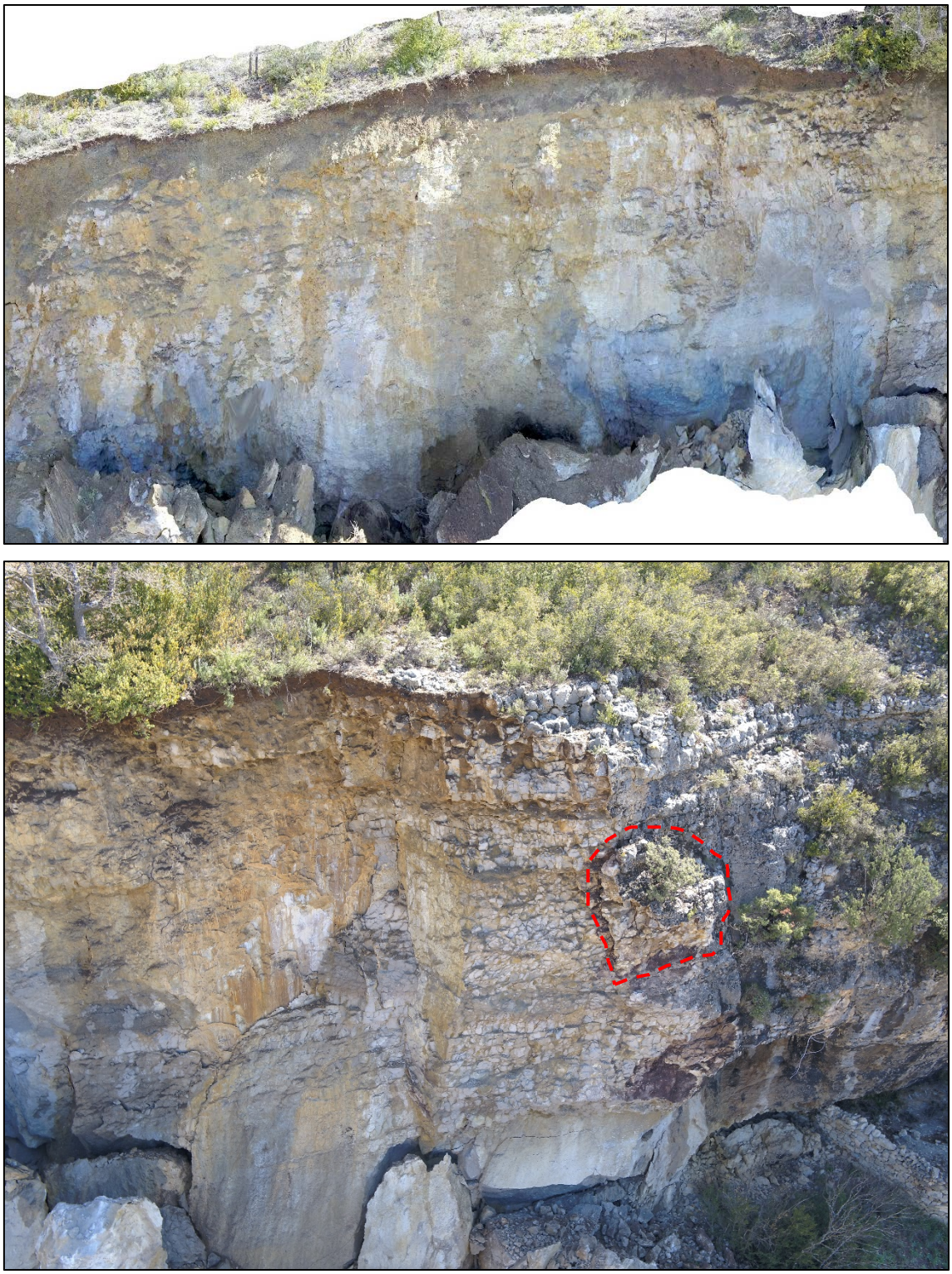

Figure 11: Up: Frontal orthophoto from Castell de Mur rockfall cliff obtained to identify unstable volumes. Down: Original picture from the drone (Castell de Mur rockfall) where an unstable rock mass can be identified.

3. Joint set identification by outcrop modelling

Joint set identification on 3D point cloud is a common activity in rock mechanics and stability analysis. There exists a number of algorithms and software products to deal with it: COLTOP 3D (Jaboyedoff et al. 2007), DiscontinuitySelfExtractor (Riquelme et al. 2014), CloudCompare (Girardeau-Montaut 2006) or GaiaGeoRoc (Assali 2014). The main ideas are the calculation of the normal on each point and define coplanarity criteria to define facets or joints sets. The normal vector calculation on each point using a defined radius of influence allows the representation of the point cloud in terms of dip direction or dip (Figure 12, left and right respectively, on Zone A of Monsaterio de Piedra case). Then, we use the plugin Facet Matching in order to identify the main joint sets on the point cloud (Figure 13).

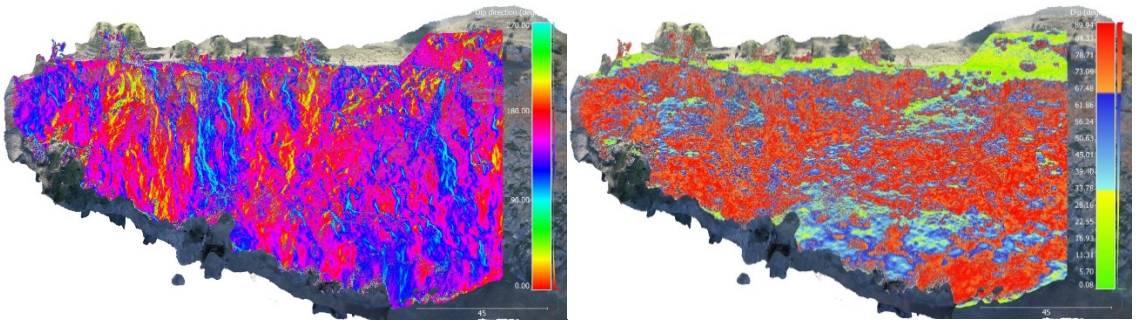

Figure 12: Dip direction and dip colored points cloud from Zone A on Monasterio de Piedra.

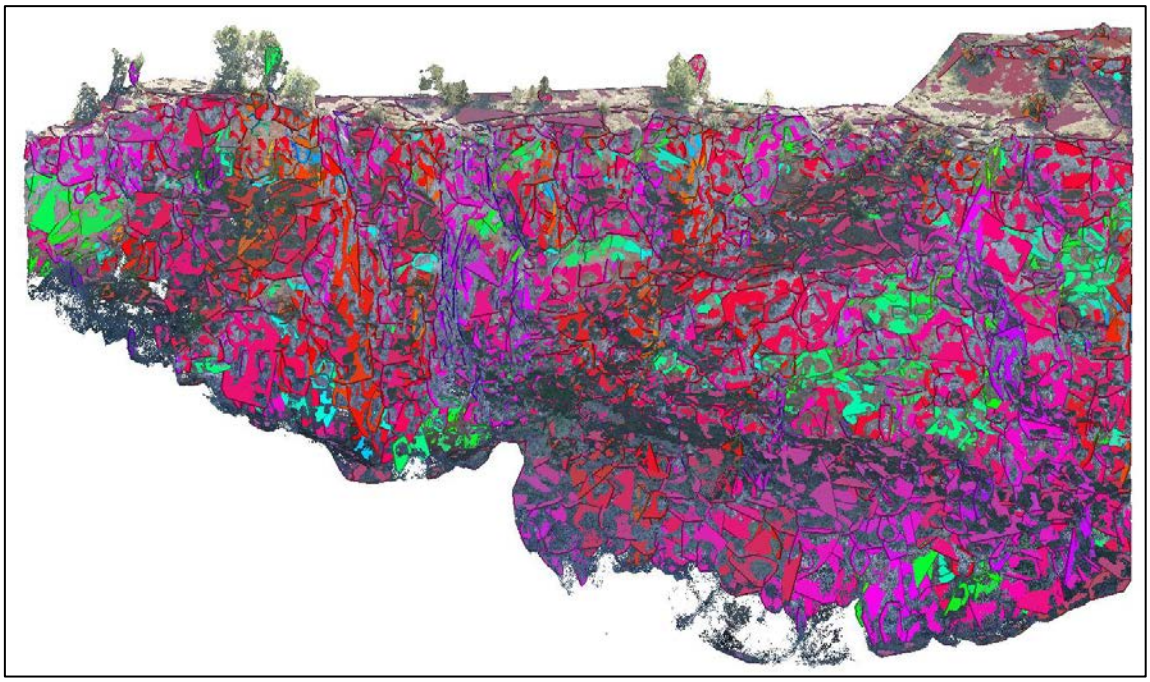

Figure 13: Identified facets with the Facet Matching plugin in Zone A on Monasterio de Piedra.

Semi-automatic identification using the Facet Matching plugin on Cloud Compare

We use the plugin Facet Matching from Cloud Compare to identify the existing joint sets in the rock mass (Dewez et al, 2016). The plugin uses the point cloud with normal vectors to create facets that are mesh format elements, with groups of points that satisfy some coplanarity criteria. Depending on the scale of the joint set that we are interested, the parameters can be modified. The plugin works with 3 parameters: (1) maximum distance, that is the maximum distance between a point and the facet assigned; (2) minimum number of points, which is the smallest allowing to create new facets; and (3) the Maximum Edge Length, controlling the maximum length a facet without including points. The last one control the perimeter of the facets and how irregular may be considering only the information from points or extrapolating to create more regular facet shapes as shown in Figure 14.

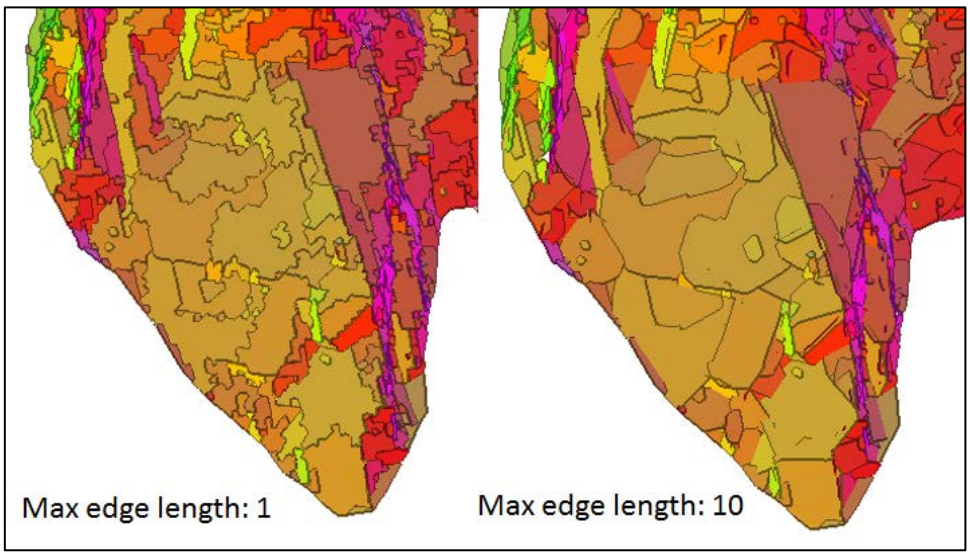

Figure 14: Identified facets with Facet Matching plugin on Cloud Compare, comparing the Maximum Edge Length parameter that control the irregularity on the defined facets perimeters.

The maximum distance is the main parameter that control the scale of our joint set identification task. If we are interested on the main morphological features which characterize cliff, then the use of high values of maximum distance allows higher tolerance between the points and the matched facets. Because of this, a more general pattern on a large scale is obtained. As the maximum distance reduces, the resolution increases, and the scale of the generated facets becomes progressively smaller (Figure 15). Decreasing the maximum distance, the coplanarity criteria becomes more restrictive and then, smaller areas of facets are obtained. For this reason, it may be wise to reduce the minimum number of points for the generation of small-size facets, related with less number of points. From our point of view, the perfect set of parameters does not exist, and depending on the scale of the joint set we are interested, the parameters should be adapted. As natural rock exposures are also fractal surfaces, similar patterns are found at different scales.

Furthermore, not all the facets generated are real joint sets, and the interpretation of the data is always necessary. Not all the facets fitted are real joints, due to any irregular plane may be adjusted with the enough maxim distance tolerance.

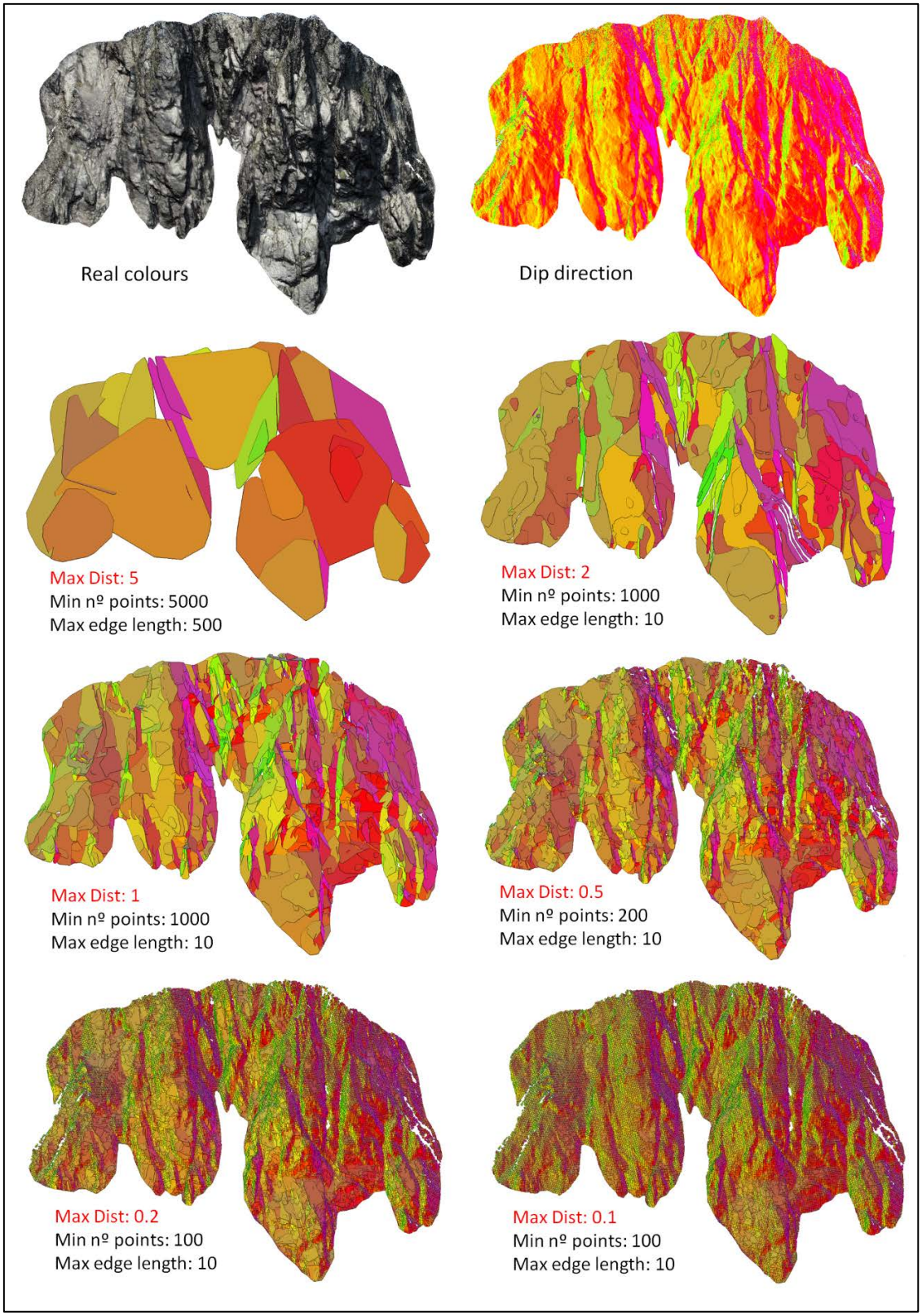

Figure 15: Facet matching plugin applied with different set of parameters using a 3D point cloud from Pala Morrano (a study site in the Aigüestortes-Sant Maurici Natural Park, Central Pyrenees).

At each slope, depending on the rock wall orientation, the joint sets may become unfavourable based on kinematic tests such as the Markland or Goodman. These joint sets can be identified, selected and exported as relevant sets on a mesh format. This is illustrated in the study of the maximum credible rockfall volume at the Borrassica slope in Andorra (Corominas et al 2018, and chapter 11). There, the main joint set that defines planar sliding mechanism (blue facets on Figure 16), the one that controls the detachment of rockfalls in the area, was selected in order to identify potentially unstable volumes. A back analysis of the dip of the scars related with this joint set can be carried out to identify the critical dip. The sliding surfaces will be used to be extrapolated inside the rock mass in order to define the base of the potential unstable volumes. Then, in order to delimitated the volumes, other joint sets are identified and modeled.

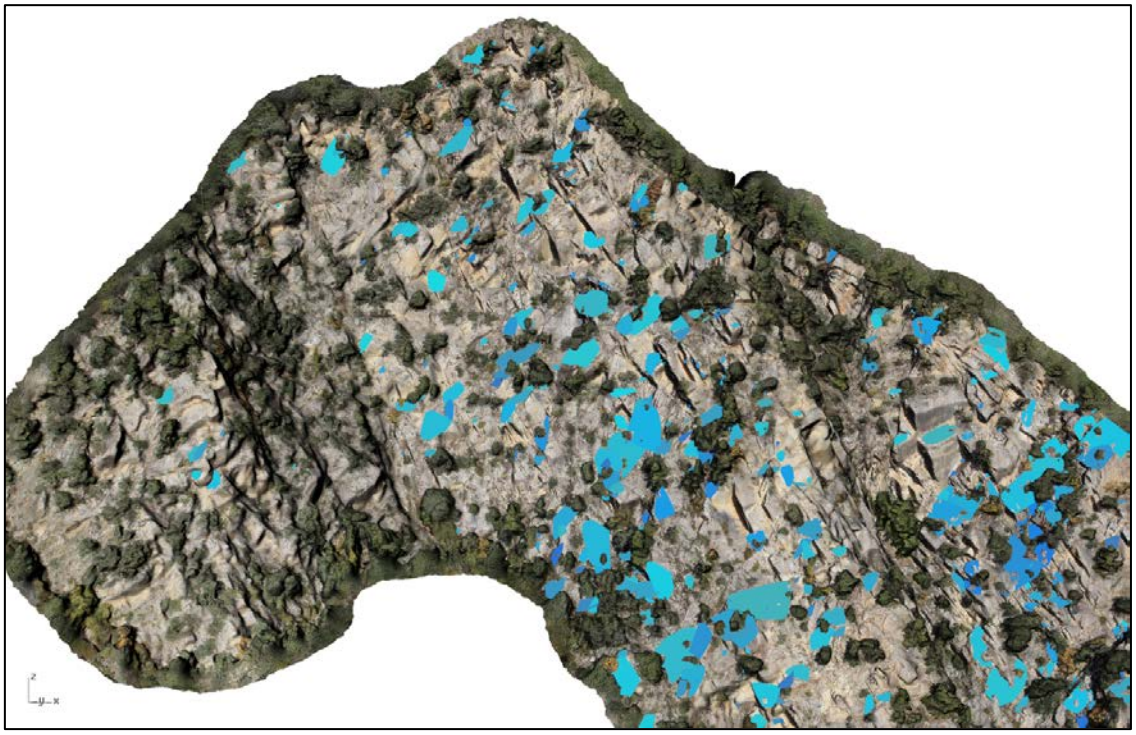

Figure 16: Joint set identified related to the sliding failures on Borrassica cliff, Andorra.

Manual joint set identification and modelling

The semi-automatic procedure to identify joint sets takes into account geometrical properties of the point cloud, namely the normal vector and coplanarity criteria. However, numerous joints do not generate relief and only their trace can be identified. To this aim, the texturized mesh is used to identify the joint traces and modelled them manually. The joints can be manual modelled using 3D modelling software like Rhinoceros, Polyworks, Blender or others. Using the case of the Borrassica slope in Andorra, the unstable potential volumes are bounded by the basal cinematically unstable planes and the joint sets that define tension cracks. The potentially

unstable masses were manually modelled using Rhinoceros (Figure 17) by identifying the joint traces.

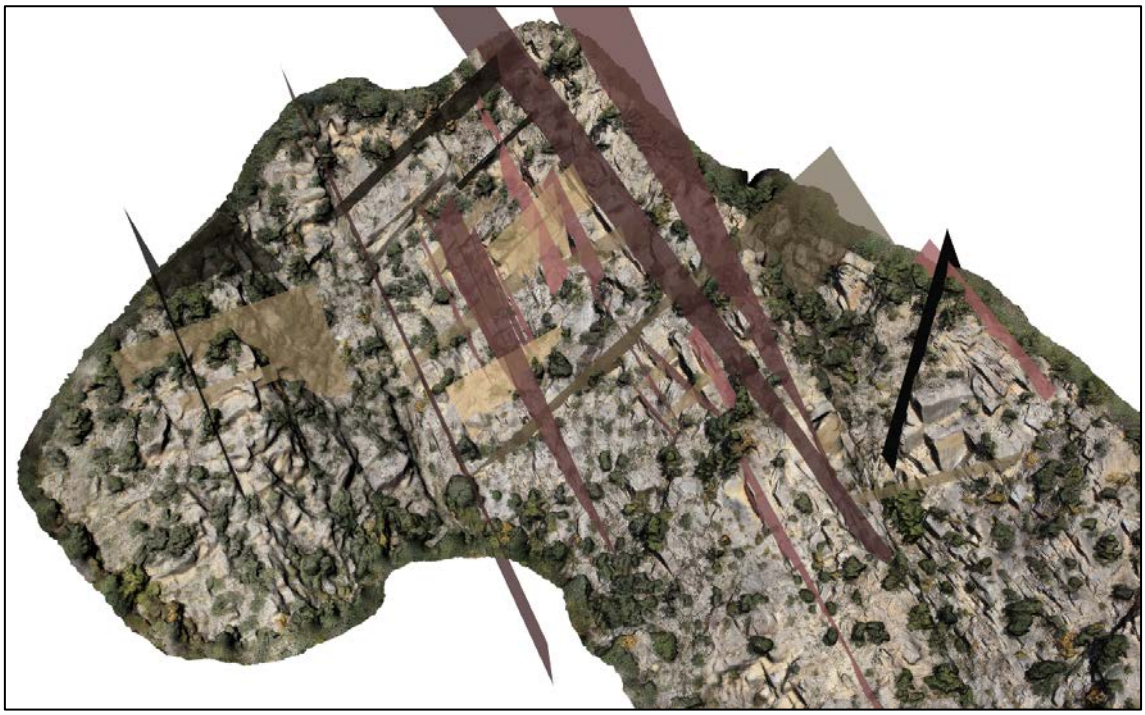

Figure 17: Manual modelling of joint sets by trace identification over 3D mesh texturized on Borrassica cliff (Andorra)

A new interesting tool is available on Cloud Compare named *Compass* (Thiele, et al 2017). This tool allows the manual selection of a group of points inside a circle to fit a plane on it. This tool can be very useful in order to measure the most relevant joint set within the point cloud used. However, the best improvement of this tool is the capability to use the point cloud information (colour, darkness, curvature, etc) in order to assist the manual joint mapping and an automatic plane definition based on the coplanarity of the points selected. The tool works especially well when the trace is clearly visible due to its color.

In Figure 18, an unstable rock mass is identified resting on a joint set that allows planar failure. The points on the base can be cropped and coloured by dip in order to analyze how the dip of this plane vary. Then, different tension joints can be modelled using the Compass tool in order to define possible unstable volumes.

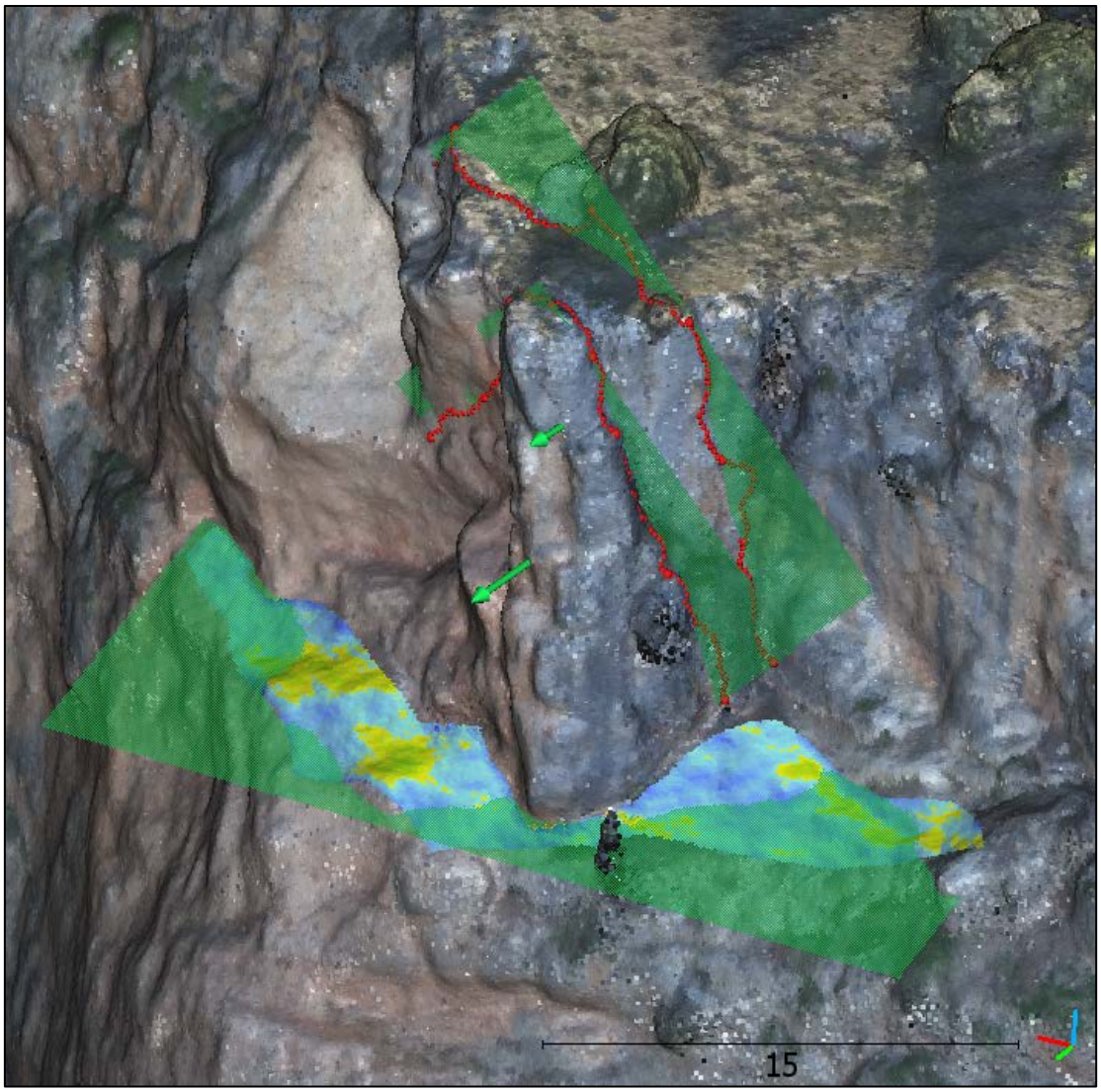

Figure 18: Joint modelling using Compass trace tool on Cloud Compare. Two possible tensile joints are modelled following the point cloud color.

4. Volume delimitation

In order to calculate a volume, it is mandatory to work with closed 3D objects. On this case, the mesh format seems to be the natural way to close a volume. The main idea is to delimitate the volume defined by the unfavorable joint sets on each defined zone. Then, in some cases, different options may be considered in order to identify different possible failures. To this end, the 3D mesh texturized is cut using the facets and the manually modeled joints in mesh formats (Figure 19, on the same example data of Figure 18)

All the delimitated volumes can be exported to different maps and to general 3D models of the zone. Some expert judgement on the evidence of instability and/or stability analysis may be used to define a range of susceptibility in order to manage the information (Figure 20)

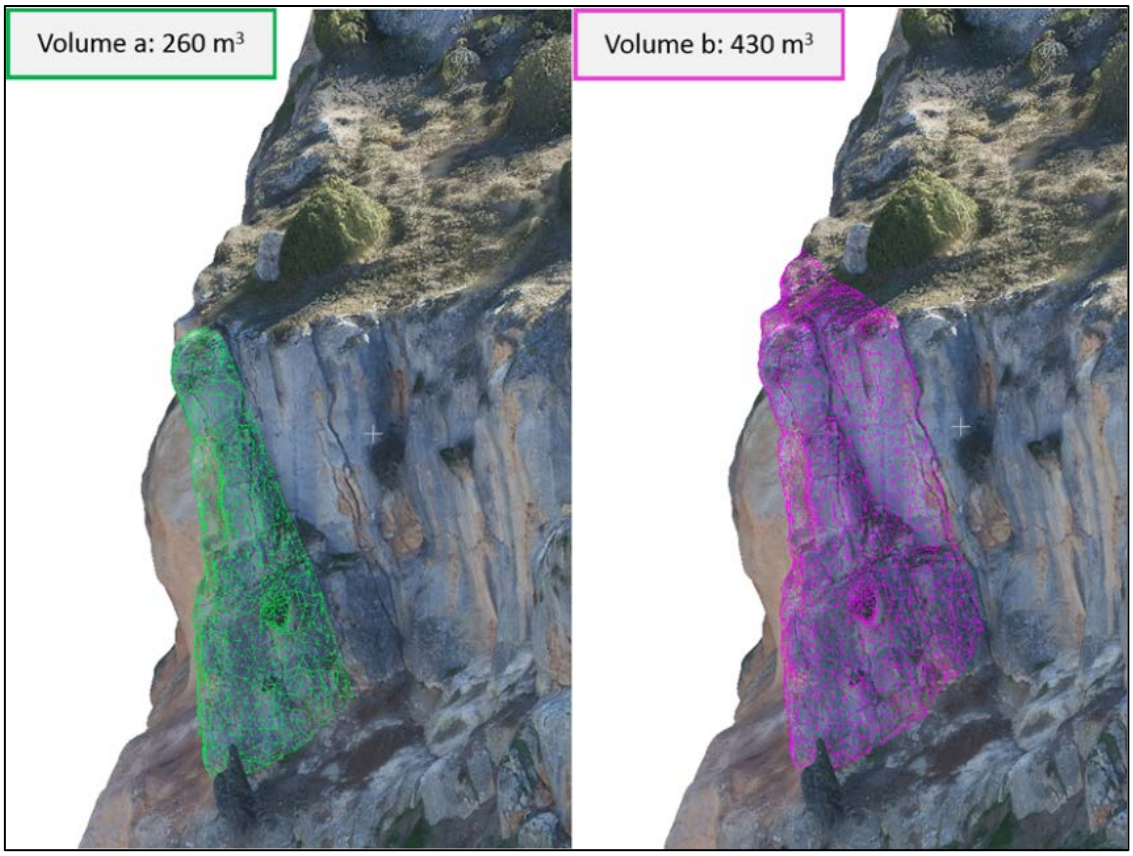

Figure 19: Volume delimitations by cutting the 3d mesh with the modelled joint sets from Figure 15.

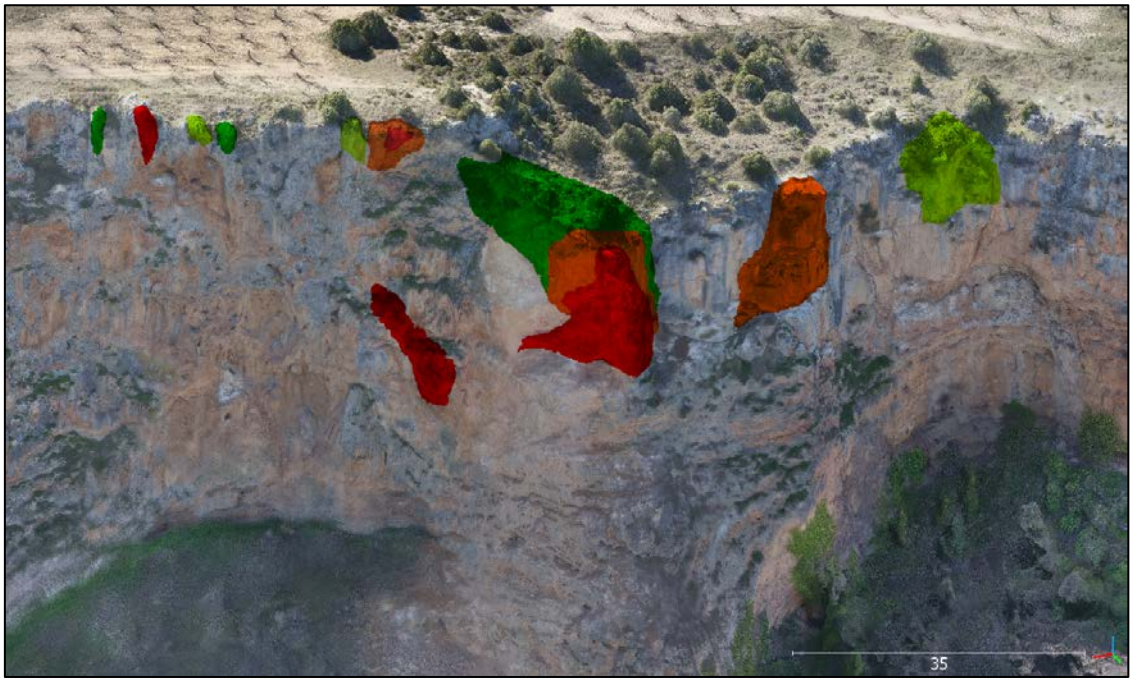

Figure 20: Delimitated unstable volumes on a 3D texturized model as inventory, ranged by susceptibility from low (green) to high (red).

The representation of the identified volumes in 3D models is not just an aesthetic issue. Often, the unstable volumes that cannot be represented appropriately in classical zenital maps or images, due to they are located in the same vertical section (Figure 21), or directly on overhang zones (Figure 22) that are completed occluded is orthophotos and topographic maps.

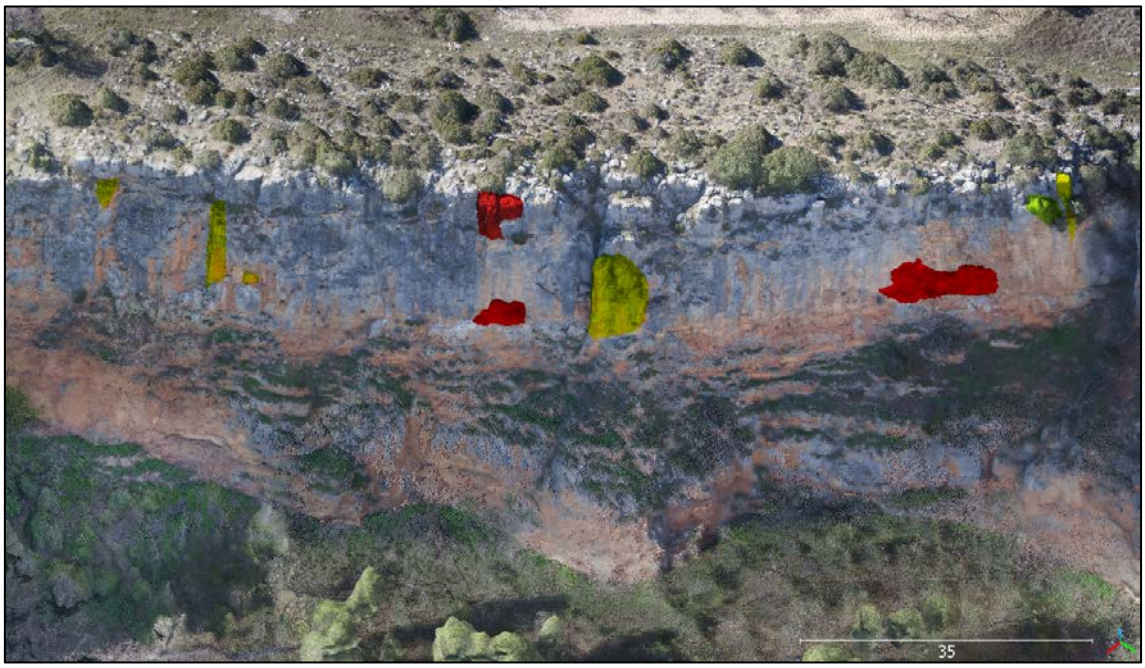

Figure 21: Delimitated unstable volumes on a 3D texturized model as inventory, ranged by susceptibility from low (yellow) to high (red).

Figure 22: Delimitated unstable volumes on a 3D texturized model as inventory, ranged by susceptibility from low (green) to high (red).

5. Conclusions

The use of UAV systems combined with the digital photogrammetric techniques creates a new era of data acquisition in geological risk assessment. The techniques and the methodologies shown in this chapter allow the generatin of high resolution ortophotos, DEM, coutour lines, as well as frontal or obliques orthophotos, the 3D point cloud and 3D texturized mesh. The flexibility of the tool is very useful to acquiere data just after and event or with the periodicity required.

It is important to know the legislation of each country about the use of UAV. It is also important have a detailed knowledge about the devices used, the drone and the camera, and decide which kind of drone and camera should be better on each case.

The methodologies will change fast, as the technology and the algorithms are in continuous developing. By now, the procedure shown on this chapter is our methodology to obtain an important part of the field data. Start with an accurately planification of the flight plan and a safety execution. Continue with the digital photogrammetric processing in order to obtain the 3D points cloud and classify it in order to work with clean data without vegetation. Few algorithms may be used to identify the joints pattern based on the point cloud coplanarity, as well as for manual modelling. It is important to keep in mind that all surfaces may be adjusted with a plane with the enough tolerances, and the supervision of real joints sets is required to select the adjusting parametrs on each scenario. Depending on the scenario scale and the interesting joints pattern, the adjusting parametrers will be defined and testes in an iterative process. Finally, the manual selection of points to fit a plane, and the manual modelling using the Compass tool (Cloud Compare) or 3D texturized meshes (for exemple in Rhinoceros) will be very useful.

The unstable rock volumes may be identified using a very safe methodology, reducing the time or complety avoiding the exposition to the higher hazardous zones, and at the same time, obtaining a high quality information from the scenario.

References:

Assali, P., Grussenmeyer, P., Villemin, T., Pollet, N. and Viguier, F. (2014) Surveying and modeling of rock discontinuities by terrestrial laser scanning and photogrammetry: Semi-automatic approaches for linear outcrop inspection. J. of Struct. 25 Geol., 66: 102-114, doi:10.1016/j.jsg.2014.05.014, 2014.

Corominas J, Mavrouli O & Ruiz-Carulla R, (2018) Magnitude and Frequency relations: are there geological constraints to the rockfall size? Landslides Landslides, Volume 15 Issue 5, pages: 829-845. https://doi.org/10.1007/s10346-017-0910-z

Corominas J, Matas G & Ruiz-Carulla R, (2018) Quantitative Analysis of Risk due to Fragmental Rockfalls. Landslides. (paper submitted)

Dewez T, Girardeau-Montaut D, Allanic C, Rohmer J (2016) Facets: A CloudCompare plugin to extract geological planes from unstructured 3d point clouds. XXIII ISPRS Congress, Jul 2016, Prague, Czech Republic. XLI-B5, pp.799-804, 2016, International Archives of the Photogrammetry Remote Sensing and Spatial Information Sciences. 〈10.5194/isprs-archives-XLI-B5-799-2016

Girardeau-Montaut (2006) Detection de Changement sur des Données Géométriques 3D", D. PhD manuscript (french), Signal & Images Processing, Telecom Paris

Jaboyedoff M, Metzger R, Oppikofer T, Couture R, Derron MH, Locat J, Turmel D (2007) New insight techniques to analyze rock-slope relief using DEM and 3D-imaging cloud points: COLTOP-3D software, in: Rock mechanics: Meeting Society's challenges and demands, Proceedings of the 1st Canada – U.S. Rock Mechanics Symposium, edited by: Eberhardt, E., Stead, D., and Morrison, T., Vancouver, Canada, 27–31 May, Taylor & Francis, London, UK, 1, 61–68

Riquelme A, Abellán A, Tomás R, Jaboyedoff M (2014) A New Approach for Semi-Automatic Rock Mass Joints Recognition from 3D Point Clouds. Computers & Geosciences 68. Elsevier: 38–52. doi:10.1016/j.cageo.2014.03.014.

Thiele ST, Grose L, Samsu A, Micklethwaite S, Vollgger SA, Cruden AR (2017) Rapid, semi-automatic fracture and contact mapping for point clouds, images and geophysical data. Solid Earth, 8: 1241-12535.

6. Fragmental rockfall inventory

Original unpublished chapter

Abstract: After the improvements on UAV and digital photogrammetric techniques, the rockfalls presented in Chapter 3 were revisited as well as new ones. A new field works campaing was carried out obtaining, from the UAV surveys, the 3D models of each scenario, high resolution ortophotos and the scar 3D models in detail, allowing the generation of cartographies, real terrain profiles, detached volume reconstructions, joint pattern characterization and IBSD estimations. Our research plan is based on the emprical data collected on this inventory of natural fragmental rockfalls. The fragmentation model proposed on the PART III is calibrated with the data collected.

Keywords: rockfall, fragmental rockfall, block size distribution, inventory, 3D models

1.Introduction

The bases of our research looks to empirical data from natural behavior, starting from the measurements of natural fragmental rockfall events, collecting how much data as possible on each case. 7 rockfall cases are inventoried to represent different fragmentation scenarios, in terms of failure mechanism, lithology (Limestone, Sandstone, Conglomerate and Schist), total volume detached (between 2 m^3 and 10.000 m^3), and different slopes and terrain conditions.

We tested in laboratory three samples of rock of each event, obtaining the mineralogical description, the density, the uniaxial compressive strength, the Young modulus, the Poison ratio and the tensile strength. The total volume detached reconstructed (IBSD) and the total volume estimated on the deposit (RBSD) may differ, but less than a 10-20%. Part of this volume lost is interpreted as dust or fragments too small to be measured in the field.

The relevant data collected are presented in Table 1. Notice that just for these 7 cases, we measured manually more than 7200 fragments with a tape, taking 3 distance of each fragment. Based on this, we consider the RBSD obtained a well-defined description of the volumes of the fragments of the inventoried rockfall events and a good data quality in order to calibrate fragmentation models.

Table 1: Rockfall inventory cases, summary data, rock properties and measured fragments.

ROCKFALL INVENTORY	**1.PdG**	**2.Omells**	**3.Lluca**	**4.Gurp**	**5.MdP**	**6.Malanyeu**	**7.Cadi**
Failure Mechanism	Slide	Toe erosion slide	Toppling	Toppling	Toppling Slide	Toppling	Slide
Lithology	Schist	Sandstone	Sandstone	Conglomerate	Limestone	Limestone	Limestone
Total Volume RBSD (m^3)	2.6	4.2	10.7	100	900	4350	6351
Total Volume IBSD(m^3)	2.61	4.2	10.7	100	997	4945	7663
ROCK PROPERTIES							
Density(kg/cm3)	2.72	2.35	2.46	2.69	2.5	2.64	2.68
RMR	76	64	72	82	70	74	60
Tensile Strength (Mpa)	6.53	2.03	2.07	5.47	10.00	7.03	12.10
UCS (MPa)	32.17	21.38	21.77	38.36	35	13.33	35.29
E Young (MPa)	17385	5185	730	74831	20000	12992	22761
Poisson	0.27	0.006	0.18	0.21	0.1	0.05	0.07
FRAGMENTS MEASURED							
RBSD Total number blocks	116	48	78	500	10790	28788	60980
RBSD nº of measured blocks	116	48	78	500	2256	2721	1524
Min. Vol. Measured (m^3)	0.0001	0.0007	0.0007	0.01	0.001	0.0001	0.01
Max. Vol. Measured (m^3)	0.28	1.1	8.5	22	27	445	31

The 3D models of each rockfall event obtained by UAV and digital photogrammetry technics, are very useful in order to measure distances, 2D and 3D areas, volumes, generate profiles with overhangs, create cartographies and so on. Table 2 summarize the main geometrical descriptors used for rockfalls. Bigger total rockfall volumes tends to increase all the others geometrical descriptors, however, the Coef. of correlation r-squared with the 3D scar area is 0.99 (Figure 1).

Table 2: Summary of geometrical descriptors measured on the 3D models of each scenario:

SCENARIO & DEPOSIT	1.PdG	2.Omells	3.Lluca	4.Gurp	5.MdP	6.Malanyeu	7.Cadi
Scar 3D Area (m^2)	9.55	15	32	87	578	2120	3532
Total Cliff Height (m)	15	3.3	6.8	100	50	70	150
1th Impact Height (m)	12	1	0.6	39	35	10	50
CoG Height (m)	13	5	2.8	110	60	80	230
Max. Height difference (m)	13	14.5	6.6	150	70	100	520
Max. Runout (m)	5	22	9.2	152	70	130	710
Max. Volume Runout (m)	5	3	5.6	152	40	80	200
Reach Angle (degrees)	69	33	36	45	45	38	36
Deposit Width (m)	2.5	15	5	40	50	80	130
Deposit Area(m^2)	5	300	45	2000	4200	6000	44000
YDC Area (m^2)	5	6	35	1625	3743	1150	30000
YDC Width (m)	3	2	5	40	50	40	110
YDC Length (m)	1.7	3	3.5	63	35	50	260

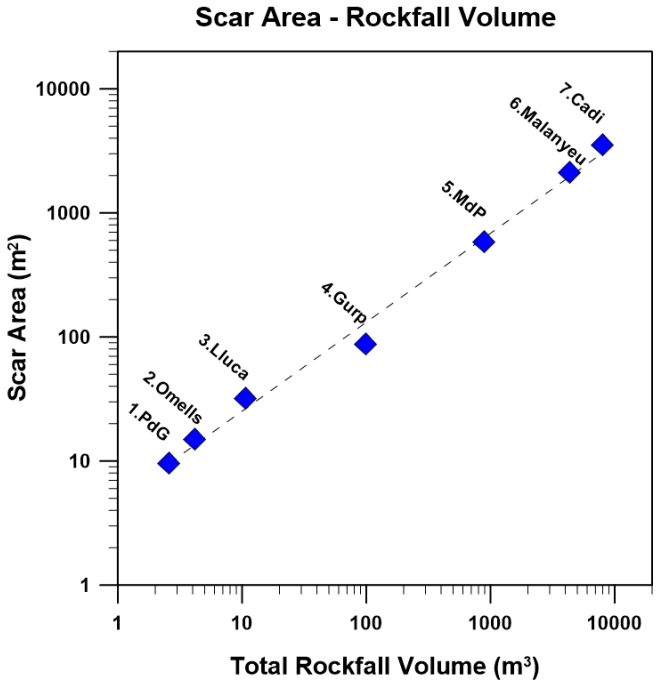

Figure 1: Scar area measured on a 3D surface and total rockfall volume of the study cases.

2. Inventoried rockfalls

Pont de Gulleri rockfall (1)

Pont de Gullerí (PdG) rockfall took place near Sant Romà de Tavèrnoles village, in Catalonia. The block size distribution (RBSD) was obtained by measuring 116 blocks on the deposit with a tape. The sum of the volumes estimates the total detached rock mass volume in 2.6 m^3. The cliff is composed of Cambro-Ordivician schists with a high persistence joint pattern. The fallen blocks observed on the deposit are bounded by preexisting joints (Figure 2). This allows us to assume that the detached rock mass was mainly disaggregated following the joint pattern. Only few block shows fresh breaks. The minimum block volume measured is $1.2*10^{-4}$ m^3, and the maximum is 0.28 m^3. The rock mass impact against a wall of an old stone house creating a hole of 1 meter of height and 0.5 meters of width, considering the case as an obstructed rockfall from propagation point of view.

Figure 2: Deposit of the Pont de Gulleri (PdG) rockfall event, stopped against a stone home wall.

From fragmentation point of view, this is a case where disaggregation is predominant over pure breakage, where the RBSD from the deposit should be very similar to the original IBSD from the cliff. In this case, the blocks weren't break to much, and a high survival rate should define a results very controlled by the original IBSD.

Lluçà rockfall (2)

The second rockfall take place on the village of Lluçà, center of Catalonia, with a detached volume of 10.7 m^3. The rupture mechanism is predominantly toppling caused by differential erosion of the underlying weak rocks over a flat terrain. The rock is grey sandstone of Upper Eocene age. The detached mass was a single block bounded by two joints filled with roots. The latter might have facilitated their development. The fallen blocks show fresh faces generated by the impact and abundant fine material generated by the breakage. We measured 77 blocks, with a minimum volume of $6.7*10^{-4}$ m^3 and a maximum volume of 8.47 m^3 that represent an important part of the whole deposit as a clearly large fragment (Figure 3). The cartography of the event (Figure 4) shows this large block or part of the rock mass not affected by breakage, and the smaller fragments ejected a little bit further due to the breakage.

Figure 3: Picture of the Lluçà rockfall case inventoried. A huge block conserve the main part of the total rock mass detached.

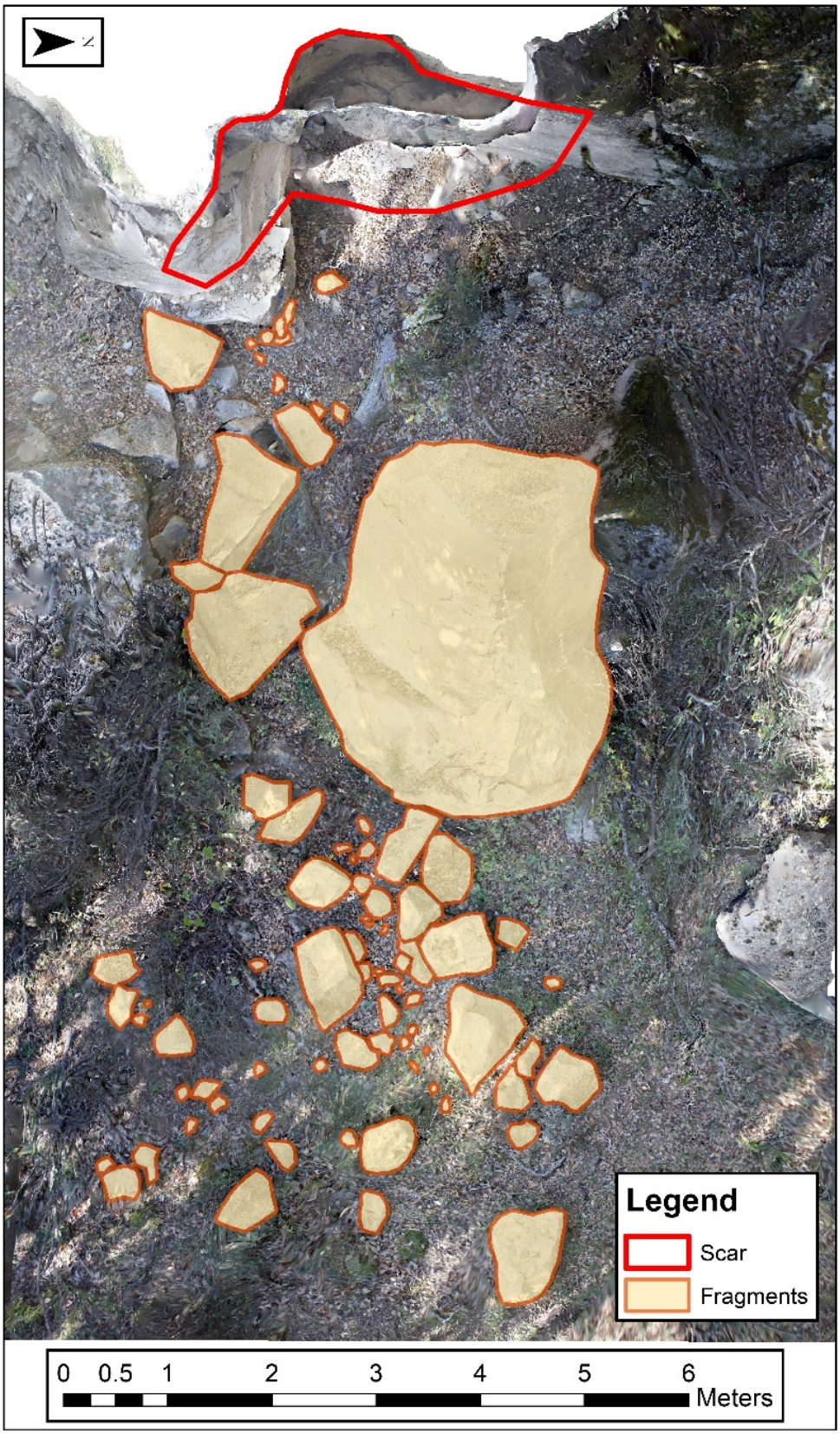

Figure 4: Deposit cartography of the Lluçà rockfall case inventoried.

Omells de Na Gaia rockfall (3)

The Omells de Na Gaia rockfall is a small-size rockfall that propagated on a stepped soft ground. It initiated with a free fall of 1 meter, and the farthest block stopped by impacting on a wall at 22 meters from the source. In the lowest part, the blocks trajectories crossed a paved road and damaged a barrier (Figure 5). The detached rock mass is sandstone of Oligocene age with a total volume of 4.2 m^3. We measured 48 blocks, with a minimum and maximum volume of $7*10^{-4}$ and 1.1 $m^{3,}$ respectively.

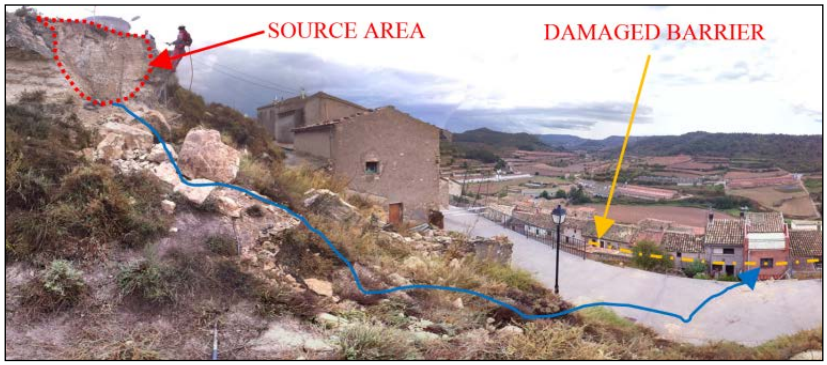

Figure 5: Panoramic photography of the Omells de Na Gaia (Omells) rockfall inventoried.

The blocks generated by fragmentation show fresh faces formed by the breakage as well as pre-existing discontinuities, mostly sedimentary planes. The fragmentation of the rock mass affects the trajectories of the blocks, modifying the impact energies (Figure 6).

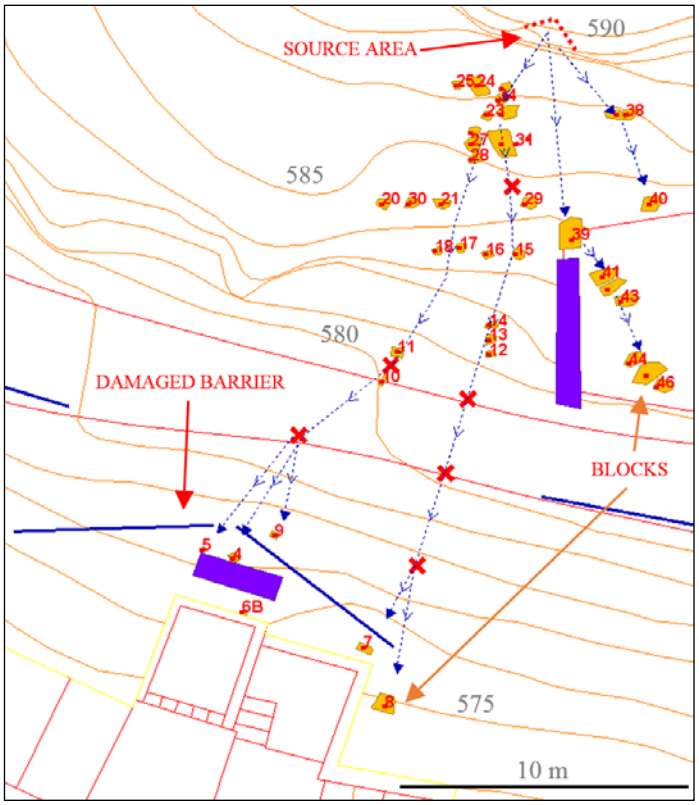

Figure 6: Omells de Na Gaia rockfall cartography with dispersion of trajectories due to fragmentation.

Gurp rockfall (4)

On 5th of April of 2016, a rock mass of 100 m^3 deatached from the top af cliff of 100 m close to the village of Gurp, in the Conca de Tremp area in Catalonia (Figure 7). The rock mass falls impacting against the slope and creating an explosive fragmentation event (Figure 8), defining a Young Debris Cover (YDC) zone. The quaternary silts and clays from the ground were ejected in a cloud of dust with little fragments, covering the trees until 5 meters of height. The central part of the YDC erase completely the trees and the vegetation. 3 major blocks achieve the lower part of the profile, crossing a field. Two of them, with volume close to the 20 m^3, cross the entire field producing important craters with the shape of the boulders (Figure 9), and finally stopping against a road.

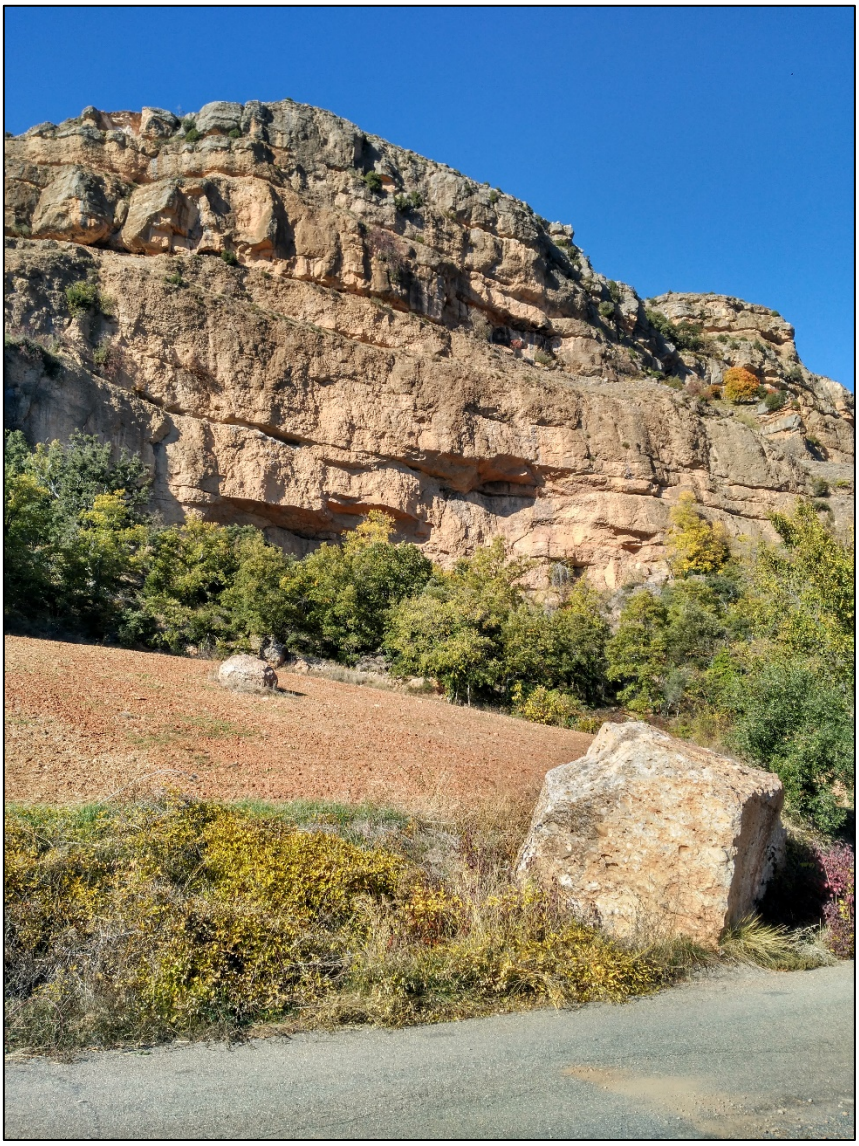

Figure 7: Photography of the Gurp rockfall. Two blouders of 20 m^3 stop against a road. See also the cartography of Figure

Figure 8: Photography of the main impact zone on the Gurp rockfall. Trees and vegetation were completely erased, and a cloud of dust and clays covers the trees until 7 meters of height.

A photogrammetric UAV flight allows us the generation of 3D models, ortophotos and the topographic cartographies necessaries to describe the case. 500 blocks were measured using a tape. The 500 blocks were delimitated in a high resolution ortophoto (2 cm/px) obtaining also an areal distribution of fragments. However, the RBSD used on this study is the obtained by measuring 3 distance of each fragment on field works, avoiding the area to volume conversions and the assumptions for this.

Figure 9: Trace craters of one of the two boulders that cross the field reaching the road on Grup rockfall.

The cartography of the Gurp rockfall (Figure 10) shows a “body shape” rockfall: with the scar as the head; the YDC as the main body of the deposit; and some arms and legs as Large Scattered Blocks (LSB) that shows more lateral dispersion or longer runouts. This is a very interesting case study example, due to it is a common pattern on fragmental rockfalls where the inventories are focused on the 2 or 3 major blocks that reach the road, and not in the rest of the deposit. Then, possible reconstruction of this rockfall event using the larger boulders without considering the fragmentation phenomenon could be erroneous in terms of restitution coefficients or energy dissipations hypothesis.

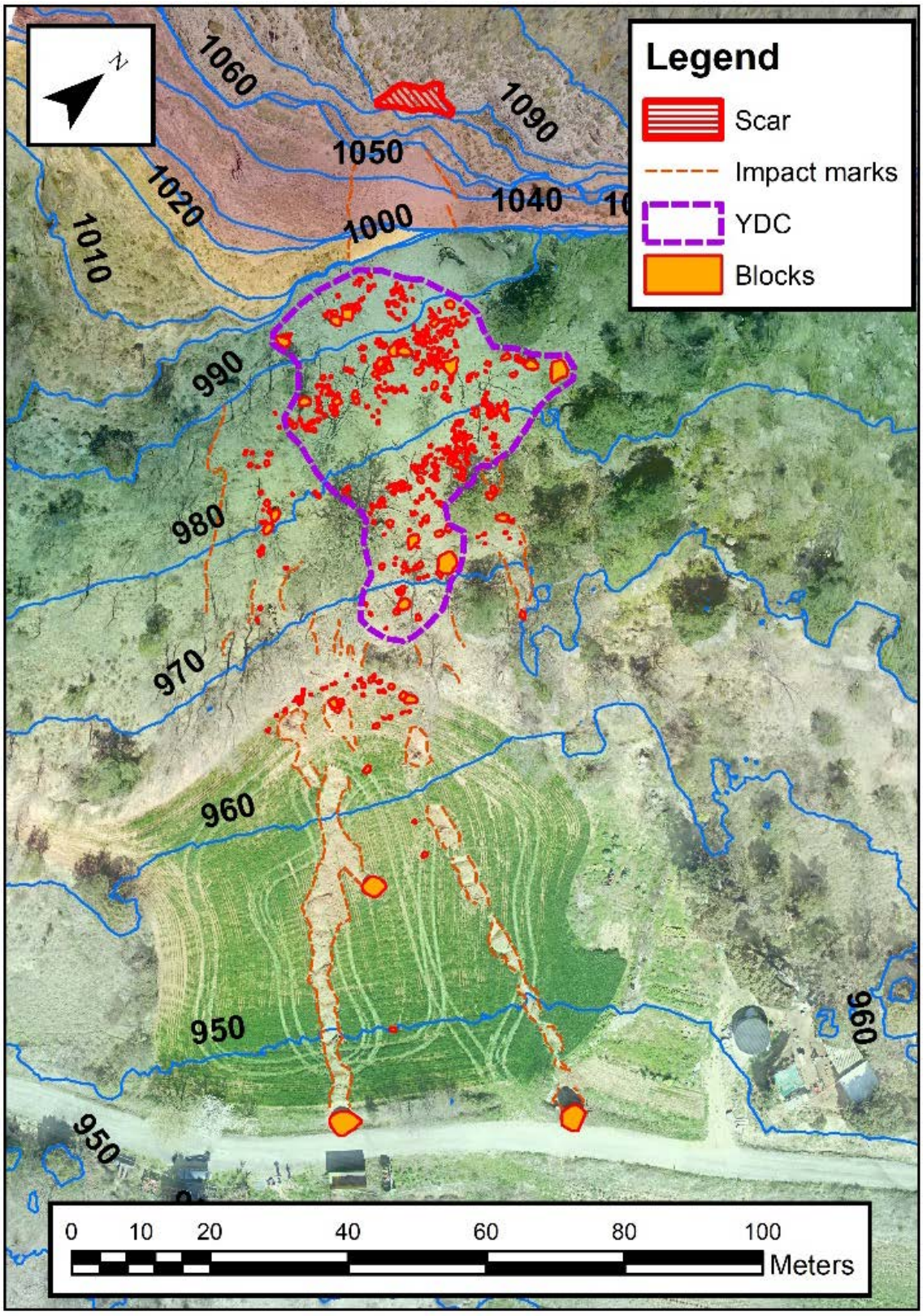

Figure 10: Gurp rockfall cartography with the scar, the Young Debris Cover zone and 500 blocks elaborated over an ortophoto, the topographic cartography and colored by the digital elevation model.

Monasterio de Piedra rockfall (5)

Monasterio de Piedra is a natural park near Calatayud (Spain), with some trails to visit cascades, lakes, rivers, and a beautiful chalk rock massif landscape with different vegetation and fishes, becoming a familiar attraction. On April of 2017, an important rockfall occurs involving 1000 m^3, reaching a visitor's trail (Figure 11). Part of the 50 meters of the deposit width impact against a dynamic barrier that has been completely turned down. The size of the blocks observed on the dynamic barrier are not enough to reach the maximum kinetic energy of these barriers (5000 KJ). However, the multiple and simultaneous impacts with these huge number of fragments allow to reach the maximum energy and total volume that these barriers resist. At the same, the rockfall width and density of blocks, increase to 1 the probability to impact against a vital part of the barrier, like a pile or the anchors. The vegetation was completely erased and the distal part of the deposit falls on the water lake.

Figure 11: UAV photography of the Monasterio de Piedra (MdP or Calatayud) rockfall inventoried.

An UAV flight was carried out obtaining the 3D model and the others cartographic products. A specific flight was carried out to obtain a high resolution model from the scar, and another from the deposit, obtaining a ground sample distance of 5 mm and 7 mm respectively (using a DJI Inspire 2 with X5S camera with 20 – 30 meters of distance or height). However, we trust on

manual measurements, and more than 2200 fragments were measured by a tape, part of them in two sampling plots with the methodology used before in (Ruiz-Carulla et al, 2015).

The obtained ortophoto reveal some blocks under the water (Figure 12). The deposit shows a very compact shape, where the whole deposit may be considered as Young Debris Cover, without large scattered blocks, in part, due to the topography, with a step before the lake on one side, and the flat trail also with the lake on the other side.

Fragmentation seems to affect also in the final position of the center of geometry of the deposit, reducing the runout of the blocks due to the decrease of each volume, the energy dedicated on breakage and the mutual interactions between the blocks. The own blocks generate a roughness on the talus slope that can stop the propagation of the smaller blocks.

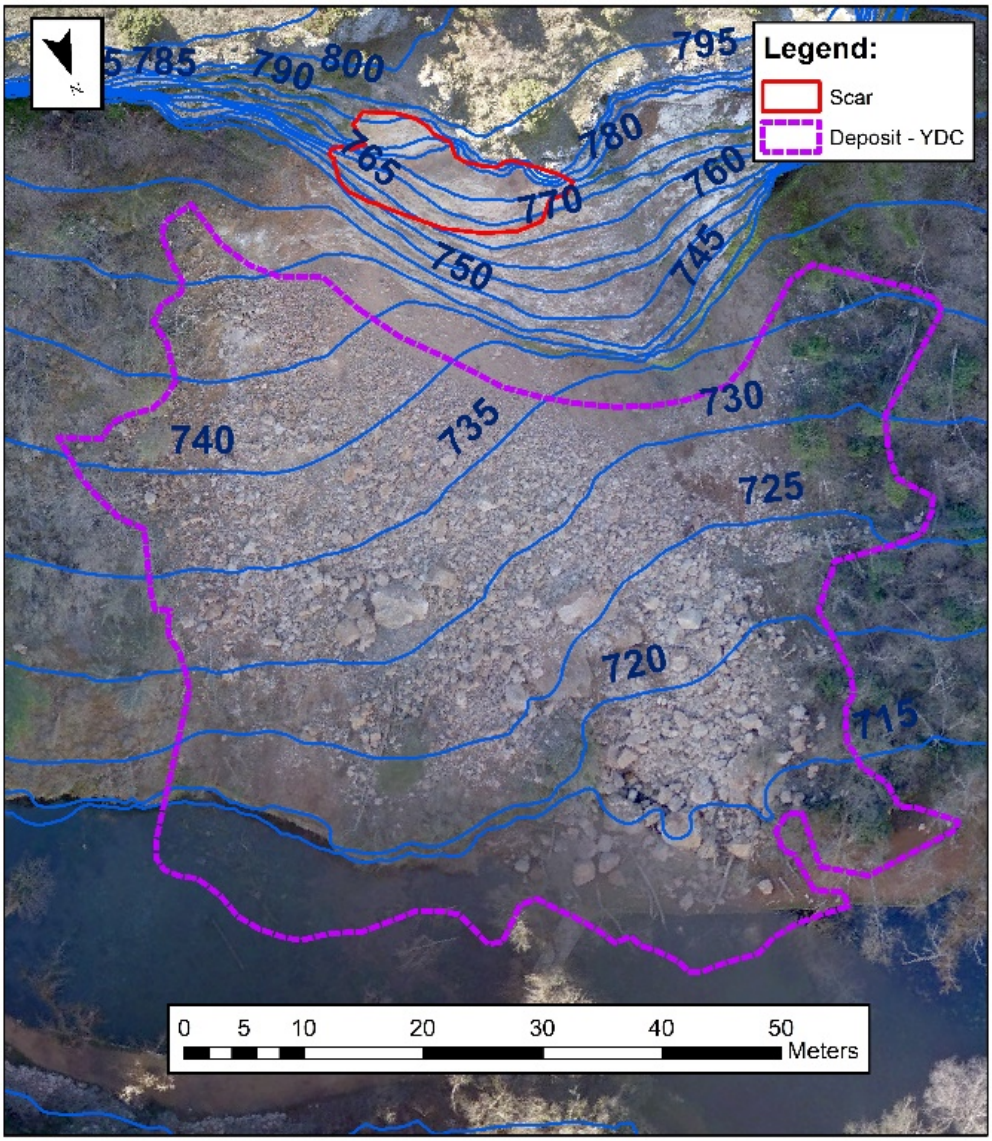

Figure 12: Cartography of the Monasterio de Piedra (MdP or Calatayud) rockfall.

Malanyeu rockfall (6)

The Malanyeu rockfall is an important rockfall, with a total volume detached close to 5000 m^3, characterized by a remarkable scar formed by two main joint sets and the stratification of the Maastrichtian limestone rock (Figure 13). The free fall height is less than 10 meters, however, may be considered as 80 meters due to the apparent direct toppling failure mechanism. The maximum run-out distance is 100 meters, reaching the valley bottom (Figure 14).

In this case, the fragmental rockfall generated a more or less continuous Young Debris Cover in the upper part of the deposit with a high concentration of small-size blocks. We measured 2721 blocks, part of them on 3 sampling plots, with a minimum volume of $4.2*10^{-5}$ m^3 and a maximum volume of 445 m^3 (the maximum inventoried fragment). The deposit includes 7 blocks greater than 100 m^3, and more than 60 blocks greater than 10m^3. The faces of the larger blocks are mostly preexisting discontinuities in the rock mass (joints and bedding surfaces).

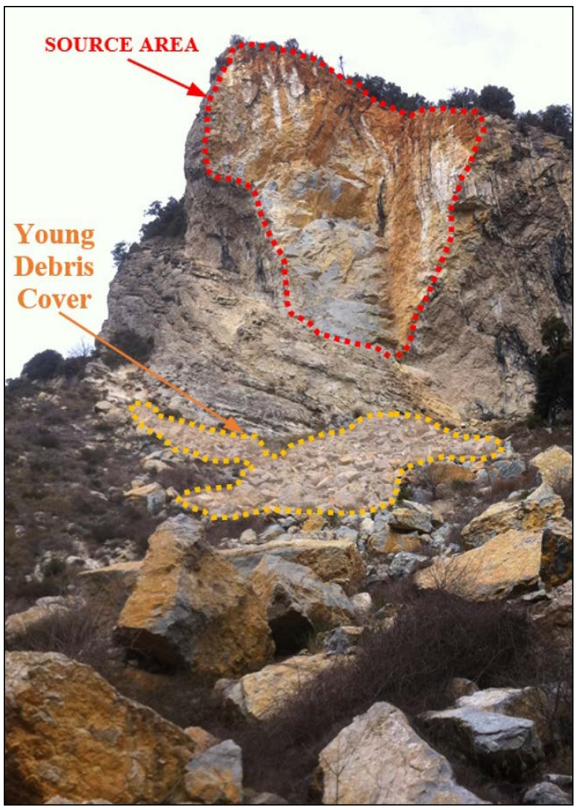

Figure 13. View of the Malanyeu rockfall.

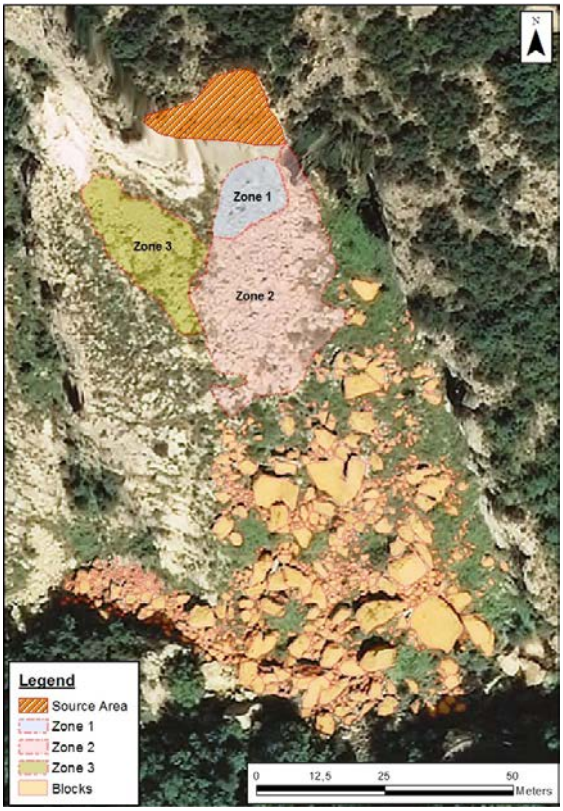

Figure 14: Malanyeu rockfall cartography.

This case corresponds to a large fragmental rockfall where the fragmentation is related to both the disaggregation of the rock mass along preexisting discontinuities (joints and bedding planes), and pure breakage. A proof of this is the presence of huge blocks, bounded by preexisting discontinuities in the lower part of the deposit and, on the other side, the blocks of the YDC, showing multiple new fresh faces.

Cadi rockfall (7)

The last and the bigger rockfall, with 10.000 m^3 involved, is located in Cadi Sierra, in the Eastern Pyrenees, near the village of Vilanova de Banat. The case has been studied and published on (Ruiz-Carulla et al, 2015 and 2016). The cliff is made of limestone of Paleocene age. The free fall height is 40-50 m, and the maximum run-out distance is 740 m. The first impacts generated a YDC of 30.000 m^2. We measured more than 1500 blocks: 1252 blocks in 6 sampling plots and 272 as Large Scattered Blocks (LSB). The minimum and maximum block volume measured is $1.53*10^{-3}$ and 30.8 m^3, respectively.

The blocks deposited have an irregular shape, showing fresh faces related to the breakage and some faces defined by the preexisting joints. Field observations suggest that the deposit was mainly originated by breakage. This is confirmed by the large number of small and medium blocks and the predominance of fresh faces in the blocks. The scenario, with a remarkable scar on red and brown colors over the grey limestone cliff (Figure 15), have a large talus to propagate the blocks with 35º degrees of slope without obstructions. However, we observe how as much volume is involved on a rockfall event, more feasible is the interaction between blocks, and also the comminution of the own rock mass on its bottom on the first impact zone creating the YDC.

Figure 15: Cadi rockfall, with red and brown colors on the scar and a long talus to propagate the blocks.

3. Scenario characterisation and detached volume reconstruction

Rockfall profiles

The reach angle may be used to study the runout and the mobility of a rockfall. We measured the reach angle of each cases from profiles obtained from 3D point clouds. (Figures 16 and 17).

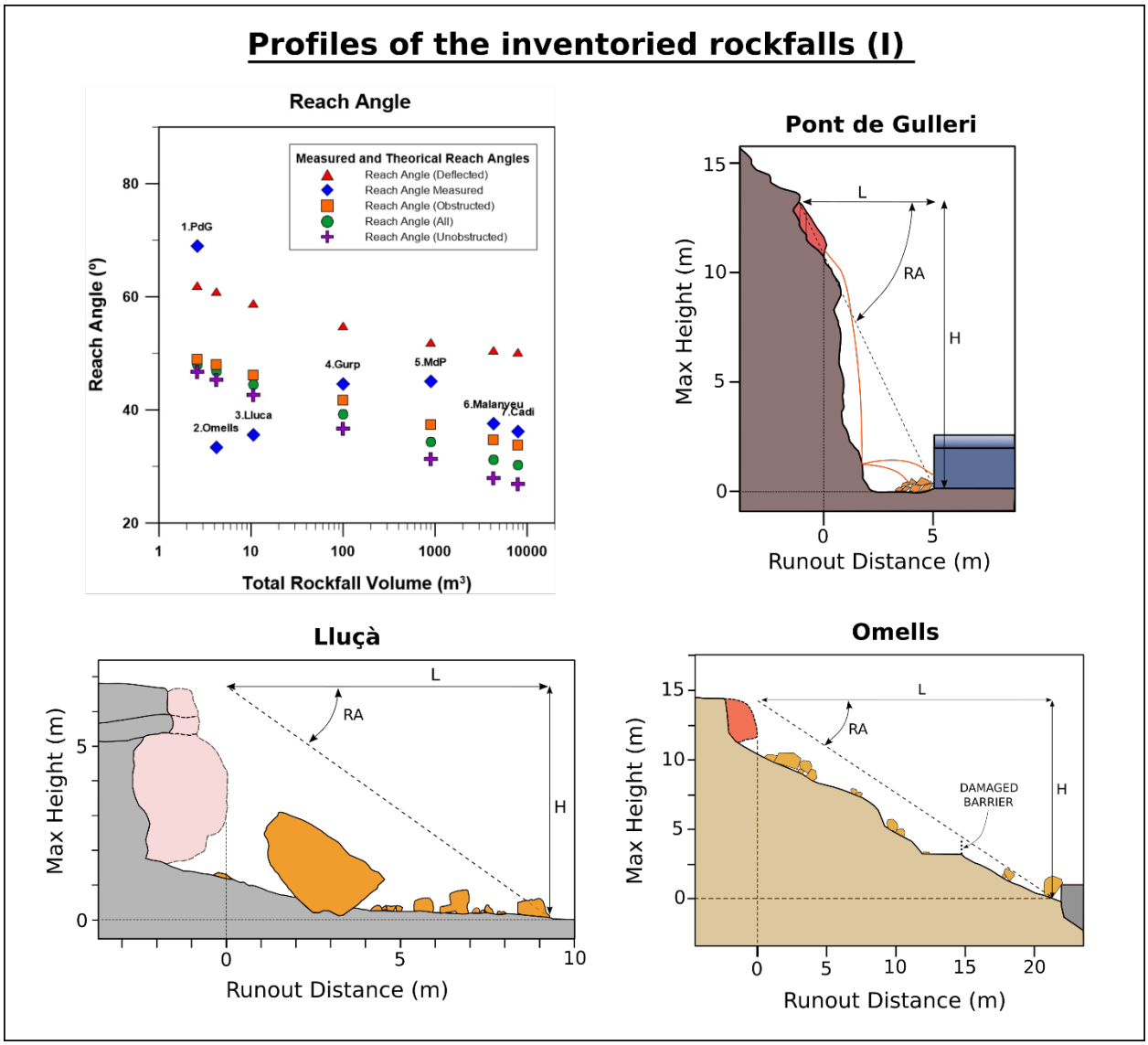

Figure 16: Reach angle of each inventoried rockfall and profiles of PdG, Omells and Lluçà cases.

The reach angle can be calculated with the empirical estimations (Corominas 1996) for scenarios of unobstructed, obstructed, deflected or all the cases mean. Based on this, we compare the measured reach angles from the inventory to the theoretical reach angles on different scenarios (Figure 16 upper left). Pont de Gulleri case have an abnormal reach angle of 70º degrees, a clearly obstructed case due to the old house. Llucà and Omells events shows lower reach angle than the expected, due to the fragmentation may produce ejected fragments that increase their mobility. However, the fragments with smaller volume can easily be stopped. The other four cases, from

100 m^3 to 10000 m^3, shows a reach angle between obstructed and deflected expectative, being fragmentation another phenomenon that may reduce the runout of a rockfall.

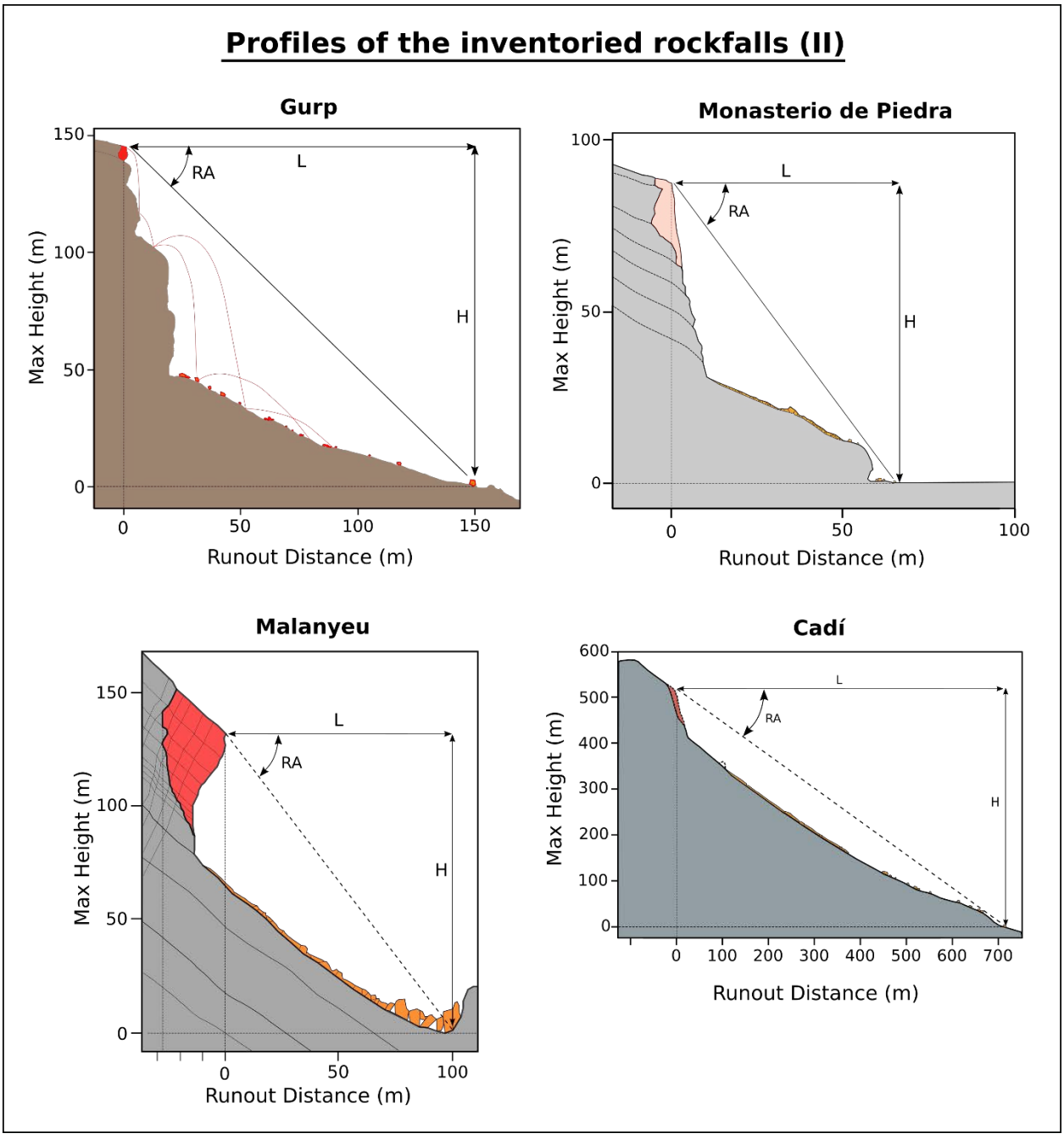

Figure 17: Profiles of Gurp, Monasterio de Piedra, Malaneyu and Cadi inventoried rockfalls.

Scar and deposit dimensions

The 3D models of each rockfall event obtained by UAV and digital photogrammetry technics, are very useful in order to measure distances, 2D and 3D areas, volumes, generate profiles with overhangs, create cartographies and so on. Table 2 (presented before) summarize the main geometrical descriptors used for rockfalls. Bigger total rockfall volumes tends to increase all the others geometrical descriptors, however, the Coef. of correlation r-squared with the 3D scar area is 0.99, and with the maximum runout and maximum deposit width are 0.78 and 0.84 respectively (Figure 18).

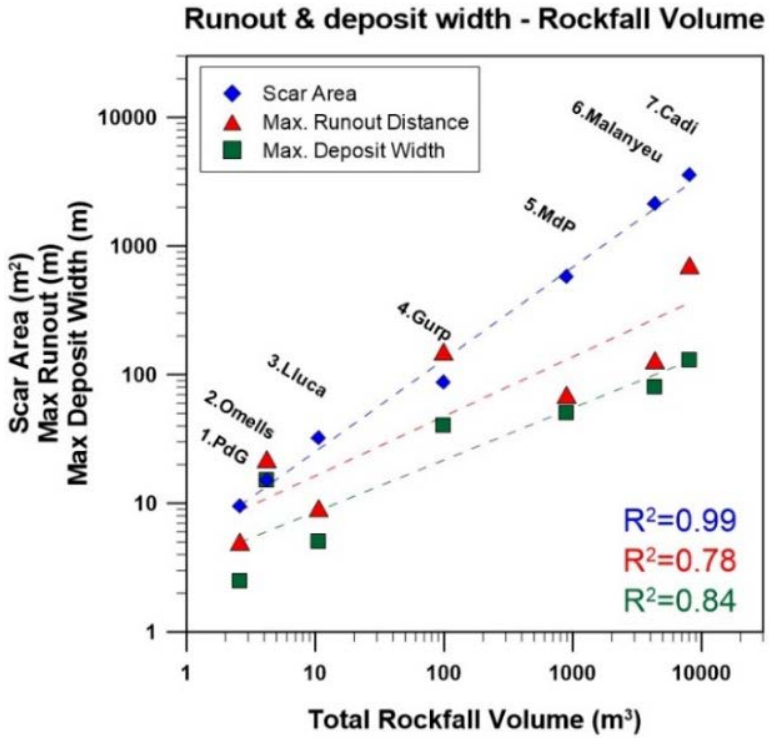

Figure 18: Correlation between scar 3D area, max. runout, max deposit width and total rockfall volume.

In order to characterize the fragmentation scenario, we consider very relevant the part of the cliff with high slopes (>45º) where the tendency is to accelerate and is the "energetic part" (colored from yellow to red on 3D models of Figures 19, 20 and 21), and the part of the slopes where the main impact and the rest of the propagation take place, with lower slopes (<45º) where the blocks tends to break or stop (colored from green to blue), related also with the type of propagation. Only Lluçà 3D model is colored by height of the fragments due to the scenario is very flat. Notice how on Gurp scenario (Figure 20, up), a blue zone on the half of the cliff can be identified, being a lower slope part of the profile that may produce impacts with high trajectory variation and also breakage.

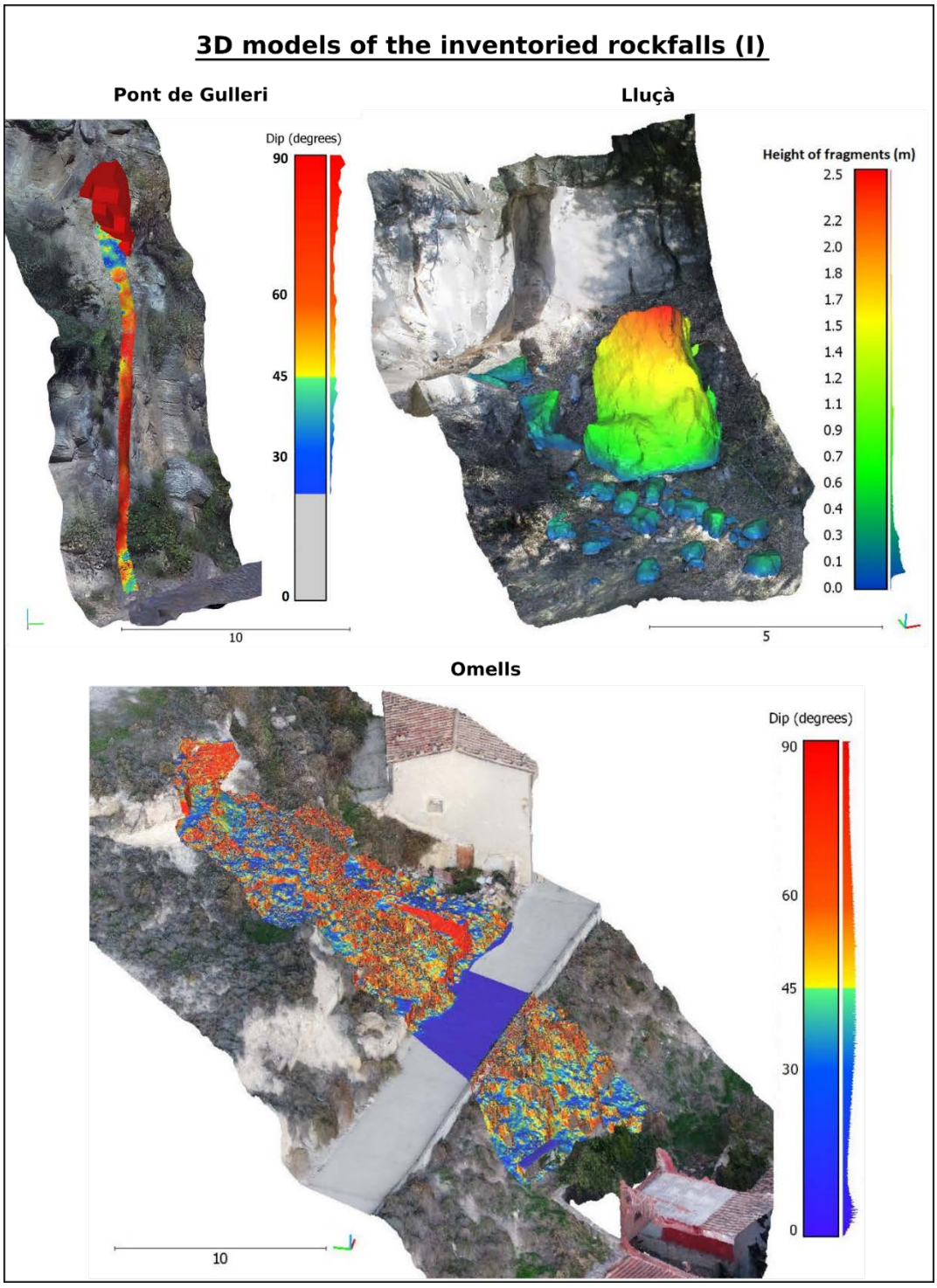

Figure 19: 3D models of Pont de Gulleri, Lluçà and Omells rockfalls, coloring the rockfall zone by higher or lower than 45º of slope. Lluça rockfall is colored by the height of the fragments.

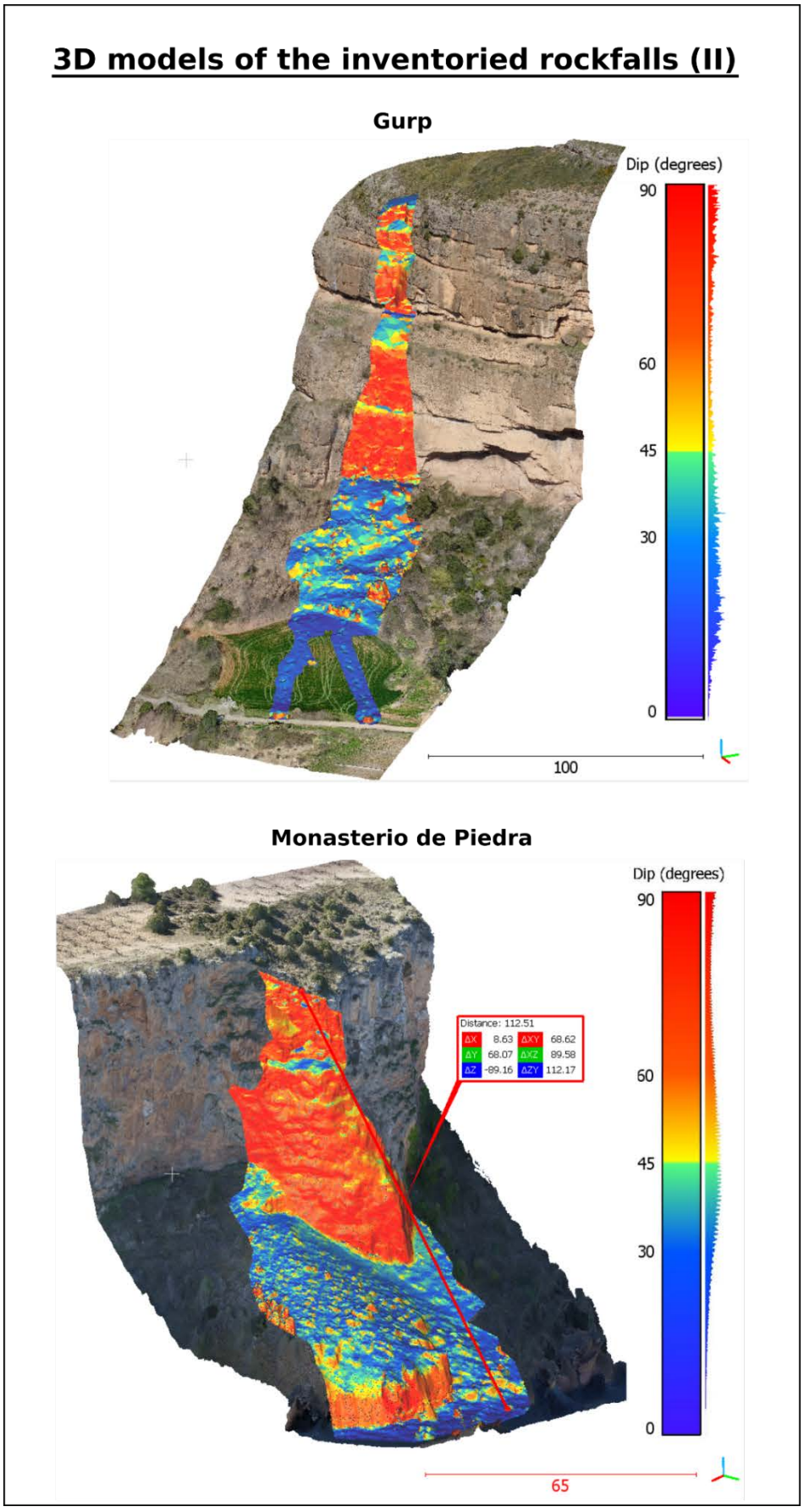

Figure 20: 3D models of Gurp and Monasterio de Piedra rockfalls, coloring the zone affected by the rockfall by higher or lower than 45º of slope.

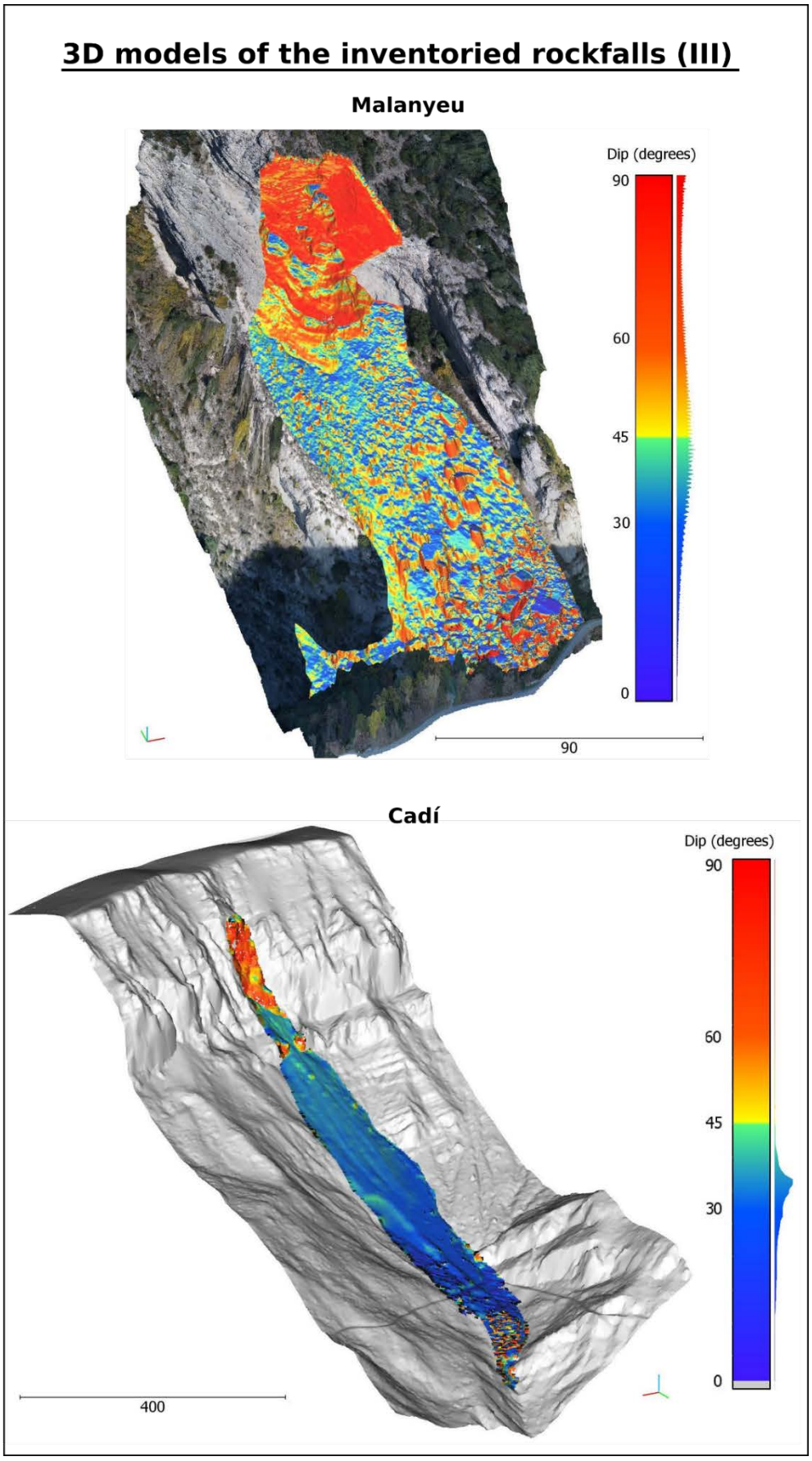

Figure 21: 3D models of Malanyeu and Cadi rockfalls, coloring the zone affected by the rockfall by higher or lower than 45º of slope. Cadí model obtained from Catalan Cartographic and Geologic Institute data.

Reconstruction of the detached rock mass and generation of the IBSD

The RFFM requires initiators, which can be individual rock blocks or rock masses that include one or more discontinuity sets predefining a group of blocks. The characterization of the latter requires the 3D reconstruction of the detached volume and the generation of the IBSD based on a discrete fracture network (DFN). This task requires considering several assumptions and hypotheses.

The detached rockfall volume at each site was calculated following the methodology described in Ruiz-Carulla et al. (2015). The detached volume is calculated by subtracting the Digital Surface Model (DSM, 3d mesh surface) of the cliff before and after the event. The DSM before the event is based on the LIDAR point cloud provided by the Cartographic and Geological Institute of Catalonia (ICGC), except for the case of Monasterio de Piedra, provided by the National Geographic Institute of Spain. When the morphology of the cliff and/or pictures before the event are available, we manually modified the DSM in order to reproduce the before scenario on the more realistic morphology possible.

The DSM of the cliff after the event was generated from pictures taken with UAV (DJI Inspire 2, X5S camera), except in the case of Vilanova de Banat where the DSM after the event was obtained from ground pictures taken with a camera Nikon D90, in all cases, with the subsequent photogrammetry treatment. The difference between the DSM of the scar before and after the rockfall yielded a detached rock mass volumes presented at table 1 (Total Volume from IBSD).

The joint set characterization is based on 3D point cloud analysis combining semi-automatic and manual modelling. The joint pattern characterization was carried out using the plugins Facet Matching (Dewez et al., 2016) on Cloud Compare (Girardeau-Montaut 2006), and also the tool Compass (Thiele et al. 2017). The parameters used on Facet Matching to define the fitted facets are accommodated to the scale of the joints. High tolerances, allowing high values of the minimum distance between the 3d points and the facet planes, will define facets with larger areas. Depending on the scale of each scar, the parameters used should be calibrated and the results supervised. Often, can be useful the manual selection of well-defined planes and adjusting a facet using the Compass tool, also for joint trace identification. Combining the semi-automatic and the manual joints defined, a well detailed Discrete Fracture Network (DFN) can be exported in mesh formats. The total volume detached reconstructed and the DFN can be handle in a 3D modelling software (CloudComapre, Rhinoceros, Polyworks, etc) to create an IBSD cutting the volume with the DFN. The main hypothesis on this step is the infinite persistence of the modelled joints. The joints used are located on its real position based on adjusted facets or by manual modelling.

The 3D blocks created composing the IBSD are listed and both the volume and the 3D surface area of each block, is measured. The list of volumes is used as input for the fragmentation model. The list of the areas and the accumulated area of the rock blocks will be compared to the areas of the new surfaces created by fragmentation. The number of joint sets, number of blocks on each IBSD, maximum and minimum blocks and minimum spacing are summarized on Table 3.

Table 3: Summary of IBSD characteristics

IBSD	**1.PdG**	**2.Omells**	**3.Lluçà**	**4.Gurp**	**5.MdP**	**6.Malanyeu**	**7.Cadi**
Nº of joint sets	5	3	4	5	5	4	5
IBSD Total number of blocks	40	3	5	14	19	95	6800
Min. Block Volume (m^3)	0.0001	0.0007	0.0007	0.0015	0.001	0.0015	0.01
Max. Block Volume (m^3)	0.28	4	10.7	30	96	492	45
Min joint spacing	0.3	0.2	2	0.5	1	3	1

The scar 3d models can be plotted in terms of dip direction or dip, and the semi-automatic and manual joint characterization allows to export mean planes or hundreds of data to obtain the mean or modals planes. In the case of a scar, the discrete fractures modelled may be the important measure and also its location. We used the DFN to cut the reconstructed volumes to obtain the IBSD as shown in Figures 22 and 23. Cadi case is already published on (Ruiz-Carulla et al, 2016, however some actualization has been carried out).

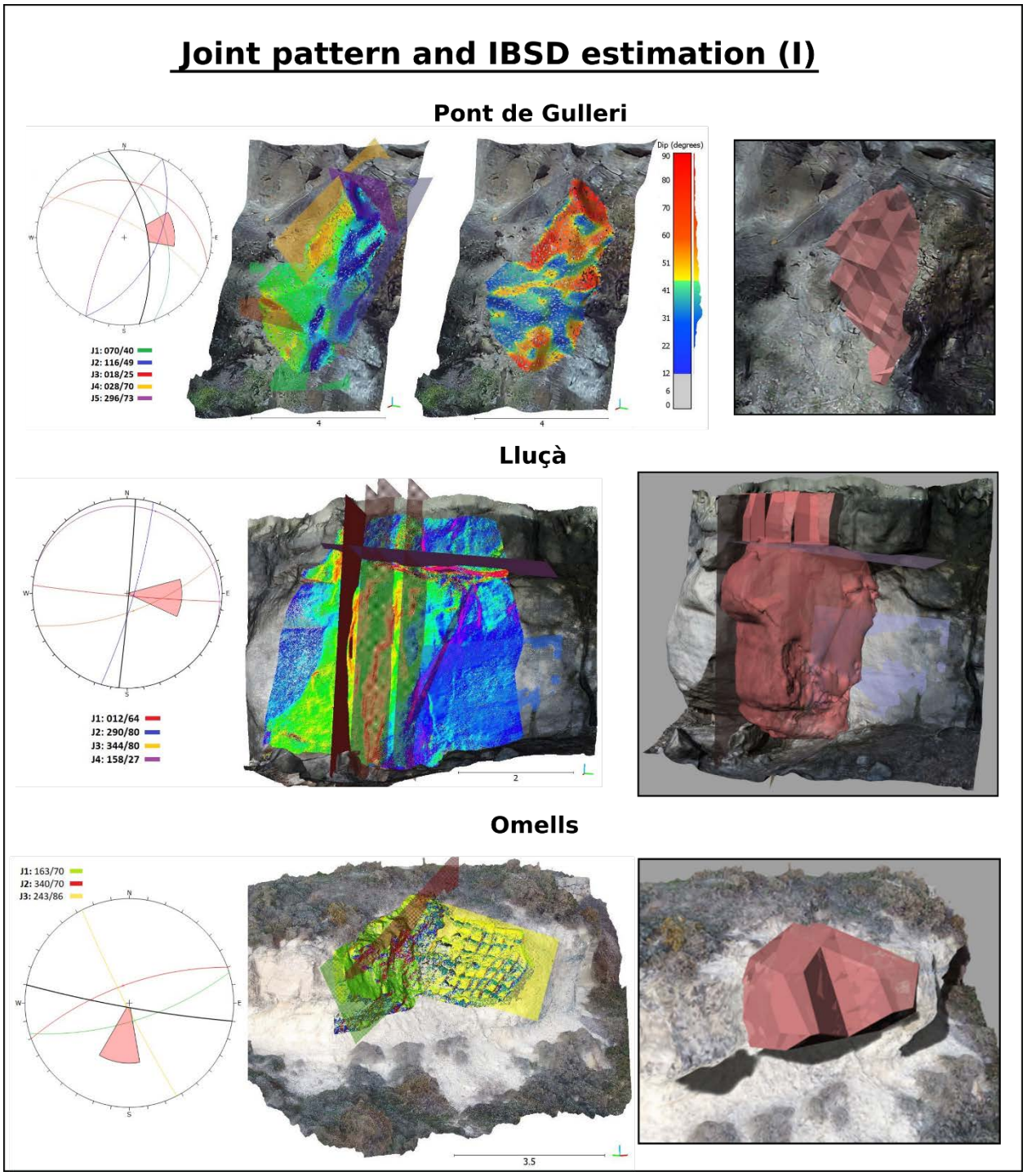

Figure 22: Stereographic projection of the joint sets identified on the 3D model of the scar, used to cut the reconstructed detached volumes in order to estimate the IBSD of Pont de Gulleri, Lluçà and Omells cases.

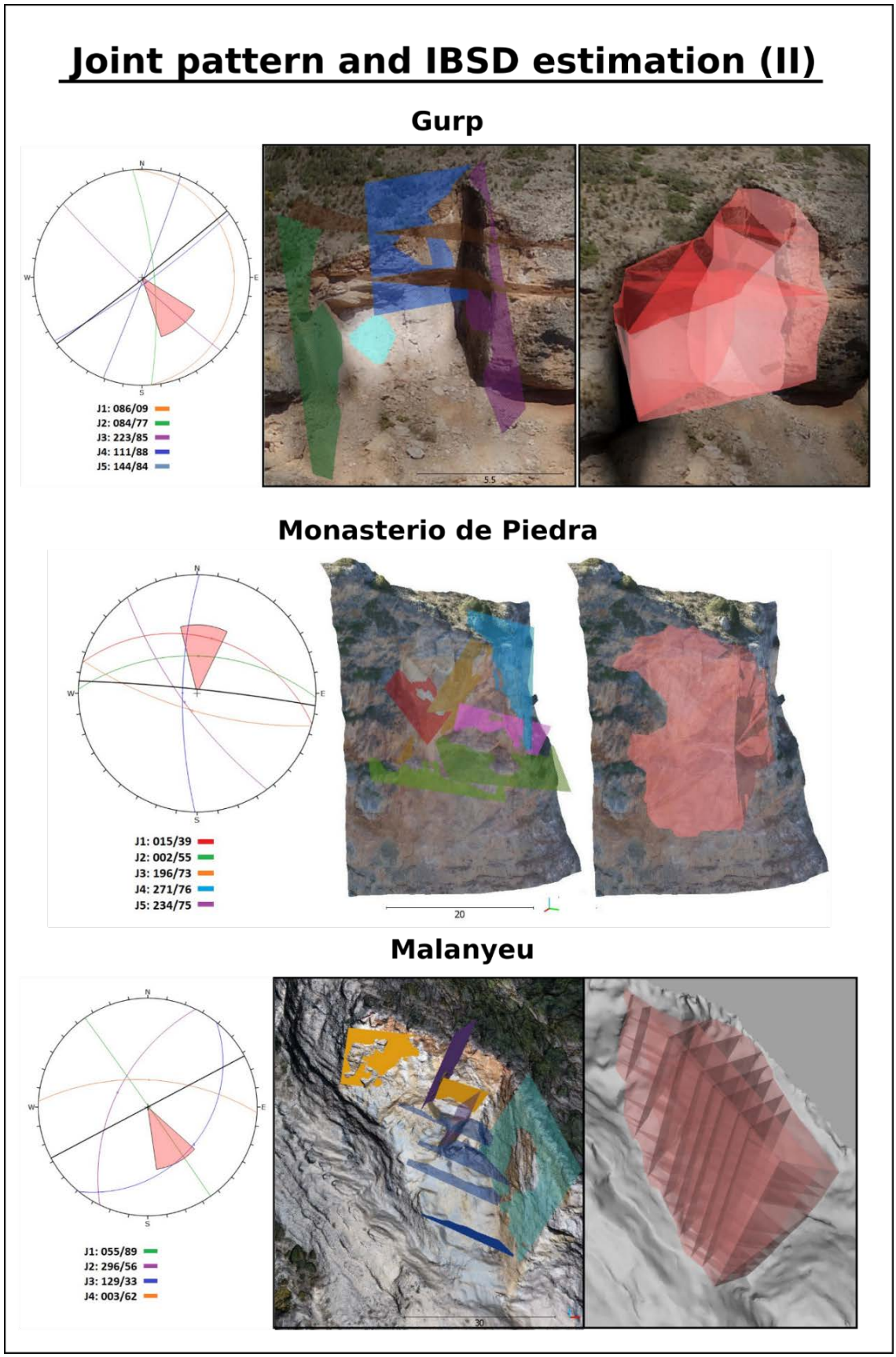

Figure 23: Stereographic projection of the joint sets identified on the 3D models of the scar, used to cut the reconstructed detached volumes in order to estimate the IBSD of Gurp, Monasterio and Malanyeu cases.

4. Rockfall block size distribution collected

From our point of view, the most important information collected on the rockfall inventory is the RBSD from each deposit (Figure 24, left). The data is used on the calibration process of the fractal fragmentation model proposed on Chapter 9 and 10. Also the IBSD will be used as input data for the fragmentation model. The total number of blocks from the IBSD and from the RBSD are plotted on Figure 24 (right), as well as the total number of blocks reproduced by the Rockfall Fractal fragmentation model (Chapter 10: calibration process), showing a very good agrrement.

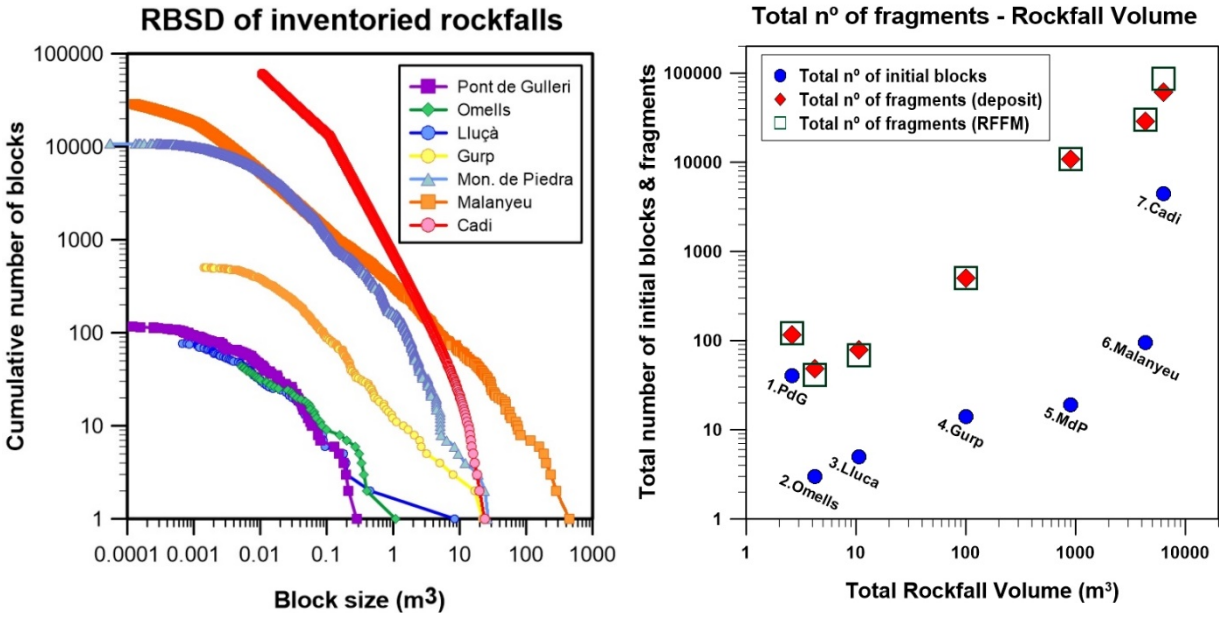

Figure 24: RBSD collected on the rockfall inventory (lefr). Total number of blocks from the IBSD and the RBSD collected, as well as the results of the fragmentation model proposed on chapter 9 and 19 (right)

5. Conclusions

The use of UAV and digital photogrammetry allow the obtention of very high resolution orthophotos, very useful for cartography proposes and to identify blocks and elements that on the field may be difficult to observe. The 3D models with high degree of detail are very useful also for profile generation, scenario analysis, and for the reconstruction of the detached rock mass. On the same way, the detailed 3D models from the scar allow the joint pattern characterization to be used on unstable rock mass identification and for IBSD estimations. The definition of the IBSD implies take some assumptions about the persistent of the joints. Howerver, the joints used are located on their real position and from real plane measurements or trace modeling. The data collected (specially the RBSD and the IBSD) will be very useful in order to calibrate the proposed fragmetattion model as well as other research lines, like trajectory simulators or RBSD measurement from raster or 3D point cloud segmetation analysis.

PART II

Real-scale fragmentation tests

7- Analysis of rock block fragmentation by means of real-scale test

8- Comparative analysis of 4 real-scale fragmentation tests

7. Analysis of rock block fragmentation by means of real-scale test

This chapter reproduces the article published in the proceedings of the International Symposium on Landslides held in 2016 in Naples, on the results of drop tests carried out in a quarry and the characteristics of the rock fragments volume distribution.

Publication reference:
R. Ruiz-Carulla, G. Matas, A. Prades, J.A. Gili, J. Corominas, N. Lantada, F. Buill, O. Mavrouli, M.A. Núñez-Andrés, J. Moya (2016). Analysis of rock block fragmentation by means of real-scale test. Internation Symposium Rock Slope Stability 2016, Proceedings

Abstract:

Rockfalls are frequent instability processes in road cuts, open pit mines and quarries, steep slopes and cliffs (Cruden & Varnes, 1996). Quite often the detached rock masses become fragmented after the first impacts on the ground. Knowing the size and trajectory of the blocks resulting from the fragmentation is critical in determining the impact energies on the exposed elements and protection structures (Jaboyedoff et al. 2005; Corominas et al. 2012). In this work we present the results of two real scale rock fall tests carried out as part of the activities of the research project Rockrisk (rockrisk.upc.edu/en). The aim of the project is to quantify the risk induced by rockfalls, improving the tools to prevent, to protect and to mitigate its effects.

Keywords: rockfall test, fragmentation, quarry

1. Real-scale rockfall test design

Two real scale rock fall tests were carried out in a limestone quarry located at Vallirana (Barcelona, Spain). Test site 1 (TS#1) was a single benched slope (Figure 1, left) while test site 2 (TS#2) was a three benched slope. The total fall height, including the bulldozer blade height, was 16.5 m for TS#1 and 27.5 m for TS#2. A total of 56 blocks with volumes ranging between 0.2 and 4.8 m^3 were released (30 for TS#1 and 26 for TS#2). The block size and the strength of rock surface (Schmidt L-hammer rebound) were measured before the tests. A 'circular photogrammetric survey' was realized block per block which allowed to build 3D models of each block for precise volume and center of gravity measurements (Figure 1, center).

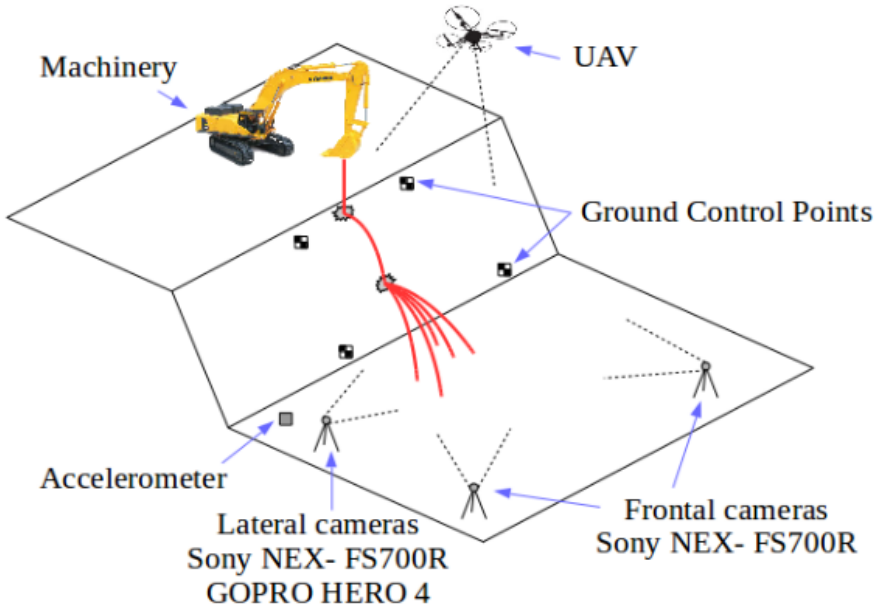

Figure 1: Left: TS#1 monitoring scheme.

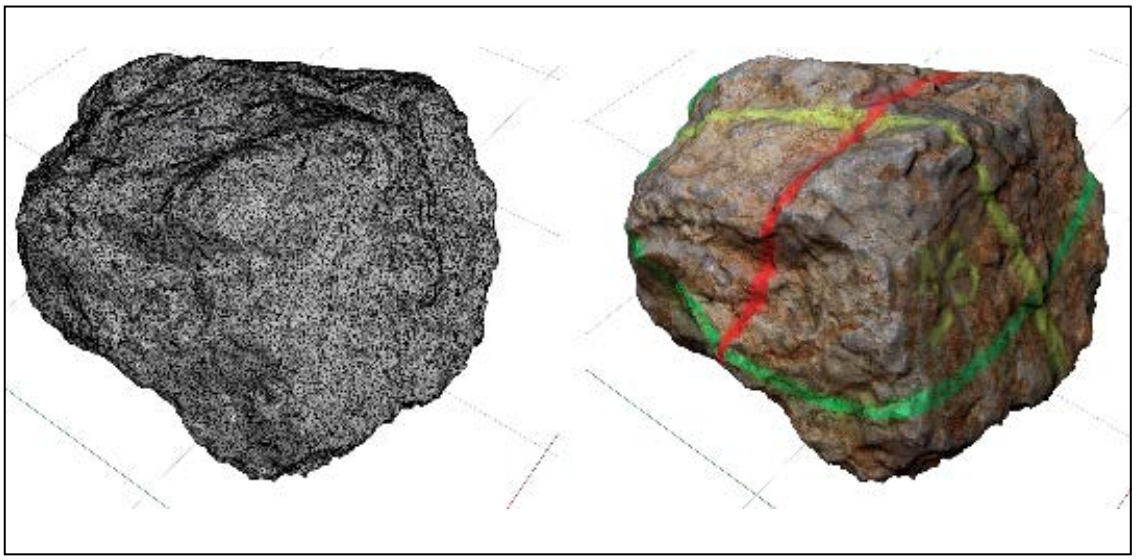

Figure 2: 3d model reconstruction by digital photogrammetry of a block before be tested.

Figure 3: Frame of TS#1 block #19.

The tests were recorded using three High-Speed (HS) and High-Definition cameras Sony NEX-FS700R at 400fps and two GOPRO Hero4 for a general view of the scene. Six Ground Control Points (GCP) where placed on the slopes to georeference the images while the location of the rock fragments was recorded using Unmanned Aerial Vehicles (UAV). An accelerometer was also installed to capture the seismic signal induced by the impacts. Figure 1 left, shows the location of the sensors for TS#1. The HS cameras were strategically placed to provide a three-dimensional multi-view (with one extra camera). The shots were synchronized using a flashlight visible from all cameras. The high frame rate allows visualizing precisely how a block is fragmented (Figure 1, right).

2. Test results

The kinematic reconstruction of each rock release has been made by video-triangulating the approximate position of the center of gravity of the block using a code developed by us. The velocity and the energy at the impact point have been computed using the trajectories obtained with this methodology. 19 over 30 blocks and 21 over 26 blocks broke at TS#1 and 2 respectively, generating a Block Size Distribution (BSD) of fragments. In Figure 2 we plot the original block volumes and the BSD for all the fragments generated in TS#1 and 2.

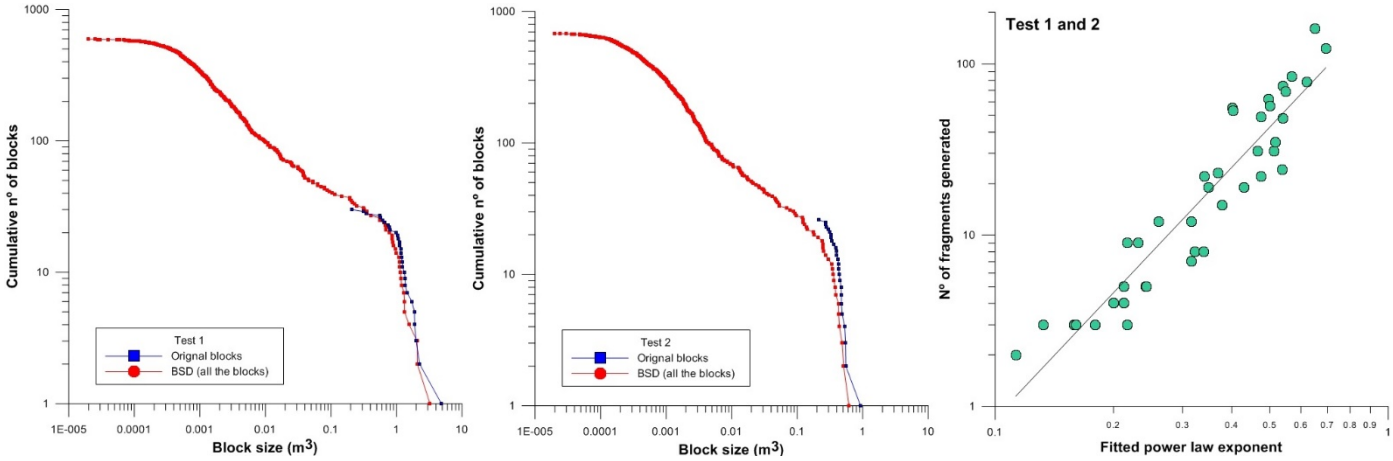

Figure 2: Original Block Volumes and the Block Size Distribution (Left: TS#1: Center: TS#2); Right: Nº of fragments generated versus the exponent of the fitted power law for each fragmented block

The BSD generated from each broken block may be well fitted by a power law. It shows a rollover effect under 10^{-4} m^3. The total volume of the generated fragments under 0.2 m^3 (the smallest block tested) represents the 33% of the total volume of the blocks. The exponent of the fitted power law at each BSD increases with the total number of fragments generated (Figure 2, right). Using the high speed videos, the velocity of each block before the impact was measured, allowing the calculation of the kinetic energies, which range between 100 and 600 KJ. No meaningful relation was observed between the kinetic energy or the Schmidt Hammer values and the number of fragments generated (Figure 3). These results suggest that other factors such as the presence of fissures in the blocks or the impact location must be taken into account. The maximum run-out distance measured from the bottom of the wall was 20 m and the maximum dispersion angle measured from the impact point was 120º.

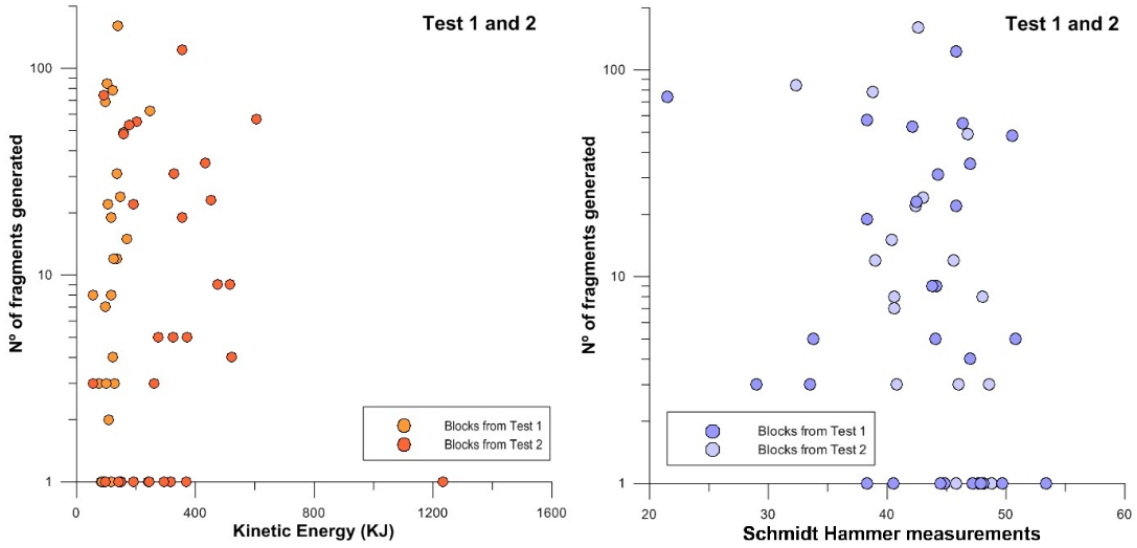

Figure 3: Nº of fragments generated versus Kinetic Energy (Left) and versus Mean value of Schmidt Hammer measures (Right)

3.Concluding remarks

The results indicate that the size distribution of rockfall fragments can be expressed by power laws, which exponents are indicators of the degree of fragmentation. The fragmentation of the blocks induces a higher dispersion angle. Although an energy threshold could be expected for the breakage of the blocks, the kinetic energies measured and the Schmidt hammer values shows poor correlations with the number of fragments generated.

REFERENCES

Corominas J, Mavrouli O, Santana D, Moya J (2012). Simplified approach for obtaining the block volume distribution of fragmental rockfalls. In Eberhardt E, Froese C, Turner AK, Leroueil S (eds). Landslides and engineered slopes. Taylor and Francis. 2:1159–1164

Cruden MD, and Varnes JD (1996). Landslide types and processes. In Turner, A.K. and Schuster, R.L., editors, Landslides: investigation and mitigation. Washington DC: Transport Research Board, 36–75.

Giacomini A, Buzzi O, Renard B, Giani GP (2009). Experimental studies on fragmentation of rock falls on impact with rock. Int. J. of Rock Mechanics & Mining Sciences. Vol 46, Pages 708-715. Elseiver

Jaboyedoff M, Dudt JP, Labiouse V (2005). An attempt to refine rockfall hazard zoning based on the kinetic energy, frequency and fragmentation degree. Nat Hazards Earth Syst Sci 5:621–632

8. Comparative analysis of 4 real-scale fragmentation tests

Original unpublished chapter

Abstract: Real-scale fragmentation tests provide high quality data in order to study the fragmentation phenomenon on rockfalls. In the real scale tests carried out, the initial rock mass is well known in terms of both volume and shape, thanks to the 3D photogrammetric reconstruction. The fragments size distribution for each block tested, was measured by hand using a tape. The successive tests allowed obtaining a range of behaviors from the series of blocks dropped under the same conditions. We carried out drop tests in four different scenarios, testing a total of 124 blocks and measuring 2907 fragments. The survival rate (Sr), which is the proportion of the block that remain intact (or the maximum fragment volume over the initial volume) shows a wide range of values. The number of fragments produced and the Sr are the parameters that characterize the fragmentation phenomenon. Finally, influence of the local conditions of each test site is also discussed.

Keywords: rockfall, fragmental rockfall, block size distribution

1. Introduction

The study of fragmentation phenomenon in natural rockfalls involves important uncertainties particularly on the size and characteristics of the initially detached rock mass and in the deposit of fragments. Real-scale fragmentation test (Figure 1 and 2) may provide high quality data in a very controlled scenario with the possibility to repeat the test several times. We performed four real-scale fragmentation test in quarries dropping rock blocks of volumes ranging between 0.17 m^3 and 5 m^3. The main features recorded during the tests are: initial volume using a tape and a 3D photogrammetric reconstruction, volume of fragments, blocks trajectories (using 3 high speed video cameras), and recording of the seismic waves. Distancemeters and targets as well as UAV flights were used for the 3D scenario reconstruction. In this chapter, we will focus only on the data from initial volumes and the final block size distributions of fragments.

Figure 1: Picture of real-scale fragmentation test on a quarry (Test 4).

Figure 2: Breaking instant of a block on the 4th real´-scale fragmentation test.

2. Experimental set up

The real-scale test were carried out at 4 different experimental set ups (Figure 3). The geometry are benches on quarries with height from 11 meters to 20 meters, however, the blocks are released from a greater height using the machinery. An UAV flight was used to generate high resolution 3D models of each experimental setting, as well as ortophotos and profiles that may display the slope angle at each point. The impact point surface has a variable inclination ranging from 42º to 71º. The heights and slope angles are shown in Figure 4.

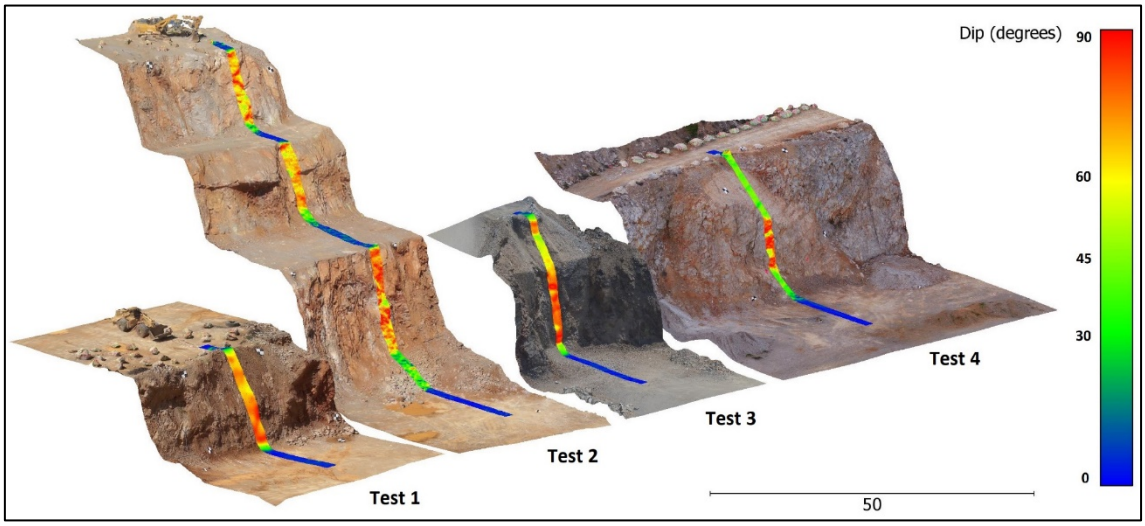

Figure 3: 3D models of the 4 fragmentation test settings, coloured according to the local slope angle.

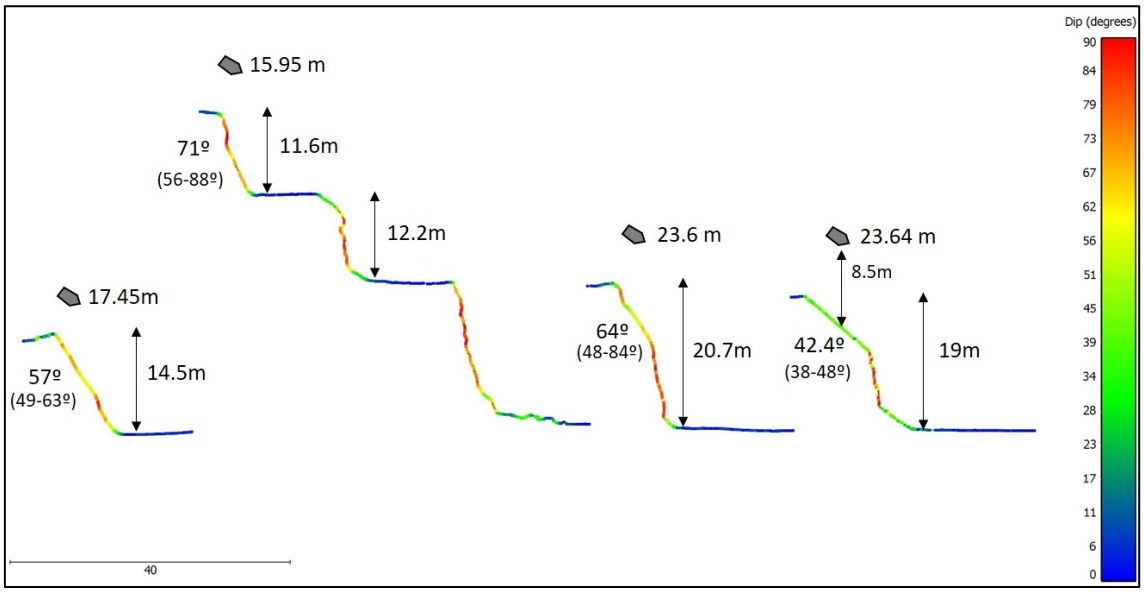

Figure 4: Profiles of the 4 settings. Local slope angles are represented with a color code and both the height of drop and the average angle of the impact surface are indicated as well.

3. Initial block volume and fragments measurements

Before the test, the block volumes were measured one by one using two different procedures: (a) by means of a tape, measuring 3 lengths of the block, assuming a prismatic shape and (b) using a set of 30 to 60 pictures to create a high resolution 3D model by means of digital photogrammetric techniques (Figure 5). After each test, all the fragments generated by the breakage of the blocks were measured with a tape up to a certain minimum size. Ideally, the sum of the fragment volumes should yield the initial volume (Figure 6, 7 and 8).

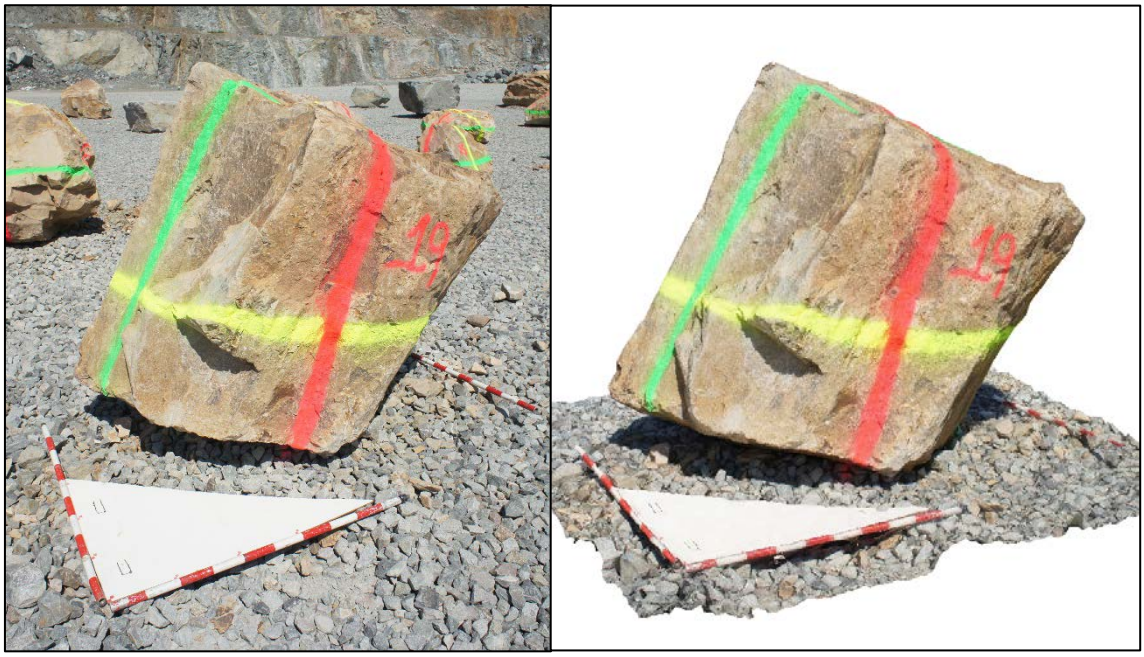

Figure 5: Picture of a block with rules to be scaled (left) and the 3D model obtained (right)

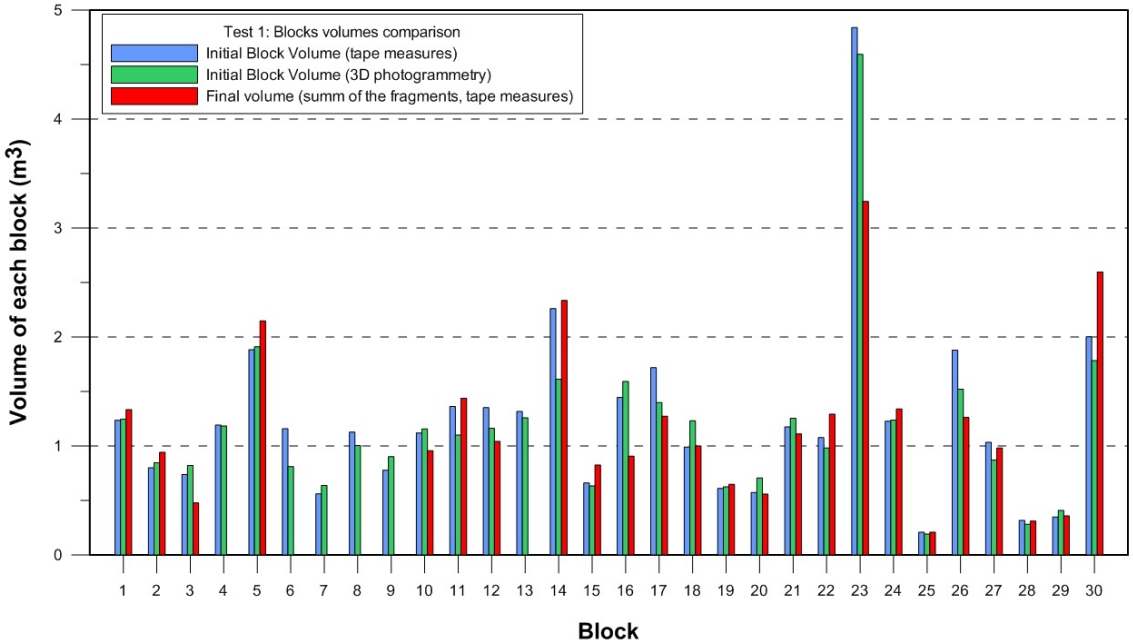

Figure 6: Initial block volume measured with a tape, 3D models and sum of fragment's volumes originated during the drop test, in test 1.

However, a fraction of the broken block is lost because the fragments are too small to be measured. In test 2, some of the initial blocks could not be reconstructed in 3d due to the lack of time to take the images. The volumes calculated using the 3D models are considered as ground truth.

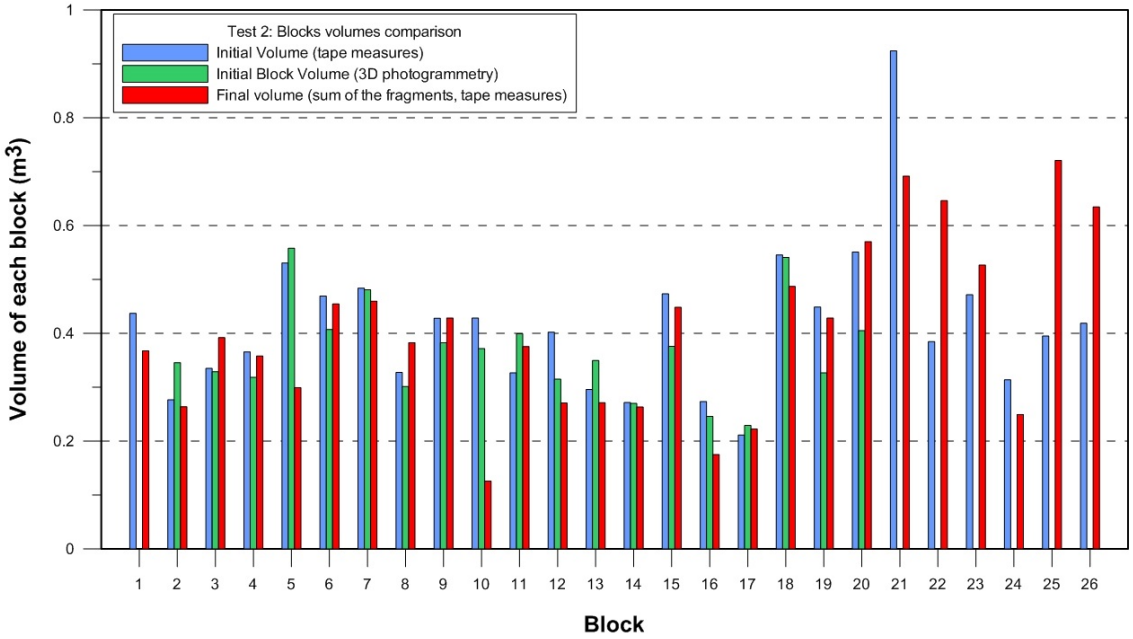

Figure 7: Initial block volumes measured with a tape, 3D models and sum of fragment's volumes originated during the drop test in test 2.

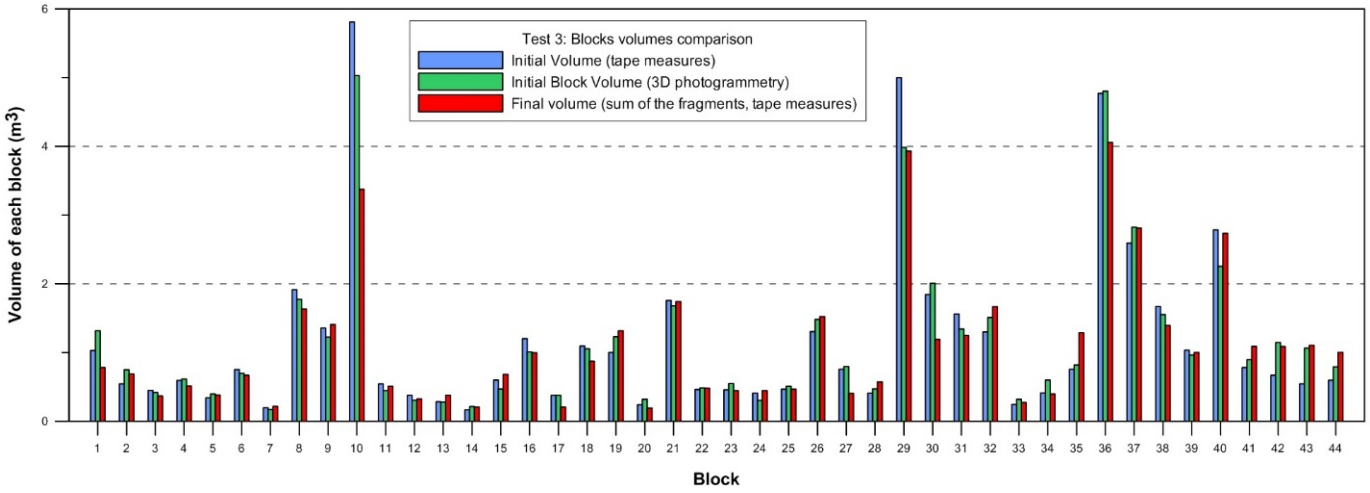

Figure 8: Initial block volumes measured with a tape, 3D models and sum of fragment's volumes originated during the drop test in test 3.

A drone flight of the park of blocks before the tests at the testing site 4 was carried out. From the flight pictures, a 3D point cloud was generated. The classification of the points of the point cloud in ground points and not ground points has allowed the automatic segmentation of the blocks (Figure 9). Two different approaches were used to obtain the volume of the initial blocks from the UAV surveys: (1) Creating a mesh and cutting the blocks at their base with another mesh created only with the ground points. Then, each volume is a closed 3D reconstructed mesh with

a defined volume; (2) A 2.5D volume calculation is used based on a high resolution digital elevation model. The base was also a surface, also in raster, created with the ground points. In both cases, the topographical surface (base surface) is not considered as a flat surface due to the presence irregularities of the ground that might be the source of important errors (Figure 10).

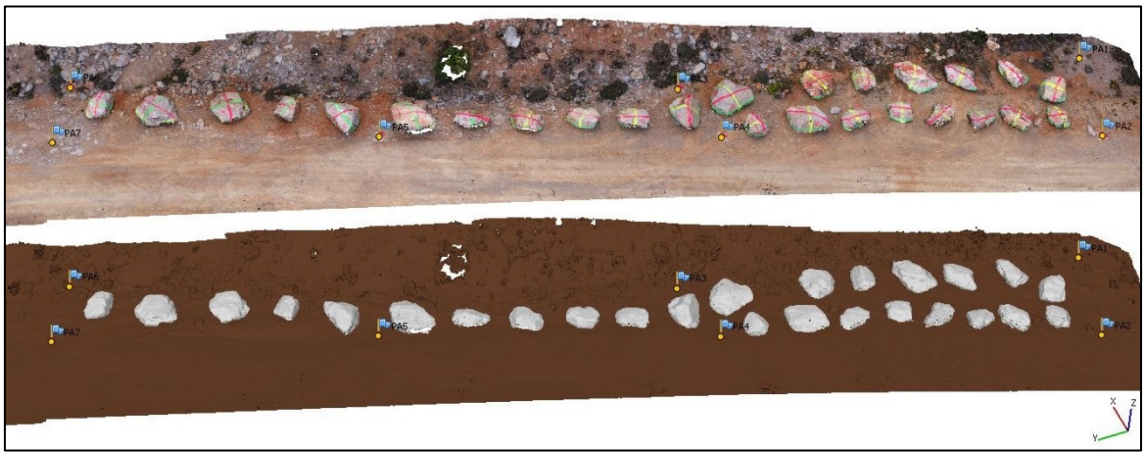

Figure 9: Blocks before test 4: Point cloud in real color (up) and point cloud classified in ground or not ground (down).

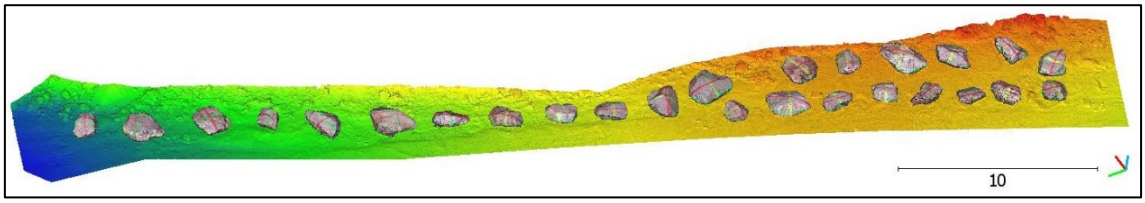

Figure 10: Blocks before test 4: Point cloud of blocks in real color and ground colored by altitude.

Therefore, the initial volume of the blocks in testing site 4 was calculated using 4 techniques (Figure 11): tape measurements; 3D photogrammetric reconstruction by pictures; 3D mesh reconstruction from UAV surveys; and 2.5D volume calculation based on DEM (also from UAV surveys).

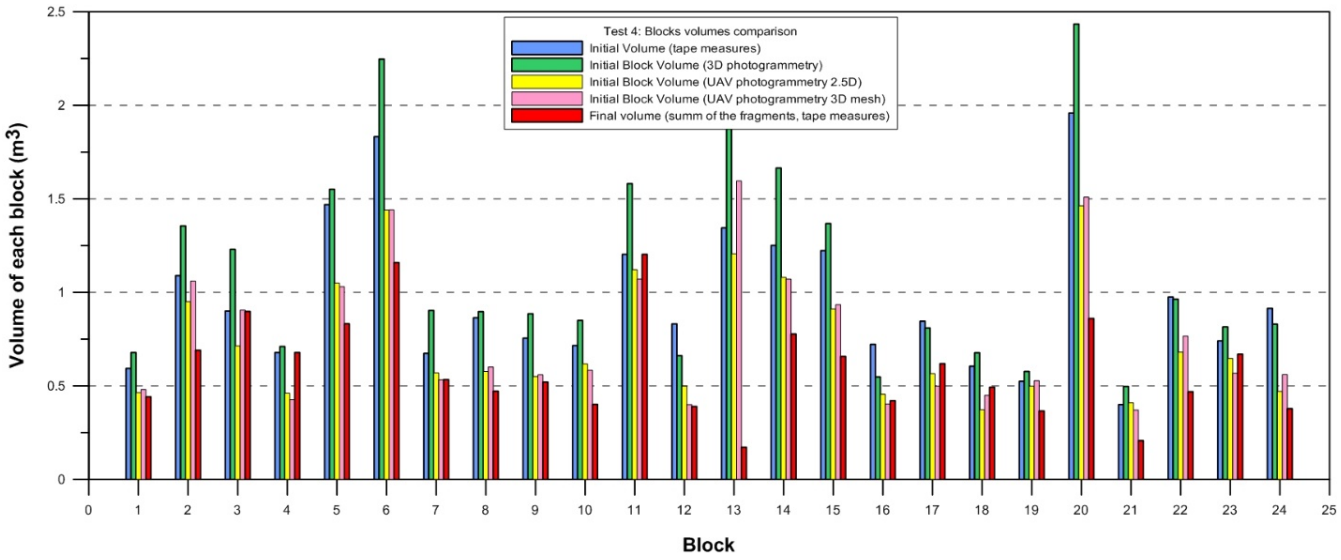

Figure 11: Initial block volume by tape, 3D model, from UAV surveys using a mesh or using a DEM estimation, and sum of fragments volumes, on test 4.

In the testing site 4, the volumes obtained from the measurement with a tape of all the fragments after each block test are smaller than the rest of techniques used. This looks like a bias due to we change the personnel in charge of the measurements with the tape and may underestimate the volumes of the fragments of each measure.

4. Deposit volume reconstruction by UAV photogrammetric survey

A flight with a UAV Inspire 2 Pro was carried out after each test. A 3D reconstruction is obtained by means of digital photogrammetric techniques. A first flight was carried out before the tests to generate a reference surface as an initial stage. This model was cleaned and smoothed in other to obtain a homogeneous and regular surface.

The point cloud of the block B2 at the testing site 4 was cropped taking the deposited fragments. A cloud to cloud difference between the fragments point cloud and the reference surface is used to calculate the volume of the fragments defining a minimum height of difference. The point cloud is filtered by means of a minimum different to the reference surface in order to select the fragments. The point cloud with the fragments is used to obtain the total volume of the fragments using the "Volume 2.5D" tool on CloudCompare (Figure 12), comparing against the reference surface. In the case of B2, the total volume obtained is 1.57 m^3 using a cell size of 5 cm.

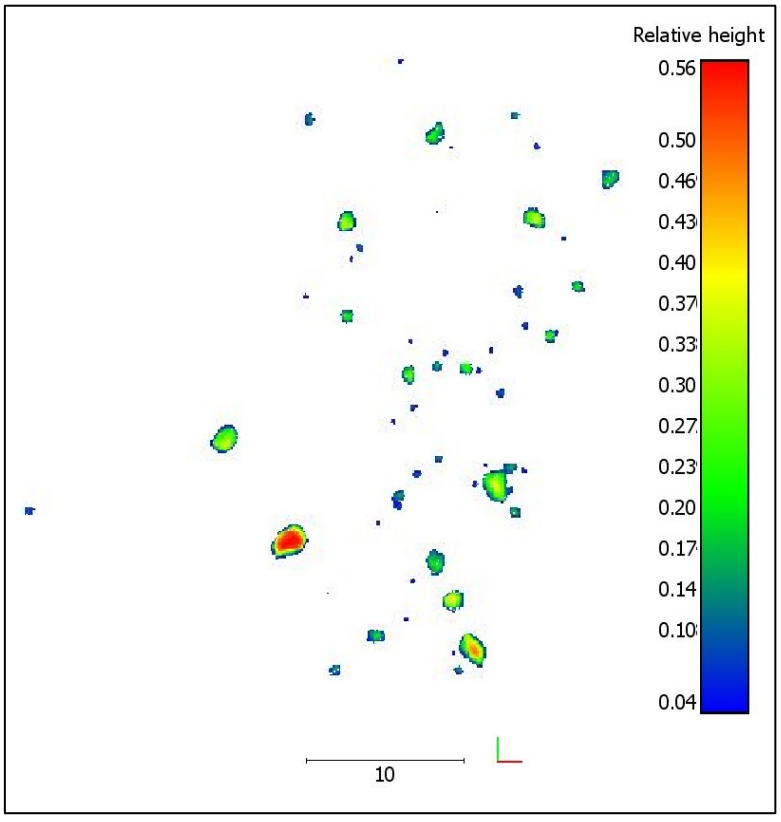

Figure 12: 2.5D volume calculation the fragments of the block B2 of test 4, based on a point cloud comparison and a minim diference of 4 cm against the point cloud of the initial and clean scenario.

An alternative volume estimation is carried out by using the point cloud of the fragments and apply a surface reconstruction in order to obtain a mesh. The reconstruction obtained create an important part of volume under the ground. In order to eliminate this part of the fragments that are not real, the reference surface point cloud can be cropped focused on the deposit and converted also in a mesh to be used to cut the fragments mesh. The result is a mesh of fragments base delimited by the ground mesh (Figure 13). Then, a simple volume request gives the 1.315 m^3 of volume estimated. Then, a final volume estimation techniques comparison is shown on the next bars chart for the volume estimation of the block B2 from the test 4 (Figure 14), ranging from 0.65 m^3 to 1.57 m^3.

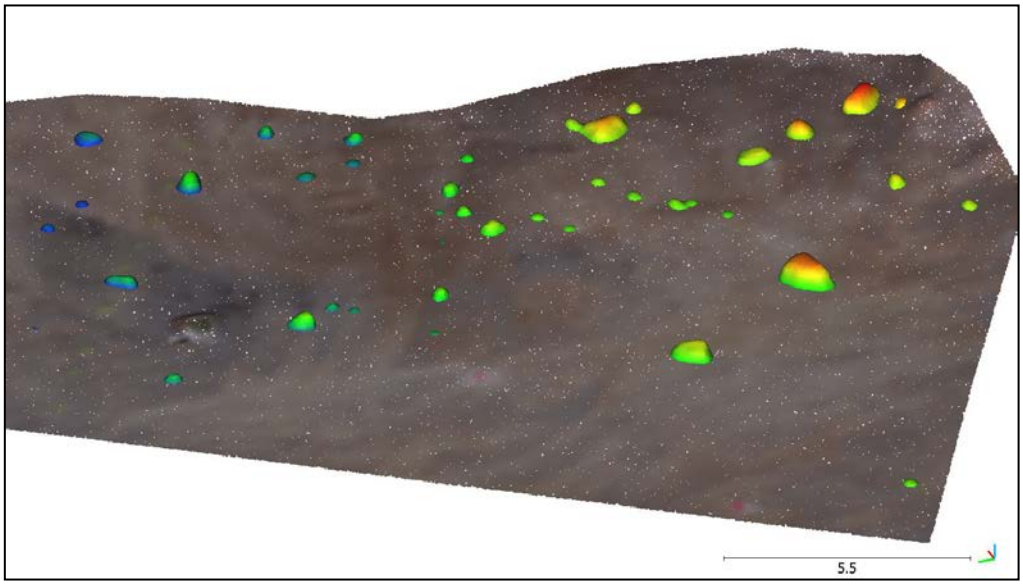

Figure 13: Mesh of framgents cutted with a ground base mesh to avoid unreal volumes under the ground.

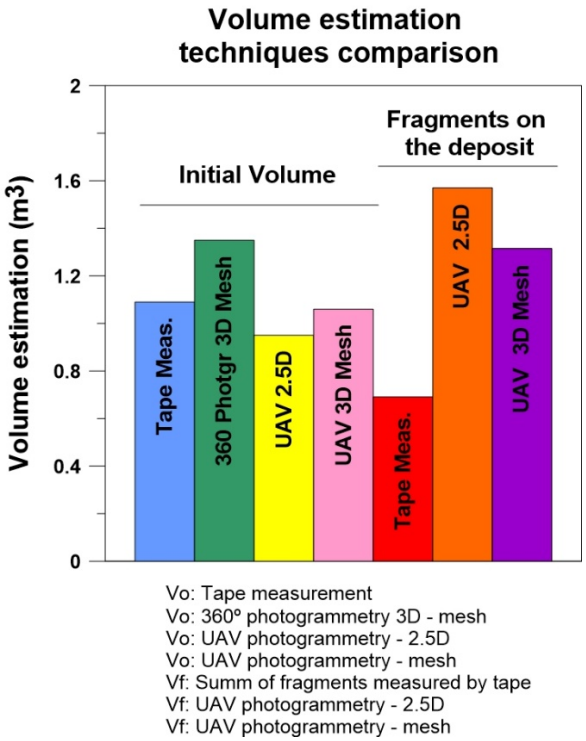

Figure 14: Volume estimation comparison from initial volume and fragments on the deposit.

5. Number of fragments generated

Figure 15 and Table 1 show the number of fragments measured for each block dropped, arranged test by test. Test 1 has 6 trials that generate more than 40 fragments, and one with more than 120 fragments generated. Test 2 shows 4 blocks that generates more than 50 fragments, and one with more than 160 fragments. Test 3 shows a lack of fragmentation, with a low number of fragments per block and a lot of blocks without fragmentation. Finally, test 4 shows high fragmentation with more than 40 fragments generated in most of the blocks. A Multiply Factor (MF) may be used to estimate how fragments produce per block each scenario as a mean, from 9 to 50 in our tests.

Table 1: Number of initial blocs, fragments measured and multiply factor of each test and in total.

	Test 1	Test 2	Test 3	Test 4	Total
Nº of Blocks tested	30	26	44	24	124
Fragments measured	594	680	392	1241	2907
Multiply Factor (MF)	19.8	26.1	8.9	51.7	23.4

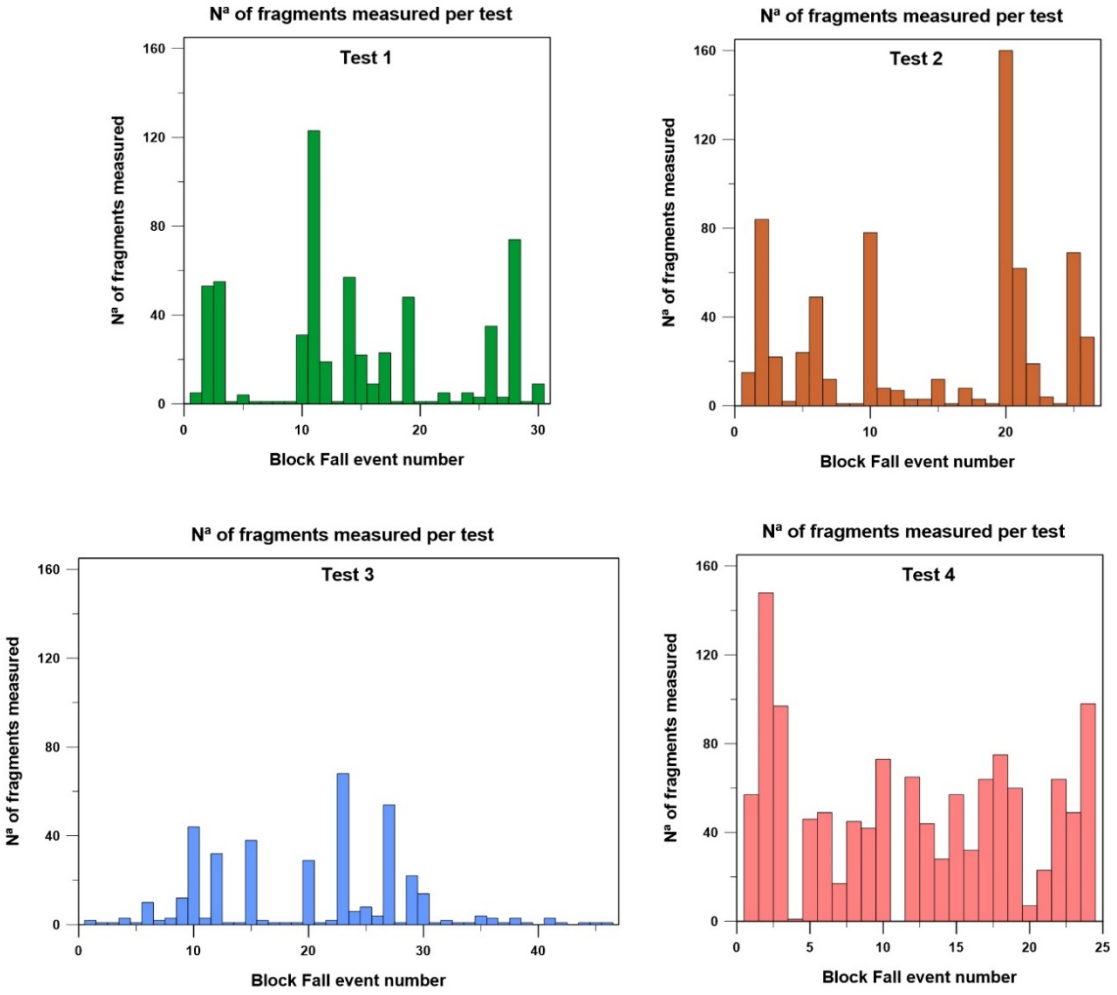

Figure 15: Number of fragments measured for each block dropped, arranged by testing sites (from 1 to 4).

6. Block Size Distributions

We measured all the block volumes of each testing site before they were dropped and plotted as a list of initial volumes (blue, Figure 16). Then, all the fragments measured at each test were added in a single list of fragments and sorted also by volume, yielding the RBSD of the tests (red, Figure 17). It is interesting to observe how the obtained distributions are similar to the distributions observed on natural rockfalls. The biggest fragments of the RBSD are the remains of the originals blocks. The arrangement of the biggest fragments of the RBSD is parallel to the original block volume distribution. The rest of the fragments fit roughly to a power law, with a less steep slope or exponent. Finally, the distribution shows rollover. Notice that the distribution of the original blocks and the largest fragments at the test site 3 are very close due to the lack of breakage. Instead, the distributions are more separately due to the intense breakage at test site 4.

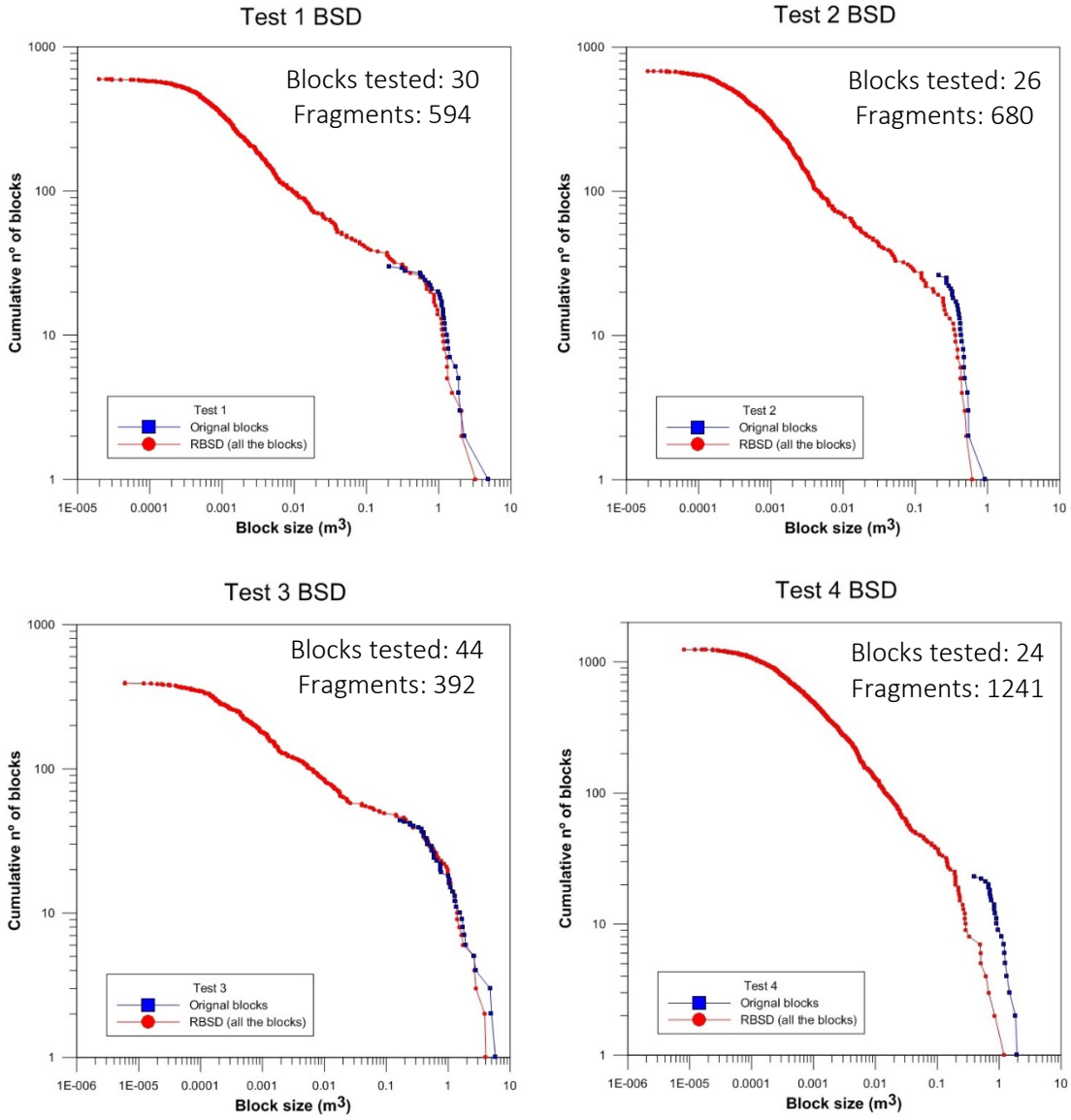

Figure 16: Original blocks volumes distribution (like an IBSD) and RBSD (all the fragments measured together) for each test.

We plot all the fragments' distributions obtained from each block tested, arranged also by testing sites (Figure 17). We have coloured the distributions defining three classes: low, medium and high values of the exponent of the fitted power law (slope of the power law). In this way, we can observe the variation of the breakage at each testing site. In test site 1, we observe blocks that remain intact (single points without line) and blocks that progressively breaks more and more until reaching the maximum (>100 fragments). Test site 2 may be differenciate by the blocks that generate more or less than 20 fragments, with a change of tendency of the exponent of the fitted power laws. Most of the blocks at the testing site # 3did not break. The majority of the fragments distributions show low exponent of the fitted power laws. Finally, the distributions of the fragments volumes of the test site 4 show mostly high exponents of the fitted power law and a high number of fragments generated. Just looking the legend, the green colors indicates how much the blocks breaks creating steeped distributions.

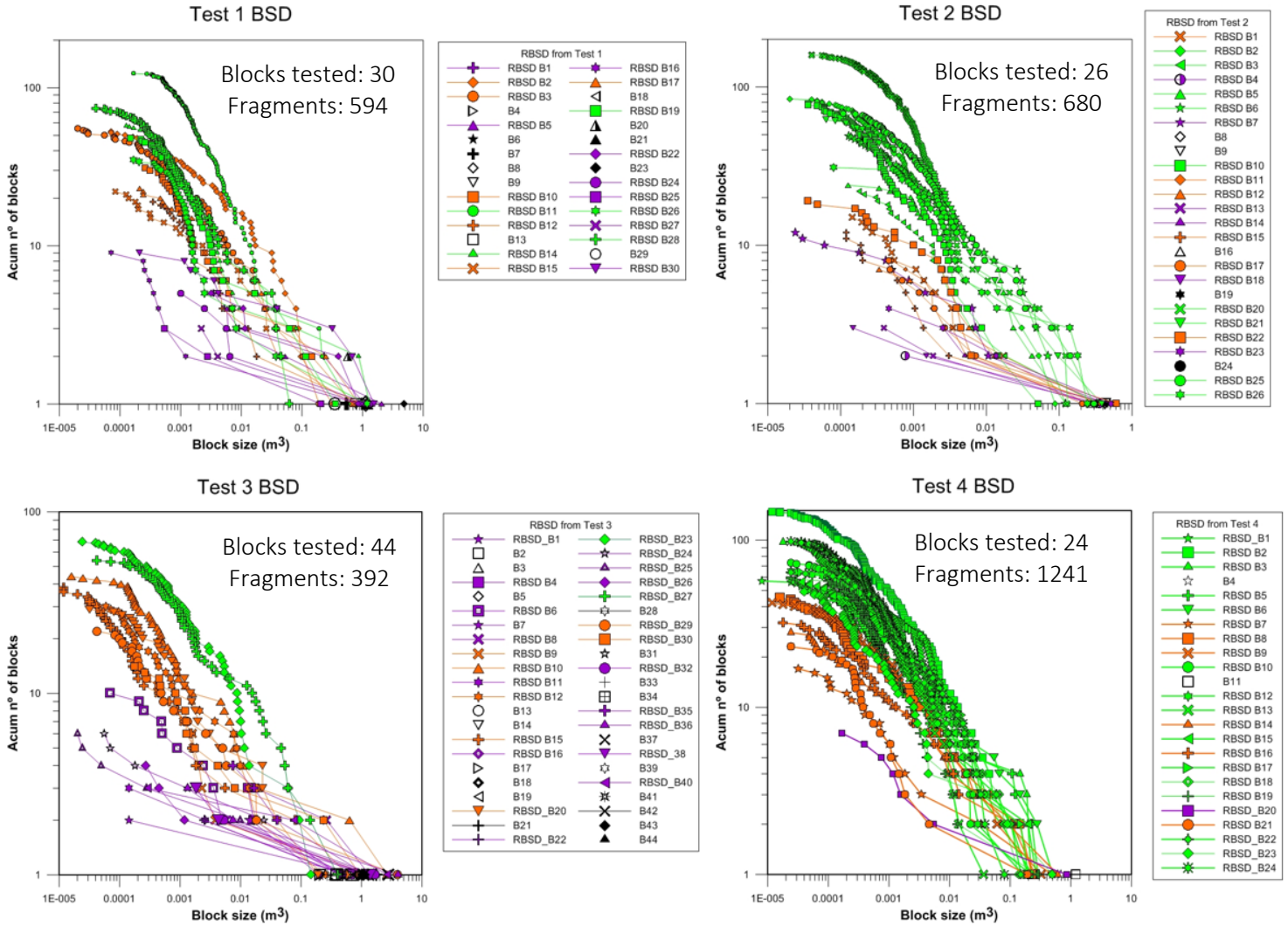

Figure 17: Block size distributions of all the fragments measured on each block dropped, arrenged by test site. The distributions are colored by: low, medium and high value of the exponent of the fitted power law.

The number of fragments generated is directly correlated to the exponent of the fitted power law of the fragments' size distribution (Figure 18, left). It is interesting to observe the contrasting behavior of testing sites 3 and 4, with respectively, low and high values of the number of fragments and exponent of the fitted power laws. Adding the information of the natural fragmental rockfall inventory (purple dots in Figure 18, right), the trend is kept with the increase of the number of fragments and also for exponents. Each block size distribution has two important limits, the maximum fragment, that control the bottom right position of the BSD, and the total number of fragments, that implies higher slope for higher values of fragments.

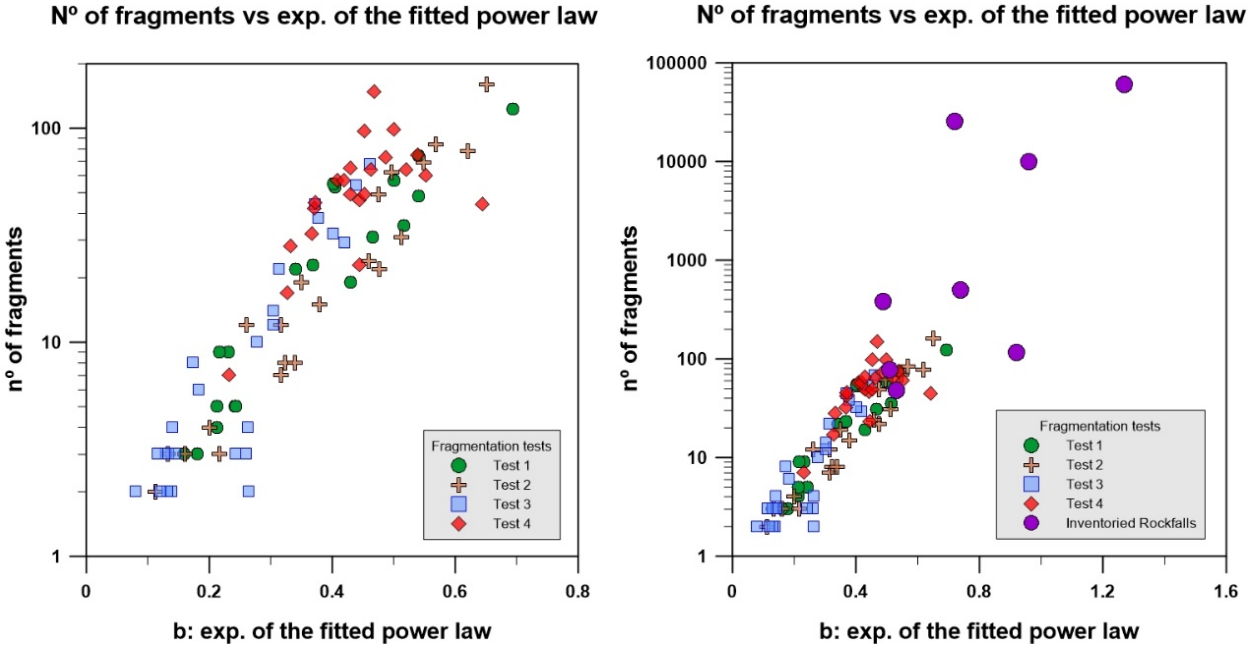

Figure 18: Correlation between the number of fragments and the exponent of the fitted power laws of the BSD obtained from the real-scale fragmentation tests (left) and adding the data of the natural fragmental rockfall inventory (right).

7. Survival rate

The Survival rate (*Sr*) is the largest fragment volume measured over the initial volume. Then, a *Sr=1* means that the block remains intact. Two blocks with the same *Sr* may produce different number of blocks. Then, the *Sr* and the number of fragments are necessary to characterize fragmentation results. Figure 19 (left) shows the Survival rate and the number of fragments produced in each block tested. As the *Sr* decreases (the size of largest fragment remaining reduces), the number of fragments produced increases. However, it is not a direct relation, and the same number of fragments can be generated within a wide range of Sr and vice versa. The Sr

in the tests performed can not be directly related to the potential energy as shown in Figure 19 (right) exemplifying that is not possible stablish a fixed energetic threshold. All the blocks of each testing site were dropped from the same height, however, the potential energy varies as each block has its own volume

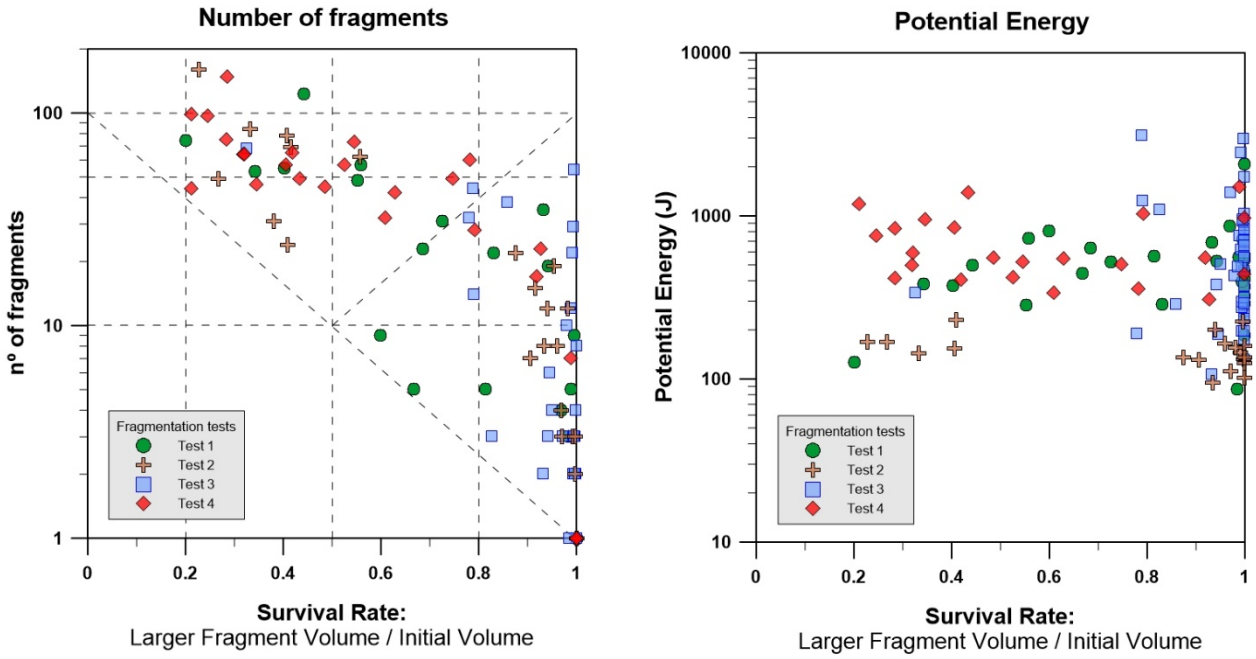

Figure 19: (left) show the Survival rate and the number of fragments produced in each block tested.

Plotting the number of fragments versus Sr separately by testing sites (Figure 20), a distinct behavior is observed. Blocks at Testing site #1 may remain virtually intact or completely breaks with *Sr* ranging from 1 to 0.2, progressively increasing the number of blocks. Some of the blocks break impacting against the slope while others when impacting against the flat ground below. The impact angle, the block shape, the relative orientation between the anisotropies of the rock and the impact direction, and the rigidity of the ground at the impact point, control the fragmentation process. Blocks from testing site # 2 may be grouped in two sets of *Sr>0.85* or *Sr<0.55* with less or more than 20 fragments respectively. In this case, blocks impacting on a more rigid substrate, generate a higher number of fragments and low values of *Sr*. Testing site # 3 is a very steeped slope with a flat surface below composed of soft materials. Due to this, the blocks impact tangentially to the slope surface and fall on the soft ground surface below. None of the blocks broke during the impact on the slope. Most of the blocks in the Testing site # 3 remained virtually intact, with high values of *Sr* (>0.8-0.9). Despite of these high values of *Sr*, the number of blocks ranges from 1 (no breakage) to 50. Only a block that impacted against other deposited block, (similar rigidity), broke showing a *Sr* close to 0,3 producing more than 50 fragments. On the other side, Tests at site # 4 were carried out dropping the blocks 8,5 meters above a fault plane of 42º

of slope and a total height of 23,6 m. As the fault plane (see Figure 4) is highly rigid (the same as the rocks or higher) and the slope geometry allows an important normal component of the impact force, the blocks break in a very explosive way, most of them producing more than 40 fragments up to more than 100. However, the Sr ranges from 1 (or 0.8) to 0.2. Testing sites # 3 and 4 show opposite behavior, highlighting the importance of the terrain rigidity and impact angle.

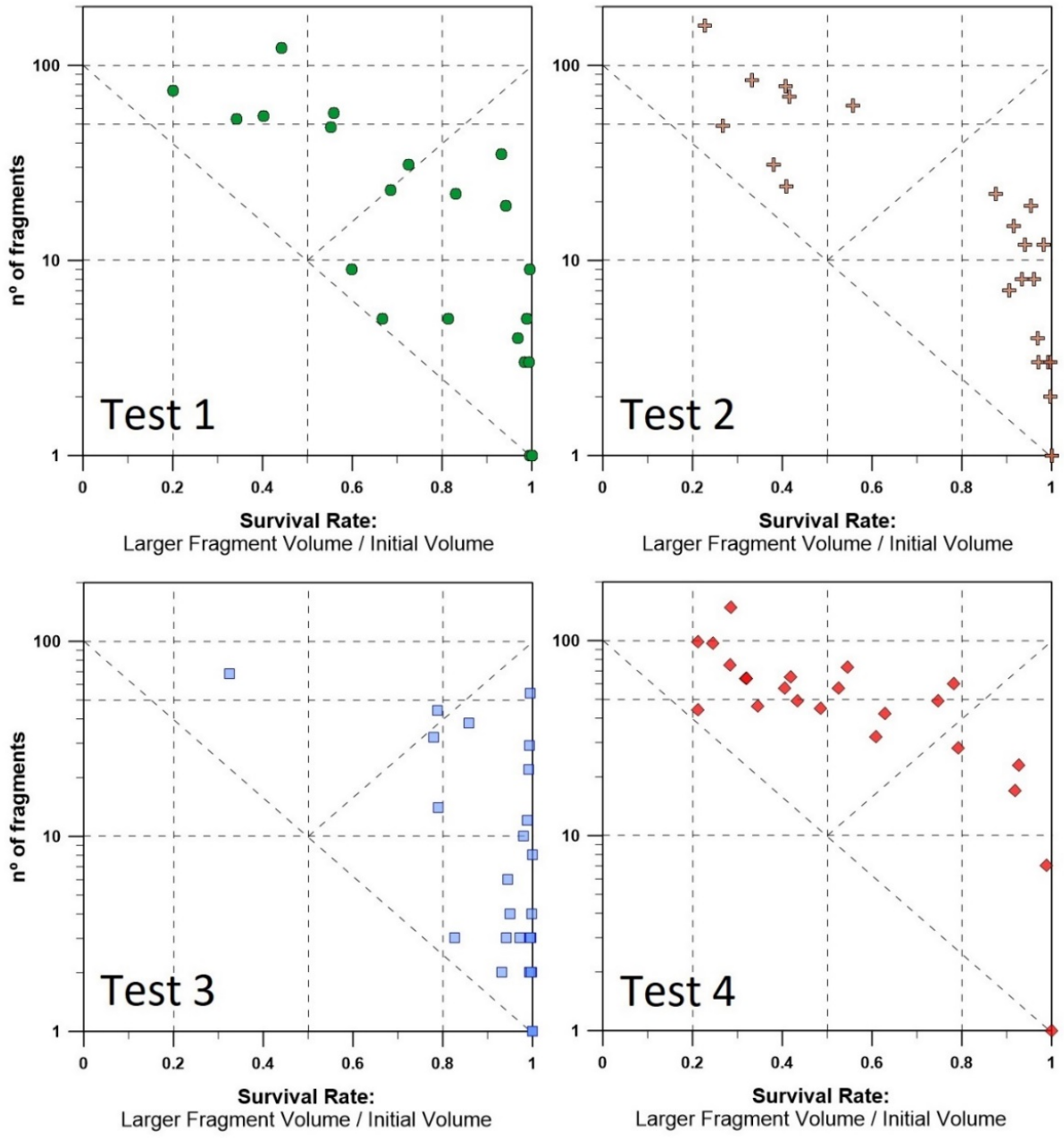

Figure 20: Survival rate versus number of fragments produced on each block tested separtly by test sites.

8. Conclusions and further works

Real-scale fragmentation tests allow the measurement and observation of the rock fragmentation phenomenon in a very controlled scenario and with the capability of to repeat the experiment. The results show large variations of the breakage behavior for the same conditions within each test. Test by test, we can identify different behavior, just using the multiply factor MF (mean number of fragments produced per block tested), from a low value of 9 on test site 3 to a high value of 50 on test site 4, being 20 and 26 in test site 1 and 2 respectively; or looking to the number total number of fragments generated or the exponent of the fitted power laws. We propose the combination of the Survival rate and the number of fragments as descriptor of the fragmentation. Different behaviors were observed at the testing sites. All range of fragmentation features are observed in Testing site # 1. Two groups of behaviors are observed in Testing site #2, the ones that break and the ones that not too much. Testing site # 3, involved very soft terrain of the ground surface. Most of the blocks remain unbroken, with $Sr > 0.85$, but producing fragments between 2 to 100 fragments. At the other end, testing site # 4, Sr ranges from 0.2 to 0.8, but most of the blocks generate more than 40 fragments. Based on these observations, we conclude that, despite some trends are identified, the fragmentation cannot be modelled in a deterministic way.

The rigidity or capacity to absorb energy of the terrain is found a main controlling factor of fragmentation. Similarly occurs with the impact angle. Other parameters such as the relative impact direction of the main rock block anisotropies (fissures or planes of weakness of the block) as well of the type of impact (vertex, edge or face) are features that can be hardly taken into account in the simulations. Only discrete elements methods can deal with these features and the deterministic modelling of real events is still a challenge.

The capture of the block's images, obtaining a 3D reconstruction of the shape and volume before the test is used not only for the analysis of fragmentation but also for the analysis of the trajectory of the block and for obtaining the kinematic parameters.

The UAV flight over block fragments has provided orthophotos and the 3D point clouds. The point cloud thus generated is used to obtain the center of each fragment as well as its stopping point (Figure 21). It will be used in future research lines for statistics about fragment distribution, the divergence of the trajectories of the fragments, as well for calibration purposes of trajectory simulators considering fragmentation like the one developed by Matas (2017) (exemple, Figure 22).

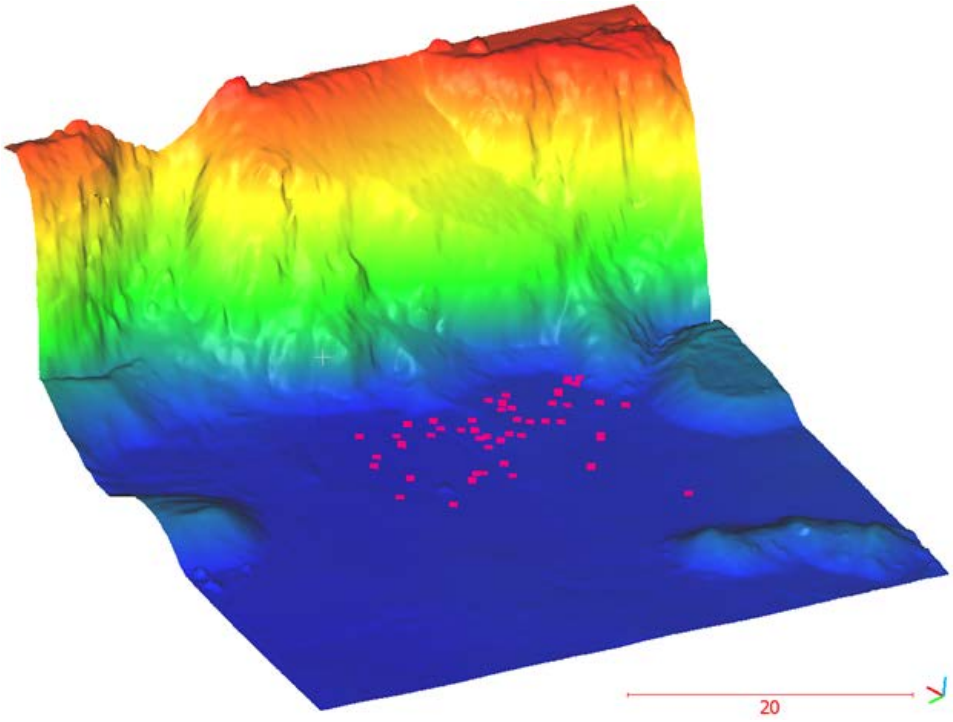

Figure 21: 3D model of the initial clean scenario with the center of each fragment identified (pink points).

Figure 22 show an example of the trajectory simulator considering fragmentation with the trajectories colored by fragments velocity (provided by Gerard Matas).

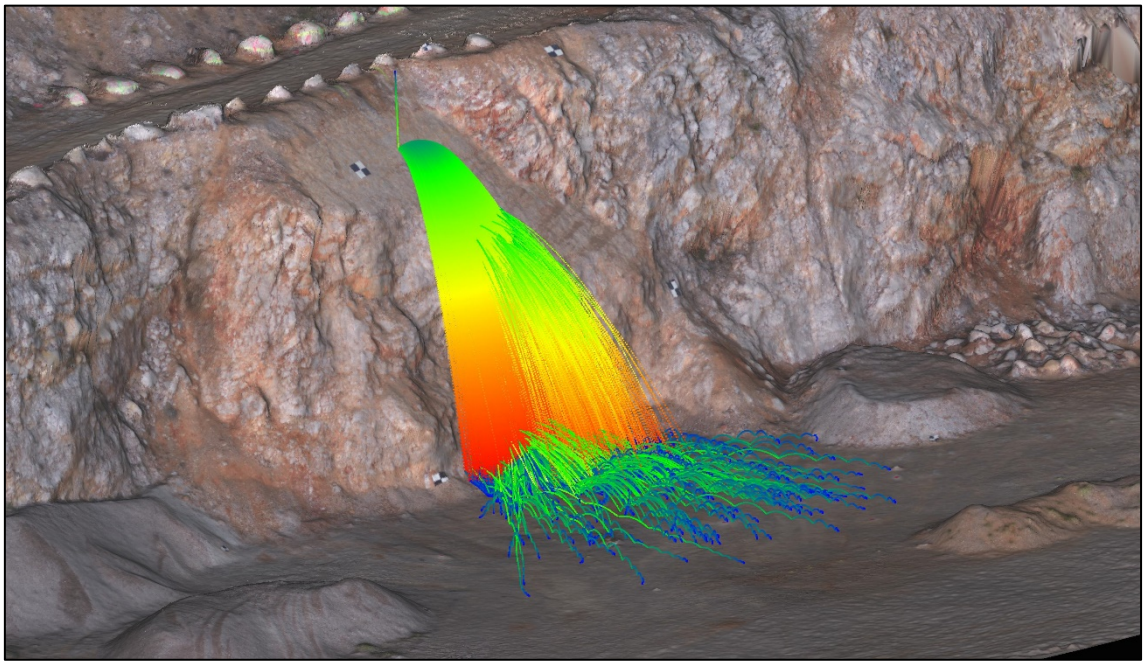

Figure 22: 3D simulation of a block tested on a trajectory simulator considering fragmentation developed by Gerard Matas (Matas et al, 2017)

The use of high-speed cameras triangulation allows the videogrammetry reconstruction of the blocks trajectories during the test (Prades et al, 2017), and the velocity calculation decomposed by its components. Figure 23 presents an example of a trajectory reconstructed colored by the velocity in the vertical (Z) direction, being evident the impact against the slope by the change from red (high) to green (low) vertical velocity.

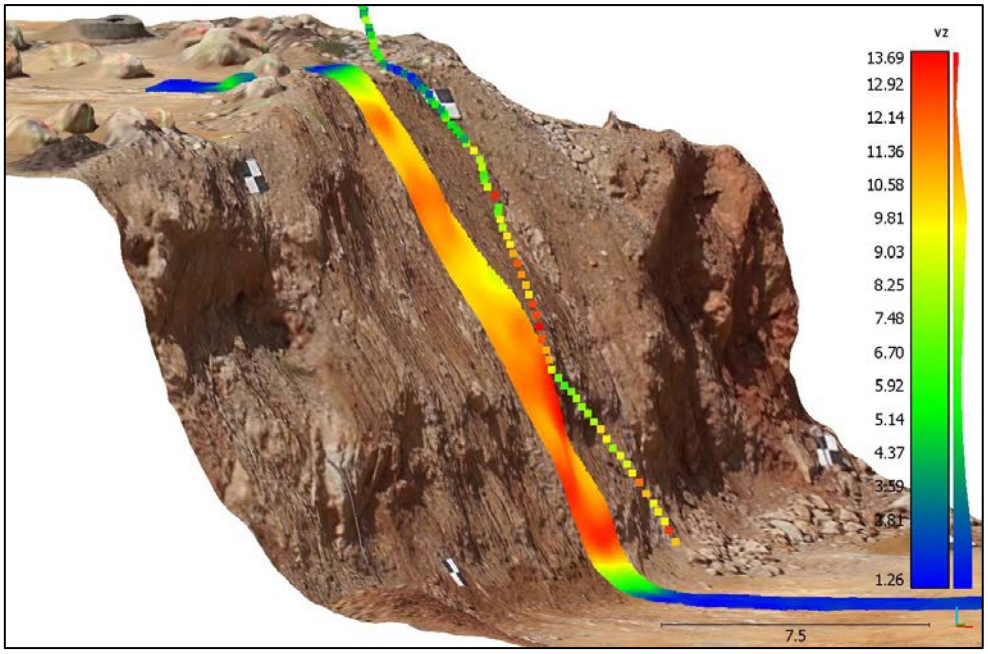

Figure 23: 3d models of the test site 1, with the central part colored by dip angle, and the trajectory of a tested block reconstructed by means of videogrammetry based on highi speed cameras recordings.

The real-scale fragmentation tests therefore provide a large amount of high-quality data that we will be precoessed in the future: energies, impact angles, initial block fractures studies, as well as all the information needed in order to calibrate fragmentation models, propagation models and discrete elements methods.

References

Matas, G., Lantada, N., Corominas, J., Gili, J., Ruiz, R., Prades, (2017) A. RockGIS: a GIS-based model for the analysis of fragmentation in rockfalls. "Landslides", Octubre 2017, vol. 14, núm. 5, p. 1565–1578.

Prades A., Matas G., Núñez-Andrés M.A., Buill F., Lantada N., Corominas J. (2017) DetermInación de trayectorias de bloques rocosos en ensayos mediante videogrametría.Primer Congreso en Ingeniería Geomática (CIGEO(abrir en una ventana nueva)), 5-6 de julio de 2017, Valencia (España).

PART III

Rockfall Fractal Fragmentation Model

9- A fractal fragmentation model for rockfalls

10- Performance of a fractal fragmentation model for rockfalls

9. A fractal fragmentation model for rockfalls

Publication reference:

Ruiz-Carulla R, Corominas J & Mavrouli O (2017). A fractal fragmentation model for rockfalls. Landslides, Volume 14 , Issue 3, Pages: 875-879. doi.org/10.1007/s10346-016-0773-8

Abstract:

The impact-induced rock mass fragmentation in a rockfall is analyzed by comparing the In Situ Block Size Distribution (IBSD) of the rock mass detached from the cliff face and the resultant Rockfall Block Size Distribution (RBSD) of the rockfall fragments on the slope. The analysis of several inventoried rockfall events suggests that the volumes of the rockfall fragments can be characterized by a power law distribution. We propose the application of a three-parameter Rockfall Fractal Fragmentation Model (RFFM) for the transformation of the IBSD into the RBSD. A Discrete Fracture Network model is used to simulate the discontinuity pattern of the detached rock mass and to generate the IBSD. Each block of the IBSD of the detached rock mass is an initiator. A survival rate is included to express the proportion of the unbroken blocks after the impact on the ground surface. The model was calibrated using the volume distribution of a rockfall event in Vilanova de Banat in the Cadí Sierra, Eastern Pyrenees, Spain. The RBSD was obtained directly in the field, by measuring the rock blocks fragments deposited on the slope. The IBSD and the RBSD were fitted by exponential and power-law functions, respectively. The results show that the proposed fractal model can successfully generate the RBSD from the IBSD and indicate the model parameter values for the case study.

Keywords: rockfall, fragmentation model, fractal, fragmental rockfall, block size distribution

1. Introduction:

A fragmental rockfall is characterized by the separation of the rockfall mass into smaller pieces after impact upon the ground surface (Evans and Hungr, 1993). The generated individual rock fragments move as independent rigid bodies, which propagate with different velocities and follow divergent trajectories (Figure 1). Fragmental rockfalls are distinguished from rock avalanches as, during the latter, the mass of fragments moves in a flow-like mode. The deposit of a fragmental rockfall consists of blocks of different sizes scattered on the ground surface (Figure 1). In the case of large fragmental rockfalls (thousands to tens of thousands of cubic meters) a more or less continuous Young Debris Cover (YDC) is formed. The size distribution of the deposit depends on the fragmentation degree.

Rock fragmentation is the progressive change in the particle size of an initial rock mass by application of actions. Incorporating the fragmentation in rockfall analysis is fundamental in many aspects. For hazard and risk assessments, its effect on the number, magnitude and intensity (kinetic energy) of the rock blocks is major (Corominas et al. 2012; Ruiz-Carulla et al. 2015, Jaboyedoff et al. 2005). As the rockfall mass splits into pieces, the number of blocks is multiplied (Corominas and Mavrouli, 2013) and their energy changes (Agliardi and Crosta, 2003). This affects their trajectories and run-out, as well the encounter probability with elements at risk (e.g. building, people, vehicle) and their destructive potential. Therefore, a rockfall analysis considering large unbroken rockfall masses may produce unrealistic results (Okura et al. 2000; Dorren 2003) and instead the fragmentation should be taken into account. Fragmentation may also affect the propagation mode in rockfalls, rockslides and rock avalanches, modify the location of the front of the deposit and the position of the final center of gravity (Haug et al. 2016). The design of protection structures such as barriers and rockfall sheds also requires data for the number and size of the rock blocks after fragmentation.

Although, rock fragmentation has been frequently observed during rockfalls it is rarely considered for the rockfall analysis. This can be attributed to the complexity of the physical process. Many parameters may have an influence such as the presence of discontinuities in the boulders including their persistence, aperture and orientation at the moment of the impact, the intact and joined rock resistance, the impacting energy, rigidity of ground conditions, impact angle and velocity (Dussage et al. 2003; Wang and Tonon, 2010). Further references on the advances regarding the fragmentation process and analysis are given in section 2 of this paper.

Important contributions on the analysis of the rock fragmentation come from the field of blast design and rock avalanche analysis. To the knowledge of the authors, there are almost no rockfall

kinematic models to simulate the fragmentation of the rock mass in the case of fragmental rockfalls. An exception is the model incorporated at the trajectory analysis software Hy-Stone (Wang, 2009), which applies a trained neural network to determine the mass and velocities of the fragments right after the impact.

This work aims to contribute to the modeling of the fragmentation of fragmental rockfalls, through the proposal of a three-parameter rockfall fractal fragmentation model, RFFM (section 3). The model is based on the assumption that the fragmentation can be considered as a transformation from the state with the In Situ Block Size Distribution (IBSD) at the cliff face (Lu and Latham, 1999) and the resultant Rockfall Block Size Distribution (RBSD) (Hantz, 2014; Ruiz-Carulla et al. 2015). This assumption is supported by the relationship between the intact rock properties and discontinuity structure of the rock mass, with the fragmentation degree and has been proved efficient for the characterization of the blastability of rocks (Lu, 1997). The proposed transition model from the IBSD to the RBSD is a three-parameter fractal model, based on that of Perfect (1997), where the resulting number-size distribution of fragments depends on the probability of failure, $P(b)$; a survival rate, Sr; and a scaling factor, b.

Using field-obtained data from a large rockfall event that occurred in 2011 in Vilanova de Banat in the Cadí Sierra, Eastern Pyrenees, Spain, we explore the applicability of the proposed fragmentation model (section 4). We investigate the potential for calibration of the three parameters that are involved in the calculation of the RBSD using the proposed model, to fit the observed deposits.

Section 5 discusses the efficiency of the proposed model and the main controlling factors. It also casts a light on the points to focus on, for developing and advancing the model with a view to general application.

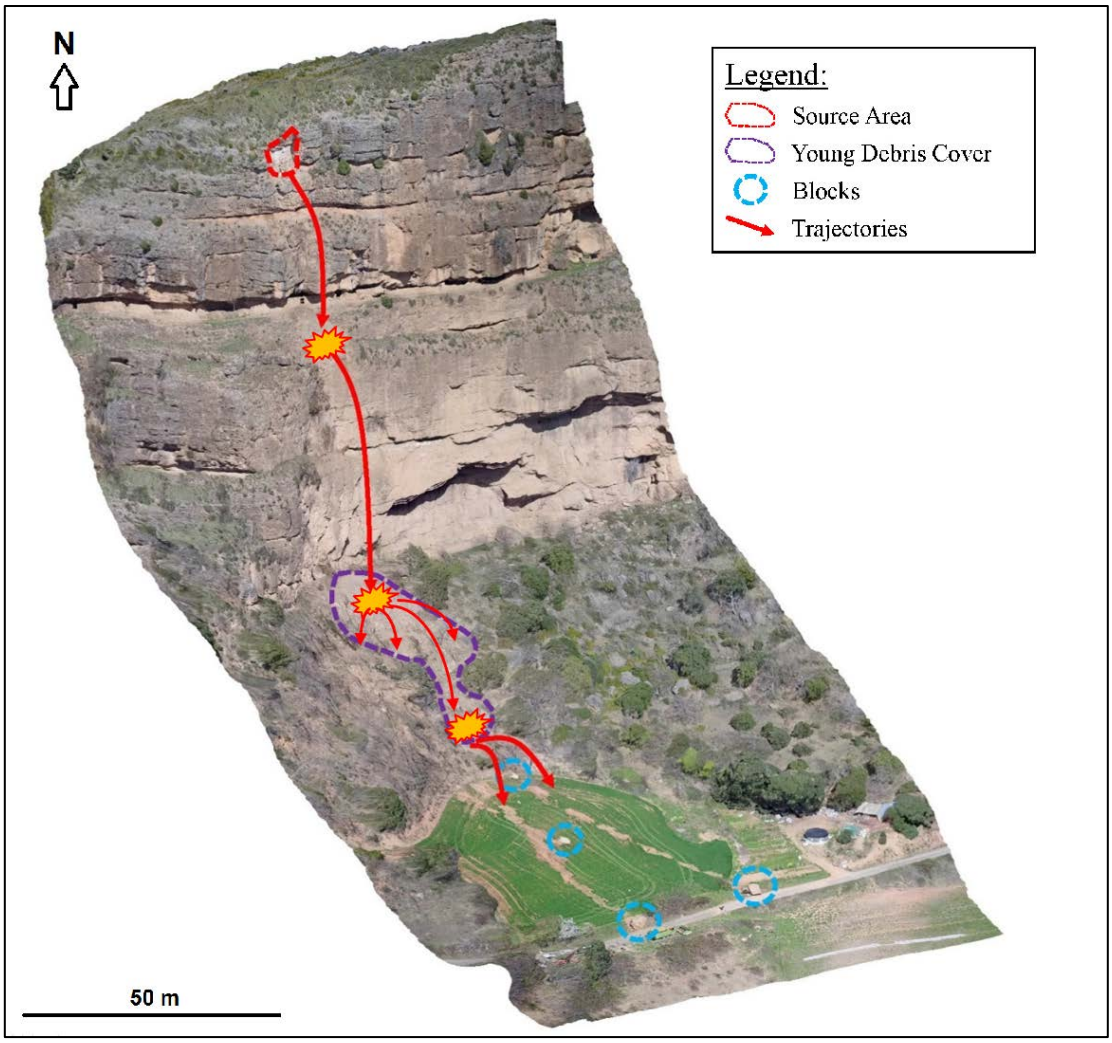

Fig. 1. Fragmental rockfall at Gurp, Central Pyrenees, Spain. A Young Debris Cover (YDC) is formed just below the rockfall source (purple polygon). Four large individual blocks (blue circles) followed both independent and divergent trajectories after the impact on the ground.

2. Rock Fragmentation

Rock fragmentation is a topic that has been addressed in a variety of scientific disciplines, such as in structural geology interested in the fracture pattern of rocks as the result of the tectonic activity (Molnar et al. 2007; Sammis and King, 2007); in fracture mechanics for the analysis of the response of cracks to both static and dynamic loading (Atkinson, 1987); in the assessment of the performance of the drilling equipment, mechanical excavators, tunnel boring machines (TBM), and for the consumption of disc cutters (Bakar et al. 2014); and in the mining industry, interested in the size distribution of muck piles after blasting and on the subsequent crushing and grinding (Aler et al. 1996; Morin et al. 2006; Kulatilake et al. 2010; Sanchidrián et al. 2014). At rock mass instabilities the fragmentation of the detached rock mass has been acknowledged by several researchers either for rockfalls (Dussauge 2003, Giacomini et al. 2009, Wang and Tonon

2010, Agliardi et al. 2009, Crosta et al. 2015) or for rock avalanches (Locat et al. 2006; Crosta et al. 2007; Davies et al. 1999; Hewitt, 1998, 1999; Hermanns et al. 2006; McSaveney and Davis, 2007; Weidinger et al. 2014).

Different types of mechanisms are invoked to explain the progressive change in grain size by application of actions. Crushing, grinding, comminution, fragmentation and dynamic fragmentation are the mechanisms usually quoted (Crosta et al. 2007). Fragmentation can occur as a result of dynamic crack propagation during compressive or tensile loading (dynamic fragmentation) or due to stress waves and their reflection during impact loading (ballistic fragmentation).

Davies et al. (1999) introduced the term fragmentation to describe the breaking of rocks into pieces smaller than those defined by the joint system of the parent rock mass. Nevertheless, for the purposes of this paper, fragmentation is used as a generic and inclusive term, meaning the division of an initial rock block or rock mass caused by either the breakage of the rock pieces, the disaggregation of joint-determined blocks, or both (Ruiz-Carulla et al. 2015). The breakage takes place under stresses that exceed the strength of the intact rock, resulting into new fractures.

2.1 Characterizing the fragmentation degree

The characterization of the rock fragmentations involves the measuring of the block size of the fragments. This is commonly performed either manually or by means of image analysis, the latter considering different assumptions for the extraction of block volumes from the image data (Locat et al. 2006, Crosta et al. 2007).

A range of descriptors can be used for the fragment size characterization. The d_{50} diameter or the mean size before and after the fragmentation are frequently used. In mine blasting, Kuznetsov (1973) associated the latter with the explosive energy and powder factors. Locat et al. (2006) also determined the degree of fragmentation for rock avalanches, by comparing the mean diameters of the blocks within the intact rock mass and the deposited fragments. Cunningham (1983 & 1987) further introduced a uniformity index “n”, depending on blast characteristics to describe the block size variation. Having obtained the mean size and the uniformity coefficient, statistical distributions can be fitted to the sizes of the fragmented blocks. The Rosin-Ramler model (Latham et al. 2006, Morin et al. 2006, Gheibie et al. 2009, Kulatilake et al. 2010 and Hudaverdi et al. 2010) is one of the most commonly used in rock blast fragmentation. Alternatively, if data are available, the characterization can be realized based on the block size distribution BSD of the

entire fragmented deposit (Hardin, 1985). The BSD is typically represented as a grain size curve, in terms of percentage of material passing a certain size in a length unit as millimeters or meters, typically with 3 or 4 orders of magnitude of sizes.

The observation of different BSD has indicated that the fragments size follows a fractal distribution or power law (Turcotte 1986 & 1992, Poulton et al. 1990, Crum 1990, Hartmann 1969, Xu et al. 2016, and Peng et al. 2009. The power-law gradient is variable and it increases with the intensity of the fragmentation process (Hartmann 1969). Turcotte (1986) added that the fragmentation is often a scale invariant process, and the preexisting zones or planes of weakness where failure occurs exist on all scales. Crosta et al. (2007) collecting data for the deposit of a rock avalanche indicated that its size distribution is characterized by a fractal dimension that was found consistent with other rock avalanche deposits (Dunning, 2006). Perfect (1997) discussed the use of the fractal theory and presented alternative models to analyze fragmentation in rock and soils.

The authors reported a fractal pattern in the volume distribution of six inventoried rockfalls in the Pyrenees, Catalonia, which exponents range between 0.5 and 1.3 (Ruiz-Carulla et al. 2016). The obtained RBSD from the direct measure of the blocks deposited in each inventoried rockfall are plotted in Figure 2 in terms of relative frequency versus block size in cubic meters. Table 1 shows the characteristics of each case. The mentioned literature and our empirical observation supports the use of fractal patterns to perform a fragmentation analysis of fragmental rockfalls.

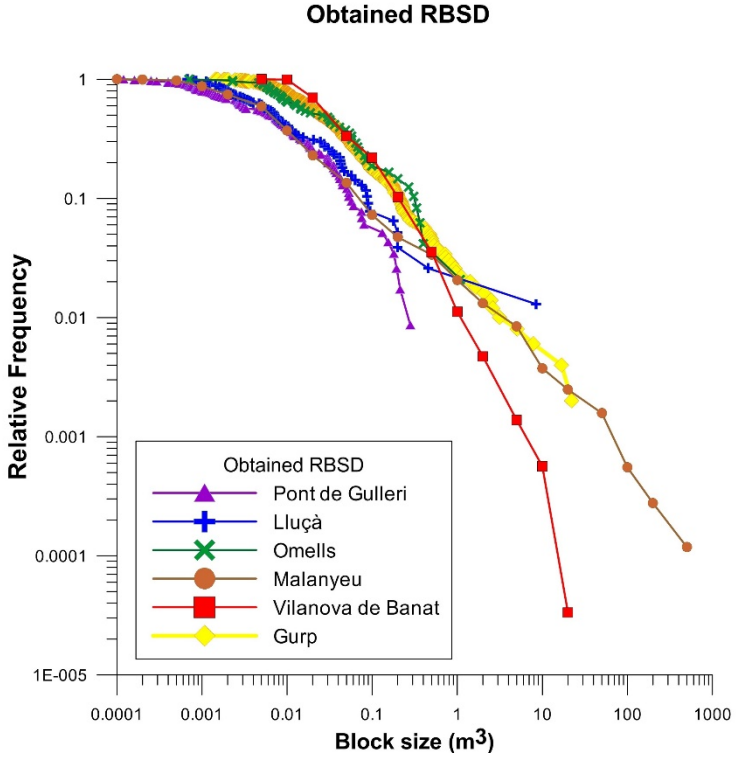

Fig. 2: Rockfall Block Size Distribution (RBSD) from 6 fragmental rockfalls events inventoried in Catalonia.

Table 1: Characteristics of the inventoried rockfalls:

	Pont de Gulleri	Lluçà	Omells	Malanyeu	Vilanova de Banat	Gurp
Lithology	Schist	Sandstone	Sandstone	Limestone	Limestone	Conglomerate
Total rockfall volume (m^3)	2.6	10.7	4.2	5000	10000	100
Max block size (m^3)	0.28	8.5	1.1	445	31	22
Min block volume measured (m^3)	0.0001	0.0007	0.0007	0.0001	0.01	0.01
Nº of blocks measured	116	78	48	2721	1524	500
Nº of blocks estimated	116	78	48	25500	60000	500
Exponent of the fitted power law	0.92	0.51	0.53	0.72	1.27	0.74
Min block vol considered for fitting (m^3)	0.001	0.001	0.01	0.001	0.01	0.01
R^2 of the fitted power law	0.94	0.95	0.89	0.98	0.95	0.98

2.2 Obtaining the BSD from the IBSD

The influence of the IBSD of the rock mass in the BSD is well known in the mining industry. Latham et al. (1999) focused on the blasting energy needed to convert the IBSD into a new fragment-size distribution. Locat et al. (2006) analyzed the fragmentation in rock avalanches comparing as well the IBSD and the BSD of the deposit, and assessed the equivalent energy for the generation of the latter. To determine fragment sizes produced during a dynamic event, Grady (1982) and Grady and Kipp (1987) adopted an energy approach to the dynamic loading regime in which a balance between local kinetic energy and fracture energy is made. Lu (1997) proposed models for the transition of the size distribution of the initial rock mass to the size distribution of the fragments after blasting. Alternative approaches include the use of Rock Engineering Systems (RES) to study the influence of each controlling parameter of the fragmentation phenomenon by blasting and predict the resultant fragment size distribution (Faramarzi et al. 2013), multivariate analysis (Aler et al. 1996, Chakraborty et al. 2004 and Hudaverdi et al. 2010), Monte Carlo simulations (Morin and Ficarazzo, 2006) or neural network and artificial intelligence methods (Kutilake et al. 2010, Monjezi et al. 2009, Saavedra et al. 2006).

There is a scarcity of models for the prediction of fragmentation in the case of rock instabilities. Viero et al. (2012) carried out a mass balance of a rockfall case. They calculated that 80% of the material was converted in a cloud of dust. The real scale tests of Giacomini et al. (2009) and Gili et al. (2016) for fragmental rockfalls indicate the complexity in predicting the size distribution of the fragments based on impact energy thresholds. Wang & Tonon (2010) used a Discrete Element Method, DEM, code to simulate impact-induced rock fragmentation in rockfall analysis, and developed a trained neural network code that was integrated into the HY-STONE trajectory software (Crosta & Agliardi 2003). Bowman et al. (2014) studied the effect of the IBSD on the

fragmentation and the runout of collapsed chalk cliffs. They performed several laboratory tests using different block assemblages and their findings for the amount of fragmentation showed consistency with use of Hardin (1985) breakage parameters for the definition of how much fragmentation has taken place during a breakage event related with the total runout of the rock mass. Charrière et al. (2015) also presented a model to calculate the successive block size distribution after fragmentation during a rock slide, which describes the breaking of a cubic block into two fragments with a random volume ratio, and in their turn their successive breaking in two more fragments each, for a chosen number of cycles. Further work is needed to develop transition models from the IBSD to the RBSD for fragmental rockfalls.

3. A Rockfall Fractal Fragmentation Model

This study defines different scenarios for the fragmentation of the rockfalls (Figure 3). The detached mass from a cliff may consist of an individual block or a rock mass. In case of an individual block, when hitting on the ground it can either remain intact or break if there is enough impact energy (Figure 3a and b, respectively). Alternatively, failure may consist of the detachment of a coherent rock mass including joint sets. Within the rock mass, individual blocks of different sizes and shapes are present due to the mutual intersection of the joint sets. The range of volumes of these blocks is characterized by the IBSD. After its detachment from the rock wall and/or due to a low energy impact on the ground, the rock mass disaggregates. In this case, the block fragments are basically bounded by the preexisting joints and the RBSD generated is similar to the initial IBSD (Figure 3c). If the impact energy is enough to break the blocks, the generated RBSD will differ from the initial IBSD (Figure 3d). Different volume distribution of fragments (RBSD) should be expected from an initial IBSD which must reflect the predominant mechanisms involved in the fall. The RBSD can be used therefore to characterize the fragmentation phenomenon and to identify the predominant mechanism as disaggregation, pure breakage or a combination of both.

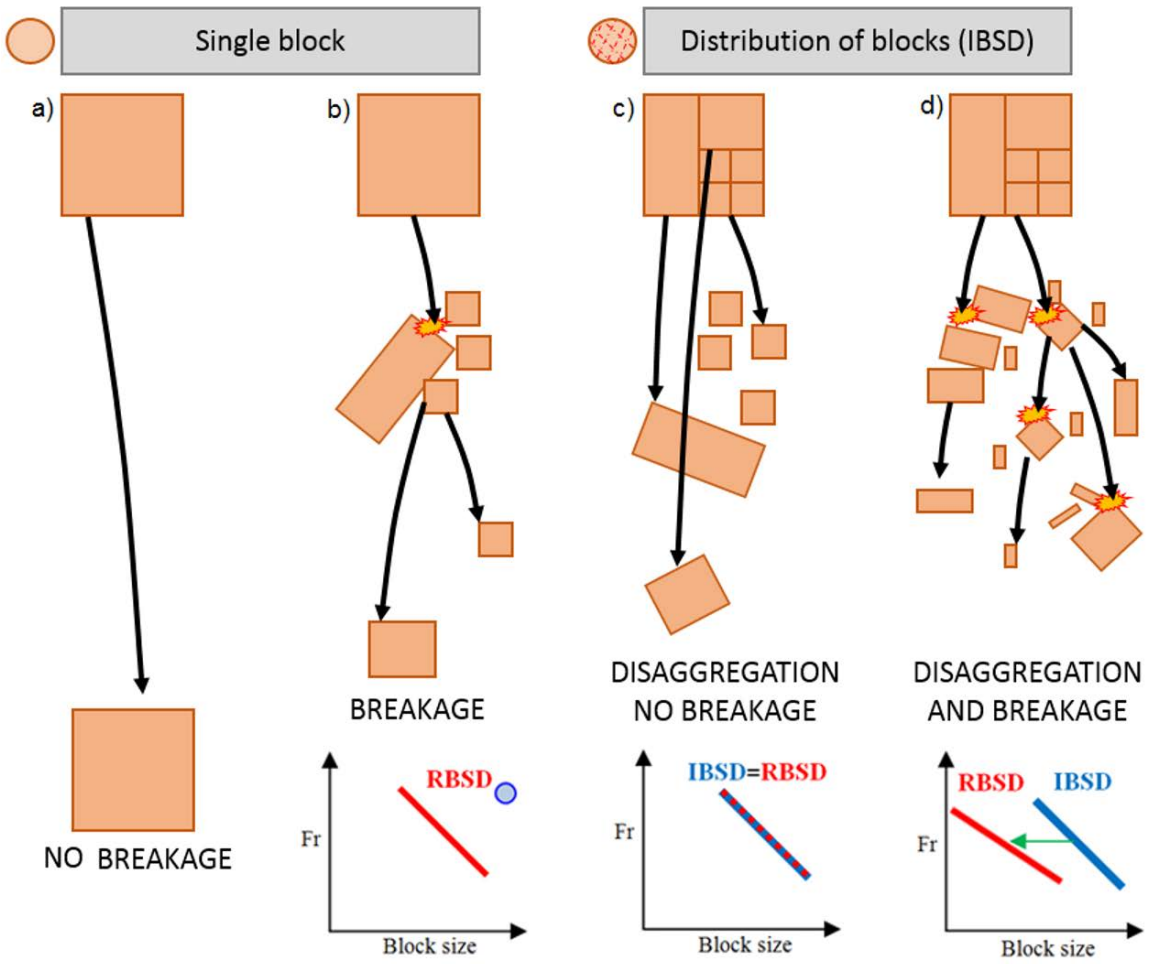

Fig. 3: Considered mechanisms in the fragmentation of falling rock blocks and rock masses. Conceptual schemes of changes in the block size distribution in the case of fragmentation by: a) lack of breakage of a single block; b) Breakage of a single block; c) Disaggregation of the rock mass through the preexisting joints; c) Disaggregation and breakage of the detached rock mass.

We proposed a Rockfall Fractal Fragmentation model RFFM that can express the aforementioned scenarios. In this model, the fragmentation of the rock mass initiates with the disaggregation of the rock mass along preexisting discontinuities and continues with the breakage of the rock blocks generating new fresh faces. Based on this, we consider the disaggregation of the mass, as controlled by the joint pattern, the first step for the fragmentation.

The RFFM proposed is based on the generic fractal fragmentation model of Perfect (1997). The model uses an initiator, which is either a single block or the individual blocks forming a rock mass. According to the model, if breakage does not takes place the initial volume distribution is preserved (Figure 3a and 3c). If the impact energy is high enough, the individual blocks will break either all of them or a percentage only (Figure 3b and 3d). Each broken block will produce a new distribution of fragments. The model is used to generate a RBSD from an initial IBSD. The

fragmentation is assumed as scale-invariant, although the model may also perform as scale-variant.

The RFFM considers a cubic block of unit length that breaks into smaller pieces following a power law. Fractals are hierarchical, often highly irregular, geometric systems generated using iterative algorithms with relatively simple scaling rules (Mandelbrot, 1982). The size distribution of elements in a fractal system is given by (Eq.1):

$$N(1/b^i) = k\left[1/b^i\right]^{-D}; i = 0,1,2...\infty \qquad \text{Eq. 1}$$

Where $N(1/b^i)$ is the total number of fragments at the *i*th level of hierarchy; *k* is the number of initiators of unit length; *b* is a scaling factor >1, that define the geometric proportion between the original block and the generated blocks; and D is the fractal dimension. N is rounded to the lower nearest integer.

The actual number of fragments produced depends on the probability of failure at the *i*th level, $P(1/b^i)$, which is defined as:

$$P(1/b^i) = n_i \frac{\left[N(1/b^j)/N(1/b^{i+1})\right]}{\left[N(1/b^j)/N(1/b^i)\right]}; j = i+1 \qquad \text{Eq. 2}$$

and then $$P(1/b^i) = n_i / b^3 \qquad \text{Eq. 3}$$

Where n_i is the number of fragments generated in the *i*th level. $P(1/b^i)$ is the proportion of block that breaks. The $P(1/b^i)$ can be physically related to subunit interfaces and their boundary strength, like in the case of fractured rocks, these interfaces represent preexisting planes of weakness, like anisotropy or non-persistent joints (Perfect, 1997). If the probability of failure is scale-invariant $P(1/b^i) = P(1/b^{i+1})$, it can be expressed as:

$$P(1/b^i) = b^{Df-3} \qquad \text{Eq. 4}$$

$$\text{or } D_f = 3 + \frac{\log\left[P(1/b_i)\right]}{\log\left[b\right]} \qquad \text{Eq. 5}$$

Where D_f is the fragmentation fractal dimension. The range for the probability of failure is $b^{-3} < P(1/b^i) < 1$. When $P(1/b^i)=1$ *and* $D_f=3$ the whole block is fragmented, while for $P(1/b^i) \leq b^{-3}$ the block remains unbroken.

The scale-invariant case is the simplest version of the fractal fragmentation model, where the parameters to be calibrated are the scaling factor *b* and the probability of failure $P(1/b^i)$. Looking for the physical interpretation of the probability of failure, if the block impact energy on the

ground is low, the probability of failure is almost b^{-3}, and in the opposite scenario, if the block impacts energy is high, the probability of failure is close to 1.

An example of how the model works is presented in the Figure 4. A simple cubic block is considered as the initiator (original block). Defining the geometric factor as b=2 the original block contains 8 possible breakables blocks. The probability of failure 1/8, defines the threshold for new block generation. For values of $P(1/b^i)$ below 1/8, the block will remain unbroken. For values just above 1/8, new blocks will be generated. The example shows the cases of: $P(1/b^i)=2/8=0.25$, where 2 blocks are generated; $P(1/b^i)=3/8$ where 3 blocks are generated and the case where $P(1/b^i)=4/8=0.5$ where 4 blocks are generated. $P(1/b^i)$ can take values up to 8/8 or 1, where the whole original block will be fragmented generating 8 new blocks. The number of new blocks generated is a natural number. The example shows that the same generation rules over the blocks apply for successive iterations. This example is scale-invariant, where $P(1/b^i)= P(1/b^{i+1})$, then, $P(1/b^1)= P(1/b^2)$.

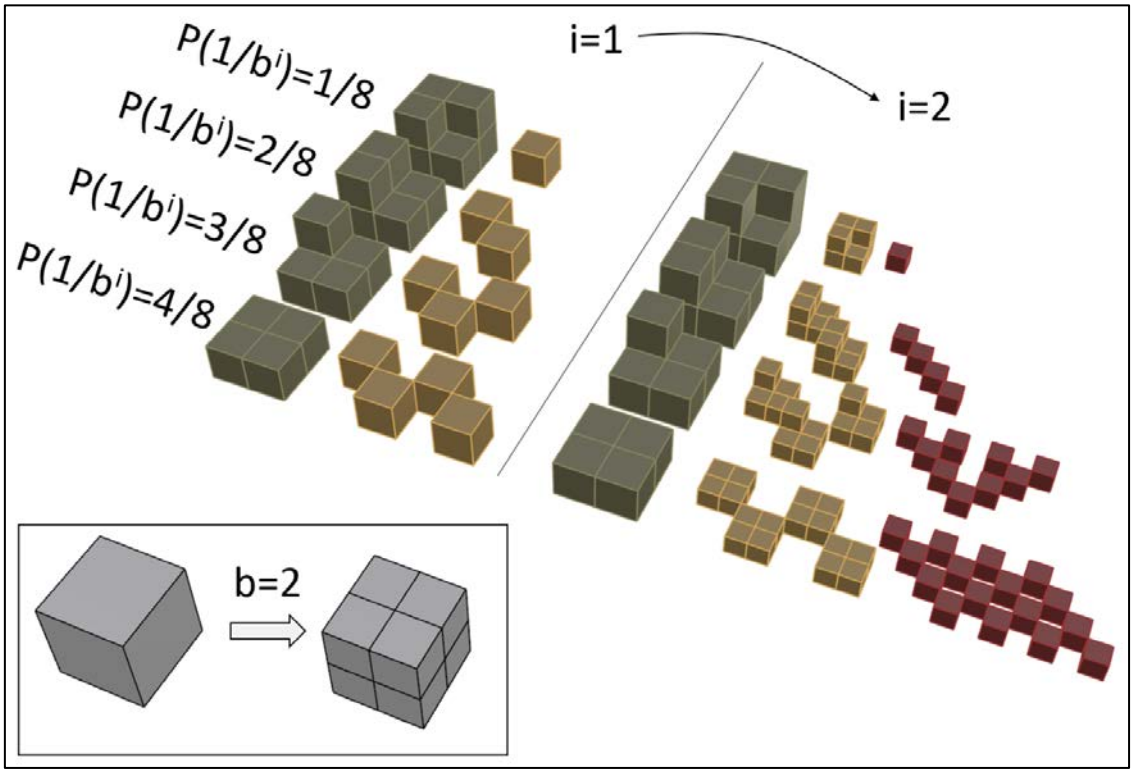

Fig. 4: Scheme of the fractal fragmentation model (scale-invariant) using b=2 and examples of smaller block generation for $P(1/b^i)=1/8$, 2/8, 3/8 and 4/8=0.5, considering 1 or 2 iterations.

One of the limitations of the model is that the blocks generated at each iteration have exactly the same volume. The real block size distribution obtained from the field measurements shows a progressive decrease of the volume of the blocks in a continuous variation. To avoid this limitation, Perfect (1997) proposed to apply the model using the cumulative number of fragments in terms of l/l_{max} where l_{max} is the maximum fragment size (length), and l is the size (length) of

each fragment generated. With this procedure, the $1/b^i$ is substituted by l/l_{max}. This methodology could be useful when considering the scenario in which only one single block is detached.

We have modified the model of Perfect (1997) to adapt the fractal fragmentation model to the case of rockfalls. The first modification is that the number k refers to an individual rock block (k=1) for the fragmentation of a single rock block, or to the IBSD if a rock mass is analyzed instead. In the latter case the IBSD should first be classified into bins. The second modification is the idea that not all the blocks will be fragmented. We define the Survival rate, *Sr*, as the ratio of blocks of each block size bin that remain unbroken after propagation. According to this, the final scheme of the fractal fragmentation model proposed for rockfalls is shown in the Fig.5 for a given IBSD classification bin.

A simple example is presented here (Figure 5): We assume 3 blocks in the bin 1-2 m^3 of the IBSD. We define the survival rate i.e., *Sr=0.33*. In this case, 33% of the blocks from the IBSD will survive the propagation, and will be added directly to the RBSD. The rest 66% of the blocks of this bin will be fragmented using the fractal law. We used a mean volume for each bin to represent the volume of the blocks inside it. (Using *b=2; $P(1/b^i)$=0.5 ; Sr=0.33 and 2 iterations*)

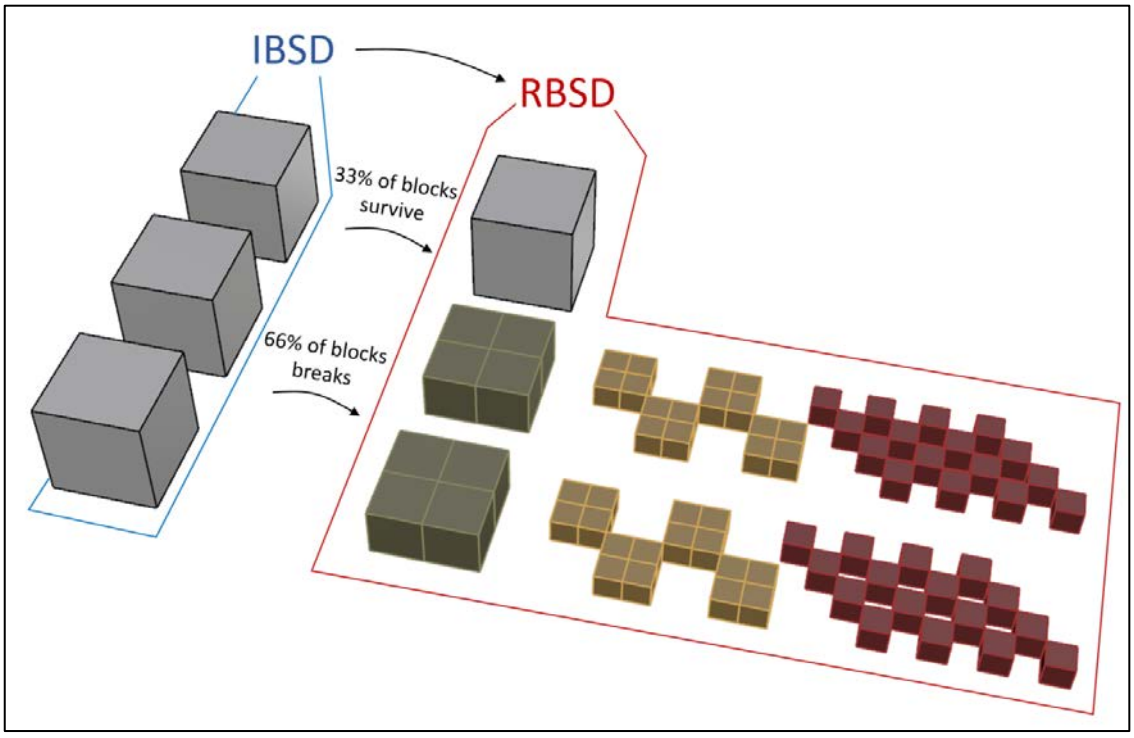

Fig. 5: Scheme of the fractal fragmentation model applied over a bin 1-2 m^3 with 3 blocks (average size 1.5m^3) from the IBSD with a survival rate *Sr=0.33*, probability of failure *$P(1/b^i)$=0.5*, scaling factor *b=2 and using 2 iterations.*

The geometric factor "b" controls the change of the average size. The number of blocks increases when the geometric factor "b" increases, allowing the generation of a larger number of fragments

with two or three orders of magnitude smaller than the original blocks (Figure 6 A), also due to the use of two iterations. When "b" increases, the d_{50} (median) of the generated block size distributions decreases, as Figure 6 shows, (B plot in terms of % of material passing versus block size in cubic meters). The comparison of the geometric factor influence shown in Figure 6 is realized using two iterations, and considering the $P(1/b^i)=1$, that implies a $D=3$, and a $Sr=0$.

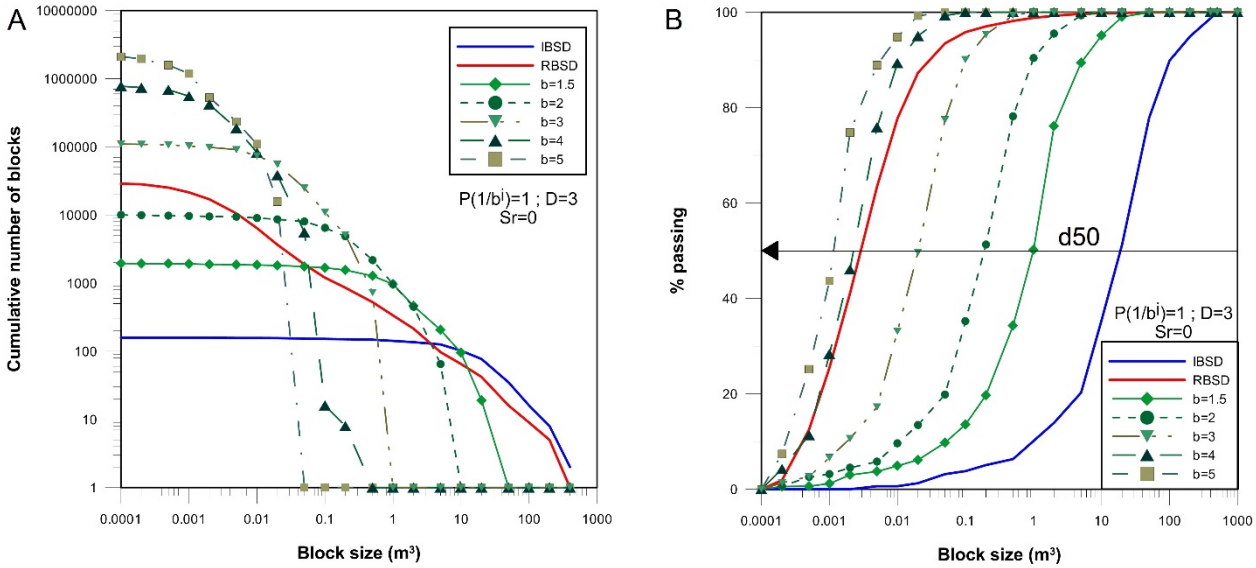

Fig.6: Effect of the geometric factor b considering a $P(1/b^i)=1$, that implies a $D=3$, and a $Sr=0$. Notice that the increase of the b-factor generates the increase of the number of blocks (A) and the reduction of the d_{50} size (B).

With a $P(1/b^i)=1$, the effect of the fractal behavior is less evident because each fragment is fully broken in all the possible blocks of volume defined by the geometric factor "b". The same "b" effect analysis was carried out using a $P(1/b^i)=0.5$ (as the case of $P(1/b^i)=4/8$ in the example of Figure 4). In this case, as shown in Figure 7, the fractal behavior of the model is more evident as the block size distributions generated is well fitted by a power law in the log-log plot.

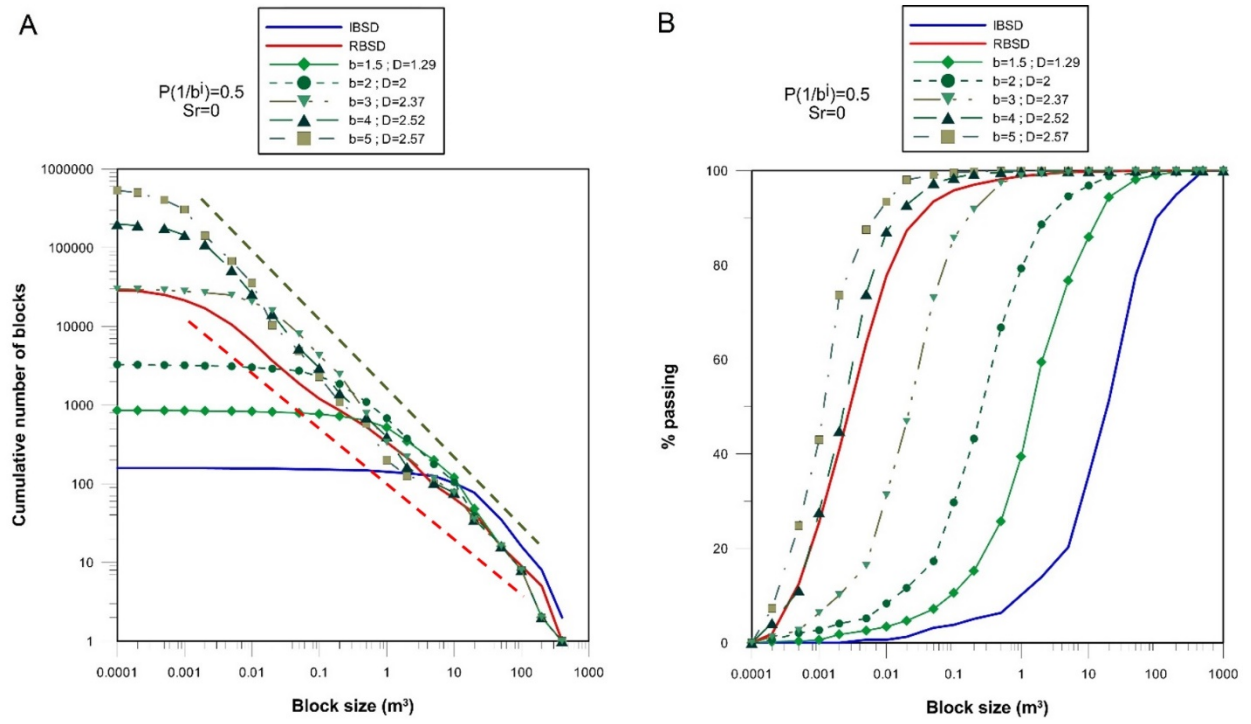

Fig.7: Effect of the geometric factor "b" considering a $P(1/b^i)=0.5$ and a $Sr=0$. (A) The upper and lower envelopes of the fitted power laws are shown as dashed lines.

Field observations indicate that during a rockfall, not all the blocks break (Figure 8) and in the extreme case just blocks bounded by preexisting joints are found (pure disaggregation). To simulate this, the survival rate is introduced. For high survival rates, the breakage is minimal. For the particular case of $Sr=1$, the distribution obtained will be identical to the IBSD.

Fig.8: Example of a fragmental rockfall where the RBSD is very similar to the original IBSD. The rock mass was disaggregated along preexisting joint faces and no new fresh faces were generated by breakage

The proposed model considers only the IBSD and the final RBSD, however, it can run several cycles with different model parameters to characterize the high energy conditions from the first impacts (with higher probability of failure and lower survival rate) and the following impacts (with lower probability of failure and higher survival rate). In this case, the results from the first impacts should be used as an input again in the model to use it with another set of parameters for the rest of the impacts with a lower energy scenario (Fig. 9).

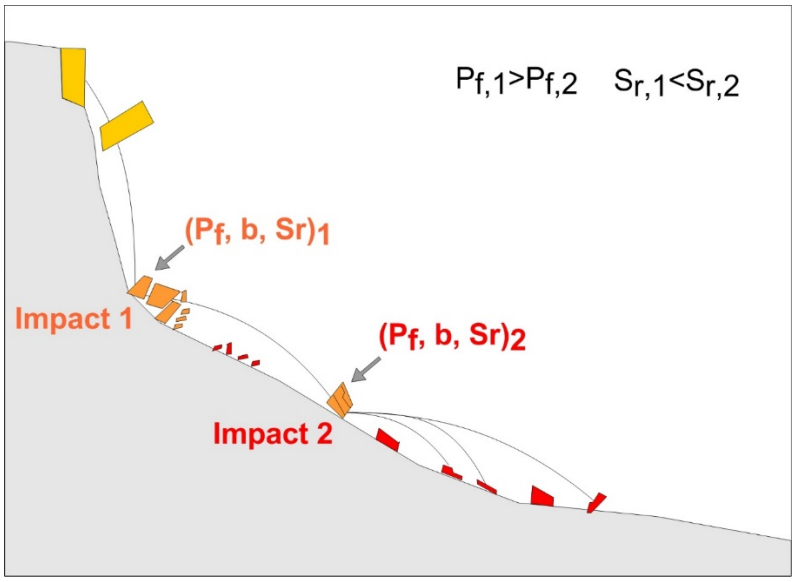

Fig. 9: Scheme of the cycle method in which different model parameters are used to simulate the scenarios generated by the successive impacts.

4. Application of the RFFM to a the rockfall event of Serra del Cadí

The model has been applied to a large fragmental rockfall event that occurred in November 2011 in the Cadí massif, Eastern Pyrenees, near Vilanova de Banat hamlet. The source area is a fault zone composed of Eocene limestones. The rockfall detached a mass of about 10000 m^3 and the young debris cover (YDC) extending over an area of 30000 m^2 (Figure 10).

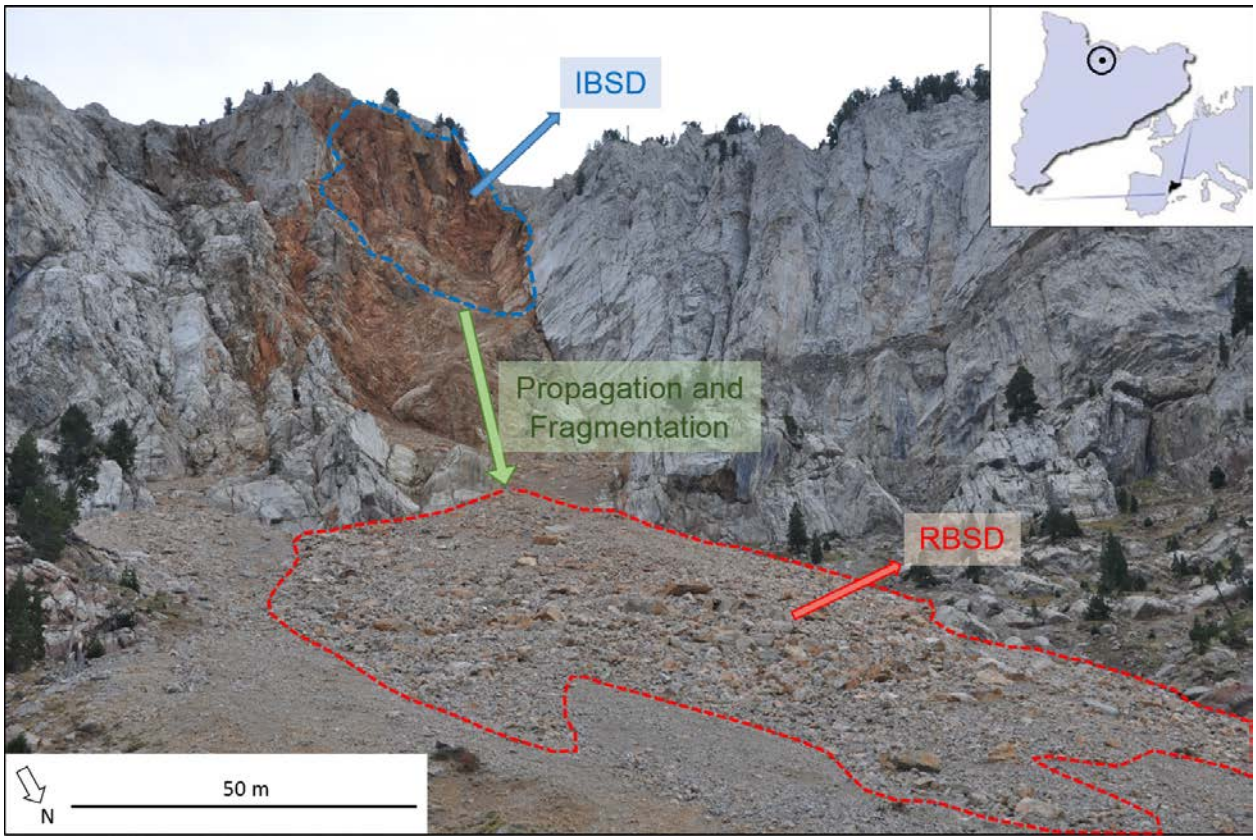

Fig.10: Rockfall event occurred in November 2011 in Cadí massif, Eastern Pyrenees, Spain. The source area is delimited by a dashed blue line, where the IBSD is estimated. The deposit is delimited by a dashed red line, where the measurements to obtain the RBSD were performed.

We obtained the RBSD measuring the deposit, the IBSD by reconstructing the joint pattern of the missing rock mass at the cliff and applied the RFFM to convert the original IBSD (estimated) to the RBSD (measured). This task has been carried out by an error minimization process in which the model parameters have been calibrated. Even though several solutions are possible, the model coefficients obtained vary only within a limited range of values.

4.1 Obtaining the RBSD

In small rockfall events, it is feasible to manually measure all the blocks in situ and thus obtain the RBSD. In the case of large fragmental rockfalls, the measurement of all blocks becomes a tedious task that is often limited by access and economical restrictions. We developed a methodology to obtain the RBSD in the case of large fragmental rockfalls (Ruiz-Carulla et al. 2015). Mid-size to large fragmental rockfalls often generate a more or less continuous Young Debris Cover (YDC) of smaller debris and Large Scattered Blocks (LSB). Given the difficulty in measuring the volume of all the blocks in the YDC, we defined several size-homogeneous zones and Sampling Plots (SP) inside them (Figure 11). The SP have a square shape and variable

dimensions proportional to the size of the blocks. All blocks (over a certain size) inside each SP were measured. The block size distribution obtained at each SP is extrapolated to the corresponding size-homogeneous zone, according to the ratio between the respective areas (Ruiz-Carulla et al. 2015). All the Large Scattered Blocks were measured and georeferenced individually. The volumes of all the blocks were measured in the field as the product of three dimensions, assuming that their shape is prismatic. Finally, all the block size distributions were added to generate the RBSD representative of the whole rockfall deposit.

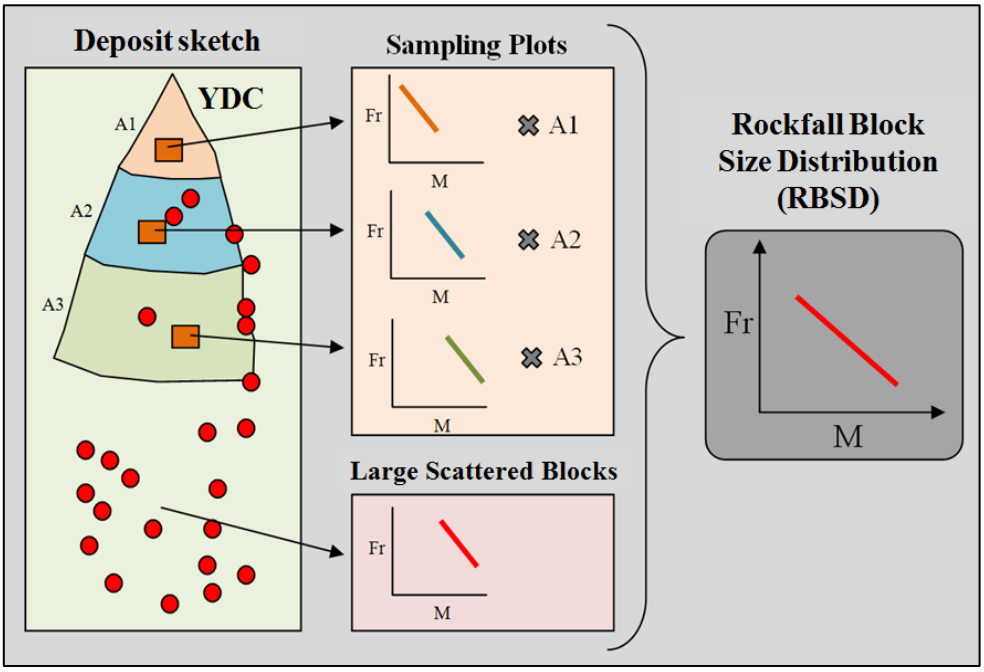

Fig .11 Scheme of the methodology to obtain the RBSD in the case of large fragmental rockfalls (Ruiz-Carulla et al. 2015)

We measured 272 Large Scaterred Blocks (LSB) and 1252 blocks within 6 Sampling Plots (SP). The volume of the biggest measured boulder is 30.8 m^3, and the measured maximum runout distance from the source area is 683 m. The area of the Sampling Plots ranges between 25 m^2 and 400 m^2. The area of the plots increases with the size of the largest blocks found inside the plot. The minimum block size measured was 0.015 m^3. Further details of the procedure followed are included in Ruiz-Carulla et al. (2015). The volume of the overall rockfall deposit calculated with this procedure is approximately 8000 m^3, and it includes more than 60000 blocks larger than 0.015 m^3.

4.2 Generation of the IBSD

Different methods to generate the IBSD of a cliff are available. Some of them use statistical simulations of the joint pattern based on data obtained from scanlines. The lack of accessibility

often forces the measurements being collected at the bottom of the rock wall, which may not represent the fracture pattern at the source. This issue has been discussed in the literature and several procedures have been proposed to overcome it (Da Gama, 1977: Miles, 1972; Hudson and Priest, 1979; Lu and Latham, 1999; Kalenchuk et al. 2006; Stavropoulou, 2014; Elmouttie and Poropat, 2012). The common idea is to use the field measurements of the joints set attributes to develop algorithms which generate stochastically combinations of the joint sets that follow the statistical distributions fitted in the real field measurements. A Monte Carlo simulation of the joint spacing, the location, and the orientation, and considering either fully or partially persistent joints, may be performed to generate Discrete Fracture Networks (DFN). The volume and shape of blocks obtained in this way can be measured. Some limitations may appear related to the number of joint sets, typically 3, and whether they intersect at right angles or not. In any case, the effect of the persistence of the joints in a simulated IBSD is found more significant than the angle between the joint sets used (Kim et al. 2006).

Alternatively, 3D Digital Surface Models (DSM) of the rock wall may be prepared with either digital photogrammetry or LiDAR, which allow obtaining the actual joint pattern at the source area (Brideau et al. 2012; Firpo et al. 2011; Gates et al. 2012; Haneberg et al. 2006; Lato et al. 2012; Pate et al. 2011; Riquelme et al. 2016; Sturzenegger et al. 2009). The discontinuities can be extracted either from 3D point clouds (Riquelme et al. 2014) or 3D meshes (Umili et al. 2013) of LiDAR images, by means of specialized software such as Coltop3D (Jaboyedoff et al. 2007), Cloud-Compare (Girardeau-Montaut 2006), Split-FX, or Sirovision. These methods work with geometrical concepts like the normal vector, the coplanarity of the points and clustering of vectors to define the joint pattern. However, the joints that do not generate relief cannot be identified. Instead, digital photogrammetry (using the software Agisoft Photoscan, http://www.agisoft.com) generates DSM that have the geometrical information and also the texture, thus allowing the visual identification of traces of joints in a rock wall (Ferrero et al. 2011, Firpo et al. 2011, Haneberg et al. 2006, Gates and Haneberg 2012, Lato et al. 2012, Sturzenegger et al. 2009)

In the Cadí rockfall, the joint pattern of the rock mass was obtained by manual identification of the joints on digital images and modelling of their surfaces using Rhinoceros 3d software (http://www.rhino3d.com) over a DSM of the cliff. The procedure for the generation of the IBSD, then, involves two steps: (i) the calculation of the volume of the detached rock mass (Ruiz-Carulla et al. 2015), (ii) the overlay of the joint pattern on the detached rock mass for the generation of the IBSD. The intersection of the joint sets generates rock volumes that can be listed and provides an estimation of the IBSD. Both steps (i) and (ii) are performed by means of the Rhinoceros software. Several assumptions have been considered, namely: (a) all the joint sets have infinite persistence, and (b) the same mean dip angles and dip directions have been assigned to each

individual plane of the set. However, the location and the spacing of the joints are the real ones identified in the 3d photogrammetric model. The methodology is summarized in the following paragraphs.

The detached rockfall volume was calculated by subtracting the DSM of the cliff before and after the event. The DSM before the event is based on model provided by the Cartographic and Geological Institute of Catalonia (ICGC), while the DSM of the cliff after the event was generated from ground pictures taken with a camera Nikon D90 with a focal length of 60 mm and a resolution of 4288x2848 px (12Mp) and subsequent photogrammetry treatment. The difference between the DSM of the scar before and after the rockfall yielded a detached rock mass volume close to 10000 m^3 (Fig 12A).

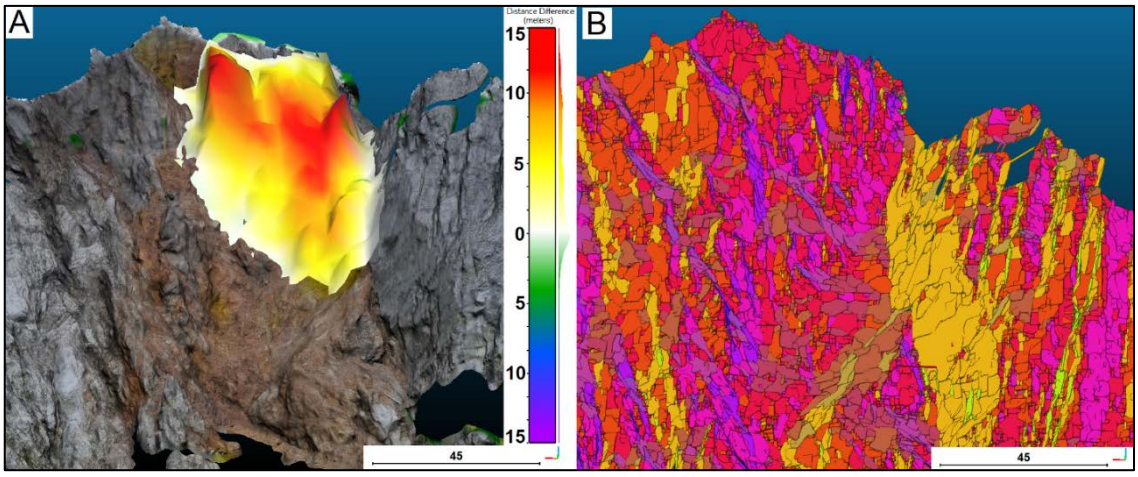

Fig.12: A) 3D photogrammetric DSM of the scar with the detached rock mass reconstructed. B) Facets based on clusters of points colored with the same dip and dip direction on the 3D photogrammetric DSM of the scar.

In order to identify the joint pattern and obtain the IBSD, we represented the DSM of the scar in terms of dip and dip direction. We draw all the joints on a picture and then we modelled the same joints over the DSM of the scar using Rhinoceros, obtaining a Discrete Fracture Network (DFN). Automatic and semi-automatic software like CloudCompare or Coltop3d allow identifying only the joints that generate relief (Fig. 12B). The manual modelling using the texture over the DSM has allowed us to define joints that do not generate relief. We identified up to 5 joint sets plotted at a stereographic representation in (Fig. 13, A) and modelled with their real spacing (Fig. 13, B).

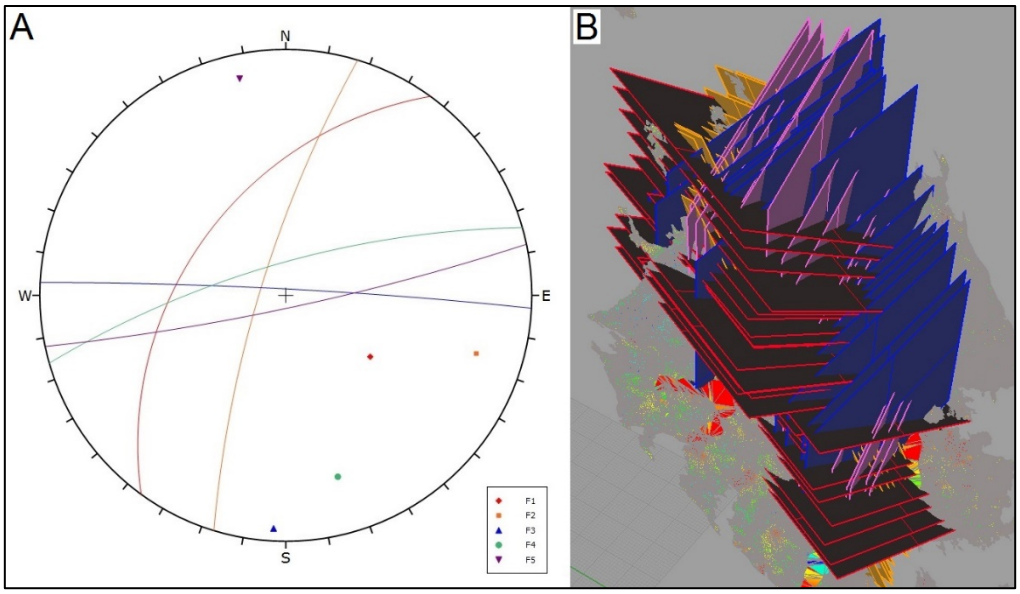

Fig. 13: Stereographic representation of the 5 joint sets (A) and the 3d modelled joints over the DSM of the scar assuming the same dip and dip direction for each joint family (B).

The detached rock mass volume is then cut by overlapping the facture pattern obtained in the previous step to it. In order to check how the shape of the detached rock mass may affect the ISBD, we have worked with two missing rock mass shapes, the one reconstructed from the scar (irregular shape) and a prismatic mass with the same volume. We have identified five joint sets which have been assumed to have an infinite persistence. However, the analysis is repeated without the less frequent set in order to account for the presence of rock bridges. The generated blocks are listed by volume and plotted in relative frequency versus block size, which is an estimation of the IBSD of the detached rock mass. Four scenarios in terms of number of joints and the shape of the overall rock mass detached have been analyzed. Figure 14 shows the joint pattern cutting the prismatic shape (A) and the same joint pattern cutting the reconstructed detached volume from the scar (B). Figure 14 (C) shows the IBSD obtained by: cutting the reconstructed detached volume using 5 joint sets (blue), cutting the prismatic shape volume using 5 joint sets (purple), 4 joint sets (pink) and using only the half part of the prismatic shape with a volume of 5000 m^3 and 4 joint sets (orange). The distribution of the volumes of the LSB is also seen (green). The IBSD generated can be well fitted by exponential laws with coefficients of determination close to 1.

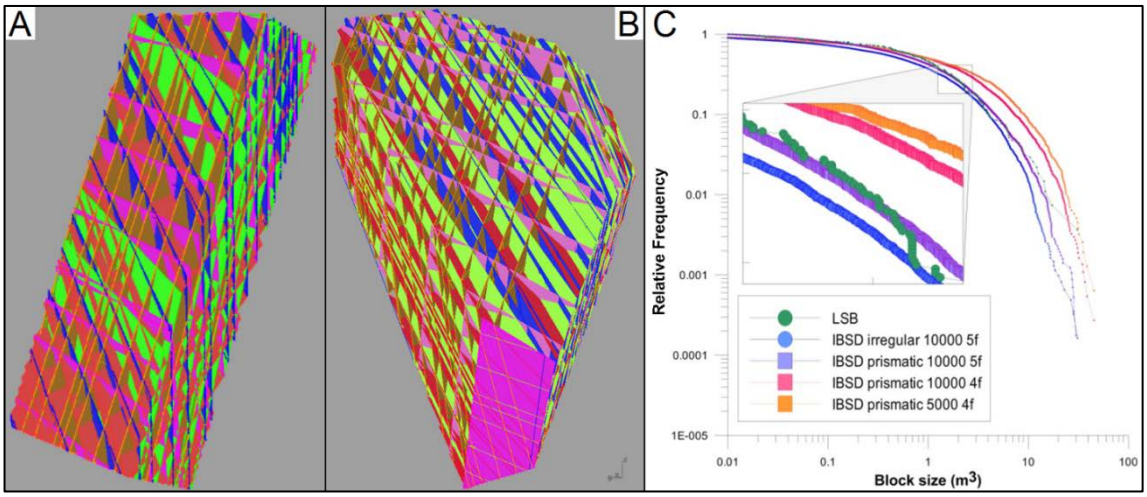

Figure 14: IBSD generated taking a prismatic volume (A) or a reconstructed irregular volume of the detached rock mass (B), and the corresponding IBSD (C) considering 4 or 5 fully persistent joint sets.

4.3 Comparison of the IBSD and RBSD

The estimated volume at the source area is approximately 10000 m^3, which is bigger than the volume of 8000 m^3 based on measured rock fall blocks. The 2000 m^3 of difference between both volumes is likely ought to the fact that approximately the 20% of the rock mass can result in dust and blocks smaller than 0.015 m^3 that were not measured in the field. In fact, by extrapolating the RBSD to a block size of 0.005 m^3, a volume of 10000 m^3 is obtained. Another possible reason for this difference is the uncertainties and the errors associated to the topographic DSM and the scar DSM.

Comparing the obtained IBSD and the RBSD we can observe changes in the shape of the distributions and in terms of both, the total number of blocks and sizes. Four IBSD were obtained considering different assumptions and all of them follow exponential laws. However, all the block size distributions for the deposits and the final RBSD are very well fitted by power laws (Ruiz-Carulla et al. 2015). Figure 15 (A) shows the IBSD obtained using the reconstructed detached volume and 5 joint sets, and the final RBSD, plotted in terms of relative frequency versus block size. By comparing them in terms of cumulative number of blocks (Figure 15, B) a significant reduction of the number of blocks bigger than one cubic meter, and a sharp increase of blocks with volumes smaller than a cubic meter are observed. The total number of blocks estimated in the IBSD is close to 6000 blocks, increasing to 60000 blocks estimated in the RBSD after the propagation and the fragmentation of the rock mass. The difference between the area defined by the IBSD and that of the RBSD is typically attributed to the fragmentation energy in blastability studies. In the case of rockfalls it must be related to the impact energy. Even though rockfall

blocks can be generated by disaggregation of the originally detached rock mass, in what concerns the Cadí case, the substantial increase of small-size blocks indicates that block breakage is the predominant mechanism during the propagation.

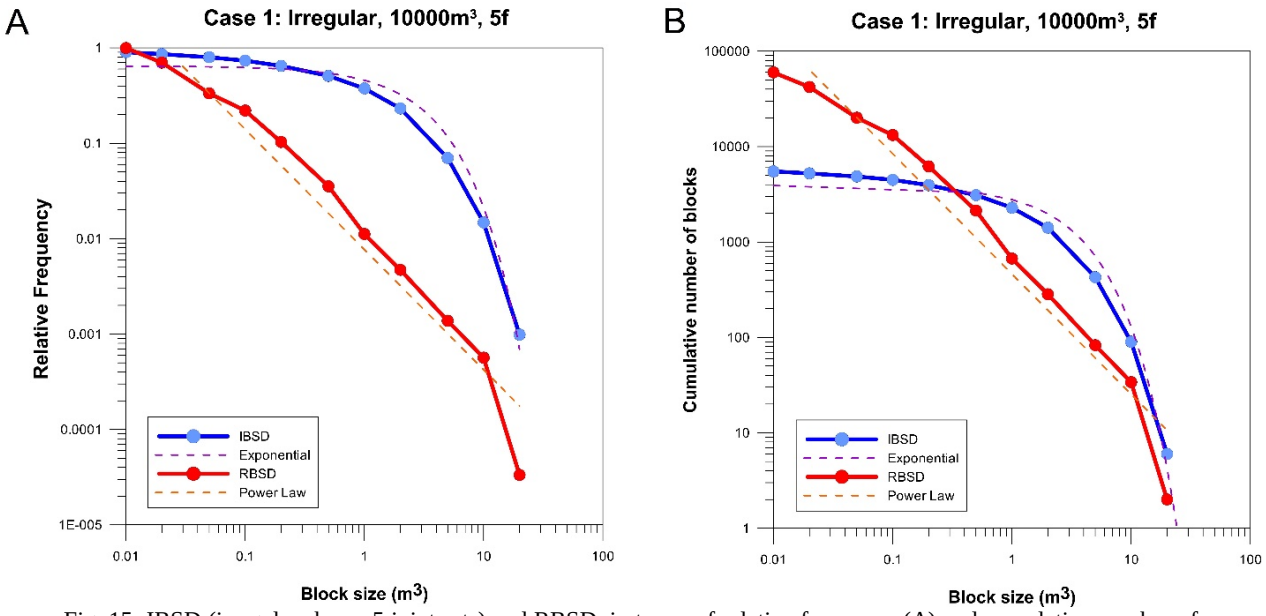

Fig. 15: IBSD (irregular shape, 5 joint sets) and RBSD, in terms of relative frequency (A) and cumulative number of blocks (B) versus block size.

As expected, the impact of the rock masses on the ground causes the reduction of both the number and size of the largest blocks and the increase of the small ones. The central size of the distribution is found around 1m^3. The number of blocks larger than this size is notably reduced. However, the large number of new blocks generated smaller than 1 m^3, and specially smaller than 0.1m^3, suggests that besides the breakage of the blocks by impact on the ground, breakage by pressing (crushing) may play an important role.

4.4 Application of the RFFM

The rockfall fractal fragmentation model RFFM was used in order to obtain the RBSD from the IBSD as an input. Three parameters have to be defined to apply the model: P_f, probability of failure; b, geometric factor; and S_r, survival rate (see Section 3). The parameters were calibrated, matching the modelled RBSD with the observed one, by a trial and error process. Four different scenarios were considered, depending on the number of joint sets and the shape of the detached rock mass, to generate the initial IBSD (Figure 14, B). The procedure allows performing several iterations in order to generate new fragments. The more the iterations performed the smaller the fragments will be. We tested performing 1 and 2 iterations to generate blocks sizes as observed in the field. Figure 16 shows the IBSD obtained from the irregular reconstructed volume, the

RBSD measured in the field and the RBSD obtained from the fragmentation model calibration using 2 iterations.

Table 1 summarizes the values of the parameters obtained for the different IBSD. We obtained a range of values: between 0.05 and 0.34 for the S_r, between 0.73 and 0.80 for the P_f and between 1.6 and 3.4 for b. We used the reduced Xi^2 test (Dussauge, 2003) to optimize the P_f, S_r and b values and to test the goodness of the results obtaining a range between 0.02 and 0.06 for the four cases of different IBSD as input and using 1 or 2 iterations. In the case of the IBSD generated using 4 joint sets, the size of the blocks of the detached rock mass is bigger than in the case of the IBSD generated using 5 joint sets. Thus, to generate the observed RBSD, it is required using a bigger geometric factor b, generating smaller fragments, or using a smaller survival rate in order to break more blocks. Using only one iteration, bigger values of the geometric factor are required to obtain the observed RBSD. Different combinations of these parameters generate very similar results.

The results show that it is possible to successfully generate the RBSD from the ISBD. The best results are obtained in the case 3 of the table 1, where the input is the IBSD based on a prismatic shape with 10000 m^3 using 4 joint sets. However, the procedure followed is a trial and error process until the fitting between both the modelled and observed RBSD is reached. Further work, is required to relate P_f, S_r and b to the local geological, geomechanical, and morphological characteristics of the detached rock mass and the slope.

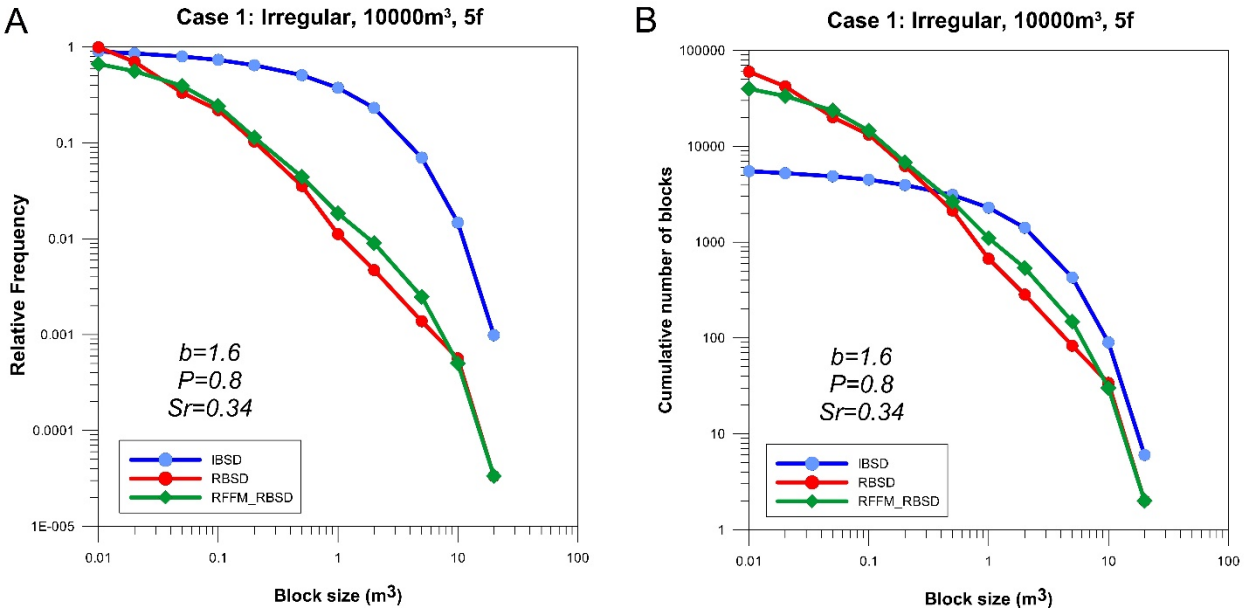

Fig. 16: IBSD (irregular shape, 5 joint sets), RBSD from the measurements in the field and RBSD generated using the Fractal Fragmentation Model; in terms of relative frequency (A) and cumulative number of blocks (B) versus block size.

Table 1: Summary of the calibrated parameters of the rockfall fractal fragmentation model, considering four (4f) and five (5f) fully persistent discontinuity sets.

IBSD	2 iterations					1 iterations				
	b	P(1/b^i)	Sr	rXi^2	D_f	b	P(1/b^i)	Sr	rXi^2	D_f
Case 1: Irreg. 10000m^3 5f	1.6	0.80	0.34	0.02	2.52	3	0.75	0.04	0.06	2.73
Case 2: Prism, 10000m^3 5f	1.75	0.75	0.20	0.03	2.48	3	0.75	0.02	0.04	2.73
Case 3: Prism. 10000m^3 4f	1.75	0.80	0.10	0.02	2.49	3	0.75	0.01	0.02	2.73
Case 4: Prism. 5000m^3 4f	2.15	0.73	0.20	0.05	2.58	3.4	0.75	0.01	0.05	2.76

Small errors in the mass balance between the IBSD and the RBSD can be justified by the use of bins for the block size classification. The use of a mean volume for each bin generates uncertainty in the calculation of the real volume of each block. Figure 17 (A) shows the volume of the rock mass for each bin in the IBSD, the observed RBSD and the RBSD generated by the fragmentation model for the mean volume of each bin. The results indicate that the RBSD generated with the RFFM tends to reduce the total volume of rock mass in bigger blocks generating volume of rock mass in smaller volumes. The difference of volume of rock mass in each bin between the IBSD and the observed RBSD or the RBSD generated by the RFFM shows the decrease of the total volume of blocks bigger than 1 m^3, and the increase of the accumulated volume of blocks smaller than 1 m^3 (Fig. 17, B).

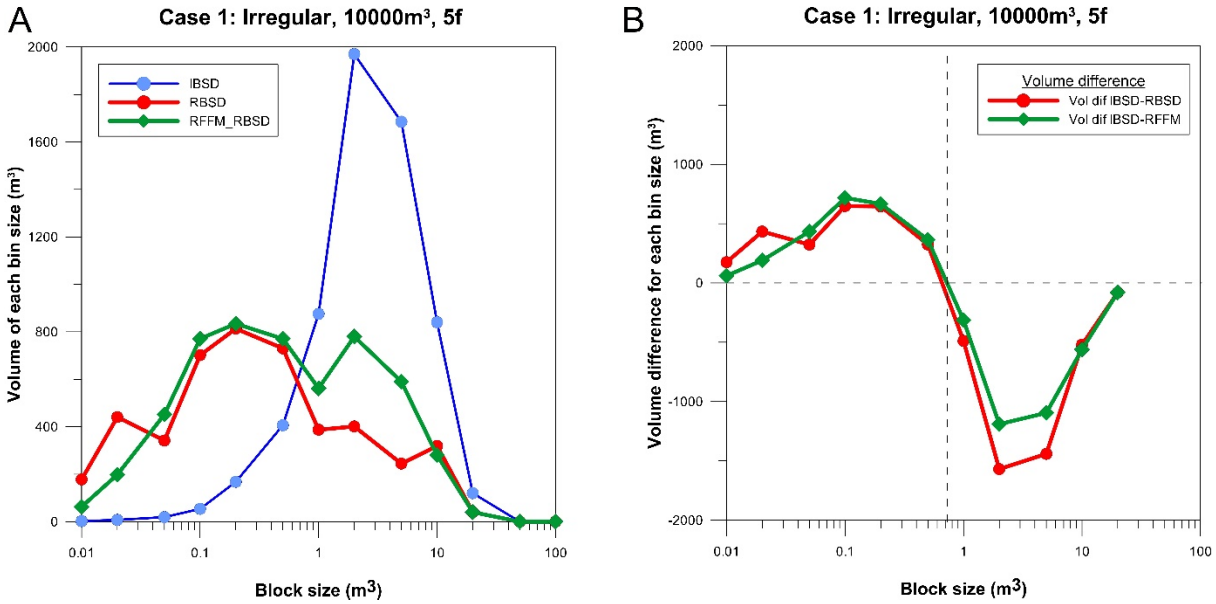

Fig. 17: A) Total rock mass volume of blocks in each bin for the IBSD, RBSD and the Rockfall Fractal Fragmentation Model results. B) Volume difference between IBSD versus RBSD and IBSD versus the RFFM results.

5. Conclusions

Few models exist for obtaining the size distribution of fragments at rockfalls. We proposed a three-parameter rockfall fractal fragmentation model RFFM to be applied to this aim. It is a transition model from the In Situ Block Distribution (IBSD), to the Rockfall Block Size Distribution, RBSD, that is based on fractal laws. The three parameters required to perform the model are: 1) the probability of failure which express the degree of breakage of each initiator block 2) the survival rate, which expresses the percentage of the blocks in a rock mass that remain unbroken, and 3) the scaling factor b, which expresses the ratio of sizes between block and its fragments. The procedure is iterative for a given number i of hierarchies. Successive iterations result in a progressively smaller fragment sizes. The fragmentation is assumed scale-invariant, although the model may also perform as scale-variant. For Sr=1, the RBSD reproduces the IBSD, as only disaggregation and no breakage takes place. The model allows the reproduction of two fragmentation mechanism defined as disaggregation and pure breakage.

An advantage of this model is that it is simple enough to be incorporated into rockfall trajectory analyses. Additionally, the proposed RFFM allows the possibility of considering different model parameters according to the energetic scenario of each impact. The minimum size of the deposit can be efficiently reproduced using proper number of iterations i.

At the proposed model, the mass balance is not fulfilled. This is due to the classification of the fragmented block sizes into bins, and the use of the lower, average and upper bin values for the calculation of the total volume after fragmentation. To overcome this problem it is possible to work with all the listed volumes from the IBSD avoiding the use of the classification in bins.

The application of the RFFM to the rockfall event of 2011 to the Sierra del Cadí, in the East Pyrenees, Spain, has shown that the model is efficient in providing with sufficient accuracy the RBSD, provided that the IBSD is known beforehand. The results of the model may vary depending on the assumptions made for the joint pattern at the rockfall source as well as the strength of the rock, the impact energy and the ground rigidity. The obtained ranges of values for the parameters were: between 0.05 and 0.34 for the S_r, between 0.73 and 0.80 for the P_f and between 1.6 and 3.4 for b. The application of the model to the case study of Sierra del Cadí has also shown that two iterations are sufficient for reproducing the block size distribution was observed in the field.

Despite of this performance, further work including more rockfall events, lithologies, heights of fall, ground surface rigidity and joint patterns, is needed before assigning beforehand values to the model parameters, in order to be able to use it as a forward predictive model.

Acknowledgments

The authors acknowledge the support of the Spanish Economy and Competitiveness Ministry to the Rockrisk research project (BIA2013-42582-P) and the support of the Ministry of Education to the first author (grant code FPU13/04252), and the support of the fellowship "Ayudas Fundación BBVA a Investigadores, Innovadores y Creadores Culturales" by the Foundation BBVA to the third author.

References

Agliardi F, Crosta G (2003) High resolution three-dimensional numerical modelling of rockfalls. International Journal of Rock Mechanics and Mining Sciences vol. 40, 4, pp. 455-471

Agliardi F, Crosta G, Frattini P (2009) Integrating rockfall risk assessment and countermeasure design by 3D modelling techniques Nat. Hazards Earth Syst. Sci., 9 , pp. 1059–1073 http://dx.doi.org/10.5194/nhess-9-1059-2009

Aler J, Du Mouza J, Arnould M (1996) Measurement of the Fragmentation Efficiency of Rock Mass Blasting and its Mining Applications. Int. J. Rock Mech. Min. Sci. & Geomech. Abstr., 33: 125-139

Atkinson BK (1987) Fracture mechanics of rock. Academic Press Inc, London. 534 pp
Bakar MZ, Gertsch LS, Rostami J (2014) Evaluation of Fragments from Disc Cutting of Dry and Saturated Sandstone. Rock Mech Rock Eng, 47:1891–1903

Bowman ET, Andrew Take W (2014) The Runout of Chalk Cliff Collapses in England and France — Case Studies and Physical Model Experiments." Landslides, Volume 12 (2), pp: 225-239. doi: 10.1007/s10346-014-0472-2

Brideau M, Sturzenegger M, Stead D, Jaboyedoff M, Lawrence M, Roberts N, Ward B, Millard T, Clague J (2012) "Stability Analysis of the 2007 Chehalis Lake Landslide Based on Long-

Range Terrestrial Photogrammetry and Airborne LiDAR Data." Landslides 9: 75–91. doi:10.1007/s10346-011-0286-4.

Chakraborty AK, Raina AK, Ramulu M, Choudhury PB, Haldar A, Sahu P (2004) Parametric study to develop guidelines for blast fragmentation improvement in jointed and massive formations. Eng Geol, 73: 105–16.

Charrière M, Humair F, Froese C, Jaboyedoff M, Pedrazzini A, Longchamp C (2015) From the source are to the deposit: Collapse, fragmentation, and propagation of the Frank Slide. Geological Society of America Bulletin. doi: 10.1130/B31243.1

Corominas J, Mavrouli O, Santana D, Moya J (2012) Simplified approach for obtaining the block volume distribution of fragmental rockfalls. A: International Symposium on Landslides. "Landslides and Engineered Slopes". Banff: CRC Press. Taylor & Francies Group, 2013, p. 1159-1164.

Corominas, J, Mavrouli O (2013) Estimation quantitative du risque (QRA) pour les bâtiments induit par des éboulements rocheux: état des lieux. Mémoire Societé Vadoise des Sciences Naturelles, 25: 229-242

Crosta GB, Frattini P, Fusi F (2007) Fragmentation in the Val Pola rock avalanche, Italian Alps. Journal of Geophysical Research, 112: p. F01006

Crosta GB, Agliardi F, Frattini P, Lari S, Lollino G (2015) Key Issues in Rock Fall Modeling, Hazard and Risk Assessment for Rockfall Protection. Engineering Geology for Society and Territory, Volume 2, pp: 43-58. doi: 10.1007/978-3-319-09057-3_4

Crum SV (1990) Fractal concepts applied to bench-blast fragmentation. in: Proc. 3rd US Rock Mech. Symp. Rotterdam: Balkema, pp. 913-919

Cunningham CVB, (1983) The Kuz-Ram model for prediction of fragmentation from blasting. In: Proceedings of the First International Symposium on Rock Fragmentation by Blasting, 22–26 August , Lulea, Sweden, pp. 439–454

Cunningham CVB (1987) Fragmentation estimations and Kuz-Ram model – four years on. Proceedings of second International Symposium on rock fragmentation by blasting, Keystone, Colorado, p.475–87

Da Gama C D (1977) Computer model for block size analysis of jointed rock masses. In 15th APCOM symposium, Brisbane, Australia, pp 305-315

Davies TR, McSaveney MJ, Hodgson KA (1999) A fragmentation-spreading model for long-runout rock avalanches. Canadian Geotechnical Journal, 36: 1096-1110

Dussauge C, Grasso J, Helmstetter A (2003) Statistical Analysis of Rock Fall Volume Distributions: Implications for Rock fall Dynamics. Journal of Geophysical Research B 108 (B6) 2286, doi: 10.1029/2001JB000650

Dorren LKA (2003) A review of rockfall mechanics and modeling approaches. Progress in Physical Geography 27 (1): 69– 87

Dunning, S. A. (2006), The grain-size distribution of rock avalanche deposits in valley-confined settings, Ital. J. Eng. Geol. Environ., 1,117 – 121

Elmouttie MK, Poropat GV (2012). A Method to Estimate In Situ Block Size Distribution. Rock Mechanics and Rock Engineering, 45(3), 401–407. doi:10.1007/s00603-011-0175-0
Evans S, Hungr O (1993) The assessment of rockfall hazard at the base of talus slopes. Canadian Geotechnical Journal 30 :620-636

Faramarzi F, Mansouri H, Ebrahimi Farsangi MA (2013) A Rock Engineering Systems Based Model to Predict Rock Fragmentation by Blasting. International Journal of Rock Mechanics and Mining Sciences 60: 82–94. doi:10.1016/j.ijrmms.2012.12.045.

Ferrero AM, Migliazza M, Roncella R, Segalini A (2011) Rock cliffs hazard analysis based on remote geostructural surveys: The Campione del Garda case study (Lake Garda, Northern Italy). Geomorphology 125: pp 457-471

Firpo G, Salvini R, Francioni M, Ranjith P (2011) Use of Digital Terrestrial Photogrammetry in rocky slope stability analysis by Distinct Elements Numerical Methods. International Journal of rock Mechanics and Mining Sciences 48:1045-1054

Gates WCB, Haneberg WC (2012) Comparison of Standard Structural Mapping Results to 3-D Photogrammetric Model Results : Boundary Transformer Banks Rockfall. American Rock Mechanics Association 12: 368.

Gheibie S, Aghababaei H, Hoseinie S H, Pourrahimian Y (2009) Modified Kuz – Ram fragmentation model and its use at the Sungun Copper Mine. International Journal od Rock Mechanics & Mining Sciences 46: 967-973. doi:10.1016/j.ijrmms.2009.05.003

Giacomini A, Buzzi O, Renard B & Giani, G P (2009) Experimental studies on fragmentation of rock falls on impact with rock surfaces. Int J Rock Mech Min Sci 46:708–715

Gili JA, Ruiz-Carulla R, Matas G, Corominas J, Lantada N, Núñez MA, Mavrouli O, Buill F, Moya J, Prades A, Moreno S (2016) Experimental study on rockfall fragmentation: in situ test design and firsts results. International Symposium Landslides 2016 (ISL2016), pp 983-990, Napoli (Italia)

Girardeau-Montaut (2006) Detection de Changement sur des Données Géométriques 3D", D. PhD manuscript (french), Signal & Images Processing, Telecom Paris

Grady DE (1982) Local inertial effects in dynamic fragmentation, Journal of Applied Physics, 53: pp 322-5.

Grady DE, Kipp ME (1987) Dynamic fragmentation of rock. Fracture Mechanics of Rock, Atkinson, B.K. Ed., Academic Press, San Diego, California, 429-475.

Haneberg WC, Norrish NI, Findley DP (2006) Digital Outcrop Characterization for 3-D Structural Mapping and Rock Slope Design along Interstate 90 near Snoqualmie Pass, Washington.” Proceedings 57th Annual Highway Geology Symposium, 1–14.

Hantz D, Rossetti JP, Servant F, D'Amato J (2014) Etude de la distribution des blocs dans un éboulement pour l’évaluation de l’aléa. Proceedings of Rock Slope Stability 2014, Marrakesh, Morocco

Hardin BO (1985) Crushing of soil particles. J Geotech Eng 111(10):1177–1191

Hartmann W K (1969) Terrestrial, lunar and interplanetary rock fragmentation. Icarus 10 (2): 201–213. doi:10.1016/0019-1035(69)90022-0

Hermanns RL, Blikra LH, Naumann M, Nilsen B, Panthi KK, Stromeyer D, Longva O (2006) Examples of multiple rock-slope collapses from Köfels (Ötz valley, Austria) and western Norway. Eng. Geol. 83, 94–108

Haug ØT, Rosenau M, Leever K, Oncken O (2016) On the energy budgets of fragmenting rockfalls and rockslides: Insights from experiments, J. Geophys. Res. Earth Surface, 121, 1310–1327, doi:10.1002/2014JF003406.

Hewitt K, (1998) Catastrophic landslides and their effects on the Upper Indus streams, Karakoram Himalaya, northern Pakistan. Geomorphology 26, 47–80

Hewitt K, (1999) Quaternary moraines vs catastrophic rock avalanches in the Karakoram Himalaya, Northern Pakistan. Quat. Res. 51, 220–237

Hudaverdi T, Kuzu C, Fisne A (2010) Investigation of the blast fragmentation using the mean fragment size and fragmentation index. International Journal Rock Mechanics & Minning Science, Volume 56, pp: 136-145. http://dx.doi.org/10.1016/j.ijrmms.2012.07.028.

Hudson JA, Priest SD (1979) Discontinuities and rock mass geometry. International Journal Rock Mechanics Minning Science Geomech Abstr 16: 339-362

Jaboyedoff M, Dudt JP, Labiouse V (2005) An attempt to refine rockfall hazard zoning based on the kinetic energy, frequency and fragmentation degree. Natural Hazards and Earth System Sciences 5: 621–632

Jaboyedoff M, Metzger R, Oppikofer T, Couture R, Derron MH, Locat J, Turmel D (2007) New insight techniques to analyze rock-slope relief using DEM and 3D-imaging cloud points: COLTOP-3D software, in: Rock mechanics: Meeting Society's challenges and demands, Proceedings of the 1st Canada – U.S. Rock Mechanics Symposium, edited by: Eberhardt, E., Stead, D., and Morrison, T., Vancouver, Canada, 27–31 May, Taylor & Francis, London, UK, 1, 61–68

Kalenchuk KS, Diederichs MS, McKinnon S (2006) Characterizing block geometry in jointed rockmasses. International Journal of Rock Mechanics and Mining Sciences 43: 1212-1225

Kim BH, Cai M, Kaiser PK, Yang HS (2006) Estimation of Block Sizes for Rock Masses with Non-persistent Joints. Rock Mechanics and Rock Engineering, 40(2), 169–192. doi:10.1007/s00603-006-0093-8

Kulatilake PSHW, Qiong W, Hudaverdi T, Kuzu C (2010) Mean particle size prediction in rock blast fragmentation using neural networks. Engineering Geology, 114: 298–311 doi:10.1016/j.enggeo.2010.05.008

Kuznetsov VM (1973). The mean diameter of fragments formed by blasting rock. Journal of Mining Science. 9: 144–148.

Latham J, Meulen J, Dupray S (2006) Prediction of fragmentation and yield curves with reference to armourstone production. Engineering Geology 87: 60–74 doi:10.1016/j.enggeo.2006.05.005
Latham J, and Ping Lu. 1999. Development of an Assessment System for the Blastability of Rock Masses. International Journal of Rock Mechanics and Mining Sciences 36: 41–55.

Lato M, Kemeny J, Harrap R M, Bevan G. (2012) Rock Bench Establishing a Common Repository and Standars for Assessing Rockmass Characteristics Using LIDAR and Photogrammetry. Computers & Geosciences 50, pp:106–14.

Locat P, Couture R, Leroueil S, Locat S (2006) Fragmentation Energy in Rock Avalanches. Canadian Geotechnical Journal 851 (20060135): 830–51. doi:10.1139/T06-045

Lu P, Latham JP (1999) Developments in the assessment of in-situ block size distributions in rock masses. Rock Mechanics and Rock Engineering, 32: 29-49

Lu P (1997) The characterization and analysis of in-situ and blasted block-size distributions and the blastability of rock masses (Doctoral dissertation). Available at https://qmro.qmul.ac.uk/jspui/handle/123456789/1626. (last accessed on june 2016).

Mandelbrot B (1982) La geometría fractal de la naturaleza. Tusquets, ISBN 8483105497, 9788483105498

McSaveney M, Davies T (2007) Rockslides and their motion. In K.Sassa, H. Fukuoka, F. Wang and G. Wang (editors). Progress in Landslide Science, chapter 8: 113-133

Miles RE (1972) The random division of space. In: Advances in applied probability, supplement: proceedings of the symposium on statistical and probabilistic problems in metallurgy, Vol 4, pp 243-266

Molnar P, Anderson RS, Anderson SP (2007) Tectonics, fracturing of rock, and erosion. Journal of Geophysical Research, 112, F03014, doi:10.1029/2005JF000433

Monjezi M, Rezaee M, Yazdian Varjani A (2009) Prediction of rock fragmentation due to blasting in Gol-E-Gohar iron mine, using fuzzy logic. Int J Rock Mech Min Sci ; 46 : 1273–80

Morin MA, Ficarazzo F (2006) Monte Carlo simulation as a tool to predict blasting fragmentation based on the Kuz–Ram model. Computers & Geosciences, 32: 352–359 doi:10.1016/j.cageo.2005.06.022

Okura Y, Kitahara H, Sammori T, Kawanami A (2000) The effects of rockfall volume on runout distance. Engineering Geology 58(2):109–124

Pate K and Haneberg WC (2011) Photogrammetric and LiDAR 3-D Rock Slope Discontinuity Mapping and Interpretation Surveys to Improve Baseline Information for Supporting Design and Construction of Capital Improvement Projects at Hydroelectric Facilities." American Rock Mechanics Association, 520

Peng S, Zhi-wei X, Hou-quan Z, Yong-nian He (2009) Evolution of Blast Induced Rock Damage and Fragmentation Prediction. In The 6th International Conference on Mining Science & Technology, 585–91

Perfect E (1997) Fractal models for the fragmentation of rocks and soils: a review. Engineering Geology 48:185-198

Poulton MM, Mojtabai N, Farmer IW (1990) Scale invariant behaviour of massive and fragments rock. mt J. Rock Mech. Mi Sci. & Geomech. Abstr., 27(3), pp. 219-221

Riquelme A, Abellán A, Tomás R, Jaboyedoff M (2014) A New Approach for Semi-Automatic Rock Mass Joints Recognition from 3D Point Clouds. Computers & Geosciences 68. Elsevier: 38–52. doi:10.1016/j.cageo.2014.03.014.

Riquelme A, Tomás R, Abellan A (2016) Characterization of Rock Slopes through Slope Mass Rating Using 3D Point Clouds. International Journal of Rock Mechanics and Mining Sciences, 84, pp: 165-176. doi:10.1016/j.ijrmms.2015.12.008.

Ruiz-Carulla R, Corominas J, Mavrouli O (2015) A Methodology to Obtain the Block Size Distribution of Fragmental Rockfall Deposits. Landslides 12 (4): 815–25. doi:10.1007/s10346-015-0600-7.

Ruiz-Carulla R, Corominas J, Mavrouli O (2016) Comparison of block size distribution in rockfalls. International Symposium on Landslides 2016 (ISL2016), pp: 1767-1774, Napoli (Italia).

Saavedra JC, Katsabanis PD, Pelley CW, Kelebek S (2006) A neural network model for fragmentation by blasting. In: Proceedings of the 8th international symposium on rock fragmentation by blasting. Santiago, Chile; p. 200–6

Sammis CG, King GCP (2007) Mechanical origin of power law scaling in fault zone rock. Geophysical Research Letters, 34. doi: 10.1029/2006GL028548

Sanchidrián JA, Ouchterlony F, Segarra P, Moser P (2014) Size distribution functions for rock fragments. International Journal of Rock Mechanics & Mining Sciences, 71: 381–394

Stavropoulou, M (2014) Discontinuity Frequency and Block Volume Distribution in Rock Masses. International Journal of Rock Mechanics and Mining Sciences 65. Elsevier: 62–74. doi:10.1016/j.ijrmms.2013.11.003

Sturzenegger M, Stead D (2009) Close-range terrestrial digital photogrammetry and terrestrial scanning for discontinuity characterization on rock cuts. Engineering Geology 106:163-182

Turcotte D (1986) Fractals and Fragmentation. Journal of Geophysical Research 91. NO B2: Pages 1921-1926

Turcotte D (1992) Fractals and Chaos in Geology and Geophysics, 221 pp. Cambridge, New York. Cambridge University Press.

Umili G, Ferrero A, Einstein HH (2013) Computers & Geosciences A New Method for Automatic Discontinuity Traces Sampling on Rock Mass 3D Model. Computers and Geosciences 51: 182–92. doi:10.1016/j.cageo.2012.07.026.

Viero A, Furlanis S, Squarzoni C, Teza G, Galgaro A, Gianola P (2012) Dynamics and mass balance of the Cima Una rockfall (Eastern Alps, Italy). Landslides 10:393-408 doi: 10.1007/s10346-012-0338-4

Wang, Y. (2009). Three-dimensional rock-fall analysis with impact fragmentation and fly-rock modeling. PhD Thesis, University of Austin, Texas.

Wang, Y, Tonon, F (2010) Discrete Element Modelling of Rock Fragmentation upon Impact in Rock Fall Analysis. Rock Mech Rock Eng 44: 23–35

Weidinger JT, Korup O, Munack H, Alternberger U, Dunning SA, Tippelt G, Lottermoser W (2014) Giant rockslides from the inside. Earth and Planetary Science Letters 389: 62–73

Xu Y, Song D, Chu F (2016) Approach to the Weibull modulus based on fractal fragmentation of particles. Powder Technology 292, Elseiver: 99-107. http://dx.doi.org/10.1016/j.powtec.2016.01.021

10. Performance of a rockfall fractal fragmentation model

Publication reference:

Ruiz-Carulla R & Corominas J (2018). A performance of a rockfall fractal fragmentation model. (to be submitted)

Ruiz-Carulla R & Corominas J

Division of Geotechnical Engineering and Geosciences

Department of Civil and Environmental Engineering. Universitat Politècnica de Catalunya-BarcelonaTech

Abstract:

We present the performance of the rockfall fractal fragmentation model developed by Ruiz-Carulla et al. (2017). The parameters of the model are calibrated by back analysis using data of seven fragmental rockfall events. The model has been upgraded and additional capabilities are added. The input of the model is either a single block or a rock mass characterized by its In situ Block Size Distribution (IBSD). Some recommendations are given on how to obtain the latter using the UAV, photogrammetric techniques, 3D point cloud analysis and joint pattern characterization. The deposited fragments volume distribution (Rockfall Block Size Distribution) of several rockfall events, is measured in the field to describe the deposit and calibrate the fragmentation model. The model may run considering scale-invariant or scale-variant breakage condition over several orders of magnitude. The results of the calibrated model fit well to the volume distributions observed. In addition, the model is able to calculate the amount of the new fresh surfaces generated by breakage, which is related to the fragmentation energy.

Keywords: rockfall, fragmentation model, rockfall inventory, fragmental rockfall, block size distribution

1. Introduction:

Fragmentation of a rock mass is the reduction in particle size due to an external action. Despite the increasing number of studies on rockfalls, the fragmentation as consequence of the impact of a rock mass on the ground surface is a process poorly understood. The detached volume may consist of either an individual block or a jointed rock mass. In the latter, the intersection of the joints individualizes rock blocks whose volumetric distribution is the In-situ Block Size Distribution (IBSD). The size distribution of the fragments generated as result of the impact and breakage of the initial blocks is the Rockfall Block Size Distribution (RBSD). The fragmentation may be quantified by comparing of the block size distributions before and after the impact (Ruiz-Carulla et al. 2017).

To simulate fragmentation, we proposed a Rockfall Fractal Fragmentation Model (RFFM) (Ruiz-Carulla et al. 2017) based on an original approach of Perfect (1997). The RFFM uses three parameters to calculate the number and size distribution of the resultant fragments: the probability of failure, $P(1/b^i)$ that expresses degree of breakage of each initiator block; a survival rate, *Sr* or percentage of unbroken blocks after the impact; and a scaling factor, *b* that defines the ratio of sizes between block and its fragment.

The present study presents the calibration of the model parameters using seven fragmental rockfall events. In addition, the model has been upgraded to overcome some of the limitations found in the previous version of Ruiz-Carulla et al. (2017). Specifically, the fact the RFFM does not preserve the mass balance (due to the use of bins) and the difficulty to simulate adequately the RBSD in case of the breakage of an individual rock block. Finally, the model has been improved by allowing the scale-variant behavior in order to reproduce RBSD with irregular shapes.

We explain the improvements of the fractal fragmentation model in section 2, the performance of the model using 7 inventoried rockfall cases in section 3, and the results and discussion in section 4.

2. Upgrade of the Rockfall Fractal Fragmentation Model (RFFM)

The RFFM of (Ruiz-Carulla et al, 2017), generates a block size distribution (RBSD) from a single block or a list of blocks (IBSD). Each broken block will produce a new distribution of fragments using the main equation for fractal systems (Perfect, 1997), which is written as (Eq.1):

$$N(1/b^i) = k\left[1/b^i\right]^{-D}; i = 0,1,2...\infty \qquad \text{Eq. 1}$$

Where $N(1/b^i)$ is the total number of fragments at the *i*th level of hierarchy; *k* is the number of initiators of unit length; *b* is a scaling factor >1, that define the geometric proportion between the original block and the generated blocks; and D_f is the fractal dimension. N is rounded to the lower nearest integer. The actual number of fragments produced depends on the probability of failure at the *i*th level, $P(1/b^i)$, which is defined as:

$$P(1/b^i) = n_i / b^3 \qquad \text{Eq. 2}$$

Where n_i is the number of fragments generated in the *i*th level. $P(1/b^i)$ expresses the proportion of block that breaks. If the probability of failure is scale-invariant $P(1/b^i) = P(1/b^{i+1})$, it can be expressed as:

$$P(1/b^i) = b^{Df-3} \qquad \text{Eq. 3}$$

$$\text{or } D_f = 3 + \frac{\log\left[P(1/b_i)\right]}{\log\left[b\right]} \qquad \text{Eq. 4}$$

Where D_f is the fragmentation fractal dimension. The probability of failure ranges between $b^{-3}<P(1/b^i)<1$. When $P(1/b^i)=1$ *and* $D_f=3$ the whole block is fragmented, while for $P(1/b^i) \leq b^{-3}$ the block remains unbroken.

In the case of scale variant (or scale-dependent) behavior, the number of fragments generated changes with the scale. Then, the probability of failure is (Perfect, 1997):

$$P(1/b^i) = 1 - q(b^i)^r \qquad \text{Eq. 5}$$

Where *"Sr"* is the probability of survival as defined by Perfect (1997) with a slightly different meaning than the survival rate or proportion of unbroken blocks defined by Ruiz-Carulla et al (2017). For $1/b^i < S_r^{1/r}$, the $P(1/b^i) = 0$ and the block remains unbroken. The interpretation of the survival rate is explained next. The fractal dimension for scale variant behavior is:

$$D_f = 3 + \frac{\log\left[b^r - q(b^i)^r\right]}{\log\left[b\right]} \qquad \text{Eq. 6}$$

The scale variant behavior is characterized by the change of behavior of different sizes. The increase or decrease of the strength of the rock block as the block size diminishes is simulated by the negative or positive value of *"r"*, respectively. For $r=0$, the scale variant is equal to the scale invariant case. Based on this, we adopt the scale variant case, that will become invariant for $r=0$.

As mentioned above, the RFFM of Ruiz-Carulla et al (2017) does not preserve the mass balance due to the use of bins. Each bin considers the average volume of the blocks rather than the exact volume. To solve it, we apply the model over each initiator, which can be either a single block or

each of the blocks of the IBSD. A threshold value is established for the minimum volume of the fragments generated. To comply with the mass conservation, the remaining mass below the threshold is computed as fine fraction. The newly generated fragments (RBSD) are listed by volumes. First, the largest fragment and then the rest of fragments ordered by decreasing sizes are added until either the initial block volume is completed or until the fragments become smaller than the threshold defined.

Finally, in the previous version, the RFFM is applied iteratively to distribute the mass of the blocks among the fragments. The size of the new blocks generated is a function of the number *i* of iterations. With this procedure all the fragments generated at each iteration are equally sized. This may be acceptable in case of an initial rock mass involving hundreds or thousands of blocks but it may yield unreliable results in the case of a single block initiator. Furthermore, the number of iterations modifies the shape of the RBSD and the exponent of the fitted power law.

In the upgraded model, the iteration over the geometric factor *"b"* defining the volumes in terms of ($1/b^i$) is replaced by (l/l_{max}), where *"l_{max}"* is the length of the largest fragment generated, and *"l"*, the length of each new fragment smaller generated (Perfect, 1997). This description lists the cumulative number of fragments in descending order of sizes, fragment by fragment. The resultant RBSD is a continuous and decreasing list of rock fragments.

Consequently, the Eq.1 describing the number of fragments of size *"$1/b^i$"* is rewritten in terms of the cumulative number of fragments of size greater than or equal to *"l/l_{max}"*. As we apply the model over every block, either a single volume or the blocks of the IBSD, the number of initiators is always 1 ($k=1$).

$$\mathbb{N}(l/l_{\max}) = \left[l/l_{\max}\right]^{-D_f}; l = \left[l_{\max}, l_{\min}\right] \qquad \text{Eq. 7}$$

The length *"l"* of the fragments generated starts from *"l_{max}"*, then *"l_{max}/l_{max}"* is 1, and the cumulative number of fragments for the largest fragment is 1. Then, *"l"* decreases generating *"N"* accumulated number of fragments. As we are only interested in natural numbers of fragments, we define a variable *"n"*, ranging from 1 to infinite, for the accumulated fragments generated. Thus, Eq.7 maybe rewritten as function of the number of fragments accumulated n, obtaining the length *"l"* that defines the following fragment size:

$$l = l_{\max} \cdot n^{-1/D_f}; n = 1, 2 \ldots \infty \qquad \text{Eq. 8}$$

The variable *"n"* increases until the total volume of the fragments generated equals the initial block volume.

Figure 1 illustrates the difference between *"$1/b^i$"* and "l/l_{max}". The former generates a number of equally sized fragments (Figure 1 left). Considering $P(1/b^i)=0.5$ and $b=2$, the initial volume *"Vo"* is fragmented creating 4 fragments of size *"$1/b^1$"* and the remaining unbroken portion of the block (Rem). In the second iteration, 2 of the 4 fragments generated in the first iteration break again yielding 16 new fragments of size *"$1/b^2$"*, while the remaining fragments are 2 of *"$1/b^1$"* size (from the first iteration) and the unbroken portion (Rem) of the initial block. Thus, a total of 19 blocks are generated of 3 different sizes. The use of *"l/l_{max}"*, generates an accumulated number of fragments of decreasing size (Figure 1, right) that fits better to the observations.

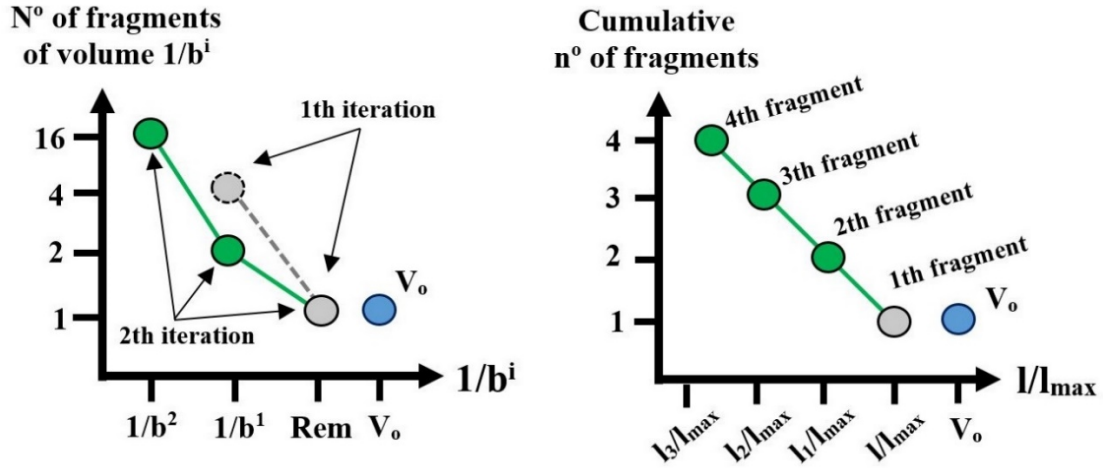

Figure 1: Comparison on fragments size distributions construction with *"$1/b^i$"* using iterations (left) or using *"l/l_{max}"* in a cumulative way (right).

Finally, to convert the characteristics lengths into volumes, the initial volume *"Vo"* is used to rescale the magnitude. The equation that generates fragment volumes in a cumulative number is:

$$Vfrag(n) = V_o \cdot l_{max} \cdot n^{-1/D_f}; n = 1, 2 \ldots \infty \qquad \text{Eq. 9}$$

The maximum length *"l_{max}"* is defined as $l_{max} = 1 - P(l/l_{max})$ on scale invariant formulation, and $l_{max} = qb^{n\wedge r}$ for the scale variant case (both by definition). Notice that "*b*" still controls the proportions between the initiator and the fragments, instead of their behavior is inversed.

Generating irregular and continuous distributions from a single block (initiator)

The upgraded RFFM can now generate block size distributions of different shapes. Figure 4 shows the results of real-scale test (Gili et al. 2016). For the sake of brevity, only four cases are plotted. These examples illustrate the capability of the upgraded RFFM to generate both irregular and continuous BSD distributions, using the scale variant behavior and the continuous generation of fragments (l/l_{max}).

Figure 3 presents the results of the fragmentation tests of the four individual blocks tested. The original size of the block was measured with digital digital photogrammetric reconstruction (blue circles in Figure 3). At each test, the block is dropped from a height of 17 meters, impacting against the ground surface and breaking in smaller fragments. We used a tape to measure 3 block dimensions of each fragment and calculate the volume assuming a prismatic shape. The volumes of the fragments define the RBSD (Rockfall Block Size Distribution) of each trial (red squares in Figure 3). Each case is used to calibrate the model parameters, minimizing the difference between the real measured volumes and the results from the RFFM (green diamonds in Figure 3). We run the model until the values of the reduced Xi^2 fall between 10^-4 and 10^-2. Under the same conditions, blocks with similar volume and mechanical properties display contrasting behavior. The may display either a survival rate of 0.95 and generate only few fragments several orders of magnitude smaller than the remaining unbroken block (Figure 3 upper left, T1-B16 case), or disintegrate with a survival rate of only 0.4 or 0.34 and producing 50, 100 or more new fragments (Figure 3, T1-B10), sometimes with a progressively curved shape distribution (Figure 3, T1-B2). Notice that by breaking less than the 20% of the block in terms of total volume (Sr = 0.817), more than 20 fragments can easily have been produced (Figure 3, T1-B12),

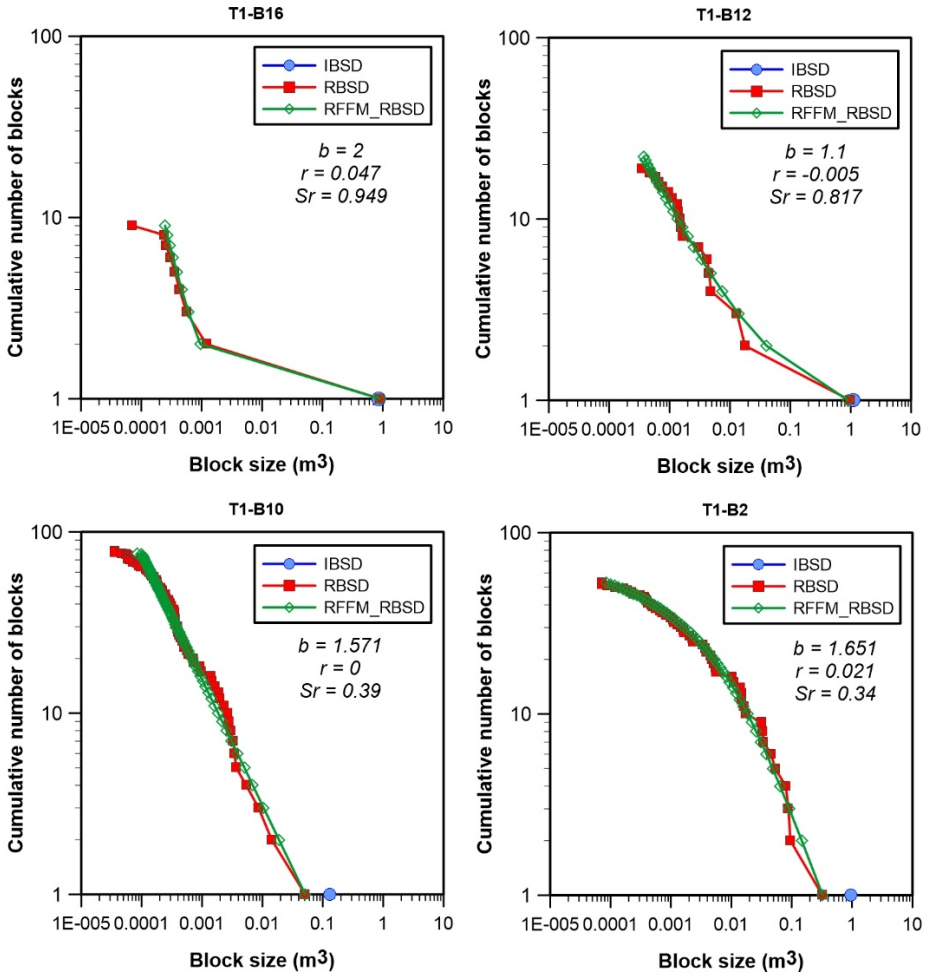

Figure 3: Calibration of the model with data from real-scale test. IBSD (blue dot) is the initial block volume. RBSD (red dots) is the fragments measured BSD, and the RFFM (green dots) is the results of the model after calibrate the parameters minimizing the reduced Xi^2.

3. Performance of the upgraded RFFM

The performance of the upgraded RFFM is tested with seven inventories rockfall events. The goals of the simulation are on one side, testing the sensitivity of the parameters and calibrate the model using a variety of detached volumes, lithologies, rock strengths, heights of fall and slope conditions. On the other hand, we aim at establishing (identifying) the relation between the model parameters and the results in order to carry out forward prediction in the future.

3.1 Inventoried rockfall events

The 7 rockfall cases analyzed in represent different fragmentation scenarios, in terms of failure mechanism, lithology (limestone, sandstone, conglomerate and schist), total volume detached (between 2 m^3 and 10.000 m^3), and different slopes and terrain conditions.

Three samples of each rockfall event were collected for the mineralogical description and testing. The parameters determined are: the rock density, the uniaxial compressive strength, the Young modulus, the Poison ratio and the tensile strength (table 1). The total volume of the detached rock mass (IBSD) and the total volume the deposit measured (RBSD) differ less than a 10-20%. The difference is interpreted as fine fraction, that corresponds to the fragments too small to be measured in the field.

The relevant data collected are presented in Table 1. Notice we measured manually three lengths of the rock fragments with a tape, totaling more than 7200 fragments. We consider the RBSD obtained an accurate description of the volume distribution of the fragmental rockfalls inventoried.

Figure 4 is a mosaic of pictures from the inventoried cases. Pont de Gulleri (PdG) rockfall is a schist with an important fracture system that defines a very blocky rock mass with a high number of planes of weakness. Omells de Na Gaia (Omells) and Lluçà (Lluca) rockfalls are sandstones with bedding defining the main weakness planes of the rock mass. Lluçà rockfall is 10 m^3 of rock that topple over a flat and soft terrain. A huge block of 8.7 m^3 remained unbroken. At Omells rockfall, the rock mass detached is scattered due to the breakage of the blocks. At Gurp rockfall, 100 m^3 of conglomerate rock mass was detached falling down 100 meters of freefall height, likely impacting at mid cliff. The main impacts at the cliff base destroyed trees (>500 m^2 affected) and produced blow of soil covering the trees. Two blocks of 20 m^3 reached the paved road after leaving a path of craters on the ground (see Figure 6 also). Monasterio de Piedra (MdP), Malanyeu

and Cadi rockfalls are rockfall cases in limestone rocks. The rock mass detached at Monasterio impacted on the ground terrain after 35 m of free fall. The impact ground is rigid and generate a substantial fragmentation. Breakage at Malanyeu was lesser and the deposit includes 7 blocks greater than 100 m^3, and more than 60 blocks greater than 10m3, with a maximum boulder of 445 m3. The Cadi rockfall is the biggest events and the rock mass detached is very jointed due to the presence of an inverse fault zone in the source area.

Figure 4: Pictures of the inventoried rockfalls.

Table 1: Rockfall inventory cases, summary data, rock properties and measured fragments.

ROCKFALL INVENTORY	1.PdG	2.Omells	3.Lluca	4.Gurp	5.MdP	6.Malanyeu	7.Cadi
Failure Mechanism	Slide	Toe erosion slide	Toppling	Toppling	Toppling Slide	Toppling	Slide
Lithology	Schist	Sandstone	Sandstone	Conglomerate	Limestone	Limestone	Limestone
Total Volume RBSD (m^3)	2.6	4.2	10.7	100	900	4350	6351
Total Volume IBSD(m^3)	2.61	4.2	10.7	100	997	4945	7663
RMR	76	64	72	82	70	74	60
ROCK PROPERTIES							
Density(kg/cm3)	2.72	2.35	2.46	2.69	2.5	2.64	2.68
Tensile Strength (Mpa)	6.53	2.03	2.07	5.47	10.00	7.03	12.10
UCS (MPa)	32.17	21.38	21.77	38.36	35	13.33	35.29
E Young (MPa)	17385	5185	730	74831	20000	12992	22761
Poisson ratio	0.27	0.006	0.18	0.21	0.1	0.05	0.07
FRAGMENTS MEASURED							
RBSD Total number blocks	116	48	78	500	10790	28788	60980
RBSD nº of measured blocks	116	48	78	500	2256	2721	1524
Min. Vol. Measured (m^3)	0.0001	0.0007	0.0007	0.001	0.001	0.0001	0.01
Max. Vol. Measured (m^3)	0.28	1.1	8.5	22	27	445	31

The 3D models of each rockfall event obtained with UAV and digital photogrammetry, were used to measure distances, 2D and 3D areas, volumes, generate profiles with overhangs, and contour maps. Table 2 summarizes the main geometrical descriptors used for rockfalls. Bigger total rockfall volumes tend to increase all geometrical descriptors, however, the Coef. of determination r-squared with the 3D scar area is 0.99 (Figure 5).

Table 2: Summary of geometrical descriptors measured on the 3D models of each scenario:

SCENARIO & DEPOSIT	1.PdG	2.Omells	3.Lluca	4.Gurp	5.MdP	6.Malanyeu	7.Cadi
Scar 3D Area (m^2)	9.55	15	32	87	578	2120	3532
Total Cliff Height (m)	15	3.3	6.8	100	50	70	150
1st Impact Height (m)	12	1	0.6	39	35	10	50
CoG Height (m)	13	5	2.8	110	60	80	230
Max. Height difference (m)	13	14.5	6.6	150	70	100	520
Max. Runout (m)	5	22	9.2	152	70	130	710
Max. Volume Runout (m)	5	3	5.6	152	40	80	200
Reach Angle (degrees)	69	33	36	45	45	38	36
Deposit Width (m)	2.5	15	5	40	50	80	130
Deposit Area(m^2)	5	300	45	2000	4200	6000	44000
YDC Area (m^2)	5	6	35	1625	3743	1150	30000
YDC Width (m)	3	2	5	40	50	40	110
YDC Length (m)	1.7	3	3.5	63	35	50	260

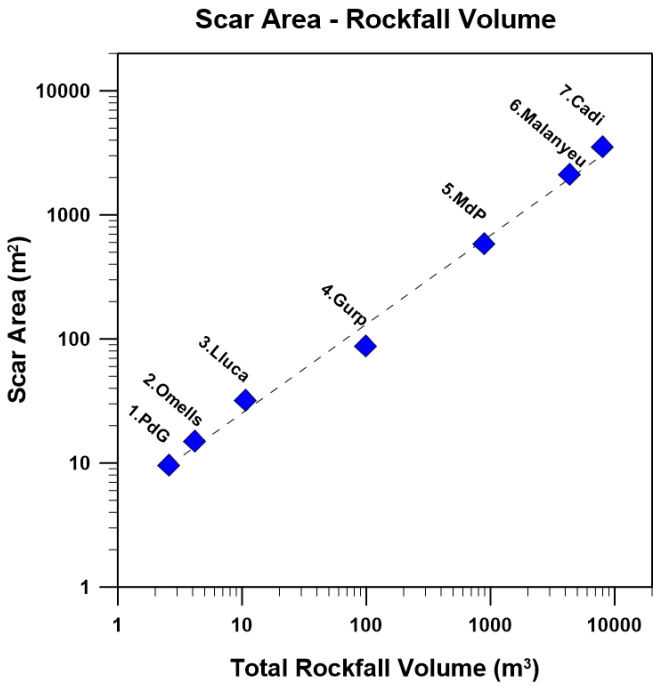

Figure 5: Scar area (SA) measured on a 3D surface and total rockfall volume (V) of the study cases, with a lineal correlation described by *SA=V*0.4476+32.963* with R^2=0.99.

In order to characterize fragmentation, the steepest part of the cliff (>45º) plays a relevant role as the falling mass tends to accelerate and is the highest "energetic part" (colored from yellow to red on 3D models of Figure 6). The less inclined part of the slope (<45º) is where the main impact and the rest of the propagation take place and where blocks tends to break or stop (coloured from green to blue), depending on the type of propagation.

At Gurp (Figure 6, up), a natural berm inclined less than 45º (blue zone located at the half of the cliff) is observed. Some trajectories may impact on this berm, causing breakage of the rock mass, thus changing the direction followed by the fragments. The gentle surfaces at the upper part of the cliff in Gurp and Monasterio de Piedra (Figure 6), define the base of the rockfall scar.

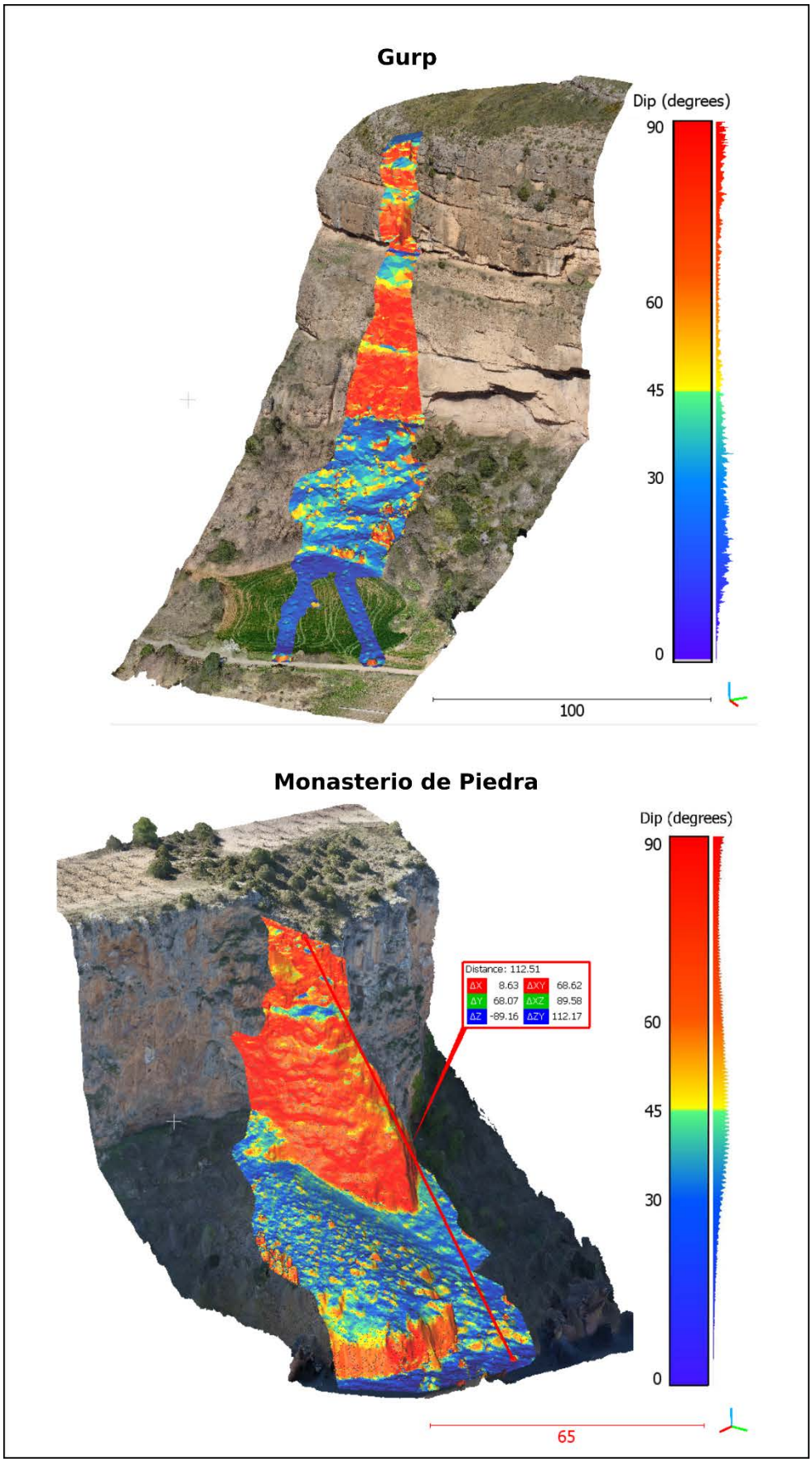

Figure 6: 3D models of Gurp and Monasterio de Piedra rockfalls, coloring the zone affected by the rockfall by higher or lower than 45º of slope.

3.2 Reconstruction of the detached rock mass and generation of the IBSD

The initiator of the model can be either an individual rock block or a rock mass intersected by one or more discontinuity sets. The characterization of the latter requires the 3D reconstruction of the detached volume and the generation of the IBSD by means of a discrete fracture network (DFN). This task requires considering several assumptions and hypotheses.

The detached rockfall volume at each site is calculated following the methodology described in Ruiz-Carulla et al. (2015). The detached volume is calculated by subtracting the Digital Surface Model (DSM, 3d mesh surface) of the cliff before and after the event. The DSM before the event is generated from the LIDAR point cloud provided by the Cartographic and Geological Institute of Catalonia (ICGC), except for the case of Monasterio de Piedra, which is provided by the National Geographic Institute of Spain. When the morphology of the cliff and/or pictures before the event are available, we manually modified the DSM in order to define the pre-event scenario as real as possible.

The DSM of the cliff after the event is generated from the pictures taken using an UAV (DJI Inspire 2, X5S camera), except in the case of Vilanova de Banat that was obtained from ground pictures taken with a camera Nikon D90.

The joint pattern identification is based on 3D point cloud analysis combining semi-automatic and manual modelling, using the plugins Facet Matching (Dewez et al., 2016) on Cloud Compare (Girardeau-Montaut 2006), and also the tool Compass (Thiele et al. 2017). The parameters of the Facet Matching to define the fitted facets are accommodated to the scale of the main joint sets. High tolerances, allowing high values of the minimum distance between the 3d points and the facet planes, will define facets with larger areas. The parameters used are calibrated according to the scale of each rockfall scar, and the results are supervised. Often, the manual selection of well-defined planes and to adjustment to a facet with the Compass tool is required, also for joint trace identification. The Discrete Fracture Network (DFN) is obtained by combining the semi-automatic and the manual detection of joints, and exported as mesh format. The total volume detached reconstructed and the DFN is handled in a 3D modelling software (Rhinoceros) to create an IBSD cutting the volume with the DFN. The joints are assumed fully persistent and placed in its real position, thus providing the actual spacing.

The 3D blocks created composing the IBSD are listed and both the volume and the 3D surface area of each block are measured. The list of volumes is the input of the fragmentation model. Both the list of the areas and the accumulated areas of the rock blocks will be compared to the areas of

the newly generated rock fragments. The joint sets, the number of blocks of each IBSD, the maximum and minimum block size and minimum spacing are summarized in Table 3 while some examples are provided in Figure 8.

Table 3: Summary of IBSD characteristics

IBSD	1.PdG	2.Omells	3.Lluçà	4.Gurp	5.MdP	6.Malanyeu	7.Cadi
Nº of joint sets	5	3	4	5	5	4	5
IBSD Total number of blocks	40	3	5	14	19	95	6800
Min. Block Volume (m^3)	0.0001	0.0007	0.0007	0.0015	0.001	0.0015	0.01
Max. Block Volume (m^3)	0.28	4	10.7	30	96	492	45
Min joint spacing	0.3	0.2	2	0.5	1	3	1

The 3d model of the scars can be plotted in terms of dip direction or dip angle. The semi-automatic and manual joint characterization allows to export only the main planes or hundreds of data to obtain the mean or modals planes. In the case of a scar, the discrete fractures manually modelled may be the best measures. The reconstructed volumes are cut with the DFN to obtain the IBSD as shown as example of Gurp, Monasterio and Malanyeu cases in Figure 7. The Cadi case is presented in Ruiz-Carulla et al (2017), following the same methodology. The block size distributions before and after the breakage were compared in a similar way than Charriere et al (2015).

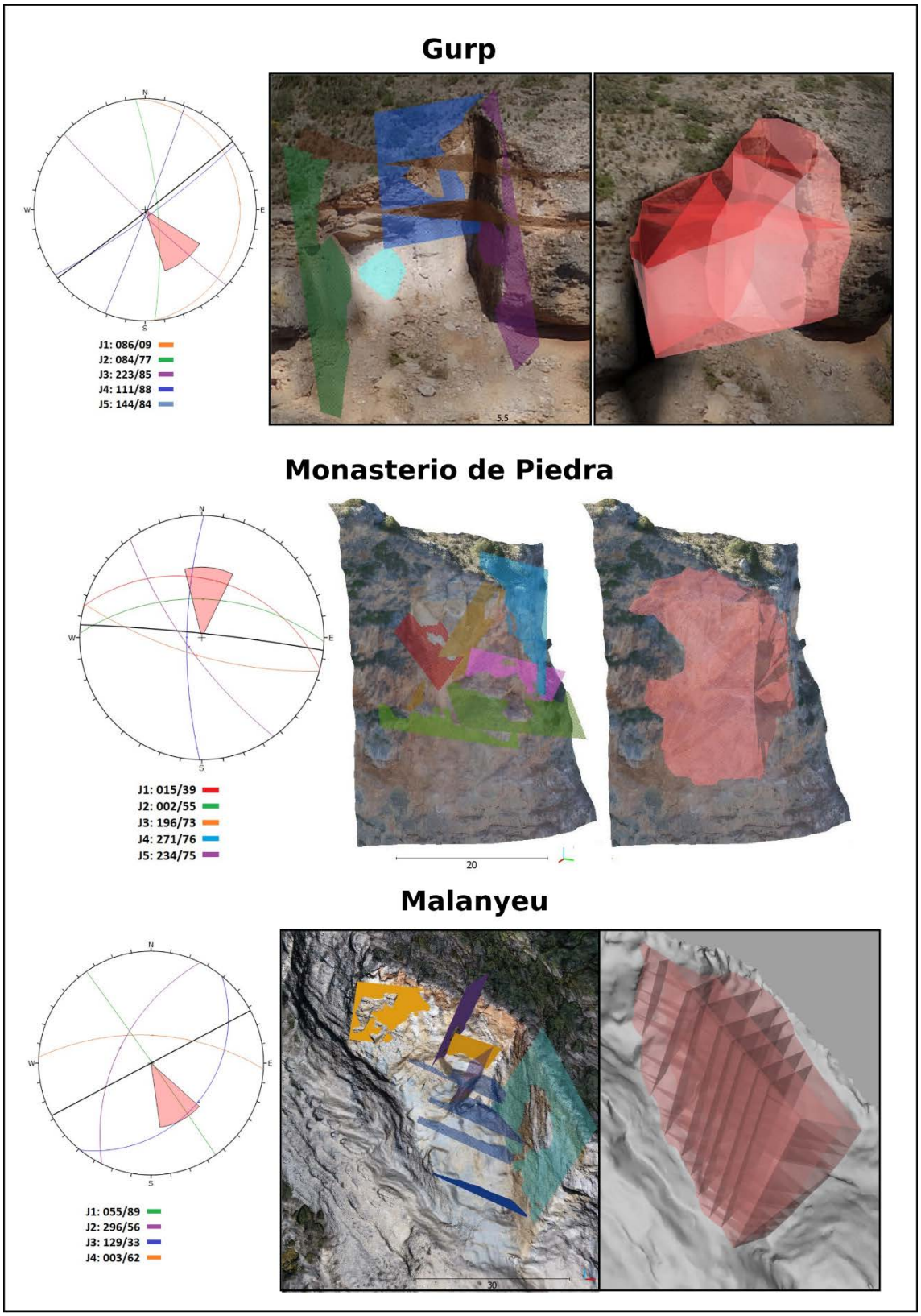

Figure 7: Stereographic projection of the joint sets identified on the 3D models of the scar. The sets have been overlaid to the detached volumes to obtain the IBSD of Gurp, Monasterio and Malanyeu events.

3.3 Calibration of the model

Rock blocks may break differently. It has been observed that blocks of the same lithology and similar size may display different fragmentation behaviour, even under controlled environmental conditions as the found in real scale drop tests in quarries (Giacomini et al 2006, Gili et al, 2016). In this study, we calibrate the model parameters using the same set of parameters *b*, and *Sr* (*q* of Perfect, 1997) for or all the blocks of each rockfall event. The resultant block size distribution (RFFM_RBSD) is fitted to the rockfall fragments distribution measured in the field (RBSD) (Figure 8 and Figure 9). We use the average parameters of the fragmentation model, despite the fact that the set of parametrs may be specific of each block, depending on the impact conditions.

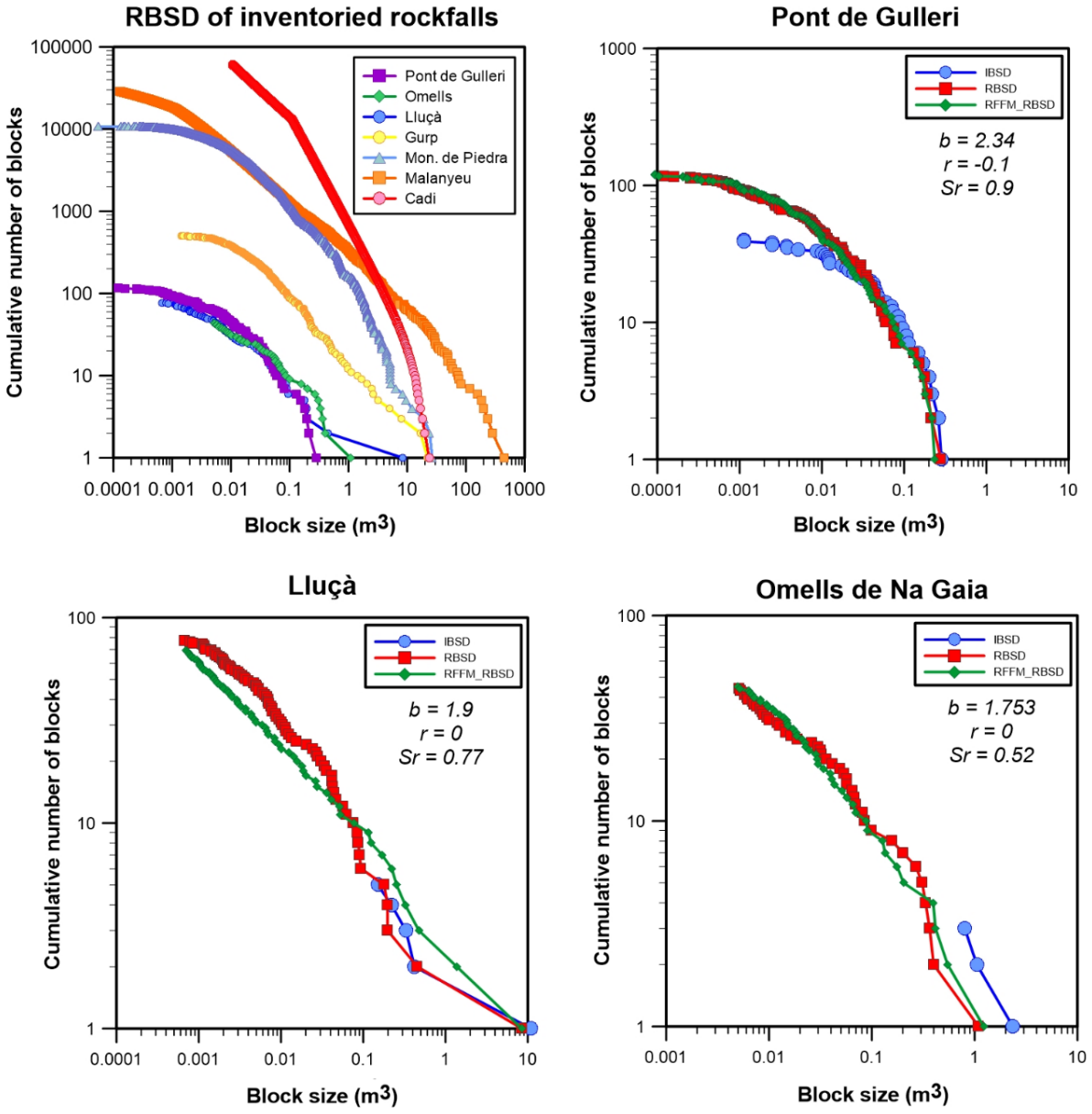

Figure 8: RBSD measured in the field (upper left) and RFFM calibrated using the RBSD and the IBSD of the Pont de Gulleri, Lluçà and Omells rockfalls.

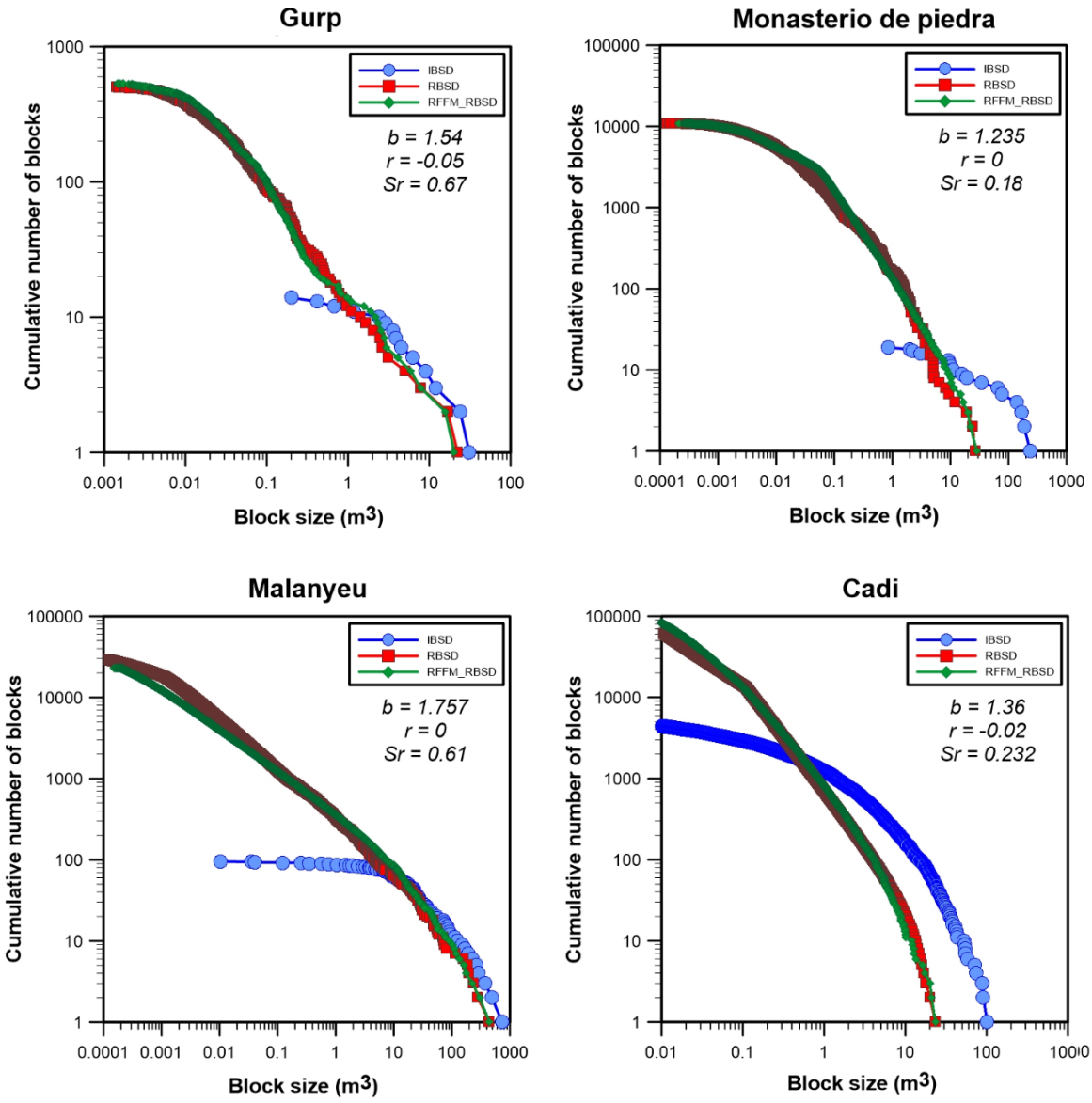

Figure 9: RFFM calibrated using the RBSD and the IBSD of the Gurp, Monasterio de Piedra, Malanyeu and Cadi rockfall events.

The biggest blocks of the deposit are the strongest ones, and their volumes are often close to the biggest blocks of the IBSD. It is worth noticing that the curve of the volume distribution of the largest fragments (either RBSD or RFFM distributions) is substantially parallel and very close to the curve of the IBSD, in all the cases. It is also interesting the change in the shape of the volume distribution for the smallest fragments. The distributions tend to flatten, evolving from a power law (straight line on a log-log plot) to an exponential curve (Figure 9). Two possible explanations are proposed for such a behavior. On one hand, the undersampling of the small-size fragments, on the other hand, the change of the pattern of breakage of the particles, when the reduction of the particle size requires the breakage of the mineralogical bonds or the rock matrix. This may

occur when the fragment size is smaller than the minimum joint spacing or weakness planes within the rock. This issue is related with the scale-variant behavior.

In order to obtain the calibrated model parameters, the reduced Chi squared (Xi_r^2**)** test is performed, comparing the fragment volumes' distribution of the RFFM and the measured RBSD, which is considered that real observation. The model parameters are summarized in Table 4. Notice the values of the geometric factor "*b"* range between 1.235 and 2.34, and the Survival rate from 0.18 to 0.9. The parameter "*r"* controls the variant or invariant behavior, yields 4 cases where it is equal to 0 (table 4), characterizing these rockfall events as a predominant invariant behavior. In all the cases, the Xi_r^2 ranges between 0.0004 and 0.018

The size of the smallest fragment measured in the field is the threshold used for the calibration of each rockfall event. The RFFM generates fragments until the minimum fragment size is reached. Then, the difference until the initial volume is considered fine fraction, in order to preserve the mass balance.

The Fractal Fragmentation Dimensions for the scale variant cases vary between a minimum and a maximum value (Dmin and Dmax in Table 4), as well as the probability of failure (Pmin and Pmax in Table 4), depending on the survival rate *"Sr"* and the exponent *"r"*.

Table 4: Summary of the model parameters calibrated and measured errors.

Rockfall	**b**	**r**	**Sr**	**Dmin**	**Dmax**	**Pmin**	**Pmax**	**Xi_r2**	**Vmin (m^3)**	**Fine fragments (m^3)**
1.PdG	2.34	-0.1	0.9	0.19	1.224	0.17	0.30	0.0001	0.0001	4.28E-08
2.Omells	1.76	0	0.52	1.701	1.701	0.48	0.48	0.0061	0.0007	0.00034
3.Lluçà	1.9	0	0.77	0.710	0.710	0.23	0.23	0.0180	0.0007	0.038
4.Gurp	1.54	-0.05	0.67	0.382	2.219	0.34	0.34	0.0054	0.0015	0.1
5.MdP	1.235	0	0.18	2.169	2.169	0.82	0.82	0.0048	0.001	62
6.Malanyeu	1.757	0	0.61	1.322	1.330	0.39	0.39	0.0049	0.0015	10
7.Cadi	1.36	-0.02	0.23	2.121	2.465	0.77	0.88	0.0022	0.01	489

4. Discussion

4.1 Survival rate

The survival rate *"Sr"* expreses the prortion of the original volume that remains unbroken and it is applied to each of the blocks of the IBSD. It defines the largest fragment *"l_{max}"* generated after the impact. In the presented calibration, the same set of model parameters are used for all the blocks of the rockfall events.

Despite the survival rate *"Sr"* (or largest fragment normalized by the total volume) has been suggested as descriptor of the degree of fragmentation (Bowman et al, 2012; Haug et al, 2016), we claim that the size of the largest fragment generated alone is not enough. Figure 10 shows two synthetic cases of the breakage of a 1 m^3 block, with the same survival rate (Sr=0.58) but with different number of fragments generated (3 on left and 10 on right). Despite being characterized with the same *"Sr"*, the scenarios generated are different. In the rockfall simulation, the results may differ substantially because the number and size of the new fragments determines the run-out, impact probabilities and the resultant kinetic energies. In risk analysis, this can have strong influence in the assessment.

Figure 10: Comparison of two synthetic cases with the same *Survival rate* and different number of fragments.

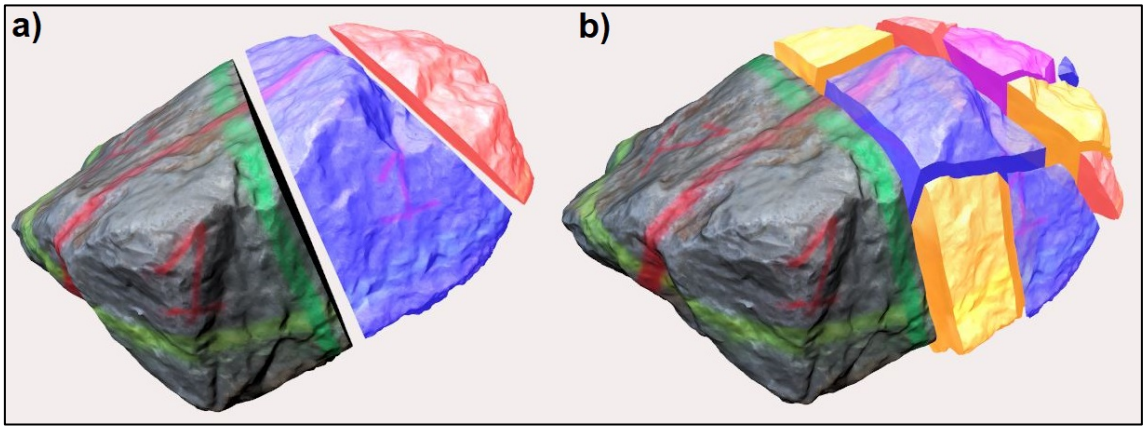

The two Block Size Distributions (BSD) shown in Figure 10, are plot in Figure 11. The largest fragment in both cases has the same volume (0.58 m3), as defined by the Survival rate, but the rest of the distribution changes due to the volumes generated in each case. The surface area of the initiator block is a 3D surface of 4.5 m^2, and the total surface area of the generated fragments increases up to 6.6 m^2 and 8.33 m^2 for the case of 3 and 10 fragments, respectively. The relation between the energy required to break the rock block and the amount of new area (fresh faces) generated in the fragments is known since long time ago. The third theory of fragmentation of Bond (1952), as unification of the first and second theories from Rittinger (1867) and Kick (1885

cited on Bond 1952) respectively, consider that the work needed to break particles of certain size although is initially proportional to their volume, it becomes proportional to the area as new surfaces are created. Consequently, besides S_r, additional descriptors are required to characterize the fragmentation process, due to the largest fragment (normalized by the initial volume as a proportion) is not enough to describe the new fragments distribution and the different energetic scenarios.

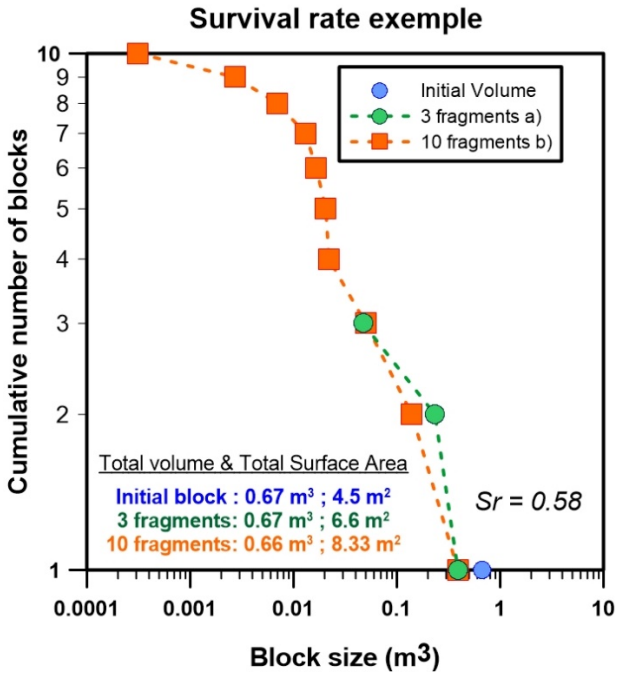

Figure 11: Comparison of two BSD from synthetic cases (Figure 2, *a* and *b)* with the same *Survival rate* and different number of fragments. Notice the increase on total surface from 4.5 $m^2$to 6.6 m^2 and 8.33 m^2.

According to the equation 6, the model parameters, "*Sr*" and "*b*", are related to the Fractal Fragmentation Dimension, and the trend can be observed graphically in the Figure 12 left. Comparing the model parameters with some rock mass properties, the RMR shows a positive correlation with the survival rate as may be expected, (Figure 12 right) however, the correlation with the geometric factor *b* is weak. Similarly occurs with the correlation with the Uniaxial Compressive Strength and the Tensile Strength (Figure 13).

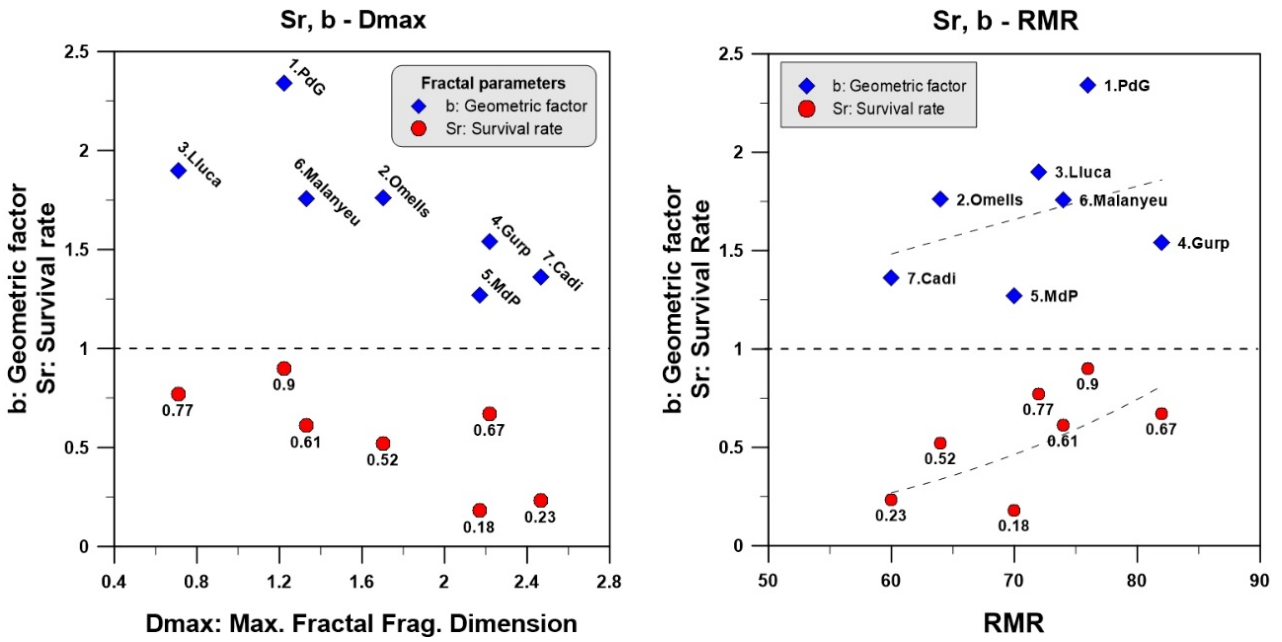

Figure 12: Calibrated model parameters *"b"* and *"Sr"* versus Max. Fractal Fragmentation Dimension (left) and Rock Mass Ratio, RMR (right).

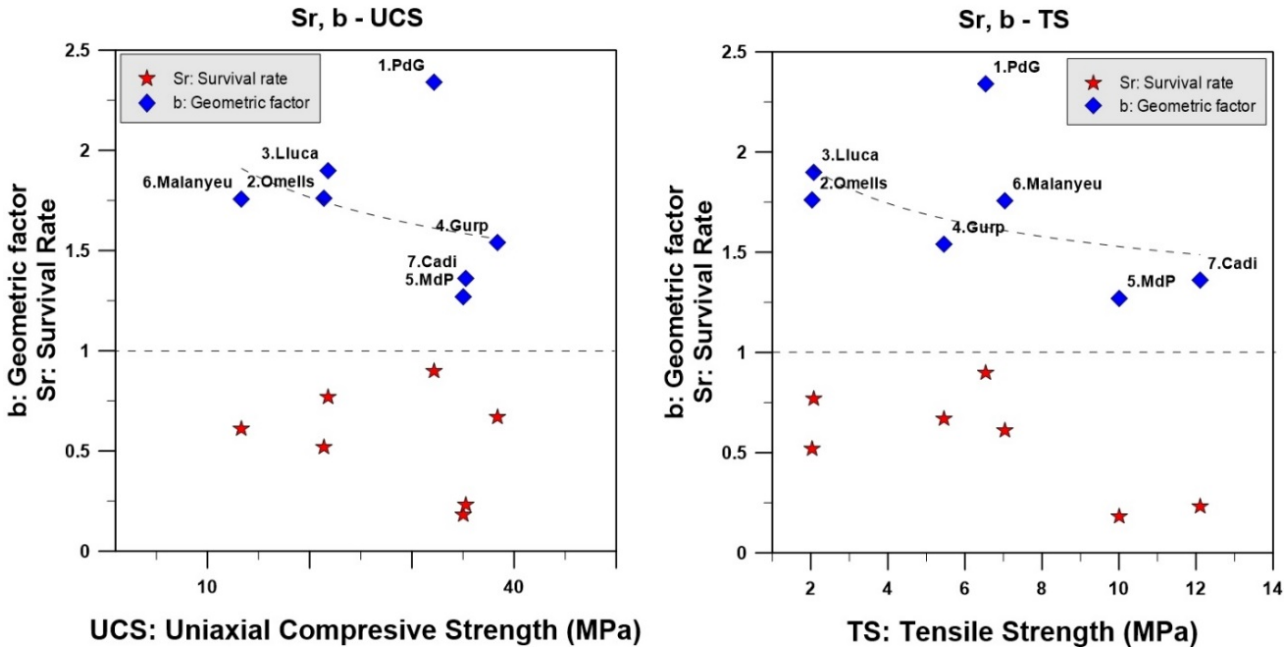

Figure 13: Calibrated model parameters *"b"* and *"Sr"* versus Uniaxial Compressive Strength (left) and Tensile Strength (right).

4.2 Number of fragments

The analysis of number of fragments generated is relevant because directly affects the probability of impact. Given the uncertainties of the quantification of the persistence of the joints, the number of initial blocks of the IBSD has to be considered a rough estimation. Instead, the total number rockfall fragments is well constraint.

Figure 14 (left) displays the total number of initial blocks (IBSD, blue dots), the deposited rockfall fragments (RBSD, red squares) and the results of the calibrated model (RFFM, green squares). The fitting the last two is satisfactory. The vertical displacement from the IBSD to both the RBSD and the RFFM shows the increase of the number of new blocks generated in each rockfall case. It is worth noticing that the total number of fragments increases as the total rockfall volume increases, as expected. Figure 14 (right) show the number of blocks normalized by the total rockfall volume. The normalized number of fragments ranges between 5 and 10 blocks/m^3 for event volumes of less than 100m^3, except in the Pont de Gulleri case, with 45 blocks/m^3.

Notice that Pont de Gulleri (PdG) and Cadi rockfalls contain more initial blocks than the expected from the observed trend. This is because the initial rock mass is intensely fractured becoming a very blocky rock mass. Monasterio de Piedra (MdP) and Malanyeu fall at the opposite end, with lesser number of initial blocks than the trend.

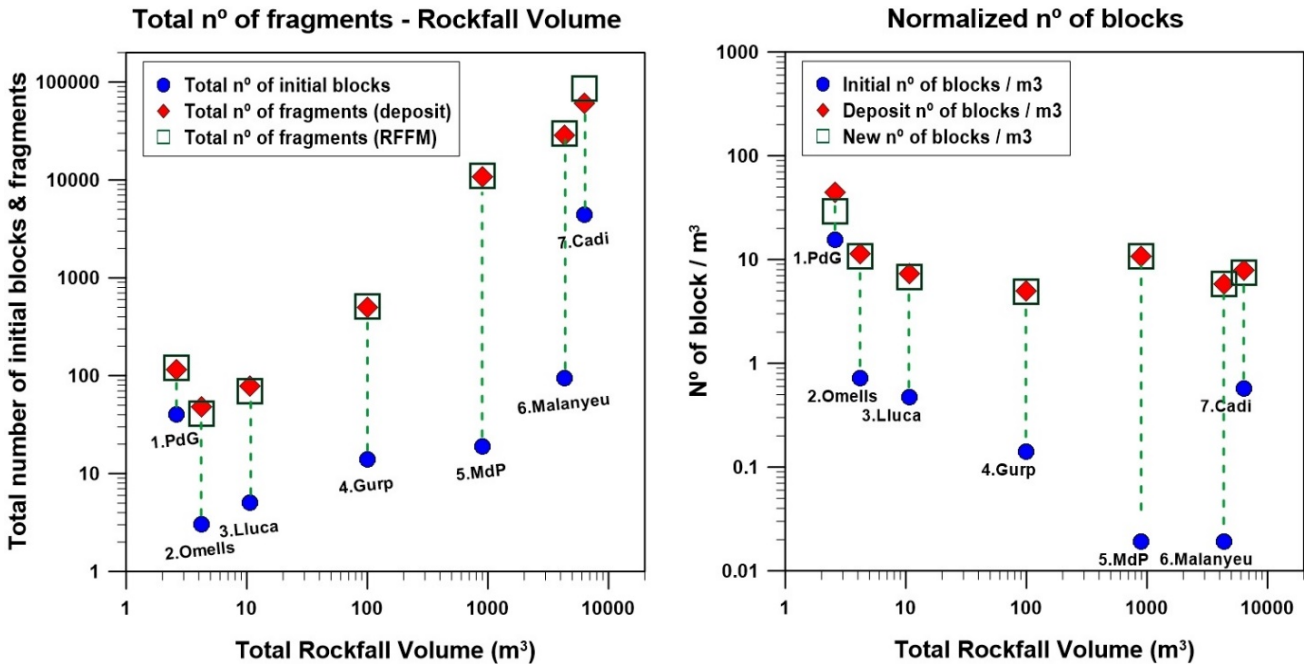

Figure 14: Left: Total number of initial blocks (of the IBSD, blue dots), fragments measured (red dots) and modelled fragments (green squares); Right: number of blocks normalized by the total rockfall volume.

4.3 Newly generated surfaces and energy

The breakage of the blocks generates new surfaces and the energy required to break the block can be related to the new area created (Kick 1885, Bond 1952, Locat et al, 2006, Crosta et al 2007). In order to analyze the latter, we measured the increase of the new surface area created.

We listed the 3D surface that bounds every block of the IBSD, and we sum all of them to obtain the total Initial Area (IA_{3D}). We also calculate the equivalent surface area of cubes having the same volume than the blocks of the IBSD (IA_{cubic}). This allows the comparison between the IA_{cubic} and the $IA_{3D,}$ being the latter bigger than the first one (blue columns in Figure 15). We also plot the rockfall scar 3D surface as the reference surface.

We define the Total Area (TA) as the total surface area of the deposited fragments, based on the the RFFM results (TA_{RFFM}) and based on the RBSD list of volumes (TA_{RBSD}) also ploted in Figure 15 (green and red columns respectively). The estimated cubic area is included in both cases because usually only the available data are a list of volumes, not the areas. Figure 15 shows that the area can reasonably be calculated from the volume.

The cubic estimation of the areas was also applied to the RBSD. We measured 3 lengths of each fragment of the inventoried rockfalls and calculated the surface area of each fragment assuming a prismatic shape. Adding all of them, we obtain the total surface area based on the 3 lengths measured (TA_{RBSD} measurements prismatic). We also used the cubic estimation based on the list of volumes measured (TA_{RBSD} measurements cubic estimation). The comparison (last two columns in Figure 15) shows that there is not significant difference between the prismatic and the cubic estimation to obtain the total surface area of the fragments.

The TA_{RBSD} (red column in Figure 15) and the TA_{RBSD} from measurements (the last two columns in Figure 15) differ in the Monasterio de Piedra (Mdp), Malanyeu and Cadi cases. This may be explained by the use of sampling plots for estimating the block size distribution of the fragments. In the other cases, all the blocks of the deposit were measured directly, and then, shows similar or equal values of TA. Furthermore, the proposed fragmentation model reproduces the TA in a satisfactory way, being the TA_{RBSD} (red column) and the TA_{RFFM} (green column) very similar in all the cases,

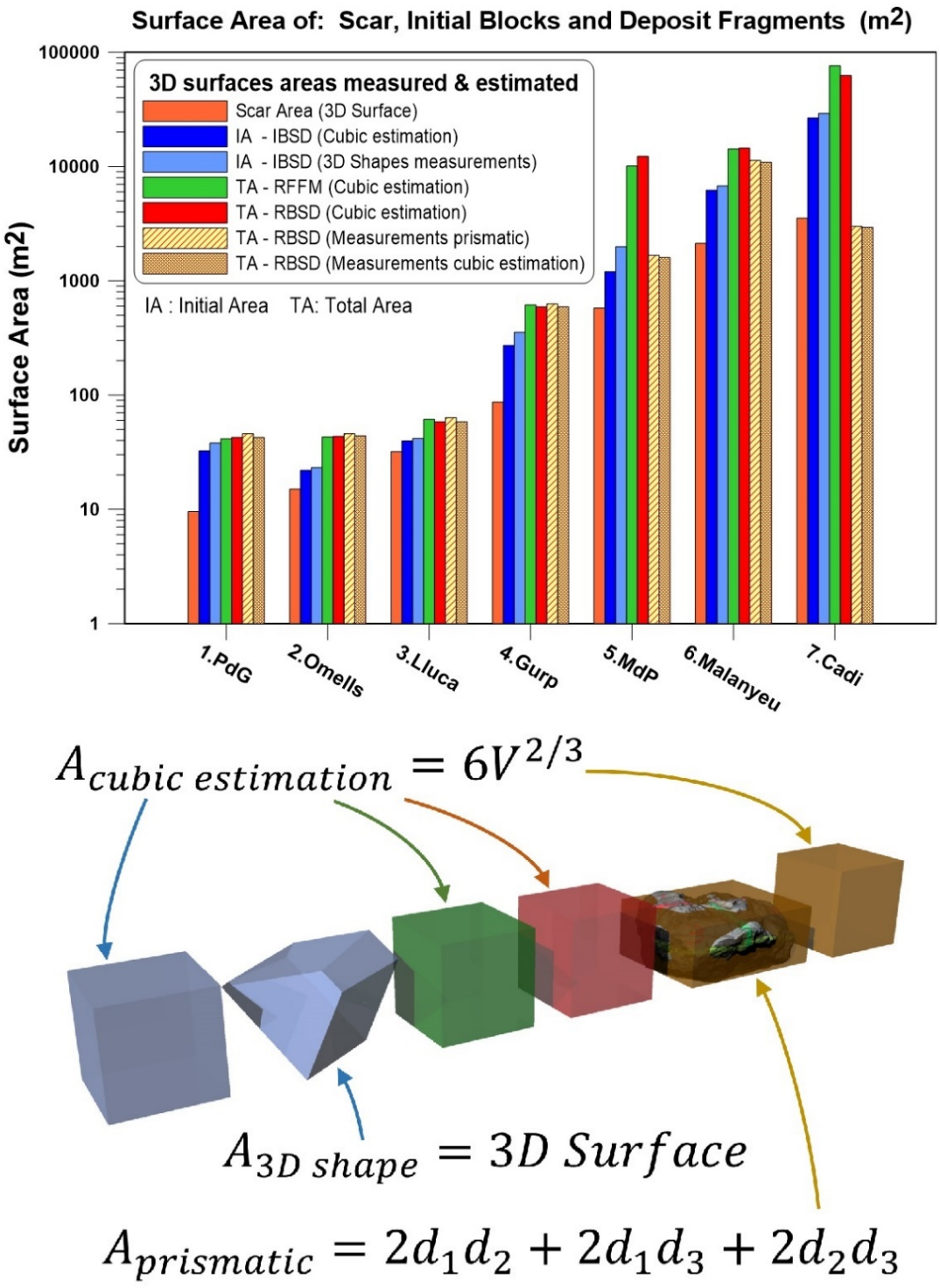

Figure 15: Surface areas calculated and/or estimated of: 3D scar surface (first column); Initial surface area (IA) from the IBSD using a cubic estimation or from 3d shapes of the blocks modelled (blue columns); Total surface area (TA) from RFFM and RBSD list of volumes using a cubic estimation (gren and red columns respectively); Total surface area (TA) from fragments measurements, assuming a prismatic shape using the distnaces measured or the cubic estimation from the list of volumes (las two columns)

The difference between the IA_{cubic} and the TA (using TA_{RBSD} or TA_{RFFM}, both cubic estimations), yields the new surface area (NA) generated by breakage, defined as: $NA_{RBSD} = TA_{RBSD} - IA_{cubic}$ and $NA_{RFFM} = TA_{RFFM} - IA_{cubic}$. A very good correlation is found by fitting a power law to the total volume of the rockfall (Figure 16, left). The coefficients of determination R-squared are 0.971 for the NA_{RFFM} and 0.96 for the NA_{RBSD}.

Spreafico et al (2017) and Blasio & Crosta (2016) stated that there exists a relation between the new surface area generated (NA) and the fragmentation energy. This is confirmed in Figure 16 right, the total potential energy of the rockfall event and the potential energy of the first impact on the ground have been plotted against the new surface area created. A power law can be fitted with coefficients of determination R-squared of 0.96 (based on Total Potential Energy) and 0.90 (based on 1st impact potential energy), both cases using the NA_{RFFM}.

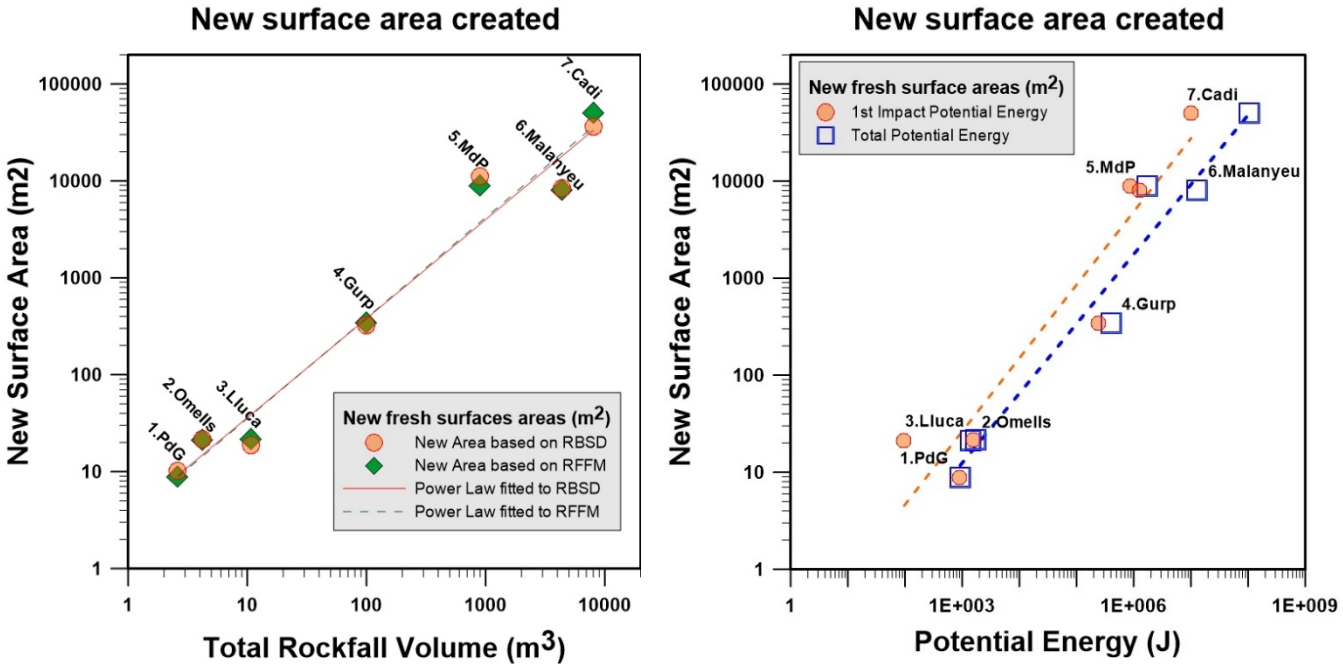

Figure 16: Left: New surface area from RBSD (NA_{RBSD}) or from RFFM (NA_{RFFM}) versus Total rockfall volume. Right: New surface area (NA_{RFFM}) versus Total Potential Energy and the 1st Impact Potential Energy.

The Specific Surface Area (SSA) is a property of solids defined as the total surface area of a material per unit volume (m^2/m^3). The total surface areas IA, TA and NA are normalized by the total rockfall volume, obtaining the Initial Specific Surface Area (ISSA), the Total Specific Surface Area (TSSA) and the New Specific Surface Area (NSSA) with units of m^2/m^3, summarized on the Table 5.

Table 5: Initial Specific Surface Area (ISSA) representing the initial state in the cliff; Total Specific Surface Area (TSSA) representing the deposited fragments; New Specific Surface Area (NSSA) representing the new surfaces related with the breakage; and the proportion of NA over TA in percentatge (equal to NSSA/TSSA).

Rockfall	Initial Area / Total volume **ISSA (m^2 /m^3)**	New Area / Total volume **NSSA (m^2 /m^3)**	Total Area / Total Volume **TSSA (m^2 /m^3)**	**NA / TA (%)**
1.PdG	12.5	3.4	15.9	21
2.Omells	5.2	5.0	10.2	49
3.Lluca	3.7	2.0	5.7	35
4.Gurp	2.7	3.4	6.1	56
5.MdP	1.3	8.8	10.1	87
6.Malanyeu	1.3	1.6	2.9	56
7.Cadi	3.5	6.5	10.0	65

Figure 17 shows the ISSA (in blue), the NSSA (stacked in orange) and the TSSA (adjacent column in red). Also the proportion of NA/TA (equal to NSSA/TSSA) is plotted as a percentage. The ISSA column represents the initial surfaces per volume unit, defining the initial degree of fracturation of the rock mass. The NSSA quantify the new area created by breakage. From our point of view of fragmentation, vertical bars represent the proportion between disaggregation (previously existing surfaces) and breakage (new surfaces).

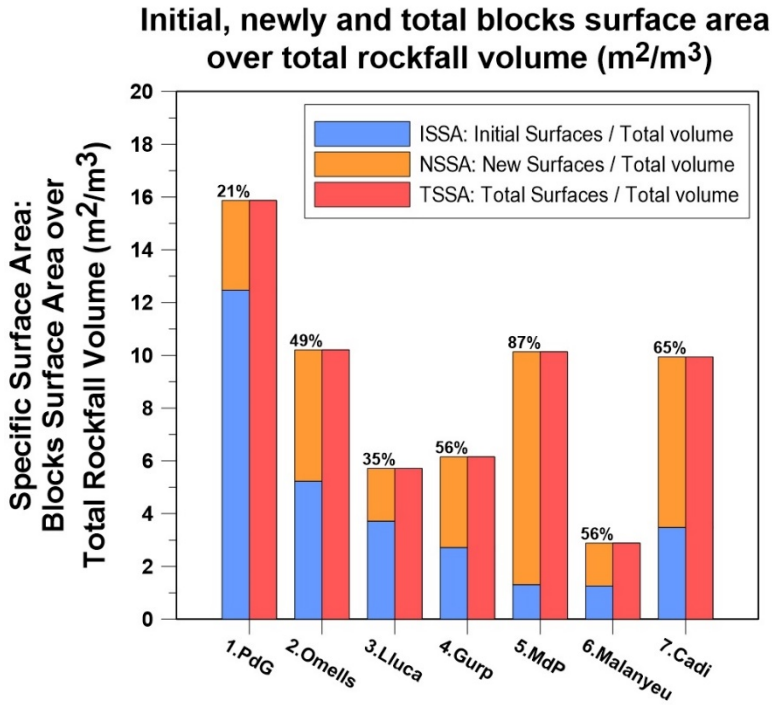

Figure 17: Initial, New and Total Specific Surface Area (ISSA, NSSA and TSSA). Left bar stacks the ISSA (in blue, from IBSD) and the NSSA generated by breakage (in orange, with the percentage that represent over the TSSA labelled on the top). Right bar represents the TSSA representing the deposited blocks (in red, from RBSD).

Pont de Gulleri case (PdG) shows the higher value of TSSA, however, only the 21% of the surfaces are related with new surfaces and breakage. It means that the 79% of the surfaces are preexisting from a very jointed rock mass as show the ISSA value of 12.5 m^2/m^3. From our point of view, the fragmentation is predomined by dissagregation on this case.

Monasterio de Piedra (MdP), Cadi and Omells events, shows TSSA values close to 10 m^2/m^3 with different proportion of newly surfaces: 87%, 65% and 49% respectively, being the Monasterio de Piedra the event with the highest breakage ratio, followed by the Cadi event. In comparison, Lluçà, Gurp and Malanyeu cases show low values of TSSA and are interpreted as events with less breakage. In the latter events, a few blocks remain unbroken or less affected: Lluçà with a block of 8,5 m^3 over the 10,7 m^3 of total detached mass; Gurp with two blocks of more than 20 m^3 over the total 100 m^3 of rockfall; and Malanyeu, where the deposit includes 7 blocks greater than 100 m^3, and more than 60 blocks greater than 10m^3, with a maximum boulder of 445 m^3.

The ISSA values of MdP and Malanyeu events are 1.3 m^2/m^3, suggesting similar initial joint pattern conditions. However, Malanyeu is 5 times bigger and MdP generates more new surfaces (TSSA of 10 m^2/m^3 compared to 3 m^2/m^3 in Malanyeu).

The model p arameters show a trend with the NA (Figure 18, left) and a distinct correlation with the proportion of NA/TA (Figure 18, right). By decreasing the geometric factor *"b"* and the survival rate *"Sr"*, the NA/TA increase, increasing the proportion of new fresh faces related to breakage.

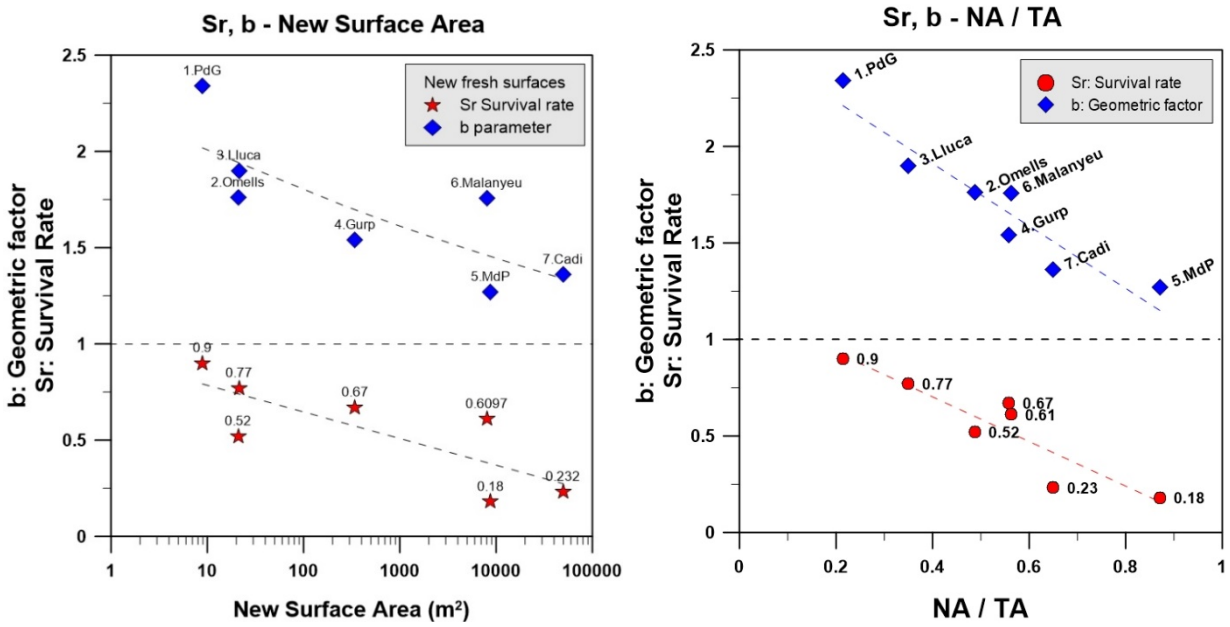

Figure 18: Model parameters "b" and "Sr" versus New Surface Area created, NA (Left), and versus the proportion of New Area over the Total Area (NA/TA).

5. Summary and conclusions

Perfect (1997) highlights the importance of describing describe the initial state of a brittle material before and after the fragmentation to study properly the phenomenon. We make efforts in order to characterize as well as possible the IBSD (In situ Block Size Distribution) and the RBSD (Rockfall Block Size Distribution) in order to improve the fragmentation understanding and to test the proposed fractal fragmentation model with real data.

UAV and digital photogrammetric techniques are very useful in order to obtain detailed 3D models of the whole scenario, and specifically, of the scar. From the latter, it is possible to reconstruct the detached volume and characterize the joint pattern. We worked with the real position of the modelled joints and assumed infinite persistence, as hypothesis (as a first approach). The reconstructed volume is cut in order to estimate the IBSD. We inventoried 7 rockfalls with total volumes ranging between 2,6 m^3 and 10.000 m^3, measuring more than 7200 fragments of the deposits (3 lengths with a tape assuming prismatic shape) in order to obtain the RBSD of each inventoried rockfall event. Using the IBSD as input, and the RBSD as real results, we calibrate the model parameters to simulate the RBSD and the estimation of the new surfaces created. Both outputs are useful for energetic estimations propagations models, and QRA analysis considering multiple impacts due to fragmentation.

The model is able to reproduce satisfactorily the measured RBSD, from the IBSD. In this paper, the model is upgraded, introducing two main improvements:

1) Avoidance of bins, working in cumulative form and conserving the mass balance: With the use of bins, all the fragments from each size bin in the IBSD is defined by an average size, and the fragments created on each iteration are equal size. Due to this, the mass balance cannot be achieved. The upgraded model uses each initial block of the IBSD (list of volumes) as initiator, and generates an accumulated number of fragments of decreasing size that fits better to the observations, specially in the case of a single block as initiator like in the real-scale fragmentation test on quarry. The model generates fragments until the sum of fragments is equal to the initiator initial volume, or until the fragments become smaller than a threshold value. The remaining mass is computed as volume of fine fragments (finer than the threshold defined). Thus, the upgraded model conserves the mass balance.

2) The use of the scale-variant behavior: Based on the RBSD measured in the deposits and from the block size distributions measured in real-scale fragmentation tests, a scale-variant (or scale-dependent) behavior is observed. The upgraded model uses the formulation proposed by Perfect

(1997) for scale-variant fragmentation. The probability of failure is defined by the probability of survival or Survival rate (*Sr*), and represents the largest unbroken part of the block normalized by the initial block volume. The survival rate controls whether a block breaks or not, being 1 for unbroken blocks. In Ruiz-Carulla et al (2017), the survival rate represented the proportion of unbroken blocks of each bin size from the IBSD. Here, the Sr is applied over each initiator instead to the global number of initial blocks. Then, a new parameter "*r*" controls de scale dependency making blocks either stronger or weaker by decreasing their size. This happens when the fragment size is smaller than the minimum joint spacing or weakness planes within the rock mass. The geometrical factor "*b*" still controls the proportion between the size of the blocks and fragments generated. The upgraded model is able to reproduce all kind of block size distributions observed in natural rockfall deposits and of real-scale fragmentation test, even when the initiator is a single block.

In this study, we calibrate the model parameters using the same set of parameters *b, r* and *Sr* for all the blocks of each rockfall event. The calibrated values of the geometric factor "*b"* range between 1.235 and 2.34, and the Survival rate from 0.18 to 0.9. The parameter "*r"* controls the variant or invariant behavior, yields 4 cases where it is equal to 0, characterizing these rockfall events as a predominant invariant behavior. In all the cases, the Xi_r^2 used to calibrate the model ranges between 0.0004 and 0.018. We use the average parameters of the fragmentation model, despite the fact that the set of parameters can be specific of each block, depending on the impact conditions. Future trajectory simulators considering fragmentation will be able apply a different set of parameters for each block at each impact. The controlling factors is the focus of our future research. By now, the capacity to absorb energy of the terrain, despite its relevance is difficult to quantify, as well as the total potential energy, the impact conditions (impact angle) and the shape of the blocks.

The RMR shows a positive correlation with the survival rate, however, the correlation with the geometric factor *b* is weak. Similarly occurs with the correlation with the Uniaxial Compressive Strength and the Tensile Strength without direct correlations. It may be noticed a relation between the 3d surface area of the scar and the total rockfall volume, as well as the number of fragments and new area created in a wide range of orders of magnitude. The new area created is related with the fragmentation energy, and seems to be directly correlated with the total rockfall volume as well as total potential energy.

The specific surface area of the initial blocks (ISSA) and the resultant fragments (TSSA) is estimated. The proportions of Initial, New and Total Specific Surface Area of the blocks characterize the fragmentation scenario. The ISSA (Initial Specific Surface Area) is the one

generated by disaggregation of the rock mass through the preexisting discontinuities, and is determined by the IBSD. There exists a direct relation between the NSSA (New Specific Surface Area) and the breakage of the rock creating new surfaces. Based on this, we interpret the more or less predominant fragmentation behavior based on the proportion of New Surface Area over Total Surface Area (NA/TA = NSSA/TSSA). The model parameters show a clear correlation with the proportion of NA/TA.

However, the number of inventoried cases is too small to generalize these findings. The fragmentation process is a very complex phenomenon where small details that may affect the final results. From real-scale fragmentation test, we observed how 30 similar blocks dropped from the same height on the same place yields Sr ranging between 0.2 and 1 (unbroken) depending on the local impact conditions and the block shape. For these reasons, a probabilistic approach of the fragmenation should still be used.

Acknowledgments

The authors acknowledge the support of the Spanish Economy and Competitiveness Ministry and the European Regional Development's funds (FEDER), to the Rockmodels research project (BIA2016-75668-P) and the support of the Ministry of Education to the first author (grant code FPU13/04252).

References

Blasio F. V., Corsta G. B. (2016) Extermly Energetic Rockfall: Some Preliminar estimates. 12th International Symposium on Landslides (ISL 2016) Landslides and Engineered Slopes. Experience, Theory and Practice – Aversa et al. (Eds) © 2016 Associazione Geotecnica Italiana, Rome, Italy, ISBN 978-1-138-02988-0.

Bond F C (1952) The third theory of comminution, Transactions of the American Institue of Mining and Metallurgical Engineers, 193. 494-495

Bowman ET, Andrew Take W (2014) The Runout of Chalk Cliff Collapses in England and France — Case Studies and Physical Model Experiments.” Landslides, Volume 12 (2), pp: 225-239. doi: 10.1007/s10346-014-0472-2

Charrière M, Humair F, Froese C, Jaboyedoff M, Pedrazzini A, Longchamp C (2015) From the source area to the deposit: Collapse, fragmentation, and propagation of the Frank Slide. Geological Society of America Bulletin. doi: 10.1130/B31243.1

Crosta GB, Frattini P, Fusi F (2007) Fragmentation in the Val Pola rock avalanche, Italian Alps. Journal of Geophysical Research, 112: p. F01006

Dewez T, Girardeau-Montaut D, Allanic C, Rohmer J (2016) Facets: A CloudCompare plugin to extract geological planes from unstructured 3d point clouds. XXIII ISPRS Congress, Jul 2016, Prague, Czech Republic. XLI-B5, pp.799-804, 2016, International Archives of the Photogrammetry Remote Sensing and Spatial Information Sciences.

Giacomini A, Buzzi O, Renard B & Giani, G P (2009) Experimental studies on fragmentation of rock falls on impact with rock surfaces. Int J Rock Mech Min Sci 46:708–715

Gili JA, Ruiz-Carulla R, Matas G, Corominas J, Lantada N, Núñez MA, Mavrouli O, Buill F, Moya J, Prades A, Moreno S (2016) Experimental study on rockfall fragmentation: in situ test design and firsts results. In: Aversa S, Cascini L, Picarelli L, Scavia C (eds) Landslides and engineered slopes, 2: 983-990.

Girardeau-Montaut (2006) Detection de Changement sur des Données Géométriques 3D", D. PhD manuscript (french), Signal & Images Processing, Telecom Paris

Haug ØT, Rosenau M, Leever K, Oncken O (2016) On the energy budgets of fragmenting rockfalls and rockslides: Insights from experiments, J. Geophys. Res. Earth Surface, 121, 1310–1327, doi:10.1002/2014JF003406.

Locat P, Couture R, Leroueil S, Locat S (2006) Fragmentation Energy in Rock Avalanches. Canadian Geotechnical Journal 851 (20060135): 830–51. doi:10.1139/T06-045

Perfect E (1997) Fractal models for the fragmentation of rocks and soils: a review. Engineering Geology 48:185-198

Rittinger, P. R. “Lehrbuch der Aufbereitungskunde,” Berlin, 1867.

Ruiz-Carulla R, Corominas J, Mavrouli O (2015) A Methodology to Obtain the Block Size Distribution of Fragmental Rockfall Deposits. Landslides 12 (4): 815–25. doi:10.1007/s10346-015-0600-7.

Ruiz-Carulla, R., Corominas, J. & Mavrouli, O. Landslides (2017) A fractal fragmentation model for rockfall. Landslides 14 (3): 875-889. doi.org/10.1007/s10346-016-0773-8

Spreafico MC, Franci F, Bitelli G, Borgatti L, Ghirotti M (2017). Intact rock bridge breakage and rock mass fragmentation upon failure: quantification using remote sensing techniques. The Photogrammetric Record Vol 32, Issue 160: Pages 513-536 https://doi.org/10.1111/phor.12225

Thiele ST, Grose L, Samsu A, Micklethwaite S, Vollgger SA, Cruden AR (2017) Rapid, semi-automatic fracture and contact mapping for point clouds, images and geophysical data. Solid Earth, 8: 1241-12535.

ANNEX A: Block size distribution from calibration process on the inventoried cases.

Block size distribution from calibration process on the inventoried cases.

Pont de Gulleri

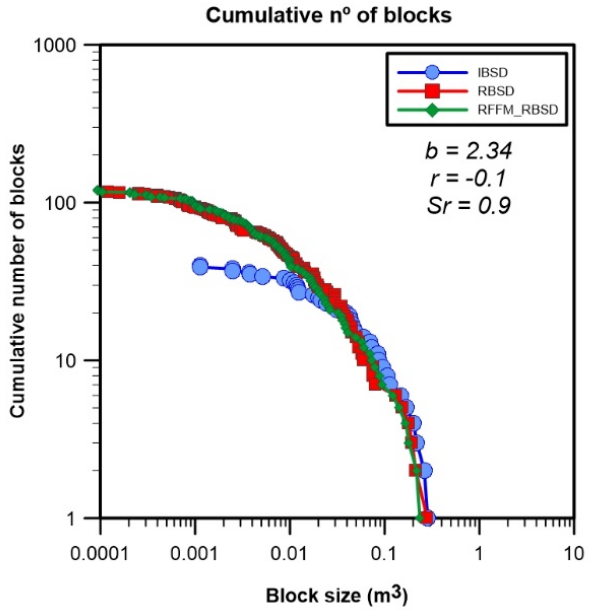

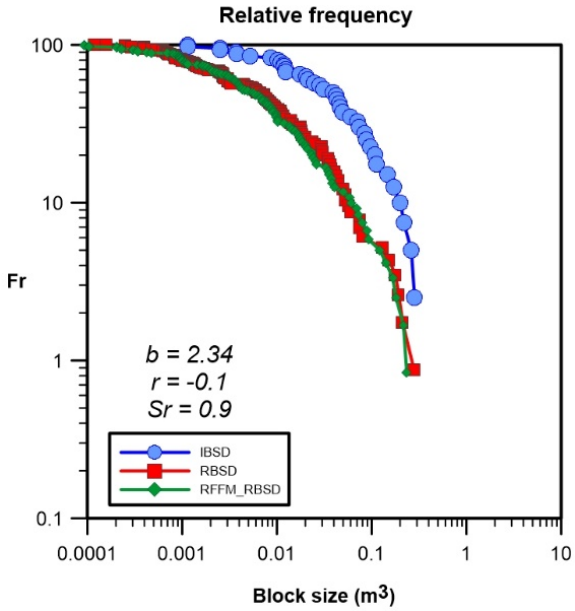

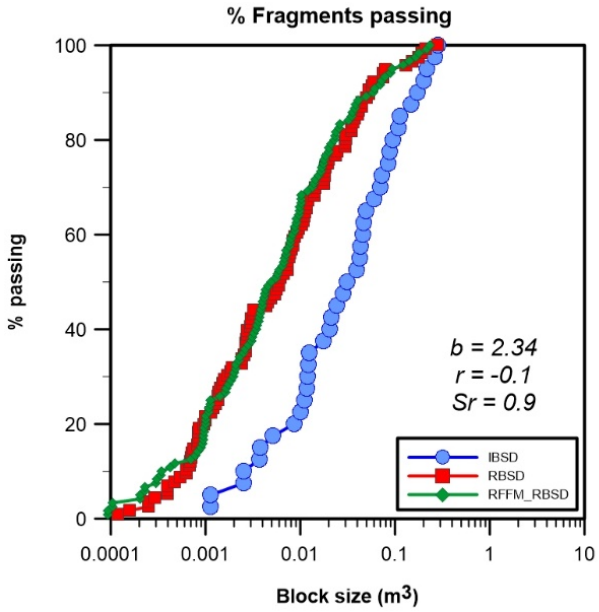

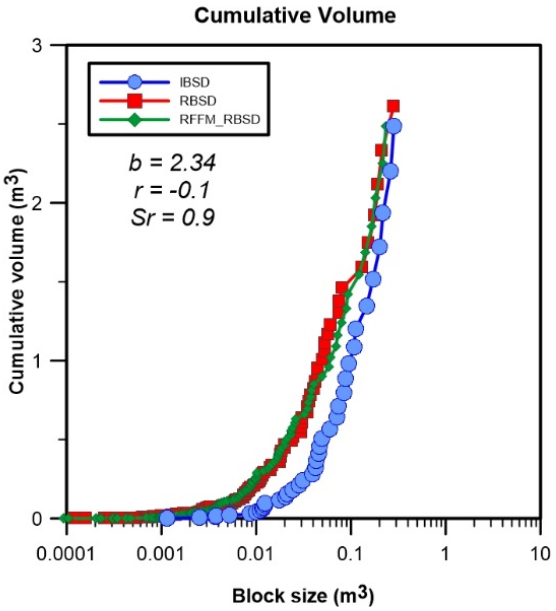

Omells de Na Gaia

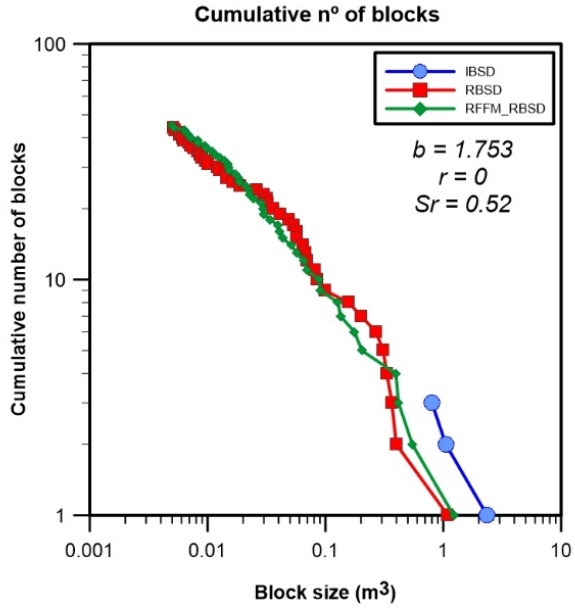

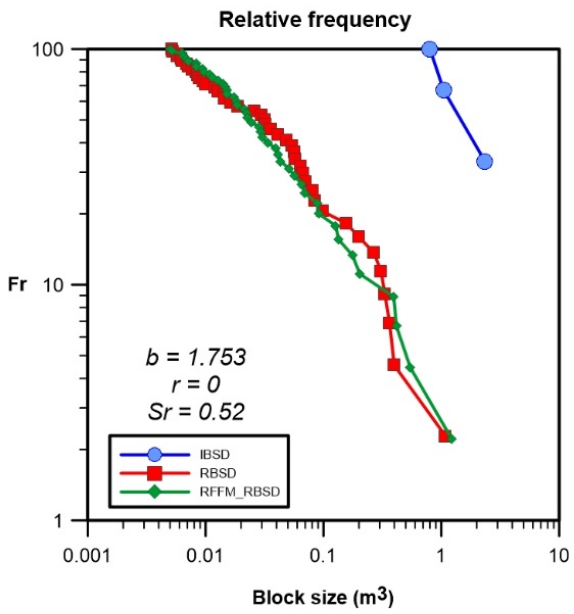

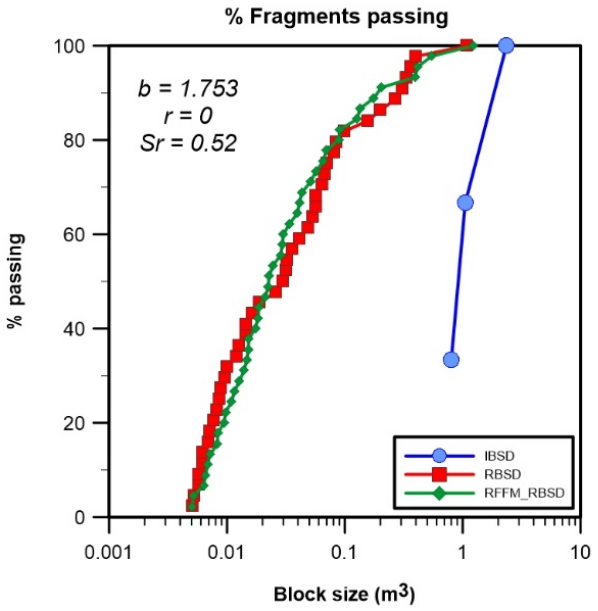

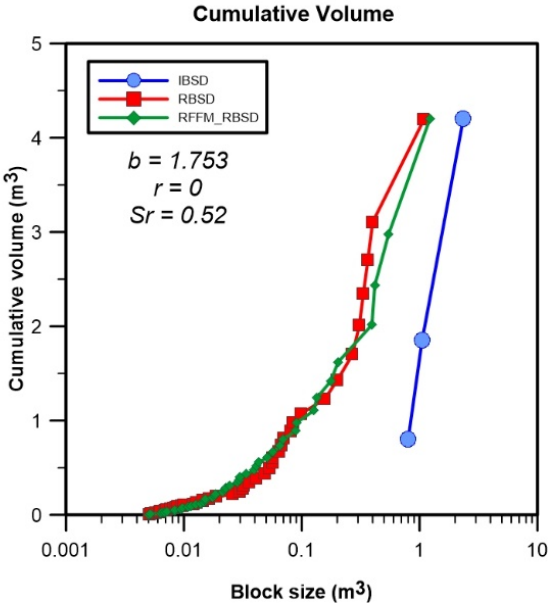

Lluçà rockfall

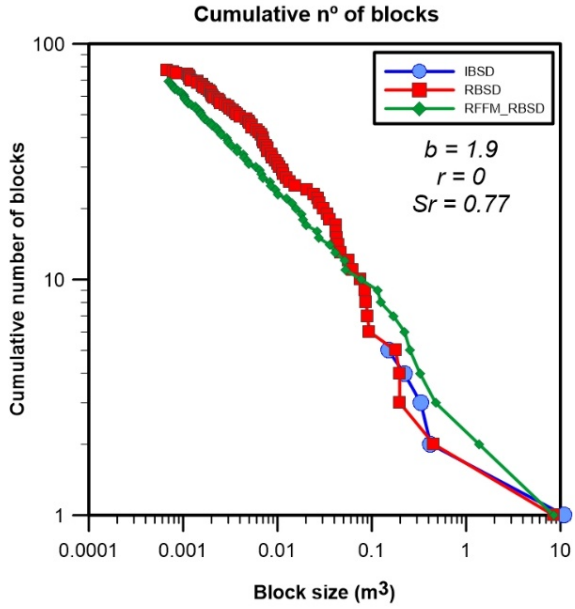

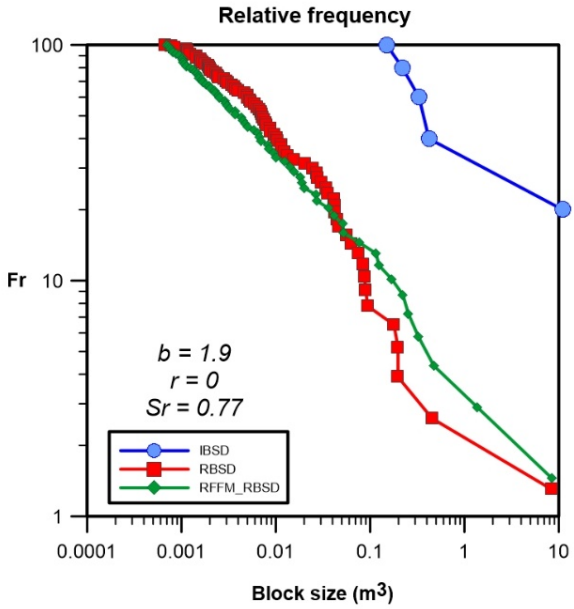

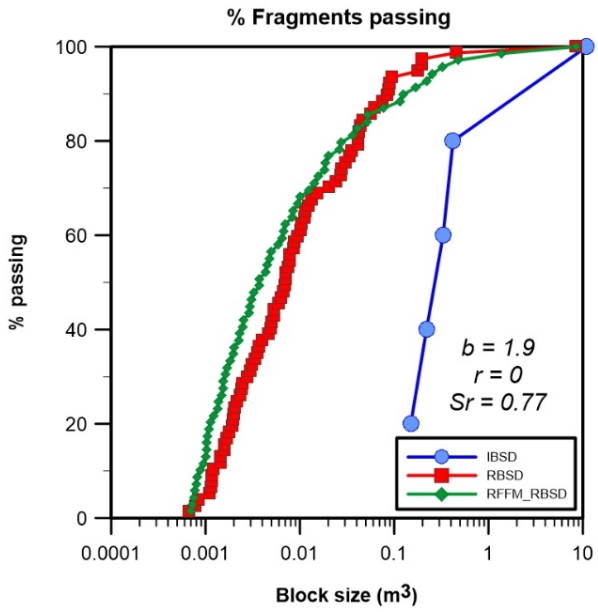

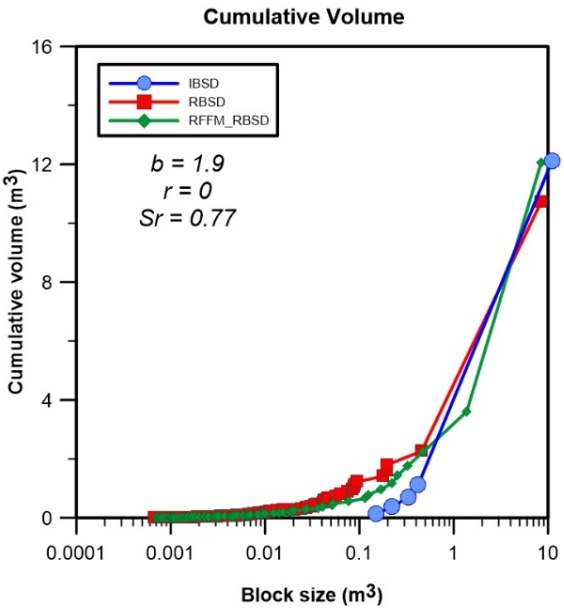

Gurp rockfall

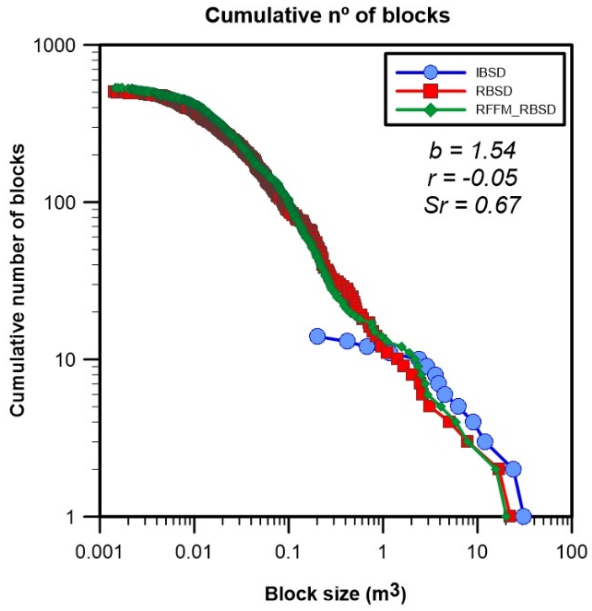

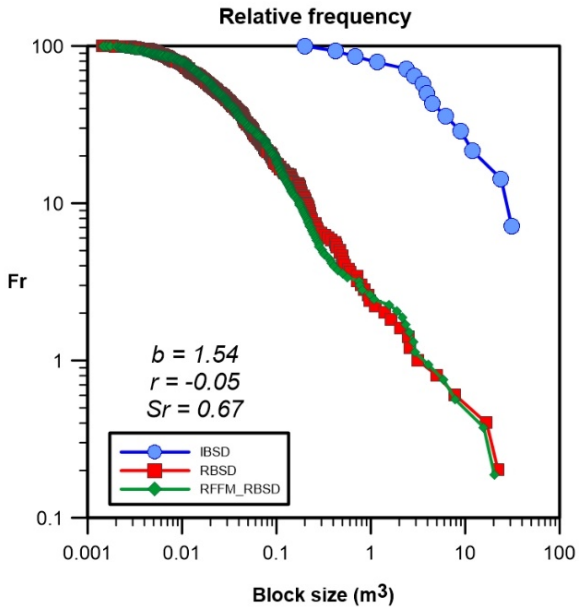

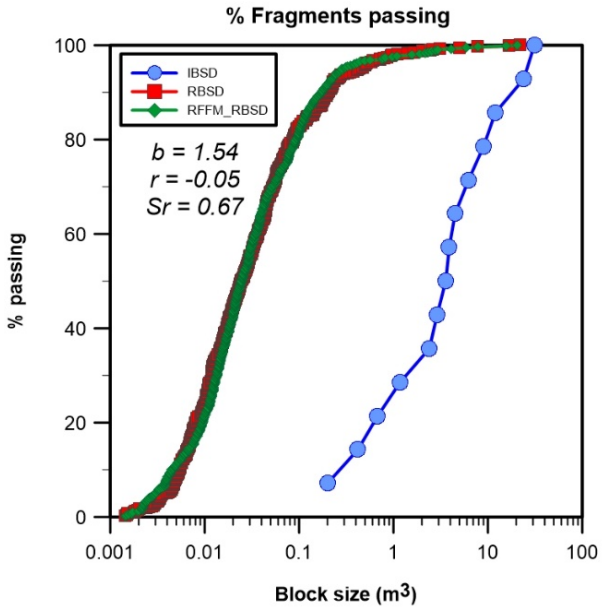

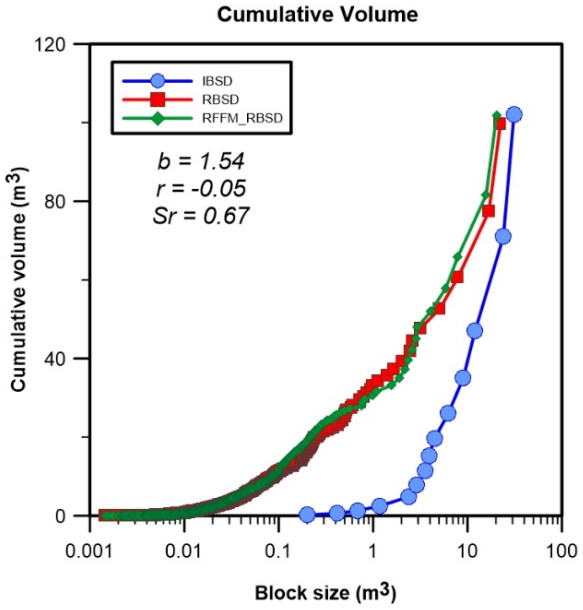

Monasterio de piedra rockfall

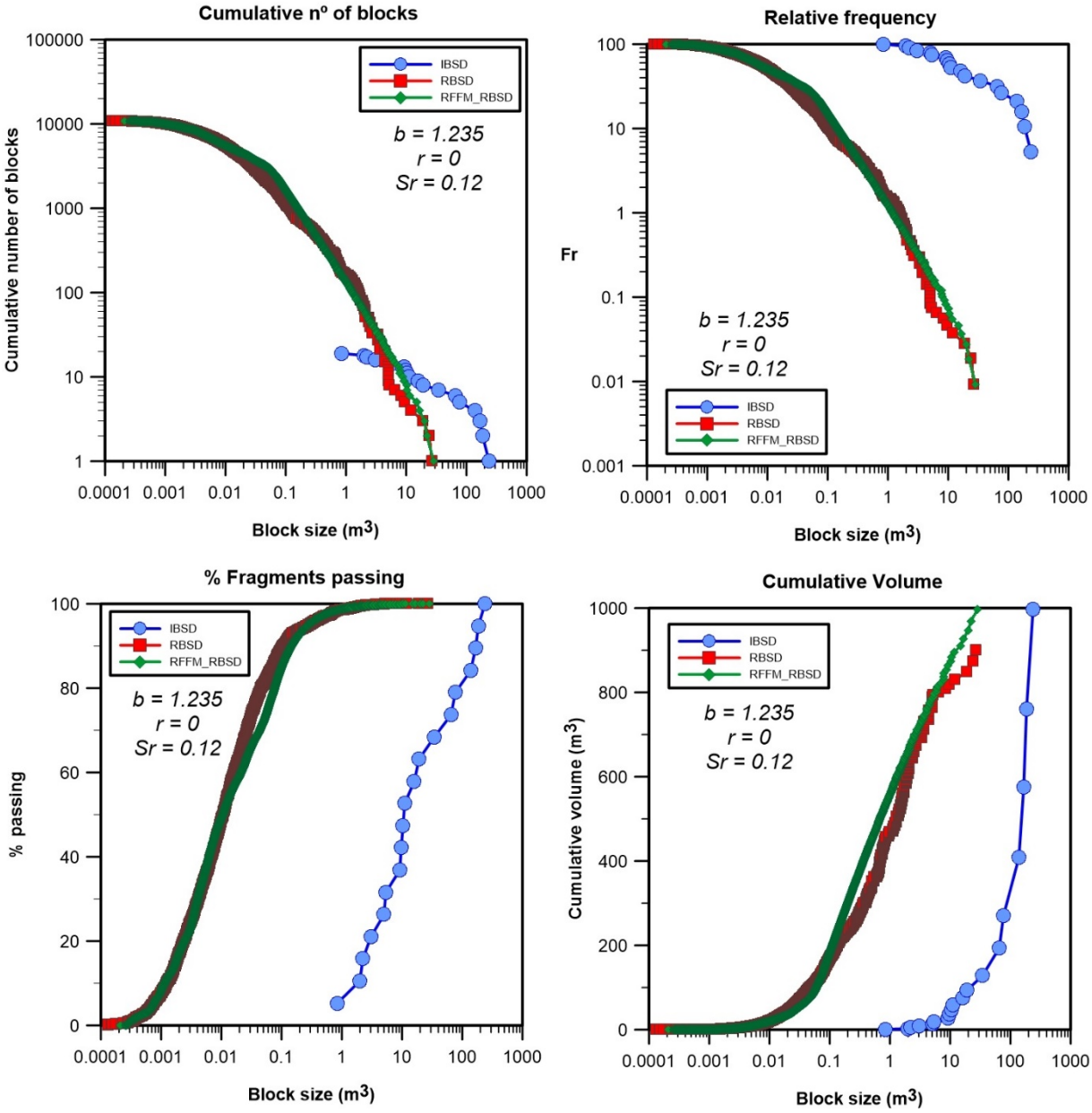

Malanyeu rockfall (SV)

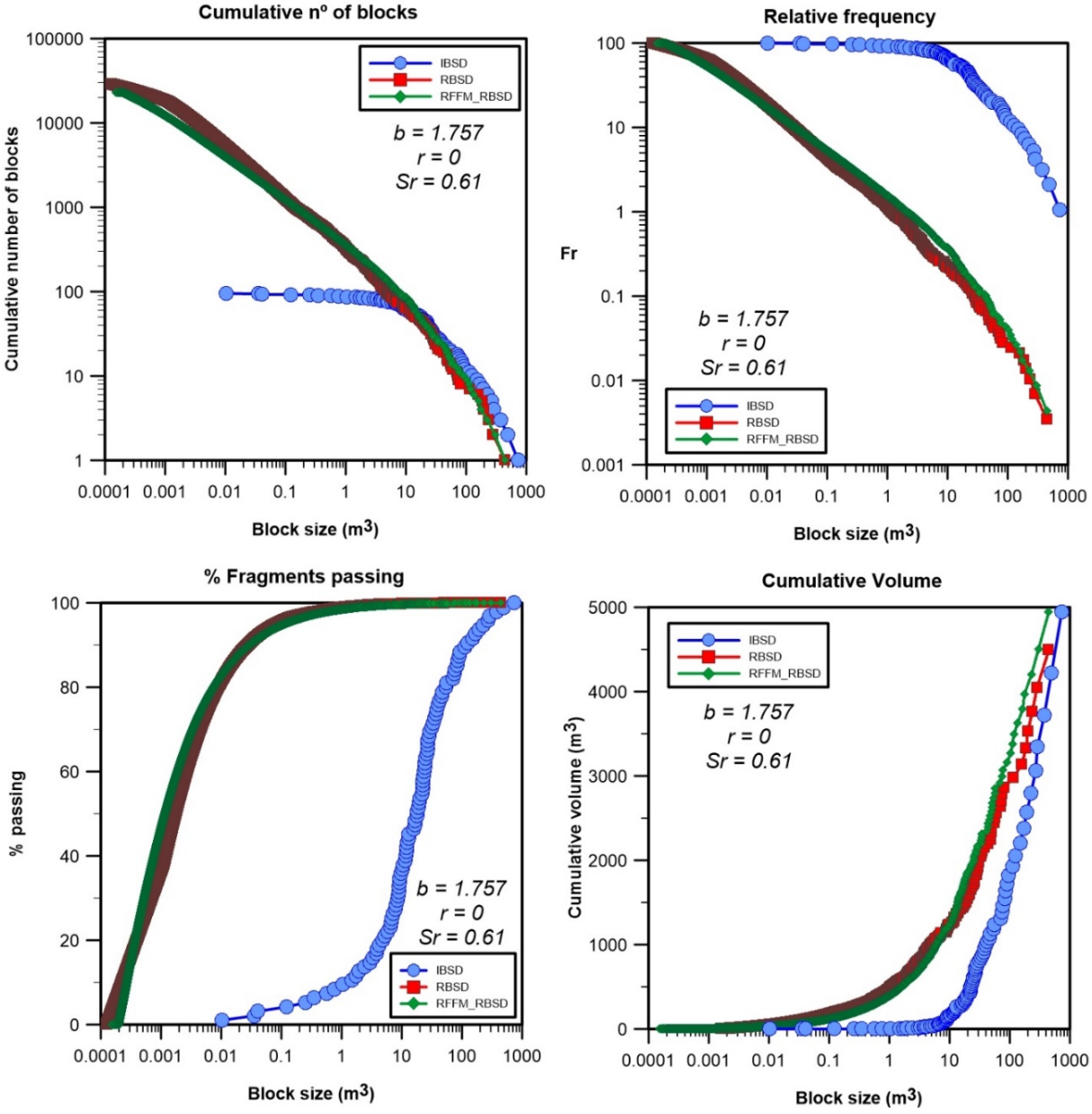

Cadi rockfall

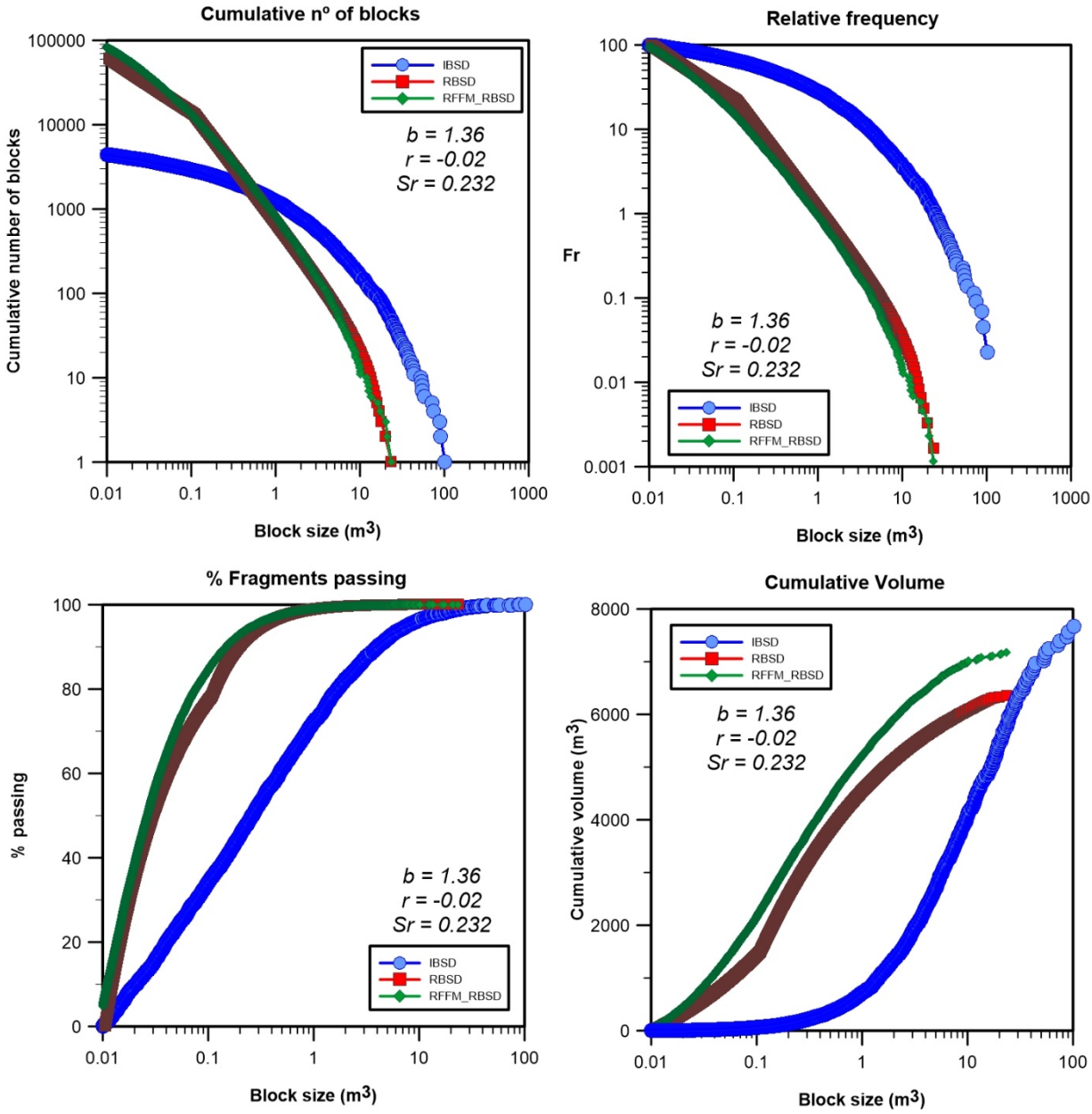

PART IV

Applications

11- Magnitude and Frequency relations: are there geological constraints to the rockfall size?

12- Quantitative Analysis of Risk due to Fragmental Rockfalls

11. Magnitude and Frequency relations: are there geological constraints to the rockfall size?

Publication reference:

Corominas J, Mavrouli O & Ruiz-Carulla R, (2018) Magnitude and Frequency relations: are there geological constraints to the rockfall size? Landslides Landslides, Volume 15 Issue 5, pages: 829-845. https://doi.org/10.1007/s10346-017-0910-z

Abstract. There exists a transition between rockfalls, large rock mass failures and rock avalanches. The magnitude and frequency relations (M/F) of the slope failure are increasingly used to assess the hazard level. The management of the rockfall risk requires the knowledge of the frequency of the events but also defining the worst case scenario, which is the one associated to the maximum expected (credible) rockfall event.

The analysis of the volume distribution of the historical rockfall events in the slopes of the Solà d'Andorra during the last 50 years, shows that they can be fitted to a power law. We argue that the extrapolation of the F-M relations far beyond the historical data is not appropriate in this case. Neither geomorphological evidences of past events nor the size of the potentially unstable rock masses identified in the slope support the occurrence of the large rockfall/rock avalanche volumes predicted by the power law. We have observed that the stability of the slope at the Solà is controlled by the presence of two sets of unfavorably dipping joints (F3, F5) that act as basal sliding planes of the detachable rock masses. The area of the basal sliding planes outcropping at the rockfall scars were measured with a Terrestrial Laser Scanner. The distribution of the areas of the basal planes may be also fitted to a power law that shows a truncation for values bigger than 50 m2 and a maximum exposed surface of 200 m^2. The analysis of the geological structure of the rock mass at the Solà d'Andorra make us conclude that the size of the failures is controlled by the fracture pattern and that the maximum size of the failure is constrained. Two sets of steeply dipping faults (F1 and F7) interrupt the other joint sets and prevent the formation of continuous failure surfaces (F3 and F5). We calculated the likelihood of generation of a large sliding surface by connecting the basal sliding planes displaced by the fault sets, with a Monte Carlo simulation. The results obtained are consistent with the size of the exposed failure surfaces measured in the slopes. We conclude that due to the structural control, large slope failures in Andorra are not randomly distributed thus confirming the findings in other mountain ranges.

Keywords: rockfall, maximum volume, structural constraints, unstable volumes identification

1. Introduction

Rockfalls are widespread phenomena in mountain ranges, coastal cliffs, volcanos, river banks, and slope cuts. Most of them take place in remote places, but they may cause significant damage in residential areas and transport corridors (Hungr et al. 1999; Chau et al. 2003; Corominas et al. 2005). They are extremely rapid processes that even in the case of small events, they exhibit high kinetic energies and damaging capability (Turner and Jayaprakash, 2012).

Cruden and Varnes (1996) defined rockfall as the detachment of a rock from a steep slope along a surface on which little or no shear displacement takes place. The detached mass experiences free fall and, after impacting on the ground, it continues by bouncing and rolling. Strictly speaking, rockfalls are individual blocks or relatively small rock masses that propagate without interaction between the most mobile fragments (Hungr el al. 2014). Rock avalanche is a large rock mass volume that propagates as granular flow, involving crushing and pulverisation of the particles (Scheidegger, 1973; Hungr et al. 2014).

Rochet (1987) distinguished: (i) falls of boulders up to few hundred of cubic meters, in which no interaction exists between the rock fragments, which follow independent trajectories; (ii) rock mass fall up to few hundreds of thousands of cubic meters in which the interaction between particles is weak as they follow independent trajectories or soon they become independent. This sort of propagation is known as fragmental rockfall (Evans and Hungr, 1993); (iii) very large rock mass fall (>105- 106 m3) showing strong interaction of particles within the moving mass with the development of internal pressures (possible fluidification) and low energy dissipation; and (iv) mass propagation (> 106 m3) that progresses mostly by a translational displacement. Differentiating between all these mechanisms is relevant because rockfalls and fragmental rockfalls are modelled as ballistic trajectories while rock avalanches are simulated as granular flows (Bourrier et al. 2013). The passage from a falling of independent particles to a granular flow is gradual and both mechanisms can coexist in some events. The transition may take place at volumes as small as 5x104m3 (Davis and McSaveney, 2002) although other authors raise it up to 107m3 (Hsü, 1978). The current practice shows that the agreement in using terms such as rockfall, rockslide and rock avalanche has not yet reached (Hungr et al. 1999; Chau et al. 2003; Dussauge-Peisser et al. 2002; Guzzetti et al. 2003; Hewitt et al. 2008). In light of these considerations, in this paper we will not consider any volumetric threshold between rockfall and rock avalanches, as recommended by Turner and Jayaprakash (2012).

The management of the rockfall hazard may be based on the Quantitative Risk Analysis (QRA). The QRA is a formal and structured framework that considers the probability and consequences

for all the credible hazard scenarios (Ho, 2004; Fell et al. 2008). The management of the rockfall risk is a challenging task. There is a demand for assessing not only the hazard and socio-economic impact in the short term but also for evaluating the consequences of large often unrecorded events. The UN/ISDR (2004) introduced the concept of living with risk in order to develop strategies and undertake actions oriented to the prevention and mitigation of the consequences in developed areas. Living with risk requires the analysis of the potentially hazardous scenarios (Brundl et al. 2009) and in particular, the scenario associated to the Maximum Credible Event (MCE).

The magnitude of landslide is expressed by either the area or volume (Corominas et al. 2014). The former is widely used for landslides because they can be readily measured from maps, aerial photographs or satellite images. The rockfall magnitude is usually expressed as the volume. Risk assessment requires considering the probability or the frequency of different magnitude scenarios for landslides (Picarelli et al. 2005; Rossi et al. 2010; Lari et al. 2014) and rockfalls (Hungr et al. 1999; Agliardi et al. 2009; Wang et al. 2014). The frequency may be expressed as a simple cumulative or non-cumulative manner (Guzzetti et el 2002) or as a frequency density (i.e. number of landslides of a given size divided by the size of the bin) (Guzzetti et al. 2003, Malamud et al. 2004).

Landslides occurring in a specific study site may be characterized by magnitude-frequency relations derived from the empirical data. These relations can be prepared using different approaches and data sources (Picarelli et el 2005): (i) landslide of different ages mapped at one time from aerial photographs and field surveys (Guzzetti et al. 2002; Malamud et al. 2004); landslides for a defined time interval (i.e. from successive aerial photographs); from triggering events such as rain storms or earthquakes (Malamud et al. 2004); from continuous inventories (Hungr et al. 1999; Guzzetti et la. 2003; Rossi et al 2010). The M-F relations often follow a power law over a limited scale range, with deviations at both high and low magnitudes (Brardinoni and Church, 2004; Guthrie and Evans, 2004). To explain the positive exponent at smaller volumes, Stark and Hovius (2001) proposed a double Pareto distribution while Malamud et al (2004) fitted an inverse-gamma distribution but in both cases the tail of the distribution follows a power law.

A scale invariance of the M/F relation has been observed over several orders of magnitudes in landslides and rockfalls, in different geological contexts and associated to different triggering events (Guzzetti et al. 2003; Marques, 2008). Malamud et al. (2004) noted that rockfalls show a behaviour different than the other types of landslides. This was attributed to the fact that rockfall involves the disintegration of the rock mass. Guzzetti et al. (2003), Dussauge et al. (2003), and Hergarten (2012) claimed that the negative exponent of the power law is similar for several rockfalls inventories. A wider review of the available literature indicates however that the scaling

parameters of the power law for rockfalls may vary between 0.4 and 0.9 according to regional differences in structural geology, morphology, hydrology and climate (Barlow et al. 2012) (see also Table 1)

Table 1. Exponents of the power law fitted distributions obtained for different rockfall inventories

Reference	Location	Length of the record (yr)	Range of volumes fitted (m^3)	number of events N	Scaling parameter b
Hungr et al. 1999	Highway 99 British Columbia,	40	10^1 to $8x10^8$	390	- 0.43
	BCR line	12	10^0 to 10^4	403	-0.4
	Highway 1		10^0 to 10^4	226	-0.7
	CP Line	22	10^0 to 10^4	918	-0.65
Gardner 1970[a]	Lake Louis	Two summers	10^{-1} to 10^3	409	-0.72
Chau et al. 2003	Hong Kong, China			201	-0.87
Dussauge-Peisser et al 2002	Upper Arly, gorge French Alps		10^0 to 10^4	59	-0.45
	Grenoble, French Alps	60	10^{-2} to 10^6	87	-0.41
	Yosemite, USA	77	10^0 to 10^5	101	-0.46
Royán et al. 2015	Puigcercós, Spain	6.87	10^{-2} to 10^2	3096	-0.72
Wang et al. 2014	Feifeng Mountain, China	200	10^0 to 10^2	27	-0.62

[a] Cited in Hungr et al 1999

The fact that different sets of rock falls and rock slides exhibit the same magnitude-frequency relation has supported the idea that the frequency of large unrecorded events can be estimated by extrapolating the power law obtained for the small-size events provided that the record of the latter is complete (Dussage-Peisser et al. 2002; Guzzetti el al., 2002, 2003; Picarelli 2005). This exercise raises the question on the range of validity of the extrapolation (Corominas and Moya, 2008). The analysis of the probability of occurrence of rockfalls along large cliffs is affected by uncertainties due to the different site-specific characteristics (Wang et al 2014), while the temporal resolution over which power laws can be applied is poorly constrained (Cruden and Hu, 1993).

The question posed here is to what extent the empirically-based models are capable to extrapolate short-term observations to the spatial and temporal scales required for reliable rockfall risk management. This requires the understanding of the scaling behaviour of rockfall processes. Two issues must be addressed. The first one is that several authors (Picarelli et al 2005; Cascini et al.

2005; Corominas and Moya 2008) argue that a major difficulty for the assumption of M/F invariance is whether the rate of landslide occurrence will persist in the future. In that respect, Cruden and Hu (1993) noticed a decay in time of the number of large landslides in the Canadian Rockies, that contradicts the stationarity implicit in the power law. The second one is the definition of the largest volume that can be predicted with the extrapolation of the M/F relations.

In this paper we attempt to address the last issue with the analysis of the rockfall activity in the Sola d'Andorra, Eastern Pyrenees. We will first present the results of the F/M of rockfalls in Andorra using historical data what can be expected from them. Secondly, we will address the definition of a cut-off value for the size of the maximum expected rockfall/rock avalanche event, and we will discuss the role of the geological factors in possible constraining the maximum volumes.

2. Rockfall hazard management in Andorra

The slopes of the Solà d'Andorra bound the right bank of the Valira d'Orient river in the Principality of Andorra. This stretch of the valley is a basin that was deepened and widened by glaciers during the Pleistocene. After the glacier retreat, a lake was formed and the basin filled with lacustrine, deltaic and colluvial sediments up to a depth of 100m. Nowadays it forms a 1km-wide alluvial valley (Turu et al. 2007).

The Solà is the lower part of the Enclar massif (2383m), extending between the urban settlements of Santa Coloma and Andorra la Vella. The rock mass is made up of highly fractured granodiorite and hornfels. The slope is characterized by the presence of V-shaped couloirs alternating with steep walls for a length of about 3km (Figure 1). The couloirs extend from 990 m to about 1300 m.a.s.l. The rockfall activity at the Santa Coloma wall has an average frequency of 1 event bigger than 1m3 every 2 years. In the last decades (since the 1960s) the maximum recorded rockfall events attained a volume of of 1000 m3 in its the Tartera de la Pica (April 1969) and 150 m3 (April, 2008) in the chute of Forat Negre. The average annual rainfall precipitation is of 1071.9 mm. Although some events occurred after rainfall episodes, a direct relation between precipitation and rockfalls could not be established so far (Copons et al. 2004). Freeze-thaw process might also play a role for the onset of the failure.

Figure 1. The slope above the town of Santa Coloma and the chute of Forat Negre.

The efforts of the Andorran administration in the management of natural hazards began in the eighties of last century (Corominas, 2007). The first global initiative took place between 1989 and 1991 with the preparation hazards maps at 1:25,000 scale, that included landslides and flood-prone areas. The main impulse in management of the natural hazards was given by the Urban and Land-Use Planning Law approved in 1998. The key points of this law in terms of hazard management are the following (Escalé, 2001): (a) the zones exposed to natural hazard cannot be developed; (b) local development plans must take into account the presence of zones exposed to natural hazards; (c) the Andorra government will commission both geological-geotechnical studies and hazard mapping. This means that the Andorra government has to provide hazard inventories, hazard zoning and regulations for management of the threatened areas. In those sites where hazard can be mitigated and reduced to an acceptable level, the Andorran government will establish the requirements of the protective works that have to be undertaken. After the implementation of the law, several studies were completed and among them: the Geotechnical and Landslide Hazard Zoning Plan of Andorra (1999-2001). The purpose of the Plan was to identify, locate and assess the natural hazards as well as the geological and geotechnical constraints that may affect future construction works in the Andorran territory. The scale of work was 1:5,000 (Corominas, 2007).

In January 1997, a falling rock block hit a building in Santa Coloma, causing an injury. This event persuaded the Andorran administration to implement the Rockfall Risk Management Master Plan (RFMP) of the Solà d'Andorra which was completed in 1998 (Copons et al. 2004). This Plan established, the restriction to the development in the most threatened sectors and it was published in the official journal of the Principality in the year 2000. The RFMP, based on a rockfall trajectographic analysis, defined an upper boundary line above which development is forbidden. Several existing buildings were already within the exclusion area. For all these cases, the RFMP contemplated the design of rockfall defenses (Copons et al. 2001). The cost of the protective works raised over 4.5 million euro (Escalé, 2001). After the construction of the fences several events have occurred with minor only consequences. However, a residual risk exists as large rockfall events might not be fully retained due to excessive energy or bouncing height (Corominas, et al. 2005).

The RFMP has been complemented with a Surveillance Plan that started in 1998. This Plan aimed at (Amigó et al. 2001): (a) the inventory of the rock falls occurring in the valley side; (b) the update and validation of the trajectographic models used to design the protective structures (rockfall paths, height of bounces, among other parameters); and (c) the detection of possible large rockfall events (exceeding thousands of m3). It is expected that before the large rock mass failure, premonitory signs such as the increase the number of small rockfall events or the opening of new fractures, could be timely identified.

The risk management practice requires assessing the scenario associated to the maximum credible event (MCE). The MCE is a very conservative estimate of the event considered sufficiently unlikely, sometimes associated to a notional return period of the order of 1,000 years (Ho, 2004). In any case, it should correspond to the largest event observed in historical data, geomorphological evidence in the area and its vicinity and any other relevant evidence from similar terrain (Ho, 2004).

We have attempted to estimate the size of rockfall events that can be expected in the future. A 50-yr length record of rockfall events bigger than 1 m3 is nowadays available in Andorra and can be considered complete since 1999. This length is similar to the length used in other M/F studies (Hungr et al. 1999; Dussauge-Peisser et al 2002). The record has been used for the construction of the M/F relation for the Solà d'Andorra. Table 2 contains the historical rockfalls inventoried and their volumes, while the plot of Figure 2 shows the relationship between the volumes and the cumulative frequency expressed as the number of events greater than a given volume per year.

Table 2. Historical rockfalls at the Solà d'Andorra and their volumes. The rockfall volumes of the boxes framed in pink are estimations based on the volume of the largest block observed. Source: Copons, 2007 and unpublished data from Surveillance Plan of the Ministry of Land Management (MOT).

Location	Year of occurrence	source	Volume (m^3)	Largest block (m^3)
Canal de la Pica	1969	Copons, 2007	1000	60
Canal Ramenada	2012	MOT	450	
Canal de la Pica	20003	Copons, 2007	300	70
Forat Negre	2008	MOT	150	32
Canal de l'Alzina	1997	Copons, 2007	125	25
Canal Ramenada	End of 1960s	Copons, 2007	100	10
Roc Sant Vicenç	2002	MOT	30	14
Forat Negre	1968	Copons, 2007	30	7.5
Forat Negre	2009	MOT	30	7
Forat Negre	2004	MOT	25	4
Canal Coll d'Eres	1983	Copons, 2007	25	7
Forat Negre	2014	MOT	20	8
Cementiri	2011	MOT	20	1.3
Forat Negre	1984	Copons, 2007	10	1
Forat Negre	2002	MOT	10	2
Forat Negre	2003	MOT	10	2.3
Canal Boneta	2001	MOT	10	
Canal Boneta	2002	MOT	10	1
Canal de la Pica	1996	Copons, 2007	10	2
Canal de la Pica	2000	MOT	10	
Forat Negre	1994	Copons, 2007	5	
Forat Negre	1996	Copons, 2007	5	
Canal de l'Alzina	1999	Copons, 2007	5	
Forat Negre	2000	MOT	4	
Forat Negre	2001	MOT	4	

The inventory includes 25 cases since the late 60s of last century. The data before 1999 might not complete and, in some events, the initial rockfall volume is not well known. For this reason, an estimate has been made (boxes highlighted in green) from the descriptions available of the events.

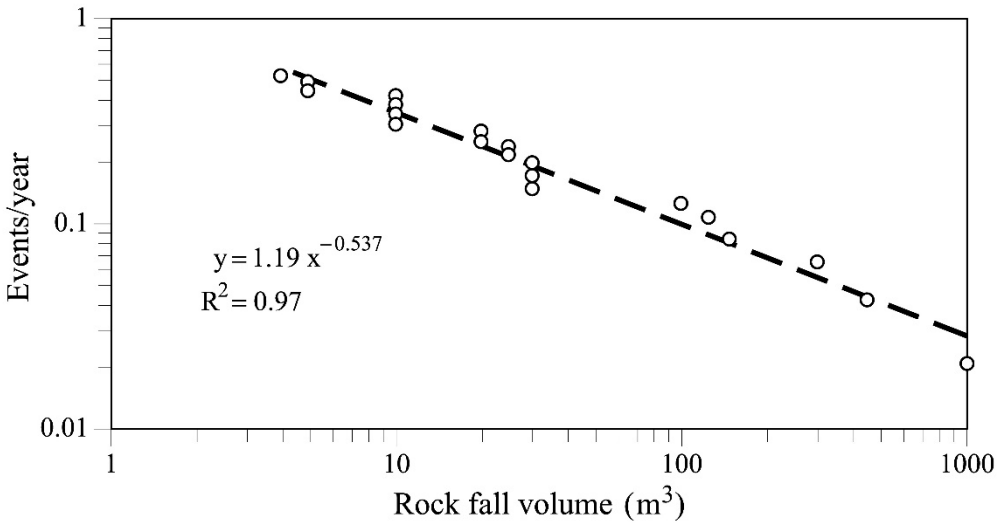

Figure 2. Relationship between the volume (m3) of the inventoried rockfall event at the Solà and the cumulative relative frequency (N events larger than a certain size per year)

The relation shown in Figure 2 fits well to the power law of Equation [1]:

$$N = 1{,}193.\ V^{-0.537} \qquad [1]$$

Being N, the number of rockfalls per year exceeding the volume V.

The extrapolation of this relationship to rockfall volumes much larger than the inventoried, would result in the frequency for each range of return periods and volumes shown in Table 3

Table 3. Cumulative frequency and return periods obtained from the extrapolation of the power law fitted to the rockfalls observed at the Solà d'Andorra during the last 50 years..

Volume range (m^3)	Fr (events/year)	Return period (years)
≥1	1.1933	0.84
≥10	0.3465	3
≥100	0.1006	10
≥1,000	0.0292	34
≥10,000	0.0085	118
≥100,000	0.0025	406
≥1,000,000	0.0007	1397

The extrapolation of the power law defines a scenario in which cliff failures with a magnitude of a hundred of thousands of cubic meters (i.e. large rock slides or rock avalanches) have a recurrence period of about 400 years.

3. Are there evidences supporting the extrapolation of M/F relation obtained at the Sola d'Andorra?

A number of studies have shown that the occurrence of large rockslides and rock avalanches has geomorphic consequences which can be deciphered by means of the analysis of the landscape. Two main distinct features of rock avalanches are the deposits and the scar left at the source (Soeters and Van Westen, 1996; Hewitt, 2002; Ballantyne and Stone, 2004).

3.1 Rockfall deposits

Rock slide and rock avalanche deposits as old as tens of thousands of years remain blanketing the valley bottoms of the main alpine chains (Voight and Pariseau, 1978; Cave and Ballantyne, 2016; Crosta et al. 2016). Some old rock-avalanche deposits are remarkably well preserved such as those of the Karakoram range (Hewitt et al. 2008) or in the northern Chilean coast (Crosta et al. 2016), partly due to semi-arid conditions of these regions. Others are less preserved because they run onto glaciers and became dispersed by ice flow or removed by the fluvial erosion (Hewitt et al. 2008). However, even in the latter case the deposits may remain for thousands of years.

The Valira d'Orient glacier resided in the Andorra la Vella basin until ca. 18 ka (Turu et al. 2016). After the glacier retreat any landslide or rockfall deposit would have emplaced on ice-free valley floor. At present, only talus deposits from rockfalls and the debris cones from debris flow events accumulate at the foot of the slopes, bounding plain of the Valira river. According to the results of Table 2, rockfalls of the order of 10,000 m3 should have occurred almost every 120 years and two events of 100,000 m3 each millennium. However, the bottom of the the Solà d'Andorra lacks of debris deposits that could be associated with the release of a large rockfall or rock avalanche. In case they had occurred, the deposits should lay over the alluvial plain of Santa Coloma. Figure 3 shows the topographic profile of the Santa Coloma slope, the alluvial plain of the Valira river, and the expected runout for different rockfall/rock avalanche sizes detached from the walls of the Solà d'Andorra. The runout has been determined using the equations for unobstructed rockfalls/rock avalanches prepared by Corominas (1996) Corominas et al. (2003).

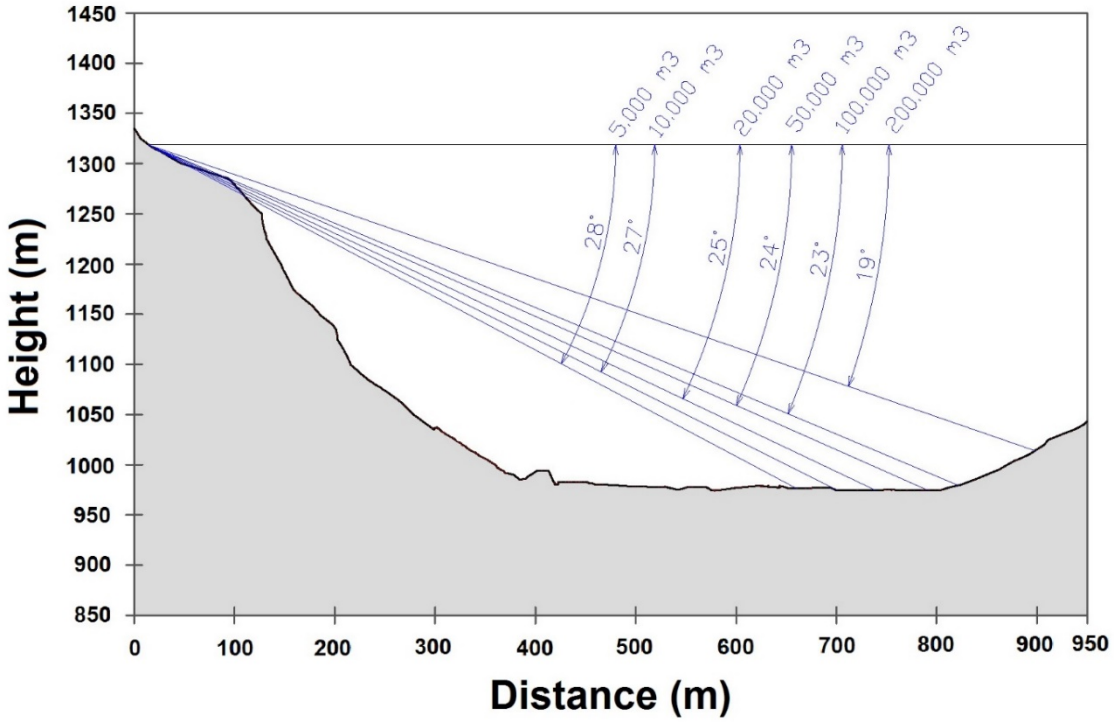

Figure 3. Maximum runout that could be achieved by rockfall events with sizes between 5,000 and 200,000 m3 originating from the slopes of the Borrassica in Santa Coloma if they had occurred in the past. The runout has been calculated following the criterion of reach angle for unobstructed rockfall events (Corominas 1996; Corominas et al. 2003).

Based on the distances obtained shown in Figure 3, rockfall events of tens of thousands of cubic meters would blanket much of the valley bottom. In the event that the volume increased to 100,000 m3 or greater, the deposits would reach the opposite slope. However, in the historical archives of the valley there is no record of events of any of these sizes. Figure 4 is an aerial photograph taken before the extensive development of the basin of Andorra la Vella and Figure 5 is the geomorphological map prepared by Turu et al (2007). Both figures show the lack of rockfall/ avalanche deposits over the valley bottom. These type of deposits have not been found either in the boreholes drilled in the fluvial plane or in the interpretation of geoelectrical surveys carried out in the basin for hydrogeological purposes (Gutiérrez-Rodríguez and Turu, 2013).

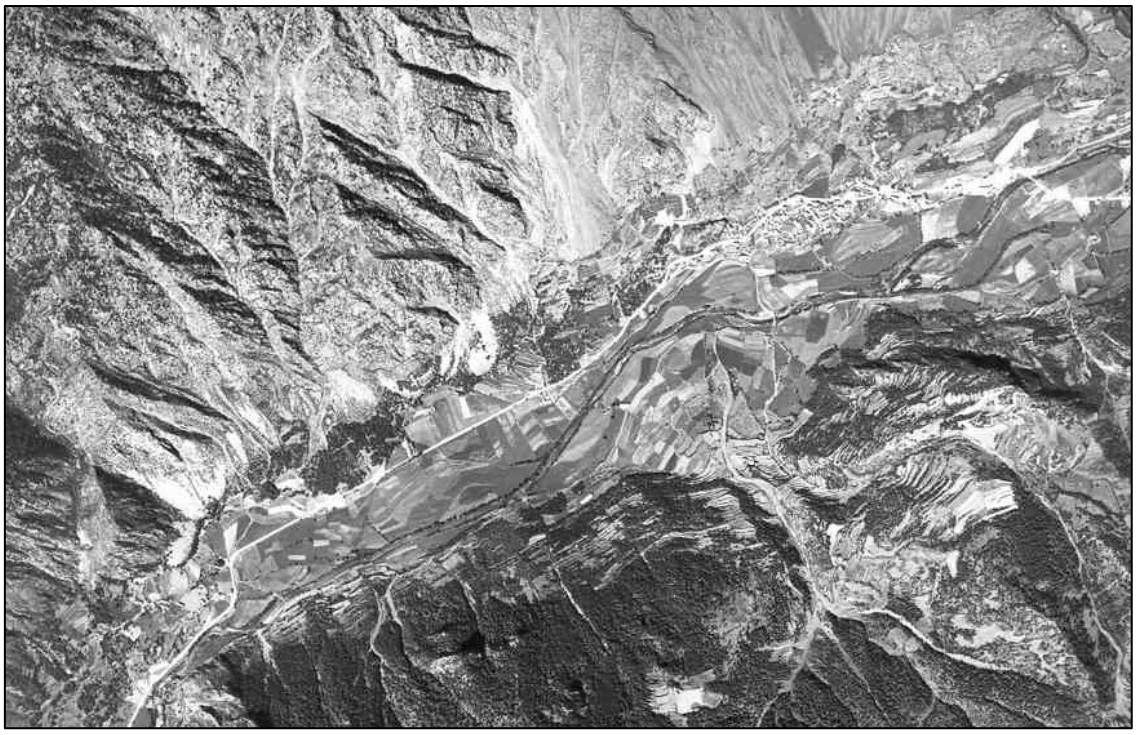

Figure 4. Aerial photograph of the Andorra la Vella basin taken in 1948.

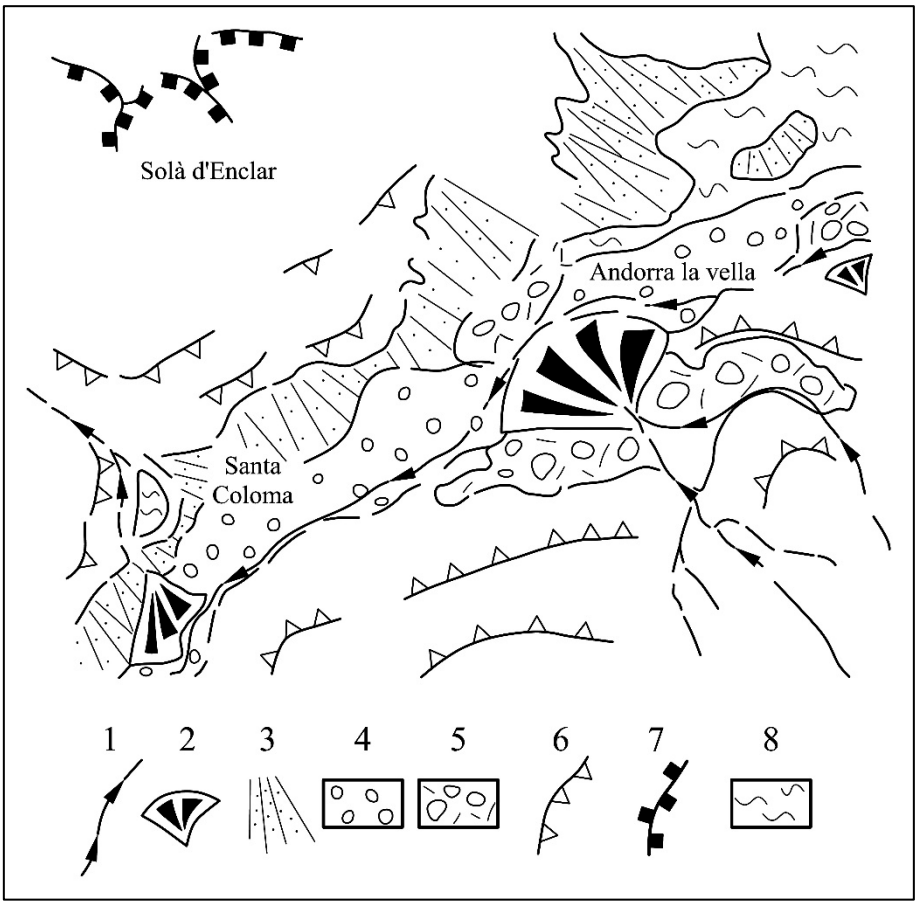

Figure 5. Geomorphological map of Santa Coloma – Andorra la Vella – Les Escaldes: (1) stream, (2) debris fan, (3) talus deposit and colluvium, (4) alluvial deposit, (5) till, (6) reconstructed glacial margins, (7) glacial cirque, (8) hummocks (modified from Turu et al. 2007).

3.2 Analysis of the rockfall scars

The availability of modern data capture techniques facilitates the analysis of the rockfall scars. Successive surveys with the TLS allow the identification and measure of the volumes missing from the rock wall (Rosser et al. 2007) and the preparation of M/F relations (Royan et al. 2014). We argue that cliff faces contain the record of rockfall events that occurred during the last hundreds or thousands of years. Each rockfall scar bounds the mass that was detached from the rock wall as a single or multiple events (Figure 6). Consequently, the volume distribution of the rockfall scars can be used as a quantitative proxy the rockfall volume distribution (Santana et al. 2012).

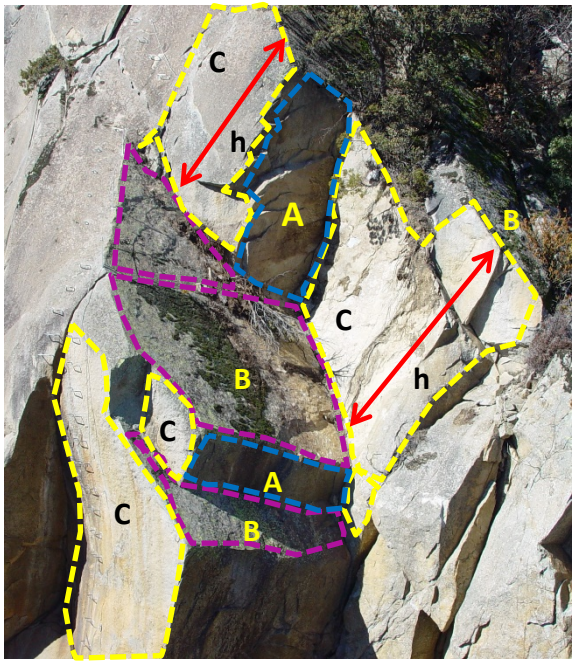

Figure 6. Rockfall scar defined by three intersecting joint sets. The detached block was resting on a basal plane (B) which is bounded by planes (A) and (C). The height of the scar (h) may involve several spacings

The dimensions of the rockfall scars can be determined from a point cloud obtained with a Terrestrial Laser Scanner, TLS. In the the Solà d'Andorra this was carried out at the slope of Borrassica-Forat Negre, following the methodology of Santana et al. (2012). Eight joint sets present in the rock mass were first identified (F1 to F8). Four sets are directly involved in the formation of the scars (Table 4).

Table 4. Dip direction and dip angle of the discontinuity sets that contribute to the formation of scars.

	Dip direction (°)	Dip angle (°)	Role
F1	54	59	Lateral plane/tension crack
F3	157	56	Basal sliding plane
F5	182	47	Basal sliding plane
F7	141	89	Tension crack

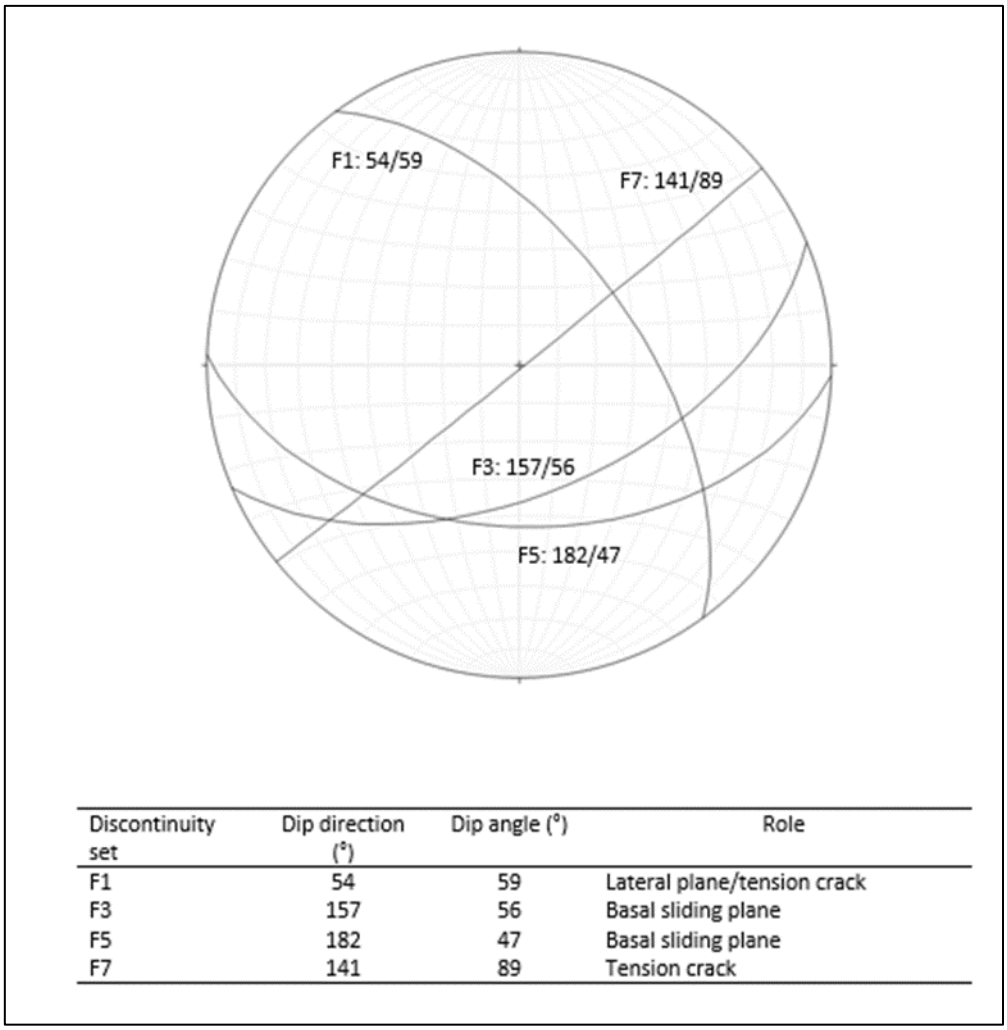

Discontinuity set	Dip direction (°)	Dip angle (°)	Role
F1	54	59	Lateral plane/tension crack
F3	157	56	Basal sliding plane
F5	182	47	Basal sliding plane
F7	141	89	Tension crack

Figure 7. Stereoplot showing the joint sets involved in the formation of unstable volumes at the slope of Borrassica-Forat Negre. The slope is mostly oriented to 180º

The observation of historical events as well as the kinematic analysis of the fracture pattern (Figure 7) show that most of the rockfalls initiate by sliding of the detached rock mass over an unfavourable dipping discontinuity plane (F3 and F5). Each rockfall scar is therefore defined by a basal plane and two tension cracks (F1, F7 joint sets). The area of each discontinuity plane and the height of the scar was obtained from the treatment of the point cloud generated with the TLS. The volume of the rockfalls was generated stochastically by combining the measured areas and the scar heights following a Monte Carlo simulation approach. The procedure accounted for stepped failures sliding over parallel discontinuity surfaces spaced less than 0.2 m. It is assumed that each scar on the slope face corresponds at least to an event.

To measure the size distribution of the missing volume from the scars, the points of the point cloud belonging to each sets were extracted and planes were adjusted to them. Afterwards, the areas were measured (Figure 8) as well as their maximum width (along the strike) and length (along the dip direction).

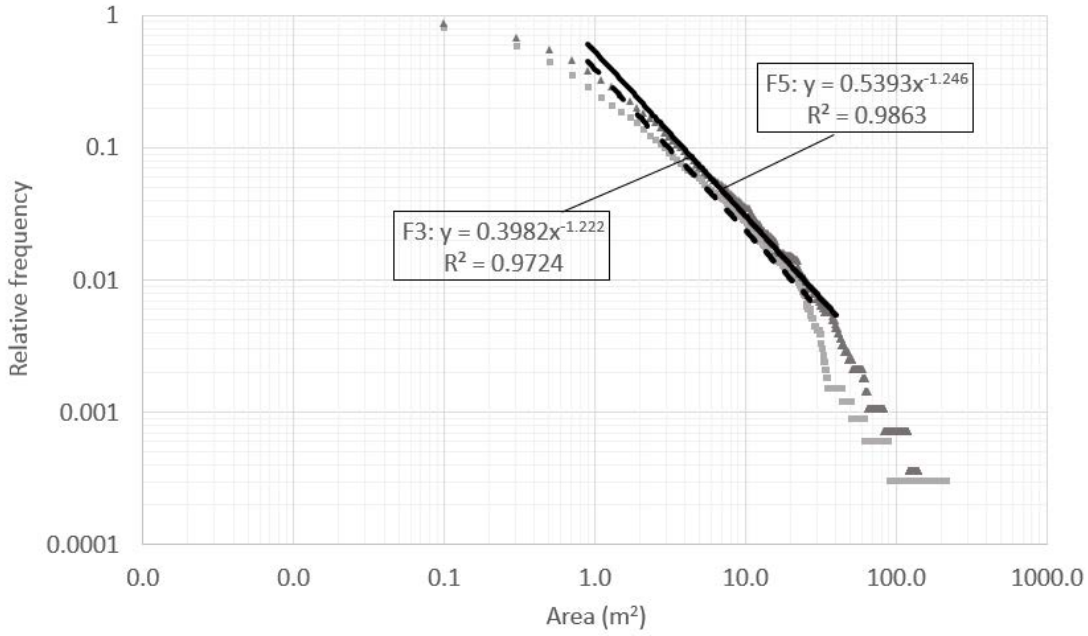

Figure 1. Magnitude (area in m^2) - Cumulative frequency of the discontinuity surfaces of the sets F3 and F5, calculated from the point cloud

The areas of F3 and F5 (basal planes of the scars) were well fitted to a power law. The scar heights were measured as intersections of the tension cracks F1 and F7. Eventually, the size distribution of the scars was calculated past a Monte Carlo simulation by the multiplication of the scar areas with the scar heights (see details in Santana et al. 2012).

The results were fitted to the f power law of Equation [2].

$$N (>V) = 1919V^{-0.92} \quad [2]$$

Where N is the number scars bigger than V and V, the volume of the scar in m3.

Five thousand scars were randomly generated, based on the observed distribution of the areas and heights, which is of the same order of magnitude of the number of scars identified on the point cloud in Borrassica-Forat Negre. The maximum scar volume calculated using this method is about 3000 m3. This volume is substantially smaller than the predicted with the extrapolation of the M/F relation of the historical rockfalls.

The analysis of large rockslides, show that the sliding surface may be a single plane or it may be composed of a series discontinuity planes and lateral release surfaces with both down-dip and laterally stepped morphology as in the Aknes (Ganerod et al. 2008) or Palliser Rockslide (Sturzenegger and Stead, 2012). In the latter case, a composite surface is generated, which is characterized by a combination of low persistence discontinuities, cross joints and broken rock bridges. Steps can be as high as 35m (Sturzenegger and Stead, 2012). The approach followed by Santana et al (2012) in the slopes of Borrassica-Forat Negre has the restriction that only step path basal surfaces involving steps heights of less than 0.2m were considered.

3.3 Identification of massive rock mass failure scars

To check the possibility of occurrence of a large stepped failure at the Borrassica-Forat Negre slope in the past, we have looked for remnant of an old rockslide or rock avalanche scar in the slope. Source areas of large rock slides and massive rock failures are usually characterized by the presence of a more or less continuous sliding surface that terminates against large lateral and or back release surfaces forming prominent scarps (Cruden 1975; 1985; Eberhardt et al 2004; Willenberg et al. 2008; Sturzenegger and Stead, 2012; Stead and Wolter, 2015). Lateral and back release surfaces can form by the presence of cross joints, by the breakage of rock bridges or by the combination of both. In highly unstable mountain fronts, adjacent scars may coalesce to form large niches several kilometres length (Crosta et al. 2016). These features can persist for millennia or even longer (Hewitt et al 2008).

The exposed basal sliding planes (failure surface) are therefore a reasonable indicator of both the occurrence and size of rock slide (rock mass failure).

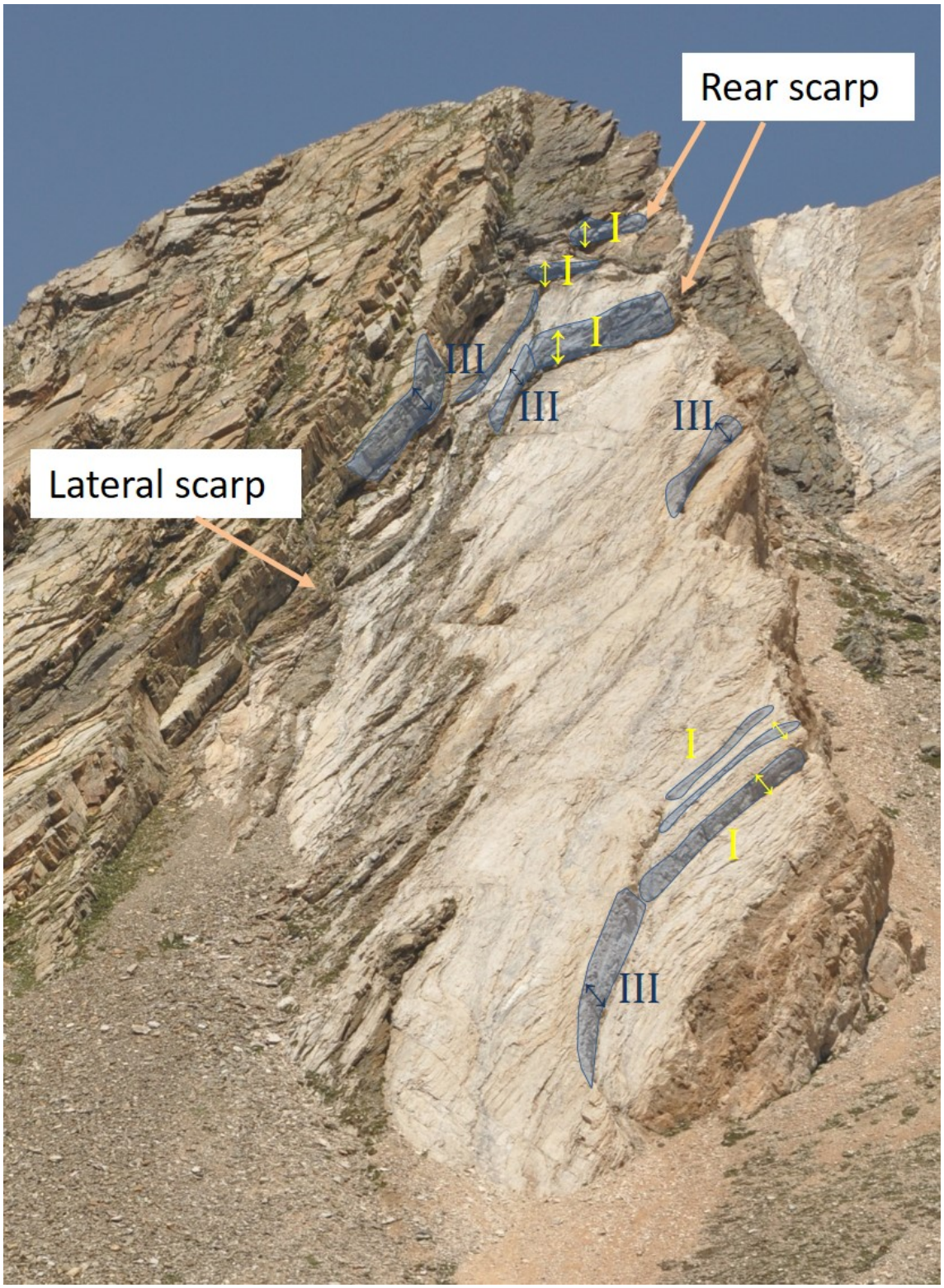

Figure 9. Type I and III steps (Sturzenegger and Stead, 2012) formed at the down-dip and laterally stepped basal failure surface of a rockslide at the Pic of Freser, Eastern Pyrenees, Spain

At the scale of the whole slope, both rear and lateral scarps and either single or step path sliding surface may be identified as a distinct macro forms (Figure 9). The steps of the stepped sliding

surfaces, can be approximated as roughness features (Wolter et al. 2014; Stead and Wolter, 2015) that can be scaled (Barton and Bandis, 1982).

We have attempted to fit a large step path surface at the slope of the Borrassica-Forat Negre, assuming that the surface can be a down-dip (type I) or a laterally (type II) stepped basal failure surface or both. We expect the large stepped failure to be composed of more or less parallel, relatively long, straight stretches alternating with steps of different heights produced by F7 joint set. The direction of the movement will follow the dip direction of either F3 or F5 joint sets. It may be also expected that lateral steps (type III) may develop in a direction more or less parallel to F1 joint set. In this case, transverse cross sections should show straight (almost horizontal) stretches alternating with the steps generated by F1 joint set, similarly to what is shown in Figure 10.

We used the program CloudCompare. to fit a large rupture surface to a sequence of down-dip stepped planes and the cross-sections. As seen in Figure 10, it is not possible to adjust a large stepped surface to Borrassica-Forat Negre slope because despite the longitudinal profile being compatible with the presence of a large stepped surface, the transverse profiles suggest otherwise. The transverse profiles show protuberances that prevent the definition of a sliding surface. We have included the profile generated in the outcrop of Pala de Morrano in the Aigüestortes-Sant Maurici National Park, Central Pyrenees, for comparison.

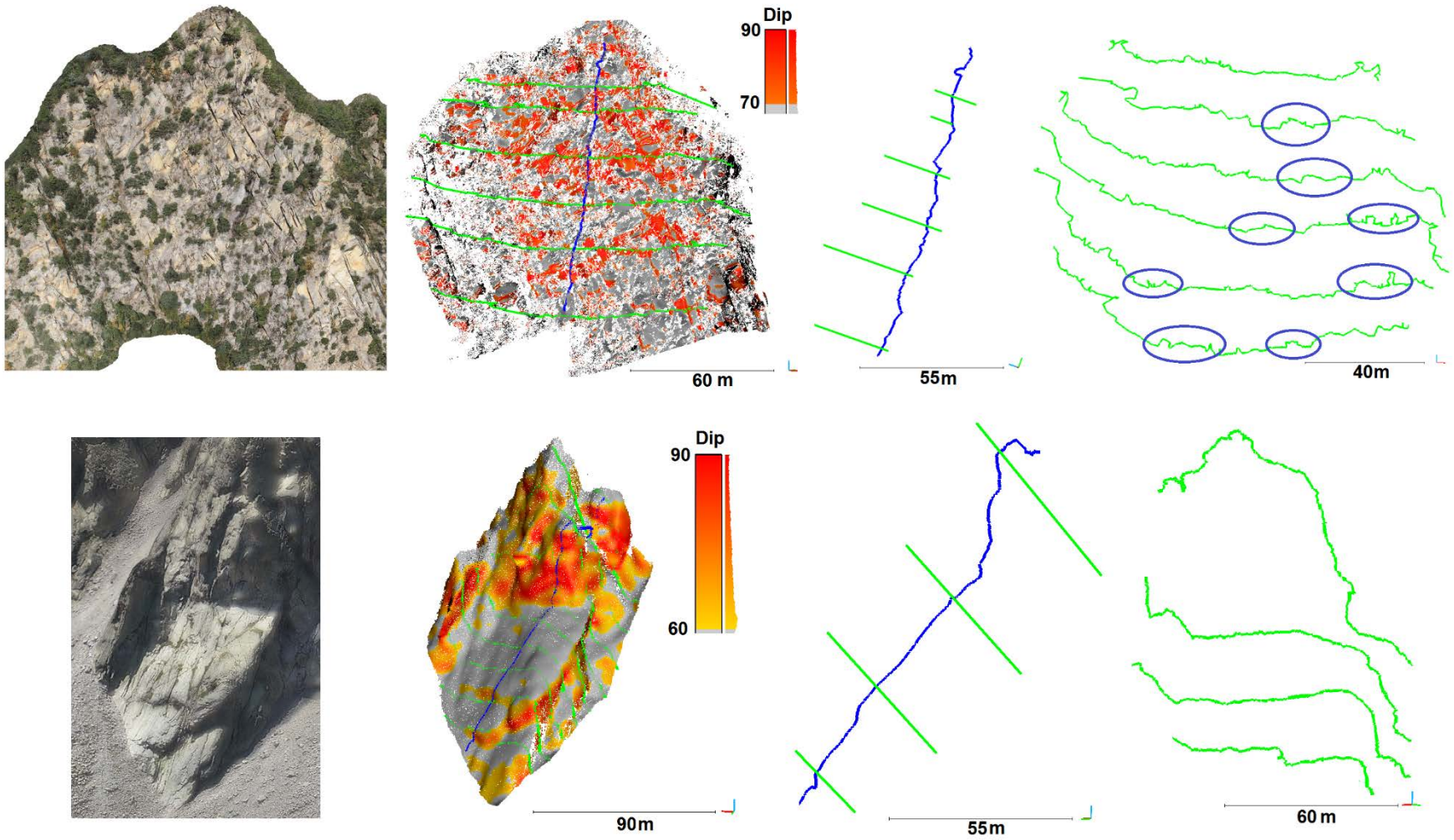

Figure 10. Top: profiles extracted from a point cloud in Pala de Morrano, Aigüestortes-Sant Maurici National Park, Eastern Pyrenees. The straight stretches of the step-path failure surface are clearly observable in both longitudinal and transverse cross-section. Bottom: profiles extracted from the point cloud of the slope of Borrassica-Forat Negre. Transverse sections exhibit protuberances that interrupt any possible large sliding surface

4. Defining the maximum credible volume

In risk management, the design of mitigation measures and the delimitation of the hazardous areas are based on analyses for a range of expected potential rockfall volumes (Corominas et al. 2005; Abruzzese et al. 2009; Agliardi et al. 2009; Li et al. 2009). The question posed in our work is what the range of validity of the historical power law is and specifically, what the largest rock slope failure or maximum credible event (MCE) can be in the Borrassica-Forat Negre slope. The MCE is usually characterized by volumes of rock masses of several orders of magnitude greater than the events commonly observed in the study area.

As already mentioned, power laws for rockfalls-rock avalanches have been verified by a range of volumes spanning several orders of magnitude as in Yosemite, U.S.A. (Guzzetti et al. 2003) but in the case of the Solà d'Andorra, the M/F calculated from the historical rockfalls differ significantly from the geological record. On the other hand, the maximum volume cannot be unlimited. It is evident that for a given slope, the failure cannot exceed the size of the slope (Guzzetti et al. 2002). In the Solà d'Andorra this would be the scenario of an unfavorably oriented fully persistent discontinuity outcropping at the base of the cliff, crossing the entire massif. However, the largest credible rockfall event is the reasonable largest event, not the largest conceivable event.

The analysis of the MCE for rockfalls is not a standardized procedure. In other scientific disciplines, concepts such as the maximum credible earthquake or the probable maximum flood were already introduced in the 90s. For earthquakes, the maximum credible event is the one that can be justified by all the known geological and seismic data (US Bureau of Reclamation, 2015). The estimation of largest hypothetical earthquake takes into account the characteristics of the fault or other seismic source and the current tectonic setting. It can be evaluated either deterministically or probabilistically. As regards the calculation of annual exceedance probabilities of maximum flood discharge, the use of data from multiple sources is recommended. Moreover, procedures have been proposed to obtain the optimal range for the credible extrapolation of the magnitudes and return periods (Swain et al. 2006). In these cases, an upper boundary for the size of the maximum event is obtained.

We assume in our work that the MCE for rockfalls is the largest reasonably conceivable slope failure that appears possible in the geographically contained slope, under the presently known or presumed geostructural and geomechanical setting. Several factors account for the occurrence of a slope failure of a given size, reflecting the complex interaction between the rock strength properties, the rock mass structure, the geomorphic context and the triggers.

4.1 MCE based on a simple kinematic analysis (Markland test)

As mentioned, the rockfall events in the Solà d'Andorra are mostly governed by the presence of unfavorably dipping joint sets (the discontinuity sets F3 and F5). The potential of a large slope failure generated by this structural setting has been analyzed by Mavrouli et al (2015) and Mavrouli and Corominas (2017). They carried out an analysis aimed at identifying large kinematically detachable rock masses on a Digital Elevation model, DEM. The potentially unstable volumes were detected by checking the compliance of the joint sets with the Markland criteria at every cell. Adjacent unstable cells on the DEM, were merged to form larger unstable zones (Figure 11).

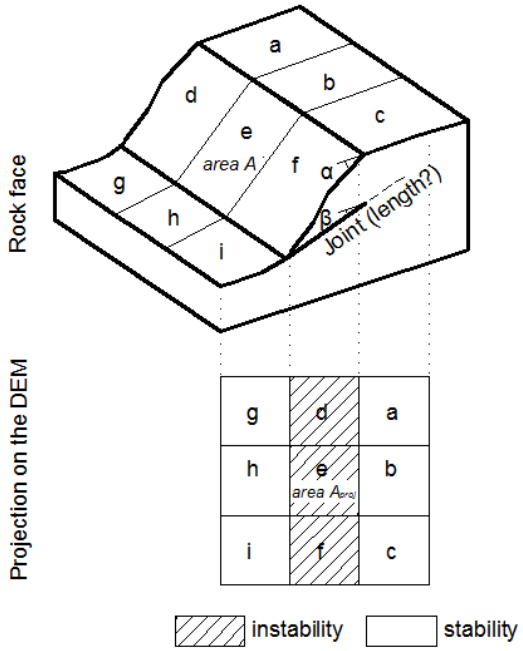

Figure 11. Rock wall and its projection on the mesh of the Digital Elevation Model. It assumes infinite lateral persistence of the unfavourable joint sets. Thus, adjacent cells which meet the requirements of the Markland test merge to form a single kinematically movable rock mass. (from Mavrouli et al. 2015)

The calculation of the volume of the detachable masses was simplified, assuming either cubic or prismatic shape of the detachable rock masses. The distribution of the potential rockfall volumes was calculated. The largest volumes obtained are of the order of 50,000 and 25,000 m3 for cubic and prismatic volumes respectively. The largest basal area was estimated at 1,361 m2.

The results may be fitted to the power laws of Equations [3] and [4].

$$N (>V) = 817.74V^{-0.572} \quad [3]$$

$$N (>V) = 952.42V^{-0.546} \quad [4]$$

For cubic and prismatic shapes, respectively and volumes V>100 m3

Where N is the number scars bigger than V and V, the volume of the scar in m3.

4.2 MCE based on discrete potentially movable volumes

We have here aproached the assessment of the MCE using an alternative way. In this procedure, we identified and calculated the volume of real rock spurs resting on unfavourable dipping basal planes (F3 / F5 sets) of the Borrassica-Forat Negre slope, with several unconstrained faces. The basal sliding surfaces are actual outcropping discontinuities that have been identified one by one. The surfaces have been extracted from the TLS-generated point cloud and confirmed with digital photos. A similar approach was used by Gigli et al. 2014.

The calculation of the volumes has been made with the program Rhinoceros. We have followed these steps:

1) Identification of rock spurs having at least three unconstrained slope faces (front, crest and lateral), permitting mobilization.
2) Location of both the basal and lateral discontinuity planes that bound the rock spur and definition of the volume of the rock mass.
3) Estimation of the volume of the rock mass formed by the intersection of these discontinuity planes with the surface topography.

An example of the procedure followed is shown in the Figure 12 (A to C).

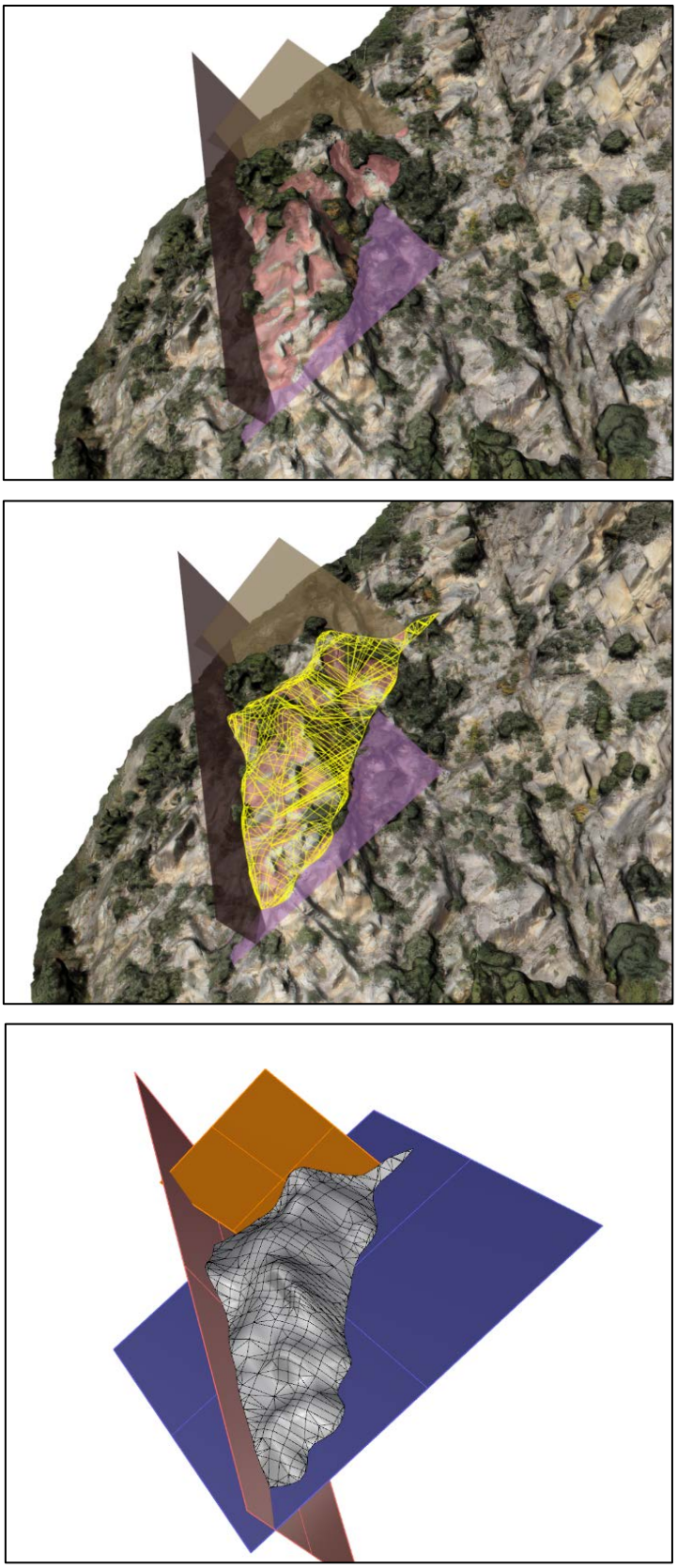

Figure 12. (A) Identification and definition of the rock spur volumes kinematically detachable at the Borrassica and Forat Negre slope. Each volume is delimited by real discontinuity planes observed in the slope and at least, three unconstrained faces; (B) Extraction of the of rock mass volume defined at (A); and

(C) Representation and calculation of the volume of rock mass defined at (A). In this case, the calculated volume is 8,000 m^3.

Following this procedure, we have characterized the five largest rock masses of the Borrassica slope resting on a basal plane, matching with the orientations of F3 or F5 joint sets whose outcrops have been double-checked in the photographs (Figure 13). Each of these rock masses is bounded by the topographic surface (open slope) and the highly persistent planes of F1 and F7 joint sets. It is assumed that the basal plane maintains its continuity under the rock mass until intersecting the persistent planes of the F1 and F7 joint sets or the topographic surface on the other side of the ridge are intersected. Table 5 shows the geometric characteristics of the volumes identified.

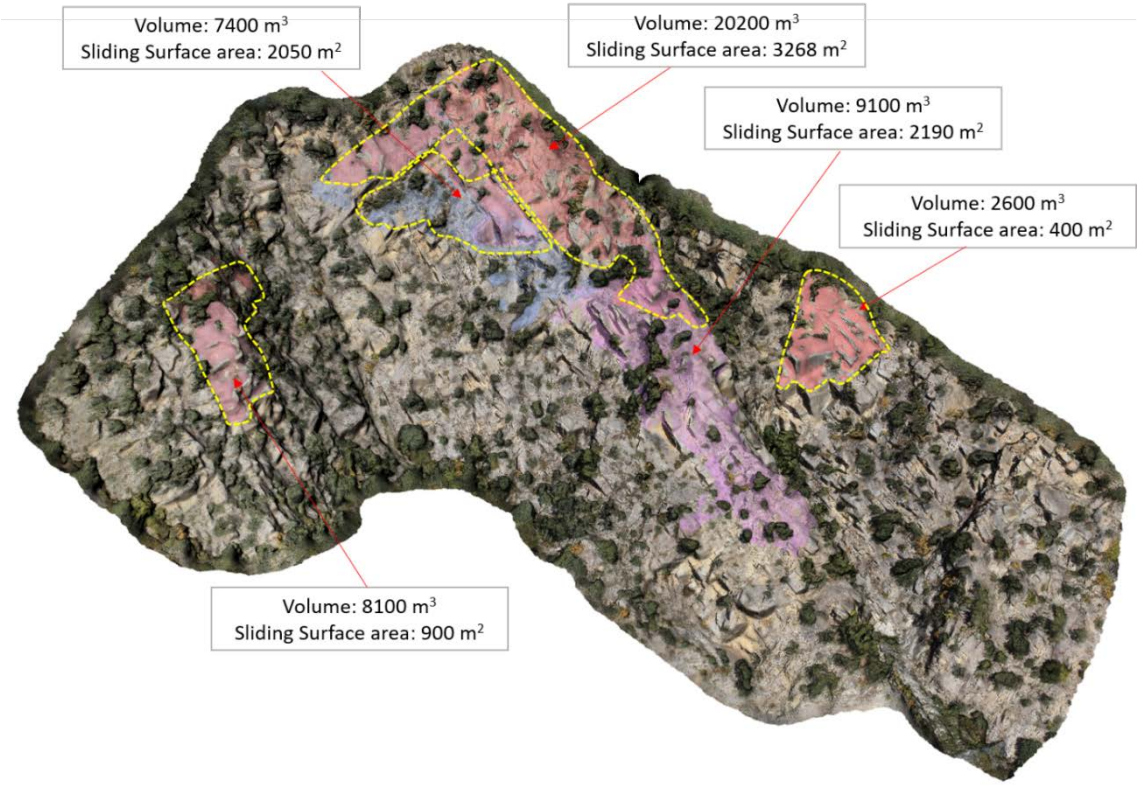

Figure 13. Texturized point cloud showing the largest volumes of rock spurs defined at the slope of Borrassica-Forat Negre

Table 5. Volumes of the rock spurs identified at the slope of Borrassica – Forat Negre

Roc spur	Basal plane area (F3 or F5 set) (m^2)	Volume of the rock mass (m^3)
BO-01	400	2600
BO-02	2190	9100
BO-03	3268	20200
BO-04	2050	7400
BO-05	900	8100

We compared the volumes and basal areas of the rock spurs with the volumes estimated from the theoretical criteria of the test Markland used in the previous section. While the largest basal area identified from the Markland test is about 1300 m2, the basal area of rock spurs is significantly bigger (up to 3270 m2). However, the calculated volumes of the rock spurs are much smaller. This is due to the assumptions made in Mavrouli et al. (2015) on the persistence of the sliding planes and for converting areas to volumes. This supports the argument that the procedure used to calculate volumes with the simple kinematic approach overestimates the volume of potentially unstable rock masses and may set the highest bound for the MCE. Using this new approach (of 5volumes), the volumes that we obtain are lower than the 50,000 m3 calculated previously.

The size distribution of scars obtained in equation [1] is the empirical evidence of rockfall events that have occurred in the past. However, the kinematically movable rock masses from individual rock spurs are scenarios that might occur in the future. Comparing the size of the largest volume calculated from the scars (approximately 3,000 m3) and that of the most prominent rock spur (20,000 m3) or of the rock wall under the criteria of the Markland test (50,000 m3) is one order of magnitude. Although the difference is remarkable, it is worth noticing that none of the procedures used is capable to justify the volumes extrapolated from the F-M relation of Figure 2.

The areas of the basal plans under the rock spurs may reach up to > 3200 m2. However, planes of this size are not observed in the basal plane of the scars, as the maximum surface measured basal plane of rupture is 213 m2 (Mavrouli and Corominas, 2017), and cannot be justified either by fitting large planes to stepped down-dip adjacent planes.

An interesting detail of the area distribution of the planes measured with TLS (Figure 8) is that a truncation of the power relationship (area - cumulative frequency) occur for both F3 and F5 joint sets, which causes a significant reduction of the number of planes over 100 area m2 in relation to what is expected from the corresponding power law.

The truncation of the relationship is not fictitious as it applies to areas that have actually been identified and measured. Truncation may have a geological reason as it will be discussed in the next section. The truncation or deviation from the trend is also observed in other rockfall records (Figure 144), thus reducing the frequency of large rockfalls several orders of magnitude in relation to the provisions of the power law (Hungr et al. 1999; Guzzetti et al. 2003; Böhme et al. 2015).

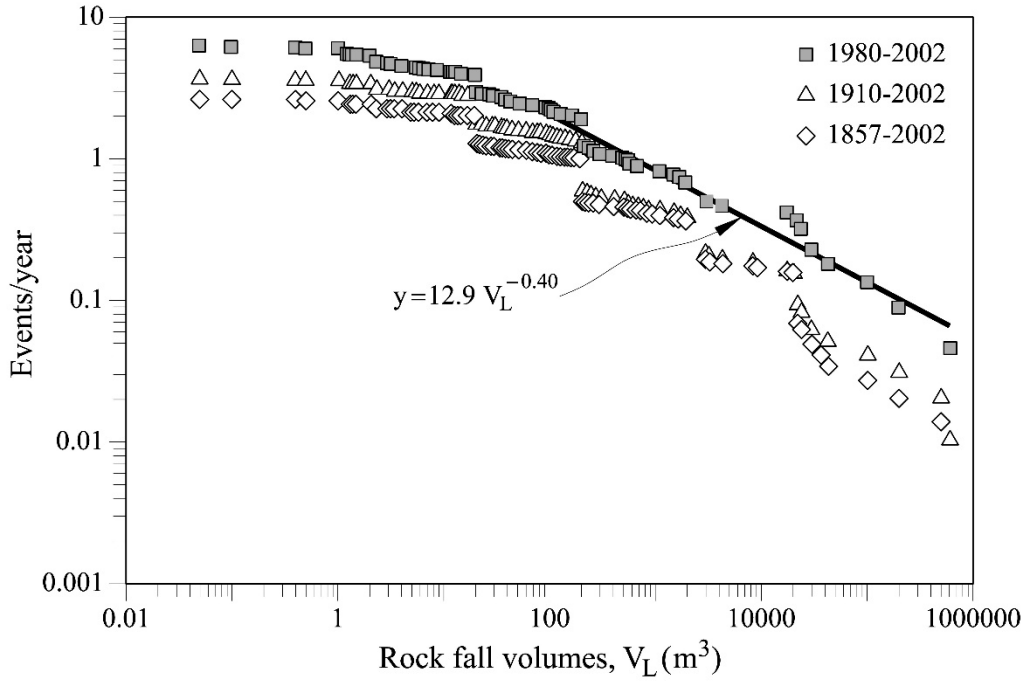

Figure 14. Truncation of the power law for rockfalls in Yosemite (from Guzzetti et al. 2003)

5. Role of the geologic structure

Lithology, structure and erosion history (i.e. glacial steepening and debutressing) are predisposing factors of rock slope failures (Evans and Clague, 1988). The role of the geologic structure for the generation of large rockslides and avalanches is well documented in the literature. The fracture pattern frequently facilitates the kinematic release of large slope failures (Guzzetti et al., 1996; Agliardi et al., 2001, 2009b; Badger, 2002; Massironi et al., 2003; Ambrosi and Crosta, 2006; Stead and Wolter, 2015). The sliding planes of large slope failures often develop along pre-existing planar features in the rock mass such as bedding planes, exfoliation joints, faults or cleavage dipping unfavourably towards de valley (Hermanns and Strecker, 1999; Keller, 2017) although in some regions this is not a requisite for the development large slope slope failures (Jarman, 2006; Cave and Ballantyne, 2016). On the contrary, the role of the geologic structure in constraining the size of the rock slope failures is less known.

In the Borrassica Forat Negre slope, Mavrouli and Corominas (2017) observed the frequent interruption of the basal planes (discontinuities F3 and F5) at their intersection with the tension crack and lateral release planes F7 and F1, respectively, which prevent the formation of large failures. Using independent procedures, they showed that the distribution of the exposed lengths along the dip of the F3 and F5 planes are similar to the distribution of the spacings of planes of F7. Furthermore, the analysis of the largest exposed lengths of F3 and F5 showed that, in some cases, these planes are up to four times longer than the maximum spacing of F7. This fact suggested that in the Forat Negre slope, the failure surface may also generate by coalescence of several (although few) unfavourable dipping F3/F5 planes and/or by brittle failure of minor rock bridges. Some of these cases were identified on photos (Figure 15). The maximum volume will therefore depend on the length of the basal plane and on the resistance of the rock bridges, if any.

Figure 15. Rockfall scar of April 20th, 2008. The failure developed over several adjacent down-dipping planes (F3) generating a stepped sliding surface (black solid line). Steps are formed F7 planes (yellow dashed polygons) and broken rock bridges. The failure is bounded laterally by planes of F1 set.

We performed a structural analysis of the joint sets of the Forat Negre looking for the reason of the interruption of the kinematically unstable joint sets that could justify the greater b-value of the scar volume distribution and a cutoff value for the largest expected volume. The field survey was carried out in the slopes of the granodiorite massif of Borrassica and Forat Negre, aiming at determining the relative chronology of the tectonic features affecting the rock mass (Figure 16). It was performed at key outcrops where discontinuities are well exposed. The outcrops were studied by combining scanlines and detailed structural observations. It is found that set F6 was formed first as it is affected by other sets that interrupt and displace its planes. A second phase is characterized by sets F2 poorly identified with LiDAR and merged with F7. They should be interpreted as conjugate faults. F3 is a joint set that could be associated to this phase. It shows high scattering and undulation with amplitude up to 20cm. The last phase is characterized by the occurrence of F1 and F4, which include both very persistent conjugate faults and joints that interrupt the rest of sets.

Fault sets (F1, F7) have a twofold role: they interrupt the continuity of the planes of the F3 and F5 joint sets; at the same time, they act as weak zones facilitating the formation of both the lateral and back release surfaces of the sliding rock masses.

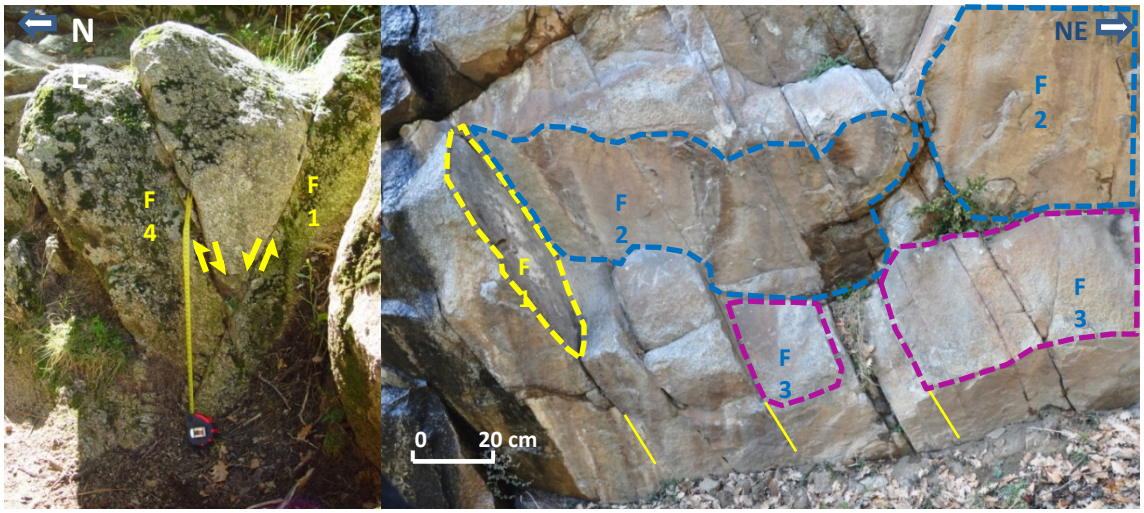

Figure 16. (left) Outcrop of conjugated faults F4 and F1; (right) intersection of planes of sets F1, F3 and F2 (from Corominas et al. 2017)

6. May the geological structure constraint the rockfall size in the Solà d'Andorra?

We have evaluated how the displacement of F1 and F7 faults affects the persistence of the F3/F5 planes (basal failure surface). We have developed a procedure for the probabilistic calculation of the distribution of the length, width and area of the planes of the sets F3 and F5, taking into account their displacement when intersected by F1 and F7 fault planes. The procedure

incorporates the probability of the F3 and F5 planes preserving or losing their continuity. The dimensions of the continuous F3 and F5 planes then depend on the number and dimensions of the sections of planes F3 and F5 between successive spacings of F1 and F7 that can be considered continuous. The continuity criterion is based on the perpendicular distance between two joints of the same set, in two successive sections. A general representation of the rock mass fracture pattern with 3 discontinuity sets is seen in Figure 17.

This threshold was selected because it was found to efficiently distinguish undulation from spacing at most cases in the study area (Santana et al. 2012), although some overlapping may exist for distances 0.10-0.25 m.

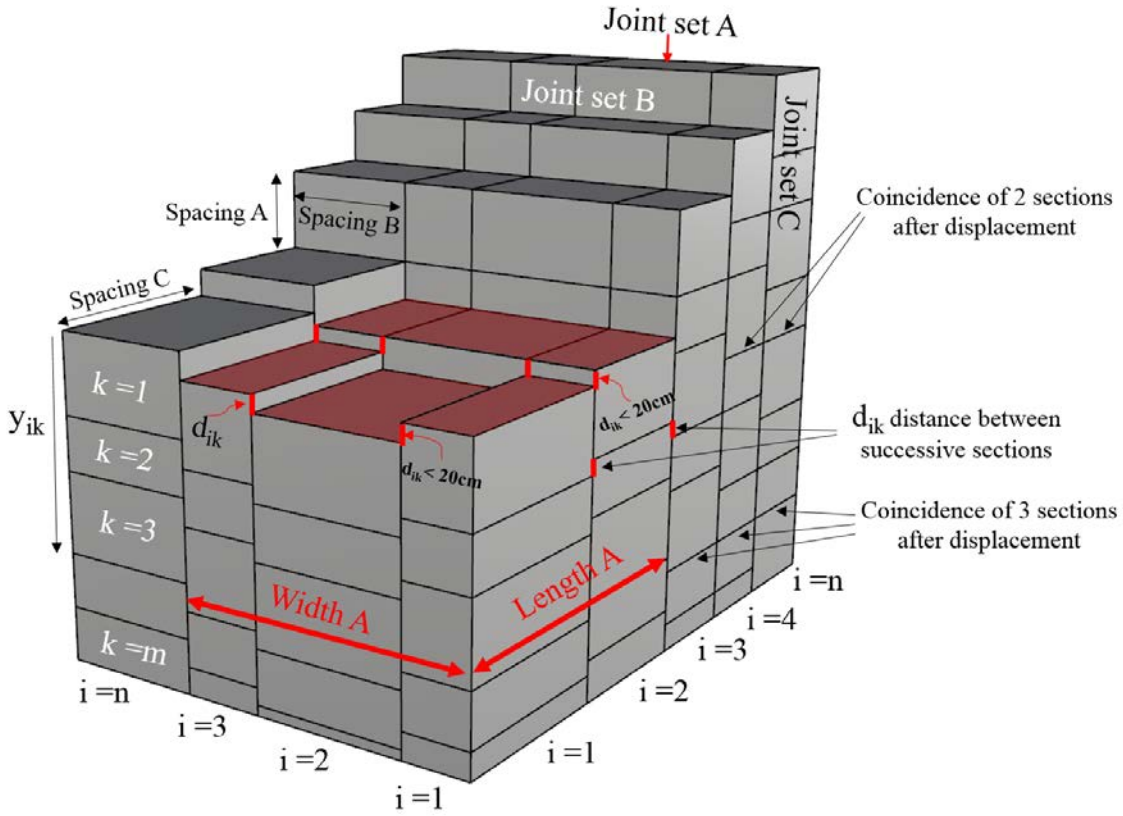

Figure 17. Rock mass with 3 discontinuity sets for the calculation of the probability mass function (pmf) of generating a continuous plane of set A containing i=1,2,3…n spacings, in the direction of length or width. At their intersection with either B or C faults, planes of set A are displaced a distance "d". If dik<0.2 m, the successive sections of plane A form a single continuous basal plane.

In Figure 17, the rock mass is composed by columns bounded by two vertical sets of faults (B and C). The columns contain "k" series of planes of the joint set A. A section of plane A may or may not lose its continuity at each intersection with planes B or C. Two sections of plane A form a continuous plane if their perpendicular distance (dik) at the intersection is smaller than 0.20 m. This threshold was selected because it was found to efficiently distinguish undulation from

spacing at most cases in the study area (Santana et al. 2012). Through this process, the size of the planes of the set A can grow by connecting a number of “i" sections that yield a displacement “dik” smaller than the threshold, in either width or length or both (Figure 17, in red).

As the displacement along each fault plane is not known, the A planes in each column were generated randomly and independently, with the only requirement to maintain the actual spacing distribution. Similarly, the spacings of sets B and C comply with their observed distribution. For the application, the joint set A corresponds to the sets F3 and F5. For F3, the joint sets B and C correspond to F7 and F1, respectively and for F5, to F1 and F7, respectively.

The application of the procedure requires as an input sample data for the spacing of the sets F3 and F5 (basal planes) and of the sets F1 and F7 (tension crack and lateral planes). The spacing data was obtained for each joint set using the Lidar point cloud of the slope face. We identified a representative sample of planes and we measured the perpendicular distance between the adjacent ones, using the software Rhinoceros®. Having obtained the discrete set of spacings S we proceeded with the following two steps which were performed for each F3 and F5.

Step 1: Calculation of the probability mass function (pmf) of a continuous plane of a given joint set being composed by i=1,2,3…n sections along a direction.

For each set, F3 and F5, we generated i=[1,2,3,...n] columns (sections), of k=[1,2,3,...m] planes within each column. Between the planes k=m-1 and k=m, there is random spacing of distance s, that takes values from the discrete spacing sets S ($s \epsilon S$) of F3/F5. The number “i" of columns represents the number of spacings F1 or F7 included between successive intersection points of the planes F3 and F5 with the sets F1 and F7. We investigated the continuity of planes F3/F5 for a maximum of 13 intersections and accordingly n=13 columns. For the calculation of the probability mass function (pmf) using the Monte Carlo method, we simulated k=5000 planes within each column.

First, the vertical distances yik of all the generated planes with i=[1,2,3,...n] and k=[1,2,3,...m] from a common reference plane with i=1 and k=1, were calculated. This permitted the identification of the minimum distance dik of each plane of a column “i” from the planes of the column “i+1” (Figure 17). As aforementioned, if the minimum distance between a plane of the column “i” from a plane of the column “i+1” was found smaller than 0.20 m, the planes were considered continuous. If not, they were considered interrupted and separate. We must take into account however, that not all the planes of joint sets F1 and F7 are fault planes.

Using the generated sample of "i" columns and ¨k¨ planes within each column, and also the distances dik, we calculated the probability mass function (pmf) of a continuous plane being composed by i=1,2,3…n sections. The probability of a continuous plane being composed by i=1,2,3…n sections, along a direction is given by Equation [4]:

$$P(i)=(\text{Number of } dik<0.2 \text{ m}/ \text{ Number of } d1k), \text{ for } i=[1,2,3,...n] \quad [4]$$

In equation [4], the "number of dik<0.2 m" is the number of measurements that fulfill the plane continuity criterion dik<0.2 m for each column "i" and all previous columns.

The pmf depends on the spacing of F3 and F5. When the spacing of a set is smaller (denser), then the probability of having longer and wider continuous planes increases.

Step 2: Calculation of the probability density function (pdf) of the length, width and area of the continuous planes

The intersection of the joint sets for the formation of the basal sliding planes is shown in Figure 17. The span of each section is determined by the spacing of the intersecting joints. Thus, using Monte Carlo simulations (N=5000 random samples), the probability density functions of the length L, width W of the planes of F3 and F5, can be assessed by Equations [5] to [8].

$$LF3=NF3 \times sF7 \quad [5]$$

$$WF3= NF3 \times sF1 \quad [6]$$

$$LF5= NF5 \times sF1 \quad [7]$$

$$WF3= NF5 \times sF7 \quad [8]$$

Where : N: number i=[1,2,3,...n] of successive discontinuities of a given set composing a continuous plane, and s: spacing s ϵ S of the intersecting set

The random sample of N follows the pmf that were calculated at step 1 for F3 and F5, and the spacings s, take random discrete values from the input spacing set of F1 and F7.
For the basal planes F3, the intersecting set in the direction of its length is F7 and in the direction of its width is F1. Respectively, for the basal planes F5, the intersecting set in the direction of its length is the F1 and of its width is the F7.

Then the distribution of the areas of the continuous planes of F3 and F5 were assessed by Eqs [9] and [10], assuming for simplicity, rectangular basal areas.

$$A\ F3 = LF3 \times WF3 \quad [9]$$

$$A\ F5 = LF5 \times WF5 \quad [10]$$

N=5000 random samples of lengths and widths, were also used for Monte Carlo simulations of the areas.

The results of step 1 for the calculation of the probability mass function of a continuous plane being composed by i=1,2,3…n spacings are presented in Figure 18, for the sets F3 and F5. Table 6 shows these probabilities. It also resumes the number of planes (values have been rounded) that is expected to contain "i" spacings, out of the total of number of planes that were identified on the point cloud for each set, that 4760 for F3 and 3920 for F5.

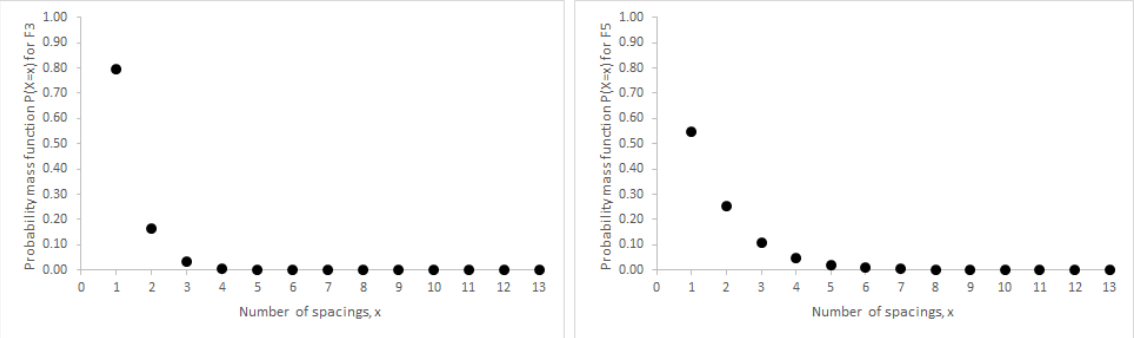

Figure 18. Probability mass function for the number of spacings of either F1 or F7 being contained in a continuous plane, for the set F3 (left) and F5 (right)

Table 6. Probability of a plane containing "i" spacings (5000 simulations) and number of planes with "i" spacings (out of 4760 for F3 and 3920 for F5)

Number of spacings contained	Probability Set F3 (±0,1)	Probability Set F5 (±0,1)	Number of planes F3	Number of planes F5
1	0.7994	0.5419	3805	2124
2	0.1606	0.2533	764	993
3	0.0320	0.1105	152	433
4	0.0064	0.0541	30	212
5	0.0012	0.0216	6	85
6	0.0004	0.0110	2	43
7	0.0000	0.0030	0	12
8	0.0000	0.0032	0	13
9	0.0000	0.0006	0	2
10	0.0000	0.0004	0	2
11	0.0000	0.0004	0	2
12	0.0000	0.0000	0	0
13	0.0000	0.0000	0	0

We compared the results from the application of this procedure with the dimensions of the exposed planes of the sets F3 and F5, as observed on the Lidar point cloud following the procedure of Santana et al. (2012).

Table 7 and Table 8 summarize the median, maximum and standard deviation that were calculated for the length, width and area of the planes of F3 and F5, as well as the respective observed values on the point cloud.

Table 7. Geometrical features of the planes F3: calculated (proposed procedure) and observed (Santana et al. 2012)

			Median	Max	Standard deviation
Calculated with Monte Carlo Simulation		Length (m)	1.1	35	1.4
		Width (m)	2.1	48	2.7
		Area (m^2)	4	584	7
Observed		Length (m)	1.0	27	1.5
		Width (m)	2.2	40	2.7
		Area (m^2)	0.7	236	10

Table 8. Geometrical features of the planes F5: calculated (proposed procedure) and observed (Santana et al. 2012)

		Median	Max	Standard deviation
Calculated with Monte Carlo Simulation	Length (m)	2.9	59	4.6
	Width (m)	1.4	50	2.5
	Area (m^2)	4	705	19
Observed	Length (m)	0.7	15	0.9
	Width (m)	0.8	20	1.2
	Area (m^2)	0.38	144	5

Values greater than those of Table 7 and Table 8 are possible with a probability of occurrence lower than 2x10-4.

The analysis of 5,000 simulations, shows that the dimensions of the generated basal surfaces for F3 are very similar to the measured with the TLS. For the basal surfaces of F5, the calculated length, width and area are bigger than the observed ones. The largest F5 basal area generated is 705 m2, which is about 5 times bigger than the largest area measured. Despite of this, the sizes of the generated basal surfaces are of the same order of magnitude than the measured using the TLS

by Santana et al. (2012). This exercise confirms that the presence of the F1 and F7 faults could restrict the extent of the F3/F5 sliding surfaces and bound the size of the potential slope failures.

7. Discussion

We argue that we should not expect a random distribution of large landslides, in particular large rockslides and rock avalanches. In some regions there may exist a truncation for large volumes (upper size limit) and that geological factors may partially explain this behaviour.

7.1 Spatial distribution of large slope failures

Rock slope failures (RSF) is a term coined frequently found in geomorphological studies that encompasses three main slope instability forms (Ballantyne, 2002; Jarman, 2006; Cave and Ballantyne, 2016): catastrophic failures in the form rockslides, rock avalanches and major toppling; deep-seated gravitational slope deformations; complex failures involving two or more of the above. In the main mountain belts, RSF are often considered as paraglacial, implying that failure was preconditioned by the preceding episode of glaciation and deglaciation (Ballanyte, 2002; McColl, 2012). Despite a number of studies have focused on RSF, the knowledge of their distribution at a regional scale, timing and causes is still incomplete. The spatial analysis of the RSF suggests that a relation exists between the occurrence of the failures and the type of geological structures, the lithologies involved, and the inherited glacier relief/geomorphological setting (Jarman, 2006) or the triggers (Cave and Ballanyte, 2016; Crosta et al. 2016).

Regional inventories of large RSF have shown that:

a) RSF are uneven spatially distributed (Whalley et al 1983; Jarman 2006; Jarman et al. 2014; Strom 2015; Keller, 2017)
b) Greater density of occurrence on some susceptible lithologies (Cave and Ballantyne, 2016) but this is not a requisite in other locations (Strom, 2015)
c) Some events are recurrent in the same location (Shang et al. 2003; Hermanns et al. 2004; Evans et al. 2009; Delaney and Evans, 2015; Strom, 2015; Crosta et al. 2016)
d) Some regions are relatively rockslides-free areas (Strom, 2015).

Literature review shows that the density of landslides varies from one region to another and large rock slope failures are not evenly distributed in mountain regions. Jarman (2006) found in the Scottish Highlands that 65% of the large slope failures were concentrated in seven main clusters while the rest were non-randomly scattered. In Iceland, large rockslides occur almost entirely on

(within) a particular lithological unit (Tertiary lavas), particularly in locations where the lava layers dip towards the valley (Whalley et al. 1983).

The first comprehensive study of large-scale rock slope failures in the Eastern Pyrenees where the Solà d'Andorra is located, identified 30 main large slope failures and further 20 smaller or uncertain cases (Jarman et al. 2014). The inventory did not show any obvious regional pattern or clustering and a surprisingly sparse population that affects 45–60 km2 or 1.5–2.0% of the 3000 km2 glaciated core of the mountain range and neighbouring fluvial valleys. From them, only 27% can be considered as large catastrophic events (rock or debris avalanches) and none of them were located in the Valira river valley. For comparison, in the Alps, 5.6% of the entire 6200 km2 montane area is affected by deep-seated gravitational slope deformations alone (Crosta et al. 2013) and up to 11% in the Upper Rhone basin (Pedrazzini et al (2016). This sparsity has been interpreted by a low-intensity glaciation and less subsequent debuttressing, relative tectonic stability and small fluvial incision (Jarman et al. 2014). When compared to other mountain ranges, the Pyrenees have been less steepened and incised by the Pleistocene glaciers. The slopes in the Valira valleys commonly rise 1000m from valley bottoms, reaching a maximum of up to1400m. In the Karakoram, the Southern Alps of New Zealand and in the Pacific Coastal Ranges of USA and Canada, the slopes usually rise 3000m and some may attain more than 6000m (Hewitt et al. 2008).

7.2 Truncation of the power laws

Many natural processes are described by power law distributions such as fault displacements (Kakimi, 1980), fault trace length (Bonnet el al 2001), earthquakes (Gutenberg and Richter, 1954). Data collected to measure the parameters of such distributions only represents samples from some underlying population. Without proper consideration of the scale and size limitations of such data, estimates of the population parameters, particularly the exponent of the power law, are likely to be biased (Pickering et al. 1995). As stated by Hovius et al. 1997, extrapolating short-term geomorphic observation to time scales pertinent to landscape development requires an understanding of the scaling behaviour of the processes involved, in particular the magnitude and frequency with which they occur (Wolman and Miller, 1960; Hovius et al. 1997). All power law and fractal characteristics in nature must have upper and lower bounds (Bonnet el al. 2001).

All the evidences suggest that an upper limit to the size of the slope failures in the Sola d'Andorra might exist. These observations are consistent with the findings of Hergarten (2012), who applied a simple model for rock detachment in the Alps, Southern Rocky Mountains and the Himalayas. He found a breakdown of the power law distributions at large events. Large slope failures occur

less frequently than predicted by the power laws and the size at which the cut-off takes place, varies from one region to other. Furthermore, the size of largest event at each region may differ more than one order of magnitude. These differences were attributed to the different geologic and climatic context although a detailed work was not carried out. Clarke and Burbank (2010) compared the occurrence of rock slope failures in Fiorland and western Southern Alps in New Zealand. These two regions are subjected to similar climate but different uplift rates and lithologies. They observed that despite failures initiate on slopes steeper than the modal hillslope angle in both regions, the frequency-magnitude distributions revealed one order of magnitude difference, being considerably smaller in Fiorland. These authors conclude based on geophysical surveys that the dense geomorphic fracturing in Fiorland appears to limit the depth and magnitude of the slope failures. Conversely, in the Southern Alps, fractures are more pervasive and result in larger and deeper landslides.

The incompleteness of the record or the use of different criteria for fitting of the power laws to the volume distributions may therefore produce significant differences in the estimation of the frequency of large events.

7.3 Role of the geological factors

The assumption of random distribution of the slope failures overlooks the basic geomechanical prerequisites (rock strength, fracture pattern, relief,..) for failure (Selby, 1992; Jarman, 2006) as it is evident that some geological contexts (i.e. steeply dipping discontinuities or weak lithologies) favour the occurrence of the slope failures. Tectonic damage has also been accounted for several stepped large rock slope failures (Brideau et al 2009). In our work, we argue that the fracture pattern (geological context) of the Solà d'Andorra plays a key role in constraining the size (defining the cutoff size) of large rockslope failures. Fault sets (F1, F7) have a twofold role: they interrupt the continuity of the planes of the F53 and F5 joint sets; at the same time, they act as weak zones facilitating the formation of both the lateral and back release surfaces of the sliding rock masses.

It is also evident that other factors can be accounted for. In alpine mountain glacial and fluvial incision of the valley bottoms causes steepening of the valley slopes that induces slope failures (Selby, 1980). In tectonically active regions, the sustained rock uplift and valley incision perpetuates this process and results in a landslide-dominated landscape (denudation) (Burbank, et al. 1996). The analysis of the slope angles distribution in tectonically active mountain belts has shown that there exists threshold conditions of slope inclination or height at which they fail readily because of limitations in material strength (Korup et al. 2007).

Therefore, the scarce number of large rock slope failures and rock avalanche deposits in Andorra should not be considered an exception. Low density of RSF has been also observed in Scotland (Cave and Ballantyne, 2016)

8. Conclusions

This paper through the analysis of the rockfall occurrence at the rock wall of Borrassica-Forat Negre of the Solà d'Andorra addresses the validity of the extrapolation of the M-F relations obtained far beyond the temporal window used for their preparation. We argue that despite the M-F relation is well fitted, there exist no evidences supporting the occurrence large slope failures (larger than 100,000m3) in the Solà d'Andorra at least, during the last 10,000 years. Neither rockslide/rock avalanche deposits were found in the Valira river valley bottom nor evident large detachment scars (rockfall cavities) are identified in the rock walls from the analysis of the TLS-generated point cloud of the outcropping surfaces.

According to the geo-structural analysis (fracture pattern) and the geomorphological evidences, the most predominant slope failure mechanism is planar sliding surfaces. The largest exposed sliding surface has an area of 200 m2 while the M-F relation of the surfaces measured is truncated at around 50m2. The volume distribution of 5000 rockfall scars generated stochastically by combining the measured areas of the basal sliding surfaces and the scar heights, which may cover a time span of several thousands of year, yielded a maximum rockfall scar volume of 3000 m3 (Santana et al. 2012). No evidences have been found that could justify the occurrence of a large stepped failure in the past.

Two independent procedures have been applied to measure the size of the kinematically detachable rockfall masses according to Markland instability criteria (Mavrouli and Corominas 2017) and the size of rock spurs lying over unfavourable dipping highly persistent joints. The largest volumes identified are of a few tens of thousands of cubic meters only. These results are consistent with the absence of rock slide or rock avalanche deposits at the bottom of the Andorra la Vella basin.

The detachment of large rock masses via step-path failures is prevented by the geological structure. The interruption of the sliding planes by two orthogonal highly persistent sets of faults (F1 and F7), restrict the development of large rock mass volumes. The volume restriction can be overcome to some extent either by coalescence of basal planes or through step-path failures involving the breakage of rock bridges. This situation however, will necessarily involve smaller

volumes than in the case of fully persistent basal joints. Because of this, we conclude that the maximum credible volume for Forat Negre is significantly smaller than the expected from the basic kinematical analysis of the rock slope. The case of Andorra provides empirical evidence that rockfall could be size-constraint due to the geological structure.

The lack of evidences of large slope failures in this reach of the Valira river valley should not be considered as an anomaly because several studies in mountainous ranges worldwide have demonstrated that large rockslides and rock avalanches are not randomly distributed in the space and that local geological and geomorphic conditions exert some control the development of the slope failures.

ACKNOWLEDGMENTS

This work has been carried out with the support of the fellowship to the third author and within the framework of the research project Rockmodels financed by the Spanish Ministry of Economy and Competitiveness (BIA2016-75668-P) and by the Government of Andorra (Edicte de 10/04/2013, BOPA nº18 17/04/2014).

References

Abbruzzese JM, Sauthier C, Labiouse V (2009) Considerations on Swiss methodologies for rock fall hazard mapping based on trajectory modelling. Nat Hazards Earth Syst Sci 9:1095-1109

Agliardi F, Crosta G, Zanchi A (2001) Structural constraints on deep-seated slope deformation kinematics. Engineering Geology 59: 83–102.

Agliardi F, Crosta GB, Frattini P (2009a) Integrating rockfall risk assessment and countermeasure design by 3D modelling techniques. Nat Hazards Earth Syst Sci, 9: 1059-1073

Agliardi F, Crosta GB, Zanchi A, Ravazzi C (2009b) Onset and timing of deep-seated gravitational slope deformations in the eastern Alps, Italy. Geomorphology 103: 113–129.

Ambrosi C, Crosta GB (2006) Large sackung along major tectonic features in the Central Italian Alps. Engineering Geology 83: 183–200

Amigó J, Altimir J, Copons R (2001) Verificación de los resultados del modelo de simulación Eurobloc a partir de casos reales de caídas de bloques rocosos. V Simposio Nacional sobre Taludes y Laderas Inestables. Madrid. Vol. 2: 653-663.

Badger TC (2002) Fracturing within anticlines and its kinematic control on slope stability. Environmental and Engineering Geoscience VIII: 19–33.

Ballantyne CK (2002) Paraglacial geomorphology. Quaternary Science Reviews 21: 1935-2017

Ballantyne CK, Stone JO (2004) The Beinn Alligin rock avalanche, NW Scotland: Cosmogenic 10Be dating, interpretation and significance. The Holocene 14: 448-453

Barlow J, Lim M, Rosser N, Petley D, Brain M, Norman E, Geer M (2012) Modeling cliff erosion using negative power law scaling of rockfalls.Geomorphology 139: 416-424

Barton N, Bandis S (1982) Effects of block size on the shear behavior of jointed rock. The 23rd U.S Symposium on Rock Mechanics, Berkeley, California. pp. 739-760

Böhme M, Oppikofer T, Jaboyedoff M, Hermanns RJ, Derron MH (2015) Analyses of past and present rock slope instabilities in a fjord valley: Implications for hazard estimations. Geomorphology 248: 464–474

Bonnet E, Bour O, Odling NE, Davy P, Main I, Cowie P, Berkowitz B (2001) Scaling of fracture systems in geological media. Reviews in Geophysics, 39: 347-383

Bourrier F, Dorren L, Hungr O (2013) The use of ballistic trajectory and granular flow models in predicting rockfall propagation. Earth Surf Processes Landforms 38: 435–440

Brardinon, F, Church M (2004) Representing the landslide magnitude–frequency relation: Capilano River Basin, British Columbia. Earth Surface Processes and Landforms 29: 115–124

Brideau MA, Yan M, Stead D (2009) The role of tectonic damage and brittle rock fracture in the development of large rock slope failures. Geomorphology 103: 30-49

Brundl M, Romang HE, Bischof N, Rheinberger CM (2009) The risk concept and its application in natural hazard risk management in Switzerland. Nat. Hazards Earth Syst. Sci., 9: 801–813

Burbank DW, Leland J, Fielding E, Anderson RS, Brozovic RS, Reid MR, Duncan C (1996) Bedrock incision, rock uplift and threshold hillslopes in the northwestern Himalayas. Nature, 379: 505-510

Cascini L, Bonnard C, Corominas J, Jibson R, Montero-Olarte J 2005. Landslide hazard and risk zoning for urban planning and development. State of the art report (SOA7). In: Hungr O, Fell R, Couture R, Eberthardt E (eds) Proceedings of the international conference on “landslide risk management”, Vancouver (Canada). Taylor and Francis, London, pp 199–235

Cave JAS, Ballantyne CK (2016) Catastrophic Rock-Slope Failures in NW Scotland: Quantitative Analysis and Implications. Scottish Geographical Journal 132: 185-209

Chau KT, Wong RCH, Liu J, Lee CF (2003) Rockfall Hazard Analysis for Hong Kong Based on Rockfall Inventory. Rock Mech Rock Eng 36: 383–408

Clarke BA, Burbank DW (2010) Bedrock fracturing, threshold hillslopes and limit to the magnitude of landslides. Earth and Planetary Science Letters 297: 577-586

Copons, R, Altimir J, Amigó J, Vilaplana JM (2001) Medotología *Eurobloc* para el estudio y protección de caídas de bloques rocosos. Principado de Andorra. V Simposio Nacional sobre Taludes y Laderas Inestables. Madrid. Vol. 2: 665-676.

Copons R, Vilaplana JM, Corominas J, Altimir J, Amigó J (2004) Rockfall risk management in high-density urban areas. The Andorran experience. In: T.Glade, M. Anderson and M.J. Crozier (eds). Landslide hazard and risk. John Wiley and Sons, Chichester. pp. 675-698.

Copons R (2007) Avaluació de la perillositat de caigudes de blocs rocosos al Solà d'Andorra la Vella. Monografies del CENMA

Corominas, J. (1996) The angle of reach as a mobility index for small and large landslides, Canadian Geotechnical Journal, 33: 260–271.

Corominas J, Copons R, Vilaplana JM, Altimir J, Amigó, J (2003) Integrated landslide susceptibility analysis and hazard assessment in the principality of Andorra. Nat Hazards, 30: 421–435

Corominas J (2007) Experience on landslide risk management in the Eastern Pyrenees (Spain and Andorra): achievements and challenges. In K. Ho and V. Li (Eds). The 2007 International Forum on Landslide Disaster Management. Hong Kong. The Hong Kong Institution of Engineers. Vol 1: 49-70

Corominas J, Copons R, Moya J, Vilaplana, J M, Altimir J, Amigó J (2005) Quantitative assessment of the residual risk in a rock fall protected area. Landslides 2: 343–357

Corominas J, Moya J (2008) A review of assessing landslide frequency for hazard zoning purposes. Eng Geol 102: 193-213

Corominas J, van Westen C, Frattini P, Cascini L, Malet JP, Fotopoulou S, Catani F, Van Den Eeckhaut M, Mavrouli O, Agliardi F, Pitilakis K, Winter MG, Pastor M, Ferlisi S, Tofani V. Hervás J, Smith JT (2014) Recommendations for the quantitative analysis of landslide risk. Bull Eng Geol Env 73: 209-263.

Crosta GB, Frattini P, Agliardi F (2013) Deep seated gravitational slope deformations in the European Alps. Tectonophysics 605: 13–33.

Crosta GB, Hermanns RL, Dehls J, Lari S, Sepulveda S (2016) Rock avalanches clusters along the northern Chile coastal scarp, Geomorphology, doi:10.1016/j.geomorph.2016.11.024

Cruden D M (1975) Major rock slides in the Rockies. Canadian Geotechnical Journal 13, 8–20.

Cruden DM (1985) Rock slope movements in the Canadian Cordillera. Canadian Geotechnical Journal 22: 528–540.

Cruden DM Varnes DJ (1996) Landslide types and processes. In, Landslides Investigation and Mitigation, A. K. Turner and R. L. Schuster, eds.: National Research Council, Transportation Research Board, Special Report 247: 36-75

Cruden DM, Hu XQ (1993) Exhausting and steady state models for predicting landslide hazards in the Canadian Rocky Mountains. Geomorphology 8: 279-285

Davies TR, McSaveney MJ (2002) Dynamic simulation of the motion of fragmenting rock avalanches. Canadian Geotechical Journal 39:789–798

Delaney KB Evans SG (2015) The 2000 Yigong landslide (Tibetian Plateau), rockslide- dammed lake and outburst flood: review, remote sensing analysis and process modeling. Geomorphology 246: 377-393

Dussauge-Peisser A, Helmstetter A, Grasso, JR, Hanz D, Desvarreux P, Jeannin M, Giraud A. (2002) Probabilistic approach to rockfall hazard assessment: potential of historical data analysis. Nat Hazards Earth Syst Sci 2: 15-26.

Dussauge C, Grasso JR, Helmstetter A (2003) Statistical analysis of rockfall volume distributions: Implications for rockfall dynamics. J Geophys Res B6 108: 2286

Eberhardt E, Stead D, Coggan JS (2004) Numerical analysis of initiation and progressive failure in natural rock slopes - the 1991 Randa rockslide. Int. J. Rock Mech. Mining Sciences 41: 69-87.

Escalé J (2001) La nova llei d'ordenament territorial a Andorra. In La Gestió dels Riscos naturals. Primeres Jornades CRECIT. Andorra la Vella. http://www.iea.ad/crecit/primeresjornades.html.

Evans SG, Clague JJ (1988) Catastrophic rock avalanches in glacial environments. In: Bonnard, C. (Ed.), 5th International Symposium on Landslides, Lausanne, Switzerland, 2, pp. 1153–1158.

Evans S, Hungr O (1993) The assessment of rockfall hazard at the base of talus slopes. Canadian Geotechnical Journal 30: 620-636

Evans SG, Bishop NF, Smoll LF, Murillo PV, Delaney KB, Oliver-Smith A (2009) A reexamination of the mechanism and human impact of catastrophic mass flows originating on Nevado Huascarán, Cordillera Blanca, Peru, in 1962 and 1970. Engineering Geology 108: 96-118.

Fell R, Corominas J, Bonnard Ch, Cascini L, Leroi E, Savage WZ (on behalf of the JTC-1 Joint Technical Committee on Landslides and Engineered Slopes) (2008) Guidelines for landslide susceptibility, hazard and risk zoning for land use planning. Eng. Geology 102: 85–98

Ganerød GV, Grøneng G, Rønning JS, Dalsegg E, Elvebakk H, Tønnesen JF, Kveldsvik V, Eiken T, Blikra LH, Braathen A (2008) Geological model of the Åknes rockslide, western Norway. Engineering Geology, 102: 1-18.

Gigli G, Frodella W, Garfagnoli F, Morelli S, Mugnai F, Menna F, Casagli N (2014) 3-D geomechanical rock mass characterization for the evaluation of rockslide susceptibility scenarios. Landslides 11: 131-140.

Guthrie R, Evans SG (2004) Analysis of landslide frequencies and characteristics in a natural system. Coastal British Columbia. Earth Surface Processes and Landforms 29, 1321–1339

Gutiérrez-Rodríguez MC, Turu V (2013) Hidrogeología de un valle glaciar: el caso de la cubeta

de Andorra (Pririneos Orientales). Parte 1: datos geoquímicos. X Simposio de Hidrogeología. Granada. http://www.igeotest.ad/igeofundacio/Activitats/Docs/PDF/Granada/articulo%20hidro%206_Parte%201e.pdf

Guttemberg B, Richter CF (1954) Seismicity of Earth and associated phenomena (2nd Ed.) Princeton University Press, Princeton, NJ.

Guzzetti F, Cardinali M, Reichenbach P (1996) The influence of structural setting and lithology on landslide type and pattern. Environmental and Engineering Geosciences 2: 531–555.

Guzzetti F, Malamud BD, Turcotte DL, Reichenbach P (2002) Power-law correlations of landslide areas in Central Italy. Earth Planet Sci Lett 195: 169-183

Guzzetti F, Reichenbach P, Wieczorek GF (2003) Rockfall hazard and risk assessment in the Yosemite Valley, California, USA. Nat Hazards Earth Syst Sci 3: 491–503.

Hergarten S (2012) Topography-based modeling of large rockfalls and application to hazard assessment, Geophys. Res. Lett. 39, L13402, doi:10.1029/2012GL052090.

Hermanns RL, Strecker MR (1999) Structural and lithological controls on large Quaternay rock avalanches (sturzstroms) in arid northwestern Argentina. Geological Society of America Bulletin, 111: 934-948

Hermanns RL, Niedermann S, Ivy-Ochs S, Kubik PW (2004) Rock avalanching into a landslide dammed lake causing multiple dam failure in Las Conchas valley (NW Argentina) - evidence from surface exposure dating and stratigraphic analyses. Landslides 1: 113 - 122.

Hewitt K, Clague JJ, Orwin JF (2008) Legacies of catastrophic rock slope failures in mountain landscapes. Earth-Sci Reviews, 87: 1–38

Ho KKS (2004) Recent advances in geotechnology for slope stabilization and landslide mitigation – perpective from Hong Kong. In: Lacerda, W.A., Ehrlich, M., Fontoura S.A.B., Sayao, A.S.F (eds) Landslides: Evaluation and Stabilization.. Taylor and Francis, London, UK. Vol. 2 pp. 1507-1560

Hsü KJ (1978) Albert Heim: observations of landslides and relevance to modern interpretations. In: Voight, B. (Ed.), Rockslides and Avalanches; 1, Natural Phenomena. Elsevier, Amsterdam, pp. 70–93.

Hovius N, Stark CP, Allen PA (1997) Supply and removal of sediment in a landslide-dominated mountain belt: Central Range, Taiwan. Journal of Geology 108: 73-89

Hungr O, Evans SG, Hazzard J (1999) Magnitude and frequency of rock falls and rock slides along the main transportation corridors of southwestern British Columbia. Canadian Geotechnical Journal, 36: 224-238

Hungr O, Leroueil S, Picarelli L (2014) The Varnes classification of landslides types, an update. Landslides 11:167-194.

Jarman D (2006) Large rock slope failures in the Highlands of Scotland: characterisation, causes

and spatial distribution. Engineering Geology, 83: 161-182

Jarman D, Calvet M, Corominas J, Delmas M, Gunnell Y (2014) Large-Scale Rock Slope Failures in the Eastern Pyrenees: Identifying a Sparse But Significant Population in Paraglacial and Parafluvial Contexts. Geogr Ann A 96 (3): 357-391.

Kakimi T (1980) Magnitude frequency relation for displacement of minor faults and its significance in crustal deformation. Bull. Geol. Society of Japan, 31: 467-487

Keller B (2017) Massive rock slope failure in Central Switzerland: history, geologic–geomorphological predisposition, types and triggers, and resulting risks. Landslides DOI 10.1007/s10346-017-0803-1

Korup O, Clague JJ, Hermanns RL, Hewitt K, Strom AL Weidinger JT (2007) Giant landslides, topography and Erosion, Earth and Planetary Science Letters 261: 578–589

Lari S, Frattini P, Crosta GB (2014) A probabilistic approach for landslide hazard analysis. Engineering Geology 182: 3-14

Li ZH, Huang HW, Xue YD, Yin J (2009) Risk assessment of rockfall hazards on highways. Georisk, 3: 147-154

Malamud BD, Turcotte DL, Guzzetti F (2004) Landslide inventories and their statistical properties. Earth Surface Processes and Landforms 29: 687–711

Marques FMSF (2008) Magnitude-frequency of sea cliff instabilities. Nat. Hazards Earth Syst. Sci. 8: 1161–1171,

Massironi M, Bistacchi A, Dal Piaz GV, Monopoli B, Schiavo A (2003) Structural control on mass-movement evolution: a case study from the Vizza Valley, Italian Eastern Alps. Eclogae Geologicae Helvetiae 96: 85–98.

Mavrouli O, Corominas J, Jaboyedoff M (2015) Size distribution for potentially unstable rock masses and in-situ rock blocks using LIDAR generated Digital Elevation Models. Rock Mechanics Rock Engineering 48: 1589-1604

Mavrouli O, Corominas J (2017) Comparing rockfall scar volumes and kinematically detachable rock masses. Engineering Geology, 219: 64–73

McColl ST (2012) Paraglacial rock-slope stability. Geomorphology, 153-154: 1-16

Pedrazzini A, Humair F, Jaboyedoff M, Tonini M (2016) Characterisation and spatial distributionof gravitational slope deformation in the Upper Rhone catchment (Western Swiss Alps). Landslides 13: 259–277

Picarelli L, Oboni F, Evans SG, Mostyn G, Fell R (2005) Hazard characterization and quantification. In O. Hungr, R. Fell, R. Couture and E. Eberthardt (editors) Landslide Risk Management. Taylor and Francis, London. pp. 27-61 ISBN: 041538043X

Pickering G., Bull, JM, Sanderson DJ (1995) Sampling power-law distributions. Tectonophysics, 248: 1-20

Rochet L (1987) Application des modeles numeriques de propagation a l'etude des eboulements

rocheux. Bull Lab Ponts et Chaussées 150/151: 84–95

Rosser N, Lim M, Petley D, Dumming S, Allison R (2007) Patterns of precursory rockfall prior to slope failure. J Geophys Res 112: F04014,

Rossi M, Witt A, Guzzetti F, Malamud B D, Peruccacci S (2010) Analysis of historical landslide time series in the Emilia-Romagna region, northern Italy. Earth Surface Processes and Landforms 35: 1123-1137

Royán MJ, Abellán A, Jaboyedoff M, Vilaplana JM, Calvet J (2014) Spatio-temporal analysis of rockfall pre-failure deformation using Terrestrial LiDAR. Landslides 11: 697–709.

Royán M J, Abellán A, Vilaplana JM. (2015) Progressive failure leading to the 3 December 2013 rockfall at Puigcercós scarp (Catalonia, Spain). Landslides 12: 585–595

Santana D, Corominas J, Mavrouli O, Garcia-Selles D (2012) Magnitude-Frequency relation for rockfalls using a Terrestrial Laser Scanner. Engineering Geology 145–146: 50-64

Scheidegger AE (1973) On the prediction of reach and velocity of catastrophic landslides. Rock Mechanics 5: 231–236.

Selby MJ (1980) A Rock mass strength classification ofr geomorphic processes: with tests from Antartica and New Zealand. Zeits. Fur Geomorphologie 24: 31-51

Selby MJ (1992) Hillslope Materials and Processes. University Press, Oxford.

Shang Y, Yang Z, Li L, Liu D,Liao Q, Wang Y (2003) A super-large landslide in Tibet in 2000: background, occurrence, disaster, and origin. Geomorphology 54: 225 - 243

Soeters R, Van Westen C J (1996) Slope instability, recognition, analysis and zonation. In: Turner, AT, Schuster, RL (ed), Landslides — Investigation and Mitigation, Transportation Research Board Special Report No 247 National Academy Press, Washington DC, pp 129-177

Stark CP, Hovius N (2001) The characterization of the landslide size distributions. Geoph. Res Letters, 28: 1091-1094

Stead, D, Wolter A (2015) A critical review of rock slope failure mechanisms: The importance of structural geology. Journal of Structural Geology, 74: 1-23

Strom A (2015) Clustering of large bedrock landslides and recurrent slope failure: implications for lands seismic hazard assessment of the Tien Shan – Djungaria region. International Journal of Geohazards and Environment, 1: 110-121

Sturzenegger M, Stead D (2012) The Palliser Rockslide, Canadian Rocky Mountains: Characterization and modeling of a stepped failure surface. Geomorphology 138: 145–161

Swain RE, England JF Jr, Bullard KL, Raff DA (2006) Guidelines for evaluating hydrologic hazards, U.S. Department of Interior, Bureau of Reclamation, Denver, CO, 83 p.

Turner AK, Jayaprakash GP (2012) Introduction. In A.K. Turner & R.L. Schuster (Eds). Rockfall characterization and control. Transportation Research Board, National Academy of Sciences. Whasington D.C. pp. 3-20

Turu V, Boulton,G, Ros X, Peña, JL, Martí C, Bordonau J, Serrano E, Sancho C, Constante A,

Pous J, González JJ, Palomar J, Herrero R, García JM (2007) Structure des grands bassins glaciaires dans le nord de la Péninsule Ibérique: comparaison entre les vallées d'Andorre (Pyerénées orientales), du Gállego (Pyrénées centrales) et du Trueba (Chaîne Cantabrique); Quaternaire, vol. 18/4, 309-325 http://quaternaire.revues.org/index1167.html

Turu V, Calvet M, Bordonau J, Gunnell Y, Delmas M, Vilaplana JM, Jalut G (2016) Did Pyrenean glaciers dance to the beat of global climatic events? Evidence from the Würmian sequence stratigraphy of an ice-dammed paleolake depocentre in Andorra. In: Quaternary Glaciation in the Mediterranean Region. Geological Society, Special Publication. London. 433.

UN/ISDR (2004) Living with Risk: A Global Review of Disaster Reduction Initiative, United Nations Publication, Geneva.

USBR (2015) Best practices in dam and levee safety risk analysis. Version 4.0 USBR, USACE. https://www.usbr.gov/ssle/damsafety/risk/BestPractices

Voight B, Pariseau WG (1978) Rockslides and avalanches: an introduction. In: Voight, B. (Ed.), Rockslides and Avalanches, 1 Natural Phenomena. Elsevier, NY, pp. 1–67.

Wang X, Frattini P, Crosta G, Zhang L, Agliardi F, Lari S, Yang Z (2014) Uncertainty assessment in quantitative rockfall risk assessment. Landslides 11:711–722

Whalley WB, Douglas GR, Jonsson A (1983) The magnitude and frequency of large rockslides in Iceland in the postglacial. Geografiska Annaler 65A: 99-110

Willenberg H, Löw S, Eberhardt E, Evans KF, Spillman T. Heinke B, Maurer H, Green AG (2008.) Internal structure and deformation of an unstable crystalline rock mass above Randa (Switzerland): part I e internal structure from integrated geological and geophysical investigations. Eng. Geology, 101: 1-14.

Wolman MG, Miller JP (1960) Magnitude and frequency of forces in geomorphic processes. Journal of Geology 68: 54–74.

Wolter A, Stead D, Clague JJ (2014) A morphologic characterisation of the 1963 Vajont Slide, Italy, using long-range terrestrial photogrammetry. Geomorphology 206 : 147-164

12. Quantitative Analysis of Risk due to Fragmental Rockfalls

Publication reference:

Corominas J, Matas G & Ruiz-Carulla R, (2018) Quantitative Analysis of Risk due to Fragmental Rockfalls (paper submitted)

Abstract:

Rockfalls are ubiquitous diffuse hazard in mountain regions, with the potential of causing victims and severely damaging buildings and infrastructures. The quantitative risk analysis (QRA) is a tool to evaluate the risk in a reproducible manner and to assess the performance of mitigation measures. Considering or not the fragmentation of the detached mass, affects significantly the results of the QRA and the risk management criteria. The number of new fragments generated increases the probability of impact while the kinetic energy of blocks and the run-out is reduced. In this paper, we present the performance of a rockfall fractal fragmentation model (Ruiz-Carulla et al. 2017), in combination with the RockGIS code (Matas et al. 2017), a rockfall propagation model that accounts for fragmentation. The inclusion of fragmentation has required the redefinition of the probability of reach and to develop a specific procedure to quantify the exposure. A worked example of QRA is carried out at the Monasterio de Piedra, Spain. The results show that fragmentation has a significant but contrasting effect in the calculation of risk. The overall risk may be reduced if the slope where blocks propagate is both long and gentle enough before reaching the analyzed section. The reason is that, compared to the unfragmented rock masses, the new fragments generate short travel distances with lesser kinetic energy. This effect vanishes in case of large rockfalls. Conversely, the risk increases if rock blocks propagate over steep slopes and the distance to the analyzed section is short. The reason is that the exposure increments due to the generation of a cone of fragments. Our simulations also shown that the segregation of the visitors flow has only a minor influence in the results of the risk analysis. Finally, the consideration of fragmentation provides additional criteria for the assessing the efficiency of the rockfall protective measures.

Keyworks: rockfall, fragmentation, Quantitative Risk Analysis, modelling, case study

1. Introduction

Rockfalls are one of the most ubiquitous diffuse hazard in mountain regions. Despite the vast majority of rockfalls are local small-size events, the aggregated damage they cause and the number of casualties is high (Hungr et al. 1999; Chau et al. 2003). Compared to other landslide types, such as the slow moving landslides, rockfalls may become much more damaging due to the high impact velocity of the rock blocks (Turner and Jayaprakash, 2012).

Cruden and Varnes (1996) defined a rockfall as the detachment of a rock mass from a steep slope, that experiences free fall and, after impacting on the ground, it continues by bouncing and rolling. Despite this definition can be applied to events with volumes ranging many orders of magnitude (from less than 1 m3 up to >106m3), in this paper we will refer to rockfall events of less than 5x104m3, which is the size proposed as the transition from rockfalls to rock avalanches (Davis and McSaveney, 2002).

A complete rockfall study involves several issues (Volkwein et al 2011). On one side, the characterization of the source and the predisposing conditions (Mozzocola and Hudson, 1996; Guzzetti et al. 2003; Marquínez et al. 2003; Jaboyedoff et al. 2004; Loye et al. 2009), which control the occurrence and frequency of the events. On the other side, the dynamics of the falling masses, which determines the trajectory, velocity, runout, and therefore, the consequences (Giani et al. 2004; Bourrier and Hungr, 2011; Asteriou et al. 2012). Rockfall simulations are strongly affected by the stochasticity of all the processes involved (Bourrier et al. 2012; Gischig et al. 2015; Macciotta et al. 2015; Preh et al. 2015).

The analysis of rockfalls has improved significantly during the last years. The use of 3D rockfall models has been generalized (Guzzetti et al. 2002; Lan et al . 2007; Dorren 2012; Gischig et al. 2015). These models highlight the relevance for the modelling results of the input parameters such as the scale dependency of topographic features (Agliardi and Crosta, 2003; Lan et al. 2010; Corona et al. 2017), the resolution of the DEM (Crosta and Agliardi, 2004; Lambert, et al. 2013); or the ground stiffness (Dorren et al. 2006; Wyllie, 2014). Modelling requires a substantial effort in calibration, which is usually carried out by trial and error approach, for parameter optimization. To this aim, minimum amount of quality data is needed (Crosta and Agliardi, 2004; Bourrier et al. 2009; Frattini et al. 2013; Macciota et al. 2014). The criteria used for calibration include among others: the percentage of simulated blocks stopping close to the actual blocks; the passing frequencies through reference sections and maximum run-out distances; the mean values and standard deviations of passing heights and translational kinetic energies (Stoffel et al. 2006; Bourrier et al. 2009; Frattini et al. 2013).

Rockfall hazard and risk analysis has also benefited of the improvement of data capture techniques and of the availability of 3D rockfall propagation models. This kind of analyses is often carried out for land use planning purposes (Raetzo et al. 2002; Copons et al. 2003; Corominas, et al. 2005) and for management of infrastructures (Hungr et al. 1999; Budetta, 2004; Guzzetti et al. 2004; Macciotta et al. 2016). It requires identifying the potential rockfall source areas and accounting for the processes affecting the descending mass, the knowledge of the trajectory, passing height and velocity at each point along the path as well as the stopping point or runout (Guzzetti et al. 2002; Dorren et al. 2011). The analysis of the rockfall hazard is a very demanding due to the complexity of the mechanisms involved and the intrinsic stochasticity (Agliardi et al 2009).

The quantitative analysis of risk (hereinafter QRA) of slope instabilities has undergone remarkable development in recent years (Chau and Lee, 2002; Lee, 2004; Fell et al. 2008). The objective of the QRA is to evaluate the consequences (i.e. damages, casualties) in case of occurrence of the event and their associated probabilities. The QRA provides an objective evaluation of risk because the assumptions and uncertainties are declared (Straub and Schubert, 2008). It yields reproducible results, which allow the analysis of different scenarios and the comparison of their results. The interpretation of the QRA results may be carried out in terms of risk acceptability criteria (Corominas and Mavrouli, 2011; Corominas et al. 2014).

In QRA, for each potential rockfall source, the probability of occurrence of the event, the trajectories of the falling blocks, the kinetic energies and the passing heights for the points along their path, and the stopping points must be determined. For rockfalls, risk (R) is expressed as follows (adapted from Fell et al. 2005; Hungr and Beckie, 1998; Agliardi et al. 2009):

$$R = \sum_{j=1}^{J} \sum_{i=1}^{I} N_i . P(X/D)_i . P(T/X)_j . V_{ij} \qquad [1]$$

where:

R: risk due to the detachment from a cliff of a rock mass of magnitude (volume) “i” on an exposed element “j” located at a reference distance “x” from the source.

Ni: the annual frequency of rockfalls of volume class “i”.

P (X │ D)i: the probability that the detached rock mass of the size class “i” reaches a point located at a distance “x” from the source,

P (T │ X): the exposure or the probability that an element “j” be in the trajectory of the rock fall at the distance “x”, at the timing of the arrival of the rock fall debris.

Vij: the vulnerability of an exposed element “j” being impacted by a block of magnitude “i”

The summation indicates that the expression of the risk is calculated for a range of rockfall magnitudes (volumes) because each one is characterized by a probability of occurrence, runout, and probability of impact. Therefore, the consequences are specific of each rockfall volume. Basically, hazard grows with the mean frequency and with the intensity of the rockfall event (Jaboyedoff et al. 2005; Labiouse and Abruzzese 2011; Agliardi et al. 2009).
P (X │ D) or reach probability is usually calculated with propagation models, which take into account initial volume, the topography and characteristics of the path, the stiffness of the ground, as well as the presence of obstacles. Hundreds or thousands of trajectories can be generated with rockfall models and P (X │ D) is calculated as the proportion of rockfall events that travel up to the reference point or section, for each rockfall magnitude. A refinement of the analysis is achieved by determining the spatial distribution of the velocity, kinetic energy (or intensity) of the blocks.

The procedure for evaluating exposure of elements moving along linear features has long been known, but only a few practical examples have been recently published for its calculation (Roberds, 2005; Ferlisi et al., 2012, Nicolet et al., 2016; Macciotta et al. 2016). It is usually performed for infrastructures such as roads, railways and it is applicable to trail paths as well. Hazard and risk are calculated either for the whole length of the infrastructure or in some selected sections (stretches).

The exposure of people walking along a trail is the probability of a person (or group of persons) being in the trajectory of the rockfall at the moment of its occurrence. The exposure, P (T │ X) is therefore dependent on the number of moving exposed elements and the width of the section affected by the rockfall event. For people in movement, the encounter probability with a rockfall is as follows (adapted from Nicolet et al., 2016):

$$P(T/S) = \frac{f_p.(w_r + l_p)}{24 .1000 .v_p} \qquad [2]$$

where:
fp: flow of visitors (persons/day)
Wr: width of the rockfall debris front (m)
lp: length of the trail occupied of the person or group of persons (m)
vp: is the mean velocity of the person or group of persons (km/h)

In this expression, a uniformly distributed flow of elements or constant moving element frequency is usually assumed (Macciotta et al. 2016).

In the practical examples mentioned above, only intact blocks are considered. However, rockfall masses often fragment along the path. Fragmentation consists of the separation of the initial mass into several smaller pieces, which follow both independent and divergent trajectories. Fragmentation can appear during the initial instants in which the rock mass is detached from the cliff but it becomes evident upon the first impact(s) on the ground surface. The rock mass can be either dislodged by the separation of the blocks delimited by discontinuities, broken or both (Ruiz-Carulla et al. 2015). Rockfalls that experience fragmentation along the path are called fragmental rockfalls (Evans and Hungr, 1993).

The fragmentation has received little attention in the scientific literature despite being a process often observed in rockfalls. Its analysis is affected to great uncertainty because the variables involved cannot be determined with confidence (Dussauge et al. 2003; Wang and Tonon 2010; Hantz et al. 2014). Among these variables, the presence of discontinuities in the initial rock mass, their persistence, orientation relative to the ground surface at the time of impact, energy and angle of impact and the ground stiffness have to be considered. Several researchers, have shown fractal models may be adequate to characterize the phenomenon of fragmentation of rock masses and to estimate the number and size of the resultant blocks (Turcotte, 1986; Perfect, 1997; Crosta et al. 2007). The volume distributions of the fragments of some inventoried rockfall events and from real scale tests confirm the power-law distribution of the fragments. They also show that different exponents may be obtained in different locations and/or contexts (Ruiz-Carulla et al., 2016; Gili et al. 2016). Based on these field observations we developed a rockfall fractal fragmentation model (RFFM) which simulates rockfall fragmentation (Ruiz-Carulla et al. 2017). The model is based on a generic fractal fragmentation model of Perfect (1997) in which a cubic block of unit length, is broken into small pieces according to a power law. Either an intact block or a detached rock mass characterized by an in situ block size distribution (IBSD) is used as input of the model. The results consist of a block size distribution of the rockfall fragments (RBSD). The RFFM can be integrated into the RockGIS (Matas et al. 2017). The latter is a GIS-Based model that simulates stochastically the fragmentation of rockfalls, considering a lumped mass approach. It requires as input data the digital surface model, land use map and the rockfall sources. In RockGIS, the fragmentation initiates by the disaggregation of the detached rock mass through the pre-existing discontinuities. An energy threshold has to be defined in order to determine whether the rock block breaks or not at each impact upon the ground surface. The distribution of the initial mass between the set of newly generated rock fragments is carried out stochastically, according to a power law. The envelop of the trajectories of the new rock fragments downslope, defines a cone and the remaining energy after the impact and subsequent breakage is distributed proportionally to the mass of each fragment. All fragments generated propagate downslope and the process continues iteratively until all fragments stop.

In this paper, we present the effect of the rockfall fragmentation in the results of the QRA. To this end, we have analyzed two scenarios within the premises of the Monasterio de Piedra, Spain. Although the risk will be quantified, our aim is to show how the risk assessment procedure has to be adapted to take into account fragmentation and how it affects the results and their interpretation.

2. QRA of fragmental rockfalls

The QRA for fragmental rockfalls has some specificities. Fragmentation causes the initial mass being redistributed among the new generated fragments. The overall effect is that the smaller fragments travel shorter distances and mobilize lesser kinetic energy, thus reducing P (X │ D) and the intensity of impacts (Corominas et al. 2012). Furthermore, the maximum bouncing height of the blocks, which is an important parameter for the design of the rockfall protection barriers, it is also affected by the size of the fragments (Agliardi et al. 2009). On the contrary, the probability of impact on the exposed element, P (T │ X), increases substantially with the fragmentation because a number of new fragments are generated and due to the divergence of the trajectories, which enlarges the area affected by the trajectories (Jaboyedoff et al. 2005; Corominas et al. 2012; Ruiz-Carulla et al. 2015). Despite all these effects have been known for some time, to the authors' knowledge, no attempt has been made so far to quantify the effect of rockfall fragmentation on the runout, the velocity of the rock blocks, the exposure and, consequently on hazard and risk.

The risk analysis of fragmental rockfall requires the redefinition of the way how both the reach probability P (X │ D) and the exposure P (T │ X) are calculated. Compared to the analysis of individual rock blocks, fragmentation may produce paradoxical results in the computation of P (X │ D) The simplest way to assess the probability of reach is to calculate the percentage of all simulated block trajectories that cross a point, reference line or area (Guzzetti et al., 2002; Jaboyedoff et al 2005). However, when the rock mass fragments, this procedure may yield probabilities >1. The reason is that fragmentation may generate a number of rock fragments which are able to reach the reference point or section, much higher that the number of initiators. To overcome this, here the P (X│ D). is calculated as the proportion of the simulated events that reach the point or reference section, regardless whether it consist of one fragment only, or several fragments. The number of fragments, however, will be considered in the calculation of the exposure.

The encounter probability or exposure P (T │ X) has to consider both the width of the falling mass (Wr) and the length of the trail (lp) occupied by the person or group of persons (Nicolet et al. 2016). It is calculated with equation [2], whose parameters are shown in Figure 1.

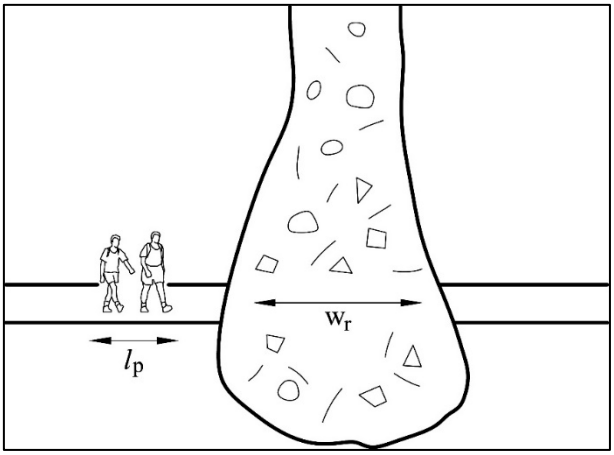

Figure 1. Length of the affected section and of the exposed element or elements used in equation [2]

Equation [2] is used for a variety of hazardous processes such as mudslides, snow avalanches, or debris flows. These type of slope movements progress downslope forming a continuous front, whose width is Wr.

For fragmental rockfalls this scenario is somehow different. After the impact of the falling rock mass on the ground and its fragmentation, the rock fragments follow divergent trajectories that can be simplified as forming a cone (Figure 2). In plan view, the affected area is defined by the projected cone of fragments. The width of the cone (wcx) varies (e.g. increases) with the downslope travelled distance (x).

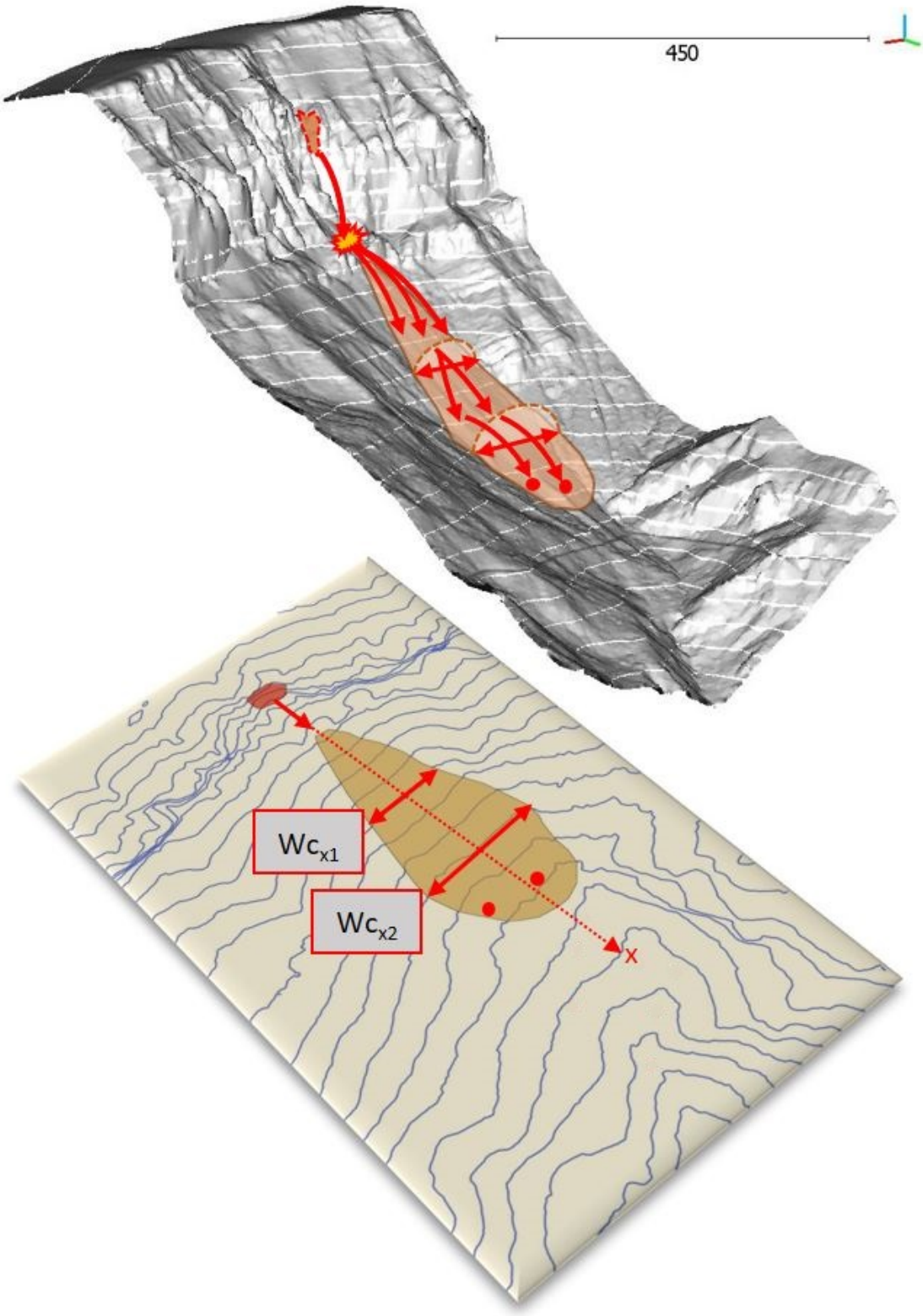

Figure 2. Sketch of the fragmentation of a falling rockfall mass upon its impact on the ground surface. The projected width of the cone of fragments (Wc) generated varies with the distance (x) to the rockfall source.

Therefore, Wcx is spatially dependent and must be calculated at each point or analyzed section. Large rockfall events may form a continuous front (Figure 3 B), in this case Wr=Wcx (equation [2]). However, in case of small to mid-size events (usually, up to several hundred of cubic meters), the rock fragments might not completely occupy the width (wcx) of the cone defined by the trajectories (Figure 3 A).

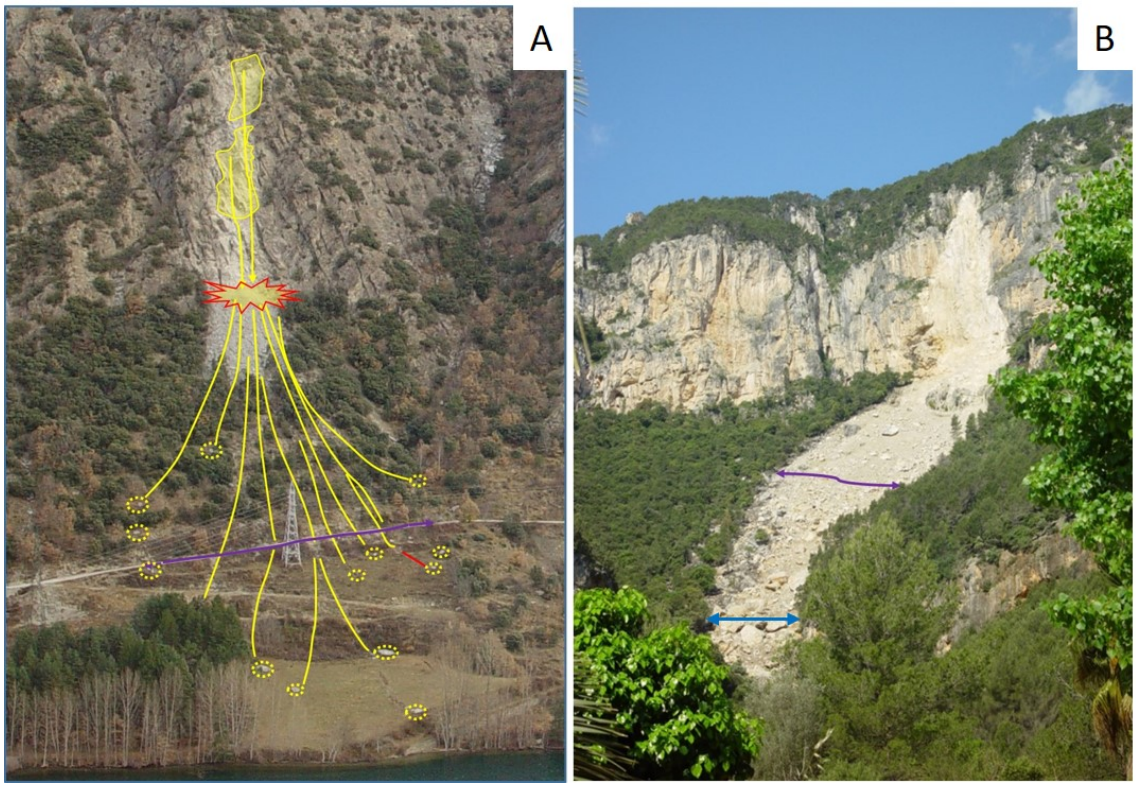

Figure 3 A: young debris cover generated at the point of impact of the falling mass (red polygon). At the section of analysis (purple line), the divergent trajectories of the scattered blocks form a discontinuous debris front. B: Massive rockfall event. The the rockfall debris form continuous front which is wider in the middle part of the slope than in the lowest one (purple lines).

In case of a discontinuous cone, the width of the rockfall (Wr) in equation [2] is calculated considering the fraction of the cone width actually occupied by the blocks. By increasing the size of the rockfall and the number of fragments, the proportion of the rockfall width (Wr) actually occupied by the rock blocks growths until it reaches the whole cone width (Wcx). To the sole effect of estimating Wr in equation [2], here we assume that all the rock fragments reaching the analyzed section located at a distance "x" from the source, are equally sized to the modal block size (Wmx). The number of blocks reaching the analyzed section are counted in each simulation. Thus, the rockfall width Wr is:

$$Wr = n.\ Wmx \qquad [3]$$

Where “n” is the number of blocks reaching the analyzed trail section (at a distance “x”)
Wmx: is the modal block width reaching the analyzed trail section at a distance “x” from the source

If $n.Wm \geq Wcx$, then $Wr = Wcx$
Where Wcx is the width of the cone of trajectories at a distance “x” from the source

As example, let’s assume that a 50 m3 rockfall generates trajectories forming a 10m-width cone at a distance of 100m from the source and the modal width Wm100 of the fragments generated is 1 m. In case of one, five, ten, or fifteen fragments reaching the reference line, Wr is respectively: 0.1 Wcx, 0.5 Wcx, Wcx. and Wcx.

In large rockfall events (> 103 m3), the rock fragments usually generate a continuous young debris cover (YDC) (Figure 3 B) although large scattered blocks may travel far away from it. For the YDC, Wr = Wcx. For scattered blocks travelling farther away from the YDC, equation [3] has to be used.

3. The site: Monasterio de Piedra, a case study in Spain

The Monasterio de Piedra is a protected natural space located in the lower reach of the River Piedra, in the central Iberian Range, NE Spain, a NW–SE trending alpine intraplate fold belt (Figure 4). The climate is predominantly of a continental Mediterranean type with strong seasonal contrasts. The mean annual precipitation is around 400mm. The geological setting corresponds to a series of Mesozoic carbonate materials, Miocene detrital formations and Quaternary tufa (Arenas et al. 2014). The River Piedra incised and down cut the carbonate rock during the Quaternary forming a number of small gorges and canyons, in which thick Pleistocene and Holocene tufa deposits were generated (Osácar et al. 2013). One of these gorges extends around the Lago del Espejo (Mirror lake), whose 100m-high cliffs are composed of a sequence of dolostones and limestones of Upper Cretaceous age. At the base of the cliffs predominate finely stratified limestone (30 to 50 cm-thick layers) while in the upper part the strata are massive white limestones (Figure 5). In addition to the stratification, which displays different dip angle at both sides of the lake, the rock mass is crossed by two main orthogonal joint sets (figure 6). This carbonate formation is also affected by dissolution processes that left karstic features easily identifiable in the outcrops.

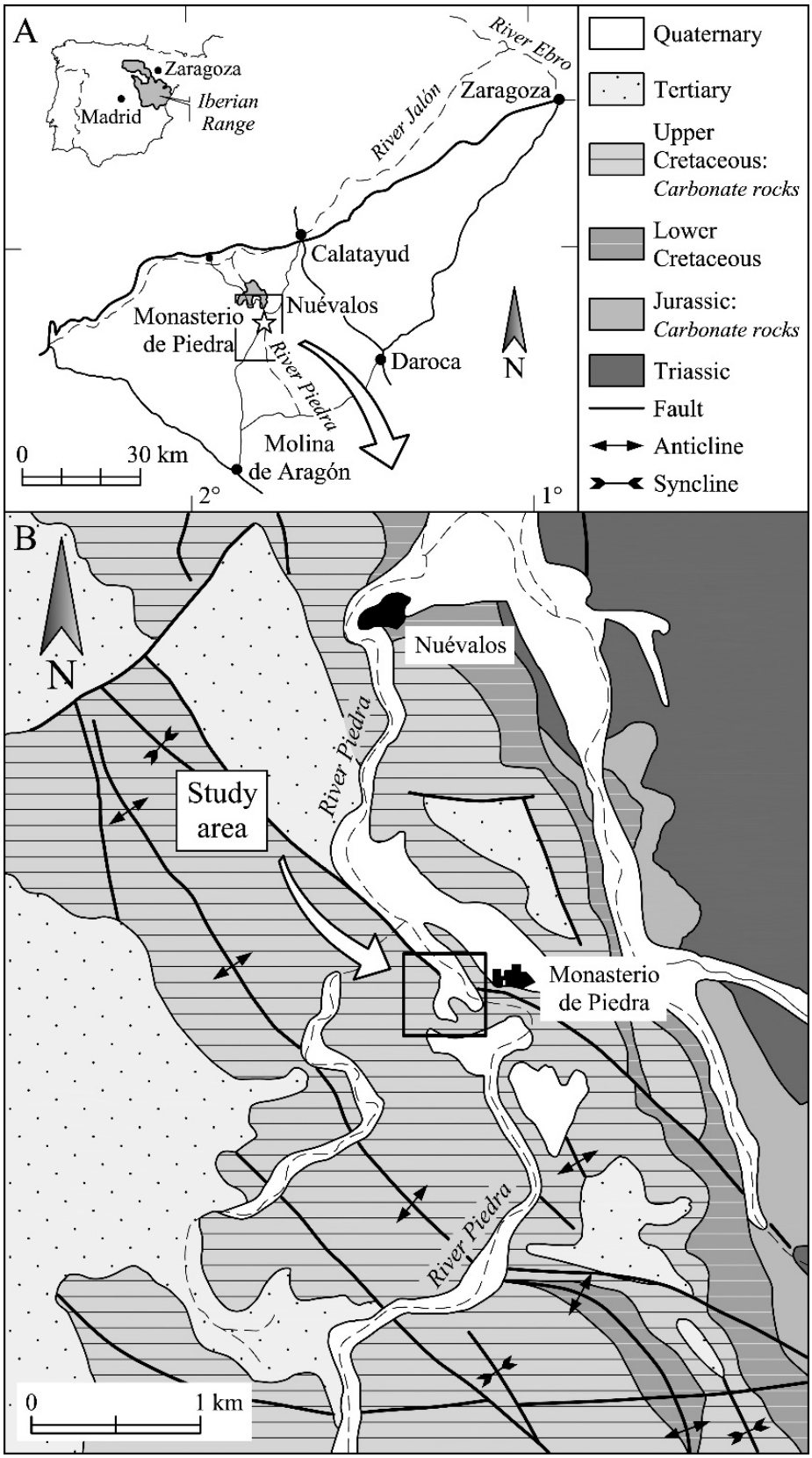

Figure 4. (top) Geographical location and (bottom) geological sketch of the Monasterio de Piedra area (modified from Osácar et al. 2013)

Figure 5. Overall view of the cliffs around the Lago del Espejo (Mirrow lake) and the trail at Monasterio de Piedra. At the foot of the cliff, in the background, the rockfall debris of February 2017. On the lower right slope, between the trees, several rockfall barriers have been installed. On the left, the steep cliff of Peña del Diablo (Devil's rock)

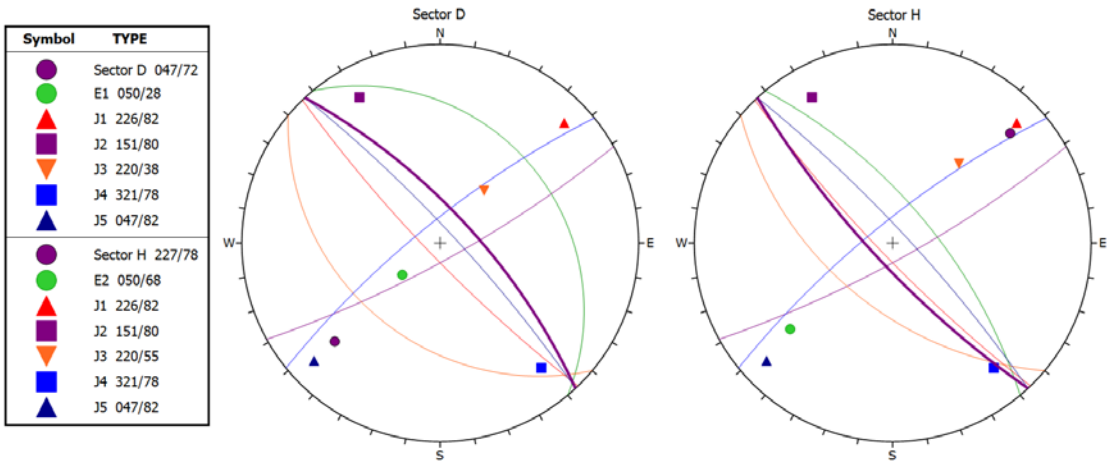

Figure 6. Main discontinuity sets present at the rock mass that form the cliffs around the Lago del Espejo. Cliff sector D is located at the SW margin of the lake and Cliff Sector H is located at the NE margin (Peña del Diablo). The cliff and bedding planes represented by purple and green color great circles, respectively.

The stability of the rock masses is determined by both the rock strength and discontinuities. Limestone and dolostone rocks outcropping at the Piedra river gorge are highly resistant materials, allowing them to form vertical slopes of more than a hundred meters high. In the Monasterio de Piedra, the stability is mainly associated to the presence of discontinuities (stratification, joints, faults, among others) since they facilitate the individualization of the rock blocks although the failure mechanism is complex. Back analyzed failures sometimes do not comply with the criterion of kinematic instability (Hoek and Bray, 1981) because the toppling mechanism is mostly driven by rock deterioration and slaking processes (Figure 7A) or if they comply, they may be constrained by the presence of rock bridges (Figure 7B). Using an Unmanned Aerial Vehicle (UAV) more than 40 potentially unstable rock masses bigger than 10m3 where identified on the cliffs around the lake.

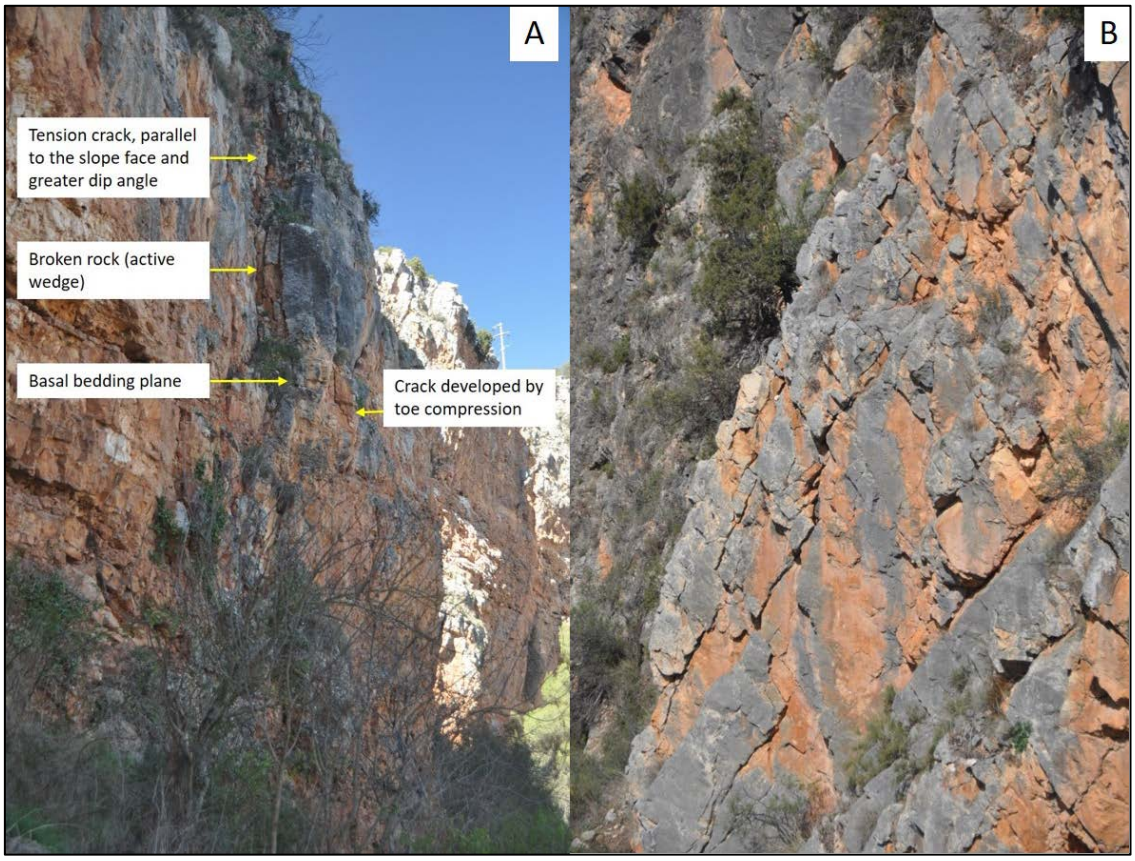

Figure 7. (A) Potentially unstable rock column at the cliff face. None of the two joints bounding the rock the block: the tension crack and the basal plane (stratification), meet the criterion of kinematic instability. Nevertheless, the base of the column is cracking due to its compression and slaking. Loose rock fragments filling the tension crack, favor the development of toppling. (B) partial view of the cliff of the Peña del Diablo. Bedding is dipping to the right while two orthogonal joint set facilitate the generation of potential planar failures.

On February 17th, 2017 a rock mass of about 800 m3 detached from the cliff above the Lago del Espejo in Monaterio de Piedra, Spain (Figure 8). The mass fell from a 60m height and fragmented upon the impact on the ground. The debris extended downslope up to the lake, burying a section of the visitors trail. Several modules of the rockfall barrier of 1500 kJ, located just below the cliff, were destroyed. Previously, in October 1986 another rockfall event of a volume of about 600m3 occurred, generating a young debris cover of 500m2 approximately. Its source is located close to that of the 2017 event.

Figure 8. left: general view of the rockfall event of February 2017.

A QRA has been carried out in the premises of the Lago del Espejo in the Monasterio de Piedra to assess the risk considering different scenarios. The quantification of the risk is based on equation [1]. We present here the results of the QRA with emphasis on the influence of the fragmentation on the resulting hazard and risk as well as the lessons for the management of the site. The analysis is performed at a variable distance "x" from the cliff, which corresponds to two alternative trails around the Lago del Espejo used by the visitors (Figure 9). One trail runs along the SW margin of the lake, separated from cliff by a gentle slope and the other by the NE margin, just under the Peña del Diablo. For the sake of brevity, the analysis of only one section of each trail is presented here.

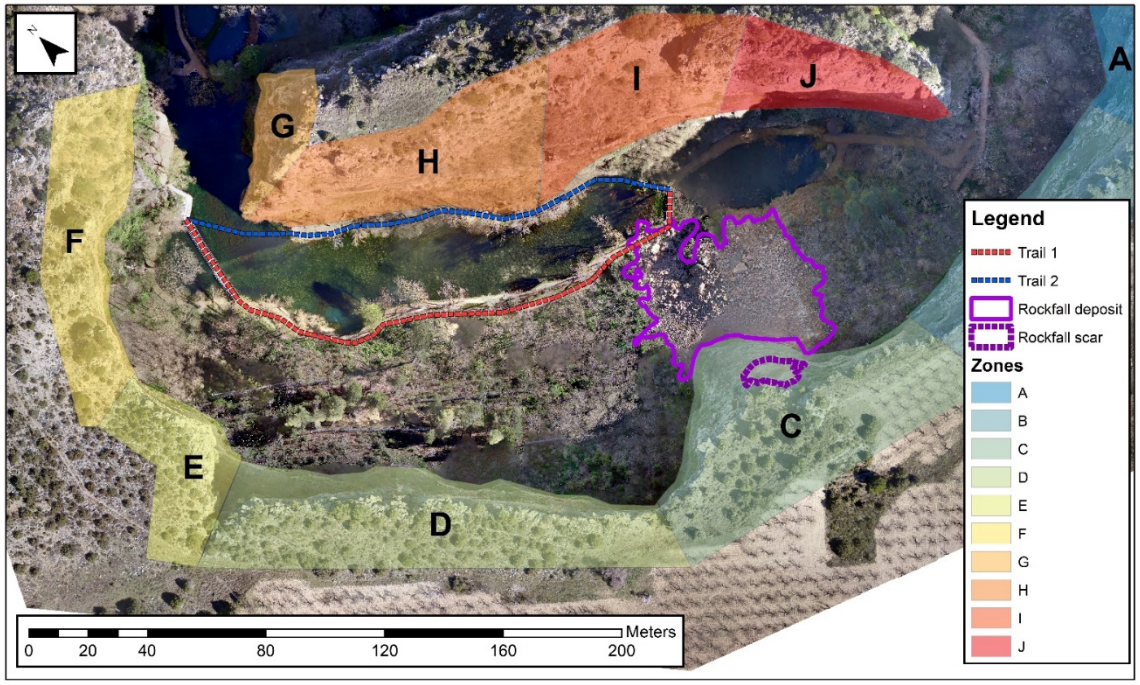

Figure 9. Orthoimage of the cliff sectors contributing to the rockfall hazard to the two trail sections analyzed (red and blue discontinuous lines). Each sector presents conditions of homogeneity in relation to stability. The location of the rockfall event of February 2017 is also shown (purple lines).

Scenarios analyzed/considered and assumptions

Trail is threatened by rockfalls originated from the cliffs of sectors D-C. The rockfalls propagate over a partially forested gentle slope. Below the cliff sector D, five flexible rockfall fences of 1500kJ capacity were built in 2002, one of them was destroyed by the event of 2017. Trail 2 is threatened by rockfalls originated from cliff H of the Peña del Diablo.

Table 1. Characteristics of the two alternative trails analyzed.

Trail section	Trail section length (m)	Length of the contributing cliff (m)	Proportion of the contributing cliffs
1	194.8	294.1	0.319
2	143.9	132.0	0.143

The frequency of rockfalls assigned to each trail section is the value that corresponds to it according to the proportion of contributing cliff.

Two scenarios are analyzed: (1) the original situation without any protection work; (2) presence of the 1500 kJ-capacity barriers (for trail 1 only)

The estimation of the risk on moving elements from the binomial theorem (Bunce et al., 1997), is based on several simplifying assumptions such as the flow of visitors is uniformly distributed in space and time, and it is independent of the rockfalls. All the exposed elements (visitors) occupy the same space. Similarly, rock falls are distributed uniformly in time and space along the cliffs (Hantz, 2011), and their occurrence is independent of the flow of visitors. Two flows of visitors will be considered here (see Table 6): uniformly distributed flow and segregated flow.

In this type of analysis, the geological structure and slope geometry is basically ignored. Each rockfall that reaches the section of the trail around the Lago del Espejo is a Bernouilli trial with binary result: whether there is impact or not on the target object (visitor or group of visitors) (Hungr and Beckie, 1998; Agliardi et al. 2009).

The source areas of the rockfalls are homogeneously distributed along the crest line of the cliffs (294 sources, one every meter). This hypothesis accommodates well to the large-size potentially detachable rock masses identified but it is quite conservative for mid-size rockfalls (up to 50 m3) because a percentage of them originates in middle and lower sectors of the cliff face. Failures from the mid-lowest cliff sectors will produce smaller kinetic energies and run-out.

This case study analyses the risk associated to the direct impact of rockfalls on visitors walking around the lake premises. Other circumstances such as people stopping for a while in the trail (for instance, working, resting, picnicking or camping) or wandering out of the trail, are beyond the scope of this analysis.

In what follows, we present how the different components of equation 1 have been determined.

Frequency of the rockfall events (Ni)

The first step consist of calculating the average frequency of rockfalls. Using the available information of the rockfall inventories as done in other case studies (Bunce et al. 1997; Lee and Jones, 2004; Hungr et al. 1999; Guzetti et al. 2002; Ferlisi et al. 2012). There exists no complete record of rockfall events that affected the Monasterio de Piedra premises. We prepared the magnitude-frequency relation of rockfall events at the site, using two sources: (i) the count of rock blocks intercepted by the barriers installed 15 years ago (in 2002), and (ii) the inventory of three large events (>400 m3), two historical (1986 and 2017) and the third of unknown age.
A total of 209 rock blocks were measured in four barriers. The volume distribution of the blocks covers three orders of magnitude and it fits to a potential law (Figure 10). The distribution is similar to that observed in other locations affected by rockfalls (e.g. Hungr et al., 1999; Dussage-Peisser et al. 2002; Guzzetti et al., 2003).

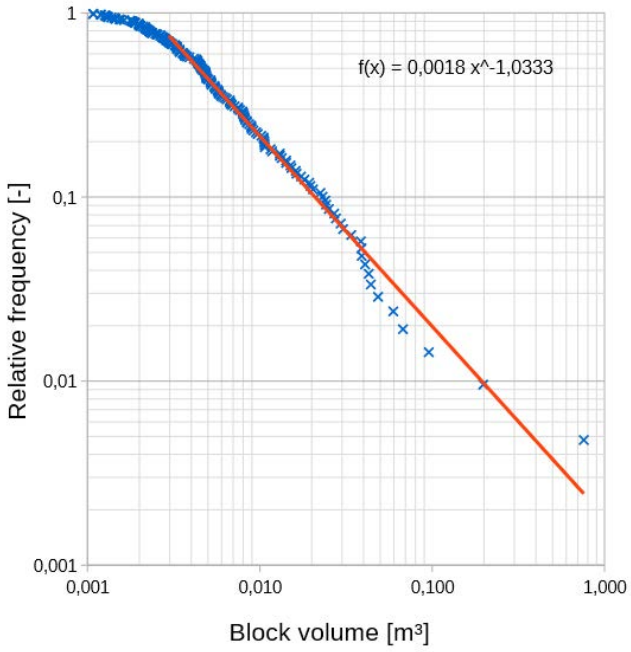

Figure 10. Volume distribution of the rock blocks retained in the four rockfall fences

The rockfall rate obtained in the barriers during the 15 years since their installation is 14 events / year. This value is only an approximate estimation of the frequency because some small-size blocks did not reach the fences (a small percentage) while some of the blocks retained could be part of the same fragmental rockfall event, thus underestimating its size.

The fences collect the rockfalls originated within the cliff section D only. Because of this, the frequency-magnitude relation has been extrapolated to the whole cliff length around the Lago del Espejo. In addition, the three large rockfalls inventoried were also included. The corrected

frequency and the volumetric distribution of the events (arranged in bins) is presented in Table 2. The extrapolated frequency relation yields an accumulated volume of rock fall debris of about 4200 m3 in 1000 years. Considering the exposed surface of all cliffs around the Lago del Espejo, which is 57600 m2 (921 m in length and 60 m in height), a denudation rate of the cliffs of 76 mm/ka is obtained. This rate is of the same order of magnitude as the observed in the same regional climatic context (Sancho et al., 1988; Gutiérrez et al., 2001). Because of this, we consider the extrapolation representative.

Table 2. Frequency of rockfall events by the extrapolation of the volumes retained in the barriers and of the three major events identified to the 921m of accumulated length of cliffs.

Volume class	Rockfall volume (m^3)	Events/yr	Annual volume m^3/yr	Volume (m^3) per ka	Cumulative volume (m^3) in 1 ka
A	≤ 0.005	45.1463	0.226	226	226
	$0.005 < x \leq 0{,}05$	5.9514	0.298	298	523
B	$0{,}05 < x \leq 0{,}5$	0.7846	0.392	392	916
C	$0{,}5 < x \leq 5$	0.1034	0.517	517	1433
D	$5 < x \leq 50$	0.0136	0.682	682	2114
E	$50 < x \leq 500$	0.0018	0.899	899	3013
F	$500 < x$	0.0002	1.185	1185	**4198**

Reach probability P (X │ D)i

To calculate P (X │ D)i, the probability of the rockfall event reaching the study section of the trails, we used the RockGIS simulation program developed by our research group, whose details and characteristics are explained in Matas et al. 2017.

The parameters of the model for both fragmentation and propagation were calibrated using the rockfall event of February 2017, the location of a few blocks (volume ranging between 0.5 and 5m3) that were removed from the cliff during scaling works carried out in March 2015 (Figure 11), and the blocks retained at the rockfall barriers. The fragmentation law was calibrated with the 2017 event, using the in-situ block size distribution (IBSD) estimated from the rockfall source captured with a drone and measurement in the field of the rockfall blocks size distribution (RBSD), following the approach described in Ruiz-Carulla et al. (2015). Figure 12, Figure 13 and Figure 14, show the results of the simulation of the 2017 rockfall event and the ISBD and RBSD

obtained. The spatial distribution of rock fragments and the run-out distances were checked using the procedure described in Matas et al. (2017).

Figure 11. Blocks resting at the bottom of cliff B. These blocks were removed from the cliff during the scaling works carried out in 2015 and are used to calibrate the RockGIS model.

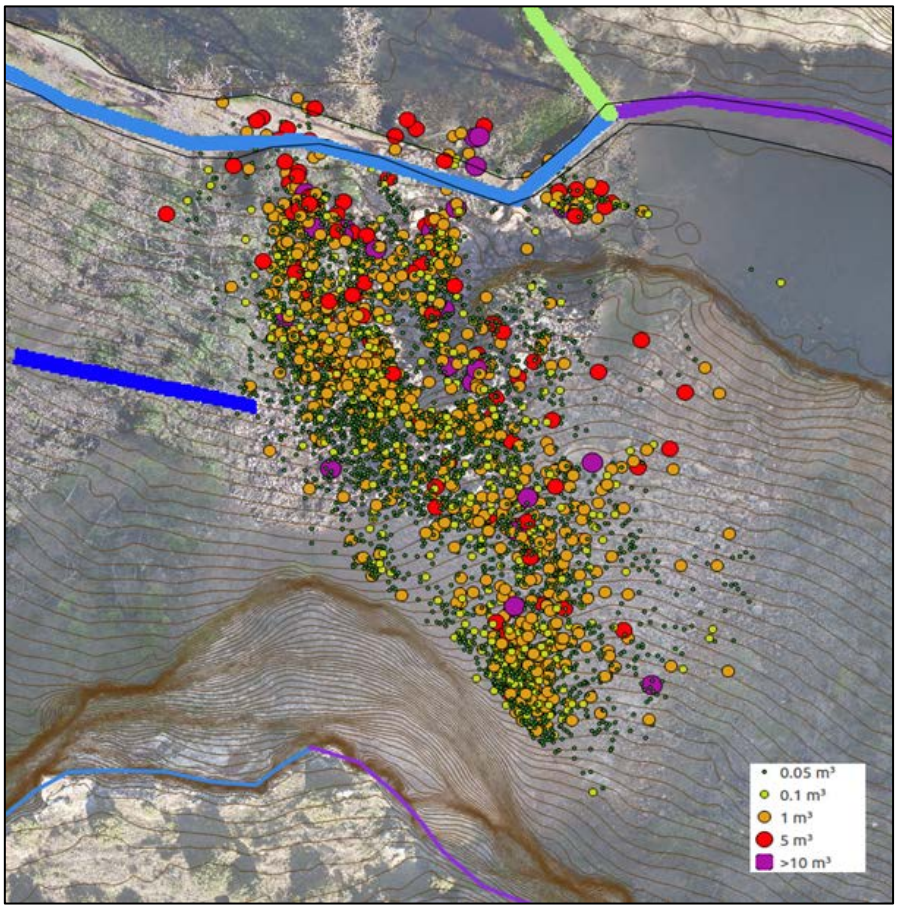

Figure 12. Simulation of the rockfall event of February 2017. The rock block volume is indicated by the size and color of the circles

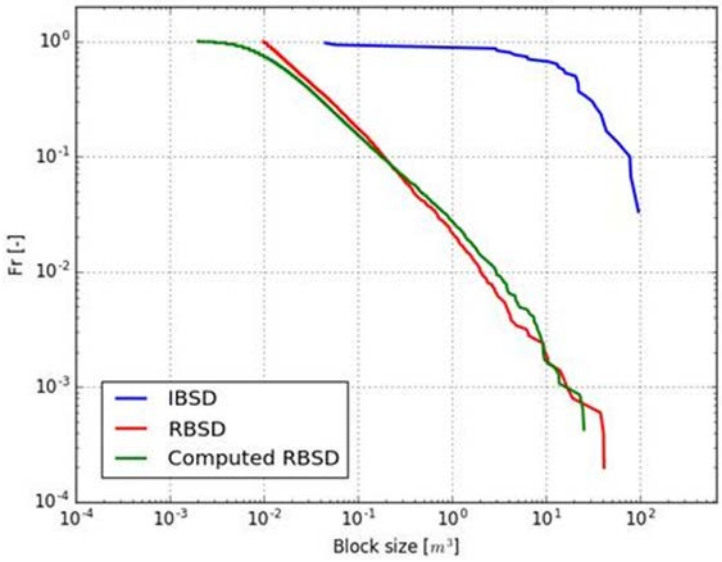

Figure 13. In situ block size distribution (IBSD) of the rock mass detached in February 2017 and both the computed and observed rock block size distribution (RBSD) of the fragments.

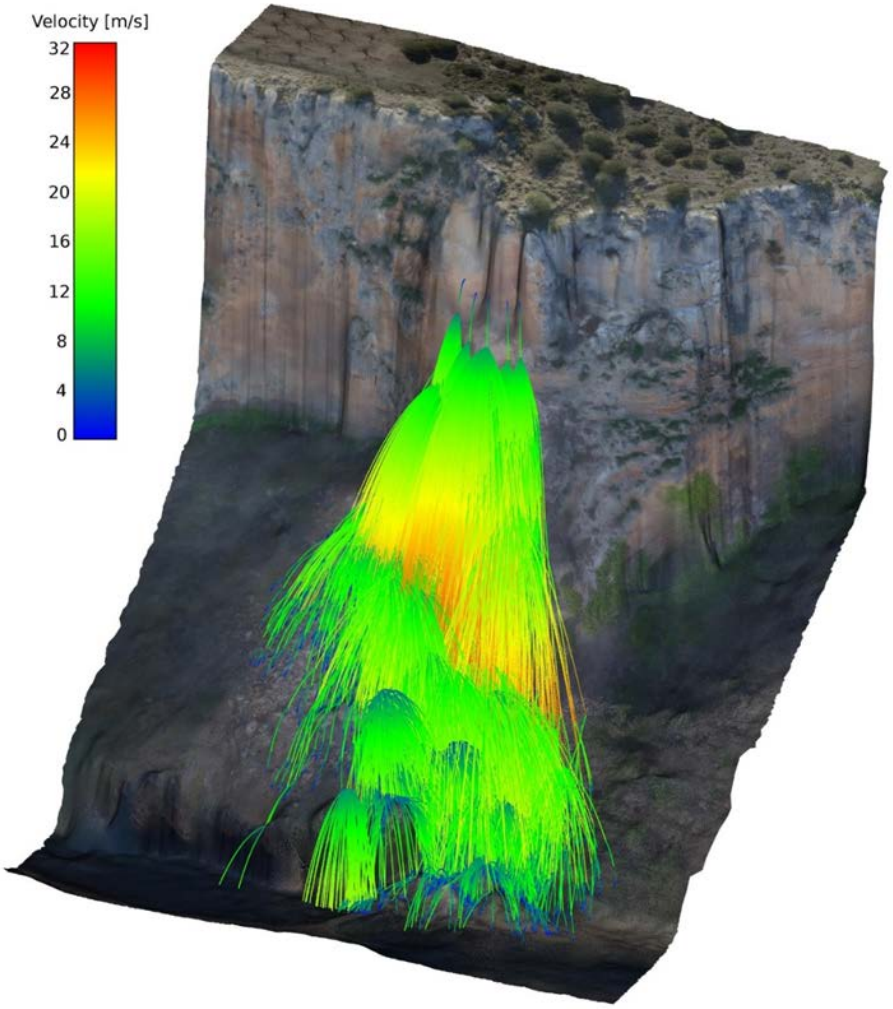

Figure 14. Simulation of the rockfall event of February 2017. The velocity of the falling blocks is illustrated by means of the color code.

The calibration has accounted for the fact that low-velocity impacts are considered relatively elastic while high-velocity impacts consume additional energy through plastic deformation of the ground and breakage of the rock blocks, producing smaller rebounds (Pfeiffer and Bowen, 1989; Dorren 2012). Therefore, for the determination of the normal restitution factor Rn, the hyperbolic formulation adapted from Gischig et al. (2015) is used. Figure 15 shows the normal restitution factors for different block sizes. The figure corresponds to the factor for impacts with the medium stiff ground, for impacts on sound rock surfaces the Rn for the lowest velocities has been incremented from 0.68 to 0.91.

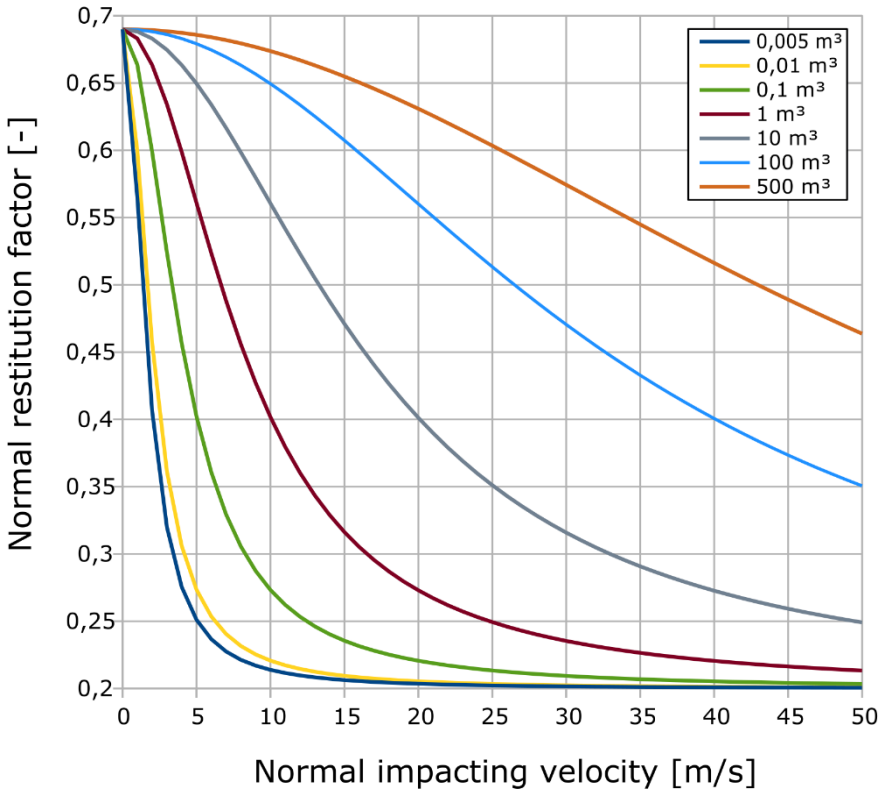

Figure 15. Normal restitution coefficients depending on the volume and the normal impact velocity in the case of isolated blocks (<10m3) (adapted from Gischig et al. 2015).

The trajectory analysis considers a rockfall source every 1m (294 and 132 potential rockfall sources, for trail 1 and 2, respectively). Each source releases 100 rock masses than remain intact along the path and 10 rock masses that fragment, totaling 29,400 and 2,940 simulations respectively for trail 1 and 13200 and 1320 for trail 2.

The effect of fragmentation on the rockfall runout is illustrated in Figure 16. For the sake of visualization only one trajectory of intact rockfall from a few selected detachment sources is shown (top). For the same reason, only one fragmental rockfall event is shown as well (bottom). In the latter, the trajectories of the rock fragments are also displayed. The quantitative results are

summarized in Table 3. Proportion of rockfall trajectories P(X|D) reaching the trail sections for both with (F) and without fragmentation (NF).

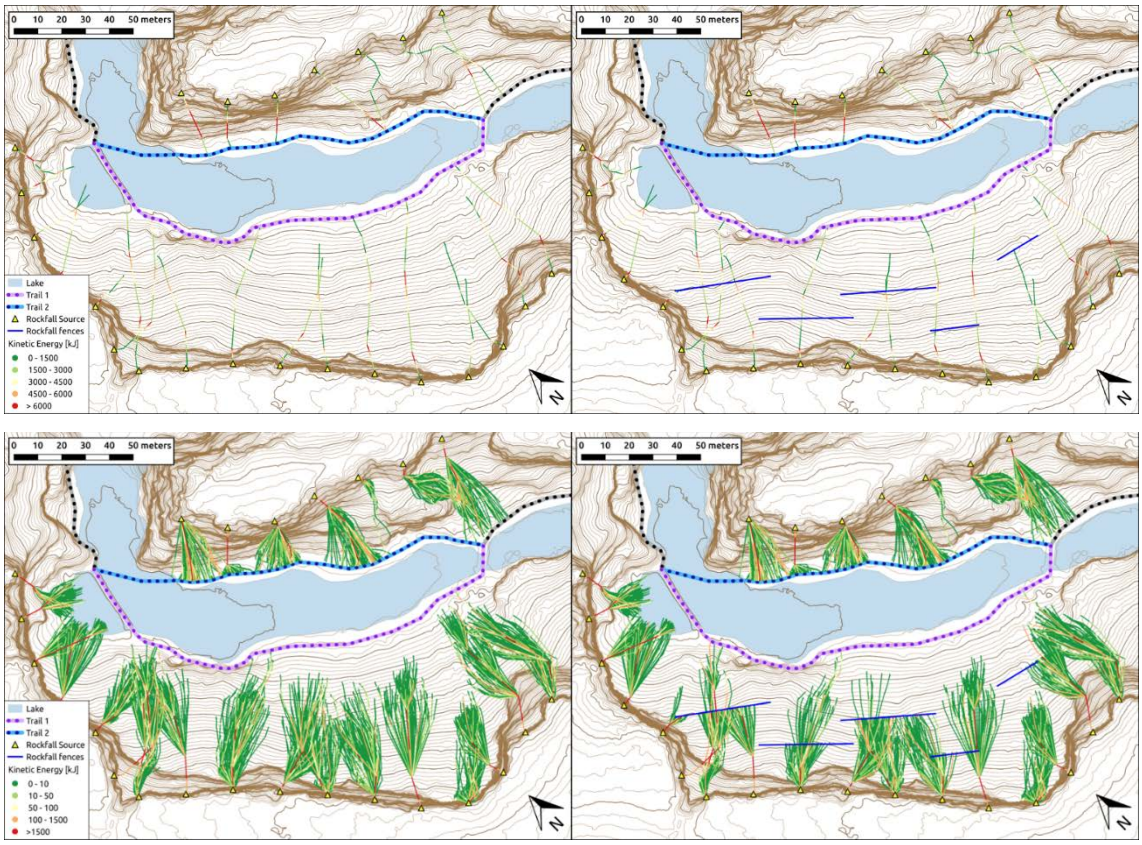

Figure 16. Top: trajectories of rockfall masses of 10m^3 without fragmentation. Considering the presence (right) or absence of rockfall barriers; Bottom: trajectories of 10m3 rockfall masses with fragmentation. Considering the presence (right) or absence of rockfall barriers; The existing rockfall barrier are represented by blue lines. The kinetic energies are displayed following a color code (from high to low: red orange, yellow and green).

The runout is strongly affected by both the size of the event and fragmentation. The positive relation of the size of the rockfall event with the runout is illustrated by the examples shown. Only 12% of the modelled smallest rockfalls (<0.05m3) reach the trail section 1 compared to the 87% in case of occurrence of the largest events (>500m3). This effect is less evident in trail section 2 because the slope is steeper. Despite of this, in trail section 2, 61% of the smallest rockfalls reach the trail while virtually all the rockfall events larger than 50m3 as well. For fragmental rockfalls reaching the trail means that at least one block fragment has arrived to the trail section analyzed. The results of Figure 16 and Table 3show that fragmentation may strongly affect propagation if the slope is both gentle and long enough. None of the simulated rockfall events smaller than 0.5m3 is able to reach trail section 1. However, the influence of fragmentation on the reduction of the runout vanishes progressively with the increase of the rockfall size. Thus, for rockfall volumes larger than 50 m3, the runout reduction is barely perceptible. On the other hand, on trail section

2 that runs under the steep slope of the Peña del Diablo, the fragmentation only has a minor effect on the distance traveled by the blocks.

Table 3. Proportion of rockfall trajectories P(X|D) reaching the trail sections for both with (F) and without fragmentation (NF)

	Trail Section 1				Trail Section 2	
Rockfall volume (m^3)	Natural state		Flexible fences 1500kJ		Natural state	
	NF	F	NF	F	NF	F
<0,05	0.1194	0	0.0220	0	0.6105	0.2940
0,05 < x <0,5	0.3280	0	0.0647	0	0.8394	0.5700
0,5 < x <5	0.5896	0.0425	0.1455	0.0124	0.9446	0.7910
5 < x <50	0.7647	0.2327	0.7361	0.1310	0.9699	0.9515
50 < x <500	0.8320	0.6309	0.8312	0.5135	0.9792	0.9886
>500	0.8735	0,7996	0.8736	0.7574	0.9820	0.9917

The RockGIS code allows counting the number of blocks reaching the section. This information will be used to calculate the exposure as it will be shown in the following chapters.

Exposure P (T │ X)$_i$

The probability of the rockfall encountering visitors at a distance "x" from the source, P (T │ X), takes into account two components: the probability that the person or group of persons is located within the rockfall trajectory at the moment of its occurrence and the width of the trail section intersected by the cone of rock fragments (W_r) (equation 2). In the simulation of intact rock fall masses, W_r is the width of the fallen rock block assuming a cubic shape. For fragmental rockfalls, W_r is the fraction of the cone of debris width W_{cx} actually occupied by the rock fragments calculated with the information provided by the RockGIS code

Fragmentation of rockfalls generates a completely different scenario (see example of $10m^3$ in **Error! Reference source not found.**). First, fragmentation generates a number of divergent trajectories. In the study area, the width of the cone of block fragments (W_{cx}) increases with the distance (x) from the source and with the number of impacts. Compared to unbroken rock blocks, the length of the trail section intersected by the rock fragments (W_{cx}) is found to increase up to an order of magnitude (**Error! Reference source not found.**). This has a direct effect on the exposure.

Table 4. Wcx values for different fragmental rockfall volumes, calculated with the RockGIS code

Rockfall volume (m^3)	Trail section 1		Trail section 2	
	Intact blocks	fragmental	Intact blocks	fragmental
<0,05	0.2	None reaching	0.2	6
0,05 < x <0,5	0.8	None reaching	0.8	9
0,5 < x <5	1.5	17.5	1.5	13
5 < x <50	3.5	20	3.5	18
50 < x <500	8	40	8	25
>500	10	55	10	32

The modal size and number "n" of fragments reaching the analyzed section provided by RockGIS code are included in equation 3 to calculate Wr. An example is provided in Figure 17 and Table 5. The annual frequency of a 10 m3 fragmental rockfall event is assigned as 10-2. To calculate P(X|D) a total of 10 trajectories are simulated. The number of rock fragments reaching the trail section in each simulation are counted. In the example of Figure 17 only 21% of the trajectories (reach probability=1-0.79) of the simulated fragmental rockfall events, reach the trail. This percentage may be split considering the number of fragments that reach the trail in each simulation. Thus, the trail is intersected by only one rock fragment in 6.5% of the simulated trajectories (reach probability=0.855-0.79); by 2 rock fragments in 2% of the simulated trajectories (reach probability=0.875-0.855); by 3 rock fragments in 1% of the simulated trajectories; by 4 rock fragments in 1% of the simulated trajectories; by 5 or more rock fragments in 10.5% of the simulated trajectories.

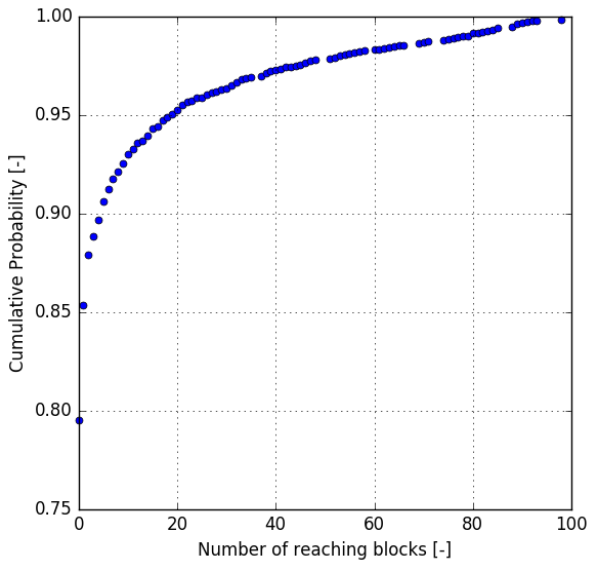

Figure 17 Cumulative probability of the simulated trajectories for each number of reaching fragments, in the case of a 10m3 fragmental rockfall.

In case of block fragments with a modal width (Wmx) of 1m and a width of the cone of fragments (Wcx) of 5m at its intersection with the trail, the equations 3, yields the results shown at Table 5.

Table 5.Value of Wr and its associated probability for the case example of a 10-m3 fragmental rockfall occurring with an annual frequency of 10-2, and considering the reach probability for one or more blocks of figure 18. In the example, the block fragments have a modal with (Wm) of 1 m and the width of the cone of fragments at its intersections with trail is Wcx=5m.

Distribution of the daily visitors flow (≈700 visitors) in groups				
type	individuals	Groups of 2	Groups of 4	Groups of 10
percentage	10%	45%	35%	10%
# of persons	70	313	243	70
# of sets	70	157	61	7

This procedure for estimating Wr in fragmental rockfall events must be repeated for each rockfall size and for each analyzed trail section.

The exposure, P (T │ X) also requires considering the number and velocity of the visitors or, in other words, the flow of visitors (fp). During the last 16 years, the Monasterio de Piedra natural site has received an average number of 250,040 visitors per year (696 ≈ 700 visitors/day). Most QRA studies for infrastructures such as roads and railways, assume a continuous (constant) flow of vehicles (Hungr et al. 1999; Ferlisi et al. 2012; Nicolet et al. 2016). This assumption is arguable in the case of Lago del Espejo as the visitors usually walk in small groups. For this reason, we have carried out two calculations:

- Uniformly distributed flow of visitors
- Flow of visitors distributed in groups as follows: 10% individuals, 45% in couples, 35% in groups of 4 people, 10% in groups of 10 people (Table 6)

Table 6. Distribution of the visitors' flow within the premises of the Lago del Espejo, used in the QRA

Distribution of the daily visitors flow (≈700 visitors) in groups				
type	individuals	Groups of 2	Groups of 4	Groups of 10
percentage	10%	45%	35%	10%
# of persons	70	313	243	70
# of sets	70	157	61	7

In equation 2, all the visitors whatever they are individuals or groups of any size, move at an average speed (vp) of 2 km/h. The width or length of the person (lp) is assumed 0.5m as suggested by Hantz (2011).

Risk calculation

Different vulnerability values are heuristically assigned based on the size of the rock block and the number of persons in the group (Table 7Table 7). For risk calculation purposes, the assigned vulnerability is multiplied by the number of persons to obtain number of victims. Thus, a vulnerability value of 1 for a group of 4, implies 4 victims.

Table 7. Estimated vulnerability values for different rockfall sizes and groups of visitors.

Rockfall volume (m^3)	# persons			
	individuals	Groups of 2	Groups of 4	Groups of 10
≤ 0,05	0.5	0.3	0.1	0.05
0,05 a ≤0,5	0.9	0.6	0.3	0.2
0,5 a ≤5	1.0	0.9	0.6	0.4
5 a ≤50	1.0	1.0	0.8	0.8
50 a ≤500	1.0	1.0	1.0	1.0
> 500	1.0	1.0	1.0	1.0

The risk is calculated for each of the six rockfall magnitude classes because each one is characterized by a specific probability of occurrence, runout, impact probability and vulnerability

4. Results

The results are summarized in tables 8 to 13. The two following scenarios are analyzed:

Scenario 1

Corresponds to the initial situation, without the presence of flexible rockfall protection fences, for intact (non fragmented) rockfall masses and for fragmental rockfalls and for an uniformly distributed flow of visitors (Table 8 and Table 9) and segregated flow of visitors (Table 10 and Table 11)

Table 8. Individual risk (annual probability of loss of life) for intact (top) and fragmental (bottom) rockfalls at the trail section 1. A uniformly distributed flow of visitors (700 visitors/day) is considered

Trail Section 1 length: 194,8m					
Unfragmented rockfalls					
Class M_i (m^3)	Ni	P(X:D)	P(T:X)	V	Risk
≤ 0,05	16.31851	0.1194	0.010	0.5	0.009945
0,05 a ≤0,5	0.25049	0.3280	0.019	0.9	0.001402
0,5 a ≤5	0.03301	0.5896	0.022	1.0	0.000426
5 a ≤50	0.00434	0.7647	0.066	1.0	0.000218
50 a ≤500	0.00057	0.8320	0.124	1.0	0.000059
> 500	0.00008	0.8735	0.153	1.0	0.000010
Annual probability of loss of life					**0.012060**
Fragmental rockfalls					
≤ 0,05	16.31851	0.0000	0.0000	0.5	0.000000
0,05 a ≤0,5	0.25049	0.0000	0.0000	0.9	0.000000
0,5 a ≤5	0.03301	0.0425	0.0338	1.0	0.000047
5 a ≤50	0.00434	0.2327	0.1204	1.0	0.000122
50 a ≤500	0.00057	0.6309	0.3738	1.0	0.000136
> 500	0.00008	0.7996	0.6778	1.0	0.000042
Annual probability of loss of life					**0.000346**

Table 9. Individual risk (annual probability of loss of life) for intact (top) and fragmental (bottom) rockfalls at the trail section 2. A uniformly distributed flow of visitors (700 visitors/day) is considered

Trail Section 2 length: 143.9m					
Non fragmented rockfalls					
Class M_i (m^3)	Ni	P(X:D)	P(T:X)	V	Risk
≤ 0,05	7.32419	0.6105	0.010	0.5	0.022823
0,05 a ≤0,5	0.11243	0.8394	0.019	0.9	0.001610
0,5 a ≤5	0.01482	0.9446	0.022	1.0	0.000306
5 a ≤50	0.00195	0.9699	0.066	1.0	0.000124
50 a ≤500	0.00026	0.9792	0.124	1.0	0.000031
> 500	0.00003	0.9820	0.153	1.0	0.000005
Annual probability of loss of life					**0.024900**
Fragmental rockfalls					
≤ 0,05	7.32419	0.2940	0.0407	0.5	0.043771
0,05 a ≤0,5	0.11243	0.5700	0.0620	0.9	0.003579
0,5 a ≤5	0.01482	0.7908	0.1561	1.0	0.001829
5 a ≤50	0.00195	0.9507	0.2443	1.0	0.000453
50 a ≤500	0.00026	0.9886	0.3668	1.0	0.000094
> 500	0.00003	0.9917	0.4718	1.0	0.000016
Annual probability of loss of life					**0.049741**

Table 10. Risk segregated by groups of visitors for unfragmented and fragmental rockfall events at trail section 1.

Volume	Events/yr		Unfragmented rock falls					Fragmental rockfalls			
Class M_i	Ni	P(X:D)	P(T:X)	V	#persons	Risk	P(X:D)	P(T:X)	V	#persons	Risk
≤ 0,05	16.31851	0.1194	0.001021	0.5	1	0.000995	0.0000	0.0000	0.5	1	0.000000
0,05 a ≤0,5	0.25049	0.3280	0.001896	0.9	1	0.000140	0.0000	0.0000	0.9	1	0.000000
0,5 a ≤5	0.03301	0.5896	0.002188	1.0	1	0.000043	0.0425	0.0034	1.0	1	0.000005
5 a ≤50	0.00434	0.7647	0.006563	1.0	1	0.000022	0.2327	0.0120	1.0	1	0.000012
50 a ≤500	0.00057	0.8320	0.012396	1.0	1	0.000006	0.6309	0.0374	1.0	1	0.000014
> 500	0.00008	0.8735	0.015313	1.0	1	0.000001	0.7996	0.0678	1.0	1	0.000004
Individuals (10% visitors)						**0.001210**					**0.000035**
≤ 0,05	16.31851	0.1194	0.003925	0.3	2	0.004589	0.0000	0.0000	0.3	2	0.000000
0,05 a ≤0,5	0.25049	0.3280	0.005888	0.6	2	0.000580	0.0000	0.0000	0.6	2	0.000000
0,5 a ≤5	0.03301	0.5896	0.006542	0.9	2	0.000229	0.0425	0.0092	0.9	2	0.000023
5 a ≤50	0.00434	0.7647	0.014719	1.0	2	0.000098	0.2327	0.0286	1.0	2	0.000058
50 a ≤500	0.00057	0.8320	0.029438	1.0	2	0.000028	0.6309	0.0855	1.0	2	0.000062
> 500	0.00008	0.8735	0.035979	1.0	2	0.000005	0.7996	0.1537	1.0	2	0.000019
Groups of 2 (45% of visitors)						**0.005529**					**0.000162**
≤ 0,05	16.31851	0.1194	0.002160	0.1	4	0.001684	0.0000	0.0000	0.1	4	0.000000
0,05 a ≤0,5	0.25049	0.3280	0.002923	0.3	4	0.000288	0.0000	0.0000	0.3	4	0.000000
0,5 a ≤5	0.03301	0.5896	0.003177	0.6	4	0.000148	0.0425	0.0042	0.6	4	0.000014
5 a ≤50	0.00434	0.7647	0.006990	0.8	4	0.000074	0.2327	0.0118	0.8	4	0.000038
50 a ≤500	0.00057	0.8320	0.012073	1.0	4	0.000023	0.6309	0.0338	1.0	4	0.000049
> 500	0.00008	0.8735	0.014615	1.0	4	0.000004	0.7996	0.0603	1.0	4	0.000015
Groups of 4 (35% of visitors)						**0.002222**					**0.000116**
≤ 0,05	16.31851	0.1194	0.000613	0.05	10	0.000597	0.0000	0.0000	0.05	10	0.000000
0,05 a ≤0,5	0.25049	0.3280	0.000700	0.2	10	0.000115	0.0000	0.0000	0.2	10	0.000000
0,5 a ≤5	0.03301	0.5896	0.000729	0.4	10	0.000057	0.0425	0.0008	0.4	10	0.000005
5 a ≤50	0.00434	0.7647	0.001167	0.8	10	0.000031	0.2327	0.0017	0.8	10	0.000014
50 a ≤500	0.00057	0.8320	0.001750	1.0	10	0.000008	0.6309	0.0042	1.0	10	0.000015
> 500	0.00008	0.8735	0.002042	1.0	10	0.000001	0.7996	0.0073	1.0	10	0.000004
Groups of 10 (10% of visitors)						0.000809					0.000038
		Overall risk for unfragmented rockfalls				**0.009766**	**Overall risk for fragmental rockfalls**				**0.000351**

Table 11. Risk segregated by groups of visitors for unfragmented and fragmental rockfall events at trail section2.

Volume	Events/yr		Unfragmented rock falls					Fragmental rockfalls			
Class M_i	Ni	P(X	P(T:X	V	#perso	Risk	P(X:D	P(T:X	V	#perso	Risk
≤ 0,05	7.32419	0.61	0.001	0.5	1	0.0022	0.2940	0.0041	0.5	1	0.0043
0,05 a	0.11243	0.83	0.002	0.9	1	0.0001	0.5700	0.0062	0.9	1	0.0003
0,5 a ≤5	0.01482	0.94	0.002	1.0	1	0.0000	0.7908	0.0156	1.0	1	0.0001
5 a ≤50	0.00195	0.96	0.007	1.0	1	0.0000	0.9507	0.0244	1.0	1	0.0000
50 a ≤500	0.00026	0.97	0.012	1.0	1	0.0000	0.9886	0.0367	1.0	1	0.0000
> 500	0.00003	0.98	0.015	1.0	1	0.0000	0.9917	0.0472	1.0	1	0.0000
Individuals (10% visitors)						**0.0024**					**0.0049**
≤ 0,05	7.32419	0.61	0.0039	0.3	2	0.0105	0.2940	0.0108	0.3	2	0.0138
0,05 a	0.11243	0.83	0.0058	0.6	2	0.0006	0.5700	0.0156	0.6	2	0.0011
0,5 a ≤5	0.01482	0.94	0.0065	0.9	2	0.0001	0.7908	0.0366	0.9	2	0.0007
5 a ≤50	0.00195	0.96	0.0163	1.0	2	0.0000	0.9507	0.0564	1.0	2	0.0002
50 a ≤500	0.00026	0.97	0.0294	1.0	2	0.0000	0.9886	0.0839	1.0	2	0.0000
> 500	0.00003	0.98	0.0359	1.0	2	0.0000	0.9917	0.1075	1.0	2	0.0000
Groups of 2 (45% of						**0.0114**					**0.0161**
≤ 0,05	7.32419	0,.6	0.0021	0.1	4	0.0038	0.2940	0.0048	0.1	4	0.0041
0,05 a	0.11243	0.83	0.0029	0.3	4	0.0003	0.5700	0.0067	0.3	4	0.0005
0,5 a ≤5	0.01482	0.94	0.0031	0.6	4	0.0001	0.7908	0.0149	0.6	4	0.0004
5 a ≤50	0.00195	0.96	0.0069	0.8	4	0.0000	0.9507	0.0226	0.8	4	0.0001
50 a ≤500	0.00026	0.97	0.0120	1.0	4	0.0000	0.9886	0.0332	1.0	4	0.0000
> 500	0.00003	0.98	0.0146	1.0	4	0.0000	0.9917	0.0424	1.0	4	0.0000
Groups of 4 (35% of						**0.0043**					**0.0052**
≤ 0,05	7.32419	0.61	0.0006	0.05	10	0.0013	0.2940	0.0009	0.05	10	0.0009
0,05 a	0.11243	0.83	0.0007	0.2	10	0.0001	0.5700	0.0011	0.2	10	0.0001
0,5 a ≤5	0.01482	0.94	0.0007	0.4	10	0.0000	0.7908	0.0021	0.4	10	0.0000
5 a ≤50	0.00195	0.96	0.0011	0.8	10	0.0000	0.9507	0.0030	0.8	10	0.0000
50 a ≤500	0.00026	0.97	0.0017	1.0	10	0.0000	0.9886	0.0042	1.0	10	0.0000
> 500	0.00003	0.98	0.0020	1.0	10	0.0000	0.9917	0.0052	1.0	10	0.0000
Groups of 10 (10% of						**0.0015**					**0.0012**
		Overall risk for unfragmented rockfalls				**0.0198**	Overall risk for fragmental rockfalls				**0.0276**

Some contrasting results of the rockfall fragmentation must be highlighted from Table 8 and Table 10. On one side in the example of trail section 1, fragmentation reduces the risk totally for rockfall volumes of less than 0.5m3. This is because fragmentation prevents the rock fragments from reaching the trail section that is, P(X:D)=0. On the opposite side, for rockfall volumes larger than 50m3, fragmentation raises the risk to the visitors. The reason is that the generation of the cone of fragments increases substantially the exposure or the P(T:X) value, particularly for large rockfall events whose fragments virtually occupy the whole Wcx. In contrast, for rockfall volumes ranging between 0.5 and 50m3, the increase of exposure is either partially or fully compensated by the reduction of the runout.

As shown in Table 10 and, as it will be discussed later in this chapter, the mentioned effects have a direct consequence on the overall risk value as most of the risk originate from high-frequency small-magnitude rockfall events, the runout of which is strongly affected by the fragmentation. Instead, the runout of large rockfall events (>50m3) is only slightly affected (from 0.3 to 0.63 and from 0.87 to 0.80 for rockfalls in the range of 50 – 500 m3 and over 500m3, respectively. The annual probability of loss of life for a uniformly distributed flow of individual visitors is reduced from 1.2·10-2 to 3.5·10-4, which is almost two orders of magnitude. The segregation of the visitors flow in groups has only a minor influence in the results. For non-fragmented rockfalls the annual probability of loss of life is reduced from 1.21·10-2 to 9.8·10-3 while for fragmental rockfalls it remains virtually the same as 3.5·10-4.

The analysis of trail section 2 of Table 9 shows that risk has increased for all the range of rockfall volumes, without exception. In this case, the slight reduction of the probability of reach P(X:D) that fragmentation causes, does not compensate the increase of exposure. As the slope of trail 2 is steeper and shorter than section trail 1, Wcx is narrower. This is confirmed by the results of Table 11, for the segregated flow of visitors. Quantitatively the increase of risk is mostly due to the small rockfall events (volumes <0.5m3)

Scenario 2

The situation considering the presence of flexible rockfall protection fences is analyzed for trail section 1 only. It is carried out for both the unfragmented rockfall masses and for fragmental rockfalls and for uniformly distributed flow of visitors (table 12) and segregated flow of visitors (table 13).

Furthermore, this analysis allows assessing the performance of the rockfall fences in terms of its spatial arrangement and their efficiency to cope with the fragmental rockfalls.

Table 12. Individual risk (annual probability of loss of life) for intact (top) and fragmental (bottom) rockfalls considering the presence of flexible rockfall protection fences. Uniformly distributed flow of visitors (700 visitors/day) is considered.

Section length: 194,8m					
Unfragmented rockfalls					
Class M_i (m^3)	Ni	P(X:D)	P(T:X)	V	Risk
≤ 0,05	16.31851	0.0220	0.010208	0.5	0.001832
0,05 a ≤0,5	0.25049	0.0647	0.018958	0.9	0.000277
0,5 a ≤5	0.03301	0.1455	0.021875	1.0	0.000105
5 a ≤50	0.00434	0.7361	0.065625	1.0	0.000210
50 a ≤500	0.00057	0.8312	0.123958	1.0	0.000059
> 500	0.00008	0.8737	0.153125	1.0	0.000010
Annual probability of loss of life					**0.00249**
Fragmental rockfalls					
0,00121 ≤ 0,05	16.31851	0.0000	0.0000	0.5	0.000000
0,05 a ≤0,5	0.25049	0.0000	0.0000	0.9	0.000000
0,5 a ≤5	0.03301	0.0122	0.0370	1.0	0.000015
5 a ≤50	0.00434	0.1310	0.1216	1.0	0.000069
50 a ≤500	0.00057	0.5135	0.3590	1.0	0.000106
> 500	0.00008	0.7574	0.6504	1.0	0.000038
Annual probability of loss of life					**0.000228**

Table 13. Residual risk remaining after the construction of 1500kJ rockfall fences, segregated by groups of visitors for unfragmented and fragmental rockfall events.

Volume	Events/yr		**Unfragmented rock falls**					**Fragmental rockfalls**			
Class M_i (m^3)	Ni	P(X:D)	P(T:X)	V	**#persons**	Risk	P(X:D)	P(T:X)	V	**#persons**	Risk
≤ 0,05	16.31851	0.0220	0.001021	0.5	1	0.000183	0.0000	0.0000	0.5	1	0.000000
0,05 a ≤0,5	0.25049	0.0647	0.001896	0.9	1	0.000028	0.0000	0.0000	0.9	1	0.000000
0,5 a ≤5	0.03301	0.1455	0.002188	1.0	1	0.000011	0.0122	0.0037	1.0	1	0.000001
5 a ≤50	0.00434	0.7361	0.006563	1.0	1	0.000021	0.1310	0.0122	1.0	1	0.000006
50 a ≤500	0.00057	0.8312	0.012396	1.0	1	0.000006	0.5135	0.0359	1.0	1	0.000010
> 500	0.00008	0.8737	0.015313	1.0	1	0.000001	0.7574	0.0650	1.0	1	0.000003
Individuals (10% visitors)						**0.00025**					**0.000023**
≤ 0,05	16.31851	0.0220	0.003925	0.3	2	0.000845	0.0000	0.0000	0.3	2	0.000000
0,05 a ≤0,5	0.25049	0.0647	0.005888	0.6	2	0.000114	0.0000	0.0000	0.6	2	0.000000
0,5 a ≤5	0.03301	0.1455	0.006542	0.9	2	0.000057	0.0122	0.0099	0.9	2	0.000007
5 a ≤50	0.00434	0.7361	0.014719	1.0	2	0.000094	0.1310	0.0289	1.0	2	0.000033
50 a ≤500	0.00057	0.8312	0.029438	1.0	2	0.000028	0.5135	0.0821	1.0	2	0.000048
> 500	0.00008	0.8737	0.035979	1.0	2	0.000005	0.7574	0.1475	1.0	2	0.000017
Groups of 2 (45% of visitors)						**0.00114**					**0.000106**
≤ 0,05	16.31851	0.0220	0.002160	0.1	4	0.000310	0.0000	0.000	0.1	4	0.000000
0,05 a ≤0,5	0.25049	0.0647	0.002923	0.3	4	0.000057	0.0000	0.000	0.3	4	0.000000
0,5 a ≤5	0.03301	0.1455	0.003177	0.6	4	0.000037	0.0122	0.004	0.6	4	0.000004
5 a ≤50	0.00434	0.7361	0.006990	0.8	4	0.000071	0.1310	0.012	0.8	4	0.000022
50 a ≤500	0.00057	0.8312	0.012073	1.0	4	0.000023	0.5135	0.033	1.0	4	0.000038
> 500	0.00008	0.8737	0.014615	1.0	4	0.000004	0.7574	0.058	1.0	4	0.000013
Groups of 4 (35% of visitors)						**0.00050**					**0.000078**
≤ 0,05	16.31851	0.0220	0.000613	0.05	10	0.000110	0.0000	0.000	0.05	10	0.000000
0,05 a ≤0,5	0.25049	0.0647	0.000700	0.2	10	0.000023	0.0000	0.000	0.2	10	0.000000
0,5 a ≤5	0.03301	0.1455	0.000729	0.4	10	0.000014	0.0122	0.001	0.4	10	0.000001
5 a ≤50	0.00434	0.7361	0.001167	0.8	10	0.000030	0.1310	0.002	0.8	10	0.000008
50 a ≤500	0.00057	0.8312	0.001750	1.0	10	0.000008	0.5135	0.004	1.0	10	0.000012
> 500	0.00008	0.8737	0.002042	1.0	10	0.000001	0.7574	0.007	1.0	10	0.000004
Groups of 10 (10% of visitors)						**0.000186**					**0.000025**
		Overall risk for unfragmented				**0.002081**	Overall risk for fragmental				**0.000232**

In this scenario, fragmentation reduces the overall risk by an order of magnitude. The effects observed in the natural conditions, such as the runout reduction and the increase of exposure are found here as well. However, the efficacy of the flexible rockfall fences in halting the falling blocks and the subsequent risk reduction is better observed in the analysis of unfragmented rockfalls. There is a reduction of 80% of the annual risk for both the uniformly distributed flow of visitors and the segregated flow of visitors (from 0.012 to 0.0025 and from 0.0098 to 0.0021, respectively). Most of the reduction is due to the trapping of small-size rockfall events. The reduction of risk for fragmental rockfall is less significant. The annual risk is reduced to around 35% for both the uniformly distributed flow of visitors and the segregated flow of visitors (from 0.00035 to 0.00023). The reason is that most of the mid and large-size fragmental rockfalls cannot be stopped by the fences. There exist however an additional cause for this particular example. The probability of reach P(X:D) for fragmental rockfalls in the volume range of 0.5 to 5m3, has been reduced from 0.04 to 0.01 only. This contrast with the significant reduction observed for the non-fragmented events which is from 0.59 to 0.15. The explanation for such a behavior is found in Figure 16. A small percentage of modelled trajectories are not intercepted by the fences while some rebounds are higher than the height of the fences. This percentage cannot be reduced unless further protection works are carried out.

A significant percentage (over 50%) of the large rockfalls for both unfragmented and fragmental rockfalls reach the trail. The existing protection fences are not capable to intercept their trajectories. It is worth noticing however, that for the range of fragmental rockfall volumes between 5 and 50m3, the reach probability is reduced up to 0.13.

5. Discussion

Rockfall simulation is highly sensitive to the quality of the input data (Van Westen et al. 2008). In the example of Monasterio de Piedra, we worked with a high-resolution DEM (0.2x0.2m) generated from digital images captured with a drone. There are, however, several sources of uncertainty in all the steps followed. Because of this, the example we provide is not aimed at yielding a precise value of risk but to highlight the effect of fragmentation in the value on risk and in the interpretation of the results.

The first source of uncertainty is the frequency-magnitude relation, which has been prepared using a 15-yr record of rock blocks trapped in the existing fences. It is assumed that each block corresponds to one independent event obviating the fact that several of the retained blocks might be fragments belonging to the same rockfall event. This assumption underestimates the magnitude

of the events (all the blocks trapped are less than1m3). Conversely, rock blocks located upslope of the flexible fences were not count because their age cannot be constraint, which underestimates their frequency. At the other end, three large rockfall events (>500m3) were identified on the slopes bordering the lake. The age of two samples of tufa deposited at the bottom of the river Piedra valley, close to the Lago del Espejo are respectively 760±45 and 945±45 yr BP (Sancho et al. 2010). These values yield the minimum age of the gorge and consequently, of the length of the rockfall series obtained. They are consistent with the erosion rate of Table 2 and with the magnitude-frequency relation prepared for the study area. Another source of uncertainty are the rockfall release points. All the detachment points are assumed homogeneously distributed along the crest line of the cliffs. Although this hypothesis fits well for large rockfall volumes, it is clearly conservative for both small and mid-size events (up to 50 m3) since a percentage of them originates in middle and lower sectors of the cliff face and, therefore, they develop lower kinetic energies and run-out. Furthermore, despite the RockGIS model has been calibrated with the rockfall event of 2017 and with the back analysis of the blocks released during scaling works in 2015, the model is based on a lumped mass approach whose restrictions are already known. The roughness is included in the restitution factors and is assumed constant for the whole slope while the vegetation has not been considered. Finally, the exposure is calculated considering a variable debris front width (Wr). calculated based on the modal rock block size (Wmx) rather than the actual size distribution of the blocks reaching the analyzed section.

In spite of all the uncertainties and limitations of the approach, the results indicate that fragmentation affects strongly the results of the risk analysis. However, the consequences are not obvious and must be checked at each location or analyzed section. The main reason is that both the reach probability and the exposure are spatially dependent. This contrasting behavior is observed in the two trail sections analyzed.

The risk in trail section 1 is clearly benefited by the fragmentation. The length of the propagation slope facilitates the occurrence of additional impacts that, due to the smaller size of the newly generated fragments, a higher energy is dissipated (Figure 15) and consequently, travel shorter distances. As the volume of the rock fall increases, so does the size of the blocks, the divergence of the trajectories (Wcx), and the exposure $P(T \mid X)$, thereby partially compensating the reduction of the run out. The analysis of trail section 2 of Table 11 provides a different perspective, as due to the steepness of the slope, most of the new fragments generated are able to reach the section of analysis. In this case, the beneficial effect of the fragmentation on the run-out is lost. We must take into account that the topography also affects the trajectories and consequently, an effect on both the run-out and the exposure. This is illustrated by the Figure 3B, where the initially divergent flow of debris finally converge at the lowest part of the slope, thus reducing Wcx.

The analysis of the design remedial measures is beyond the scope of this paper. The scenario analyzed with flexible rockfall fences considers the present conditions at the site. The simulations show that the efficacy of the fences for mid-size events increases with the fragmentation. After the impact, the velocity of the broken mass is transferred to the smaller rock fragments, whose energies are substantially reduced. In that respect, fragmentation improves the efficiency of the protections. In the example of trail section 1, the existing barriers intercept virtually all (98.8%) the fragments generated by the 0.5 to 5 m3 rockfall events, and a high percentage (87%) of the fragments generated by the 5 to 50 m3 rockfall events. The analysis also shows that a few trajectories may avoid the barriers by either passing between them or by bouncing over them. However, the interpretation of the performance of the rockfall fences must take into account the various assumptions of the analysis. First and most importantly, the analysis does not account for the multiple block impacts. Furthermore, no damage function is applied to the fences. In the simulations, all impacts with kinetic energies below 1500 kJ are trapped without affecting the future performance of the fence. This is an arguable assumption as the performance of the rockfall fences is much complex. The efficiency of the fence may decrease below the maximum impact load (Duffy and Badger, 2012; Volkwein et al. 2011) while small blocks with kinetic energy lower than the design values, may puncture the fence panel by the bullet effect (Spadari et al. 2012). As consequence, our evaluation most likely overestimates the efficiency of the existing barriers.

6. Conclusions

The quantitative risk analysis of fragmental rockfall has to confront a variety of challenges related to the evaluation the occurrence probability or frequency of the events, the runout modelling and the behavior of the falling mass. It must also account for the uncertainties due to inherently complex physical processes involved and the stochastic variability of all the relevant parameters. This is the first attempt to address the QRA of fragmental rockfalls. It is carried out with simulations using the RockGIS code and considering a fragmentation law for the falling rock masses. Despite all the limitations, the example we present highlights the relevance of the fragmentation for the exposed elements and in the quantification of the risk.

One of the most important effects of fragmentation is on the rockfall runout. Fragmentation may significantly reduce the rockfall propagation if the slope is both gentle and long enough. This is clearly illustrated in the analysis of trail section 1 in the Monasterio de Piedra. None of the rock fragments of the small size (<0.5m3) fragmented rock masses reaches the trail section. This is the reason for the substantial reduction (more than one order of magnitude) compared to the value of risk for intact blocks for this magnitude range. However, the favorable effect of fragmentation

vanishes when rockfalls propagate along steep slopes. The blocks can hardly stop and the generated cone of fragments increase the exposure, as shown in the analysis of trail section 2. Considering fragmentation in the risk analysis forces the redefinition of the reach probability P(X | D) because a paradoxical situation may appear if a number of block fragments bigger than the number of initiators attain the distance of the analyzed section. In addition, our analysis has required a new procedure to quantify the exposure. The fragmentation due to the impact of small to mid-size rock masses (e.g. <100m3) on the ground, generates divergent trajectories of the new fragments, which define a cone. The projected width of the cone of the ground surface determines the length of the trail section affected by the arrival of rock fragments (Wcx). The procedure followed includes the calculation of the number of fragments that reach the section and the proportion that they really occupy of the debris front width (Wr). An important effect of fragmentation is that the exposure P(T:X) is spatially dependent, as shown by the variability of the cone of fragments.

In the worked example, for rockfall events larger than 50 m3, fragmentation increases notably the exposure or the impact probability, due to the generation of the cone of fragments. In the case of trail section 1, the increase is counterbalanced by the reduction of the runout. The results show that the value of risk associated to both unfragmented and fragmental rockfalls is similar but the contribution of factors is different. This fact has to be taken into account in order not to reach misleading conclusions.

The performance of the existing protection flexible fences has been analyzed as well. The efficacy of rockfall fences for rockfall events up to 50m3 increases with the fragmentation. This fact opens the possibility of using this type of protections to manage the risk. However, additional work is needed on the performance of these structures before the efficiency and the residual risk could be evaluated reliably.

In summary, fragmentation has both a significant and contrasting effect on the calculation of risk and it should not be obviated in risk analysis. Risk is significantly reduced if the slope where blocs propagate is both long and gentle enough. In this case, the new fragments generated mobilize less energy and can be trapped by the topographic irregularities, obstacles and the protection measures. Conversely, a wide range of block sizes are able to reach the trails located either next or below steep slopes. In such a situation, fragmentation increases notably risk by generating of cone of fragments, which increase exposure of visitors. Our simulations also shown that the segregation of visitors's flow has only a minor influence in the results of the risk analysis. The analysis of fragmentation is not straightforward. It requires the availability of a diversity of input data and working with high-resolution DEM. The use of the RockGIS propagation model

entails the multiparametric calibration and validation. The simulations illustrate the importance of the topography in the generation of preferential trajectories and the sensitivity of both run out and the kinetic energies of the blocks to the fragmentation criteria as shown in Matas et al. 2017.

ACKNOWLEDGEMENTS

This work has been carried out with the support of the fellowship to the last two authors and within the framework of the research project Rockmodels financed by the Spanish Ministry of Economy and Competitiveness and the European Regional Development's funds (FEDER), (BIA2016- 75668-P, AEI/FEDER, UE) and by the grants to the second and third authors (BES-2014-069795 and FPU13/04252, respectively). We also appreciate all the facilities provided by Monasterio de Piedra S.A. to carry out this work.

References

Agliardi F, Crosta GB (2003) High resolution three-dimensional numerical modelling of rockfalls. International Journal of Rock Mechanics and Mining Sciences 40: 455-471

Agliardi F, Crosta GB, Frattini P (2009) Integrating rockfall risk assessment and countermeasure design by 3D modelling techniques.Nat Hazards Earth Syst Sci 9:1059–1073

Areans C, Vázquez-Urbez M, Auqué L, Sancho C, Osácar C, Pardo G (2014) Intrinsic and extrinsic controls of spatial and temporal variations in modern fluvial tufa sedimentation: A thirteen-year record from a semi-arid environment. Sedimentology 61: 90–132

Asteriou P, Saroglou H, Tsiambaos (2012) Geotechnical and kinematic parameters affecting the coefficients of restitution for rock fall analysis. International Journal of Rock Mechanics & Mining Sciences 54: 103–113

Bourrier F, Hungr O (2011) Rockfall dynamics: a critical review of collision and rebound models. In: Lambert S, Nicot F (ed) Rockfall Engineering, ISTE Ltd- John Wiley and Sons, Inc., Hoboken, 175-209, doi:10.1002/9781118601532. Ch6

Bourrier F, Dorren L, Nicot F, Berger F, Darve F (2009) Toward objective rockfall trajectory simulation using a stochastic impact model. Geomorphology, 110: 68-79

Bourrier F, Berger F, Tardif P, Dorren L, Hungr O (2012) Rockfall rebound: comparison of detailed field experiments and alternative modelling approaches. Earth Surface Processes and Landforms, 37: 656-665

Budetta P (2004) Assessment of rockfall risk along roads. Nat Hazards Earth Syst Sci 4:71–81

Bunce CM, Cruden D M, Morgenstern N R (1997) Assessment of the hazard from rock fall on a highway, Can. Geotech. J 34: 344–356

Chau KT, Wong RCH, Liu J, Lee CF (2003) Rockfall Hazard Analysis for Hong Kong Based on Rockfall Inventory. Rock Mech Rock Eng 36: 383–408

Chen G, Zheng L, Zhang Y, Wu J (2013) Numerical Simulation in Rockfall Analysis: A Close Comparison of 2-D and 3-D DDA. Rock Mechanics Rock Engineering 46: 527. https://doi.org/10.1007/s00603-012-0360-9

Copons R, Vilaplana JM, Corominas J, Altimir J, Amigó J (2004) Rockfall risk management in high-density urban areas. The Andorran experience. In: Glade T, Anderson M, Crozier MJ (ed). Landslide hazard and risk. John Wiley and Sons, Chichester, pp 675-698

Corominas J Mavrouli O (2011) Rockfall quantitative risk assessment. In: Lambert S, Nicot F (ed) Rockfall Engineering, ISTE Ltd John Wiley and Sons, Inc., Hoboken, 255–301, doi:10.1002/9781118601532. ch8

Corominas J, van Westen C, Frattini P, Cascini L, Malet JP, Fotopoulou S, Catani F, Van Den Eeckhaut M, Mavrouli O, Agliardi F, Pitilakis K, Winter MG, Pastor M, Ferlisi S, Tofani V, Hervás J, Smith JT (2014) Recommendations for the quantitative analysis of landslide risk. Bull Eng Geology Environment, 73: 209-263

Corona C, Lopez-Saez J, Favillier A, Mainieri R, Eckert N, Trappmann D, Stoffel M, Bourrier F, Berger F (2017) Modeling rockfall frequency and bounce height from three-dimensional simulation process models and growth disturbances in submontane broadleaved trees. Geomorphology 281: 66-77

Crosta GB, Agliardi F (2004) Parametric evaluation of 3D dispersion of rockfall trajectories. Nat Hazards Earth Syst Sci 4:583–598

Crosta GB, Frattini P, Fusi N (2007) Fragmentation in the Val Pola rock avalanche, Italian Alps. Journal of Geophysical Res., 112, F01006, DOI: 10.1029/2005JF000455

Davies TR, McSaveney MJ (2002) Dynamic simulation of the motion of fragmenting rock avalanches. Canadian Geotechical Journal 39:789–798

Dorren LK (2003). A review of rockfall mechanics and modelling approaches. Progress in Physical Geography, 27(1), 69–87.

Dorren LKA (2012) Rockyfor3D (v5.1) revealed—transparent description of the complete 3D rockfall model. http://www.ecorisq.org/

Dorren, LKA, Berger F, Putters US (2006). Real-size experiments and 3-D simulation of rockfall on forested and non-forested slopes. Nat Hazards Earth Syst Sci, 6: 145-153

Dorren L, Domaas U, Kronholm K, Labiouse V (2011). Methods for predicting rockfall trajectories and run-out zones. In: Rockfall Engineering, edited by: Lambert, S. and Nicot, F., ISTE Ltd- John Wiley and Sons, Inc., Hoboken, 143-173, doi:10.1002/9781118601532. Ch5

Duffy JD, Badger TC (2012). Flexible rockfall fences. In Turner and Schuster (Eds). Rockfall characterization and control. Transportation Research Board, Washington D.C. pp. 526-563

Dussauge-Peisser, A., Helmstetter, A., Grasso, J.-R, Hanz, D., Desvarreux, P., Jeannin, M., Giraud, A. 2002. Probabilistic approach to rockfall hazard assessment: potential of historical data analysis. Natural Hazards and Earth System Sciences, 2, 15-26.

Evans S, Hungr O (1993). The assessment of rockfall hazard at the base of talus slopes. Canadian Geotechnical Journal 30: 620-636

Fell R, Ho KKS, Lacasse S, Leroi E (2005) A framework for landslide risk assessment and management. In: Hungr O, Fell R, Couture R, Eberhardt E (ed) Landslide Risk Management, Taylor and Francis, London, 3–26

Ferlisi S, Cascini L, Corominas J, Matano F (2012) Rockfall risk assessment to persons travelling in vehicles along a road: the case study of the Amalfi coastal road (southern Italy). Nat Hazards 62:691–721

Frattini P, Crosta GB, Agliardi F, Imposimato S (2013) Challenging Calibration in 3D Rockfall Modelling. In: Margottini C, Canuti P, Sassa K. (ed) Landslide Science and Practice. Springer, Berlin, Heidelberg. pp. 169-175

Giani GP, Giacomini A, Migliazza M, Segalini A (2004) Experimental and Theoretical Studies to Improve Rock Fall Analysis and Protection Work Design. Rock Mechanics and Rock Engineering 37: 369-389.

Gili JA, Ruiz-Carulla R, Matas G, Corominas J, Lantada N, Núñez MA, Mavrouli O, Buill F, Moya J, Prades A, Moreno S (2016) Experimental study on rockfall fragmentation: in situ test design and firsts results. In: Aversa S, Cascini L, Picarelli L, Scavia C (ed) Landslides and engineered slopes, 2: 983-990.

Gischig V, Hungr O, Mitchell A, Bourrier F (2015) Pierre3D - a 3D stochastic rock fall simulator based on random ground roughness and hyperbolic restitution factors. Canadian Geotechnical Journal 52: 1360-1373. DOI10.1139/cgj-2014-0312

Gutierrez Elorza M, Sesé Martínez VH (2001) Multiple talus flatirons, variations of scarp retreat rates and the evolution of slopes in Almazán Basin (semi-arid central Spain). Geomorphology 38: 19–29.

Guzzetti F, Crosta, GB, Detti R, Agliardi F (2002) STONE: A computer program for the three-dimensional simulation of rock-falls. Computers & Geosciences, 28: 1079–1093.

Guzzetti F, Reichenbach P, Wieczorek GF (2003) Rockfall hazard and risk assessment in the Yosemite Valley. California, USA Natural Hazards and Earth System Sciences 3: 491-503

Guzzetti F, Reichenbach, P, Ghigi S (2004) Rockfall hazard and risk assessment along a transportation corridor in the Nera Valley, central Italy. Environmental Management, 34 : 191-208

Hantz D (2011) Quantitative assessment of diffuse rock fall hazard along a cliff foot, Nat. Hazards Earth Syst. Sci., 11, 1303–1309, doi:10.5194/nhess-11-1303-2011, 2011

Hungr O, Beckie RD (1998) Assessment of the hazard from rock fall on a highway: Discussion, Can. Geotech. J., 35, 409, doi:10.1139/cgj-35-2-409

Hungr O, Evans SG, Hazzard J (1999) Magnitude and frequency of rock falls and rock slides along the main transportation corridors of southwestern British Columbia. Canadian Geotechnical Journal, 36: 224-238

Jaboyedoff M, Baillifard F, Philippossian F, Rouiller JD (2004) Assessing fracture occurrence using weighted fracturing density a step towards estimating rock instability hazard. Nat Hazards and Earth System Sciences. 4: 83–93

Jaboyedoff M., Labiouse V. (2011) Technical Note: Preliminary estimation of rockfall runout zones. Nat Hazards and Earth System Science, 11: 819–828.

Jaboyedoff M, Dudt JP, Labiouse V (2005) An attempt to refine rockfall hazard zoning based on the kinetic energy, frequency and fragmentation degree, Nat. Hazards Earth Syst. Sci., 5, 621–632

Lan H, Martin CD, Lim CH. (2007) RockFall analyst: A GIS extension for three-dimensional and spatially distributed rockfall hazard modeling. Computers & Geosciences, 33: 262-279

Lan H, Martin CD, Zhou CH, Lim CH. (2010). Rockfall hazard analysis using LiDAR and spatial modeling. Geomorphology, 118: 213-223. doi.org/10.1016/j.geomorph.2010.01.002

Lee EM, Jones DKC (2004) Landslide Risk Assessment. Thomas Telford, London, pp 454

Loye A, Jaboyedoff M, Pedrazzini A (2009) Identification of potential rockfall source areas at a regional scale using a DEM-based geomorphometric analysis. Nat. Hazards Earth Syst. Sci., 9: 1643–1653

Macciotta R, Martin CD, Cruden DM (2015) Probabilistic estimation of rockfall height and kinetic energy based on a three-dimensional trajectory model and Monte Carlo simulation. Landslide 15: 757-772. doi:10.1007/s10346-014-0503-z

Macciotta R, Martin CD, Morgenstern NR, Cruden D.M (2016) Quantitative risk assessment of slope hazards along a section of railway in the Canadian Cordillera – a methodology considering the uncertainty in the results, Landslides, 13: 15-117, doi:10.1007/s10346-014-0551-4, 2015.

Marquínez J, Menéndez Duarte R, Farias P, Jiménez Sánchez M (2003) Predictive GIS-based Model of Rockfall Activity in Mountain Cliffs. Natural Hazards, 30: 341–360,

Matas G, Lantada N, Corominas J, Gili JA, Ruiz-Carulla R, Prades A. (2017). RockGIS: a GIS-based model for the analysis of fragmentation in rockfalls. Landslides, 14: 1565–1578

Mazzoccola DF, Hudson JA. (1996) A comprehensive method of rock mass characterization for indicating natural slope instability. Q J Eng. Geol. Hydrogeology 29: 37–56,

Michoud C, Derron MH, Horton, P, Jaboyedoff M, Baillifard FJ, Loye A, Nicolet P, Pedrazzini A, Queyrel A. (2012) Rockfall hazard and risk assessments along roads at a regional scale: example in Swiss Alps, Nat. Hazards Earth Syst. Sci., 12, 615–629, doi:10.5194/nhess-12-615-2012

Nicolet P, Jaboyedoff M, Cloutier C, Crosta G, Lévy S. (2016) Brief Communication: On direct impact probability of landslides on vehicles. Nat Hazards and Earth System Sciences 16, 995-1004

Osácar MC, Arenas C, Vázquez-Urbez M, Sancho C, Auqué LF, Pardo G (2013) Environmental factors controlling the $\delta^{13}C$ and $\delta^{18}O$ variatins of recent fluvial tufas: a 12-year record from the Monasterio de Piedra Natural Park (NE Iberian Peninsula). Journal of Sedimentary Research 83: 309-322

Perfect E (1997) Fractal models for the fragmentation of rocks and soils: a review. Eng Geology 48: 185-198

Pfeiffer T, Bowen T. (1989) Computer simulation of rockfalls. Bull Association of Eng Geologists, XXVI: 135–146. doi:10.2113/gseegeosci. xxvi.1.135

Preh A, Mitchell A, Hungr O, Kolenprat B. (2015) Stochastic analysis of rockfall dynamics in quarry slopes. Int J Rock Mech Min Sciences 80: 57-66.

Raetzo H, Lateltin O, Bollinger D, Tripet JP (2002) Hazard assessment in Switzerland – Code of practice for mass movements. Bull Eng. Geol. Environ., 61, 263–268, 2002.

Ruiz-Carulla R, Corominas J, Mavrouli O (2015) A Methodology to Obtain the Block Size Distribution of Fragmental Rockfall Deposits. Landslides 12: 815–25.

Ruiz-Carulla R, Corominas J, Mavrouli O (2016) Comparison of block size distribution in rockfalls. In: Aversa S, Cascini L, Picarelli L, Scavia C (eds) Landslides and engineered slopes 3: 1767-1774

Ruiz-Carulla R., Corominas J, Mavrouli O (2017) A fractal fragmentation model for rockfalls. Landslides 14: 875-889

Sancho C, Gutiérrez M, Peña JL, Burillo F. (1988) A quantitative approach to scarp retreat starting from triangular slope facets, central Ebro Basin, Spain. Catena Suppl 13: 139–146

Spadari M, Giacomini A, Buzzi O, Hambleton JP (2012) Prediction of the Bullet Effect for Rockfall Barriers: a Scaling Approach. Rock Mech Rock Eng 45: 131-144

Stoffel M, Wehrli A, Kühne R, Dorren LKA, Perret S, Kienholz H (2006) Assessing the protective effect of mountain forests against rockfall using a 3D simulation model. Forest Ecology and Management 225: 113-122

Straub D, Schubert M (2008) Modeling and managing uncertainties in rock-fall hazards. Georisk, 2: 1-15

Turcotte DL (1986) Fractals and fragmentation. Journal of Geophysical Research. Solid earth 91: 1921-1926. DOI: 10.1029/JB091iB02p01921

Turner AK, Duffy JD (2012) Modeling and prediction of rockfall. In: Turner AK, Schuster RL (ed) Rockfall: characterization and control. Transportation Research Board, National Research Council, Washington, DC, pp 334–406

Turner AK, Jayaprakash GP (2012) Introduction. In Turner AK, Schuster RL (ed). Rockfall characterization and control. Transportation Research Board, National Academy of Sciences. Whasington D.C. pp. 3-20

Volkwein A, Schellenberg K, Labiouse V, Agliardi F, Berger F, Bourrier F, Dorren LKA, Gerber W, Jaboyedoff M (2011) Rockfall characterisation and structural protection—a review. Nat Hazards Earth Syst 11:2617–2651

Van Westen CJ, Castellanos E, Kuriakose SL (2008) Spatial data for landslide susceptibility, hazard, and vulnerability assessment: an overview. Eng Geol 102(3):112–131

Wang Y, Tonon F (2011) Discrete element modeling of rock fragmentation upon impact in rock fall analysis. Rock Mech Rock Eng 44:23–35. doi: 10.1007/s00603-010-0110-9

Wyllie DC (2014) Calibration of rock fall modeling parameters. Int J Rock Mech Min Sci 67:170–180. doi: 10.1016/j.ijrmms.2013.10.002